PHOTOCATALYSIS FOR ENVIRONMENTAL APPLICATIONS

EDITED BY: Fan Dong, Sen Zhang and Yuxin Zhang
PUBLISHED IN: Frontiers in Chemistry

frontiers Research Topics

frontiers

ISSN 1664-8714
ISBN 978-2-88945-902-5
DOI 10.3389/978-2-88945-902-5

About Frontiers

Frontiers is more than just an open-access publisher of scholarly articles: it is a pioneering approach to the world of academia, radically improving the way scholarly research is managed. The grand vision of Frontiers is a world where all people have an equal opportunity to seek, share and generate knowledge. Frontiers provides immediate and permanent online open access to all its publications, but this alone is not enough to realize our grand goals.

Frontiers Journal Series

The Frontiers Journal Series is a multi-tier and interdisciplinary set of open-access, online journals, promising a paradigm shift from the current review, selection and dissemination processes in academic publishing. All Frontiers journals are driven by researchers for researchers; therefore, they constitute a service to the scholarly community. At the same time, the Frontiers Journal Series operates on a revolutionary invention, the tiered publishing system, initially addressing specific communities of scholars, and gradually climbing up to broader public understanding, thus serving the interests of the lay society, too.

Dedication to Quality

Each Frontiers article is a landmark of the highest quality, thanks to genuinely collaborative interactions between authors and review editors, who include some of the world's best academicians. Research must be certified by peers before entering a stream of knowledge that may eventually reach the public - and shape society; therefore, Frontiers only applies the most rigorous and unbiased reviews.
Frontiers revolutionizes research publishing by freely delivering the most outstanding research, evaluated with no bias from both the academic and social point of view. By applying the most advanced information technologies, Frontiers is catapulting scholarly publishing into a new generation.

What are Frontiers Research Topics?

Frontiers Research Topics are very popular trademarks of the Frontiers Journals Series: they are collections of at least ten articles, all centered on a particular subject. With their unique mix of varied contributions from Original Research to Review Articles, Frontiers Research Topics unify the most influential researchers, the latest key findings and historical advances in a hot research area! Find out more on how to host your own Frontiers Research Topic or contribute to one as an author by contacting the Frontiers Editorial Office: researchtopics@frontiersin.org

PHOTOCATALYSIS FOR ENVIRONMENTAL APPLICATIONS

Topic Editors:
Fan Dong, Chongqing Technology and Business University, China; University of Electronic Science and Technology of China, China
Sen Zhang, University of Virginia, United States
Yuxin Zhang, Chongqing University, China

Citation: Dong, F., Zhang, S., Zhang, Y., eds. (2019). Photocatalysis for Environmental Applications. Lausanne: Frontiers Media. doi: 10.3389/978-2-88945-902-5

Table of Contents

frontiers in Chemistry

EDITORIAL
published: 01 May 2019
doi: 10.3389/fchem.2019.00303

Editorial: Photocatalysis for Environmental Applications

Fan Dong[1,2]*, *Yuxin Zhang*[3]* and *Sen Zhang*[4]*

[1] Chongqing Key Laboratory of Catalysis and New Environmental Materials, Engineering Research Center for Waste Oil Recovery Technology and Equipment of Ministry of Education, College of Environment and Resources, Chongqing Technology and Business University, Chongqing, China, [2] Research Center for Environmental Science & Technology, Institute of Fundamental and Frontier Sciences, University of Electronic Science and Technology of China, Chengdu, China, [3] College of Materials Science and Engineering, Chongqing University, Chongqing, China, [4] Department of Chemistry, University of Virginia, Charlottesville, VA, United States

Keywords: photocatalysis, environmental catalysis, air pollution, reaction mechanism, nanomaterials

Editorial on the Research Topic

Photocatalysis for Environmental Applications

Environmental pollution is one of the major challenges because of the rapid development of urbanization and industrialization. Considering this environmental challenge, providing a clean environment for human beings is very important for the sustainability. The nanostructured photocatalysts with intriguing physiochemical property have offered opportunities to solve the issue of environmental sustainability (Chen et al., 2019; Huo et al., 2019; Li J. et al., 2019). In recent years, significant advances have been witnessed on the synthesis and application of photocatalyst in environmental remediation (He et al., 2018a; Li et al., 2018c; Li X. et al., 2018, 2019; Wang et al., 2018c). These new photocatalysts have enabled wide applications in the air purification, wastewater treatment, and so on (Cui et al., 2018; He et al., 2018b; Li et al., 2018b; Xiong et al., 2018) The rapid development in catalysis science, nanoscience, and materials enable the significant advances in new strategies for the controlled preparation, photocatalysis reaction mechanism, and structure-activity relationship of photocatalysts (Dong et al., 2018a; Li et al., 2018a; Wang et al., 2018a,b). The structural features of photocatalysts can be further tuned to achieve enhanced photocatalytic performance in environmental applications (Dong et al., 2018b; Li X. et al., 2018; Wang et al., 2018d).

The rapid development in photocatalysis for environment has inspired this interesting Research Topic. We have invited scientists worldwide to contribute original research and review articles which could enhance our understanding of the key problems in environmental applications of nanostructured photocatalysts. The original articles describing the photocatalysts for environmental control, and for sustainable development have been accepted for publication after peered review. In this topic issue, the readers will find very interesting results covering the following aspects (1) design and synthesis of photocatalysts with new morphology and active catalytic sites; (2) photocatalysts for green synthesis; (3) photocatalysts for CO_2 conversion to solar fules; (4) photocatalysts for wastewater treatment and air purification; and (5) revealing the photocatalysis reaction mechanism as applied in environmental problems.

For the g-C_3N_4 based photocatalysts, Guan et al. synthesized Ti_4O_7/g-C_3N_4 composites by a low temperature method. The enhanced photocatalytic activity for Ti_4O_7/g-C_3N_4 could be ascribed to the promoted charge separation and photoabsorption efficiency. Yang et al. fabricated a monolithic g-C_3N_4/melamine sponge by a cost-effective ultrasonic-coating method. The monolithic g-C_3N_4/melamine demonstrated high photocatalytic activity for NO removal and CO_2 reduction. Guan et al. prepared the Ti_4O_7/g-C_3N_4 photocatalysts by a hydrolysis method. The Ti_4O_7/g-C_3N_4 exhibited remarkably improved photocatalytic activity for hypophosphite oxidation, which can be

OPEN ACCESS

Edited by:
Simelys Hernández, Polytechnic University of Turin, Italy

Reviewed by:
Fatwa Abdi, Helmholtz-Zentrum Berlin für Materialien und Energie, Helmholtz-Gemeinschaft Deutscher Forschungszentren (HZ), Germany

***Correspondence:**
Fan Dong
dfctbu@126.com
Yuxin Zhang
zhangyuxin@cqu.edu.cn
Sen Zhang
sz3t@virginia.edu

Specialty section:
This article was submitted to Catalysis and Photocatalysis, a section of the journal Frontiers in Chemistry

Received: *12 February 2019*
Accepted: *16 April 2019*
Published: *01 May 2019*

Citation:
Dong F, Zhang Y and Zhang S (2019) Editorial: Photocatalysis for Environmental Applications. Front. Chem. 7:303. doi: 10.3389/fchem.2019.00303

ascribed to the heterojunction structure of Ti_4O_7/g-C_3N_4 that enhanced charge carrier efficiency (Guan et al.).

Xu et al. prepared $BiVO_4$ by a facile method and conducted a trapping experiment to study the free radical transformation mechanisms. They identified •OH and h^+ as the main active radicals for oxidation. Han et al. developed a new photoelectrochemical (PEC) technology for simultaneous SO_2 removal and H_2 production. The enhanced H_2 production and SO_2 removal efficiency can be attributed to the improved charge carrier transfer after Mo doping (Han et al.). Regmi et al. reviewed recent advances on the microbial decontamination by photocatalysts and their possible mechanisms are highlighted.

Cui et al. fabricated the Ag_3PO_4/MoS_2 nanocomposites and revealed that the improved performance of Ag_3PO_4/MoS_2 can be ascribed to wide spectra response, efficient charge separation and enhanced oxidation capacity. He et al. developed a two-step ZnO-modified strategy to immobilize the catalyst on rGO sheets. The high ammonia degradation efficiency of ZnO/Cu/rGO can be attributed to the enhanced ROSs production efficiency and the activated interfacial catalytic sites. Shi et al. prepare high energy faceted TiO_2 nanosheets by calcination of $TiOF_2$ cubes. The 500°C-calcined sample exhibits the highest photocatalytic activity for removal of acetone owing to the high energy TiO_2-NSs and the surface adsorbed fluorine.

Kim et al. synthesized the nitrogen doped TiO_2 by a novel plasma electrolysis method. The 0.4 at.% N doped TiO_2 catalyst showed the highest photocatalytic performance. Xu et al. developed a BiOCl/$NaNbO_3$ p-n heterojunction by an *in-situ* method. The BiOCl/$NaNbO_3$ composites exhibited much enhanced photocatalytic activity attributed to the formation of p-n junction between $NaNbO_3$ and BiOCl that facilitated the charge separation (Xu et al.). Ren et al. synthesized the AgBr@Ag modified titanium phosphate composites. The AgBr@Ag/titanium phosphate exhibited higher photocatalytic activity and the photocatalytic degradation mechanisms were proposed.

She et al. reported selective activation of saturated C–H bond to generate the high-value-added chemicals on Ni-doped CdS nanoparticles. The high photocatalytic performance can be attributed to the cubic and hexagonal phases, Ni-doping and the charge carriers separation. Li et al. synthesized Au/$BiFeO_3$ homojunctions via a simple method. The Au1.2-BFO showed efficient photocatalytic activity due to the hierarchical structure, SPR effect of Au particles, and the defects (Li et al.). Zhang and Liang fabricated the new 2D g-C_3N_4@BiOCl/$Bi_{12}O_{17}Cl_2$ by a facile approach, which showed enhanced visible light absorption and electron-hole separation efficiency and thus highly enhanced photocatalytic activity for NO removal.

At last, as the Guest Editors of this topic issue, we would like to appreciate all the authors for the contributed articles and thank for all the referees for their comments on the manuscripts. We hope that the readers will find the results in articles of this topic issue interesting and useful for their research. Finally, we appreciate the editorial staff of Frontiers in Chemistry for their work in publishing of this topic issue.

AUTHOR CONTRIBUTIONS

All authors listed have made a substantial, direct and intellectual contribution to the work, and approved it for publication.

REFERENCES

Chen, P., Wang, H., Liu, H., Ni, Z., Li, J., Zhou, Y., et al. (2019). Directional electron delivery and enhanced reactants activation enable efficient photocatalytic air purification on amorphous carbon nitride Co-Functionalized with O/La. *Appl. Catal. B Environ.* 242, 19–30. doi: 10.1016/j.apcatb.2018.09.078

Cui, W., Li, J., Sun, Y., Wang, H., Jiang, G., Lee, S., et al. (2018). Enhancing ROS generation and suppressing toxic intermediate production inphotocatalytic NO oxidation on O/Ba co-functionalized amorphous carbon nitride. *Appl. Catal. B Environ.* 237, 938–946. doi: 10.1016/j.apcatb.2018.06.071

Dong, X., Li, J., Xing, Q., Zhou, Y., Huang, H., and Dong, F. (2018a). The activation of reactants and intermediates promotes the selective photocatalytic NO conversion on electron-localized Sr-intercalated g-C_3N_4. *Appl. Catal. B Environ.* 232, 69–76. doi: 10.1016/j.apcatb.2018.03.054

Dong, X., Zhang, W., Sun, Y., Li, J., Cen, W., Cui, Z., et al. (2018b). Visible light induced charge transfer pathway and photocatalysis mechanism on Bi semimetal@defective BiOBr hierarchical microspheres. *J. Catal.* 357, 41–50. doi: 10.1016/j.jcat.2017.10.004

He, W., Sun, Y., Jiang, G., Huang, H., Zhang, X., and Dong, F. (2018b). Activation of amorphous Bi_2WO_6 with synchronous Bi metal and Bi_2O_3 coupling: photocatalysis mechanism and reaction pathway. *Appl. Catal. B Environ.* 232, 340–347. doi: 10.1016/j.apcatb.2018.03.047

He, W., Sun, Y., Jiang, G., Li, Y., Zhang, X., Zhang, Y., et al. (2018a). Defective Bi_4MoO_9/Bi metal core/shell heterostructure: enhanced visible light photocatalysis and reaction mechanism. *Appl. Catal. B Environ.* 239, 619–627. doi: 10.1016/j.apcatb.2018.08.064

Huo, W., Dong, X., Li, J., Liu, M., Liu, X., Zhang, Y., et al. (2019). Synthesis of Bi_2WO_6 with gradient oxygen vacancies for highly photocatalytic NO oxidation and mechanism study. *Chem. Eng. J.* 361, 129–138. doi: 10.1016/j.cej.2018.12.071

Li, J., Dong, X., Sun, Y., Cen, W., and Dong, F. (2018a). Facet-dependent interfacial charge separation and transfer in plasmonic photocatalysts, *Appl. Catal. B Environ.* 226, 269–277. doi: 10.1016/j.apcatb.2017.12.057

Li, J., Dong, X., Sun, Y., Jiang, G., Chu, Y., Lee, S., et al. (2018b). Tailoring the rate-determining step in photocatalysis via localized excess electrons for efficient and safe air cleaning. *Appl. Catal. B Environ.* 239, 187–195. doi: 10.1016/j.apcatb.2018.08.019

Li, J., Zhang, W., Ran, M., Sun, Y., Huang, H., and Dong, F. (2019). Synergistic integration of Bi metal and phosphate defects on hexagonal and monoclinic $BiPO_4$: enhanced photocatalysis and reaction mechanism. *Appl. Catal. B Environ.* 243, 313–321. doi: 10.1016/j.apcatb.2018.10.055

Li, J., Zhang, Z., Cui, W., Wang, H., Cen, W., Johnson, G., et al. (2018c). The spatially oriented charge flow and photocatalysis mechanism on internal van der waals heterostructures enhanced g-C_3N_4. *ACS Catal.* 8, 8376–8385. doi: 10.1021/acscatal.8b02459

Li, X., Zhang, W., Cui, W., Sun, Y., Jiang, G., Zhang, Y., et al. (2018). Bismuth Spheres Assembled on Graphene Oxide: Directional Charge Transfer Enhances Plasmonic Photocatalysis and In Situ DRIFTS Studies. *Appl. Catal. B Environ.* 221, 482–489. doi: 10.1016/j.apcatb.2017.09.046

Li, X., Zhang, W., Li, J., Jiang, G., Zhou, Y., Lee, S., et al. (2019). Transformation pathway and toxic intermediates inhibition of photocatalytic NO removal on designed Bi metal@defective $Bi_2O_2SiO_3$, *Appl. Catal. B Environ.* 241, 187–195. doi: 10.1016/j.apcatb.2018.09.032

Wang, H., He, W., Dong, X., Wang, H., and Dong, F. (2018a). *In situ* FT-IR investigation on the reaction mechanism of visible light photocatalytic NO oxidation with defective g-C_3N_4. *Sci. Bull.* 63,117–125. doi: 10.1016/j.scib.2017.12.013

Wang, H., Sun, Y., He, W., Zhou, Y., Lee, S., and Dong, F. (2018c). Visible light induced electrons transfer from semiconductor to insulator enables efficient photocatalytic activity on insulator-based heterojunctions. *Nanoscale* 10, 15513–15520. doi: 10.1039/C8NR03845G

Wang, H., Sun, Y., Jiang, G., Zhang, Y., Huang, H., Wu, Z., et al. (2018b). Unraveling the mechanisms of visible light photocatalytic NO purification on earth-abundant insulator-based core-shell heterojunctions. *Environ. Sci. Technol.* 52, 1479–1487. doi: 10.1021/acs.est.7b05457

Wang, H., Zhang, W., Li, X., Li, J., Cen, W., Li, Q., et al. (2018d). Highly enhanced visible light photocatalysis and *in situ* FT-IR studies on Bi metal@defective BiOCl hierarchical microspheres. *Appl. Catal. B Environ.* 225, 218–227. doi: 10.1016/j.apcatb.2017.11.079

Xiong, T., Wang, H., Zhou, Y., Sun, Y., Cen, W., Huang, H., et al. (2018). KCl-mediated dual electronic channels in layered g-C_3N_4 for enhanced visible light photocatalytic NO removal. *Nanoscale* 10, 8066–8074. doi: 10.1039/C8NR01433G

Conflict of Interest Statement: The authors declare that the research was conducted in the absence of any commercial or financial relationships that could be construed as a potential conflict of interest.

frontiers in Chemistry

ORIGINAL RESEARCH
published: 11 April 2019
doi: 10.3389/fchem.2019.00231

Facile Synthesis of Ternary g-C_3N_4@BiOCl/$Bi_{12}O_{17}Cl_2$ Composites With Excellent Visible Light Photocatalytic Activity for NO Removal

Wendong Zhang and Yi Liang*

Chongqing Key Laboratory of Inorganic Functional Materials, Department of Scientific Research Management, Chongqing Normal University, Chongqing, China

OPEN ACCESS

Edited by:
Nicolas Keller, l'Environnement et la Santé (ICPEES), France

Reviewed by:
Dong Guohui, Shaanxi University of Science and Technology, China
Bitao Liu, Chongqing University of Arts and Sciences, China
Liwu Zhang, Fudan University, China

****Correspondence:***
Wendong Zhang
w5i1@163.com

Specialty section:
This article was submitted to Catalysis and Photocatalysis, a section of the journal Frontiers in Chemistry

Received: *19 August 2018*
Accepted: *25 March 2019*
Published: *11 April 2019*

Citation:
Zhang W and Liang Y (2019) Facile Synthesis of Ternary g-C_3N_4@BiOCl/$Bi_{12}O_{17}Cl_2$ Composites With Excellent Visible Light Photocatalytic Activity for NO Removal. Front. Chem. 7:231. doi: 10.3389/fchem.2019.00231

In this study, novel two-dimensional (2D) g-C_3N_4@BiOCl/$Bi_{12}O_{17}Cl_2$ composites have been fabricated through a facile deposition-precipitation process. The as-prepared photocatalysts were characterized by XRD, SEM, TEM, XPS, UV-vis DRS, PL, Photocurrent, EIS, ESR, and N_2 adsorption-desorption. The photocatalytic activities were investigated through NO removal test in gas under visible light irradiation ($\lambda > 420$ nm). The g-C_3N_4@BiOCl/$Bi_{12}O_{17}Cl_2$ composites exhibit enhanced visible light absorption and photo-induced electron-hole separation efficiency, compared with pristine g-C_3N_4 and BiOCl/$Bi_{12}O_{17}Cl_2$. The intimated contact interfaces between g-C_3N_4 and BiOCl/$Bi_{12}O_{17}Cl_2$ nanosheets are responsible for the more efficient photochemical interactions. The present work provides a new direction to develop a class of ternary g-C_3N_4-based visible-light-driven photocatalysts for environmental purification.

Keywords: facile synthesis, g-C_3N_4@BiOCl/$Bi_{12}O_{17}Cl_2$, visible light, photocatalytic activity, nitrogen oxide (NO) removal

INTRODUCTION

In the past decades, with the rapid development of modern industrial society, a large amount of highly harmful and toxic contaminants have been discharged into environmental system, which have been the focus of world attention (Han et al., 2017; Li et al., 2018). It remains a great challenge to completely achieve the degradation of environmental contaminants through the conventional treatment process, especially for the low-level concentrations of contaminants (Jiang et al., 2017, 2018; Zhong et al., 2017).

Photocatalysis, as a novel technique, have potential application in degradation low-level concentrations of environmental contaminants under visible-light irradiation (Xiong et al., 2015; Zheng and Zhang, 2016; Guan et al., 2017; Jin et al., 2018). Up to now, although a large number of photocatalysts have been explored for environmental purification, most of them still suffer from the limited utilization of solar light, resulting in quite low visible light photocatalytic activity (Chibac et al., 2017; Zhang et al., 2017). Hence, it is desirable to develop highly efficient visible-light-driven photocatalysts for satisfying the requirements of practical applications.

Currently, graphitic carbon nitride (g-C_3N_4), an organic semiconductor photocatalyst, has attracted intensive research interest in energy conversion and environmental remediation fields, largely due to its typical physicochemical properties, such as suitable band gap, good chemical and thermal stability, environmental friendly, etc (Wang et al., 2011; Dong and Zhang, 2013; Dong et al., 2015). However, the photocatalytic efficiency of g-C_3N_4 is far below the requirement of practical applications, mainly due to its fast recombination of photo-excited electron-hole pairs. So far, various strategies have been developed to improve the photocatalytic performance of g-C_3N_4, including electronic structure engineering, nanostructure optimization, and heterojunction construction (Cao et al., 2015; Zhao et al., 2015; Ong et al., 2016). Furthermore, it is well-known that the g-C_3N_4 nanosheets can provide a good two-dimensional surface and interface platform for growth of other nanostructured semiconductors. In particular, the heterojunction with other semiconductor photocatalysts has been regarded as an attractive and effective solution in enabling the efficient separation of photo-excited electron-hole pairs, which not only helps to prolong the life-time of photo-excited charge carriers, but also endows g-C_3N_4-based heterojunctions with more abundant active sites, leading to the significantly enhancement of photocatalytic performance. Successful examples include g-C_3N_4/TiO_2 (Wei et al., 2016), g-C_3N_4/MoS_2 (Hou et al., 2013), g-C_3N_4/BiOBr (Sun et al., 2014), g-C_3N_4/WO_3 (Huang et al., 2013), g-C_3N_4/CdS (Liu, 2015), g-C_3N_4/g-C_3N_4 (Dong et al., 2013), g-C_3N_4/$(BiO)_2CO_3$ (Zhang et al., 2014), g-C_3N_4/graphene (Kim et al., 2016), and g-C_3N_4/Ag (Olga et al., 2016), etc. However, little information about ternary g-C_3N_4@BiOCl/$Bi_{12}O_{17}Cl_2$ heterojunction for visible light photocatalytic removal of NO has been reported.

Here, we report a highly cost-effective method based on the *in situ* self-assembly of BiOCl/$Bi_{12}O_{17}Cl_2$ binary nanoplates onto the surface of g-C_3N_4 nanosheets at room temperature. It takes into consideration advantages of well-matched band structures among g-C_3N_4, BiOCl and $Bi_{12}O_{17}Cl_2$, the as-prepared ternary g-C_3N_4@BiOCl/$Bi_{12}O_{17}Cl_2$ heterojunctions exhibit apparent characteristics including larger surface area, improved visible light absorption ability, and efficient separation of photo-induced charge carries, which are extremely favorable for improving the photocatalytic activity.

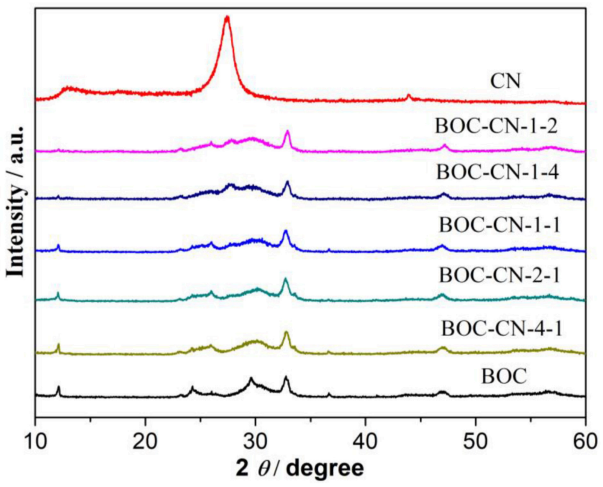

FIGURE 1 | The XRD patterns of the BOC, CN, and BOC-CN samples.

Fabrication of g-C_3N_4@BiOCl/$Bi_{12}O_{17}Cl_2$ Composites

The pure g-C_3N_4 nanosheets and TiO_2 powders were fabricated according to the previous reports (Dong et al., 2011; Zhang et al., 2014), respectively. It's a typical synthesize that 1.33 g of $BiCl_3$ and 0.25 g of as-obtained g-C_3N_4 were added to 50 mL absolute ethyl alcohol and then were ultrasonicated for 30 min. Afterwards, dripping 12.6 mL of NaOH solution (2.0 mol/L) dropwise into $BiCl_3$ solution and then stirring vigorously for 4 h at room temperature. After that, filtering and washing the resulting precipitate for times with distilled water and ethanol. The final samples were obtained after drying under vacuum at 60°C for 24 h. Five types of samples were prepared. The mass rations of BiOCl/$Bi_{12}O_{17}Cl_2$ to g-C_3N_4 are 1:2, 1:4, 1:1, 2:1, and 4:1, respectively. Accordingly, the final samples were labeled as BOC-CN-1-2, BOC-CN-1-4, BOC-CN-1-1, BOC-CN-2-1, and BOC-CN-4-1, respectively. The pure BiOCl/$Bi_{12}O_{17}Cl_2$ samples were synthesized under the same conditions without adding g-C_3N_4 nanosheets, and the g-C_3N_4@BiOCl/$Bi_{12}O_{17}Cl_2$ sample was labeled as BOC.

Materials Characterization

In a typical analysis of the crystal phase of the as-obtained samples, X-ray diffraction with Cu Kα radiation (XRD: model D/max RA, Japan) was applied. Meanwhile scanning electron microscope (SEM, JEOL model JSM-6490, Japan) and transmission electron microscopy (TEM: JEM-2010, Japan) were utilized to characterize the morphology and structure. And the surface properties were examined by X-ray photoelectron spectroscopy with Al Kα X-rays ($h\nu = 1486.6$ eV) radiation operated at 150 W (XPS: Thermo ESCALAB 250, USA). By using a Scan UV-vis spectrophotometer (UV-vis DRS: UV-2450, Shimadzu, Japan) equipped with an integrating sphere assembly and $BaSO_4$ as reflectance sample, the UV-vis diffuse reflection spectra was gained. Nitrogen adsorption-desorption was conducted on a nitrogen adsorption apparatus (ASAP 2020, USA) to insure the specific surface areas and total pore volumes. Photoluminescence (PL: F-7000, HITACHI, Japan) was used to investigate the charge transfer properties. ESR spectrometer (FLsp920, England) was applied to detect the electron spin resonance (ESR) signals of •OH and $\bullet O_2^-$, respectively. The photocurrent measurements (CHI 660B electrochemical system: Shanghai, China) and electrochemical impedance spectroscopy (EIS) were carried out to analyze the photo-generated charge separation properties. All the samples were degassed at 150°C prior to measurements.

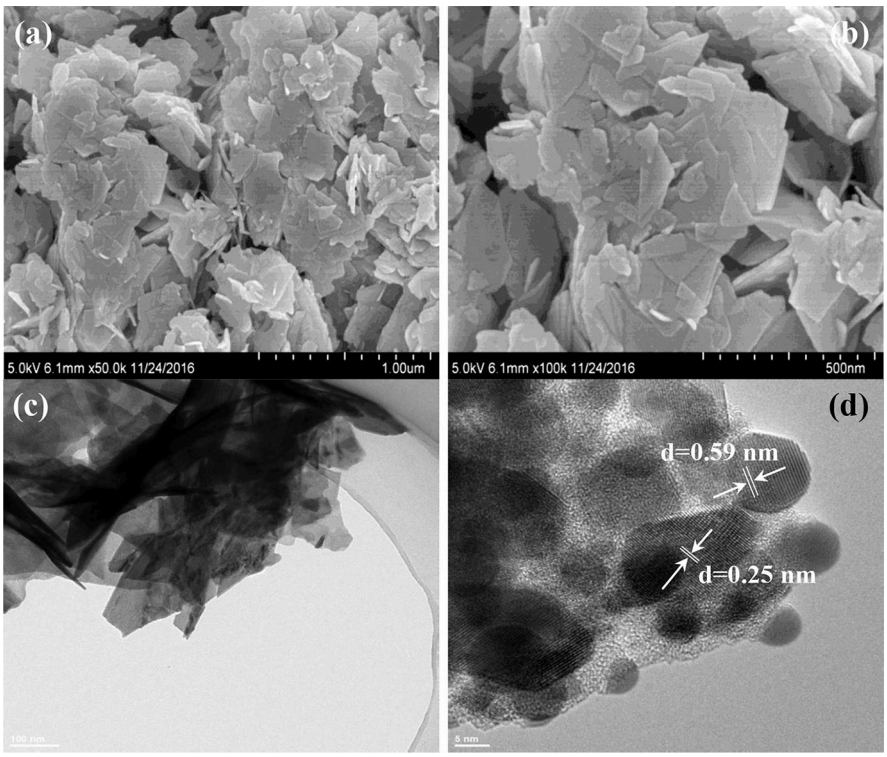

FIGURE 2 | SEM **(a,b)** and TEM **(c,d)** images of BOC samples.

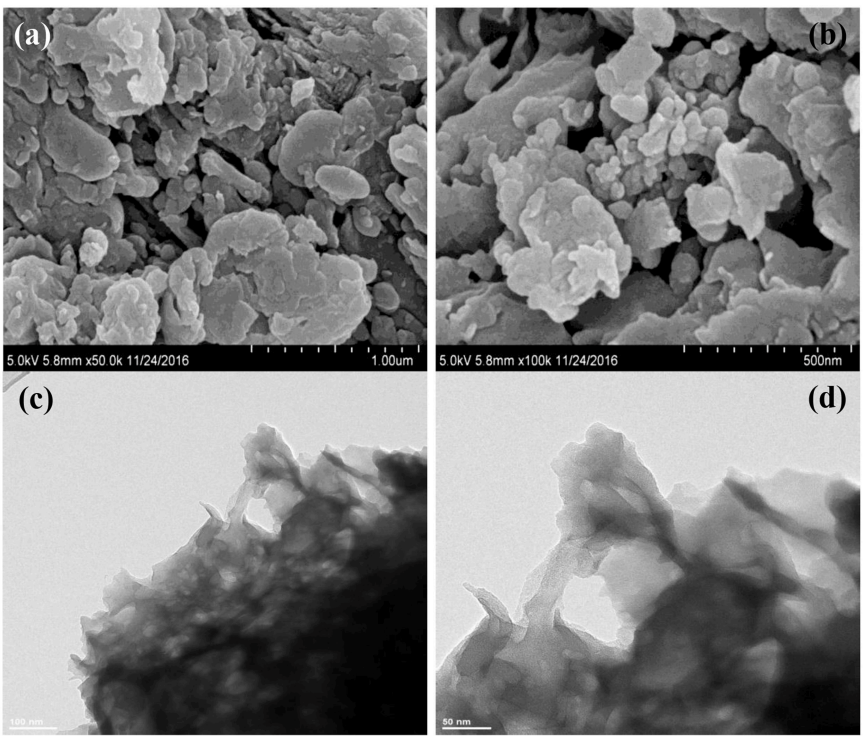

FIGURE 3 | SEM **(a,b)** and TEM **(c,d)** images of CN samples.

Appraisement of Photocatalytic Activity

The photocatalytic activity was investigated by removal of NO at ppb (1×10^{-9}) levels in a continuous flow reactor at ambient temperature. The volume of the rectangular reactor, made of stainless steel and covered with Saint-Glass, was 4.5 L (30 × 15 × 10 cm). A 100-W commercial tungsten halogen lamp (THL100, Beijing, China) was vertically placed outside the reactor, and the light spectra range (see **Supplementary Figure 1**) from 350 to 2,400 nm. A UV cut-off filter (Aike UBG-420, Shenzhen, China) was adopted to remove UV light in the light beam. Photocatalyst (0.2 g) was coated onto a dish with a diameter of 12.0 cm, and the irradiance received by the photocatalyst powder is about 0.66 W/cm^2. The coated dish was then pretreated at 70°C to remove water in the suspension. The catalyst adhesion on the dish was firm enough to avoid the erosion (or removal) of the catalyst during air flowing. The NO gas was acquired from a compressed gas cylinder at a concentration of 100×10^{-6} NO (N_2 balance, BOC gas). The initial concentration of NO was diluted to about 500×10^{-9} by the air stream. The desired relative humidity (RH) level of the NO flow was controlled at 50% by passing the zero air streams through a humidification chamber. The gas streams were premixed completely by a gas blender, and the flow rate was controlled at 2.4 L·min^{-1} by a mass flow controller. After the adsorption-desorption equilibrium was achieved, the lamp was turned on. The concentration of NO was continuously measured by a chemiluminescence NO analyzer (Thermo Environmental Instruments Inc., 42i-TL), which monitors NO, NO_2, and NO_x (NO_x represents NO + NO_2) with a sampling rate of 1.0 L·min^{-1}. The removal ratio (η) of NO was calculated by η (%) = (1-C/C_0) ×100%, where C and C_0 are concentrations of NO in the outlet stream and the feeding stream, respectively.

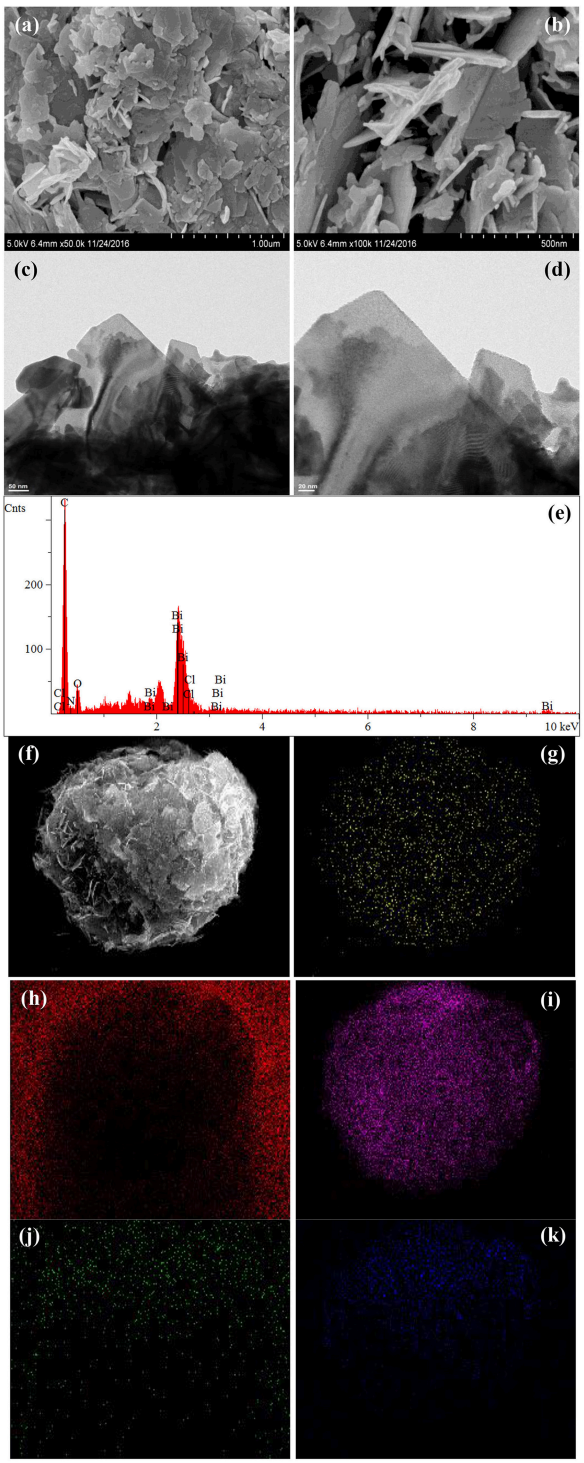

FIGURE 4 | SEM **(a,b)** and TEM **(c,d)** images of BOC-CN. EDS elemental mapping **(e–k)** of the same region, indicating the spatial distribution of Bi **(g)**, C **(h)**, Cl **(i)**, N **(j),** and O **(k)**, respectively.

RESULTS AND DISCUSSION

The phase structures of the obtained samples were investigated by XRD patterns. As shown in **Figure 1**, the BOC sample exhibits typical XRD peaks of BiOCl and $Bi_{12}O_{17}Cl_2$ (He et al., 2016; Huang et al., 2016), thus suggesting the formation of BiOCl/$Bi_{12}O_{17}Cl_2$ heterojunctions, the result is good agreement with the previous reports (Zhang et al., 2017). For the pure CN sample, the typical diffraction peaks appeared at 27.4 and 13.1° are indexed to the g-C_3N_4 (002) and (100) planes (Wang et al., 2011; Cao et al., 2015), respectively. Based on further observation, the peak intensity of the CN decreased with increasing BOC content, implying that interactions exist between the BOC and CN. Finally, two peaks of CN cannot be observed in the BOC-CN composites, which can be ascribed to a good dispersion of BOC onto the surface of CN.

The morphologies and microstructures of BOC, CN, and BOC-CN were characterized by SEM and TEM. For BOC samples (**Figure 2**), the layered and irregular microstructures consist of smooth nanosheets with different sizes. Moreover, there are two different fringes with the lattice spacing of 0.59 and 0.25 nm (**Figure 2d**), which can be indexed to the (006) crystal plane of $Bi_{12}O_{17}Cl_2$ and (003) crystal plane of BiOCl, respectively. For CN samples (**Figure 3**), it presents the lamellar morphology is composed of numerous nanosheets with a much looser pore structure. As shown in **Figures 4a–d**, the BOC-CN composites

also consist of a large number of layered nanosheets with different shapes. Obviously, the BOC nanosheets were *in situ* growth on the surface of g-C_3N_4, resulting in the formation of closely interface in g-C_3N_4@BiOCl/$Bi_{12}O_{17}Cl_2$ composites, which is beneficial for the separation and transfer of the photo-induced electron-hole pairs. The surface element dispersion state of BOC-CN composites are studied by EDS mapping. As shown in **Figures 4e–k**, the Bi, C, Cl, N, and O elements are uniformly distributed in BOC-CN samples.

The XPS measurements were applied to verify the composition and chemical state of the elements. Two peaks at 159.1 and 164.3 eV are consistent with $Bi4f_{7/2}$ and $Bi4f_{5/2}$ (**Figure 5A**), respectively. The XPS spectrum for Cl shows two peaks at 197.8 and 199.4 eV attributed to $Cl2p_{3/2}$ and $Cl2p_{1/2}$ (**Figure 5B**), respectively. The peak centered at 530.3 eV that corresponds to the binding energy of O 1s (**Figure 5C**) (Bi et al., 2016; Zhang et al., 2017). The C peak at 284.8 eV can be ascribed to the adventitious carbon atom. **Figure 5D** shows one peak at 288.5 is identified as overlapped peaks of N-C=N and the O-C=O. Two different peaks are observed in **Figure 5E**, the N peak at 398.9 eV correspond to the C=N-C and the N

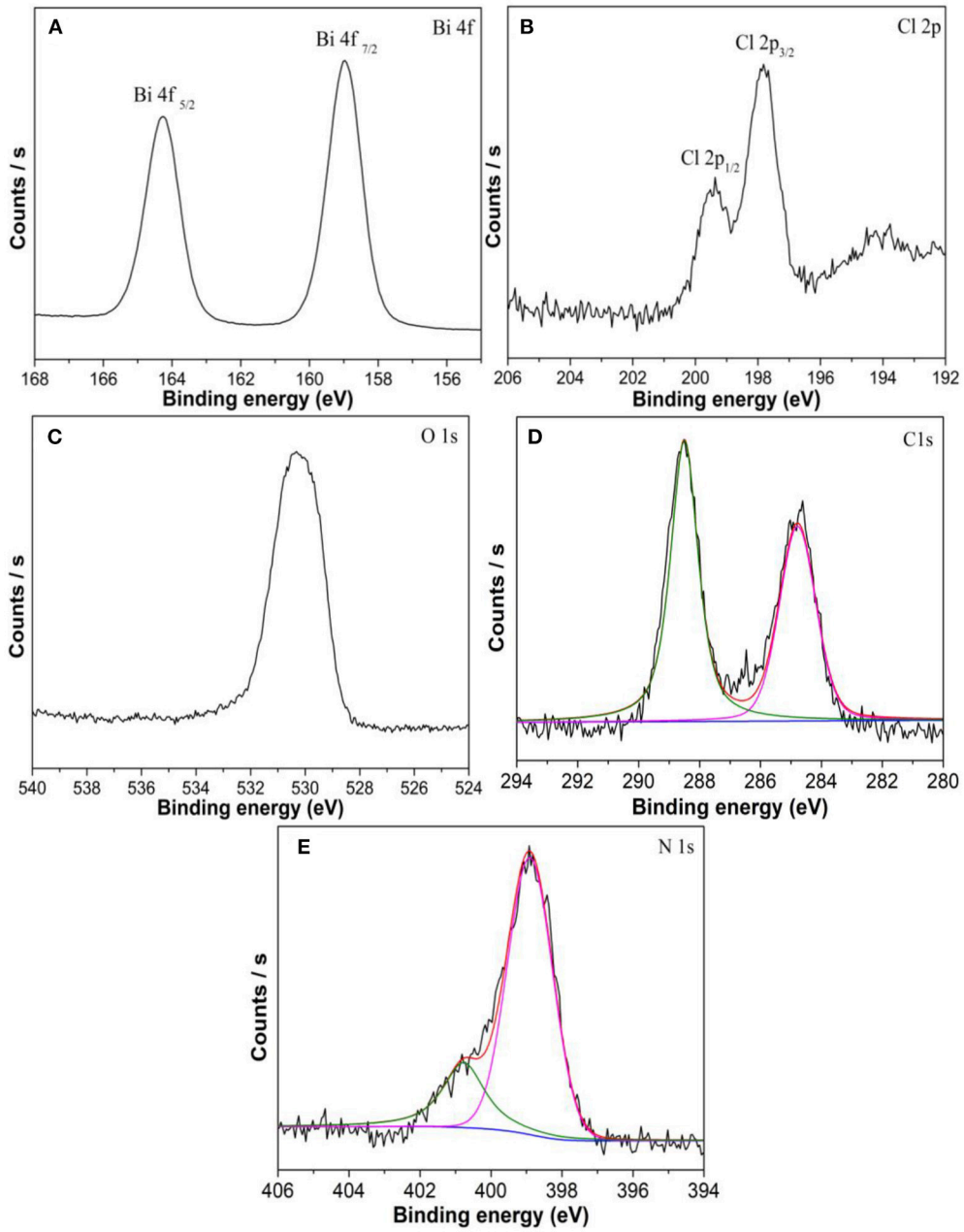

FIGURE 5 | XPS spectra of **(A)** Bi 4f, **(B)** Cl 2p, **(C)** O1s, **(D)** C1s, and **(E)** N1s in BOC-CN.

peak at 400.8 eV is attributed to the residual amino groups (Zhang et al., 2014).

The optical absorption property of the as-obtained samples was investigated by UV-vis DRS. As can be seen from **Figure 6A**, BOC and CN exhibit absorbance edge around 550 and 475 nm, respectively, displaying that BOC and CN possess good visible light absorption ability. Interestingly, BOC-CN-4-1 shows relatively stronger visible light absorption ability lies in the range of 550–800 nm, because of the synergetic effect between BOC and CN. **Figure 6B** shows the PL spectra for BOC, CN,

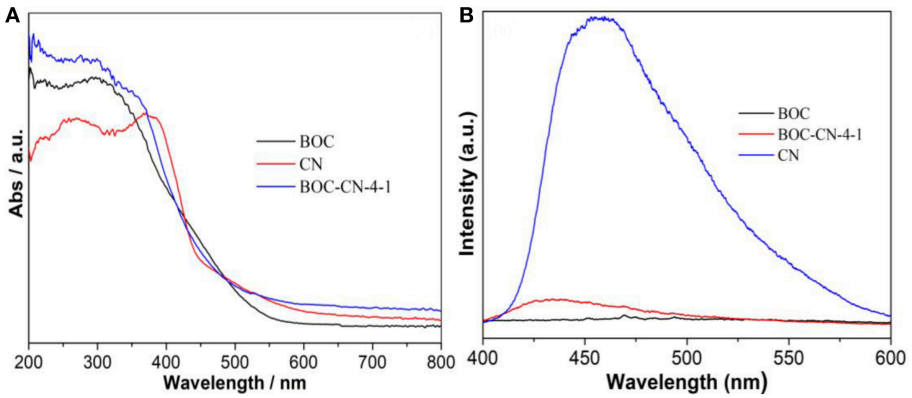

FIGURE 6 | UV-vis diffuse reflectance spectra **(A)** and PL spectra **(B)** for the BOC, CN, and BOC-CN-4-1 samples.

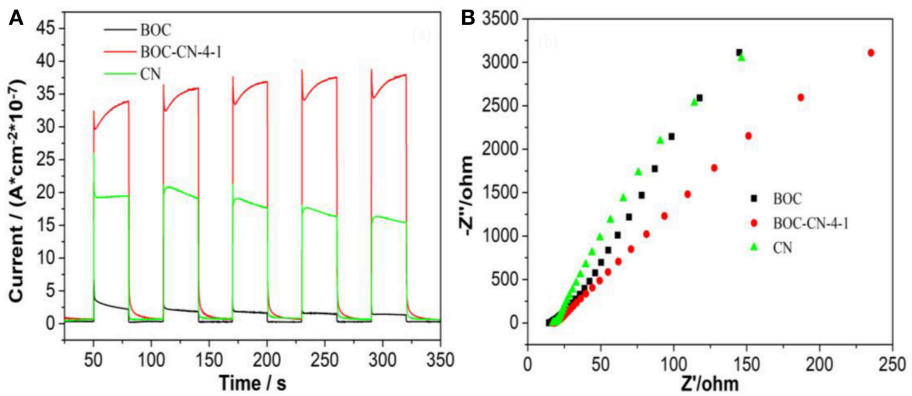

FIGURE 7 | Photocurrent response **(A)** and Nyquist plots **(B)** for BOC, CN, and BOC-CN-4-1 samples under visible light irradiation ($\lambda \geq 420$ nm, $[Na_2SO_4] = 0.5$ M).

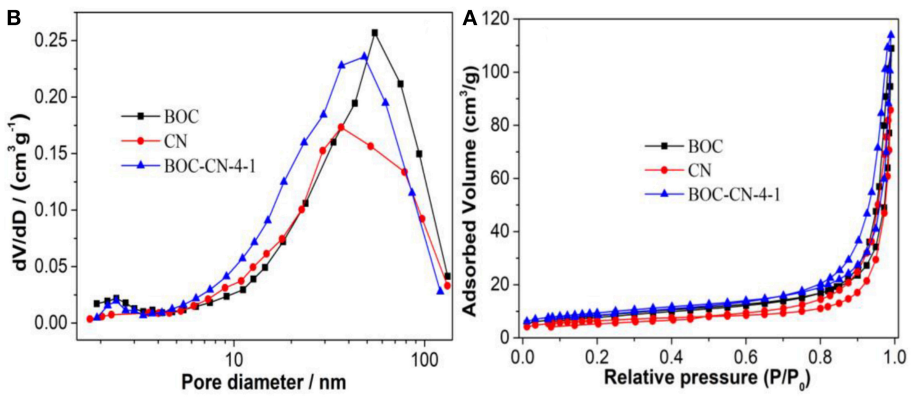

FIGURE 8 | The adsorption-desorption isotherms **(A)** and pore size distribution curves **(B)** of BOC, CN, and BOC-CN-4-1 samples.

and BOC-CN-4-1 using the exciting light of 320 nm. Compared to CN, the PL intensity of BOC-CN-4-1 significantly decreases, demonstrating that the interface interaction between BOC and CN could inhibit the recombination rate of photo-generated electrons and holes.

The photocurrent and electrochemical impedance experiments were used to investigated the photo-generated charges separation and transfer property of BOC, CN, and BOC-CN-4-1 samples under visible light irradiation (Zhang et al., 2018a). Compared with the pure BOC and CN, it was interesting to find that BOC-CN-4-1 exhibits significantly enhanced photocurrent density (**Figure 7A**), suggesting that BOC-CN-4-1 possesses higher photo-generated charge separation property. As can be seen from the **Figure 7B**, the arc radius on the EIS Nyquist plot of BOC-CN-4-1 was smaller than that of the pure BOC and CN, demonstrating that BOC-CN-4-1 has much more efficient photo-generated charge separation and transfer property.

Figure 8A shows that the adsorption-desorption isotherms of all the samples are type IV according to the IUPAC classification, demonstrating that all the samples have mesopores (Dong et al., 2013; Zhang et al., 2014). However, the typical H3 hysteresis loop at low pressure can be ascribed to the aggregation of nanosheets with slit-like pores. **Figure 8B** further confirms the presence of mesopores in BOC, CN, and BOC-CN samples. In addition,

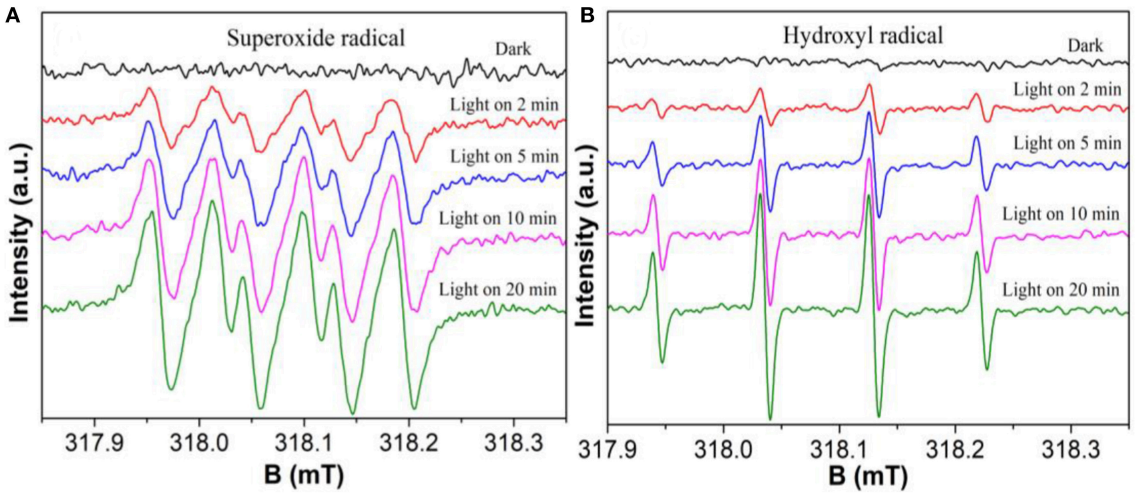

FIGURE 9 | DMPO spin-trapping ESR spectra of BOC-CN-4-1 in methanol dispersion for DMPO-•O_2^- **(A)**, and in aqueous dispersion for DMPO-•OH **(B)**, respectively.

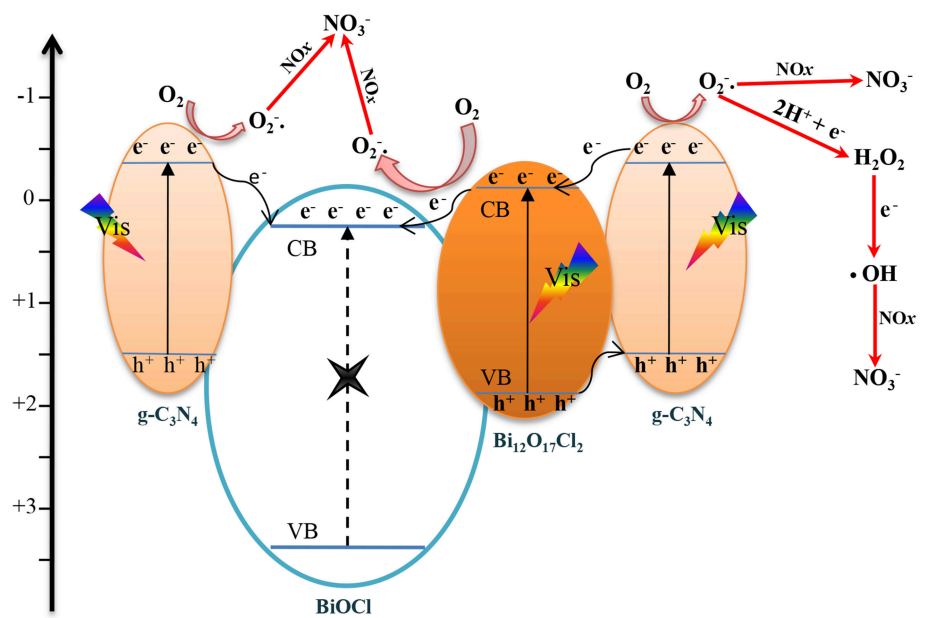

FIGURE 10 | The proposed schematic mechanism for the photocatalytic reation at the BOC-CN heterojunction interface.

the specific surface area (S_{BET}) and total pore volume (V_p) are 32.8 m^2/g and 0.176 cm^3/g for BOC-CN composites, which are higher than those of pure BOC (29.7 m^2/g and 0.168 cm^3/g) and CN (21.8 m^2/g and 0.132 cm^3/g), the enlarged S_{BET} and V_p of BOC-CN composites can be attributed to the stack of nanosheets layered by layered. The enlarged S_{BET} and V_p of BOC-CN composites can facilitate the reactants adsorb and transfer, and provide more active sites for the photocatalytic reaction.

The electron spin resonance (ESR) experiments were further used to confirm the active species during the photocatalytic reaction process under visible light irradiation. As shown in **Figures 9A,B**, the superoxide ($\bullet O_2^-$) radicals and hydroxyl ($\bullet$OH) radicals have been successfully detected by the ESR technique, respectively. Moreover, the intensity of all peaks increase significantly with the irradiation time, demonstrating that $\bullet O_2^-$ and $\bullet$OH are continuously generated during the reaction. The result shows that both $\bullet O_2^-$ and $\bullet$OH are the main photocatalytic reaction active species. The formation of $\bullet O_2^-$ and $\bullet$OH from the photochemical reaction shows in Equations 1–3 (Zhang et al., 2018a).

$$e^- + O_2 \rightarrow \bullet O_2^- \quad (1)$$

$$\bullet O_2^- + 2H^+ + e^- \rightarrow H_2O_2 \quad (2)$$

$$H_2O_2 + e^- \rightarrow \bullet OH + OH^- \quad (3)$$

Furthermore, the possible mechanism for the photocatalytic reaction at the BOC-CN interface are presented in **Figure 10**. After the visible light irradiation, the $Bi_{12}O_{17}Cl_2$ and g-C_3N_4 can be excited and then produce electron-hole pairs (Dong et al., 2013; Zhang et al., 2018b). On the one hand, the excited electrons in CB of g-C_3N_4 can directly transfer to CB of BiOCl (Zhang et al., 2013). On the other hand, the excited holes in VB of $Bi_{12}O_{17}Cl_2$ can transfer to VB of g-C_3N_4, the excited electrons in CB of g-C_3N_4 can transfer to CB of $Bi_{12}O_{17}Cl_2$, and the electrons can further transfer to the CB of BiOCl from the CB of $Bi_{12}O_{17}Cl_2$, the band structures of the three components are well-matched resulting in efficient separation and transfer of the photo-induced carriers. Hence, the suitable band structures clearly show that the efficient electron-hole pair separation plays critical role in improving the photochemical reaction (Zhang et al., 2013, 2014).

The visible-light-induced photocatalytic activities of the TiO_2, BOC, CN, and BOC-CN samples toward NO were revealed in **Figure 11A**. The pure BOC and CN only removed 36.2 and 14.6% of NO after 30 min visible light irradiation due to its fast recombination of photo-induced carriers, respectively. However, the visible-light-induced photocatalytic activities of the TiO_2 sample can be neglected under the same conditions, indicating that the activity does not result from a UV-A light induced photocatalytic activity due to some trace of UV-A light after the cut-off filter. When the heterojunction was formed, the NO removal ratio over BOC-CN composites was increased to 46.8%. For ruling out and evidencing the NO degradation, the adsorption experiment of the optimized BOC-CN-4-1was carried out under dark condition, the result shows that adsorption property of NO over the BOC-CN-4-1-dark sample can also be ignored. The photocatalytic stability experiment of the BOC-CN-4-1 sample was evaluated by repeating the reaction for five runs under visible light irradiation. As shown in in **Figure 11B**, the photocatalytic performance shows slightly loss after five run, indicating that BOC-CN-4-1 photocatalyst possesses good photocatalytic stability. Interestingly, the BOC-CN composites exhibit even higher visible light photocatalytic activity than that of BiOBr/C_3N_4 (removal rate of 32.7%) and p-doped g-C_3N_4 (removal rate of 42.3%) (Sun et al., 2014; Zhang et al., 2016). The enhanced photocatalytic activity of BOC-CN can be attributed to the synergistic contribution of BOC and g-C_3N_4 with respect to the suitable band structure, enlarged S_{BET} and V_p, improved visible light absorption, and efficient photo-induced carrier separation at the interface of BOC and g-C_3N_4 (Dong et al., 2013; Hou et al., 2013; Sun et al., 2014; Liu, 2015; Wei et al., 2016).

CONCLUSION

In summary, we have synthesized ternary BOC-CN heterojunctions with outstanding visible light photocatalytic

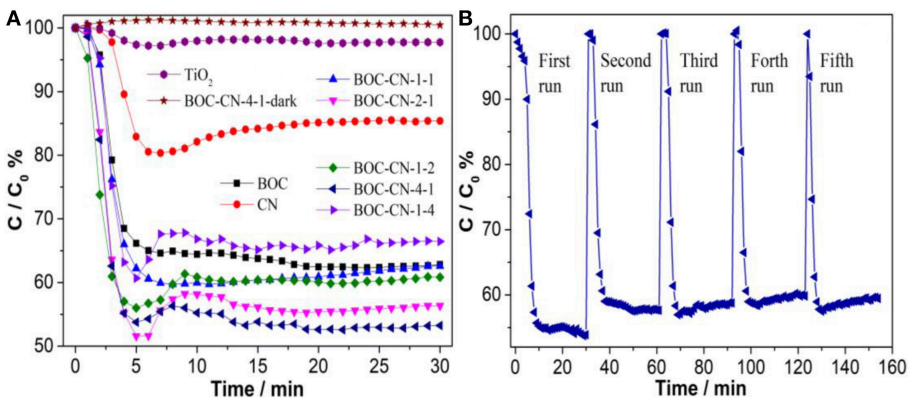

FIGURE 11 | (A) Photocatalytic removal of NO over the as-obtained samples, **(B)** cycling runs of the BOC-CN-4-1 composite in air under visible light irradiation (λ > 420 nm).

performance by self-assembly of BiOCl/$Bi_{12}O_{17}Cl_2$ nanosheets on the surface of g-C_3N_4 nanosheets via a chemical deposition-precipitation method. The results reveal that g-C_3N_4, BiOCl, and $Bi_{12}O_{17}Cl_2$ possess well-matched band structures, which is helpful to the separation and transport of photo-induced carriers. This work provides a new perspective for the design and fabrication of high performance and stable BiOCl/$Bi_{12}O_{17}Cl_2$-based photocatalysts via a facile method at room temperature.

AUTHOR CONTRIBUTIONS

WZ: experiment, data analysis, and paper writing. YL: paper writing.

FUNDING

This research is financially supported by the National Natural Science Foundation of China (No. 51708078), Natural Science Foundation of Chongqing (CSTC, 2018jcyjA1040), and the Chongqing Postdoctoral Science Foundation funded project (No. Xm2016027).

SUPPLEMENTARY MATERIAL

The Supplementary Material for this article can be found online at: https://www.frontiersin.org/articles/10.3389/fchem.2019.00231/full#supplementary-material

Supplementary Figure 1 | The light spectra range of tungsten halogen lamp.

REFERENCES

Bi, C. J., Cao, J., Lina, H. L., Wang, Y. J., and Chen, S. F. (2016). Enhanced photocatalytic activity of $Bi_{12}O_{17}Cl_2$ through loading Pt quantum dots as a highly efficient electron capturer. *Appl. Catal. B Environ.* 195, 132–140. doi: 10.1016/j.apcatb.2016.05.011

Cao, S., Low, J., Yu, J., and Jaroniec, M. (2015). Polymeric photocatalysts based on graphitic carbon nitride. *Adv. Mater. Weinheim.* 27, 2150–2176. doi: 10.1002/adma.201500033

Chibac, A. L., Buruiana, T., Melinte, V., and Buruiana, E. C. (2017). Photocatalysis applications of some hybrid polymeric composites incorporating TiO_2 nanoparticles and their combinations with SiO_2/Fe_2O_3. *Beilstein J. Nanotechnol.* 8, 272–286. doi: 10.3762/bjnano.8.30

Dong, F., Guo, S., Wang, H. Q., Li, X. F., and Wu, Z. B. (2011). Enhancement of the visible light photocatalytic activity of c-doped TiO_2 nanomaterials prepared by a green synthetic approach. *J. Phys. Chem. C.* 115, 13285–13292. doi: 10.1021/jp111916q

Dong, F., Zhao, Z., Xiong, T., Ni, Z., Zhang, W., and Sun, Y. (2013). *In situ* construction of g-C_3N_4/g-C_3N_4 metal-free heterojunction for enhanced visible-light photocatalysis. *ACS Appl. Mater. Interface* 5, 11392–11401. doi: 10.1021/am403653a

Dong, G. H., Ho, W. K., Li, Y. H., and Zhang, L. Z. (2015). Facile synthesis of porous graphene-like carbon nitride ($C_6N_9H_3$) with excellent photocatalytic activity for NO removal. *Appl. Catal. B Environ.* 174–175, 477–485. doi: 10.1016/j.apcatb.2015.03.035

Dong, G. H., and Zhang, L. Z. (2013). Synthesis and enhanced Cr(VI) photoreduction property of formate anion containing graphitic carbon nitride. *J. Phys. Chem. C.* 117, 4062–4068. doi: 10.1021/jp3115226

Guan, W., Zhang, Z. H., Tian, S. C., and Du, J. W. (2017). Ti_4O_7/g-C_3N_4 for visible light photocatalytic oxidation of hypophosphite: effect of mass ratio of Ti_4O_7/g-C_3N_4. *Front. Chem.* 8:313. doi: 10.3389/fchem.2018.00313

Han, J., Zheng, X. Z., Zhang, L. W., Fu, H. B., and Chen, J. M. (2017). Removal of SO_2 on a nanoporous photoelectrode with simultaneous H_2 production. *Environ. Sci. Nano* 4, 834–842. doi: 10.1039/C6EN00638H

He, G. P., Xing, C. L., Xiao, X., Hu, R. P., Zuo, X. X., and Nan, J. M. (2016). Facile synthesis of flower-like $Bi_{12}O_{17}Cl_2$/β-Bi_2O_3 composites with enhanced visible light photocatalytic performance for the degradation of 4-tert-butylphenol. *Appl. Catal. B Environ.* 170–171, 1–9. doi: 10.1016/j.apcatb.2015.01.015

Hou, Y., Lauren, A. B., Zhang, J., Zhang, G., Zhu, Y., Wang, X., et al. (2013). Layered nanojunctions for hydrogen-evolution catalysis. *Angew. Chem. Int. Ed.* 52, 1–6. doi: 10.1002/anie.201210294

Huang, H. W., Xiao, K., He, Y., Zhang, T. R., Dong, F., Du, X., et al. (2016). Rational design on 3D hierarchical bismuth oxyiodides via *in situ* self-template phase transformation and phase-junction construction for optimizing photocatalysis against diverse contaminants. *Appl. Catal. B Environ.* 199, 75–86. doi: 10.1016/j.apcatb.2016.10.082

Huang, L., Xu, H., Li, Y., Li, H., Cheng, X., and Xia, J. (2013). Visible-light-induced WO_3/g-C_3N_4 composites with enhanced photocatalytic activity. *Dalton. Trans.* 42, 8606–8616. doi: 10.1039/C3DT00115F

Jiang, G., Lan, M., Zhang, Z., Lv, X., Lou, Z., Xu, X., et al. (2017). Identification of active hydrogen species on palladium nanoparticles for an enhanced electrocatalytic hydrodechlorination of 2,4-dichlorophenol in water. *Environ. Sci. Technol.* 51, 7599–7605. doi: 10.1021/acs.est.7b01128

Jiang, G. M., Wang, K. F., Li, J. Y., Fu, W. Y., Zhang, Z. Y., Johnson, G., et al. (2018). Electrocatalytic hydrodechlorination of 2,4-dichlorophenol over palladium nanoparticles and its pH-mediated tug-of-war with hydrogen evolution. *Chem. Eng.J.* 348, 26–34. doi: 10.1016/j.cej.2018.04.173

Jin, S., Dong, G. H., Luo, J. M., Ma, F. Y., and Wang, C. Y. (2018). Improved photocatalytic NO removal activity of $SrTiO_3$ by using $SrCO_3$ as a new co-catalyst. *Appl. Catal. B Environ.* 227, 24–34. doi: 10.1016/j.apcatb.2018.01.020

Kim, S. Y., Oh, J., Park, S., Shim, Y., and Park, S. (2016). Production of metal-free composites composed of graphite oxide and oxidized carbon nitride nanodots and their enhanced photocatalytic performances. *Chem. Eur. J.* 22, 5142–5145. doi: 10.1002/chem.201505100

Li, Y. H., Wu, X. F., Ho, W. K., Lv, K. L., Li, Q., Li, M., et al. (2018). Graphene-induced formation of visible-light-responsive SnO_2-Zn_2SnO_4 Z-scheme photocatalyst with surface vacancy for the enhanced photoreactivity towards NO and acetone oxidation. *Chem. Eng.J.* 336, 200–210. doi: 10.1016/j.cej.2017.11.045

Liu, J. J. (2015). Origin of high photocatalytic efficiency in monolayer g-C_3N_4/CdS heterostructure: a hybrid DFT study. *J. Phys. Chem. C* 119, 28417–28423. doi: 10.1021/acs.jpcc.5b09092

Olga, F. C., Mario, J. M. B., Marcos, F. G., and Anna, K. (2016). Interface effects in sunlight-driven Ag/g-C_3N_4 composite catalysts: study of the toluene photodegradation quantum efficiency. *ACS Appl. Mater. Interface* 8, 2617–2627. doi: 10.1021/acsami.5b10434

Ong, W. J., Tan, L. L., Ng, Y. H., Yong, S. T., and Chai, S. P. (2016). Graphitic carbon nitride (g-C_3N_4)-based photocatalysts for artificial photosynthesis and environmental remediation: are we a step closer to achieving sustainability? *Chem. Rev.* 116, 7159–7329. doi: 10.1021/acs.chemrev.6b00075

Sun, Y., Zhang, W., Xiong, T., Zhao, Z., Dong, F., Wang, R., et al. (2014). Growth of BiOBr nanosheets on C_3N_4 nanosheets to construct two-dimensional nanojunctions with enhanced photoreactivity for NO removal. *J. Colloid. Interf. Sci.* 418, 317–323. doi: 10.1016/J.JCIS.2013.12.037

Wang, Y., Wang, X. C., and Antonietti, M. (2011). Polymeric graphitic carbon nitride as a heterogeneous organocatalyst: from photochemistry to multipurpose catalysis to sustainable chemistry. *Angew. Chem. Int. Ed.* 50, 2–24. doi: 10.1002/anie.201101182

Wei, X., Shao, C., Li, X., Lu, N., Wang, K., Zhang, Z., et al. (2016). Facile *in situ* synthesis of plasmonic nanoparticles-decorated g-C_3N_4/TiO_2 heterojunction nanofibers and comparison study of their photosynergistic effects for efficient photocatalytic H_2 evolution. *Nanoscale* 8, 11034–11043. doi: 10.1039/C6NR01491G

Xiong, T., Zhang, H. J., Zhang, Y. X., and Dong, F. (2015). Ternary Ag/AgCl/$BiOIO_3$ composites for enhanced visible-light-driven photocatalysis. *Chin. J. Catal.* 8, 784–788. doi: 10.1016/S1872-2067(15)60980-9

Zhang, R. Y., Wan, W. C., Li, D. W., Dong, F., and Zhou, Y. (2017). Three-dimensional MoS_2/reduced graphene oxide aerogel as a

macroscopic visible-light photocatalyst. *Chin. J. Catal.* 2, 313–320. doi: 10.1016/S1872-2067(16)62568-8

Zhang, W., Sun, Y., Dong, F., Zhang, W., Duan, S., and Zhang, Q. (2014). Facile synthesis of organic–inorganic layered nanojunctions of g-C_3N_4/$(BiO)_2CO_3$ as efficient visible light photocatalyst. *Dalton. Trans.* 43, 12026–12036. doi: 10.1039/c4dt00513a

Zhang, W. D., Dong, X. A., Bin, J., Zhong, J. B., Sun, Y. J., and Dong, F. (2018a). 2D BiOCl/$Bi_{12}O_{17}Cl_2$ nanojunction: enhanced visible light photocatalytic NO removal and in situ DRIFTS investigation. *Appl. Surf. Sci.* 430, 571–577. doi: 10.1016/j.apsusc.2017.06.186

Zhang, W. D., Dong, X. A., Liang, Y., Sun, Y. J., and Dong, F. (2018b). Ag/AgCl nanoparticles assembled on BiOCl/$Bi_{12}O_{17}Cl_2$nanosheets: enhanced plasmonic visible light photocatalysis and *in situ* DRIFTS investigation. *Appl. Surf. Sci.* 455, 236–243. doi: 10.1016/j.apsusc.2018.05.171

Zhang, W. D., Zhang, J., Dong, F., and Zhang, Y. X. (2016). Facile synthesis of *in situ* phosphorus-doped g-C_3N_4 with enhanced visible light photocatalytic property for NO purification. *RSC Adv.* 6, 88085–88089. doi: 10.1039/C6RA18349B

Zhang, W. D., Zhang, Q., and Dong, F. (2013).Visible-light photocatalytic removal of NO in air over BiOX (X = Cl, Br, I) single-crystal nanoplates prepared at room temperature. *Ind. Eng. Chem. Res.* 52, 6740–6746. doi: 10.1021/ie400615f

Zhao, Z., Sun, Y., and Dong, F. (2015). Graphitic carbon nitride based nanocomposites: a review. *Nanoscale* 7, 15–37. doi: 10.1039/C4NR03008G

Zheng, X. Z., and Zhang, L. W. (2016). Photonic nanostructures for solar energy conversion. *Energy Environ. Sci.* 9, 2511–2532. doi: 10.1039/C6EE01182A

Zhong, H. Y., Wang, H., Liu, X., Liu, C., Liu, G. Y., Tian, Y., et al. (2017). Degradation and characteristic changes of organic matter in sewage sludge using vermi-biofilter system. *Chemosphere* 180, 57–64. doi: 10.1016/j.chemosphere.2017.03.121

Conflict of Interest Statement: The authors declare that the research was conducted in the absence of any commercial or financial relationships that could be construed as a potential conflict of interest.

frontiers in Chemistry

ORIGINAL RESEARCH
published: 04 January 2019
doi: 10.3389/fchem.2018.00649

In situ Synthesis of Au-Induced Hierarchical Nanofibers/Nanoflakes Structured $BiFeO_3$ Homojunction Photocatalyst With Enhanced Photocatalytic Activity

Yan'an Li[1], Jiao Li[1], Long Chen[1]*, Haibin Sun[1], Hua Zhang[1], Hong Guo[2] and Liu Feng[2]*

[1] School of Materials Science and Engineering, Shandong University of Technology, Zibo, China, [2] Analysis & Testing Center, Shandong University of Technology, Zibo, China

In order to further improve the photocatalytic performance of $BiFeO_3$ (BFO), novel Au-induced hierarchical nanofibers/nanoflakes structured $BiFeO_3$ homojunctions (Au_x-BFO, x = 0, 0. 6, 1.2, 1.8, 2.4 wt%) were *in situ* synthesized through a simple reduction method with assist of sodium citrate under the analogous hydrothermal environment. The effect of loading amount of Au nanoparticles (NPs) on the physicochemical properties and photocatalytic activity was investigated in detail. The $Au_{1.2}$-BFO NFs sample show the best photocatalytic activity (85.76%), much higher than that for pure BFO samples (49.49%), mainly due to the hierarchical nanofibers/nanoflakes structured homojunction, the surface plasmon resonance (SPR) effect of Au NPs, as well as the presence of defects (Fe^{2+}/Fe^{3+} pairs and oxygen vacancy). Furthermore, the possible formation mechanism of the unique homojunction and the enhanced photocatalytic mechanism for the degradation of methylene blue (MB) dye are proposed. It is proven that holes (h^+) play the decisive role in the photocatalytic process. The present work provides a fascinating way to synthesize efficient homojunctions for the degradation of organic pollutes.

Keywords: bismuth ferrite, homojunction, SPR effect, defects, photodegradation

OPEN ACCESS

Edited by:
Yuxin Zhang,
Chongqing University, China

Reviewed by:
Dong Guohui,
Shaanxi University of Science and Technology, China
Xiaoying Liu,
Chongqing Technology and Business University, China

****Correspondence:***
Jiao Li
haiyan9943@163.com
Long Chen
lchen830@sdut.edu.cn

Specialty section:
This article was submitted to Catalysis and Photocatalysis, a section of the journal Frontiers in Chemistry

Received: *03 September 2018*
Accepted: *12 December 2018*
Published: *04 January 2019*

Citation:
Li Y, Li J, Chen L, Sun H, Zhang H, Guo H and Feng L (2019) In situ Synthesis of Au-Induced Hierarchical Nanofibers/Nanoflakes Structured $BiFeO_3$ Homojunction Photocatalyst With Enhanced Photocatalytic Activity. Front. Chem. 6:649. doi: 10.3389/fchem.2018.00649

INTRODUCTION

Nowadays, energy crisis and environmental deterioration issues are severely detrimental for economic development and human health (Wang et al., 2013). Semiconductor photocatalysis as an efficient and green technology can convert solar energy into chemical energy to dispose of these issues (Wang et al., 2013; Wang H. et al., 2017). In order to fully exploit the solar energy, it is necessary to explore visible light responsive photocatalysts with excellent photocatalytic activities (Zhang et al., 2017).

Among the variety of visible-light-driven semiconductor materials, $BiFeO_3$ (BFO) has attracted a great deal of attention due to its narrow band gap (2.2∼2.5 eV), good chemical stability and low cost (Wang et al., 2013; Niu et al., 2015). In addition, the room temperature multiferroic property makes it easily recovered from the treated water to avoid the secondary pollution (Zhang et al., 2017). However, the rapid recombination rate of photogenerated electron-hole pairs and low quantum yield limit its practical application (Huo et al., 2011; Srivastav and Gajbhiye, 2012; Niu et al., 2015). Therefore, much efforts have been made to improve its photocatalytic performance, such as element doping (Wang et al., 2012; Ahmada et al., 2017; Irfan et al., 2017; Yang et al., 2018),

morphology control (Mohan and Subramanian, 2013; Zhang Q. et al., 2016), noble metal deposition (Li S. et al., 2013; Zhang et al., 2015), and semiconductor coupling (Li Z. et al., 2013; Humayun et al., 2016).

Compared to that of bulk materials, the reduced radial dimension and the extremely large surface-to-volume ratio of one-dimension (1D) nanofibrous structure can promote the rapid transfer of photogenerated charge carriers to the surface, and thus enhance the separation efficiency (Li S. et al., 2013). Furthermore, the perpendicular transport direction of photogenerated electrons and holes can further effectively inhibit the recombination of photogenerated electron-hole pairs (Mohan and Subramanian, 2013). Therefore, the synthesis of BFO sample with nanofibrous structure is in favor of enhancing the photocatalytic activity.

Noble metal (e.g., Ag, Au, Pt, etc.) deposition is also an efficient way to enhance the photocatalytic activity (Li et al., 2015; Niu et al., 2015; Zhang et al., 2015). Among them, Au nanoparticles (NPs) exhibit excellent a chemical stability and a characteristic absorption peak in the visible wavelength range due to the strong surface plasmon resonance (SPR) effect (Li S. et al., 2013; Li et al., 2015). The deposited Au NPs can not only act as electron-trapping centers to reduce the recombination rate of photogenerated electron-hole pairs, but also can act as light harvesters enhancing the light absorbing ability and as catalytic sites for the photocatalytic reaction (Lin et al., 2017; Chiu et al., 2018). Significantly, the formed Schottky junctions between Au NPs and BFO nanofibers (NFs) can adjust the interfacial band structure and thus promote the separation and transfer of photogenerated charge carriers.

In comparison with heterojunction built with different semiconductors. Besides the band alignment of two semiconductors, the creation of heterojunctions is also dependent on other properties of semiconductor, such as electron affinity and work function (Ye et al., 2017). The homojunction is constructed by the same semiconductor materials with different crystal phases, exposing facets or semiconductor types, *etc.*, which can avoid the disadvantages of heterojunction fabrication (Huang et al., 2017). The enhanced photocatalytic activity of heterojunctions or homojunctions is mainly dependent on the space charge accumulation or depletion at the interfaces of two phases (Ye et al., 2017).The homojunction structure can also introduce an internal field to effectively facilitate surface charge separation, retard the recombination of photogenerated carriers, and thus remarkably improve the photocatalytic performance. However, there are few reports on the fabrication of BFO homojunction, especially for the aspect of *in situ* synthesis.

In this work, an distinctive Au NPs deposited BFO homojunction, in which BFO nanoflakes are assembled on the surface of BFO NFs, was *in situ* synthesized through a simple reduction method under the analogous hydrothermal environment. The effect of loading amount of Au NPs on the physicochemical properties and photocatalytic activity was investigated in detail. Furthermore, it proposed a possible formation mechanism of the unique homojunction and the enhanced photocatalytic mechanism for the degradation of methylene blue (MB) dye over Au_x-BFO NFs under simulated solar light irradiation.

EXPERIMENTAL

Preparation of Au_X-BFO NFs

BFO NFs (Au_x-BFO NFs, $x = 0$ wt%) were prepared *via* a sol-gel method combined with an electrospinning technique. All the chemical reagents used for the synthesis were analytical grade. Bismuth nitrate ($Bi(NO_3)_3{\cdot}5H_2O$) and ferric nitrate ($Fe(NO_3)_3{\cdot}9H_2O$) with the Bi: Fe molar ratio of 1.11:1 (to make up for the loss of Bi ions during the calcination process) were dispersed in methylglycol by ultrasonic to form a homogeneous solution. Then the viscosity and pH value of the solution were adjusted by 2.5 mL of glacial acetic acid, called solution A. g of poly(vinylpyrrolidone) (PVP, $Mw = 1{,}300{,}000$) was added to the mixed solvent of N'N-dimethylformamide (DMF) and ethanol with the volume ratio of 2:1, called solution B. Solution B was added dropwise to solution A with constantly stirring for 24 h to form the pre-spinning solution which has a pH of 2.0. The pre-spinning solution was loaded into a plastic syringe connected with a stainless needle and then fixed onto the electrospinning system. An optimized high voltage of 15 kV was applied to the needle with the flow rate of 0.4 mL/h. The distance was 20 cm from the needle to the rotating drum collector. The as-spun NFs were dried at 60°C for 4 h, calcined at 350°C for 30 min with a heating rate of 2°C/min, and then calcined at 600°C for 120 min with a heating rate of 5°C/min in air.

Au NPs deposited BFO NFs (Au_x-BFO NFs, $x = 0.6$, 1.2, 1.8, 2.4 wt%) were synthesized by a simple reduction method with sodium citrate. In a typical procedure, 57.38 mg of BFO NFs were first dispersed in 50 mL of deionized water, followed by adding a certain amount of $HAuCl_4$ (3 mmol/L) and sodium citrate (0.04 mol/L). Then the suspension was kept stirring at 150°C for 30 min in oil bath. After cooled to room temperature naturally, the obtained products were centrifuged, washed with deionized water and absolute ethanol for several times, and then dried at 80°C for 24 h. The loading amount of Au NPs on BFO NFs were 0.6, 1.2, 1.8, and 2.4 wt% (mass ratio of Au to BFO), which were defined as $Au_{0.6}$-BFO NFs, $Au_{1.2}$-BFO NFs, $Au_{1.8}$-BFO NFs, and $Au_{2.4}$-BFO NFs, respectively.

Characterization

The phase structures were identified by X-ray diffraction (XRD; D8 Advance, Bruker AXS, German) with Cu Kα radiation ($\lambda = 1.5418$ Å) at 40 kV and 50 mA in a 2θ ranging from 20 to 70°. The morphologies were observed by field emission scanning electron microscope (FE-SEM; Sirion 200, FEI, USA). The transmission electron microscopy (TEM) and high resolution TEM (HRTEM) were performed at a field emission transmission electron microscope (TEM; Tecnai G2 F20 S-TWIN, FEI, USA) with an accelerating voltage of 200 kV. UV-vis diffuse reflectance spectra (DRS) were measured at room temperature by UV-Vis spectrometer (UV-Vis; UV-3600plus, Shimadzu, Japan) with the wavelength range of 350–800 nm using $BaSO_4$ as a reflectance. The measurements of magnetic properties were carried out by a superconducting quantum interference device magnetometer

(FM, MPMS XL-7, Qunatum Design, USA). The element chemical states were characterized by X-ray photoelectron spectrometer (XPS; PHI-5300, PHI, USA) with an Al Kα X-ray radiation. The photoluminescence (PL) spectra were measured on the fluorescence spectrophotometer (PL; Hitachi F-4600, Hitachi, Japan) with the excitation wavelength of 230 nm and a 150 W xenon lamp as the light source.

Photocatalytic Activity Evaluation

Twenty five milligram of Au_x-BFO NFs were added to 30 mL of 10 mg/L MB solution with ultrasound for 10 min. After stirring in the dark for 30 min to reach the adsorption-desorption equilibrium, the suspension system was exposed to simulated solar light irradiation (CHF-XM-500W xenon lamp, Beijing Perfactlight Company, China). During the photocatalytic reaction process, the suspension was taken out at every 30 min interval and centrifuged to remove the photocatalyst. The MB concentration was measured by a UV-vis spectrophotometer at the wavelength of 666 nm.

RESULTS AND DISCUSSION

XRD Analysis

The XRD patterns of Au_x-BFO NFs ($x = 0$, 0.6, 1.2, 1.8, 2.4 wt%) are shown in **Figure 1**. All the diffraction peaks of pure BFO NFs can be indexed to the rhombohedral perovskite structure with *R3m* space group of the $BiFeO_3$ phase (JCPDS card no. 86–1518) (Chen et al., 2017). The strong diffraction peaks also imply the good crystallinity. In addition, the crystalline structures of BFO NFs are not changed after depositing Au NPs.

Microstructures

Figure 2 shows the SEM images of Au_x-BFO NFs ($x = 0$, 0.6, 1.2, 1.8, 2.4 wt%). It can be seen from **Figure 2A** that the pure BFO NFs exhibit an uniform nanofibrous structure with compactly packed and continuous nanoparticles. The diameter of BFO NFs is about 100–200 nm. As shown in **Figures 2B–E**, there is no obvious change of the nanofibrous structure for BFO NFs with Au NPs deposition, but some thin nanoflakes are embedded in the surface of nanofibers, and the number of nanoflakes increases with the increase of the loading amount of Au NPs.

The EDS mapping is performed to clarify the chemical composition and element distribution in $Au_{1.2}$-BFO NFs, as shown in **Figure 3**. It can be clearly seen that Bi, Fe, and O elements are uniformly distributed throughout the single nanofiber (**Figures 3A–D**). Au NPs are dispersed well on BFO NFs, instead of agglomerating together (**Figure 3E**). More importantly, The EDS result (**Figure 3F**) recorded at the "+" position in **Figure 3A** shows that the main elements of the nanoflake are Bi, Fe, Au, and O. It is worthy to note that the atomic ratio of Bi/Fe is almost 1:1, nearly corresponding to the composition of BFO. The trace amount of Au shows that Au NPs are also deposited on the nanoflake.

In order to further illustrate the morphology and microstructure of pure BFO NFs and $Au_{1.2}$-BFO NFs, TEM technology is used. As shown in **Figure 4A**, the pure BFO sample is nanofibrous structure compactly packed with nanoparticles. The HRTEM image in **Figure 4D** is collected from the square area in **Figure 4A**. The interplanar spacing of 0.278 nm corresponds to the (110) lattice plane of the rhombohedral perovskite BFO structure. **Figure 4B** shows the TEM image

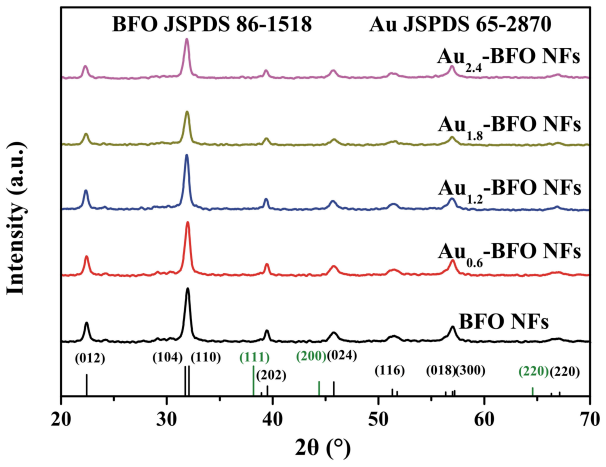

FIGURE 1 | XRD patterns of Au_x-BFO NFs ($x = 0$, 0.6, 1.2, 1.8, 2.4 wt%).

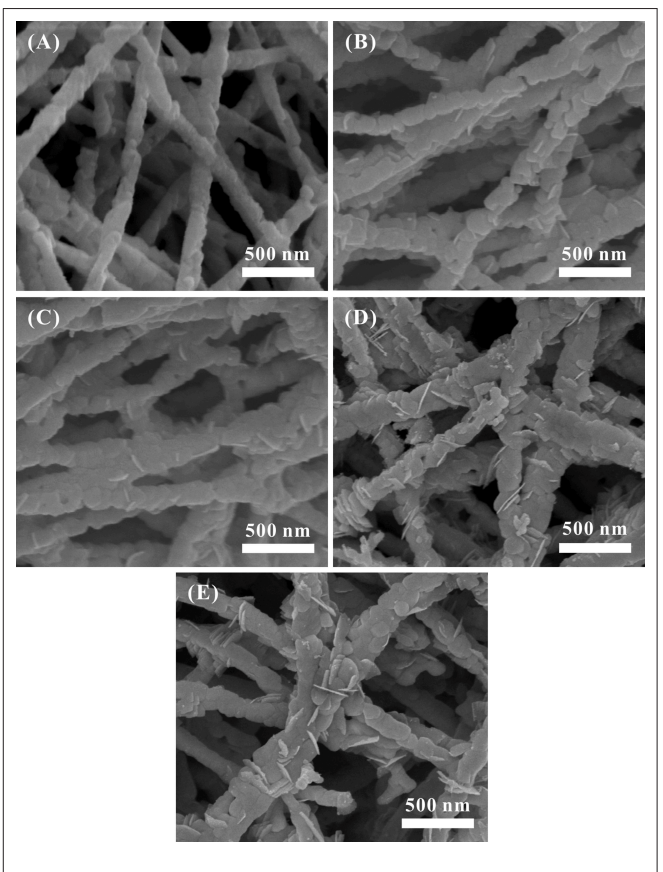

FIGURE 2 | SEM images of Au_x-BFO NFs: **(A)** $x = 0$ wt%, **(B)** $x = 0.6$ wt%, **(C)** $x = 1.2$ wt%, **(D)** $x = 1.8$ wt%, **(E)** $x = 2.4$ wt%.

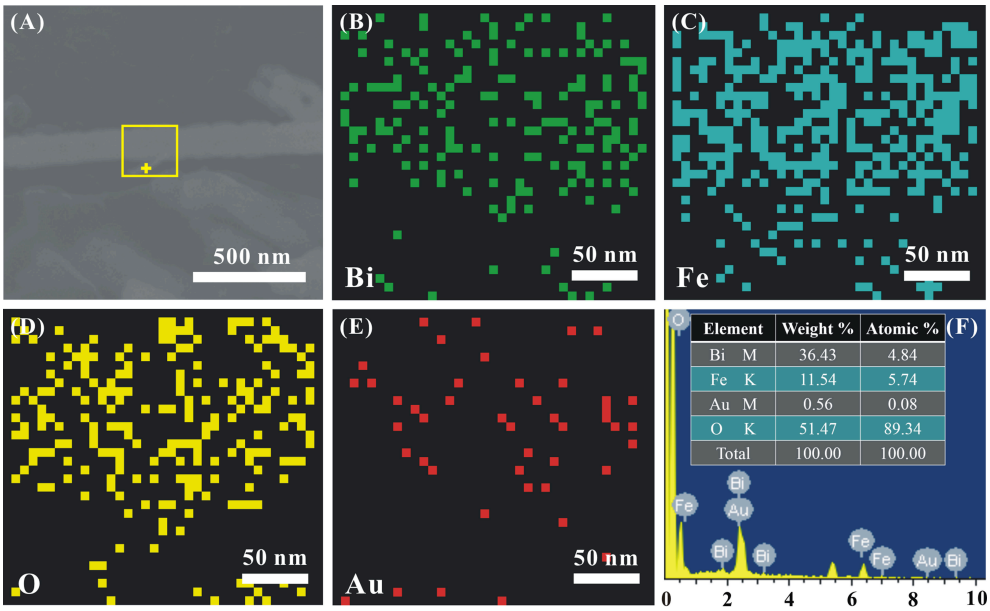

FIGURE 3 | (A) The SEM image of a single representative $Au_{1.2}$-BFO NFs, the corresponding elemental mappings of **(B)** Bi, **(C)** Fe, **(D)** O, **(E)** Au elements, and **(F)** EDS pattern.

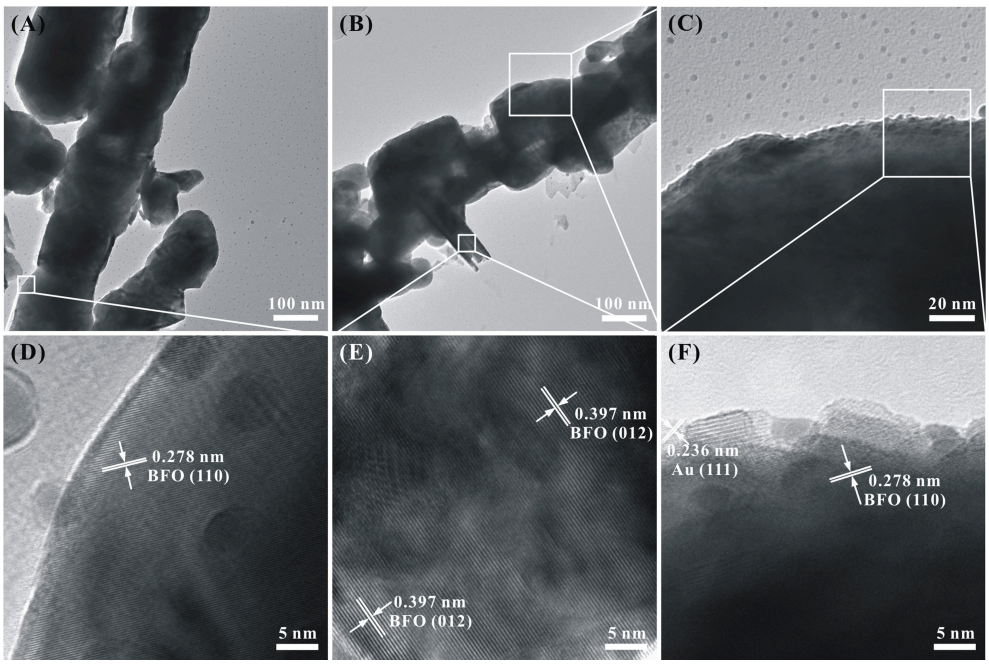

FIGURE 4 | TEM and HRTEM images of **(A,D)** pure BFO NFs and **(B,C,E,F)** $Au_{1.2}$-BFO NFs.

of $Au_{1.2}$-BFO NFs. It can be seen that the morphology is still the nanofibous structure. However, the surface of the nanofiber becomes rougher and the composed nanoparticles appear to be more prominent after depositing the Au NPs on the surface of BFO NFs. Furthermore, new nanoflake-like structures are formed and embedded in the BFO NFs. In order to confirm the structure of nanoflakes, the HRTEM is used, and the result of which is shown in **Figure 4E**. The interplanar spacing of 0.397 nm is ascribed to the (012) lattice plane of the rhombohedral perovskite BFO structure, further implying that the new formed nanoflake-like structure is indeed BFO phase. Therefore, homojunctions will be formed between BFO NFs

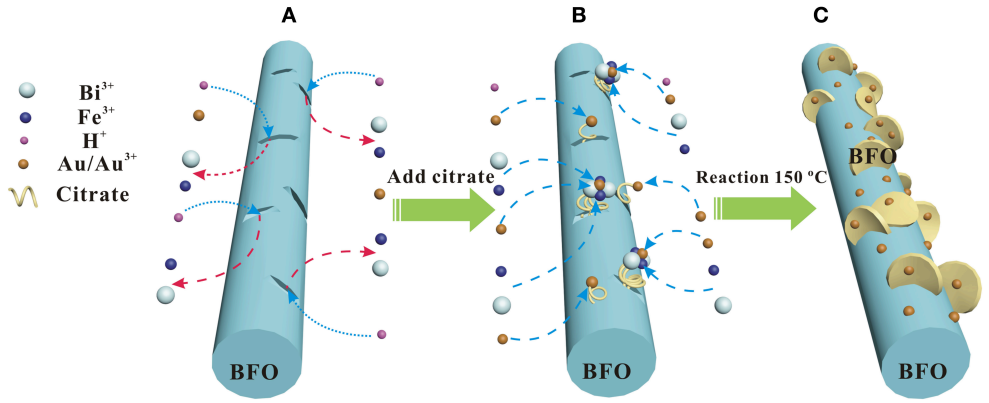

FIGURE 5 | Scheme of the possible formation mechanism of Au NPs deposited hierarchical nanofibers/nanoflakes structured BiFeO3 homojunction: **(A)** the BiFeO3 dissolution process, **(B)** metal-chelate complexes formation process, **(C)** Au NPs and nanoflake-like BiFeO3 structure formation process.

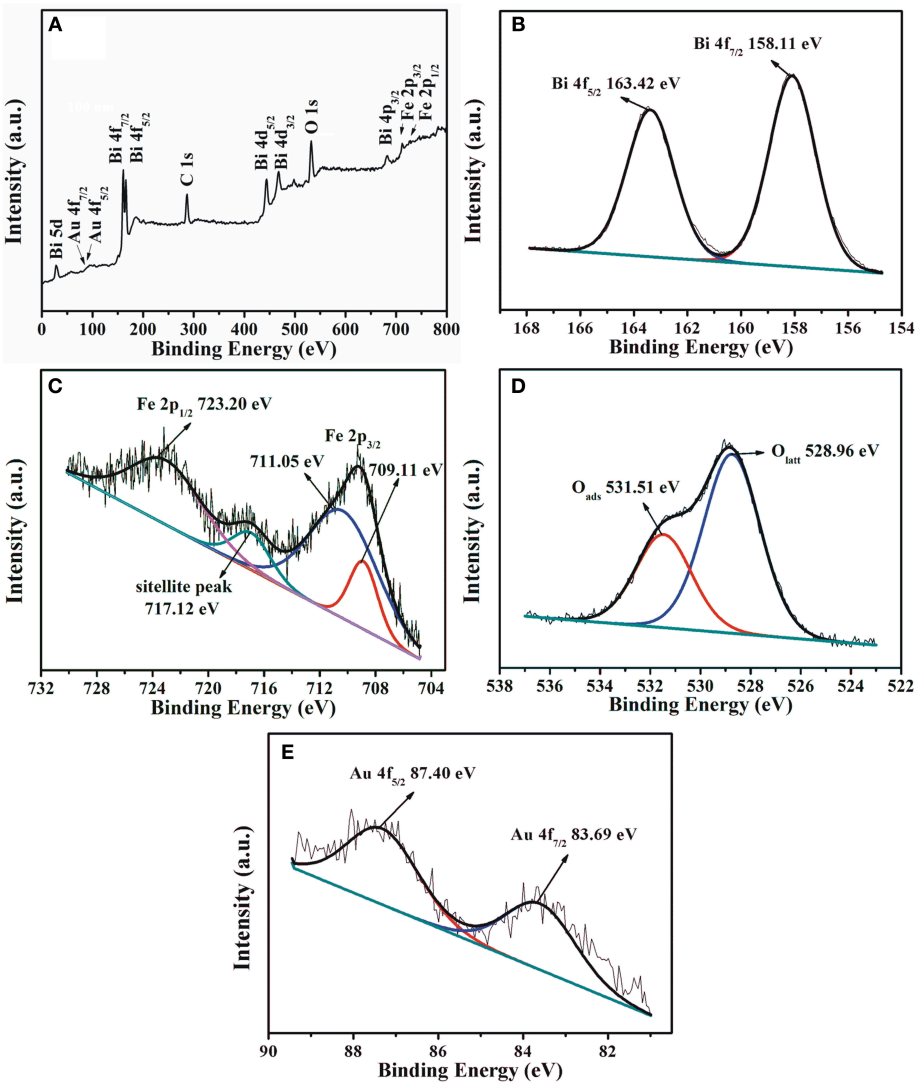

FIGURE 6 | XPS patterns of the $Au_{1.2}$-BFO NFs: **(A)** overall XPS survey, **(B)** Bi 4f, **(C)** Fe 2p, **(D)** O 1s, and **(E)** Au 4f.

and BFO nanoflakes. From **Figure 4B**, there is no obvious Au NPs deposited on the BFO surface. In order to clearly observe the deposited Au NPs, the magnified TEM image is shown in **Figure 4C**. It can be seen that Au NPs with the size of about 5 nm are indeed deposited uniformly on the BFO surface. The according HRTEM image is shown in **Figure 4F**. The interplanar spacing of 0.236 nm matches well with the (111) lattice plane of the cubic Au structure (Wang P. et al., 2017).

The possible formation mechanism of the Au NPs deposited hierarchical nanofibers/nanoflakes structured BFO homojunction is proposed in **Figure 5**. Firstly, the $HAuCl_4$ is decomposed to $AuCl_3$ and HCl in the aqueous solution. $BiFeO_3$, being regarded as the product of a combination of Bi_2O_3 and Fe_2O_3, is soluble in the weak acidic environment (Sakar et al., 2013). Therefore, the generated HCl can decompose the $BiFeO_3$ to generate Bi^{3+} and Fe^{3+} ions in the solution (**Figure 5A**). In particular, the decomposition reaction prefers to occur at the defects on the surface of BFO NFs where the higher surface energy have. The defects may be generated during the oxidation decomposition of organic material (PVP) under the high calcination temperature. Secondly, the citrate present in the solution can act as a chelating agent to react with Bi^{3+}, Fe^{3+}, and Au^{3+} ions to form stable metal-chelate complexes (**Figure 5B**). In addition, due to the presence of defects, the citrate can anchor on the surface of BFO NFs (Mudunkotuwa and Grassian, 2010). Finally, the uniform Au NPs and nanoflake-like BFO structure are formed on the surface of BFO NFs under the effect of the citric acid in the analogous hydrothermal environment (**Figure 5C**). With the increase of the $HAuCl_4$ content (the increase of the loading amount of Au NPs), more Bi^{3+} and Fe^{3+} ions pass from the defects on the surface of BFO NFs to the solution, and more nanoflake-like BFO structure are formed.

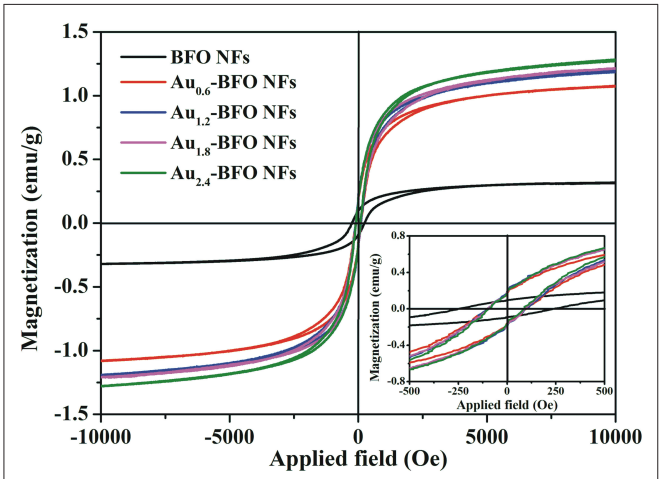

FIGURE 7 | *M–H* hysteresis loops of Au_x-BFO NFs (x = 0, 0.6, 1.2, 1.8, 2.4 wt%) measured at room-temperature; the inset shows the partially magnified curves.

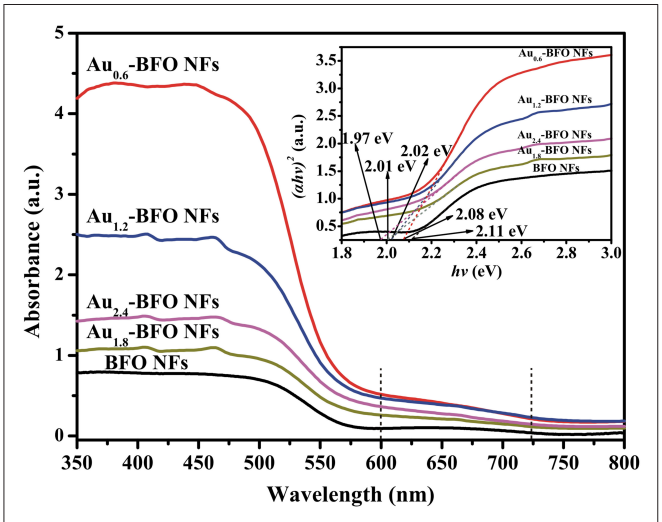

FIGURE 8 | UV–vis DRS spectra of Au_x-BFO NFs (x = 0, 0.6, 1.2, 1.8, 2.4 wt%); the inset shows the corresponding band gap energies.

XPS Analysis

The chemical state and elemental composition of $Au_{1.2}$-BFO NFs are analyzed by XPS technology. According to the overall XPS survey (**Figure 6A**), only Bi, Fe, O, Au, and C elements can be detected in the sample. The peak of C 1s located at 284.5 eV is used for calibration (Dou et al., 2015; Chen et al., 2016). As shown in **Figure 6B**, the two peaks centered at around 158.11 eV and 163.42 eV can be assigned to the binding energy of Bi $4f_{7/2}$ and Bi $4f_{5/2}$, respectively. It is confirmed that the bismuth species in $Au_{1.2}$-BFO NFs is the oxidation state of +3. From the high resolution XPS spectra of Fe 2p in **Figure 6C**, the three peaks located at 710.79, 717.12, and 723.20 eV can be ascribed to the Fe $2p_{3/2}$, satellite, and Fe $2p_{1/2}$ peaks, respectively. In addition, the Fe $2p_{3/2}$ peak can be fitted into two peaks located at 711.05 and 709.11 eV, which are attributed to Fe^{3+} and Fe^{2+} species, respectively (Wu et al., 2016). The presence of Fe^{2+} species may come from the reduction of Fe^{3+} species by citric acid under high temperature environment. In order to meet

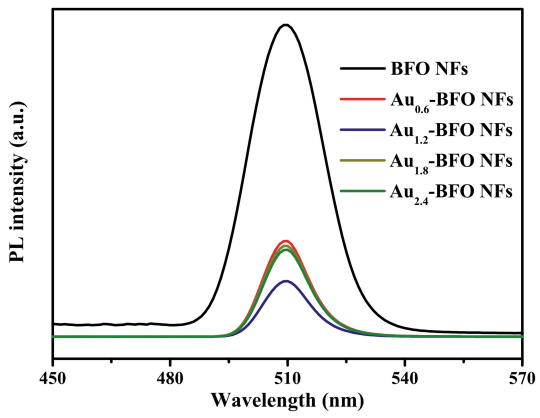

FIGURE 9 | PL spectra of Au_x-BFO NFs (x = 0, 0.6, 1.2, 1.8, 2.4 wt%) at the excitation wavelength of 230 nm.

the requirement of charge equilibrium, oxygen vacancy should be formed accompanied by the Fe^{2+} species. The O 1s curve in **Figure 6D** can be splitted into two peaks with Lorentzian-Gaussian function. The peaks at 531.51 and 528.96 eV can be ascribed to the surface adsorbed oxygen (O_{ads}) and lattice oxygen (O_{latt}) species, respectively (Bharathkumar et al., 2016; Chen et al., 2016). The O_{ads} species may originate from the –OH groups bonded to the metal cations in the oxygen defcient region (Guo et al., 2016; Sun et al., 2017), which can be converted to oxygen-related free radicals to participate in the photocatalytic reaction. Moreover, the more O_{ads} species usually mean the more oxygen vacancies it possesses, and also the better photocatalytic activity. From **Figure 6E**, the binding energies of 83.69 eV and 87.40 eV are ascribed to the Au $4f_{7/2}$ and Au $4f_{5/2}$ peaks, respectively, indicating that the gold is present in the form of metallic gold (Au^0) in the $Au_{1.2}$-BFO NFs. This can be ascribed to the reduction by citric acid under high temperature environment. Therefore, the metallic gold have been successfully deposited on the surface of BFO NFs. Whereas, the binding energies of Au 4f in the $Au_{1.2}$-BFO NFs are 0.3 eV below the standard binding energy of a metallic gold foil (Jovic et al., 2013), indicating the existence of electron transfer from BFO NFs to Au NPs for the different Fermi levels (Li S. et al., 2013). In addition, the loading amount of Au NPs is measured to be 1.14%, almost equal to the theoretical value of 1.2%.

Ferromagnetism Analysis

In order to investigate the effect of Au on the magnetic property of Au_x-BFO NFs, the room-temperature magnetic hysteresis (*M-H*) loops are shown in **Figure 7**. It can be seen that all BFO NFs exhibit the weak-ferromagnetic (FM) characters, which is due to the suppressed cycloidal spin structure and the coexistence of Fe^{3+} and Fe^{2+}, thereby resulting in the FM spins in the system (Xu et al., 2014; Modak et al., 2016). The pure BFO NFs show the saturation magnetization (*Ms*) value of 0.32 emu/g. When Au NPs are deposited on the surface of BFO NFs, the *Ms* value is enhanced with the increase in the loading amount of Au NPs. The *Ms* values are 1.07, 1.19, 1.22, and 1.27 emu/g for BFO NFs with the loading amount of Au NPs of $x = 0.6$, 1.2, 1.8, and 2.4 wt%, respectively. The gradually enhanced magnetic properties of Au_x-BFO NFs could be attributed to the new formed nanoflake-like structures, where the confined dimensions (15 nm) facilitate the enhancement of FM properties (Chauhan et al., 2012). In addition, the rather large magnetic moment of Au NPs explains the enhanced magnetic properties with increase in loading amount of Au NPs (Nealon et al., 2012). From the inset of **Figure 7**, an obvious off-center displacement in magnetic field axis is shown in the *M–H* curves. This can be ascribed to the exchange bias (EB) effect of antiferromagnet (AFM) - FM ordering in BFO NFs, where the AFM-core/FM-shell-like structure can be formed in the well-defined 1D structure (Sakar et al., 2016). Compared to that of the pure BFO NFs, the off-center displacement of Au_x-BFO NFs is relatively less pronounced, which is ascribed to the enhanced FM spins caused by the emergence of nanoflake-like structures.

Optical Properties

Figure 8 shows the UV-vis DRS spectra of Au_x-BFO NFs ($x = 0$, 0.6, 1.2, 1.8, 2.4 wt%) samples. It can be seen that the pure BFO NFs exhibit excellent absorption in both UV and visible light region. The absorption edge located at 575 nm is due to the bandgap transition. When the Au NPs are deposited on the surface of BFO NFs, the optical properties are obviously enhanced. In addition, the Au_x-BFO NFs exhibit a weak absorption peak in the range of 600∼725 nm, which are attributed to the SPR effect of Au NPs (Villa et al., 2016; Wang P. et al., 2017). The enhanced absorption in visible light is in favor of boosting the photocatalytic activity. Moreover, the band gap energies can be calculated from the plots of the $(\alpha h\nu)^2$ vs. the photon energy ($h\nu$) (Xu et al., 2015; Singh et al., 2018), the

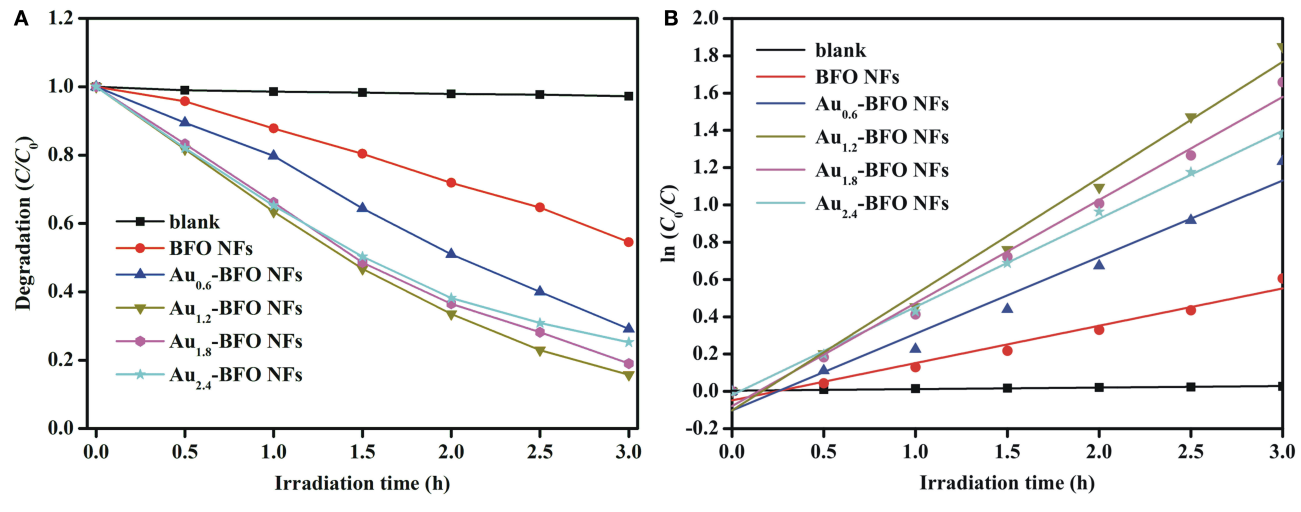

FIGURE 10 | (A) Photocatalytic degradation efficiencies of Au_x-BFO NFs ($x = 0$, 0.6, 1.2, 1.8, 2.4 wt%) on the degradation of MB dye under simulated solar light irradiation, and **(B)** kinetic linear simulation curves of MB photocatalytic degradation with Au_x-BFO NFs ($x = 0$, 0.6, 1.2, 1.8, 2.4 wt%).

results of which are shown in the inset of **Figure 8**. The band gap energies are calculated to be 2.11, 2.08, 2.02, 2.01, and 1.97 eV for the $x = 0$, 0.6, 1.2, 1.8, 2.4 wt%, respectively. It is obvious that the band gap energies decrease slightly with the increase in the loading amount of Au NPs. The possible reason is that the deposited Au NPs can produce some lower energy levels due to the formed Schottky junction at the interface between Au NPs and BFO NFs (Papadas et al., 2015).

PL Analysis

Photoluminescence (PL) spectra are extensively used to study the transfer and separation of photogenerated electron-hole pairs in the semiconductor material. The peak intensity can reflect the capture, migration and transfer efficiency of photogenerated electron-hole pairs. The lower PL intensity usually means the lower recombination rate of photogenerated electron-hole pairs, and also the higher photocatalytic activity (Tang et al., 2018). It can be seen from **Figure 9** that the PL intensity decreases obviously once the Au NPs are loaded on the surface of BFO NFs. Significantly, the PL intensity of $Au_{1.2}$-BFO NFs is the lowest. This indicates that the deposition of Au NPs on the surface of BFO NFs can efficiently inhibit the recombination of photogenerated charge carriers, which may be attributed to that the Schottky junction formed between Au NPs and BFO NFs can efficiently promote electron transfer from BFO NFs to Au NPs, and thus decreased the recombination rate of photogenerated charge carriers (Li S. et al., 2013). However, the PL intensity increases when the loading amount of Au NPs is too much. This can be ascribed to the fact that the excess amount of Au NPs can result in an increase of surface defects, which can act as recombination centers for photogenerated charge carriers, thus leading to the increase in the recombination rate. Therefore, it is necessary to deposit an appropriate amount of Au NPs on the surface of BFO NFs to promote the efficient separation of photogenerated electron-hole pairs, thus enhancing the photocatalytic activity.

Photocatalytic Activities

Figure 10A shows the photocatalytic degradation efficiencies of Au_x-BFO NFs ($x = 0$, 0.6, 1.2, 1.8, 2.4 wt%) on the degradation of MB dye under simulated solar light irradiation. For contrast, the blank experiment without any photocatalyst is carried out under the same conditions. The result shows that the MB dye is hardly degraded under simulated solar light irradiation. The degradation efficiency is only 2.77% after irradiation of 3 h. When the pure BFO sample is added to the reaction system, the degradation efficiency reaches to be 49.49% after irradiation of 3 h. However, the photocatalytic activity is still relatively poor. Once Au NPs are deposited on the surface of BFO NFs, the photocatalytic activities of Au_x-BFO NFs are obviously enhanced. The enhanced activities can be ascribed to the hierarchical nanofibers/nanoflakes structured homojunction, the SPR effect of Au NPs, as well as the presence of defects (Fe^{2+}/Fe^{3+} pairs and oxygen vacancy). In addition, the photocatalytic activity is increased and then suppressed with the increase in the loading amount of Au NPs. When the loading amount of Au NPs is 1.2%, the photocatalytic activity is the best with the photocatalytic efficiency of 85.76% after irradiation of 3 h.

To evaluate the reaction kinetics of the degradation of MB, the plot of $\ln(C_0/C)$ vs. time is plotted in **Figure 10B**, which shows the kinetics of the degradation process by the five photocatalysts which follow Langmuir-Hinshelwood pseudo first-order kineticsequation, $\ln(C_0/C) = kt$, where t is the irradiation time and k is the rate constant (Niu et al., 2015). The observed calculated rate constants k in the presence of blank sample, Au_x-BFO NFs ($x = 0$, 0.6, 1.2, 1.8, 2.4 wt%) are 8.28×10^{-3}, 200.23×10^{-3}, 411.46×10^{-3}, 623.27×10^{-3}, 552.85×10^{-3}, and 472.69×10^{-3} h^{-1}, respectively. which also indicates that the $Au_{1.2}$-BFO NFs sample exhibits the strongest photocatalytic activity among the Au_x-BFO NFs ($x = 0$, 0.6, 1.8, 2.4 wt%) samples.

In order to evaluate the stability of photocatalysts, the recycle experiment is carried out. After each recycle, the photocatalysts

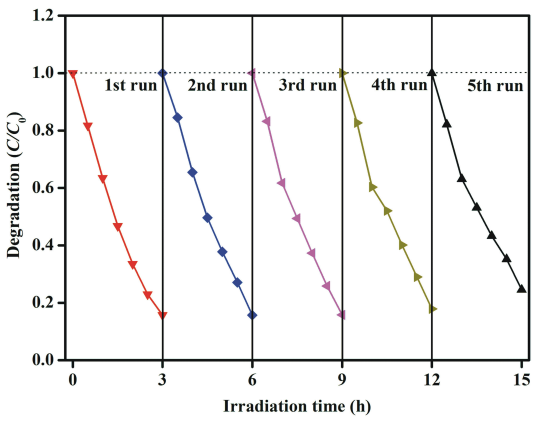

FIGURE 11 | Stability evaluation for the photocatalytic degradation of MB dye in the presence of $Au_{1.2}$-BFO NFs under simulated solar light irradiation.

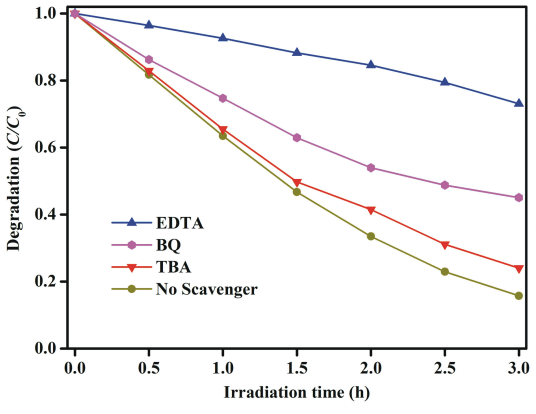

FIGURE 12 | Active species trapping experiments of photocatalytic degradation of MB dye over the $Au_{1.2}$-BFO NFs under simulated solar light irradiation with the addition of EDTA, TBA, and BQ quenchers.

are collected by simple filtration and washed with deionized water and absolute ethanol. As shown in **Figure 11**, there is no obvious loss in photocatalytic activity after five recycle test, indicating that Au_x-BFO NFs photocatalysts have good stability during the photocatalytic degradation of MB dye under simulated solar light irradiation.

In order to explore the possible reaction pathways during the photocatalytic degradation of MB dye under simulated solar light irradiation, the trapping experiments are used to determine the main active species in this reaction system. Ethylenediaminetetraacetic acid (EDTA), tertbutyl alcohol (TBA) and benzoquinone (BQ) are used as scavengers for holes (h^+), hydroxyl radicals (•OH), and superoxide radicals ($\bullet O_2^-$), respectively (Chen et al., 2016; Qiao et al., 2017; Ji et al., 2018). As can be seen from **Figure 12**, when the TBA or BQ is added, a slight reduction in MB degradation efficiency is occurred in comparison to the initial activity without addition of any scavengers, which means that $\bullet O_2^-$ and •OH radicals are not the main active species. However, the photocatalytic activity is severely suppressed when EDTA is added to the reaction system, implying that photogenerated holes are the main active species and play the decisive role in the photocatalytic activity.

Photocatalytic Mechanism

On the basis of the aforementioned experimental and active species trapping results, the possible enhanced photocatalytic mechanism is illustrated in **Figure 13**. It can be ascribed to the following aspects: (1) Nanofibers/nanoflakes structured homojunction. It is well-known that nanoflakes with ultrathin structure possess higher valence band (VB) energy than that of nanofibers with larger particle size (Weng et al., 2014). After forming homojunctions between BFO NFs and BFO nanoflakes, the staggered band potentials would introduce a new internal electrical field to provide a driving force to reduce the charge transfer barrier. The formed homojunction can promote the transfer of photogenerated holes (h^+) from the VB of BFO NFs to the VB of BFO nanoflakes, whereas photogenerated electrons (e^-) from the conduction band (CB) of BFO nanoflakes to that of BFO NFs. (2) SPR effect of Au NPs. The enhanced local electric field in the near-surface region of BFO induced by the SPR effect of Au NPs results in the further separation of photogenerated electrons and holes. The photogenerated electrons are thermodynamically favorable to transfer from the CB of BFO to Au NPs due to the Fermi energy of Au NPs is more positive than the CB potential of BFO (Li S. et al., 2013). The formed Schottky junction at the interfaces can act as trapping centers for photogenerated electrons, contributing the accumulation of photogenerated electrons at the surface of Au NPs and preventing the recombination of photogenerated electron-hole pairs. (3) Defects. The presence of Fe^{2+}/Fe^{3+} pairs located below the CB of BFO can act as electron/hole trapping centers and thus reduce the recombination rate (Zhang et al., 2014; Verma and Kotnala, 2016). In addition, the oxygen vacancy can introduce the defect state energy level and effectively regulate the band structure, thus significantly improve the separation of photogenerated charge carriers (Zhang C. et al., 2016). Under the effect of these aspects, the photocatalytic activities are remarkably enhanced.

During the process of photocatalytic reaction, a few photogenerated electrons in the CB of BFO nanoflakes can

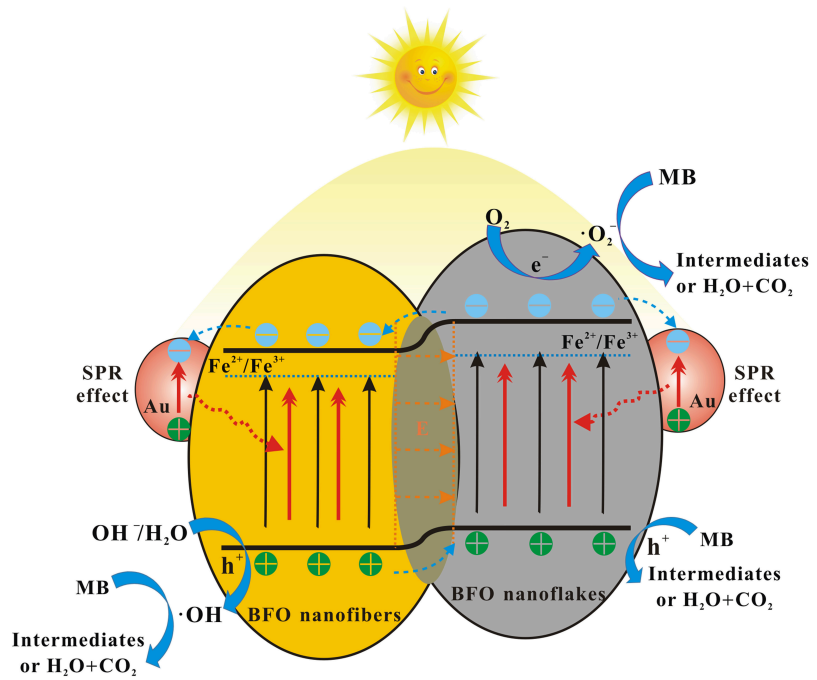

FIGURE 13 | The possible enhanced photocatalytic mechanism for the degradation of MB dye over Au_x-BFO NFs under simulated solar light irradiation.

react with oxygen molecules adsorbed on the surface to form superoxide radicals ($\bullet O_2^-$). The photogenerated electrons transferred to the Au NPs can react with Fe^{2+}/Fe^{3+} pairs and oxygen vacancy defects. Meanwhile, a little part of photogenerated holes in the VB of BFO NFs can oxidize the absorbed OH^- and H_2O to hydroxyl radicals ($\bullet$OH) (Dong et al., 2016; Hu et al., 2017). Finally, the photogenerated holes transferred the VB of BFO nanoflakes as well as the formed $\bullet O_2^-$ and $\bullet$OH species can oxidation decomposition of MB dye molecules.

CONCLUSIONS

Novel Au-induced hierarchical nanofibers/nanoflakes structured BFO homojunction (Au_x-BFO, x=0, 0.6, 1.2, 1.8, 2.4 wt%) were *in situ* synthesized by a simple reduction method under the analogous hydrothermal environment. The deposited Au NPs were distributed uniformly on the surface of BFO sample. The formed BFO nanoflakes were vertically assembled on BFO nanofibers to form a hierarchical architecture. The photocatalytic results showed that $Au_{1.2}$-BFO NFs samples exhibited the best photocatalytic activity with the photocatalytic efficiency of 85.76% after irradiation of 3 h. The remarkable enhanced photocatalytic activity could be mainly attributed to the hierarchical nanofibers/nanoflakes structured homojunction, the SPR effect of Au NPs, as well as the presence of defects (Fe^{2+}/Fe^{3+} pairs and oxygen vacancy). This work provided a novel method to design efficient homojunctions with multiple functions in solar energy utilization.

AUTHOR CONTRIBUTIONS

YL synthesized Au_x-BFO NFs samples and analyzed part of characterizations. JL is the supervisor of this research work. LC and HS helped writing. HZ analyzed Ferromagnetism measurements. HG and LF performed SEM, EDS, and TEM imaging and analyses. All authors have contributed to preparing the review article.

FUNDING

This work was supported by the National Natural Science Foundation of China (Grant No. 51702189), the Shandong Provincial Natural Science Foundation, China (Grant No. ZR2017BEM033), and Science & Technology Plan of the Education Department of Shandong Province (grant No. J18KA002).

REFERENCES

Ahmada, S., Khanb, M. A., Sarfrazc, M., Rehmana, A. U., Farooqwarsia, M., and Shakirc, I. (2017). The impact of Yb and Co on structural, magnetic, electrical and photocatalytic behavior of nanocrystalline multiferroic $BiFeO_3$ particles. *Ceram. Int.* 43, 16880–16887. doi: 10.1016/j.ceramint.2017.09.088

Bharathkumar, S., Sakar, M., and Balakumar, S. (2016). Experimental evidence for the carrier transportation enhanced visible light driven photocatalytic process in bismuth ferrite ($BiFeO_3$) one-dimensional fiber nanostructures. *J. Phys. Chem. C* 120, 18811–18821. doi: 10.1021/acs.jpcc.6b04344

Chauhan, S., Kumar, M., Chhoker, S., Katyal, S. C., Singh, H., Jewariya, M., et al. (2012). Multiferroic, magnetoelectric and optical properties of Mn doped $BiFeO_3$ nanoparticles. *Solid State Commun.* 152, 525–529. doi: 10.1016/j.ssc.2011.12.037

Chen, D., Niu, F., Qin, L., Wang, S., Zhang, N., and Huang, Y. (2017). Defective $BiFeO_3$ with surface oxygen vacancies: Facile synthesis and mechanism insight into photocatalytic performance. *Sol. Energ. Mat. Sol. C.* 171, 24–32. doi: 10.1016/j.solmat.2017.06.021

Chen, L., Meng, D., Wu, X., Wang, A., Wang, J., Wang, Y., et al. (2016). *In situ* synthesis of V^{4+} and Ce^{3+} self-doped $BiVO_4/CeO_2$ heterostructured nanocomposites with high surface areas and enhanced visible-light photocatalytic activity. *J. Phys. Chem. C* 120, 18548–18559. doi: 10.1021/acs.jpcc.6b04131

Chiu, Y. H., Chang, K. D., and Hsu, Y. J. (2018). Plasmon-mediated charge dynamics and photoactivity enhancement for Au-decorated ZnO nanocrystals. *J. Mater. Chem. A* 6, 4286–4296. doi: 10.1039/c7ta08543e

Dong, F., Li, P., Zhong, J., Liu, X., Zhang, Y., Cen, W., et al. (2016). Simultaneous Pd^{2+} doping and Pd metal deposition on $(BiO)_2CO_3$ microspheres for enhanced and stable visible light photocatalysis. *Appl. Catal. A Gen.* 510, 161–170. doi: 10.1016/j.apcata.2015.11.022

Dou, Y., Li, J., Cao, M., Su, D., Rehman, F., Zhang, J., et al. (2015). Oxidizing annealing effects on VO_2 films with different microstructures. *Appl. Surf. Sci.* 345, 232–237. doi: 10.1016/j.apsusc.2015.03.044

Guo, Y., Li, J., Gao, Z., Zhu, X., Liu, Y., Wei, Z., et al. (2016). A simple and effective method for fabricating novel p-n heterojunction photocatalyst g-$C_3N_4/Bi_4Ti_3O_{12}$ and its photocatalytic performances. *Appl. Catal. B Environ.* 192, 57–71. doi: 10.1016/j.apcatb.2016.03.054

Hu, X., Li, Y., Tian, J., Yang, H., and Cui, H. (2017). Highly efficient full solar spectrum (UV-vis-NIR) photocatalytic performance of Ag_2S quantum dot/TiO_2 nanobelt heterostructures. *J. Ind. Eng. Chem.* 45, 189–196. doi: 10.1016/j.jiec.2016.09.022

Huang, H., Xiao, K., Du, X., and Zhang, Y. (2017). Vertically aligned nanosheets-array-like BiOI homojunction: three-in-one promoting photocatalytic oxidation and reduction abilities. *ACS Sustain. Chem. Eng.* 5, 5253–5264. doi: 10.1021/acssuschemeng.7b00599

Humayun, M., Zada, A., Li, Z., Xie, M., Zhang, X., Qu, Y., et al. (2016). Enhanced visible-light activities of porous $BiFeO_3$ by coupling with nanocrystalline TiO_2 and mechanism. *Appl. Catal. B Environ.* 180, 219–226. doi: 10.1016/j.apcatb.2015.06.035

Huo, Y., Miao, M., Zhang, Y., Zhu, J., and Li, H. (2011). Aerosol-spraying preparation of a mesoporous hollow spherical $BiFeO_3$ visible photocatalyst with enhanced activity and durability. *Chem. Commun.* 47, 2089–2091. doi: 10.1039/c0cc04247a

Irfan, S., Li, L., Saleemi, A. S., and Nan, C. (2017). Enhanced photocatalytic activity of La^{3+} and Se^{4+} co-doped bismuth ferrite nanostructures. *J. Mater. Chem. A* 5, 11143–11151. doi: 10.1039/c7ta01847a

Ji, S., Dong, G., Luo, J., Ma, F., and Wang, C. (2018). Improved photocatalytic NO removal activity of $SrTiO_3$ by using $SrCO_3$ as a new co-catalyst. *Appl. Catal. B Environ.* 227, 24–34. doi: 10.1016/j.apcatb.2018.01.020

Jovic, V., Chen, W., Sun-Waterhouse, D. X., Blackford, M. G., Idriss, H., and Waterhouse, G. I. N. (2013). Effect of gold loading and TiO_2 support composition on the activity of Au/TiO_2 photocatalysts for H_2 production from ethanol-water mixtures. *J. Catal.* 305, 307–317. doi: 10.1016/j.jcat.2013.05.031

Li, Q., Hao, X., Guo, X., Dong, F., and Zhang, Y. (2015). Controlled deposition of Au on $(BiO)_2CO_3$ microspheres: the size and content of Au nanoparticles matter. *Dalton Trans.* 44, 8805–8811. doi: 10.1039/c5dt00844a

Li, S., Zhang, J., Kibria, M. G., Mi, Z., Chaker, M., Ma, D., et al. (2013). Remarkably enhanced photocatalytic activity of laser ablated Au nanoparticle decorated

$BiFeO_3$ nanowires under visible-light. *Chem. Commun.* 49, 5856–5858. doi: 10.1039/c3cc40363g

Li, Z., Shen, Y., Yang, C., Lei, Y., Guan, Y., Lin, Y., et al. (2013). Significant enhancement in the visible light photocatalytic properties of $BiFeO_3$-graphene nanohybrids. *J. Mater. Chem. A* 1, 823–829. doi: 10.1039/c2ta00141a

Lin, F., Shao, B., Li, Z., Zhang, J., Wang, H., Zhang, S., et al. (2017). Visible light photocatalysis over solid acid: enhanced by gold plasmonic effect. *Appl. Catal. B: Environ.* 218, 480–487. doi: 10.1016/j.apcatb.2017.06.076

Modak, P., Lahiri, D., and Sharma, S. M. (2016). Correlation between structure and ferromagnetism in Nano-$BiFeO_3$. *J. Phys. Chem. C* 120, 8411–8416. doi: 10.1021/acs.jpcc.6b02822

Mohan, S., and Subramanian, B. (2013). A strategy to fabricate bismuth ferrite ($BiFeO_3$) nanotubes from electrospun nanofibers and their solar light-driven photocatalytic properties. *RSC Adv.* 3, 23737–23744. doi: 10.1039/c3ra44085k

Mudunkotuwa, I. A., and Grassian, V. H. (2010). Citric acid adsorption on TiO_2 nanoparticles in aqueous suspensions at acidic and circumneutral pH: surface coverage, surface speciation, and its impact on nanoparticle-nanoparticle interactions. *J. Am. Chem. Soc.* 132, 14986–14994. doi: 10.1021/ja106091q

Nealon, G. L., Donnio, B., Greget, R., Kappler, J. P., Terazzi, E., and Gallani, J. L. (2012). Magnetism in gold nanoparticles. *Nanoscale* 4, 5244–5258. doi: 10.1039/c2nr30640a

Niu, F., Chen, D., Qin, L., Gao, T., Zhang, N., Wang, S., et al. (2015). Synthesis of Pt/$BiFeO_3$ heterostructured photocatalysts for highly efficient visible-light photocatalytic performances. *Sol. Energ. Mat. Sol. C.* 143, 386–396. doi: 10.1016/j.solmat.2015.07.008

Papadas, I., Christodoulides, J. A., Kioseoglou, G., and Armatas, G. S. (2015). A high surface area ordered mesoporous $BiFeO_3$ semiconductor with efficient water oxidation activity. *J. Mater. Chem. A* 3, 1587–1593. doi: 10.1039/c4ta05272b

Qiao, Z., Yan, T., Li, W., and Huang, B. (2017). *In situ* anion exchange synthesis of In_2S_3/$In(OH)_3$ heterostructures for efficient photocatalytic degradation of MO under solar light. *New J. Chem.* 41, 3134–3142. doi: 10.1039/c6nj04119a

Sakar, M., Balakumar, S., Saravanan, P., and Jaisankar, S. N. (2013). Annealing temperature mediated physical properties of bismuth ferrite ($BiFeO_3$) nanostructures synthesized by a novel wet chemical method. *Mater. Res. Bull.* 48, 2878–2885. doi: 10.1016/j.materresbull.2013.04.008

Sakar, M., Balakumar, S., Saravanan, P., and Jaisankar, S. N. (2016). Electric field induced formation of one-dimensional bismuth ferrite ($BiFeO_3$) nanostructures in electrospinning process. *Mater. Design* 94, 487–495. doi: 10.1016/j.matdes.2016.01.029

Singh, N., Salam, Z., Subasri, A., Sivasankar, N., and Subramania, A. (2018). Development of porous TiO_2 nanofibers by solvosonication process for high performance quantum dot sensitized solar cell. *Sol. Energ. Mat. Sol. C.* 179, 417–426. doi: 10.1016/j.solmat.2018.01.042

Srivastav, S. K., and Gajbhiye, N. S. (2012). Low temperature synthesis, structural, optical and magnetic properties of bismuth ferrite nanoparticles. *J. Am. Ceram. Soc.* 95, 3678–3682. doi: 10.1111/j.1551-2916.2012.05411.x

Sun, X., Wu, J., Li, Q., Liu, Q., Qi, Y., You, L., et al. (2017). Fabrication of $BiOIO_3$ with induced oxygen vacancies for efficient separation of the electron-hole pairs. *Appl. Catal. B Environ.* 218, 80–90. doi: 10.1016/j.apcatb.2017.06.041

Tang, L., Feng, C., Deng, Y., Zeng, G., Wang, J., Liu, Y., et al. (2018). Enhanced photocatalytic activity of ternary Ag/g-C_3N_4/$NaTaO_3$ photocatalysts under wide spectrum light radiation: the high potential band protection mechanism. *Appl. Catal. B Environ.* 230, 102–114. doi: 10.1016/j.apcatb.2018.02.031

Verma, K. C., and Kotnala, R. K. (2016). Tailoring the multiferroic behavior in $BiFeO_3$ nanostructures by Pb doping. *RSC Adv.* 6, 57727–57738. doi: 10.1039/C6RA12949H

Villa, A., Dimitratos, N., Chan-Thaw, C. E., Hammond, C., Veith, G. M., Wang, D., et al. (2016). Characterisation of gold catalysts. *Chem. Soc. Rev.* 45, 4953–4994. doi: 10.1039/c5cs00350d

Wang, B., Wang, S., Gong, L., and Zhou, Z. (2012). Structural, magnetic and photocatalytic properties of Sr^{2+}-doped $BiFeO_3$ nanoparticles based on an ultrasonic irradiation assisted self-combustion method. *Ceram. Int.* 38, 6643–6649. doi: 10.1016/j.ceramint.2012.05.051

Wang, H., Liang, L., Cheng, X., Luo, Y., and Sun, S. (2017). Facile fabrication of porous ZnS and ZnO films by coaxial electrospinning for highly efficient photodegradation of organic dyes. *Photochem. Photobiol.* 94, 17–26. doi: 10.1111/php.12836

Wang, P., Lin, Z., Su, X., and Tang, Z. (2017). Application of Au based nanomaterials in analytical science. *Nano Today* 12, 64–97. doi: 10.1016/j.nantod.2016.12.009

Wang, W., Li, N., Chi, Y., Li, Y., Yan, W., Li, X., et al. (2013). Electrospinning of magnetical bismuth ferrite nanofibers with photocatalytic activity. *Ceram. Int.* 39, 3511–3518. doi: 10.1016/j.ceramint.2012.10.175

Weng, S., Fang, Z., Wang, Z., Zheng, Z., Feng, W., and Liu, P. (2014). Construction of teethlike homojunction BiOCl (001) nanosheets by selective etching and its high photocatalytic activity. *ACS Appl. Mater. Inter.* 6, 18423–18428. doi: 10.1021/am5052526

Wu, L., Sui, W., Dong, C., Zhang, C., and Jiang, C. (2016). One-dimensional $BiFeO_3$ nanotubes: preparation, characterization, improved magnetic behaviors, and prospects. *Appl. Surf. Sci.* 384, 368–375. doi: 10.1016/j.apsusc.2016.05.043

Xu, H., Wang, H., Shen, Y., Lin, Y., and Nan, C. (2014). Photocatalytic and magnetic behaviors of $BiFeO_3$ thin films deposited on different substrates. *J. Appl. Phys.* 116, 174307. doi: 10.1063/1.4901066

Xu, W., Zheng, C., Hua, H., Yang, Q., Chen, L., Xi, Y., et al. (2015). Synthesis and photoelectrochemical properties of $CdWO_4$ and CdS/$CdWO_4$ nanostructures. *Appl. Surf. Sci.* 327, 140–148. doi: 10.1016/j.apsusc.2014.11.156

Yang, R., Sun, H., Li, J., and Li, Y. (2018). Structural, magnetic and photocatalytic properties of Sr^{2+} doped $BiFeO_3$ nanofibres fabricated by electrospinning. *Ceram. Int.* 44, 14032–14035. doi: 10.1016/j.ceramint.2018.04.256

Ye, B., Han, X., Yan, M., Zhang, H., Xi, F., Dong, X., et al. (2017). Fabrication of metal-free two dimensional/two dimensional homojunction photocatalyst using various carbon nitride nanosheets as building blocks. *J. Colloid Interf. Sci.* 507, 209–216. doi: 10.1016/j.jcis.2017.08.002

Zhang, C., Li, Y., Chu, M., Rong, N., Xiao, P., and Zhang, Y. (2016). Hydrogen-treated $BiFeO_3$ nanoparticles with enhanced photoelectrochemical performance. *RSC Adv.* 6, 24760–24767. doi: 10.1039/c5ra23699a

Zhang, H., Liu, W., Wu, P., Hai, X., Guo, M., Xi, X., et al. (2014). Novel behaviors of multiferroic properties in Na-doped $BiFeO_3$ nanoparticles. *Nanoscale* 6, 10831–10838. doi: 10.1039/c4nr02557a

Zhang, Q., Sando, D., and Nagarajan, V. (2016). Chemical route derived bismuth ferrite thin films and nanomaterials. *J. Mater. Chem. C* 4, 4092–4124. doi: 10.1039/c6tc00243a

Zhang, T., Shen, Y., Qiu, Y., Liu, Y., Xiong, R., Shi, J., et al. (2017). Facial synthesis and photoreaction mechanism of $BiFeO_3$/$Bi_2Fe_4O_9$ heterojunction nanofibers. *ACS Sustain. Chem. Eng.* 5, 4630–4636. doi: 10.1021/acssuschemeng.6b03138

Zhang, X., Wang, B., Wang, X., Xiao, X., Dai, Z., Wu, W., et al. (2015). Preparation of M@$BiFeO_3$ nanocomposites (M = Ag, Au) bowl arrays with enhanced visible light photocatalytic activity. *J. Am. Ceram. Soc.* 98, 2255–2263. doi: 10.1111/jace.13543

Conflict of Interest Statement: The authors declare that the research was conducted in the absence of any commercial or financial relationships that could be construed as a potential conflict of interest.

frontiers in Chemistry

ORIGINAL RESEARCH
published: 17 October 2018
doi: 10.3389/fchem.2018.00489

Titanium Phosphate Nanoplates Modified With AgBr@Ag Nanoparticles: A Novel Heterostructured Photocatalyst With Significantly Enhanced Visible Light Responsive Activity

*Manli Ren, Jiaqiu Bao, Peifang Wang, Chao Wang and Yanhui Ao**

Key Laboratory of Integrated Regulation and Resource Development on Shallow Lakes, Ministry of Education, College of Environment, Hohai University, Nanjing, China

AgBr@Ag modified titanium phosphate composites were fabricated through a two-step approach. The prepared samples were characterized by X-ray diffraction, scanning electron microscopy, and transmission electron microscopy. The optical properties of the composites were characterized by using UV-vis diffuse reflectance spectroscopy. The photocatalytic activities of the composites were investigated on the degradation of Rhodamine B and ciprofloxacin under visible light irradiation. AgBr@Ag/titanium phosphate was determined to exhibit considerably higher photocatalytic activity than the corresponding individual components. The mechanism on the enhancement of the photocatalytic activity was proposed based on the results of photoluminescence spectra and photocurrent measurements. Furthermore, the possible photocatalytic mechanisms of organic compounds degradation were also proposed.

Keywords: heterojunction, titanium phosphate, AgBr@Ag, photocatalysis, visible light

OPEN ACCESS

Edited by:
Fan Dong,
Chongqing Technology and Business University, China

Reviewed by:
Guohong Wang,
Hubei Normal University, China
Qizhao Wang,
Northwest Normal University, China

****Correspondence:***
Yanhui Ao
andyao@hhu.edu.cn

Specialty section:
This article was submitted to Catalysis and Photocatalysis, a section of the journal Frontiers in Chemistry

Received: *17 July 2018*
Accepted: *25 September 2018*
Published: *17 October 2018*

Citation:
Ren M, Bao J, Wang P, Wang C and Ao Y (2018) Titanium Phosphate Nanoplates Modified With AgBr@Ag Nanoparticles: A Novel Heterostructured Photocatalyst With Significantly Enhanced Visible Light Responsive Activity. Front. Chem. 6:489. doi: 10.3389/fchem.2018.00489

INTRODUCTION

Environmental pollution has become a global problem due to the accelerated development of human society (Ye et al., 2012; Sun et al., 2017; Zhang et al., 2017; Li et al., 2018a; Lu et al., 2018). Therefore, it is urgent to solve this severe problem via green technology (Liu et al., 2012; Hao et al., 2016; Zou et al., 2016; Chen et al., 2018; Feng et al., 2018; Guo et al., 2018). Currently, photocatalysis technology has recieved intense attention as an efficient technology for solving the problem of environment (Fan et al., 2013; Ao et al., 2016; Wang et al., 2016; Dong et al., 2017; Hao et al., 2017). Furthermore, it is well known that composite photocatalysts always show higher activity than the corresponding single component (Ma et al., 2018; Wang et al., 2018; Zhang et al., 2018). The improved photocatalytic activity is due to the different electronic energy levels of different components, which create an internal electric field that can accelerate the separation rate of photogenerated electrons and holes, and reduce their recombination rate (Guo et al., 2017).

Recently, titanium phosphate has been widely studied for the treatment of organic compounds. Titanium phosphate [α-$Ti(HPO_4)_2 \bullet H_2O$, hereafter TP] consists of layers of titanium atoms bonding on both plane sides of the monohydrogen phosphate groups. Water molecules located in

the interlayer region to form a network of hydrogen-bonding with phosphate groups (Ekambaram et al., 2000; Guo et al., 2013; Guo and Han, 2014; Zhu et al., 2014). However, titanium phosphate can only absorb ultraviolet light (<5% of the sunlight). Furthermore, the high recombination rate of photoinduced electron-hole pairs is still exist, which would lead to lower photocatalytic activity. Thus, it is urgent to find effective ways to improve the activity of the TP.

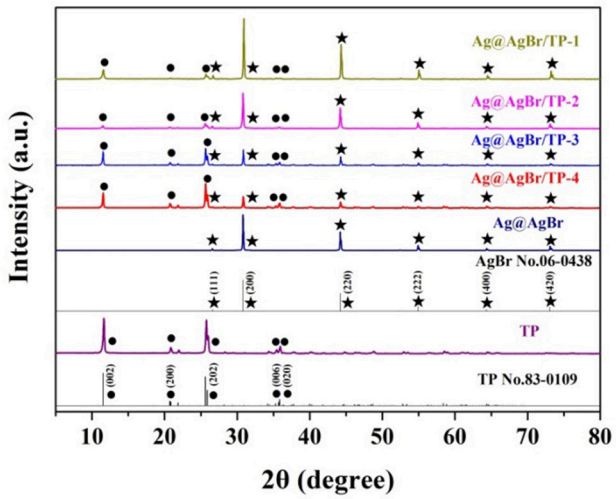

FIGURE 1 | XRD patterns of pure titanium phosphate, Ag@AgBr and Ag@AgBr/TP. The star represents AgBr.

Recently, silver halide materials have received intense attention due to their excellent visible light responsive photocatalytic activity. Silver halide@silver nanoparticles (AgNPs) based heterojunctions have been found to be excellent photocatalysts (Chen et al., 2015; Bai et al., 2016; Li et al., 2018b; Xuan et al., 2018). It has been proved that plasmon AgNPs on the surface of AgX can enhance the light absorption of the composites and accelerate the separation rate of the photogenerated charges (Daupor and Wongnawa, 2014; Li et al., 2015a,b; Ding et al., 2018; Xiao et al., 2018). Moreover, it was also considered that AgNPs decrease the recombination rate of Ag^+ with photogenerated electrons, and allow the formation of Br^0 species (photogenerated holes react with Br^- ions) that can degrade the organic compounds (Xia and Halas, 2005; Jiang et al., 2014; Zhang et al., 2015a). Therefore, it would be a good way to obtain higher visible light activated activity through the conbination of AgBr@Ag and TP.

In this work, we prepared visible light active AgBr@Ag/TP photocatalysts by a simple and feasible method. The morphology, crystal structure, optical properties, and composition of the photocatalysts were investigated. Moreover, the possible photocatalytic degradation mechanism of ciprofloxacin and the enhancement mechanism photocatalytic activity were proposed.

EXPERIMENTAL

All experimental details are shown in **Supporting Information**.

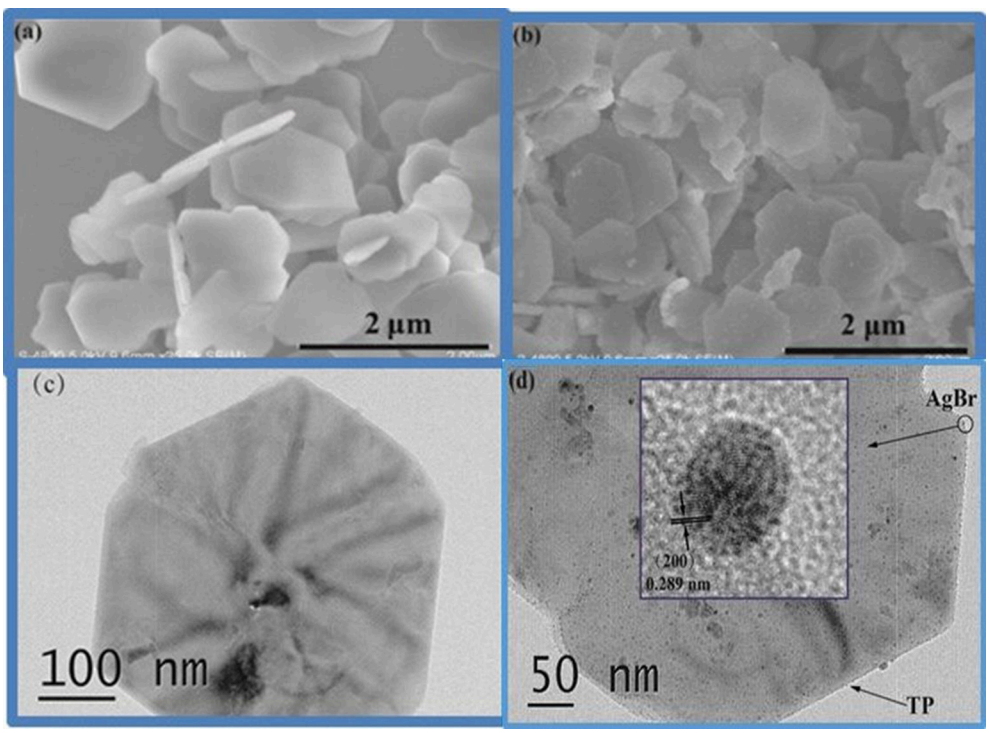

FIGURE 2 | (a) SEM image of pure titanium phosphate, **(b)** SEM image of Ag@AgBr/TP-3, **(c)** HRTEM image of pure titanium phosphate, **(d)** HRTEM image of Ag@AgBr/TP-3.

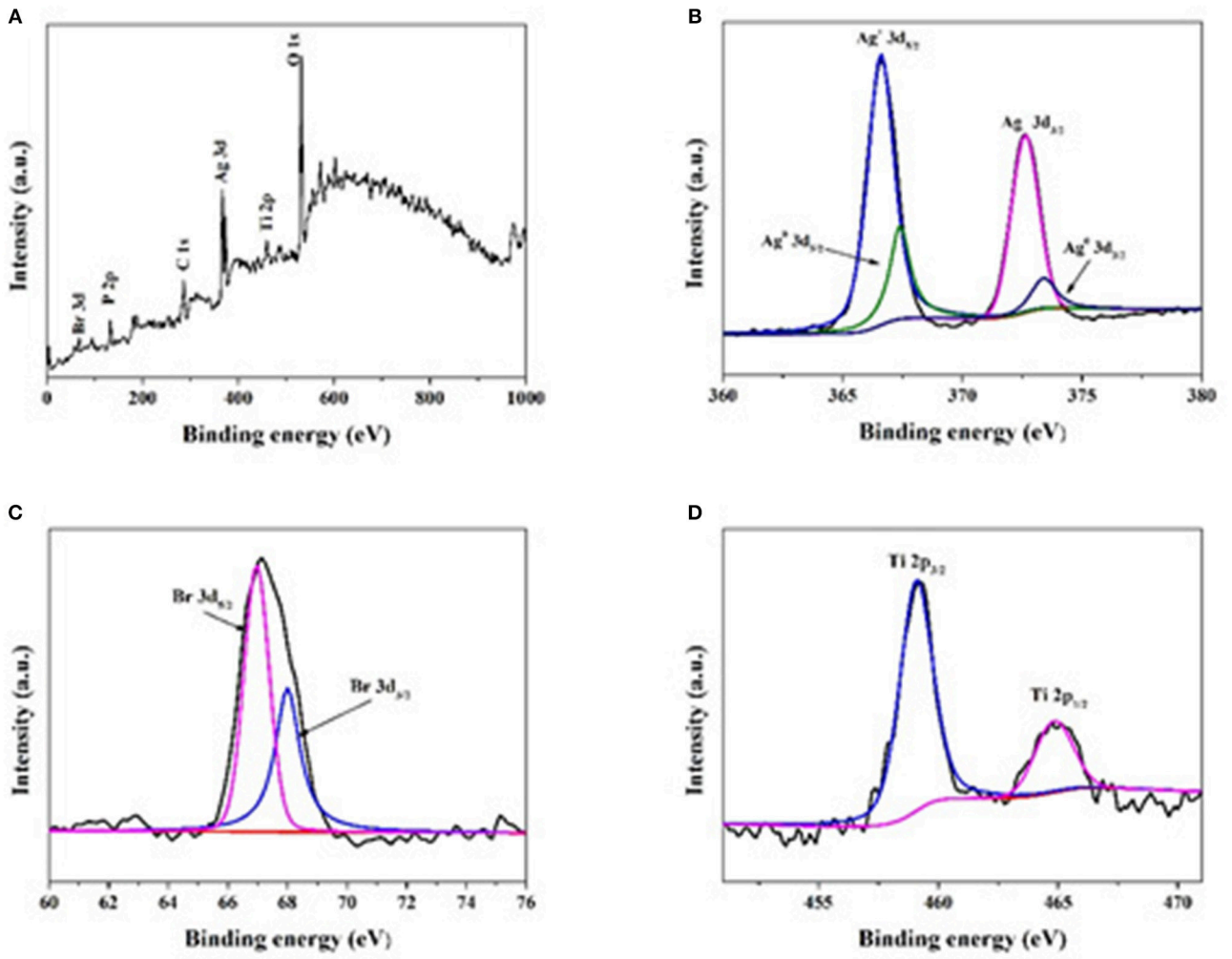

FIGURE 3 | XPS spectra of Ag@AgBr/TP-3. **(A)** The survey XPS spectrum, **(B)** Ag 3d, **(C)** Br 3d, **(D)** Ti 2p peaks related to the photocatalyst.

RESULTS AND DISCUSSION

Characterization

The phase structure was characterized by XRD, and the obtained patterns are shown in **Figure 1**. The peaks at about 11.6, 21.0, 26.0, 35.4, and 35.8° are indexed to the (002), (200), (202), (006), and (020) directions, respectively. All peaks can be ascribed to TP (JCPDS Card No: 83-0109; Ortíz-Oliveros et al., 2014; Yada et al., 2014). Diffraction peaks are also detected at 26.73, 30.96, 44.35, 55.04, 64.49, and 73.26°, which can be indexed to the (111), (200), (220), (222), (400), and (420) directions of AgBr (JCPDS Card NO: 06-0438; Chen et al., 2015; Bai et al., 2016). Furthermore, with the increasing of AgBr mass, the intensity of the characteristic peaks of AgBr increased gradually. No diffraction peaks of Ag can be observed, possibly due to its low mass, high dispersion or small size (Wang et al., 2013, 2014).

The morphologies of the composites were investigated by TEM and SEM. The obtained SEM image of pure TP is displayed in **Figure 2a**. It can be seen that the TP sample is composed

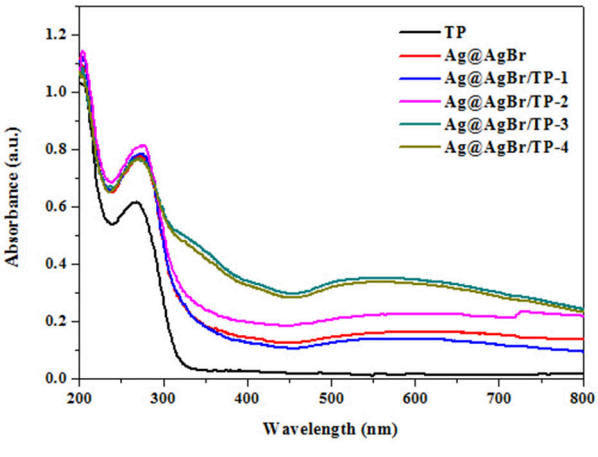

FIGURE 4 | UV-vis diffuse reflectance spectra of titanium phosphate, Ag@AgBr and Ag@AgBr/TP.

of uniform plates with sub-micrometer width and 30∼40 nm thickness. The SEM image of AgBr@Ag/TP-3 taken from **Figure 2b** displays smaller AgBr@Ag nanoparticles decorating the TP surface. The TEM image of pure TP is displayed in **Figure 2c**. It can also be seen that the titanium phosphate plate is hexagonal, which is in good agreement with the results of SEM. The TEM image of AgBr@Ag/TP is shown in **Figure 2d**. It can be seen that AgBr nanoparticles decorated the TP surface, indicating the formation of heterojunctions in the prepared samples (Cui et al., 2018). As shown in the inset of **Figure 2d**, the measured lattice spacings of 0.289 nm corresponds to the (200) lattice planes of AgBr.

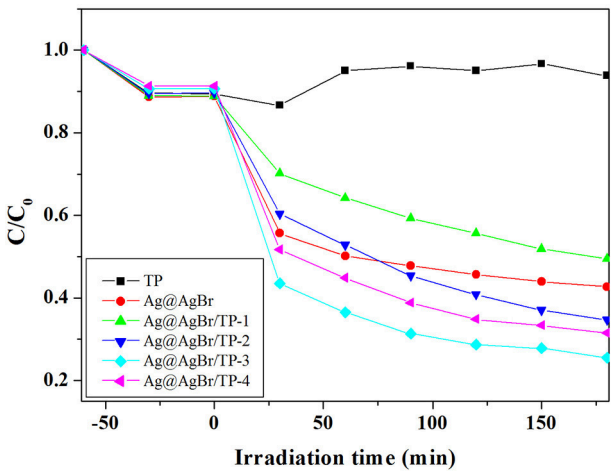

FIGURE 5 | Photocatalytic degradation of CIP over the as-prepared samples under visible light irradiation.

The elemental composition and chemical states of the elements in the composites were analyzed by XPS. The peaks of Br 3d, P 2p, Ag 3d, C 1s, Ti 2p, and O1s can be observed in **Figures 3A,B** shows the electron binding energies of Ag $3d_{5/2}$ and Ag $3d_{3/2}$ orbitals, which can be further divided into 366.6/367.4 and 372.6/373.4 eV, respectively. The peaks at 366.6 and 372.6 eV indicate the presence of Ag^{+}. Both the peak separation (6.0 eV) and peak positions (367.4 and 373.4 eV) indicate the presence of metallic form (Ag^{0}; Yang et al., 2015; Tang et al., 2017a,b). As shown in **Figure 3C**, two peaks at 68.0 and 67.0 eV corresponding to the binding energies of Br $3d_{3/2}$ and Br $3d_{5/2}$ can be found (Wang et al., 2009). All above results prove the presence of AgBr and Ag in the composite. In **Figure 3D**, the Ti peaks observed at 459.0 and

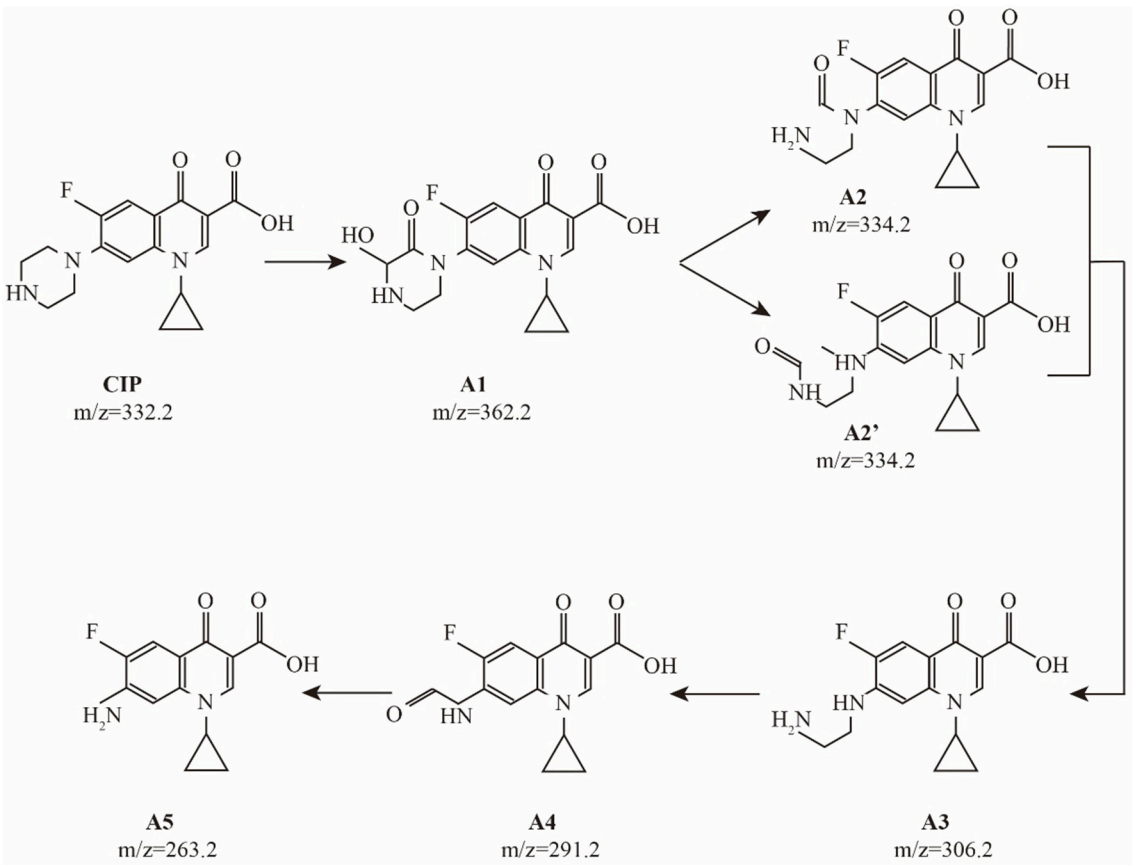

FIGURE 6 | Suggested pathways for CIP degradation.

464.8 eV can be attributed to Ti $2p_{3/2}$ and Ti $2p_{1/2}$. The peak separation of 5.8 eV for binding energy between the two peaks indicates that Ti was mainly Ti^{4+} in the composite (Yada et al., 2014).

The optical properties of photocatalysts significantly affect their photocatalytic performance (He et al., 2015). Therefore, optical properties of the composites were investigated by DRS and the obtained results are shown in **Figure 4**. Pure TP exhibited no absorption in the visible-light region, whereas the Ag@AgBr/TP composites had better absorption performance, possibly due to the deposition of AgBr and formation of AgNPs on the surface of the composites. Moreover, Ag@AgBr/TP-3 showed the highest absorption in visible light region, indicating that high absorption capability is ascribed to an optimal loading. In other words, when the loading of AgBr@Ag exceeds a critical value, the AgBr@Ag nanoparticles would agglomerate and decrease the absorption capability.

Photocatalytic Activity

To investigate the photocatalytic performance of the composites, we conducted experiments on the degradation of colorless organic pollutant (CIP) under visible light irradiation. As shown in **Figure 5**, AgBr@Ag/TP-3 displayed the highest photocatalytic activity for CIP degradation among all samples. Approximately 51.4, 44.2, 61.3, 71.5, and 65.4% of CIP was degraded in 180 min by AgBr@Ag, AgBr@Ag/TP-1, AgBr@Ag/TP-2, AgBr@Ag/TP-3, and AgBr@Ag/TP-4, respectively. Furthermore, the TP showed a low photocatalytic efficiency for CIP degradation. The degradation curve of CIP by TP exhibits a fluctuating trend. There may be some CIP molecules desorbed from the surface of TP. These results show that the Ag@AgBr/TP photocatalysts are generally effective for the degradation of colorless organic compounds.

Intermediates Analysis

Prior to the complete mineralization of CIP, there are many degradation intermediates in the photocatalytic process. The sample solution was detected by HPLC/MS during the photocatalytic degradation. Some intermediates in the photocatalytic process were identified: A1 (m/z = 362.2), A2 (m/z = 334.2), A3 (m/z = 306.2), A4 (m/z = 291.2), and A5 (m/z = 263.2). These results show that A1∼A5 are the main intermediates during the degradation process of CIP. As observed in many other oxidation system (Sturini et al., 2012), desethylene ciprofloxacin (A3) was dominant intermediate of CIP, and was formed by a net loss of C_2H_2 at the piperazinyl substituent of CIP. Prior to the formation of desethylene ciprofloxacin, two intermediates were detected. The hydroxyl keto-derivative of the piperazinyl substituent (A1) was detected to be the first oxidized intermediate on the way to the formation of A3. Apparently, the subsequent loss of CO from A1 results in the cleavage of the piperazinyl ring to form keto-derivatives A2 and A2', in which a carbonyl group remains on the N atom of aniline and alkylamine, respectively. A second loss of a CO molecule from A2 and A2' leads to the formation of desethylene ciprofloxacin (A3). The further oxidation of desethylene ciprofloxacin (A3) generated A4 with a keto group through the loss of a N atom. The decarbonylation of A4 forms aniline (A5), completely destroying the piperazinyl substituent of CIP. The probable pathways for CIP degradation are shown in **Figure 6**.

Possible Photocatalytic Mechanism

Several experiments were performed to further understand the mechanism on the enhancement of photocatalytic performance for the AgBr@Ag/TP composites. The photoluminescence (PL) spectrum was measured to investigate the recombination rate of the photogenerated electron-hole pairs. The photoluminescence spectra of the prepared samples are shown in **Figure 7**. The intensity of PL is directly proportional to the electron-hole

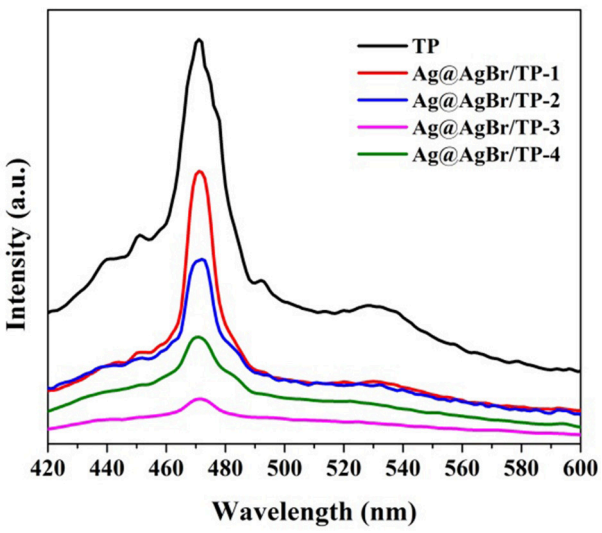

FIGURE 7 | Photoluminescence spectra of the prepared samples.

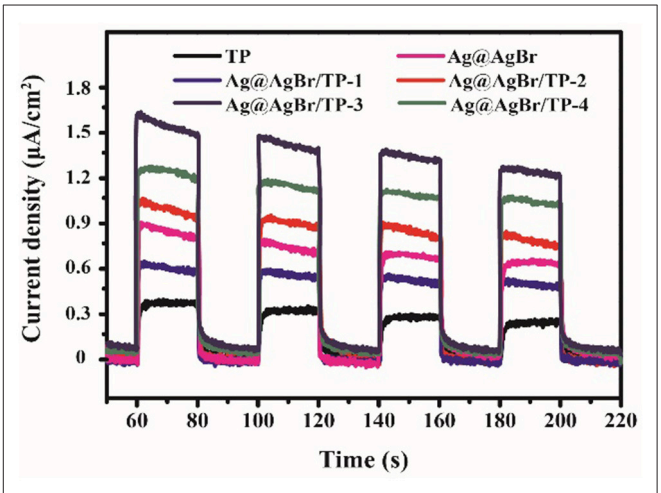

FIGURE 8 | Photocurrent of the prepared samples under visible light irradiation.

recombination rate, and lower PL intensity means lower recombination rate (Zhang et al., 2015b; Shi et al., 2016). The main emission peak of pure TP centers at ~470 nm, which was ascribed to the band gap recombination of electron-hole pairs. The PL intensity decreases significantly after the deposition of AgBr@Ag. The decreasing emission intensity of the AgBr@Ag/TP suggests that the recombination of electron-hole pairs can be suppressed after the deposition of AgBr@Ag (Xu et al., 2013). Furthermore, it can be seen that the PL intensity increase as the amount of Ag@AgBr increase to a certain value, and AgBr@Ag/TP-3 composite showed the lowest PL intensity, which means Ag@AgBr/TP-3 composite has the lowest recombination rate of photogenerated electrons-hole pairs. Therefore, it would lead to the highest photocatalytic performance. However, the PL intensity increase as the amount of Ag@AgBr increase further. It can be ascribed to the reason that superfluous Ag@AgBr nanoparticles would aggregate thus cannot form effective heterojunctions with TP. The above results demonstrate that the deposition of AgBr on TP and the formation of AgNPs on the surface of the composite can decrease the recombination efficiency and enhance the separation efficiency of the photogenerated electrons and holes.

It is well known that the efficiency of the electron-hole pairs separation significantly affects the photocatalytic performance (Jiang et al., 2011). The electrons in the valence band of photocatalysts can be activated and then transfer to the conduction band, leading to the formation of photocurrent. A higher photocurrent means higher electron-hole pairs separation rate, which induces to better photocatalytic performance (Xiang et al., 2011). **Figure 8** shows the photocurrents for different samples under 20 s intermittent visible-light irradiation with a bias of 0.3 V. The photocurrents of AgBr@Ag/TP composites are all much higher than that of TP. Moreover, AgBr@Ag/TP-3 exhibits the highest value. The results are in good agreement with the photocatalytic activity, indicating that the efficient separation of photo-induced electrons and holes results in the high photocatalytic activity.

It was demonstrated that the separation efficiency of photo-generated electrons and holes is important to the photocatalytic performance. Furthermore, the conduction band (CB) and valence band (VB) potential have a significantly effect on the separation of the photogenerated electron-hole pairs. The CB and VB potential of AgBr and TP can be obtained using Equations. (1) and (2) (Zhang et al., 2008):

$$E_{vb} = X - E_0 + 0.5E_g \quad (1)$$

$$E_{cb} = E_{vb} - E_g \quad (2)$$

where E_{vb} is the potential of VB, X is the absolute electronegativity of photocatalyst (X is 6.85 eV and 5.81 eV of TP and AgBr, respectively), E_g is the band gap energy and E_0 is the energy of free electrons (~4.5 eV). Based on these equations, the CB potential (E_{cb}) and VB potential (E_{vb}) of TP are calculated as 0.43 and 4.28 eV, while E_{cb} and E_{vb} of AgBr are calculated as 0.01 eV and 2.62 eV, respectively.

Therefore, a possible mechanism on the photocatalytic degradation of RhB by AgBr@Ag/TP under the irradiation of visible light is illustrated in **Figure 9**. The plasmon induced holes can react with Br^- and form active Br^0 atoms. The Br^0 atoms exhibit an excellent oxidation capability to oxidize organic compounds. Meanwhile, plasmon induced electrons are formed on the surface of AgNPs, part of these electrons are trapped by O_2 to produce $\bullet O_2^-$, mainly contributing to the organic compounds removal (Ye et al., 2012; Zhang and Yates, 2012; Cheng et al., 2015; Ding et al., 2018). Besides, the other electrons would transfer to the conduction band of AgBr, and then further transfer from AgBr to the conduction band of TP. Meanwhile, the h^+

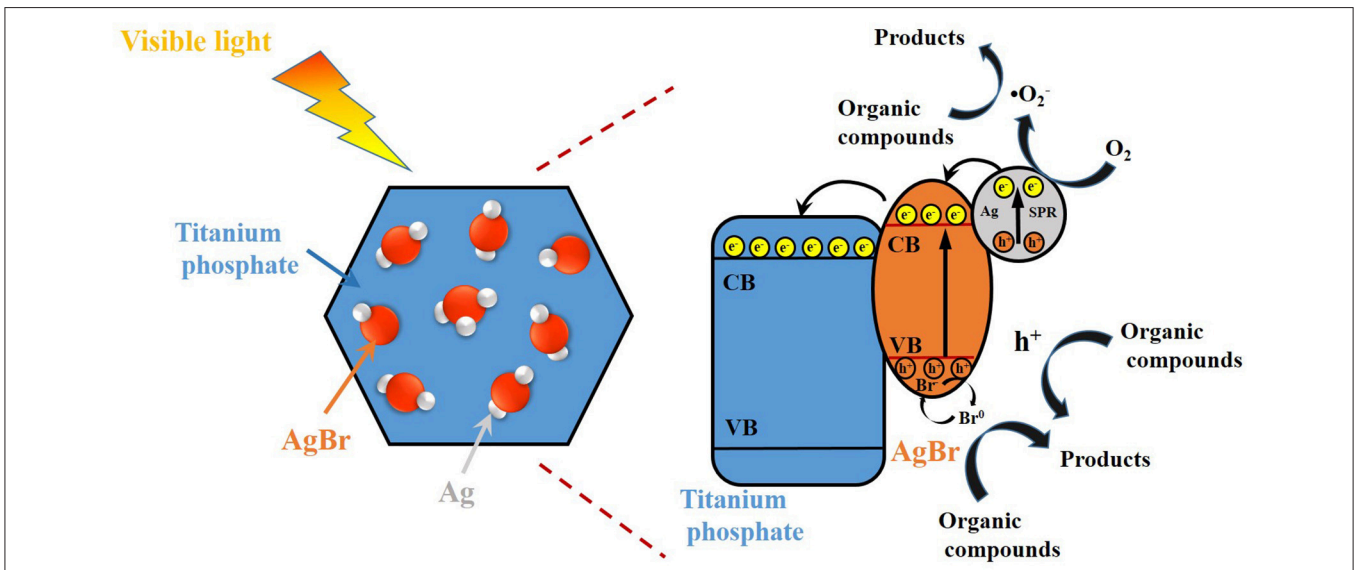

FIGURE 9 | Schematic diagram of the possible photocatalytic degradation mechanism over Ag@AgBr/TP under visible light irradiation.

stored in valence band of AgBr and TP was also involved in the organic compounds photocatalytic degradation, though they are not the dominant active species. The relevant equations are shown as following:

$$Ag + visible - light \rightarrow e^- + h^+ \quad (3)$$

$$e^- + O_2 \rightarrow \bullet O_2^- \quad (4)$$

$$h^+ + Br^- \rightarrow Br^0 \quad (5)$$

$$CIP + \bullet O_2^- (or Br^0) \rightarrow \text{degradation products} \quad (6)$$

Based on above results, the possible mechanism on the enhancement of photocatalytic activity for AgBr@Ag/TP composites can be proposed. AgBr@Ag nanoparticles deposited on TP improve the light absorption capability, as confirmed by UV-vis DRS studies. Furthermore, the heterojunctions between AgNPs, AgBr, and TP are conducive to improving the transfer rate and separation efficiency of the electron-hole pairs, and hindering the recombination of the pairs, thus inducing to the enhancement of the photocatalytic activity.

CONCLUSIONS

AgBr@Ag/TP composites exhibited higher photocatalytic performance than pure TP and AgBr@Ag, and can degrade **a typical antibiotic (CIP)** under the irradiation of visible light. The excellent photocatalytic activity can be ascribed to their enhanced visible-light absorption, low recombination and high transferring rate of the photo-generated charges, as shown by DRS, PL, and photocurrent experiments.

AUTHOR CONTRIBUTIONS

YA and CW designed the project and guided the work. MR and JB conducted the experiments and characterizations of the samples. PW revised and polished the manuscript.

ACKNOWLEDGMENTS

We are grateful for grants from National Science Funds for Creative Research Groups of China (No. 51421006), Natural Science Foundation of China (51679063), the Fundamental Research Funds for The Central Universities (2018B14514), the Key Program of National Natural Science Foundation of China (No. 91647206), the National Key Plan for Research and Development of China (2016YFC0502203), and PAPD.

SUPPLEMENTARY MATERIAL

The Supplementary Material for this article can be found online at: https://www.frontiersin.org/articles/10.3389/fchem.2018.00489/full#supplementary-material

REFERENCES

Ao, Y., Wang, K., Wang, P., Wang, C., and Hou, J. (2016). Synthesis of novel 2D-2D p-n heterojunction $BiOBr/La_2Ti_2O_7$ composite photocatalyst with enhanced photocatalytic performance under both UV and visible light irradiation. *Appl. Catal. B-Environ.* 194, 157–168. doi: 10.1016/j.apcatb.2016.04.050

Bai, Y. Y., Lu, Y., and Liu, J. K. (2016). An efficient photocatalyst for degradation of various organic dyes: Ag@ Ag_2MoO_4-AgBr composite. *J. Hazard. Mater.* 307, 26–35. doi: 10.1016/j.jhazmat.2015.12.052

Chen, D., Wang, Z., Du, Y., Yang, G., Ren, T., and Ding, H. (2015). *In situ* ionic-liquid-assisted synthesis of plasmonic photocatalyst $Ag/AgBr/g\text{-}C_3N_4$ with enhanced visible-light photocatalytic activity. *Catal. Today.* 258, 41–48. doi: 10.1016/j.cattod.2015.03.031

Chen, P., Dong, F., Ran, M., and Li, J. (2018). Synergistic photo-thermal catalytic NO purification of $MnOx/g\text{-}C_3N_4$: enhanced performance and reaction mechanism. *Chin. J. Catal.* 39, 619–629. doi: 10.1016/S1872-2067(18)63029-3

Cheng, Z., Wang, Z., Shifa, T. A., Wang, F., Zhan, X., Xu, K., et al. (2015). Au plasmonics in a WS_2-Au-$CuInS_2$ photocatalyst for significantly enhanced hydrogen generation. *Appl. Phys. Lett.* 107, 253–278. doi: 10.1063/1.4937008

Cui, X., Tian, L., Xian, X., Tang, H., and Yang, X. (2018). Solar photocatalytic water oxidation over $Ag_3PO_4/g\text{-}C_3N_4$ composite materials mediated by metallic Ag and graphene. *Appl. Surf. Sci.* 430, 108–115. doi: 10.1016/j.apsusc.2017.07.290

Daupor, H., and Wongnawa, S. (2014). Urchinlike Ag/AgCl photocatalyst: synthesis, characterization, and activity. *Appl. Catal. A-Gen.* 473, 59–69. doi: 10.1016/j.apcata.2013.12.036

Ding, K., Yu, D., Wang, W., Gao, P., and Liu, B. (2018). Fabrication of multiple hierarchical heterojunction $Ag@AgBr/BiPO_4$/r-GO with enhanced visible-light-driven photocatalytic activities towards dye degradation. *Appl. Surf. Sci.* 445, 39–49. doi: 10.1016/j.apsusc.2018.03.131

Dong, W. H., Wu, D. D., Luo, J. M., Xing, Q. J., Liu, H., Zou, J. P., et al. (2017). Coupling of photodegradation of RhB with photoreduction of CO_2 over $rGO/SrTi_{0.95}Fe_{0.05}O_{3-\delta}$ catalyst: a strategy for one-pot conversion of organic pollutants to methanol and ethanol. *J. Catal.* 349, 218–225. doi: 10.1016/j.jcat.2017.02.004

Ekambaram, S., Christian, S.erre, Gérard Férey, a. and Slavi, C., Sevov (2000). Hydrothermal synthesis and characterization of an ethylenediamine-templated mixed-valence titanium phosphate. *Chem. Mater.* 31, 444–449. doi: 10.1021/cm990492i

Fan, W., Zhang, Q., and Wang, Y. (2013). Semiconductor-based nanocomposites for photocatalytic H_2 production and CO_2 conversion. *Phys. Chem. Chem. Phys.* 15, 2632–2649. doi: 10.1039/c2cp43524a

Feng, X.Y., Wang, P.F., Hou, J., Qian, J., Wang, C., and Ao, Y. H. (2018). Oxygen vacancies and phosphorus codoped black titania coated carbon nanotube composite photocatalyst with efficient photocatalytic performance for the degradation of acetaminophen under visible light irradiation. *Chem. Engin. J.* 352: 947–956. doi: 10.1016/j.cej.2018.06.037

Guo, H., Niu, C. G., Wen, X. J., Zhang, L., Liang, C., Zhang, X. G., et al. (2017). Construction of highly efficient and stable ternary $AgBr/Ag/PbBiO_2Br$ Z-scheme photocatalyst under visible light irradiation: performance and mechanism insight. *J. Colloid Interface Sci.* 513, 852–865. doi: 10.1016/j.jcis.2017.12.010

Guo, S. Y., and Han, S. (2014). Constructing a novel hierarchical 3D flower-like nano/micro titanium phosphate with efficient hydrogen evolution from water splitting. *J. Power Sources.* 267, 9–13. doi: 10.1016/j.jpowsour.2014.05.011

Guo, S. Y., Han, S., Chi, B., Pu, J., and Li, J. (2013). Synthesis of shape-controlled mesoporous titanium phosphate nanocrystals: the hexagonal titanium phosphate with enhanced hydrogen generation from water splitting. *Int. J. Hydrogen Energy* 39, 2446–2453. doi: 10.1016/j.ijhydene.2013.12.007

Guo, Y., Wang, P., Qian, J., Ao, Y., Wang, C., and Hou, J. (2018). Phosphate group grafted twinned $BiPO_4$ with significantly enhanced photocatalytic activity:

synergistic effect of improved charge separation efficiency and redox ability. *Appl. Catal. B-Environ*. 234, 90–99. doi: 10.1016/j.apcatb.2018.04.036

Hao, R., Wang, G., Jiang, C., Tang, H., and Xu, Q. (2017). In situ hydrothermal synthesis of g-C_3N_4/TiO_2 heterojunction photocatalysts with high specific surface area for Rhodamine B degradation. *Appl. Surf. Sci*. 411, 400–410. doi: 10.1016/j.apsusc.2017.03.197

Hao, R., Wang, G., Tang, H., Sun, L., Xu, C., and Han, D. (2016). Template-free preparation of macro/mesoporous g-C_3N_4/TiO_2 heterojunction photocatalysts with enhanced visible light photocatalytic activity. *Appl. Catal. B-Environ*. 187, 47–58. doi: 10.1016/j.apcatb.2016.01.026

He, Y., Wang, Y., Zhang, L., Teng, B., and Fan, M. (2015). High-efficiency conversion of CO_2 to fuel over ZnO/g-C_3N_4 photocatalyst. *Appl. Catal. B-Environ*. 168, 1–8. doi: 10.1016/j.apcatb.2014.12.017

Jiang, J., Zhang, X., Sun, P., and Zhang, L. (2011). ZnO/BiOI heterostructures: photoinduced charge-transfer property and enhanced visible-light photocatalytic activity. *J. Phys. Chem*. 115, 20555–20564. doi: 10.1021/jp205925z

Jiang, R., Li, B., Fang, C., and Wang, J. (2014). Metal/semiconductor hybrid nanostructures for plasmon-enhanced applications. *Adv. Mater*. 26, 5274–5309. doi: 10.1002/adma.201400203

Li, S., Hu, S., Jiang, W., Liu, Y., Liu, Y., Zhou, Y., et al. (2018a). Ag_3VO_4 nanoparticles decorated $Bi_2O_2CO_3$ micro-flowers: an efficient visible-light-driven photocatalyst for the removal of toxic contaminants. *Front. Chem*. 6:255. doi: 10.3389/fchem.2018.00255

Li, S., Jiang, W., Hu, S., Liu, Y., and Liu, J. (2018b). Construction of a novel ternary Ag/AgBr/Ag_2WO_4 composite for efficient photocatalytic removal of Rhodamine B dye and tetracycline hydrochloride antibiotic. *Mater. Lett*. 224, 29–32. doi: 10.1016/j.matlet.2018.04.071

Li, W., Ma, Z., Bai, G., Hu, J., Guo, X., Dai, B., et al. (2015a). Dopamine-assisted one-step fabrication of Ag@ AgCl nanophotocatalyst with tunable morphology, composition and improved photocatalytic performance. *Appl. Catal. B-Environ*. 174, 43–48. doi: 10.1016/j.apcatb.2015.02.029

Li, X., Fang, S., Ge, L., Han, C., Qiu, P., and Liu, W. (2015b). Synthesis of flower-like Ag/AgCl-Bi_2MoO_6 plasmonic photocatalysts with enhanced visible-light photocatalytic performance. *Appl. Catal. B-Environ*. 176-177, 62–69. doi: 10.1016/j.apcatb.2015.03.042

Liu, R., Wang, P., Wang, X., Yu, H., and Yu, J. (2012). UV- and visible-light photocatalytic activity of simultaneously deposited and doped Ag/Ag(I)-TiO_2 photocatalyst. *J. Phys. Chem. C* 116, 17721–17728. doi: 10.1021/jp305774n

Lu, L., Wang, G., Zou, M., Wang, J., and Li, J. (2018). Effects of calcining temperature on formation of hierarchical TiO_2/g-C_3N_4 hybrids as an effective Z-scheme heterojunction photocatalyst. *Appl. Surf. Sci*. 441, 1012–1023. doi: 10.1016/j.apsusc.2018.02.080

Ma, L., Wang, G., Jiang, C., Bao, H., and Xu, Q. (2018). Synthesis of core-shell TiO2@g-C_3N_4 hollow microspheres for efficient photocatalytic degradation of rhodamine B under visible light. *Appl. Surf. Sci*. 430, 263–272. doi: 10.1016/j.apsusc.2017.07.282

Ortíz-Oliveros, H. B., Flores-Espinosa, R. M., Ordoñez-Regil, E., and Fernández-Valverde, S. M. (2014). Synthesis of α-Ti$(HPO_4)_2 \cdot H_2O$ and sorption of Eu (III). *Chem. Eng. J*. 236, 398–405. doi: 10.1016/j.cej,0.2013.09.103

Shi, W., Lv, H., Yuan, S., Huang, H., Liu, Y., and Kang, Z. (2016). Near-infrared light photocatalytic ability for degradation of tetracycline using carbon dots modified Ag/AgBr nanocomposites. *Sep. Purif. Technol*. 174, 75–83. doi: 10.1016/j.seppur.2016.10.005

Sturini, M., Speltini, A., Maraschi, F., Profumo, A., Pretali, L., Irastorza, E. A., et al. (2012). Photolytic and photocatalytic degradation of fluoroquinolones in untreated river water under natural sunlight. *Appl. Catal. B-Environ*. 119–120, 32–39. doi: 10.1016/j.apcatb.2012.02.008

Sun, Y., Xiao, X., Dong, X. A., Dong, F., and Zhang, W. (2017). Heterostructured BiOI@La$(OH)_3$ nanorods with enhanced visible light photocatalytic NO removal. *Chin. J. Catal*. 38, 217–226. doi: 10.1016/S1872-2067(17)62753-0

Tang, H., Chang, S., Tang, G., and Liang, W. (2017a). AgBr and g-C_3N_4 co-modified Ag_2CO_3 photocatalyst: a novel multi-heterostructured photocatalyst with enhanced photocatalytic activity. *Appl. Surf. Sci*. 391, 440–448. doi: 10.1016/j.apsusc.2016.07.021

Tang, H., Fu, Y., Chang, S., Xie, S., and Tang, G. (2017b). Construction of Ag_3PO_4 /Ag_2MoO_4 Z-scheme heterogeneous photocatalyst for the remediation of organic pollutants. *Chin. J. Catal*. 38, 337–347. doi: 10.1016/S1872-2067(16)62570-6

Wang, J., Wang, G., Wei, X., Liu, G., and Li, J. (2018). ZnO nanoparticles implanted in TiO_2 macrochannels as an effective direct Z-scheme heterojunction photocatalyst for degradation of RhB. *Appl. Surf. Sci*. 456, 666–675. doi: 10.1016/j.apsusc.2018.06.182

Wang, P., Huang, B., Qin, X., Zhang, X., Dai, Y., and Whangbo, M. H. (2009). Ag/AgBr/$WO_3 \cdot H_2O$: visible-light photocatalyst for bacteria destruction. *Inorg. Chem*. 48, 10697–10702. doi: 10.1021/ic9014652

Wang, Q., Yun, G., Bai, Y., Ning, A. N., Lian, J., Huang, H., et al. (2014). Photodegradation of rhodamine B with MoS_2/$Bi_2O_2CO_3$ composites under UV light irradiation. *Appl. Surf. Sci*. 313, 537–544. doi: 10.1016/j.apsusc.2014.06.018

Wang, W., Cheng, H., Huang, B., Lin, X., Qin, X., Zhang, X., et al. (2013). Synthesis of $Bi_2O_2CO_3$/Bi_2S_3 hierarchical microspheres with heterojunctions and their enhanced visible light-driven photocatalytic degradation of dye pollutants. *J. Colloid Interface Sci*. 402, 34–39. doi: 10.1016/j.jcis.2013.03.054

Wang, X., Li, T., Yu, R., Yu, H., and Yu, J. (2016). Highly efficient TiO_2 single-crystal photocatalyst with spatially separated Ag and F-bi-cocatalysts: orientation transfer of photogenerated charges and their rapid interfacial reaction. *J. Mater. Chem. A* 4, 8682–8689. doi: 10.1039/C6TA02039A

Xia, Y., and Halas, N. J. (2005). Shape-controlled synthesis and surface plasmonic properties of metallic nanostructures. *Mrs. Bull*. 30, 338–348. doi: 10.1557/mrs2005.96

Xiang, Q., Yu, J., and Jaroniec, M. (2011). Preparation and enhanced visible-light photocatalytic H2-production activity of graphene/C_3N_4 composites. *J. Phys. Chem. C* 115, 7355–7363. doi: 10.1021/jp200953k

Xiao, J. Q., Lin, K. S., and Yu, Y. (2018). Novel Ag@AgCl@AgBr heterostructured nanotubes as high-performance visible-light photocatalysts for decomposition of dyes. *Catal. Today* 314, 10–19. doi: 10.1016/j.cattod.2018.04.019

Xu, Y., Xu, H., Yan, J., Li, H., Huang, L., Xia, J., et al. (2013). A plasmonic photocatalyst of Ag/AgBr nanoparticles coupled with g-C_3N_4 with enhanced visible-light photocatalytic ability. *Colloid. Surface. A* 436, 474–483. doi: 10.1016/j.colsurfa.2013.06.005

Xuan, N. P., Ba, M. N., Thi, H. T., and Doan, H. V. (2018). Synthesis of Ag-AgBr/Al-MCM-41 nanocomposite and its application in photocatalytic oxidative desulfurization of dibenzothiophene. *Adv. Powder Technol*. 29, 1827–1837. doi: 10.1016/j.apt.2018.04.019

Yada, M., Inoue, Y., Sakamoto, A., Torikai, T., and Watari, T. (2014). Synthesis and controllable wettability of micro-and nanostructured titanium phosphate thin films formed on titanium plates. *Acs. Appl. Mater. Inter*. 6, 7695–7704. doi: 10.1021/am500974v

Yang, X., Tang, H., Xu, J., Antonietti, M., and Shalom, M. (2015). Silver phosphate/graphitic carbon nitride as an efficient photocatalytic tandem system for oxygen evolution. *ChemSusChem* 8, 1350–1358. doi: 10.1002/cssc.201403168

Ye, L., Liu, J., Gong, C., Tian, L., Peng, T., and Zan, L. (2012). Two Different roles of metallic Ag on Ag/AgX/BiOX (X = Cl, Br) visible light photocatalysts: surface plasmon resonance and z-scheme bridge. *ACS Catal*. 2, 1677–1683. doi: 10.1021/cs300213m

Zhang, L., Wang, G., Xiong, Z., Tang, H., and Jiang, C. (2018). Fabrication of flower-like direct Z-scheme β-Bi_2O_3/g-C_3N_4 photocatalyst with enhanced visible light photoactivity for Rhodamine B degradation. *Appl. Surf. Sci*. 436, 162–171. doi: 10.1016/j.apsusc.2017.11.280

Zhang, W., Zhao, Z., Dong, F., and Zhang, Y. (2017). Solvent-assisted synthesis of porous g-C_3N_4 with efficient visible-light photocatalytic performance for NO removal. *Chin. J. Catal*. 38, 372–378. doi: 10.1016/S1872-2067(16)62585-8

Zhang, X., Ai, Z., Falong Jia, A., and Zhang, L. (2008). Generalized one-pot synthesis, characterization, and photocatalytic activity of hierarchical BiOX (X = Cl, Br, I) nanoplate microspheres. *J. Phys. Chem. C* 112, 747–753. doi: 10.1021/jp077471t

Zhang, X., Li, R., Jia, M., Wang, S., Huang, Y., and Chen, C. (2015a). Degradation of ciprofloxacin in aqueous bismuth oxybromide (BiOBr) suspensions under

visible light irradiation: a direct hole oxidation pathway. *Chem. Eng. J.* 274, 290–297. doi: 10.1016/j.cej.2015.03.077

Zhang, Y., Gu, J., Murugananthan, M., and Zhang, Y. (2015b). Development of novel α-Fe_2O_3 /$NiTiO_3$ heterojunction nanofibers material with enhanced visible-light photocatalytic performance. *J. Alloy. Compd.* 630, 110–116. doi: 10.1016/j.jallcom.2014.12.193

Zhang, Z., and Yates, J. T. (2012). Band bending in semiconductors: chemical and physical consequences at surfaces and interfaces. *Chem. Rev.* 112, 5520–5551. doi: 10.1021/cr3000626

Zhu, Y.-P., Ma, T.-Y., Ren, T.-Z., Li, J., Du, G.-H., and Yuan, Z.-Y. (2014). Highly dispersed photoactive zinc oxide nanoparticles on mesoporous phosphonated titania hybrid. *Appl. Catal. B-Environ.* 156–157, 44–52. doi: 10.1016/j.apcatb.2014.03.001

Zou, J. P., Wu, D. D., Luo, J., Xing, Q. J., Luo, X. B., Dong, W. H., et al. (2016). A strategy for one-pot conversion of organic pollutants into useful hydrocarbons through coupling photodegradation of MB with photoreduction of CO_2. *ACS Catal.* 6, 6861–6867. doi: 10.1021/acscatal.6b01729

Conflict of Interest Statement: The authors declare that the research was conducted in the absence of any commercial or financial relationships that could be construed as a potential conflict of interest.

frontiers in Chemistry

ORIGINAL RESEARCH
published: 09 October 2018
doi: 10.3389/fchem.2018.00466

Photocatalytic Activation of Saturated C–H Bond Over the CdS Mixed-Phase Under Visible Light Irradiation

*Houde She[1], Liangshan Li[1], Hua Zhou[1], Lei Wang[1], Jingwei Huang[1] and Qizhao Wang[1,2]**

[1] College of Chemistry and Chemical Engineering, Northwest Normal University, Lanzhou, China, [2] Gansu International Scientific and Technological Cooperation Base of Water-Retention Chemical Functional Materials, Lanzhou, China

Selective activation of saturated C–H bond in hydrocarbons to produce high-value-added chemicals is of great significance for chemical synthesis and transformation. Herein, we present a facile procedure to achieve Ni-doped CdS nanoparticles with mixed (cubic and hexagonal) phases, as well as its application to the photocatalytic activation of saturated primary C–H bond of toluene and its derivatives. The photocatalytic oxidation rate of toluene into benzaldehyde of formation reached up to 216.7 $\mu molh^{-1}g^{-1}$ under visible light irradiation. The excellent photocatalytic performance of Ni(II)-doped CdS [Ni(II)/CdS] can be attributed to its unique structural assembly with cubic and hexagonal phases and also the addition of Ni ions, together taking effect in promoting the separation of photogenerated charge carriers. The possible reaction mechanism for the photocatalytic selective oxidation is illustrated in this work. The band width of the as-prepared mixed phase CdS is reduced, which can effectively expand the response range and improve photocatalytic performance.

Keywords: toluene, benzaldehyde, ion modify, mixed-phase, C–H bond, selective oxidation

OPEN ACCESS

Edited by:
Fan Dong,
Chongqing Technology and Business University, China

Reviewed by:
Zhu Gangqiang,
Shaanxi Normal University, China
Guidong Yang,
Xi'an Jiaotong University, China
Xiaole Weng,
Zhejiang University, China

***Correspondence:**
Qizhao Wang
wangqizhao@163.com;
qizhaosjtu@gmail.com

Specialty section:
This article was submitted to Catalysis and Photocatalysis, a section of the journal Frontiers in Chemistry

Received: *23 August 2018*
Accepted: *14 September 2018*
Published: *09 October 2018*

Citation:
She H, Li L, Zhou H, Wang L, Huang J and Wang Q (2018) Photocatalytic Activation of Saturated C–H Bond Over the CdS Mixed-Phase Under Visible Light Irradiation. Front. Chem. 6:466. doi: 10.3389/fchem.2018.00466

INTRODUCTION

The highly selective oxidation of inactive C–H bond in hydrocarbons to form high value-added oxygenated products under mild conditions is one of the major challenges in the industrial field (Pal et al., 2014; Yang et al., 2017). For example, toluene is a simple aromatic compound and can be selectively oxidized into benzaldehyde, benzyl alcohol, benzoic acid and benzyl benzoate, all of which are crucial intermediate for the manufacture of fine chemicals, such as pharmaceuticals, dyes, preservatives and perfume. At present, benzaldehyde is primarily synthesized via traditional route of chlorination hydrolysis of toluene. The discharges of toxic gases and organic waste bring on serious environmental concerns. Therefore, it is essential to develop an environment-friendly technique to address such problem. Photocatalysis is a promising alternative strategy that has been widely applied in the activation of C–H bond under mild conditions (Zhang et al., 2012; Hao et al., 2018) owning to its clean and low energy consumption, etc. For example, Yuan et al. reported that $BiOBr/TiO_2$ can be used in oxidation of toluene into benzaldehyde under visible light irradiation (Yuan et al., 2013). He's group (He et al., 2018) presented a toluene selective oxidation that has been carried out by $Cd_3(C_3N_3S_3)_2$/CdS porous composites under visible light irradiation. $Cd_3(C_3N_3S_3)_2$/CdS exhibits excellent performance for the transformation of toluene into benzaldehyde.

It is well-known that the CdS is economical and has been extensively employed in photocatalysis research because of its adequate band gap (2.45 eV), which is unique among photocatalytic materials (Wang et al., 2014; Cheng and Xiang, 2016; Xiang et al., 2016). Although CdS-based photocatalysts are widely studied in the field of photocatalysis (Yan et al., 2009; He et al., 2016b; Li et al., 2018) some inherent defects like high charge carrier recombination rate and photo-corrosion, debase their photocatalytic activity and practical application (He et al., 2016a). To hold back electrons-holes recombination and improve photocatalytic activity, various strategies, such as the loading of co-catalysts, forming heterojunctions have been scrupulously developed (Wang et al., 2013; Wei et al., 2017, 2018). In the past decade, Pt (Luo et al., 2015b), Au (Majeed et al., 2016; Wang et al., 2018b), Pd (Luo et al., 2015a), Ag (Gupta et al., 2017), and Ru (Nosheen et al., 2017) have been used as co-catalysts in various photocatalyst systems to enhance charge separation and surface reactions. Despite the high photocatalytic performance achieved by these noble metal-based co-catalysts contained catalyst, their use in mass production are limited due to the scarcity and high cost of them. Therefore, it is desirable to investigate new catalyst system with non-noble metal as co-catalyst, which can meet the general industrial requirements, such as low cost, high efficiency, and good durability. In this regard, many non-precious metals [such as Fe (Yan et al., 2017; Deka and Kalita, 2018), Cu (Kumar et al., 2018; Wang et al., 2018a), Co (Dong et al., 2017), Ni (Yang et al., 2018), Mo (Zhang et al., 2017)] materials have been studied as a co-catalyst to improve performance of main catalyst. In particular, nickel-based materials [such as metallic nickel, nickel ion (Song et al., 2017), nickel oxides and hydroxides (Zhang et al., 2015)] exhibit excellent activity and attract much attention as promoters for enhancing photocatalytic activity. Murugesan et al. (Murugesan et al., 2017) prepared Ba and Ni doped CdS by a spray pyrolysis method. Doping Ba and Ni can significantly improve optical performance of CdS. Besides, it has also been suggested that Ni doped CdS was prepared via an impregnation method (Yu et al., 2016), which doped samples can efficiently promotes separation of holes and electrons and consequently enhances the photocatalytic hydrogen production.

However, in the above works, only modified single phase CdS can enhance the photocatalytic activity. But, as reported by some researchers, the CdS base can also form a homojunction for enhancing its photocatalytic activity (Dai et al., 2014). The mixed-phase CdS has been reported by Zhao's group (Zhao et al., 2018), which demonstrated that the photoresponse range can be broadened to ameliorate photocatalytic activity.

In this work, we report the synthesis of Ni(II) doped CdS (Ni(II)/CdS) with mixed-phase (cubic and hexagonal) via a simple impregnation method. The Ni(II)/CdS was further used as photocatalyst in the activation of saturated primary C–H bond of toluene and its derivatives at room temperature and under two barometric pressure (0.2 MPa). The yield of benzaldehyde can reach up to 216.70 $\mu molh^{-1}g^{-1}$, which is 7.7 times higher than that of mixed-phase CdS. Controlled experiments using different radical scavenger were also conducted to elucidate the possible reaction mechanism for the selective oxidation of C–H bond in toluene over the mix phase of Ni(II)/CdS.

EXPERIMENTAL

Materials

All reagents were analytical grade and used without further purification. Benzotrifluoride (BTF) (>99%)was purchased from Aladdin Chemical Reagent Co., Ltd. Oleic acid ($C_{18}H_{34}O_2$), Cadmium nitrate tetrahydrate [$Cd(NO_3)_2{\cdot}4H_2O$], 8% of ammonium sulfide [$(NH_4)_2S$], sodium borohydride ($NaBH_4$), ethyl alcohol (C_2H_6O), toluene (>99.5%) and other chemical reagents were purchased from Sinopharm Chemical Reagent Co., Ltd.

Preparation

Synthesis of Mixed-Phase CdS

Typically, $Cd(NO_3)_2{\cdot}4H_2O$ (1.0 mmol) and oleic acid (0.0375 ml) were first dissolved in deionized water (50 mL) in a beaker placed on a magnetic stirrer for 15 min at room temperature to form solution A. $NaBH_4$ (4.0 mmol) was also dissolved in deionized water (250 mL) in a beaker placed on a magnetic stirrer at room temperature to form solution B. The two solutions were then mixed and quickly put into a microwave oven (M1-L213B, at a fixed frequency of 2,450 MHz, Guangdong midea kitchen appliances manufacturing Co., Ltd., China) followed by 20 s irradiation. The Cd nanoparticles (NPs) were collected and washed by ethyl alcohol three times, and dispersed in 20 mL ethyl alcohol to get sulfurized by adding certain amount of $(NH_4)_2S$ (2.0 mmol) and followed by 1 h stirring at room temperature. Then the yellowish products were collected and washed by ethyl alcohol three times. Finally, the products were dried in drying oven at 60°C for 4 h.

Preparation of Ni(II)-Mixed-Phase CdS Samples

The Ni(II) doped mixed phase CdS samples (Ni(II)/CdS) were synthesized by a simple impregnation method. Typically, CdS (200.0 mg) was dispersed into10.0 mL of $NiCl_2{\cdot}6H_2O$ solution and stirred at 80°C for 2 h. The products was collected and washed by deionized water several times. The amount of Ni (the weight ratio of Ni(II) to CdS) was about 0.5, 1.0, 3.0, and 5.0 wt%, respectively. Finally, the samples dried in drying oven at 60°C for 4 h.

Characterization

X-ray diffraction (XRD) patterns were acquired by a Rigaku D/MAX-2200/PCX-ray diffractometer in the angular range of 10–90° (2θ) with Cu Kα radiation (40 kV, 20 mA). UV-vis diffuse reflectance spectra (DRS) were acquired from 230 to 800 nm by a UV-vis spectrophotometer (PuXin TU-1901). The morphologies and microstructures of the samples were obtained using field emission scanning electron microscope (FE-SEM, Ultra Plus, Carl Zeiss) and transmission electron microscope (TEM, F20, FEI). X-ray photoelectron spectroscopy (XPS) was used to study the chemical compositions and the valence states by a photoelectron spectrometer (PHI5702). The photoelectrochemical (PEC) performances of photoanodes were acquired by a three-electrode system (CHI-660D Co., Shanghai, China) under a LED lamp ($\lambda > 420$ nm, CEL-LED100) illumination. A Pt wire and Ag/AgCl were used as counter

electrode and reference electrode, respectively. The working electrodes were made on the fluride-tin oxide (FTO) conductor glasses. The samples (10 mg) were homogeneously dispersed in anhydrous ethanol and ultrasound for 60 min, which were slowly dripped on FTO glasses. The electrolyte was 0.5 M Na_2SO_4 (pH = 7.35) aqueous solution in a quartz ware 0.5 V of the bias voltage was used for photoelectrochemical testing. Illumination through the back-side of FTO was used with an illumination area of about 1.0 cm^{-2}. Photoluminescence (PL) spectra of the samples were recorded by a fluorescence spectrophotometer (PE, LS-55) at room temperature, using a 390 nm excitation wavelength.

Evaluation of Photocatalytic Activity

The photocatalytic reaction was performed in a 25 mL glass bottle under visible light irradiation in this work. Typically, 0.5 mmol of substrate and 80 mg of catalyst were dispersed in the 5.0 mL of solvent (BTF) in a 25 mL glass bottle. Then the glass bottle was transferred into a closed reactor (**Figure S1**) and stirred for 30 min in dark to make the catalyst fully contact with the solution and achieve adsorption equilibrium. Meanwhile, the reactor was bubbled into oxygen molecules from a gas cylinder for 30 min at absolute pressure of 0.2 MPa. A 300 W Xe arc lamp (CEL-HXF 300, Beijing Perfectlight Co. Ltd.) with a ultraviolet cutoff filter ($\lambda < 420$ nm) was used in the following photocatalytic reaction. After 2 h of irradiation, the mixture was centrifuged to remove catalyst powders at 8,000 rmp for 5 min by a centrifuge (TG16-WS). The liquid supernatant was analyzed by a gas chromatograph (GC-9600). A series of controlled experiments were carried out similar to the photocatalytic oxidation process of toluene, except that the radical scavengers (0.1 mmol) were added to the reaction system. The conversion (Con.) rate of substrates, yield of aldehyde, and selectivity (Sel.) were defined with the following equations:

$$\text{Con.}(\%) = [(C_0 - C_1)/C_0] \times 100\% \quad (1)$$

$$\text{Yield}(\%) = (C_{aldehyde}/C_0) \times 100\% \quad (2)$$

$$\text{Sel.}(\%) = [C_{aldehyde}/(C_0 - C_1)] \times 100\% \quad (3)$$

Where C_0 is the initial concentration of substrates; C_1 and $C_{aldehyde}$ are the concentration of the remaining substrates and the corresponding aldehyde at a certain time after the photocatalytic reaction, respectively.

RESULTS AND DISCUSSION

DRS, XRD and Photoluminescence (PL) Spectra Analysis

Figure 1A shows the UV–vis diffuse reflectance spectra of mixed-phase CdS, 0.5 wt%Ni(II)/CdS, 1.0 wt%Ni(II)/CdS, 3.0 wt%Ni(II)/CdS, 5.0 wt%Ni(II)/CdS samples. All samples of the spectra display absorption in the visible-light region. The mixed-phase CdS NPs exhibit a absorption edges at 518 nm, while the

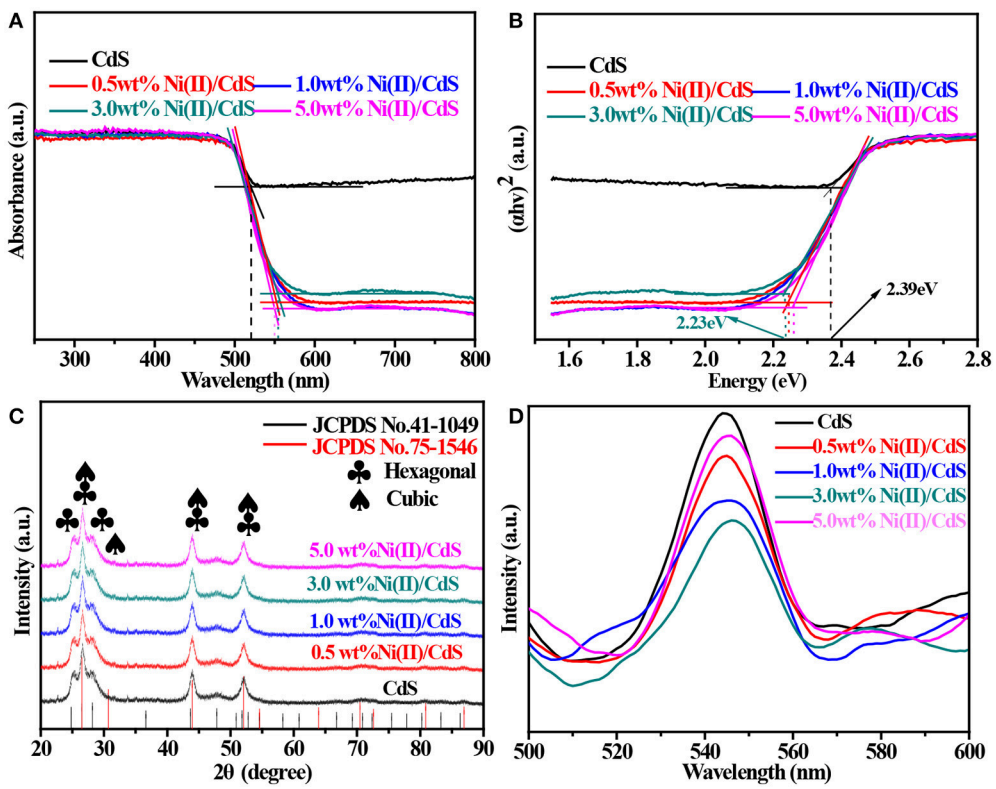

FIGURE 1 | (A) UV–vis diffuse reflectance spectra, **(B)** Tauc plots, **(C)** XRD patterns and **(D)** PL of the samples: mixed-phase CdS, 0.5 wt%Ni(II)/CdS, 1.0 wt%Ni(II)/CdS, 3.0 wt%Ni(II)/CdS, and 5.0 wt% Ni(II)/CdS.

Ni(II)/CdS samples show red shift of absorption edges compared with prestine CdS sample. In particular, the absorption edges of 3.0 wt%Ni(II)/CdS NPs was observed at 555 nm. Hence, it is clear that the modification of Ni(II) co-catalyst can significantly affect the optical absorption feature of CdS NPs. The optical band gap value has been calculated via the equation: $(\alpha hv)^2 = A(hv - Eg)$ (Su et al., 2013; Kuang et al., 2015), where α, h, A and v correspond to absorption coefficient, Planck constant, proportionality and light frequency, respectively. As shown in **Figure 1B**, the band gaps estimated are 2.39, 2.26, 2.24, 2.23 and 2.26 eV for mixed-phase CdS, 0.5 wt%Ni(II)/CdS, 1.0 wt% Ni(II)/CdS, 3.0 wt%Ni(II)/CdS and 5.0 wt%Ni(II)/CdS, respectively. The above results indicate that the Ni(II)/CdS have changed the band gap of the mixed-phase CdS. Compared with the single-phase CdS of absorption edge, the absorption edge of the mixed phase CdS is red shift. Prior to this, the cubic CdS was synthesized by a solvothermal method. In addition, the UV–vis diffuse reflectance spectra and Tauc plot are shown in **Figure S2**.

The X-ray diffraction (XRD) pattern of as-prepared CdS sample is shown in **Figure 1C**. It is evident that the sample contain hexagonal phase CdS because the peaks at 24.8, 26.5, and 28.2° correspond to the (100), (002) and (101) crystal planes (hexagonal CdS, JCPDS No. 41–1049), respectively. Meanwhile, peaks at 26.5, 44.0 and 52.1° can be indexed to (111), (220), and (311) planes of cubic phase CdS (JCPDS No. 75-1546) or (002), (110), and (112) planes of hexagonal phase CdS. So it is clear that most of the strong diffraction peaks of JCPDS No. 75–1546 (cubic phase) overlap with the peaks of JCPDS No. 41–1049 (hexagonal phase) except for the peak at 30.7°, which corresponds to (200) plane of cubic phase CdS. But it is not safe to judge the existence of cubic phase CdS from the XRD patterns simply according to this distinctive peak because the intensity of (200) peak is only one fifth of that of (111) plane due to its weak and even indiscernible signal in the whole pattern. However, the nature of mixed phases of our samples can be alternatively judged from the intensity distribution of diffraction peaks, as suggested by the peak of 26.5° corresponds to the (111) crystal plane and overlaps with the (002) crystal plane of the hexagonal phase. Noting that peak of (002) plane is not the strongest line in JCPDS No. 41-1049, it is unreasonable to conclude that the strongest peak is given at 26.5° if our samples are hexagonal phase CdS, the only possible explanation is that our sample should be mixed-phase CdS so that the diffraction wave of (111) plane (cubic CdS) will stack up with that of (002) plane (hexagonal CdS) and presents the strongest peak at 26.5°. Another possibility for the presence of the strongest peak at 26.5° can be explained by anisotropic growth of hexagonal phase CdS. The dominant growth along (002) plane will give similar result even if our sample is not mixed-phase CdS. To rule out this possibility, SEM and TEM were performed on all the samples and the results (shown in **Figure 3**) do not support this supposition. So it is now safe to demonstrate that the CdS sample should be composed of cubic CdS and hexagonal CdS. According to the patterns shown in **Figure 1C**, the same diffraction peak intensity and width as mixed-phase CdS suggests that the appearance and crystallite size of CdS NPs are not affected by doping different amount of Ni(II). Photoluminescence (PL) spectroscopy is an effective method to study the electronic structure and optical properties of semiconductor materials. **Figure 1D** shows the PL spectra of all samples at the excitation wavelength of 390 nm in room temperature. It can be seen from **Figure 1D** that the catalyst samples have a strong signal peak at a wavelength of about 540 nm. In general, a high intensity of the photoluminescent signal indicates a high recombination probability of photo-generated electrons (e^-) and holes (h^+) as well as a low photocatalytic activity (Martha et al., 2013; Wu et al., 2014; Weng et al., 2016; Cui et al., 2017a; Nie et al., 2018; She et al., 2018). In this regard, it is seen from **Figure 1D** that the activity of the catalyst 3.0 wt%Ni(II)/CdS is significantly higher than that of the other samples, which is in a good agreement with the result of catalyst activity tests.

Morphology and Microstructures Analysis

Figure 2 shows the SEM images of the mixed-phase CdS and 3.0 wt%Ni(II)/CdS. It is seen that the mixed-phase CdS sample consists of irregular particles with a size range of 20–100 nm in **Figures 2a,b**. As exhibited in the **Figures 2c,d**, 3.0 wt%Ni(II)/CdS sample is also constituted of irregular nanoparticle, and its microscopic structure is similar to that of mixed-phase CdS. But its surface is not so smooth as that of mixed-phase CdS due to the modification of Ni(II). The EDX analysis was also performed to confirm the existence of Ni element and the result is shown in **Figure 3f**. The SEM images of the 0.5 wt%Ni(II)/CdS, 1.0 wt% Ni(II)/CdS and 5.0 wt% Ni(II)/CdS are displayed in **Figure S3**, respectively. It can be clearly seen that all the samples are constituted of irregular nanoparticle with the same microscopic structure.

To study the microscopic structure and morphology of as-prepared catalysts, TEM, HRTEM, SAED, and EDX analysis were performed and the results are shown in **Figure 3**. As shown in **Figure 3b**, the lattice spacing of 0.359 and 0.335 nm can be

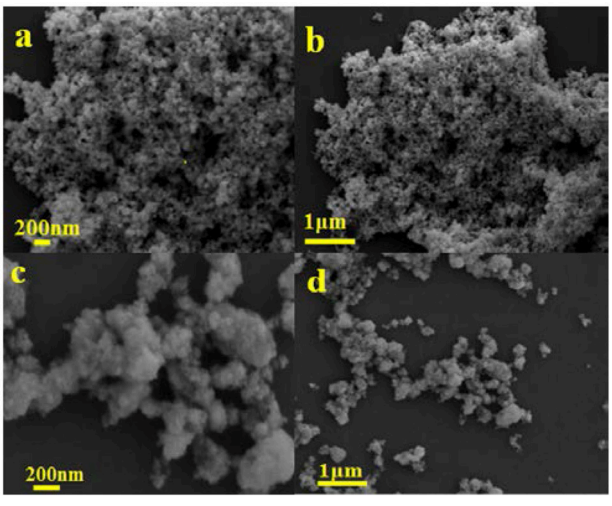

FIGURE 2 | SEM images of the mixed-phase CdS **(a,b)**, and 3.0 wt% Ni(II)/CdS **(c,d)**.

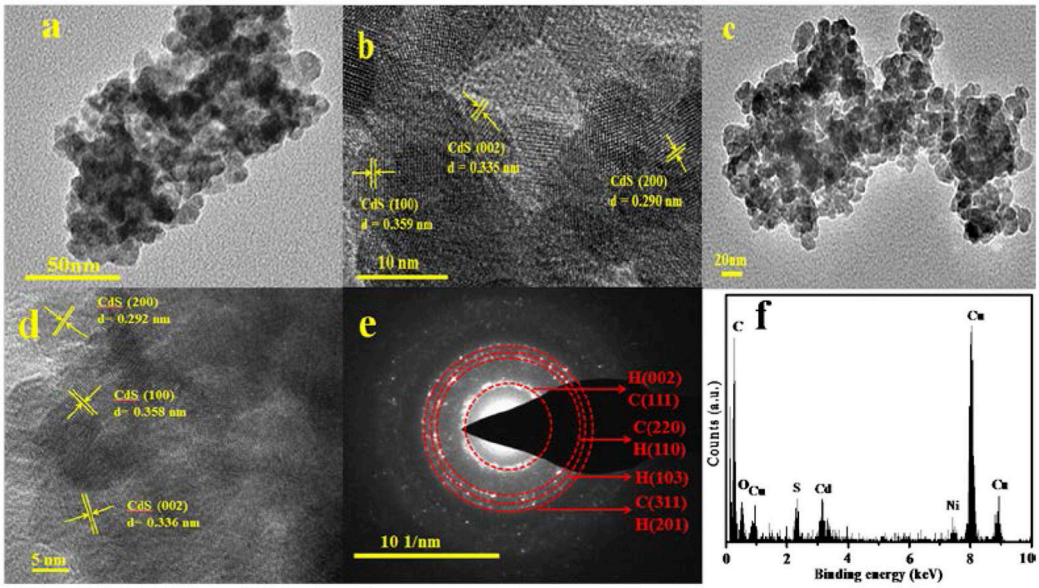

FIGURE 3 | (a) TEM image of the mixed-phase CdS, **(b)** HRTEM image of the mixed-phase CdS, **(c)** TEM image of 3.0 wt% Ni(II)/CdS, **(d)** HRTEM image of 3.0 wt% Ni(II)/CdS, **(e)** SAED pattern of 3.0 wt% Ni(II)/CdS, and **(f)** EDX of 3.0 wt% Ni(II)/CdS.

ascribed to the (100) and (002) crystal face of hexagonal phase and the spacing of 0.290 nm can be ascribed to the (200) crystal face of cubic CdS. This image analysis further confirms that the as-prepared catalysts are composed of cubic and hexagonal phase CdS NPs and is consistent with the XRD results as discussed above. Compared with prestine CdS (**Figure 3a**), it is observed that the microscopic structure and morphology of 3.0 wt%Ni(II)/CdS (**Figure 3c**) is not significantly changed. The lattice spacing of Ni is not observed in **Figure 3d**, which could be attributed to the low dosage of Ni(II) ions. As shown in **Figure 3e**, the SAED pattern shows that the sample possesses a polycrystalline nature. In addition, the energy dispersive X-ray (EDX) analysis also suggests the coexistence of Cd, S and Ni elements in **Figure 3f**.

XPS Analysis

The surface nature of the as-prepared CdS and 3.0 wt%Ni(II)/CdS samples were characterized by XPS measurements. As shown in **Figure 4A**, Cd and S elements are derived from the CdS phase, while the O element might come from H_2O (Chen et al., 2015). We can see that the peaks at the binding energy of 404.9 and 411.7 eV correspond to Cd $3d_{5/2}$ and Cd $3d_{3/2}$ in **Figure 4B** (Jin et al., 2015). **Figure 4C** indicates the S 2p peak bifurcates as two peaks of S $2p_{3/2}$ and S $2p_{1/2}$ (Xue et al., 2018), corresponding to the binding energy of 161.4 and 162.7 eV (Li et al., 2015b), respectively. As shown in the **Figure 4D** (3.0 wt%Ni(II)/CdS), the peaks at about 855.5 and 873.1 eV are attributed to Ni $2p_{3/2}$ and Ni $2p_{1/2}$ of Ni(II) (Song et al., 2017), with a spin-energy separation of 17.6 eV. The peaks at 861.3 and 879.3 eV are ascribed to the satellite peaks of Ni $2p_{3/2}$ and Ni $2p_{1/2}$, respectively (Oros-Ruiz et al., 2014, 2016). The above results also suggest that Ni(II) was successfully decorated on the surface of the CdS nanoparticles.

Electrochemical Characterization

To study the efficiency of the photogenerated electron-hole, the transient photocurrent tests were carried out on all as-prepared samples (mixed-phase CdS, 0.5 wt%Ni(II)/CdS, 1.0 wt%Ni(II)/CdS, 3.0 wt%Ni(II)/CdS and 5.0 wt%Ni(II)/CdS). As shown in **Figure 5A**, it is clear that all Ni(II)-doped samples have a higher photocurrent than that of prestine CdS, indicating that the separation efficiency of photoinduced charge carriers is improved by doping Ni(II) ions into CdS lattice. The results are consistent with the PL test results (**Figure 1D**; Zou et al., 2016). **Figure 5B** shows the electrochemical impedance spectroscopy (EIS) curves of the mixed-phase CdS and Ni(II)/CdS. Comparing the Nyquist plots circle radius of the mixed-phase CdS with that of 3.0 wt% Ni(II)/CdS, it can be observed that the radius of arc curve of 3.0 wt%Ni(II)/CdS is the shortest among all tested samples, suggesting that Ni(II) ions in CdS lattice can facilitate electron-hole separation and interfacial migration (Cui et al., 2017b). It can be also inferred that the Ni(II) ions act as a carrier for transferring electrons. **Figures 5C**, **Figure S4** show the Mott-Schottky curves of the as-prepared samples. The slopes of the two Mott-Schottky curves are all positive in the range of −0.5 and 1.2 V, indicating that the samples are n-type semiconductor, which is consistent with the reported results. The flat band potentials of CdS and 3.0 wt%Ni (II)/CdS are −0.56 and −0.51 V, respectively. The flat band potential is approximately equal to the conduction band (CB) edge for n-type semiconductors. Therefore, the CB positions of CdS and 3.0 wt%Ni (II)/CdS are approximately −0.56 and −0.51 V, respectively. The valence band (VB) edge of samples can be

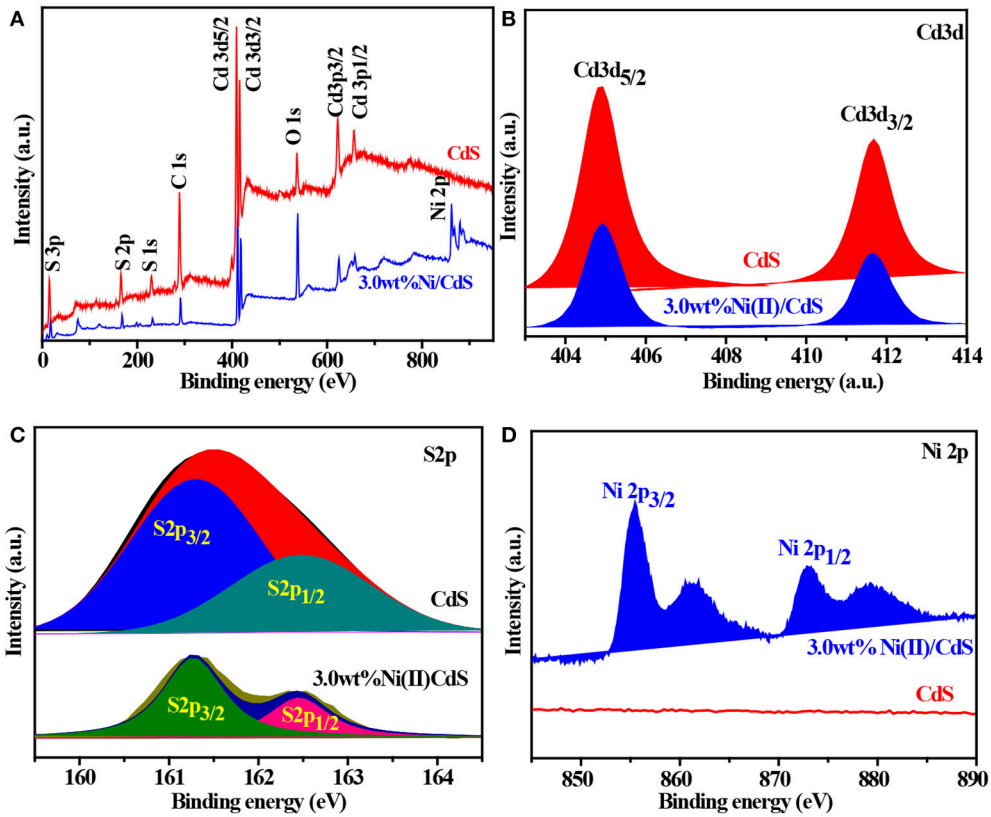

FIGURE 4 | (A) XPS survey spectra and the high-resolution XPS spectra of **(B)** Cd 3d, **(C)** S 2p, and **(D)** Ni 2p for the all samples.

determined by the following equation: $Eg = E_{VB} - E_{CB}$ (Jin et al., 2015; Wang et al., 2018c), where E_{CB} is the CB edge potential, E_{VB} is the VB edge potential, and Eg is the band gap of the semiconductors. The calculated VB positions of CdS and 3.0 wt%Ni (II)/CdS are approximately 1.83 and 1.72 V, respectively.

Photocatalytic Performance Experiment

To study the effect of amount of doping Ni(II) on the conversion level, we have tested the photocatalytic performance of the mixed-phase CdS, 0.5 wt%Ni(II)/CdS, 1.0 wt%Ni(II)/CdS, 3.0 wt%Ni(II)/CdS, and 5.0 wt%Ni(II)/CdS for selective oxidation of toluene under visible light irradiation for 2 h. It can be seen from **Table 1** that the formation rate of benzaldehyde can be improved when the amount of Ni(II) increases from 0.5 to 3.0 wt%. The formation rate of benzaldehyde can reach to 216.70 $\mu molh^{-1}g^{-1}$ using 3.0 wt%Ni(II)/CdS as catalyst after 2 h irradiation. The result suggest that 3.0 wt%Ni(II)/CdS is highly active visible-light-driven photocatalyst for the selective oxidation of primary C–H bond in toluene. As we known, metal ions may become the capture center of photogenerated electrons, and effectively suppress the recombination of photogenerated electrons and holes, thereby improving the photocatalytic activity. As the doping amount, the trapping sites of the carriers increase, which increases the carrier lifetime and improves the separation of photogenerated electron-holes. When the doping amount is increases, the carrier capture sites are increased and the carrier lifetime is extended, resulting in a great improvement in photoelectron-hole separation. Therefore, this process enhances the photocatalytic activity. However, when the doping amount is increased to a certain extent, the distance between the trapping sites of the trapping carriers becomes small, the doping ions evolve into a recombination center of electrons and holes, and the activity of the catalyst is lowered. However, when the doping amount is increased to a certain amount, the distance between the trapping sites of the trapping carriers becomes small, resulting in the doping ions evolve into a recombination center of electrons and holes. So, the photocatalyst exhibits lower photocatalytic activity. When the doping amount of 3 wt% is an optimum value, the photocatalyst exhibits the best photocatalytic activity.

To demonstrate the general applicability of the as-prepared Ni(II)/CdS photocatalysts for selective oxidation of such primary C–H bond in alkyl aromatics, the visible light photoactivity of 3.0 wt%Ni(II)/CdS toward the selective oxidation of other substituted toluenes were further tested, and the results are listed in **Table 2**. It is clear to see that the 3.0 wt%Ni(II)/CdS is also active for the oxidation of primary C–H bond of substituted toluenes to the corresponding aldehydes. The above photoactivity results suggest that the as-prepared 3.0 wt%Ni(II)/CdS, that is

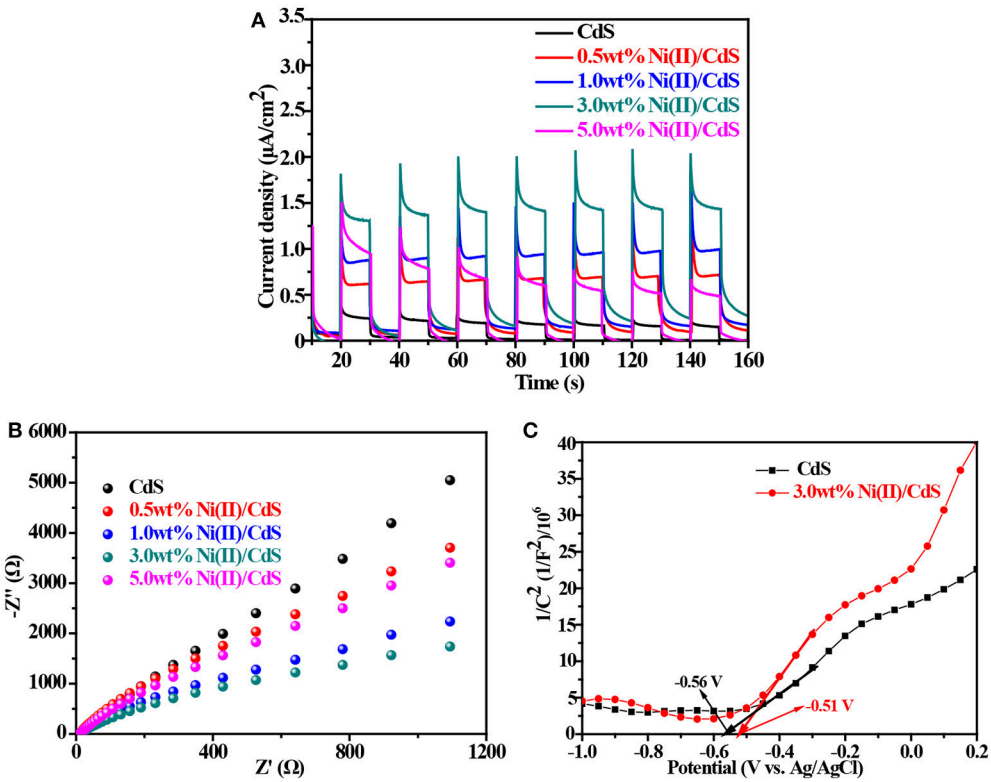

FIGURE 5 | (A) Transient photocurrent response. **(B)** Electrochemical impedance profiles. **(C)** Mott-Schottky curves of the samples.

TABLE 1 | Oxidation of toluene over the as-prepared samples under visible light irradiation for 2 h.

Entry	Catalyst	Con. (%)	Formation rate ($\mu molh^{-1}g^{-1}$)	Sel. (%)
1	CdS	3.0	27.93	100
2	0.5 wt%Ni(II)/CdS	7.7	171.08	100
3	1.0 wt%Ni(II)/CdS	8.3	189.08	100
4	3.0 wt%Ni(II)/CdS	8.8	216.70	100
5	5.0 wt%Ni(II)/CdS	7.8	179.20	100

TABLE 2 | Oxidation of toluene and substituted toluenes over the 3.0 wt%Ni(II)/CdS under visible light irradiation for 2 h.

Entry	Substrate	Product	Con. (%)	Formation rate ($\mu molh^{-1}g^{-1}$)	Sel. (%)
1			8.8	216.70	100
2		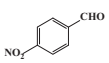	3.5	86.19	100
3		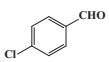	6.4	157.60	100
4			7.1	174.84	100
5			6.1	150.21	100
6			3.4	83.73	100
7		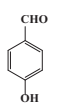	3.6	88.65	100

achieved by such a very simple method at room temperature, can be used as an efficient and visible-light-driven photocatalyst toward the selective activation of primary C–H bond in a variety of substituted toluenes.

Cycle and Possible Reaction Mechanism Experiment

The 4 times cycling test was performed over the 3.0 wt%Ni(II)/CdS to verify its stability under the same conditions. After irradiation, the reaction mixture was centrifuged to separate the catalyst, which was then washed three times with ethanol and deionized water and dried before next cycle test. In **Figure 6A**, it can be seen that the conversion of tolueneand the selectivity of benzaldehyde are almost unchanged. To further confirm the stability of our sample as catalyst, the XRD test were performed to measure the fresh 3.0 wt%Ni(II)/CdS as well as the used 3.0 wt%Ni(II)/CdS. As shown in **Figure 6B**, the

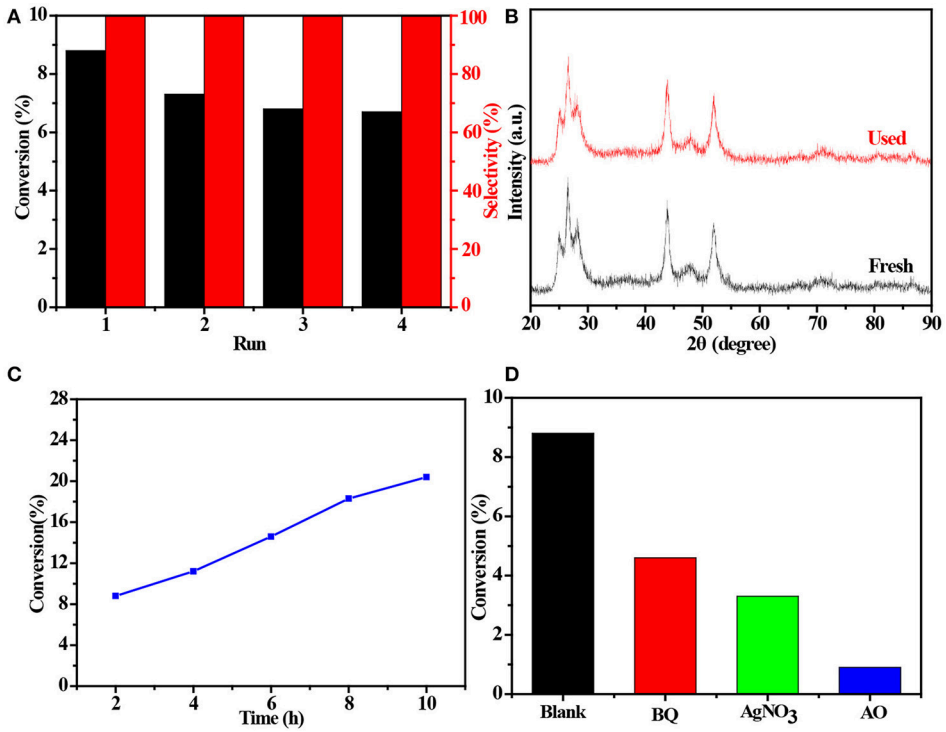

FIGURE 6 | (A) Cyclic experiments of 3.0 wt%Ni(II)/CdS to the selective oxidation of toluene to benzaldehyde under visible light irradiation for 2 h, **(B)** XRD patterns of fresh and used 3.0 wt%Ni(II)/CdS after photocatalytic reaction, **(C)** conversion of toluene under different irradiation time over 3.0 wt%Ni(II)/CdS and **(D)** control experiments using different radical scavengers for the photocatalytic selective oxidation of toluene over 3.0 wt%Ni(II)/CdS under visible light irradiation for 2 h.

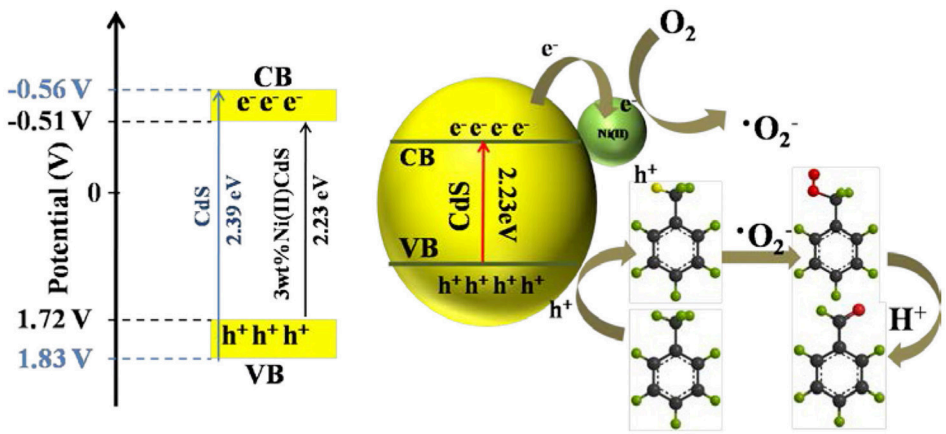

FIGURE 7 | Schematic diagram of the proposed mechanism for oxidation of toluene into benzaldehyde over 3.0 wt%Ni(II)/CdS under irradiation for 2 h.

crystal structure of 3.0 wt%Ni(II)/CdS sample does not change significantly after the photocatalytic reaction. Furthermore, considering the XRD test on stability of our sample together with the SEM images (shown in **Figure S5**) of used the 3.0 wt%Ni(II)/CdS after photocatalytic reaction, it can be inferred that the morphology and structure of the sample as photocatalyst remain unchanged during reaction, indicating that the 3.0 wt% Ni(II)/CdS composite is a stable photocatalyst for the selective oxidation of substituted toluenes to the corresponding aldehydes under the experimental conditions. Furthermore, the valence of Ni and its effect on the photocatalytic process through XPS detection of the 3.0 wt%Ni(II)/CdS after photocatalytic reaction had been analyzed. According to XPS (**Figure S6**), Cd and S present undetectable change between fresh and used 3.0

wt%Ni(II)/CdS. As shown in **Figure S6D**, two weak peaks at 850.6 and 868.9 eV can be respectively attributed to the $2p_{3/2}$ and $2p_{1/2}$ peaks of Ni metal (Li et al., 2015a), indicating the formation of the nickel metallic state of the catalyst during the photocatalytic reaction. It is considered that photogenerated electrons in the CdS CB tended to transfer to Ni(II) clusters and then effectively reduce a portion of Ni(II) to Ni^0 atoms (Weng et al., 2017). However, the combination of electrons and oxygen molecules quickly forms a process of the long-term transport of electrons. Therefore, more holes are combined with toluene to form an oxidation reaction process. This process facilitates efficient separation of carriers to ameliorate photocatalytic activity. As shown in **Figure 6C**, toluene oxidation over 3.0 wt%Ni(II)/CdS under visible light irradiation for 10 h can give a toluene conversion rate of 20.4%. It presents a great potential for the industrial synthesis for the fine chemicals. To study the role of photogenerated radical species involved in photocatalytic oxidation of toluene on 3.0 wt%Ni(II)/CdS sample under visible light irradiation and the reaction mechanism involved, a series of control experiments were carried out and the result is shown in **Figure 6D**. In the control experiments, all conditions were kept unchanged except that different scavengers (AO, BQ and $AgNO_3$) were added to capture h^+, $\bullet O_2^-$ and e^-, respectively. As shown in **Figure 6D**, ammonium oxalate (AO) scavenger was added and the conversion of toluene was almost terminated under visible light irradiation. Adding benzoquinone (BQ) or $AgNO_3$ to the reaction system also significantly suppressed the conversion of toluene. Although electrons cannot directly participate in the oxidation of toluene, it can affect the activation of oxygen molecules. A series of control experiments result suggest that the h^+ play the important role in photocatalytic oxidation of toluene over 3.0 wt%Ni(II)/CdS. The O_2 is activated by e^- to form the superoxide radicals, which acts as the main oxidant for the photocatalytic toluene process. The above results suggest that the major active species for the photocatalytic selective oxidation of toluene is h^+ rather than e^-.

Thus, the possible mechanism is proposed, as given in **Figure 7**. Compared with the common CdS of band width (2.41 eV), the band width (2.39 eV) of the mixed phase CdS is reduced. Besides, doping Ni(II) to the photocatalyst is capable of greatly enhancing its electron transport and charge separation. The photogenerated electrons of CdS can be rapidly transferred to the Ni(II) promoter because of the positive potential of Ni^{2+}/Ni^0 (−0.23 V vs. SHE, pH = 0) than the CB potential of the mixed-phase CdS (about −0.56 V, **Figure 5C**; Ran et al., 2011; Meng et al., 2018), thereby forming a long-term electron transfer process. The toluene is adsorbed on the surface of the 3.0 wt%Ni(II)/CdS and oxidized by the holes to the corresponding cationic radicals. Meanwhile, the electrons react with adsorbed O_2 to give activated oxygen species. The activated oxygen species then selectively oxidize the cationic radicals, finally leading to the formation of benzaldehyde.

According to the experimental and simulated results, the photocatalytic mechanism of oxidation of toluene coupling with was proposed as following scheme:

$$O_2 + e^- \longrightarrow \cdot O_2^- \quad (4)$$

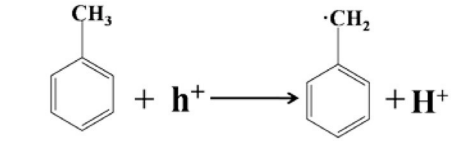

(5)

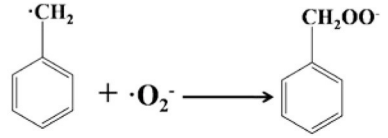

(6)

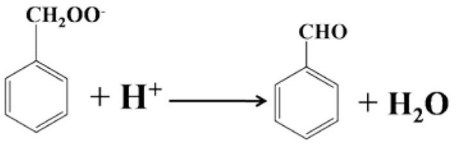

(7)

CONCLUSION

In summary, we have synthesized Ni(II)-doped cubic and hexagonal phases CdS semiconductor with nanosphere structure morphology by a simple method, which is able to be used as a well-photocatalyst to the activation of saturated primary C–H bond in toluene and substituted toluenes under mild conditions. The mixed phase CdS forms a homojunction, resulting in a reduction in its band width. It can effectively expand the response range and improve photocatalytic performance. Besides, doping Ni(II) to the photocatalyst is capable of greatly enhancing its electron transport and charge separation. The superior photocatalytic performance of Ni(II)-doped CdS is attributed to its unique structure assembly of specific morphology, which can be efficient transport and separation of photogenerated charge carriers under visible light irradiation. Mechanism research shows that Ni as a co-catalyst can improve the catalytic activity of the CdS. The as-prepared 3.0 wt%Ni(II)/CdS has highly active for the selective oxidation of inert primary C–H bond, which has great potential in photocatalytic selective activation of C–H bond to fine chemicals.

AUTHOR CONTRIBUTIONS

HS and LL designed and conducted the experiments. LL, HZ, and JH analyzed the data. HS, LL, LW, and QW wrote the paper.

FUNDING

This work was financially supported by the National Natural Science Foundation of China (21261021, 21663027, 51262028), the Science and Technology Support Project of Gansu Province (1504GKCA027), the Program for the Young Innovative Talents of Longyuan (NWNU-LKQN-15-2) and the Undergraduate Academic Innovative Research Team of Northwest Normal University.

SUPPLEMENTARY MATERIAL

The Supplementary Material for this article can be found online at: https://www.frontiersin.org/articles/10.3389/fchem.2018.00466/full#supplementary-material

REFERENCES

Chen, J., Wu, X. J., Yin, L., Li, B., Hong, X., Fan, Z., et al. (2015). One-pot synthesis of CdS nanocrystals hybridized with single-layer transition-metal dichalcogenide nanosheets for efficient photocatalytic hydrogen evolution. *Angew. Chem. Int. Ed Engl.* 54, 1210–1214. doi: 10.1002/anie.201410172

Cheng, F., and Xiang, Q. (2016). A solid-state approach to fabricate a CdS/CuS nano-heterojunction with promoted visible-light photocatalytic H_2-evolution activity. *RSC Adv.* 6, 76269–76272. doi: 10.1039/C6RA16076J

Cui, W., Li, J., Cen, W., Sun, Y., Lee, S. C., and Dong, F. (2017a). Steering the interlayer energy barrier and charge flow via bioriented transportation channels in g-C_3N_4: enhanced photocatalysis and reaction mechanism. *J. Catal.* 352, 351–360. doi: 10.1016/j.jcat.2017.05.017

Cui, W., Li, J., Dong, F., Sun, Y., Jiang, G., Cen, W., et al. (2017b). Highly efficient performance and conversion pathway of photocatalytic NO oxidation on SrO-Clusters@Amorphous carbon nitride. *Environ. Sci. Technol.* 51, 10682–10690. doi: 10.1021/acs.est.7b00974

Dai, X., Xie, M., Meng, S., Fu, X., and Chen, S. (2014). Coupled systems for selective oxidation of aromatic alcohols to aldehydes and reduction of nitrobenzene into aniline using CdS/g-C_3N_4 photocatalyst under visible light irradiation. *Appl. Catal. B Environ.* 15, 382–390. doi: 10.1016/j.apcatb.2014.04.035

Deka, K., and Kalita, M. P. C. (2018). Structural phase controlled transition metal (Fe, Co, Ni, Mn) doping in CdS nanocrystals and their optical, magnetic and photocatalytic properties. *J. Alloy Compd.* 757, 209–220. doi: 10.1016/j.jallcom.2018.04.323

Dong, Y., Kong, L., Wang, G., Jiang, P., Zhao, N., and Zhang, H. (2017). Photochemical synthesis of Co_xP as cocatalyst for boosting photocatalytic H_2 production via spatial charge separation. *Appl. Catal. B Environ.* 211, 245–251. doi: 10.1016/j.apcatb.2017.03.076

Gupta, R., Eswar, N. K., Modak, J. M., and Madras, G. (2017). Effect of morphology of zinc oxide in ZnO-CdS-Ag ternary nanocomposite towards photocatalytic inactivation of *E. coli* under UV and visible light. *Chem. Eng. J.* 307, 966–980. doi: 10.1016/j.cej.2016.08.142

Hao, H., Zhang, L., Wang, W., and Zeng, S. (2018). Modification of heterogeneous photocatalysts for selective organic synthesis. *Catal. Sci. Technol.* 8, 1229–1250. doi: 10.1039/C7CY01853C

He, J., Chen, L., Ding, D., Yang, Y. K., Au, C. T., and Yin, S. F. (2018). Facile fabrication of novel $Cd_3(C_3N_3S_3)_2$/CdS porous composites and their photocatalytic performance for toluene selective oxidation under visible light irradiation. *Appl. Catal. B Environ.* 233, 243–249. doi: 10.1016/j.apcatb.2018.04.008

He, J., Chen, L., Wang, F., Liu, Y., Chen, P., Au, C. T., et al. (2016a). CdS nanowires decorated with ultrathin MoS_2 nanosheets as an efficient photocatalyst for hydrogen evolution. *ChemSusChem* 9, 624–630. doi: 10.1002/cssc.201501544

He, J., Chen, L., Yi, Z. Q., Au, C. T., and Yin, S. F. (2016b). CdS nanorods coupled with WS_2 nanosheets for enhanced photocatalytic hydrogen evolution activity. *Ind. Eng. Chem. Res.* 55, 8327–8333. doi: 10.1021/acs.iecr.6b01511

Jin, J., Yu, J., Guo, D., Cui, C., and Ho, W. (2015). A hierarchical Z-Scheme CdS-WO_3 photocatalyst with enhanced CO_2 reduction activity. *Small* 11, 5262–5271. doi: 10.1002/smll.201500926

Kuang, P. Y., Ran, J. R., Liu, Z. Q., Wang, H. J., Li, N., Su, Y. Z., et al. (2015). Enhanced photoelectrocatalytic activity of BiOI nanoplate-zinc oxide nanorod p–n heterojunction. *Chemistry* 21, 15360–15368. doi: 10.1002/chem.201501183

Kumar, N., Pathak, T. K., Purohit, L. P., Swart, H. C., and Goswami, Y. C. (2018). Self-assembled Cu doped CdS nanostructures on flexible cellulose acetate substrates using low cost sol–gel route. *Nano Struct. Nano Objects* 16, 1–8. doi: 10.1016/j.nanoso.2018.03.001

Li, H., Yan, X., Lin, B., Xia, M., Wei, J., Yang, B., et al. (2018). Controllable spatial effect acting on photo-induced CdS@CoP@SiO_2 ball-in-ball nano-photoreactor for enhancing hydrogen evolution. *Nano Energy* 47, 481–493. doi: 10.1016/j.nanoen.2018.03.026

Li, L., Cheng, B., Wang, Y., and Yu, J. (2015a). Enhanced photocatalytic H_2-production activity of bicomponent NiO/TiO_2 composite nanofibers. *J. Colloid Interf. Sci.* 449, 115–121. doi: 10.1016/j.jcis.2014.10.072

Li, W., Feng, C., Dai, S., Yue, J., Hua, F., and Hou, H. (2015b). Fabrication of sulfur-doped g-C_3N_4/Au/CdS Z-scheme photocatalyst to improve the photocatalytic performance under visible light. *Appl. Catal. B Environ.* 168–169, 465–471. doi: 10.1016/j.apcatb.2015.01.012

Luo, M., Yao, W., Huang, C., Wu, Q., and Xu, Q. (2015a). Shape-controlled synthesis of Pd nanoparticles for effective photocatalytic hydrogen production. *RSC Adv.* 5, 40892–40898. doi: 10.1039/C5RA06352C

Luo, M., Yao, W., Huang, C., Wu, Q., and Xu, Q. (2015b). Shape effects of Pt nanoparticles on hydrogen production via Pt/CdS photocatalysts under visible light. *J. Mater. Chem. A* 3, 13884–13891. doi: 10.1039/C5TA00218D

Majeed, I., Nadeem, M. A., Al-Oufi, M., Nadeem, M. A., Waterhouse, G. I. N., Badshah, A., et al. (2016). On the role of metal particle size and surface coverage for photo-catalytic hydrogen production: a case study of the Au/CdS system. *Appl. Catal. B Environ.* 182, 266–276. doi: 10.1016/j.apcatb.2015.09.039

Martha, S., Nashim, A., and Parida, K. M. (2013). Facile synthesis of highly active g-C_3N_4 for efficient hydrogen production under visible light. *J. Mater. Chem. A* 1, 7816–7824. doi: 10.1039/c3ta10851a

Meng, A., Wu, S., Cheng, B., Yu, J., and Xu, J. (2018). Hierarchical TiO_2/$Ni(OH)_2$ composite fibers with enhanced photocatalytic CO_2 reduction performance. *J. Mater. Chem. A* 6, 4729–4736. doi: 10.1039/C7TA10073F

Murugesan, R., Sivakumar, S., Anandan, P., and Haris, M. (2017). Structural, optical and magnetic properties of Ba and Ni doped CdS thin films prepared by spray pyrolysis method. *J. Mater. Sci. Mater. Electron.* 28, 12432–12439. doi: 10.1007/s10854-017-7064-6

Nie, Y. C., Yu, F., Wang, L. C., Xing, Q. J., Liu, X., Pei, Y., et al. (2018). Photocatalytic degradation of organic pollutants coupled with simultaneous photocatalytic H_2 evolution over graphene quantum dots/Mn-N-TiO_2/g-C_3N_4 composite catalysts: performance and mechanism. *Appl. Catal. B Environ.* 227, 312–321. doi: 10.1016/j.apcatb.2018.01.033

Nosheen, E., Shah, S. M., and Iqbal, Z. (2017). Ru-dye grafted CdS and reduced graphene oxide Ru/CdS/rGO composite: an efficient and photo tuneable electrode material for solid state dye sensitized polymer solar cells. *J. Photochem. Photobiol. B* 167, 117–127. doi: 10.1016/j.jphotobiol.2016.12.034

Oros-Ruiz, S., Hernández-Gordillo, A., García-Mendoza, C., Rodríguez-Rodríguez, A. A., and Gómez, R. (2016). Comparative activity of CdS nanofibers superficially modified by Au, Cu, and Ni nanoparticles as co-catalysts for photocatalytic hydrogen production under visible light. *J. Chem. Technol. Biotechnol.* 91, 2205–2210. doi: 10.1002/jctb.4992

Oros-Ruiz, S., Zanella, R., Collins, S. E., Hernández-Gordillo, A., and Gómez, R. (2014). Photocatalytic hydrogen production by Au–M_xO_y (MAg, Cu, Ni) catalysts supported on TiO_2. *Catal. Commun.* 47, 1–6. doi: 10.1016/j.catcom.2013.12.033

Pal, N., Pramanik, M., Bhaumik, A., and Ali, M. (2014). Highly selective and direct oxidation of cyclohexane to cyclohexanone over vanadium exchanged NaY at room temperature under solvent-free conditions. *J. Mol. Catal. A Chem.* 392, 299–307. doi: 10.1016/j.molcata.2014.05.027

Ran, J., Yu, J., and Jaroniec, M. (2011). $Ni(OH)_2$ modified CdS nanorods for highly efficient visible-light-driven photocatalytic H_2 generation. *Green Chem.* 13, 2708–2713. doi: 10.1039/c1gc15465f

She, H. D., Zhou, H., Li, L. S., Wang, L., Huang, J. W., and Wang, Q. Z. (2018). Nickel-doped excess oxygen defect Titanium Dioxide for efficient selective photocatalytic oxidation of Benzyl alcohol. *ACS Sust. Chem. Eng.* doi: 10.1021/acssuschemeng.8b02217

Song, L., Chen, Z., Li, T., and Zhang, S. (2017). A novel Ni^{2+}-doped Ag_3PO_4 photocatalyst with high photocatalytic activity and enhancement mechanism. *Mater. Chem. Phys.* 186, 271–279. doi: 10.1016/j.matchemphys.2016.10.053

Su, Y. Z., Xiao, K., Liao, Z. J., Zhong, Y. H., Li, N., Chen, Y. B., et al. (2013). Directed electrochemical synthesis of ZnO/PDMcT core/shell nanorod arrays with enhanced photoelectrochemical properties. *Int. J. Hydrogen Energy* 38, 15019–15026. doi: 10.1016/j.ijhydene.2013.09.090

Wang, L., Duan, S. H., Jin, P. X., She, H. D., Huang, J. W., Lei, Z. Q., et al. (2018a). Anchored Cu(II) tetra(4-carboxylphenyl)porphyrin to P25 (TiO_2) for efficient photocatalytic ability in CO_2 reduction. *Appl. Catal. B Environ.* 239, 599–608. doi: 10.1016/j.apcatb.2018.08.007

Wang, P., Sheng, Y., Wang, F., and Yu, H. (2018b). Synergistic effect of electron-transfer mediator and interfacial catalytic active-site for the enhanced H_2-evolution performance: a case study of CdS-Au photocatalyst. *Appl. Catal. B Environ.* 220, 561–569. doi: 10.1016/j.apcatb.2017.08.080

Wang, Q. Z., Li, J. J., Bai, Y., Lian, J. H., Huang, H., Li, Z. Q., et al. (2014). Photochemical preparation of Cd/CdS photocatalysts and their efficient photocatalytic hydrogen production under visible light irradiation. *Green Chem.* 16, 2728–2735. doi: 10.1039/C3GC42466A

Wang, Q. Z., Niu, T. J., Wang, L., Yan, C. X., Huang, J. W., He, J. J., et al. (2018c). $FeF_2/BiVO_4$ heterojuction photoelectrodes and evaluation of its photoelectrochemical performance for water splitting. *Chem. Eng. J.* 337, 506–514. doi: 10.1016/j.cej.2017.12.126

Wang, Y., Wang, Y., and Xu, R. (2013). Photochemical deposition of Pt on CdS for H_2 evolution from water: markedly enhanced activity by controlling Pt reduction environment. *J. Phys. Chem. C* 117, 783–790. doi: 10.1021/jp309603c

Wei, R. B., Huang, Z. L., Gu, G. H., Wang, Z., Zeng, L., Chen, Y., et al. (2018). Dual-cocatalysts decorated rimous CdS spheres advancing highly-efficient visible-light photocatalytic hydrogen production. *Appl. Catal. B Environ.* 231, 101–107. doi: 10.1016/j.apcatb.2018.03.014

Wei, R. B., Kuang, P. Y., Cheng, H., Chen, Y. B., Long, J. Y., Zhang, M. Y., et al. (2017). Plasmon-enhanced photoelectrochemical water splitting on gold nanoparticle decorated ZnO/CdS nanotube arrays. *ACS Sust. Chem. Eng.* 5, 4249–4257. doi: 10.1021/acssuschemeng.7b00242

Weng, X., Zeng, Q., Zhang, Y., Dong, F., and Wu, Z. (2016). Facile approach for the syntheses of ultrafine TiO_2 nanocrystallites with defects and C heterojunction for photocatalytic water splitting. *ACS Sust. Chem. Eng.* 4, 4314–4320. doi: 10.1021/acssuschemeng.6b00828

Weng, X., Zhang, Y., Bi, F., Dong, F., Wu, Z., and Darr, J. A. (2017). Thermocatalytic syntheses of highly defective hybrid nano-catalysts for photocatalytic hydrogen evolution. *J. Mater. Chem. A* 5, 23766–23775. doi: 10.1039/C7TA07808K

Wu, M., Yan, J. M., Tang, X. N., Zhao, M., and Jiang, Q. (2014). Synthesis of potassium-modified graphitic carbon nitride with high photocatalytic activity for hydrogen evolution. *Chem. Sus. Chem.* 7, 2654–2658. doi: 10.1002/cssc.201402180

Xiang, Q., Cheng, F., and Lang, D. (2016). Hierarchical layered WS_2/Graphene-modified CdS nanorods for efficient photocatalytic hydrogen evolution. *Chem. Sus. Chem.* 9, 996–1002. doi: 10.1002/cssc.201501702

Xue, C., Li, H., An, H., Yang, B. L., Wei, J. J., and Yang, G. (2018). NiSx quantum dots accelerate electron transfer in $Cd_{0.8}Zn_{0.2}S$ photocatalytic system via an rGo nanosheet "Bridge" toward visible-light-driven hydrogen evolution. *ACS Catal.* 8, 1532–1545. doi: 10.1021/acscatal.7b04228

Yan, H., Yang, J., Ma, G., Wu, G., Zong, X., Lei, Z., et al. (2009). Visible-light-driven hydrogen production with extremely high quantum efficiency on Pt–PdS/CdS photocatalyst. *J. Catal.* 266, 165–168. doi: 10.1016/j.jcat.2009.06.024

Yan, X., Xue, C., Yang, B., and Yang, G. (2017). Novel three-dimensionally ordered macroporous Fe^{3+}-doped TiO_2 photocatalysts for H_2 production and degradation applications. *Appl. Surf. Sci.* 394, 248–257. doi: 10.1016/j.apsusc.2016.10.077

Yang, D., Wu, T., Chen, C., Guo, W., Liu, H., and Han, B. (2017). The highly selective aerobic oxidation of cyclohexane to cyclohexanone and cyclohexanol over V_2O_5@TiO_2 under simulated solar light irradiation. *Green Chem.* 19, 311–318. doi: 10.1039/C6GC02748B

Yang, H., Jin, Z., Liu, D., Fan, K., and Wang, G. (2018). Visible light harvesting and spatial charge separation over the creative Ni/CdS/Co_3O_4 photocatalyst. *J. Phys. Chem. C* 122, 10430–10441. doi: 10.1021/acs.jpcc.8b01666

Yu, H., Huang, X., Wang, P., and Yu, J. (2016). Enhanced photoinduced-stability and photocatalytic activity of CdS by dual amorphous cocatalysts: synergistic effect of Ti(IV)-hole cocatalyst and Ni(II)-electron cocatalyst. *J. Phys. Chem. C* 120, 3722–3730. doi: 10.1021/acs.jpcc.6b00126

Yuan, R., Fan, S., Zhou, H., Ding, Z., Lin, S., Li, Z., et al. (2013). Chlorine-radical-mediated photocatalytic activation of C–H bonds with visible light. *Angew. Chem. Int. Ed. Engl.* 52, 1035–1039. doi: 10.1002/anie.201207904

Zhang, K., Qian, S., Kim, W., Kim, J. K., Sheng, X., Lee, J. Y., et al. (2017). Double 2-dimensional H_2-evoluting catalyst tipped photocatalyst nanowires: a new avenue for high-efficiency solar to H_2 generation. *Nano Energy* 34, 481–490. doi: 10.1016/j.nanoen.2017.03.005

Zhang, L., Ding, Q., Huang, Y., Gu, H., Miao, Y. E., and Liu, T. (2015). Flexible hybrid membranes with $Ni(OH)_2$ nanoplatelets vertically grown on electrospun carbon nanofibers for high-performance supercapacitors. *ACS Appl. Mater. Interf.* 7, 22669–22677. doi: 10.1021/acsami.5b07528

Zhang, Y., Zhang, N., Tang, Z. R., and Xu, Y. J. (2012). Transforming CdS into an efficient visible light photocatalyst for selective oxidation of saturated primary C–H bonds under ambient conditions. *Chem. Sci.* 3, 2812–2822. doi: 10.1039/C2SC20603J

Zhao, N., Peng, J., Liu, G., Zhang, Y., Lei, W., Yin, Z., et al. (2018). PVP-capped CdS nanopopcorns with type-II homojunctions for highly efficient visible-light-driven organic pollutant degradation and hydrogen evolution. *J. Mater. Chem. A* doi: 10.1039/C8TA03414A

Zou, J. P., Wang, L. C., Luo, J., Nie, Y. C., Xing, Q. J., Luo, X. B., et al. (2016). Synthesis and efficient visible light photocatalytic H_2 evolution of a metal-free g-C_3N_4/graphene quantum dots hybrid photocatalyst. *Appl. Catal. B Environ.* 193, 103–109. doi: 10.1016/j.apcatb.2016.04.017

Conflict of Interest Statement: The authors declare that the research was conducted in the absence of any commercial or financial relationships that could be construed as a potential conflict of interest.

frontiers in Chemistry

ORIGINAL RESEARCH
published: 02 October 2018
doi: 10.3389/fchem.2018.00393

BiOCl Decorated $NaNbO_3$ Nanocubes: A Novel p-n Heterojunction Photocatalyst With Improved Activity for Ofloxacin Degradation

Jingjing Xu[1]*, *Bingbing Feng*[1], *Ying Wang*[1], *Yadi Qi*[1], *Junfeng Niu*[2] and *Mindong Chen*[1]

[1] Jiangsu Key Laboratory of Atmospheric Environment Monitoring and Pollution Control, School of Environmental Science and Engineering, Collaborative Innovation Center of Atmospheric Environment and Equipment Technology, Jiangsu Engineering Technology Research Center of Environmental Cleaning Materials, Nanjing University of Information Science and Technology, Nanjing, China, [2] Research Center for Eco-Environmental Engineering, Dongguan University of Technology, Dongguan, China

OPEN ACCESS

Edited by:
Fan Dong,
Chongqing Technology and Business University, China

Reviewed by:
Huogen Yu,
Wuhan University of Technology, China
Tianhua Zhou,
Fujian Institute of Research on the Structure of Matter (CAS), China

***Correspondence:**
Jingjing Xu
xujj@nuist.edu.cn

Specialty section:
This article was submitted to Catalysis and Photocatalysis, a section of the journal Frontiers in Chemistry

Received: 12 July 2018
Accepted: 14 August 2018
Published: 02 October 2018

Citation:
Xu J, Feng B, Wang Y, Qi Y, Niu J and Chen M (2018) BiOCl Decorated $NaNbO_3$ Nanocubes: A Novel p-n Heterojunction Photocatalyst With Improved Activity for Ofloxacin Degradation Front. Chem. 6:393. doi: 10.3389/fchem.2018.00393

BiOCl/$NaNbO_3$ p-n heterojunction photocatalysts with significantly improved photocatalytic performance were fabricated by a facile *in-situ* growth method. The obtained BiOCl/$NaNbO_3$ samples were characterized by UV-vis absorption spectroscopy, scanning electron microscopy (SEM), X-ray diffraction (XRD), photocurrent (PC) and photoluminescence spectroscopy (PL). The photocatalytic activity of the BiOCl/$NaNbO_3$ samples was investigated by the degradation of a typical antibiotic Ofloxacin (OFX). The experimental results showed that BiOCl/$NaNbO_3$ composites exhibited much higher photocatalytic activity for OFX degradation compared to pure $NaNbO_3$ and BiOCl. The degradation percent of OFX reached 90% within 60 min, and the apparent rate constant was about 8 times as that of pure $NaNbO_3$ and BiOCl. The improved activity can be attributed to the formation of p-n junction between $NaNbO_3$ and BiOCl. The formed p-n junction facilitated the separation of photogenerated holes and electrons, thereby enhancing photocatalytic activity. In addition, the composite photocatalyst showed satisfactory stability for the degradation of OFX. Due to the simple synthesis process, high photocatalytic activity, and the good recyclability of these composite photocatalysts, the results of this study would provide a good example for the rational design of other highly efficient heterojunction photocatalytic materials.

Keywords: photocatalysis, BiOCl, $NaNbO_3$, p–n junction, ofloxacin

INTRODUCTION

The problem of water pollution has attracted increasing attention worldwide due to many toxic pollutants continue to enter into our water bodies (Ao et al., 2016b; Li et al., 2018; Yuan et al., 2018). As a green and sustainable technology, semiconductor photocatalysis can completely eliminate most pollutants in water and air (Zhang et al., 2016, 2017a,b; Chen et al., 2018; Guo et al., 2018; He et al., 2018; Yang et al., 2018). The contaminants are degraded by hydroxyl radical or other free

radicals which are produced in the process after the absorption of light (Li et al., 2015; Cao et al., 2016; Xu et al., 2016; Yu et al., 2016; Zhang and Xiao, 2017; Han et al., 2018; Zhong et al., 2018). There are many semiconductors (such as oxides, sulfides, nitrates and silver based compounds etc.) can be served as photocatalysts to induce the degradation of pollutants.

In recent years, $NaNbO_3$ has attracted much attention due to its unique properties of nonlinear optics, ferroelectric, ionic conduction, photorefractive and photocatalytic properties (Katsumata et al., 2010; Lv et al., 2010; Li et al., 2012a, 2013; Fan et al., 2015; Qian et al., 2018). Because $NaNbO_3$ is a typical n type semiconductor with unique crystal [NbO6] angle eight-hedral crystal structure, it has the advantage of relative high transfer efficiency of electrons during the photocatalytic process (Shi et al., 2014b; Song et al., 2015). Recent studies have shown that $NaNbO_3$ can be used as an efficient photocatalyst for the evolution of H_2 and the reduction of CO_2 (Li et al., 2012b, 2014). In addition, $NaNbO_3$ also shows the ability for the decomposition of organic pollutants (Li et al., 2008; Li, 2010; Chen et al., 2014). However, because $NaNbO_3$ has a large band-gap, it cannot be used as a visible light responsive photocatalyst. Various experiments have shown that forming heterojunction with other semiconductor materials was a promising way to improve the photocatalytic activity of $NaNbO_3$. For example, an effective composite photocatalyst $NaNbO_3/WO_3$ has been proved to has stronger dye degradation activity compared with the corresponding single component (Shifu et al., 2013). Moreover, other $NaNbO_3$ based composite photocatalysts, such as $AgO_2/NaNbO_3$ (Zhang et al., 2017), $Pt/NaNbO_3$ (Liu et al., 2016) and $CdS/NaNbO_3$ (Kumar et al., 2014), were also successfully prepared for photocatalytic degradation of pollutants.

On the other hand, although BiOCl (a typical p-type oxyhalide semiconductor) has been extensively investigated in the field of photocatalysis (Ye et al., 2014; Ao et al., 2016a; Hu et al., 2016; Mao et al., 2016; Ma Y. C. et al., 2016; Wang et al., 2018). However, the recombination rate of photogenerated charges in pure phase of BiOCl is high, resulting in its limited photocatalytic activity under UV light. It has recently been found that the photocatalytic activity of BiOCl can be promoted through the formation of p-n junctions with n type semiconductors (Rajeshwar et al., 2001; Wang et al., 2012; Fang et al., 2016). The enhanced activity can be ascribed to the fact that the internal electric field at the p-n junction interface improved the separation and transfer of photo-generated charges (Yan et al., 2017). However, as far as we know, the preparation and activity of $BiOCl/NaNbO_3$ p-n heterojunction photocatalyst have not been studied yet.

In the present work, we constructed a new type of p-n heterojunction photocatalyst ($BiOCl/NaNbO_3$) by a simple *in situ* growth method. Compared with pure BiOCl and $NaNbO_3$, the composite has better photocatalytic activity for the degradation of ofloxacin (OFX). The experimental results proved that the p-n junctions formed between $BiOCl/NaNbO_3$ composites promote the transfer and separation of photogenerated electron-hole pairs, thus enhancing the photocatalytic activity.

EXPERIMENTAL

Synthesis of $NaNbO_3$ Cubes

All the reagents and materials used in this experiment were analytical grades. All of them were purchased from China pharmaceutical chemical reagents Co., Ltd. $NaNbO_3$ was directly synthesized by hydrothermal method described as following. 2 g Nb_2O_5 was added to the 120 mL NaOH solution (10 M) and stirred for 120 min before the suspension was transferred to the 200 ml Teflon-lined stainless steel autoclave. The reaction kettle was kept at 150°C for 48 h. Subsequently, the autoclave was cooled to room temperature naturally after the reaction. Then remove the reactor and precipitate it naturally, pour the supernatant out of the precipitate and centrifugate, then wash it with deionized water and ethanol for 3–5 times. Finally, the product was dried for 12 h in a vacuum oven at 60°C.

Synthesis of $BiOCl/NaNbO_3$ p–n Junction Photocatalysts

$BiOCl/NaNbO_3$ heterostructures were prepared by a simple *in-situ* growth method. A certain amount of $Bi(NO_3)_3{\cdot}5H_2O$ was added to 300 mL of ultrapure water and stirred for 1 h to form solution A. Meanwhile, $NaNbO_3$ powder was dispersed in 80 mL ultrapure water and sonicated for 30 min to form solution B. A certain amount of KCl was added to 60 mL ultrapure water to form solution C. Finally, B and C were slowly added to A under rapid stirring. Afterwards, the stirring was continued for 24 h. The product was then filtered and thoroughly washed with distilled water and ethanol before it was dried at 60°C for 24 h. By Changing the amount of $Bi(NO_3)_3{\cdot}5H_2O$ and KCl added, $NaNbO_3$/BiOCl composites with different theoretical BiOCl mass ratios of 10, 25, 75, and 100% (expressed as BN-1, BN-2, BN-3, and BN-4) were produced. In order to facilitate comparison, pure BIOCl samples are also prepared in the same way, that is to say, no $NaNbO_3$ is added in the process of making composite samples.

Characterization of Photocatalysts

The results of X ray diffraction (XRD) scanning of pure BiOCl, $NaNbO_3$ and $BiOCl/NaNbO_3$ were recorded by Shimadzu XRD 6100 X-ray diffractometer. The morphology and microstructure of the samples were characterized by scanning electron microscopy (SEM, Hitach S-4800). The band gap (Eg) of the sample was measured by UV-vis absorption spectroscopy at 200∼800 nm at room temperature, and the integrated ball attachment was installed on the ultraviolet visible spectrophotometer (UV-3600). Photocurrent (PC) and mott-Schottky (MS) were carried out on the traditional three electrode system (the electrochemical workstation of CHI-660D Chenhua chemical equipment company in Shanghai, China). The contrast electrode and the reference electrode are platinum electrodes and Ag/AgCl electrodes respectively.

Photocatalytic Activity Experiments

The experimental vessel is a double-layer quartz beaker with cooling water circulation system for photocatalytic reaction. During the experiment, the temperature of the solution can

be maintained at about 25 °C, so as to reduce the influence of temperature on the experiment. The light source used in the photocatalytic process is a 300 W xenon lamp(200 nm<λ<400 nm), and before irradiation, 25 mg photocatalyst was added to 50 mL OFX solution (5 mg/L). The suspension was stirred magnetically in the dark for 30 min to achieve adsorption/desorption equilibrium between photocatalysts and OFX. During the photocatalytic process, a certain suspension was sampled at the prescribed time intervals. The sampled suspension was centrifuged before the determination of OFX concentration.

RESULTS AND DISCUSSION

Characterizations

The XRD diagrams of pure BiOCl, $NaNbO_3$ and BiOCl/$NaNbO_3$ composites were shown in **Figure 1**. It can be seen that there are seven different diffraction peaks, which can be indexed to tetragonal BiOCl (JCPDS card number 01-0600) (Ma W. et al., 2016). Sharp and narrow diffraction peaks indicate good crystallinity for pure BiOCl. From the pattern of pure $NaNbO_3$, several main diffraction peaks can be seen at 22.7, 32.5, 46.4, 52.7, 58.1, and 68.11° corresponding to (001), (110), (002), (021), (112), and (022) planes of $NaNbO_3$ orthorhombic phases (JCPDS card number 33-1270) (Saito and Kudo, 2013). The diffraction peaks of pure BiOCl and $NaNbO_3$ and the diffraction peaks of heterostructure BiOCl/$NaNbO_3$ composites can be clearly observed by XRD diagram. In addition, when the mass ratio of BiOCl to $NaNbO_3$ increases from 10 to 100%, the diffraction peak intensity of BiOCl increases and the corresponding $NaNbO_3$ peak intensity decreases. Furthermore, when BiOCl grows on $NaNbO_3$, its diffraction peak is wider than that of pure BiOCl. This phenomenon indicates that BiOCl on the surface of $NaNbO_3$ cube has smaller particle size. The result indicates that the addition of $NaNbO_3$ can effectively inhibit the growth of BiOCl (Shang et al., 2009). XRD showed that the samples were clean and had no other phase of impurity, so the composites were basically composed of BiOCl and $NaNbO_3$.

The morphology and structure of BiOCl, $NaNbO_3$, and BiOCl/$NaNbO_3$ composites can be clearly seen by SEM characterization. The SEM image of pure BiOCl is displayed in **Figure 2a**. As can be seen from the graph, pure BiOCl is composed of regular, square like nano plates. At the same time, we can see that the synthesized $NaNbO_3$ has irregular cubic shape and smooth surface in **Figure 2b**. A typical SEM image of the BN-3 composite is shown in **Figure 2c**. It can be seen that $NaNbO_3$ cubes are anchored by BiOCl nanosheets which are thiner and smaller than pure BiOCl. During the in-sith growth process, the $NaNbO_3$ particles played a role of heterogeneity and inhibited the

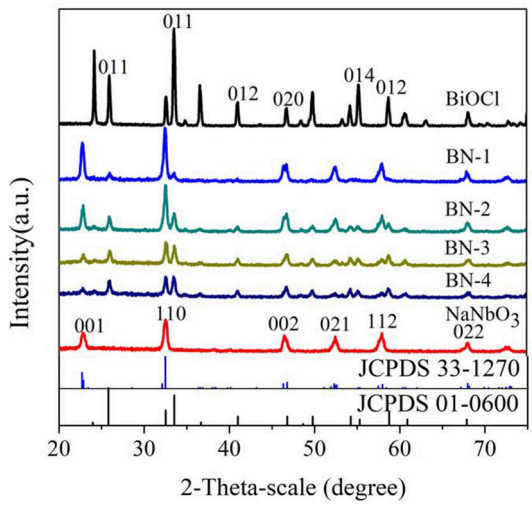

FIGURE 1 | XRD patterns of BiOCl, $NaNbO_3$, and BiOCl/$NaNbO_3$ composites with different BiOCl contents.

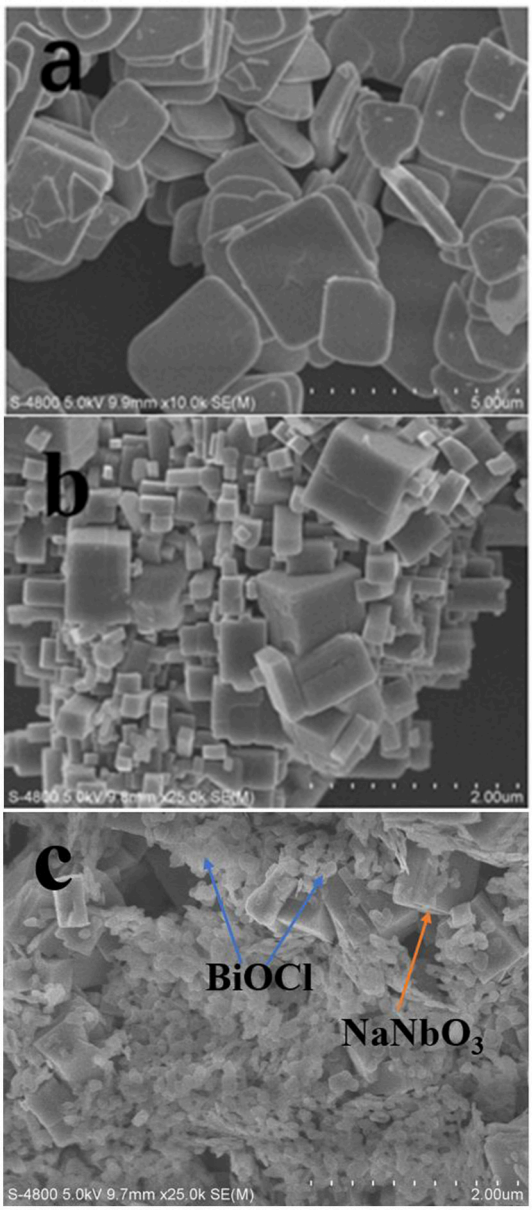

FIGURE 2 | SEM images of pure BiOCl **(a)**, NaNbO3 **(b)** and BN-3 **(c)**.

growth of BiOCl to lager ones. After analyzing the SEM image, the conclusion is in good agreement with the previous XRD analysis. BiOCl and $NaNbO_3$ form p-n junctions at the interface because of the close contact between BiOCl and $NaNbO_3$. This improves the carrier transport rate and separation efficiency in photocatalysis and helps to improve the activity.

The optical properties of the samples have a great influence on the utilization of sunlight. Therefore, UV-DRS for pure BiOCl, $NaNbO_3$ and BiOCl/$NaNbO_3$ composites are investigated. As we can see from **Figure 3**, the absorbance threshold of $NaNbO_3$ and pure BiOCl are at about 400 and 380 nm, respectively. The band-gap of photocatalysts can be obtained from the following equation:

$$Eg = 1240/\lambda,$$

where Eg is the band-gap energy and λ is the cut off wavelength. Therefore, the band gaps of $NaNbO_3$ and BiOCl prepared were 3.10 and 3.26 eV, respectively, which are similar to those reported previously (Shi et al., 2014a; Ma W. et al., 2016). It can also be seen from **Figure 3** that BiOCl/$NaNbO_3$ exhibits higher UV absoption performance compared to pure BiOCl. Furthermore, the band edge of BiOCl/$NaNbO_3$ exhibits a little red shift compared to pure BiOCl.

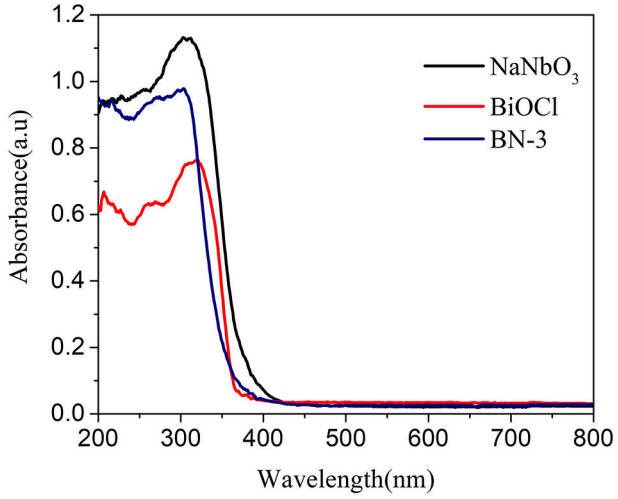

FIGURE 3 | UV-vis absorption spectra of BiOCl, $NaNbO_3$ and BN-3.

Through the band structure of the catalyst, we further explore the way of carrier transfer. The type and surface potential of $NaNbO_3$ and BiOCl semiconductors are determined by the Mott-Schottky plots. The positive tangent in the graph indicates that the sample is n type semiconductor, while the negative tangent in the graph indicates that the sample is p type semiconductor (Kuang et al., 2015). The results shown in **Figures 4A,B** show that BiOCl and $NaNbO_3$ are p-type and n-type semiconductors, respectively. In addition, the flat potential (relative to Ag/AgCl) of BiOCl and $NaNbO_3$ are 2.30 V and −0.70 V respectively through the intersection point between tangent and abscissa. According to the following equation, the potential (relative to Ag/AgCl) can be converted to a normal hydrogen electrode (NHE). (1) (Zhou et al., 2017; Liu et al., 2018):

$$E_{NHE} = E_{Ag/AgCl} + E^0_{Ag/AgCl}$$

where $E^0_{Ag/AgCl} = 0.197$ V. In particular, the maximum of the valence band (VB) is about 0.1 V lower than the flat potential of the p-type semiconductor; the minimum value of the conduction band (CB) is about 0.1 V higher than the flat potential of the n-type semiconductor (Liu et al., 2017b). Therefore, the VB position of BiOCl and the CB position of $NaNbO_3$ are 2.60 and −0.60 V (vs. NHE), respectively. The Eg of BiOCl and $NaNbO_3$ were 3.26 and 3.10, respectively. Therefore, according to Eg. (2) (Liu et al., 2017a):

$$Eg = E_{VB} - E_{CB}$$

the position of CB and VB for BiOCl and $NaNbO_3$ are −0.66 and 2.50 V, respectively.

Photocatalytic Activity

The photocatalytic activity of BiOCl/$NaNbO_3$ composites with p-n junctions is mainly studied on the degradation of OFX under UV irradiation. As shown in **Figure 5A**, In the presence of $NaNbO_3$ or BiOCl, about 20% OFX are decomposed within

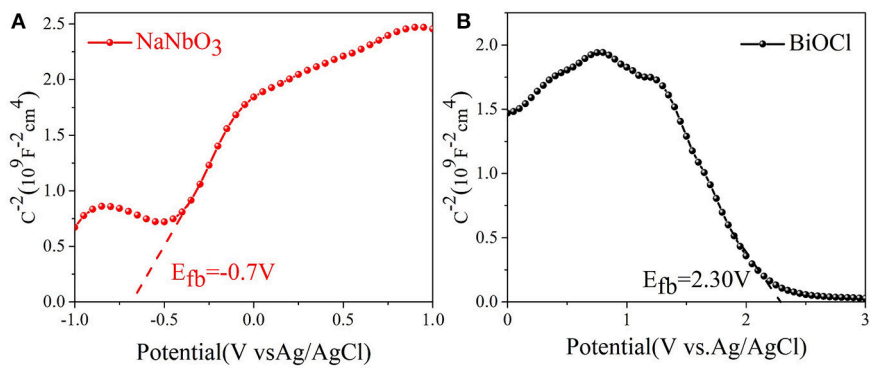

FIGURE 4 | The Mott-Schottky plots of **(A)** $NaNbO_3$ and **(B)** BiOCl.

60 min. It can also be seen that all BiOCl/$NaNbO_3$ composites exhibit significantly higher photocatalytic activity than that of pure BiOCl and $NaNbO_3$. In addition, it was found that the mass ratio of BiOCl has a significant effect on the activity of BiOCl/$NaNbO_3$ composites. Specifically, the activity increase gradually when the BiOCl content is increased from 10 to 75%. When the content of BiOCl is further increased to 100%, the activity of the sample begin to decrease. Therefore, sample BN-3 with BiOCl mass ratio of 75% exhibites the highest activity (the degradation percent of OFX is about 90% after 60 min irradiation). The time evolution of the OFX solution spectra in the degradation process by BN-3 were measured and are shown in **Figure 5B**. The absorption peak of OFX decreases as the increase of irradiation time and reaches the minimum at 60 min.

It has also been found that the photocatalytic degradation of OFX follows pseudo-first order kinetic calculated from the following formula (as shown in **Figure 5C**):

$$-\ln(C_t/C_0) = kt$$

The obtained k of OFX removal rate of pure BiOCl, $NaNbO_3$ and BiOCl /$NaNbO_3$ composites can be calculated by this formula. In **Figure 5D**, it is more clear to see that the kinetic constants of BiOCl, $NaNbO_3$, BN-1, BN-2, BN-3, and BN-4 are 0.0021, 0.002, 0.0071, 0.0094, 0.016, and 0.011 min^{-1}, respectively. Therefore, compared with the single phase BiOCl and $NaNbO_3$, the BiOCl/$NaNbO_3$ composite can promote the separation of the electron-hole pairs on the interface, thus promoting the enhancement of the photocatalytic activity.

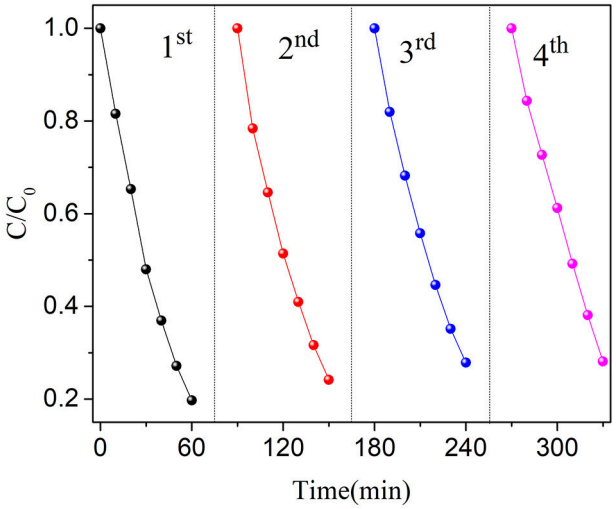

FIGURE 6 | Cyclic operation of BN-3 under UV light.

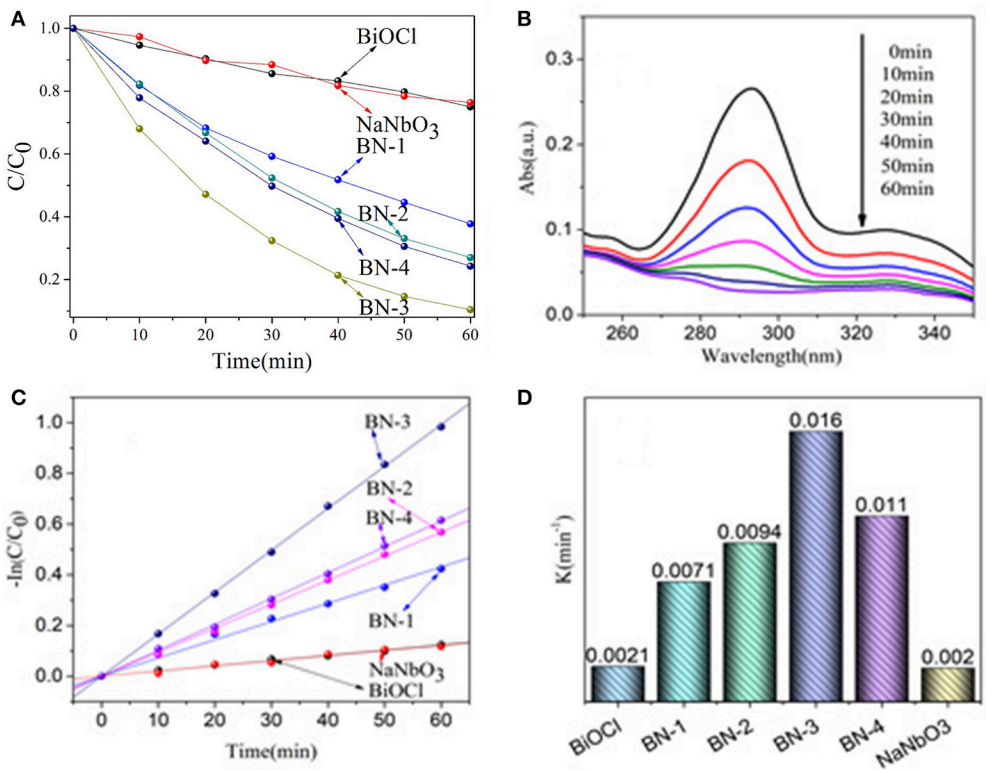

FIGURE 5 | (A) Photocatalytic activities of $NaNbO_3$, BiOCl and BiOCl/$NaNbO_3$ composites for the degradation of OFX (5 mg/L) under UV light irradiation (200 nm < λ <400 nm), **(B)** UV spectral changes of OFX in aqueous BN-3 composites dispersions as a function of irradiation time, **(C)** The kinetics of OFX degradation, and **(D)** The degradation rateconstants.

The stability of one photocatalyst is very important to the practical application. Therefore, the recycle experiments are carried out for BN-3. As shown in **Figure 6**, the photocatalytic performance of the catalyst has only slight loss after four cycles of reutilization of the photocatalyst. This experimental phenomenon indicates that the photocatalyst is stable to the photodegradation of OFX. The experimental results show that the photocatalytic degradation of organic pollutants by the prepared BiOCl/$NaNbO_3$ composites is stable, and it is of great significance for the practical application of the catalyst.

Photocatalytic Mechanism

The interfacial charge transfer kinetics between BiOCl and $NaNbO_3$ can be further elucidated by photocurrent measurements. **Figure 7** shows the photocurrent-time curves of the BiOCl, $NaNbO_3$, and BN-3 composites under an on/off cycle of intermittent UV irradiation. As shown in **Figure 7**, BN-3 composite exhibits much higher photocurrent than that of pure BiOCl and $NaNbO_3$. Therefore, the BN-3 can transfer and separate photogenerated electron hole pairs more efficiently under ultraviolet light irradiation. In addition, the photoluminescence (PL) spectra of pure BiOCl, $NaNbO_3$ and BiOCl/$NaNbO_3$ composite samples were tested to determine the separation efficiency of photo-generated charges. The excitation wavelength used in the test is 285 nm. In **Figure 8**, it is found that pure $NaNbO_3$ is the strongest relative to other sample emission peaks within the range of 350–550 nm. For pure BiOCl samples, their emission peaks are relatively weak relative to pure $NaNbO_3$. The PL luminescence strength of BN-3 composites is the lowest in the three samples. The results show that the combination of pure BiOCl and $NaNbO_3$ can effectively inhibit the recombination of electron hole pairs. The results are in good agreement with the measurement results of photocurrent.

In order to study the degradation mechanism, the main active species produced in the degradation process were determined. Therefore, three radical scavengers such as isopropanol (IPA, •OH scavenger) (Cao et al., 2012), ammonium oxalate (AO, h^+ scavenger) (Chang et al., 2013) and p-benzoquinone (BQ, $•O_{2-}$ scavenger) (Sun et al., 2017) have been added separately in the degradation systems. When BQ and AO were introduced, the degradation rate of OFX decreased significantly (see **Figure 9**). Moreover, the degradation rate of OFX was also decreased in the presence of IPA. These results indicate that h^+ and $•O_{2-}$ play an important role in the degradation process. •OH has a certain effect on the degradation of OFX. Therefore, we can conclude that the free radicals of $•O_{2-}$, h^+ and •OH in active species play a certain role in the degradation of OFX.

The formation of heterojunction in the composite system has a positive effect on the separation of photogenerated electrons and holes. Based on the above experimental results, we propose a reasonable photocatalytic mechanism for BiOCl/$NaNbO_3$ (**Scheme 1**). The enhanced photocatalytic activity of BiOCl/$NaNbO_3$ heterojunction originates from the

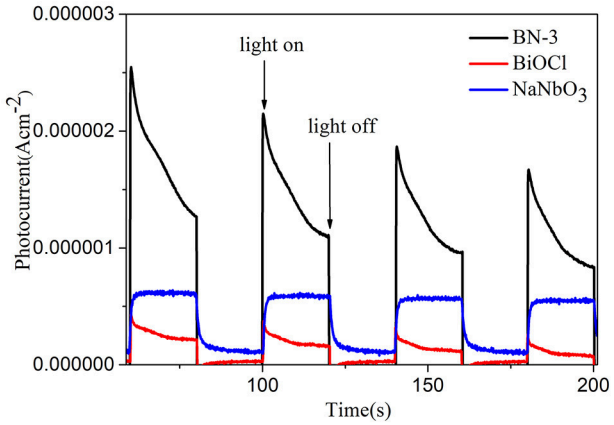

FIGURE 7 | Transient photocurrent responses for $NaNbO_3$, BiOCl, and BN-3 composite.

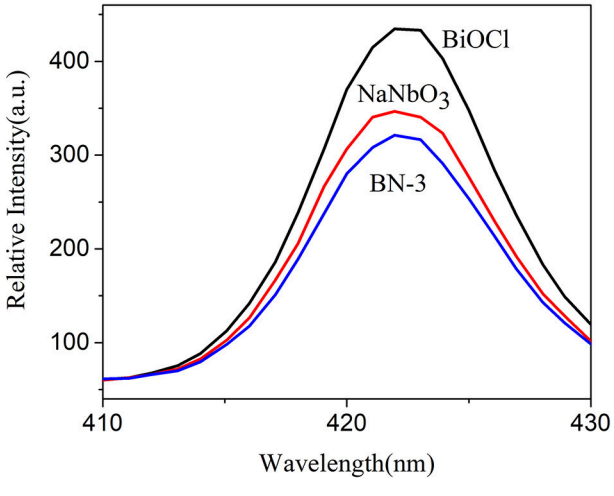

FIGURE 8 | PL emission spectra of $NaNbO_3$, BiOCl, and BN-3 composite.

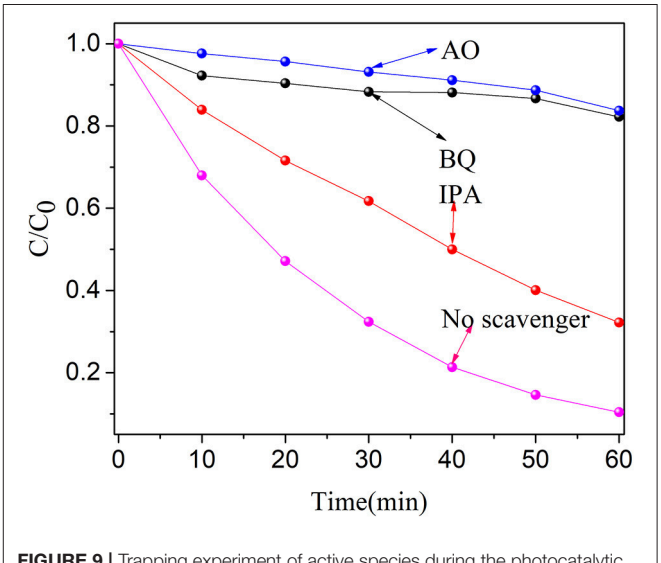

FIGURE 9 | Trapping experiment of active species during the photocatalytic degradation of OFX over BN-3 under UV light irradiation.

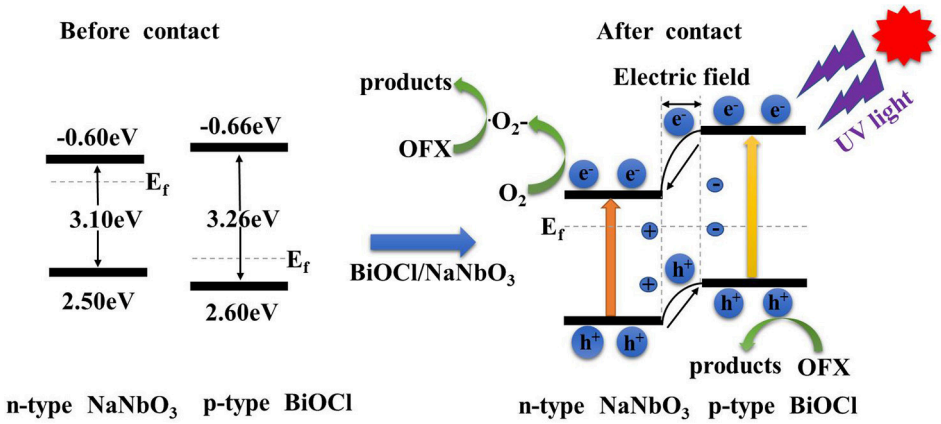

SCHEME 1 | Proposed possible mechanism of the photocatalytic degradation of pollutants over $BiOCl/NaNbO_3$ p–n junction under UV light irradiation.

unique matching band location of these two semiconductors after forming heterojunction. Based on the experimental data, we know that the band gap of BiOCl is larger than that of $NaNbO_3$. The Fermi level (E_f) of BiOCl is located near the valence band because it is a p type semiconductor, and the Fermi level of n type semiconductor $NaNbO_3$ approaches the conduction band. When the mixture of BiOCl and $NaNbO_3$ forms a p-n type heterojunction of $BiOCl/NaNbO_3$, the Fermi level of BiOCl moves upwards, while the Fermi level of the $NaNbO_3$ moves downward until the Fermi level of BiOCl and $NaNbO_3$ is at the same level. Finally, the CB position of BiOCl becomes higher than $NaNbO_3$ after moving up. At the same time, BiOCl and $NaNbO_3$ form an internal electric field in the final equilibrium state. At the same time, the valence band (VB) of $NaNbO_3$ is also lower than that of BiOCl. Due to the special band structure of the $BiOCl/NaNbO_3$ composite, the photoelectrons are excited from the VB of the BiOCl to the CB, because the special ladder like structure of the $BiOCl/NaNbO_3$ heterostructure leads to the electronic transfer from CB of BiOCl to the CB of $NaNbO_3$. Electrons stored in $NaNbO_3$'s CB can react with dissolved O_2 to form $\bullet O_{2^-}$, while the adsorbed hydroxy or H_2O molucules can also react with h^+ to form •OH or directly oxidize organic pollutants. Therefore, the formed p-n junction between BiOCl and $NaNbO_3$ provide an effective electron transfer path to reduce the recombination of electron-hole pairs, thus improving the activity of the as fabricated $BiOCl/NaNbO_3$ composites.

CONCLUSIONS

In this work, $BiOCl/NaNbO_3$ composites with p-n heterojunctions were synthesized by simple hydrothermal method. Through experiments and characterization, it is confirmed that p-n junctions formed on the interface between BiOCl and $NaNbO_3$. The results indicted that the separation efficiency of photo-generated carriers has been greatly improved because of the formation of p-n junctions. Recycle experiments showed that the composite photocatalyst exhibited good stability. The experimental results also show that pollutants are mainly degraded by h^+ and $\cdot O_{2^-}$ radicals. Therefore, $BiOCl/NaNbO_3$ heterojunction nanocomposites can be used as a highly efficient and reusable photocatalyst, which has potential applications in the removal of organic pollutants.

AUTHOR CONTRIBUTIONS

JX and MC designed the project, guided the study and polished the manuscript. BF, YW, and YQ conducted the experiments and characterized the samples. JN revised the manuscript.

ACKNOWLEDGMENTS

We are grateful for grants from the Priority Academic Program Development of Jiangsu Higher Education Institutions (PAPD).

REFERENCES

Ao, Y. H., Bao, J. Q., Wang, P. F., Wang, C., and Hou, J. (2016a). Bismuth oxychloride modified titanium phosphate nanoplates: a new p-n type heterostructured photocatalyst with high activity for the degradation of different kinds of organic pollutants. *J. Colloid Interface Sci.* 476, 71–78. doi: 10.1016/j.jcis.2016.05.021

Ao, Y. H., Wang, K. D., Wang, P. F., Wang, C., and Hou, J. (2016b). Synthesis of novel 2D-2D p-n heterojunction $BiOBr/La_2Ti_2O7$ composite photocatalyst with enhanced photocatalytic performance under both UV and visible light irradiation. *Appl. Catal. B Environ.* 194, 157–168. doi: 10.1016/j.apcatb.2016.04.050

Cao, J., Xu, B. Y., Lin, H. L., Luo, B. D., and Chen, S. F. (2012). Novel Bi2S3-sensitized BiOCl with highly visible light photocatalytic activity for the removal of rhodamine B. *Catal. Commun.* 26, 204–208. doi: 10.1016/j.catcom.2012.05.025

Cao, M., Wang, P., Ao, Y., Wang, C., Hou, J., and Qian, J. (2016). Visible light activated photocatalytic degradation of tetracycline by a magnetically separable composite photocatalyst: graphene oxide/magnetite/cerium-doped titania. *J. Colloid Interface Sci.* 467, 129–139. doi: 10.1016/j.jcis.2016.01.005

Chang, C., Zhu, L. Y., Fu, Y., and Chu, X. L. (2013). Highly active Bi/BiOI composite synthesized by one-step reaction and its capacity to degrade bisphenol A under simulated solar light irradiation. *Chem. Eng. J.* 233, 305–314. doi: 10.1016/j.cej.2013.08.048

Chen, P., Dong, F., Ran, M. X., and Li, J. R. (2018). Synergistic photo-thermal catalytic NO purification of MnOx/g-C_3N_4: enhanced performance and reaction mechanism. *Chin. J. Catal.* 39, 619–629. doi: 10.1016/S1872-2067(18)63029-3

Chen, S. F., Hu, Y. F., Ji, L., Jiang, X. L., and Fu, X. L. (2014). Preparation and characterization of direct Z-scheme photocatalyst Bi_2O_3/$NaNbO_3$ and its reaction mechanism. *Appl. Surf. Sci.* 292, 357–366. doi: 10.1016/j.apsusc.2013.11.144

Fan, M. S., Hu, B., Yan, X., Song, C. J., Chen, T. J., Feng, Y., et al. (2015). Excellent visible-light-driven photocatalytic performance of Cu_2O sensitized $NaNbO_3$ heterostructures. *New J. Chem.* 39, 6171–6177. doi: 10.1039/C5NJ00751H

Fang, S. S., Ding, C. Y., Liang, Q., Li, Z. Y., Xu, S., Peng, Y. Y., et al. (2016). *In-situ* precipitation synthesis of novel BiOCl/Ag_2CO_3 hybrids with highly e?cient visible-light-driven photocatalytic activity. *J. Alloy. Compd.* 684, 230–236. doi: 10.1016/j.jallcom.2016.05.168

Guo, Y., Wang, P. F., Qian, J., Ao, Y. H., Wang, C., and Hou, J. (2018). Phosphate group grafted twinned $BiPO_4$ with significantly enhanced photocatalytic activity: synergistic effect of improved charge separation efficiency and redox ability. *Appl. Catal. B Environ.* 234, 90–99. doi: 10.1016/j.apcatb.2018.04.036

Han, W., Liu, Z., Li, Y., Fan, X., Zhang, F., Zhang, G., et al. (2018). The promoting role of different carbon allotropes cocatalysts for semiconductors in photocatalytic energy generation and pollutants degradation. *Front. Chem.* 5:84. doi: 10.3389/fchem.2017.00084

He, S., Hou, P., Petropoulos, E., Feng, Y., Yu, Y., Xue, L., et al. (2018). High efficient visible-light photocatalytic performance of Cu/ZnO/rGO nanocomposite for decomposing of aqueous ammonia and treatment of domestic wastewater. *Front. Chem.* 6:219. doi: 10.3389/fchem.2018.00219

Hu, J. L., Wu, X. X., Huang, C. J., Fan, W. J., and Qiu, X. Q. (2016). Visible light photocatalytic activity induced by Rh(III) modification on the surface of BiOCl. *Appl. Surf. Sci.*387, 45–50. doi: 10.1016/j.apsusc.2016.06.075

Katsumata, K., Okazaki, S., Cordonier, C. E., Shichi, T., Sasaki, T., and Fujishima, A. (2010). Preparation and characterization of self-cleaning glass for vehicle with niobia nanosheets. *ACS Appl. Mater. Interfaces* 2, 1236–1241. doi: 10.1021/am100091f

Kuang, P. Y., Su, Y. Z., Chen, G. F., Luo, Z., Xing, S. Y., Li, N., et al. (2015). g-C_3N_4 decorated ZnO nanorod arrays for enhanced photoelectrocatalytic performance. *Appl. Surf. Sci.* 358, 296–303. doi: 10.1016/j.apsusc.2015.08.066

Kumar, S., Khanchandani, S., Thirumal, M., and Ganguli, A. K. (2014). Achieving enhanced visible-light-driven photocatalysis using type-II $NaNbO_3$/CdS core/shell heterostructures. *ACS Appl. Mater. Interfaces* 6, 13221–13233. doi: 10.1021/am503055n

Li, G., Kako, T., Wang, D., Zou, Z., and Ye, J. (2008). Synthesis and enhanced photocatalytic activity of $NaNbO_3$ prepared by hydrothermal and polymerized complex methods. *J. Phys. Chem. Solids* 69, 2487–2491. doi: 10.1016/j.jpcs.2008.05.001

Li, G., Yi, Z., Bai, Y., Zhang, W., and Zhang, H. (2012a). Anisotropy in photocatalytic oxidization activity of $NaNbO_3$ photocatalyst. *Dalton Trans.* 41, 10194–10198. doi: 10.1039/c2dt30593c

Li, G. Q. (2010). Photocatalytic properties of $NaNbO_3$ and $Na_{0.6}Ag_{0.4}NbO_3$ synthesized by polymerized complex method. *Mater. Chem. Phys.* 121, 42–46. doi: 10.1016/j.matchemphys.2009.12.032

Li, P., Ouyang, S., Xi, G., Kako, T., and Ye, J. H. (2012b). The effects of crystal structure and electronic structure on photocatalytic H_2 evolution and CO_2 reduction over two phases of perovskite-structured $NaNbO_3$. *J. Phys. Chem. C* 116, 7621–7628. doi: 10.1021/jp210106b

Li, P., Ouyang, S. X., Zhang, Y. J., Kako, T., and Ye, J. H. (2013). Surface-coordination-induced selective synthesis of cubic and orthorhombic $NaNbO_3$ and their photocatalytic properties. *J. Mater. Chem. A* 1, 1185–1191. doi: 10.1039/C2TA00260D

Li, P., Xu, H., Liu, L. Q., Kako, T., Umezawa, N., Abe, H., et al. (2014). Constructing cubic–orthorhombic surface-phase junctions of $NaNbO_3$ towards significant enhancement of CO_2 photoreduction. *J. Mater. Chem. A* 2, 5606–5609. doi: 10.1039/C4TA00105B

Li, Q., Li, X., Wageh, S., Al-Ghamdi, A. A., and Yu, J. (2015). CdS/Graphene nanocomposite photocatalysts. *Adv. Energy Mater.* 5:1500010. doi: 10.1002/aenm.201500010

Li, S., Hu, S., Jiang, W., Liu, Y., Liu, Y., Zhou, Y. T., et al. (2018). Ag_3VO_4 nanoparticles decorated $Bi_2O_2CO_3$ micro-flowers: an efficient visible-light-driven photocatalyst for the removal of toxic contaminants. *Front. Chem.* 6:255. doi: 10.3389/fchem.2018.00255

Liu, M. R., Hong, Q. L., Li, Q. H., Du, Y. H., Zhang, H. X., Chen, S. M., et al. (2018). Cobalt boron imidazolate framework derived cobalt nanoparticles encapsulated in B/N codoped nanocarbon as efficient bifunctional electrocatalysts for overall water splitting. *Adv. Funct. Mater.* 28:1801136. doi: 10.1002/adfm.201801136

Liu, Q. Q., Chai, Y. Y., Zhang, L., Ren, J., and Dai, W. L. (2016). Highly efficient Pt/$NaNbO_3$ nanowire photocatalyst: Its morphology effect and application in water purification and H_2 production. *Appl. Catal. B Environ.* 205, 505–513. doi: 10.1016/j.apcatb.2016.12.065

Liu, W. W., Qiao, L. L., Zhu, A. Q., Liu, Y., and Pan, J. (2017a). Constructing 2D BiOCl/C3N4 layered composite with large contact surface for visible-light-driven photocatalytic degradation. *Appl. Surf. Sci.* 426, 897–905. doi: 10.1016/j.apsusc.2017.07.225

Liu, W. W., Shang, Y. Y., Zhu, A. Q., Tan, P. F., Liu, Y., Qiao, L. L., et al. (2017b). Enhanced performance of doped BiOCl nanoplates for photocatalysis: understanding from doping insight into improved spatial carrier separation. *J.Mater. Chem. A* 5:12542–12549. doi: 10.1039/C7TA02724A

Lv, J., Kako, T., Li, Z. S., Zou, Z. G., and Ye, J. H. (2010). Synthesis and photocatalytic activities of NaNbO3 rods modified by In_2O_3 nanoparticles. *J. Phys. Chem. C* 114, 6157–6162. doi: 10.1021/jp906550t

Ma, W., Chen, L., Zhu, Y. Z., Dai, J. D., Yan, Y. S., and Li, C. X. (2016). Facile synthesis of the magnetic BiOCl/$ZnFe_2O_4$ heterostructures with enhanced photocatalytic activity under visible-light irradiation. *Colloids Surfaces A Physicochem Eng. Aspects*. 508, 135–141. doi: 10.1016/j.colsurfa.2016.08.066

Ma, Y. C., Chen, Z. W., Qu, D., and Shi, J. S. (2016). Synthesis of chemically bonded BiOCl@Bi_2WO_6 microspheres with exposed (020) Bi_2WO_6 facets and their enhanced photocatalytic activities under visible light irradiation. *Appl. Surf. Sci.* 361, 63–71. doi: 10.1016/j.apsusc.2015.11.130

Mao, D. J., Yu, A. Q., Ding, S. S., Wang, F., Yang, S. G., Sun, C., et al. (2016). One-pot synthesis of BiOCl half-shells using microemulsion droplets astemplates with highly photocatalytic performance for the degradation of ciprofloxacin. *Appl. Surf. Sci.* 389, 742–750. doi: 10.1016/j.apsusc.2016.07.178

Qian, J., Xue, Y., Ao, Y. H., Wang, P. F., and Wang, C. (2018). Hydrothermal synthesis of CeO_2/$NaNbO_3$ composites with enhanced photocatalytic performance. *Chin. J. Catal.* 39, 682–692. doi: 10.1016/S1872-2067(17)62975-9

Rajeshwar, K., de Tacconi, N. R., and Chenthamarakshan, C. R. (2001). Semiconductor-based composite materials: preparation, properties, and performance. *Chem. Mater.* 13, 2765–2782. doi: 10.1021/cm010254z

Saito, K., and Kudo, A. (2013). Fabrication of highly crystalline $SnNb_2O_6$ shell with a visible-light response on a $NaNbO_3$ nanowire core. *Inorg. Chem.* 52, 5621–5623. doi: 10.1021/ic4002175

Shang, M., Wang, W. Z., Zhang, L., and Zhou, L. (2009). 3D Bi_2WO_6/TiO_2 hierarchical heterostructure: controllable synthesis and enhanced visible photocatalytic degradation performances. *J. Phys. Chem. C* 113, 14727–14731. doi: 10.1021/jp9045808

Shi, H. F., Chen, G. Q., Zhang, C. L., and Zou, Z. G. (2014b). Polymeric g-C_3N_4 coupled with $NaNbO_3$ nanowires toward enhanced photocatalytic reduction of CO_2 into renewable fuel. *ACS Catal.* 4, 3637–3643. doi: 10.1021/cs500848f

Shi, H. F., Chen, G. Q., and Zou, Z. G. (2014a). Platinum loaded $NaNbO_3$-xNx with nanostep surface nanostructures toward enhanced visible-light photocatalytic activity. *Appl. Catal. B Environ.* 156, 378–384. doi: 10.1016/j.apcatb.2014.03.036

Shifu, C., Ji, L., Tang, W. M., and Fu, X. L. (2013). Fabrication, characterization and mechanism of a novel Z-scheme photocatalyst $NaNbO_3$/WO_3 with enhanced photocatalytic activity. *Dalton Trans.* 42, 10759–10768. doi: 10.1039/c3dt50699a

Song, C. J., Fan, M. S., Hu, B., Chen, T. J., Wang, L. P., and Shi, W. D. (2015). Synthesis of a g-C_3N_4-sensitized and $NaNbO_3$-substrated II-type heterojunction with enhanced photocatalytic degradation activity. *Cryst. Eng. Comm.* 17, 4575–4583. doi: 10.1039/C5CE00622H

Sun, M., Yan, Q., Shao, Y., Wang, C. Q., Yan, T., Ji, P. G., et al. (2017). Facile fabrication of BiOI decorated $NaNbO_3$ cubes: a p–n junction photocatalyst with improved visible-light activity. *Appl. Surf. Sci.* 416, 288–295. doi: 10.1016/j.apsusc.2017.04.136

Wang, D. H., Gao, G. Q., Zhang, Y. W., Zhou, L. S., Xu, A. W., and Chen, W. (2012). Nanosheet-constructed porous BiOCl with dominant {001} facets for superior photosensitized degradation. *Nanoscale* 4, 7780–7785. doi: 10.1039/c2nr32533k

Wang, H., Zhang, W. D., Li, X. W., Li, J. Y., Cen, W. L., Li, Q. Y., et al. (2018). Highly enhanced visible light photocatalysis and *in situ* FT-IR studies on Bi metal@defective BiOCl hierarchical microspheres. *Appl. Catal. B Environ.* 225, 218–227. doi: 10.1016/j.apcatb.2017.11.079

Xu, Y., Mo, Y. P., Tian, J., Wang, P., Yu, H. G., and Yu, J. G. (2016). The synergistic effect of graphitic N and pyrrolic N for the enhanced photocatalytic performance of nitrogen-doped graphene/TiO2 nanocomposites. *Appl. Catal. B Environ.* 181, 810–817. doi: 10.1016/j.apcatb.2015.08.049

Yan, M., Hua, Y. Q., Zhu, F. F., Gu, W., Jiang, J. H., Shen, H. Q., et al. (2017). Fabrication of nitrogen doped graphene quantum dots-BiOI/$MnNb_2O_6$ p–n junction photocatalysts with enhanced visible light efficiency in photocatalytic degradation of antibiotics. *Appl. Catal. B Environ.* 202, 518–527. doi: 10.1016/j.apcatb.2016.09.039

Yang, Y., Zhang, Q., Zhang, R. Y., Ran, T., Wan, W. C., and Zhou, Y. (2018). Compressible and recyclable monolithic g-C_3N_4/melamine sponge: a facile ultrasonic-coating approach and enhanced visible-light photocatalytic activity. *Front. Chem.* 6:156. doi: 10.3389/fchem.2018.00156

Ye, L. Q., Su, Y. R., Jin, X. L., Xie, H., and Zhang, C. (2014). Recent advances in BiOX (X = Cl, Br and I) photocatalysts: synthesis modification, facet effects and mechanisms. *Environ. Sci. Nano.* 1, 90–112. doi: 10.1039/c3en00098b

Yu, H. G., Xiao, P., Tian, J., Wang, F. Z., and Yu, J. G. (2016). Phenylamine-functionalized rGO/TiO_2 photocatalysts: spatially separated adsorption sites and tunable photocatalytic selectivity. *ACS Appl. Mat. Interfaces* 8, 29470–29477. doi: 10.1021/acsami.6b09903

Yuan, X. Z., Wang, H., Wang, J. J., Zeng, G. M., Chen, X. H., Wu, Z. B., et al. (2018). Near-infrared-driven Cr (VI) reduction in aqueous solution based on a MoS_2/Sb_2S_3 photocatalyst. *Catal. Sci. Technol.* 8, 1545–1554. doi: 10.1039/C7CY02531A

Zhang, B. B., Zhang, D. F., Xi, Z. S., Wang, P. F., Pu, X. P., Shao, X., et al. (2017). Synthesis of $Ag_2O/NaNbO_3$ p-n junction photocatalysts with improved visible light photocatalytic activities. *Sep. Purification Technol.* 178, 130–137. doi: 10.1016/j.seppur.2017.01.031

Zhang, J. F., Wageh, S., Al-Ghamdic, A., and Yu, J. G. (2016). New understanding on the different photocatalytic activity of wurtzite and zinc-blende CdS. *Appl. Catal. B Environ.* 192, 101–107. doi: 10.1016/j.apcatb.2016.03.058

Zhang, J. Y., Xiao, F. X. (2017). Modulation of interfacial charge transfer by self-assembly of single-layer graphene enwrapped one-dimensional semiconductors toward photo redox catalysis. *J. Mat. Chem. A.* 5, 23681–23693. doi: 10.1039/C7TA08415C

Zhang, W. D., Liu, X. L., Dong, X. A., Dong, F., and Zhang, Y. X. (2017a). Facile synthesis of $Bi_{12}O_{17}Br_2$ and $Bi_4O_5Br_2$ nanosheets: *in situ* DRIFTS investigation of photocatalytic NO oxidation conversion pathway. *Chin. J. Catal.* 38, 2030–2038. doi: 10.1016/S1872-2067(17)62941-3

Zhang, W. D., Zhao, Z. W., Dong, F., and Zhang, Y. X. (2017b). Solvent-assisted synthesis of porous g-C_3N_4 with efficient visible-light photocatalytic performance for NO removal. *Chin. J. Catal.* 38, 372–378. doi: 10.1016/S1872-2067(16)62585-8

Zhong, Y. X., Liu, Y. H., Wu, S., Zhu, Y., Chen, H. B., and Yu, X. (2018). Facile fabrication of BiOI/BiOCl immobilized films with improved visible light photocatalytic performance. *Front. Chem.* 6:58. doi: 10.3389/fchem.2018.00058

Zhou, T. H., Du, Y. H., Wang, D. P., Yin, S. M., Tu, W. G., Chen, Z., et al. (2017). Phosphonate-based metal-organic framework derived Co-P-C hybrid as an efficient electrocatalyst for oxygen evolution reaction. *ACS Catal.* 7:6000–6007. doi: 10.1021/acscatal.7b00937

Conflict of Interest Statement: The authors declare that the research was conducted in the absence of any commercial or financial relationships that could be construed as a potential conflict of interest.

frontiers in Chemistry

ORIGINAL RESEARCH
published: 02 October 2018
doi: 10.3389/fchem.2018.00458

A Novel Synthetic Method for N Doped TiO_2 Nanoparticles Through Plasma-Assisted Electrolysis and Photocatalytic Activity in the Visible Region

Tae Hyung Kim[1], *Gwang-Myeong Go*[2], *Hong-Baek Cho*[2], *Yoseb Song*[2], *Chan-Gi Lee*[1]* and *Yong-Ho Choa*[2]*

[1] Advanced Materials and Processing Center, Institute for Advanced Engineering (IAE), Yongin, South Korea, [2] Department of Fusion Chemical Engineering, Hanyang University, Ansan, South Korea

Nitrogen doped TiO_2 (N-TiO_2) nanoparticles were synthesized via a novel plasma enhanced electrolysis method using bulk titanium (Ti) as a source material and nitric acid as the nitrogen dopant. This method possesses remarkable merits with regard to the direct-metal synthesis of nanoparticles with its one-step process, eco-friendliness, and its ability to be mass produced. The nanoparticles were synthesized from bulk Ti metal and dipped in 5–15 mmol of a nitric acid electrolyte under the application of AC 500 V, the minimum range of voltage to generate plasma. By controlling the electrolyte concentration, the nanoparticle size distribution could be tuned between 12.1 and 24.7 nm using repulsion forces via variations in pH. The prepared N-TiO_2 nanoparticles were calcined at between 100 and 300°C to determine their photocatalytic efficiency within the visible-light region, which depended on their crystal structure and N doping content. Analysis showed that the temperature treatment yielded an anatase TiO_2 crystalline structure when the N doping content was varied from 0.4 to 0.54 at.%. In particular, the 0.4 at.% N doped TiO_2 catalyst exhibited the highest catalytic performance with quadruple efficiency compared to the P-25 standard TiO_2 nanoparticles, which featured a 91% degradation of methyl orange organic dye within 300 min. This solid-liquid reaction based on plasma enhanced electrolysis could open new pathways with regard to high purity mass producible ceramic nanoparticles with advanced properties.

Keywords: plasma enhanced electrolysis, amorphous N-doped TiO_2, visible region photocatalyst, metal-direct synthesis, nanoparticle synthesis

OPEN ACCESS

Edited by:
Fan Dong,
Chongqing Technology and Business University, China

Reviewed by:
Guohong Wang,
Hubei Normal University, China
Jingyu Wang,
Huazhong University of Science and Technology, China

***Correspondence:**
Chan-Gi Lee
cglee@iae.re.kr
Yong-Ho Choa
choa15@hanyang.ac.kr

Specialty section:
This article was submitted to Catalysis and Photocatalysis, a section of the journal Frontiers in Chemistry

Received: *06 July 2018*
Accepted: *13 September 2018*
Published: *02 October 2018*

Citation:
Kim TH, Go G-M, Cho H-B, Song Y, Lee C-G and Choa Y-H (2018) A Novel Synthetic Method for N Doped TiO_2 Nanoparticles Through Plasma-Assisted Electrolysis and Photocatalytic Activity in the Visible Region. Front. Chem. 6:458. doi: 10.3389/fchem.2018.00458

INTRODUCTION

Intensive research has been performed to produce highly photocatalytic titanium dioxide (TiO_2) nanoparticles (Ba-abbad et al., 2012; Mattioli et al., 2014; Vukoje et al., 2016) for a large application space, including water splitting (Galinska and Walendziewski, 2005; Ni et al., 2007; Tang et al., 2008) and industrial pollutant degradation (Liu et al., 2010; Lin et al., 2012; Dong et al., 2015). However, crystalline TiO_2 nanoparticles possess limited photocatalytic activity due to their wide band gap regardless of crystal structure from anatase to rutile (anatase ~ 3.2 eV, rutile ~ 3.0 eV);

the nanoparticles only absorb within the UV region, comprising a small portion of sunlight of <5% of the solar flux. Thus, to efficiently enhance the photocatalytic activity, many researchers have focused on utilizing the visible region, which contains nearly half of the energy from sunlight (∼45%) by doping metal cations (Ag, C, Zn, etc.) into the Ti lattice (Cao et al., 2008; Aware and Jadhav, 2015). However, cation dopants located at d-states within the band gap act as trap centers for excited electron and holes, which can additionally shift the conduction band below the redox potential (Wu et al., 2007). Thus, some drawbacks exist such as a low thermal stability and can act as recombination centers in the form of charge carriers. Alternatively, anion dopants such as N, S, and P have attracted considerable attention due to their intrinsic properties, which possess similar characteristics to oxygen. Among those anions, nitrogen appears to be the most plausible ingredient to be investigated for doping with the formation of a metastable center, low ionization energy state, and reduced atomic size (Dunnill et al., 2011). The light absorption range can thus be extended into the visible region (up to 380 nm) through existing p-states near the valance band (Scanlon et al., 2013).

The preparation of N-TiO_2 nanoparticles has been extensively studied with aqueous-based chemical processes such as sol-gel (Yu et al., 2007; Dunnill et al., 2011; Caratto et al., 2012), hydrothermal (Zhou et al., 2011), solvothermal (Li and Liu, 2009; Yang et al., 2010), and polymeric precursor methods (Soares et al., 2011; Yu et al., 2017) being the most frequently employed. These are general methods for the preparation of nanoparticles that can be used to control morphology, structure, and particle size. However, synthetic conditions such as the solution temperature, pH, reaction time, and precursor ratio must be sensitively controlled. Moreover, long reaction times and drying processes are essential in order to obtain highly pure and crystalline nanoparticles, making mass production difficult. To overcome these drawbacks, a noble synthetic strategy using plasma enhanced electrolysis was adopted herein. The process utilizes a small amount of electrolyte, characterizes a quick production time, and entails the direct synthesis of nanoparticles from bulk metal in a manner suitable for mass production. Furthermore, this technology is environmental friendly due to employing a reusable electrolyte and not requiring an additional nitrogen source such as ammonia (Gao et al., 2014).

Here we report a novel method for the preparation of interstitial N-TiO_2 nanoparticles by bulk-direct synthesis using an eco-friendly and mass producible method via plasma enhanced electrolysis, enhancing photocatalytic activity through the narrowing of band gap structures, which will widen the light absorption region into the visible spectrum. During the nanoparticle synthetic process, arc plasma was formed on the metal surface, creating gaseous anionic species that subsequently reacted with cationic Ti species to grow into N-TiO_2 through nucleation. The relationship between N doping content and nanoparticle crystallinity, which primarily affected the photocatalytic efficiency was analyzed and elucidated by comparing samples prepared through the variation of electrolyte concentrations and calcination temperatures.

MATERIALS AND METHODS

Synthesis of Amorphous N-TiO_2 Nanoparticles

Figure 1 shows a brief schematic diagram for the synthesis of N-TiO_2 nanoparticles by the generation of plasma. A Ti metal plate (99.99% purity) was first washed twice with acetone and deionized water in order to remove other possible impurities. The organic-free Ti plate was hanged in 1 L of a nitric acid electrolyte in the middle of a double-jacket reactor. The Ti metal was connected to an anode and stainless steel mesh (SUS 304, 60 mesh) with a cylindrical shape that was connected to the cathode; the shape of the cathode was designed to radially impart an equal supply of electric voltage to the metal surface. The solution temperature was controlled using a bath circulator and stirred with a magnetic bar to exchange heat efficiently under the high temperature plasma reaction. After the initial generation of plasma on the metal surface, the voltage and current density of the power supply was maintained at certain conditions such as AC 500 V at 100 Hz for 10 min to synthesize nanoparticles continuously; the nitric acid concentration was varied from 5 to 15 mmol to observe the effect of the electrolyte concentration on the morphology of TiO_2. After the reaction, the nanoparticle suspension was centrifuged to remove the remaining electrolyte and dried in a vacuum oven at 80°C for 24 h. The as-synthesized powders were calcined at different temperatures: 100, 150, 200, 250, and 300°C to transform amorphous TiO_2 into the crystalline anatase phase to investigate their respective photocatalytic activity.

Sample Characterization

Scanning electron microscopy (SEM) images were obtained with a Hitachi S-4800/Horiba EX-250 to analyze the morphology of the synthesized N-TiO_2 nanoparticles. High-resolution transmission electron microscopy (HR-TEM) images were obtained with a JEOL, JEM-2100F to measure and calculate lattice parameters with selected area electron diffraction (SAED) patterns. The nanoparticle crystallinity and structures were analyzed with a RigaKu D/MAX-2500/PC X-ray diffractometer (XRD) using Cu $K\alpha_1$ radiation ($\lambda = 1.54$ nm 2θ range between 20 and 80°). X-ray photoelectron spectroscopy (XPS) was performed with a Thermofisher Scientific K-Alpha+ MXP10. The photocatalytic activity of the N-TiO_2 nanoparticles was assessed by analyzing the visible region efficiency of the decomposing methyl orange (MO, Sigma-Aldrich Co.) solution in a dark chamber equipped with a UV cut-off filter (Edmund Optics, 400–50 mm Diameter, OD 2 long pass filter) and a 300 W Zenon lamp. While being exposed to visible light, degraded methyl orange was collected with nanoparticles at 2 h intervals and separated via centrifugation. After separation, a Dong-il Shimadzu Co. UV-2600 UV-vis spectrophotometer was employed to calculate the photocatalytic activity. To compare the recombination rates of the samples, photoluminescence (PL) measurements were performed using a 290 nm laser (Horiba, Nanolog) as the excitation source at room temperature.

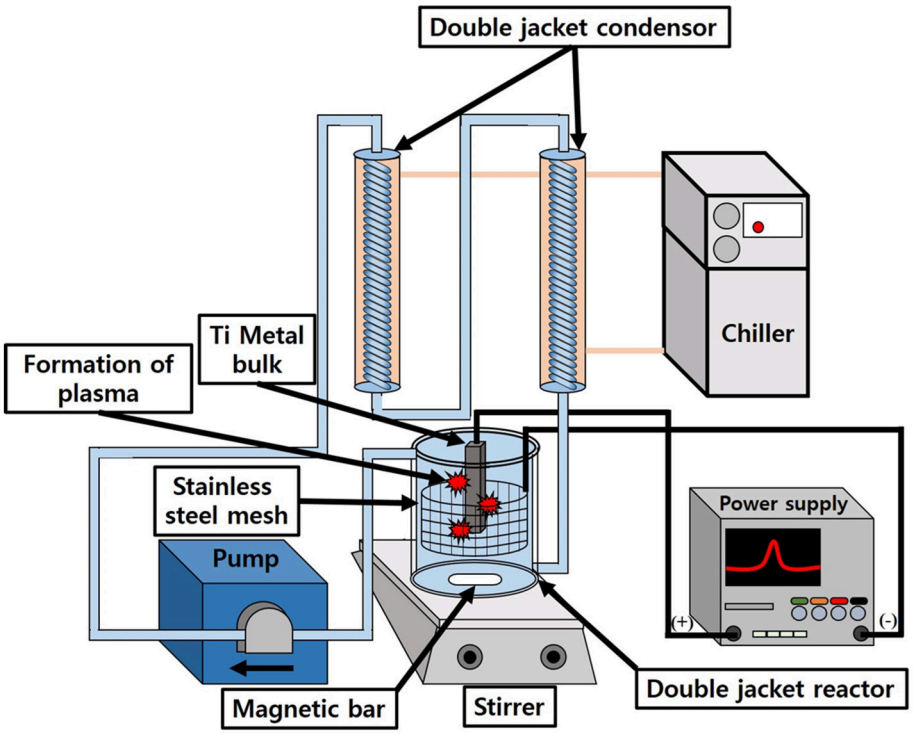

FIGURE 1 | Schematic diagram for liquid-based plasma enhanced electrolysis.

Photocatalytic Activity Analysis

The photocatalytic efficiency of the N-TiO_2 samples was compared after various degrees of heat treatment: 100, 150, 200, 250, and 300°C for 4 h to transform the crystal structure and yield variations with regard to the degree of N doping with Degussa P-25 standard TiO_2 nanoparticles. After calcination, 100 mg of nanoparticles were added and mixed with 100 ml of a 1×10^{-5} mol/L MO organic dye solution to measure the decomposition efficiency of each sample. The 100 mg/L powder mixed MO solution was sonicated for 10 min prior to the degradation step to enhance solution dispersity. The well-dispersed organic solution was placed in a dark chamber and stirred for an additional 30 min for stability. The degradation process was performed in a double-jacketed reactor to control the solution temperature and was irradiated with light using a 300 W Xe lamp with a UV cut-off filter. The reaction solution was collected every 2 h and analyzed via UV-vis spectroscopy to calculate the degradation efficiency for a 6 h long reaction.

RESULTS AND DISCUSSION

Synthesis of N-TiO_2 Nanoparticles

Figures 2a–c show the TiO_2 nanoparticle morphologies produced at different concentrations of nitric acid. The particle size distribution analyzed via SEM decreased between the range of 12.1–24.7 nm as the nitric acid concentration was increased (size distribution in **Figure 2d**). The mean particle size decreased to 24.7, 19.4, and 12.1 nm at concentrations of 5, 10, and 15 mmol, respectively. It could be seen that at lower concentrations, some rod-like nanoparticle shapes could be found. Irregular shaped nanoparticles indicated unbalanced nanoparticle synthesis between the nucleation and growth steps. At higher concentrations with a lower pH electrolyte, more uniform and non-agglomerated nanoparticles could be produced. This could be attributed to two factors; repulsion forces and balance between the nucleation and growth steps (Alqadi et al., 2014). When the electrolyte solution pH decreased to lower values, ions such as OH^-, which reacted with metal ions, scarcely existed and facilitated a slower nucleation and growth process. This also increased repulsion forces between nanoparticles, thus producing much more uniform nanoparticles with a smaller size distribution than at higher pH values (Wu et al., 2011). At higher electrolyte concentrations, the solution conductivity increased due to a larger quantity of ionized ions such as H^+ and SO_4^- (when H_2SO_4 was used as an electrolyte), yielding a higher current density that was related to the plasma intensity; this would produce transparent solutions without forming colloid nanoparticles, thus necessitating the use of additional reducing agents (Kim et al., 2016). As a result, 15 mmol was the optimum nitric acid concentration for nanoparticle synthesis.

Figures 2d,e show size distribution and XRD data for the synthesized amorphous N-TiO_2 nanoparticles. The size distribution showed the nanoparticles ranging from 12.1 to 24.7 nm (**Figure 2d**); the size deviation increased noticeably from ±4.7 to ±22.2 nm as the electrolyte concentration increased. A broad peak at the lower degree with no other specific peaks

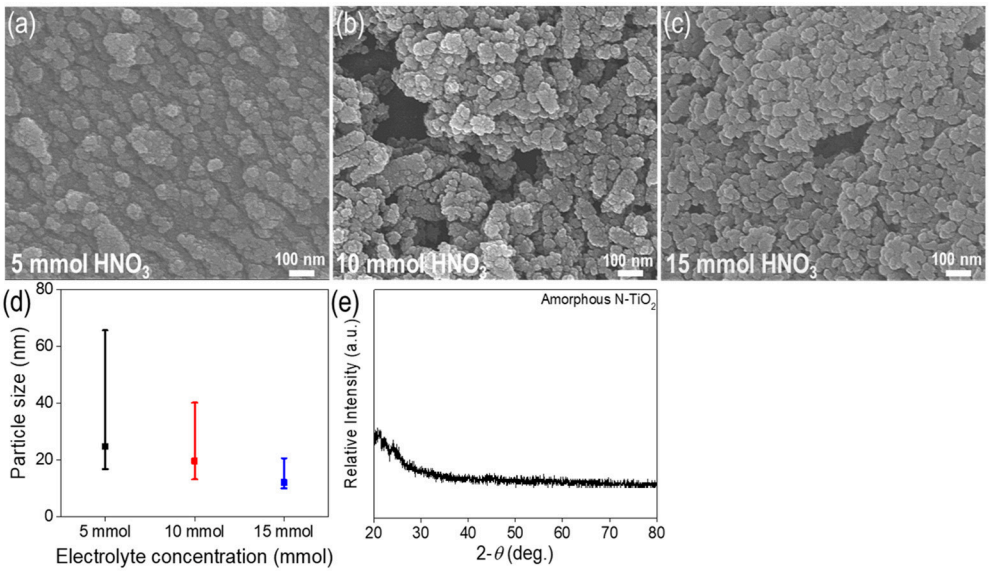

FIGURE 2 | Characterization of N-TiO_2 nanoparticles with various electrolyte concentrations,SEM images of **(a)** 5 mmol, **(b)** 10 mmol, **(c)** 15 mmol, **(d)** the size distribution and **(e)** XRD data.

in the XRD data (**Figure 2e**) indicated the pristine amorphous structure of N-TiO_2. Moreover, no peaks for the Ti bulk metal starting material were detected, implying that Ti was completely transformed to TiO_2 nanoparticles by adopting the plasma enhanced electrolysis process. If detached from the metal surface, the particle peaks would exhibit XRD peaks for bulk Ti and several irregularly shaped particles.

After the synthesis of nanoparticles using a 15 mmol electrolyte concentration, amorphous N-TiO_2 nanoparticles were calcined at various temperatures to compare the XRD peaks between the treated nanoparticles in **Figure 3**. The as-prepared amorphous N-TiO_2 nanoparticles revealed that the amorphous phase was transformed to a metastable anatase structure after being calcined at 100, 150, 200, 250, and 300°C for 4 h. In **Figure 3A**, analyzed peaks for the (101), (004), (200), and (105) lattice planes matched those for anatase TiO_2 (JCPDS card no. 21-1272) and no nitrogen source peaks were detected, which indicated that nitrogen was perfectly doped into the TiO_2 lattice (as confirmed in **Figure 6**). With an increase in calcination temperature, the XRD peak intensity also increased, indicating that the calcination temperature enhanced the crystallinity of the N-TiO_2 nanoparticles with a deformation of amorphous bonding between atoms during calcination. Additional evidence for nitrogen doping was observed by a shift in the enlarged peak of the (101) lattice in **Figure 3B**. Due to the larger atomic radius of nitrogen compared to oxygen (N^{3-} = 171 Ã > O^{2-} = 140 Ã), a large degree of nitrogen doping would lead to XRD peak broadening effects. A reduction in doping with an increase in the calcination temperature could shift the peak to much higher diffraction angles compared to non-doped TiO_2 (Sun et al., 2016). This result will be compared and identified via XPS and PL analysis in later sections.

To analyze a non-agglomerated single nanoparticle, a well-dispersed colloid solution was loaded onto a Cu grid to perform TEM analysis. According to the TEM images of amorphous N-TiO_2 structures in **Figures 4a,b**, there were no signs of lattice fringes in the nanoparticles that matched the XRD analysis in **Figure 2**. The primary particle size distribution of amorphous N-TiO_2 in **Figure 4c** revealed a primary mean particle size of 6.57 nm, which was smaller than that in the SEM images mentioned previously (in **Figure 2**). After calcination at 200°C, the polycrystalline structure with a ring SAED pattern identified the anatase phase of N-TiO_2 with a lattice plane of (101), (004), (200), and (105) in **Figures 4d–f**. The mean primary particle size was 8.37 nm, indicating a minor growth in morphology after calcination (**Figure 4g**).

XPS Analysis of N-TiO_2 Nanoparticles From Different Calcination Temperatures

The N doping concentration in the TiO_2 lattice primarily influenced the electronic structure according to the doping position and state. Thus, synthesized N-TiO_2 nanoparticles at different calcination temperatures were analyzed via XPS to compare the dopant tendency, as can be seen in **Figure 5**. The 1s peak located at 284.8 eV was used to calculate the peak shift. The peak at 398.7 eV in **Figures 5A,B** was evidence of the replacement of N dopants instead of O sites with N-Ti-O bonds (Mohamed et al., 2015)**.** When the N 1s state at 399.6 eV, which was identical and compared to the interstitial doping state with N-Ti-O bonds (**Figure 5C**), it could be confirmed that the N concentration decreased dramatically from 0.54 to 0.4 at.% by increasing the calcination temperature and lowering the intensity of the N peak, as summarized in **Figure 5D**, which was consistent with that reported by Cheng et al. (2012). To discuss the interstitial

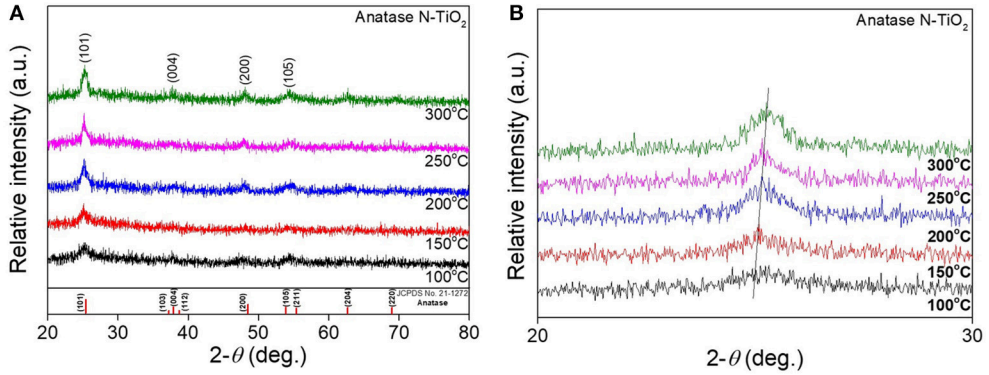

FIGURE 3 | XRD analysis of **(A)** N-TiO_2 nanoparticles at different calcination temperature and **(B)** an enlarged (101) peak.

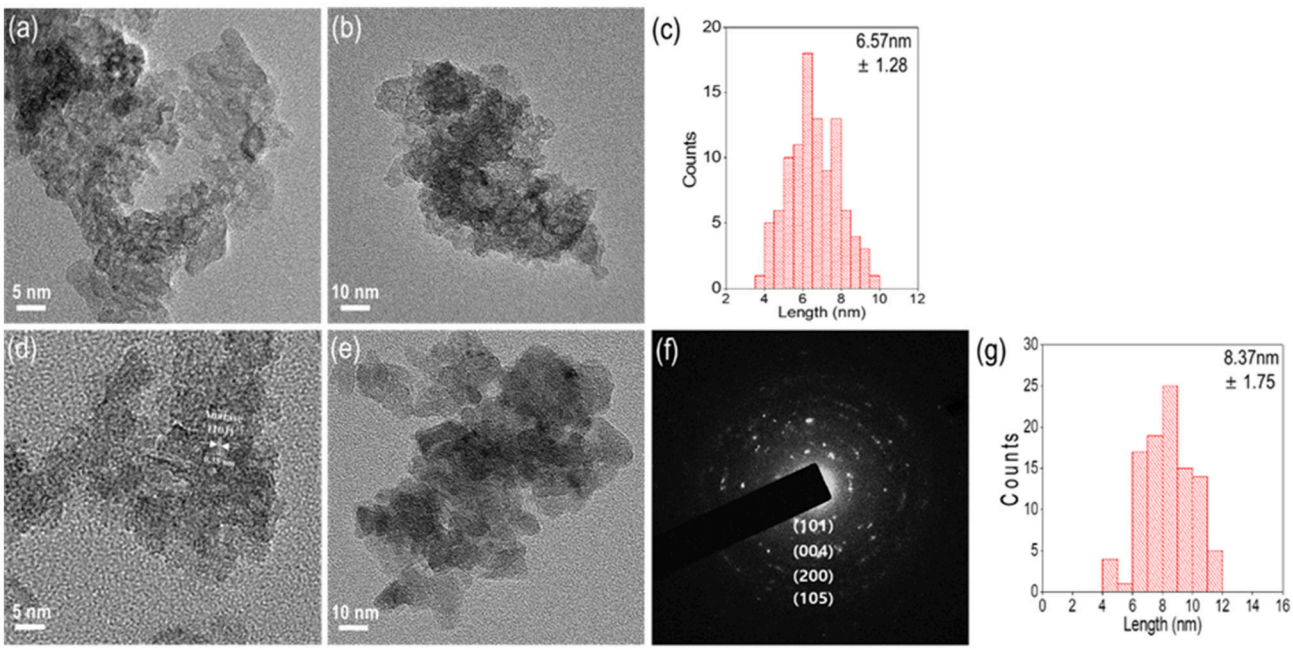

FIGURE 4 | TEM images of an N-TiO_2 nanoparticle synthesized at 15 mmol electrolyte under **(a)** amorphous high resolution, **(b)** low resolution, **(c)** size distribution, **(d)** 200°C calcined anatase high resolution, **(e)** low resolution, **(f)** anatase SAED pattern, and **(g)** the size distribution.

and substitutional N doping states in TiO_2 lattices, the energy conservation law equation was adapted:

$$E_f = E_{TiO_2:N} - E_{TiO_2} - \frac{m}{2}E_{N_2} + \frac{n}{2}E_{O_2}, \quad (1)$$

where $E_{TiO_2:N}$ and E_{TiO_2} are the total energies for N-doped TiO_2 and pure TiO_2, E_{N_2} and E_{O_2} indicate the gas energies of N_2 and O_2 molecules, and m and n are integers of doped N atoms and substituted O atoms. According to this theory, energies tended to increase when the N doping level increased by acting as a formed impurity, making it more difficult to achieve a higher doping condition. Also, doping with N atoms in the lattice instead of O atoms required greater bonding energies; interstitial doping was more generally preferable (Zhao and Liu, 2008). In this scenario, the plasma enhanced electrolysis reaction using 5–15 mmol nitric acid could only yield interstitial N doped TiO_2 nanoparticles.

Band Gap Analysis Depending on N Content

Figure 6 and **Figure S1** shows the diffuse reflectance spectra of Degussa P-25, amorphous, and various N-TiO_2 nanoparticle samples calcined at 100, 150, 200, 250, and 300°C, which possess various N doping molar ratios. The peaks of each sample showed absorptions between 300 and 400 nm in **Figure 6A** and the enlarged peaks in **Figure 6B**, which exhibited a calculated band gap of 3.4, 3.0, 2.96, 2.94, 2.94, 2.97, and 2.98 eV, respectively. The

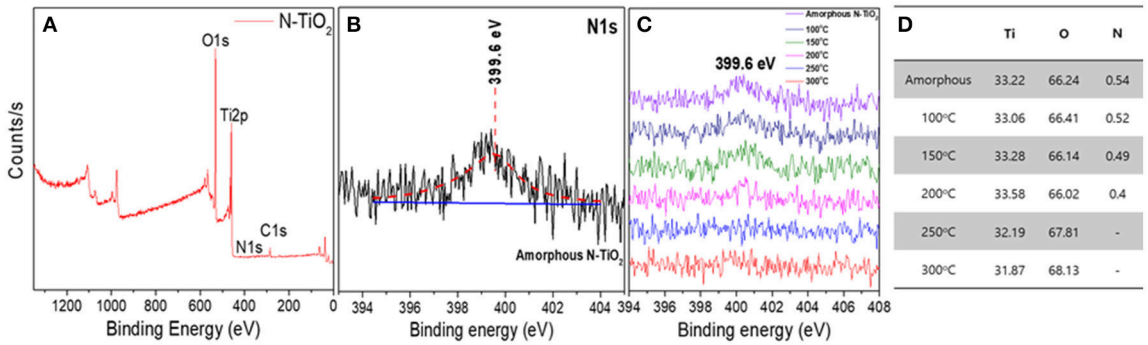

FIGURE 5 | (A) XPS analysis of amorphous N-TiO_2 showing **(B)** an enlarged N1s peak, **(C)** N1s peak at various calcination temperature, and **(D)** the elemental content.

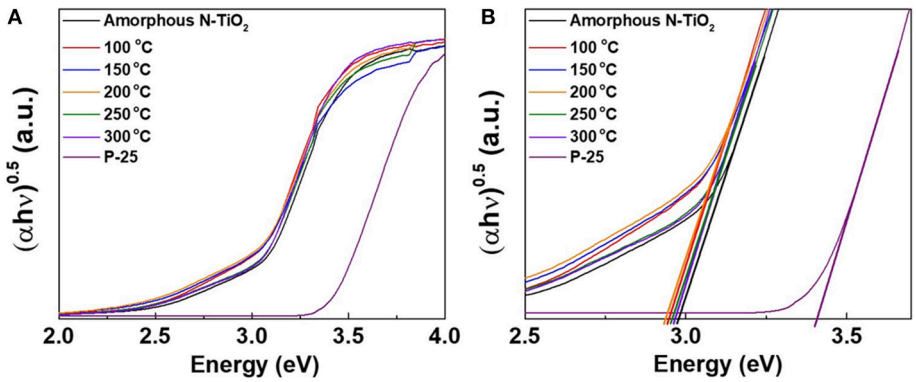

FIGURE 6 | (A) Band gap analysis using UV-vis spectroscopy at different calcination temperature and **(B)** enlarged band gap peaks.

band gap values exhibited a tendency to red shift toward lower wavelengths with an increase in N doping content that strongly affected the absorption region. Thus, it could be anticipated that nitrogen sources from nitric acid reacted with Ti ions during plasma generation in a form of interstitial doping and modifying the energy state of the TiO_2 nanoparticle band gap, which could be reduced toward the visible region.

Photocatalytic Activity Depending on N Doping Content and Crystallinity

To observe and compare photocatalytic activity depending on the calcination temperature and N doping content ratio, samples were mixed with a 1×10^{-5} MO solution and the degradation efficiency was analyzed. In **Figures 7A–H**, the as-prepared solution was irradiated with visible light (>400 nm) and the photocatalytic decomposition process was initiated. Degussa P-25 in **Figure 7A**, a standard TiO_2 nanopowder, exhibited a reduced degradation activity of the MO solution, which was only 21% under visible region irradiation. The calcined samples in **Figures 7B–F** at 100–300°C of the anatase phase with various degrees of N doping and crystallinity exhibited an enhanced maximum efficiency activity of 91% that was 4 times greater than the degradation performance of P-25 within a reaction period of 6 h. The 200°C calcined N-TiO_2 nanoparticles in **Figure 7D** yielded the greatest photodegradation results and recyclability was measured by cycling test in **Figure S2**. These results indicated that the anatase structure with 0.4 at.% N doping performed much better than the P-25 standard nanoparticles; the other calcination temperature samples yielded somewhat unpredictable phenomena, which should be discussed with regard to crystallinity and N doping content. The band gap of TiO_2 generally depended on the electron state of the doping species and content. Among those, the N doping effect was widely accepted; in the TiO_2 crystalline lattice, N incorporated and modified the electronic band structure, forming an N 2p band above the original O 2p valance band leading to the formation of a narrower band gap of minimum 2.5 eV and shifting the absorption region toward that of visible light. Undoped anatase TiO_2 structure has larger band gap of 3.2 eV, which cannot be excited with visible light. On the other hand, when the N-doped TiO_2 was exposed in the visible region, valence band at N 2p state above original O 2p reduces band gap and generates electrons in the conduction band while remaining holes in the valence band. The generated electrons on conduction band captures oxygen molecules in solution which produces highly reactive superoxide anions and hydroxyl radicals on the surface while holes in the valence band produces highly oxidative hydroxyl radicals by reacting with OH^- ions (Ansari

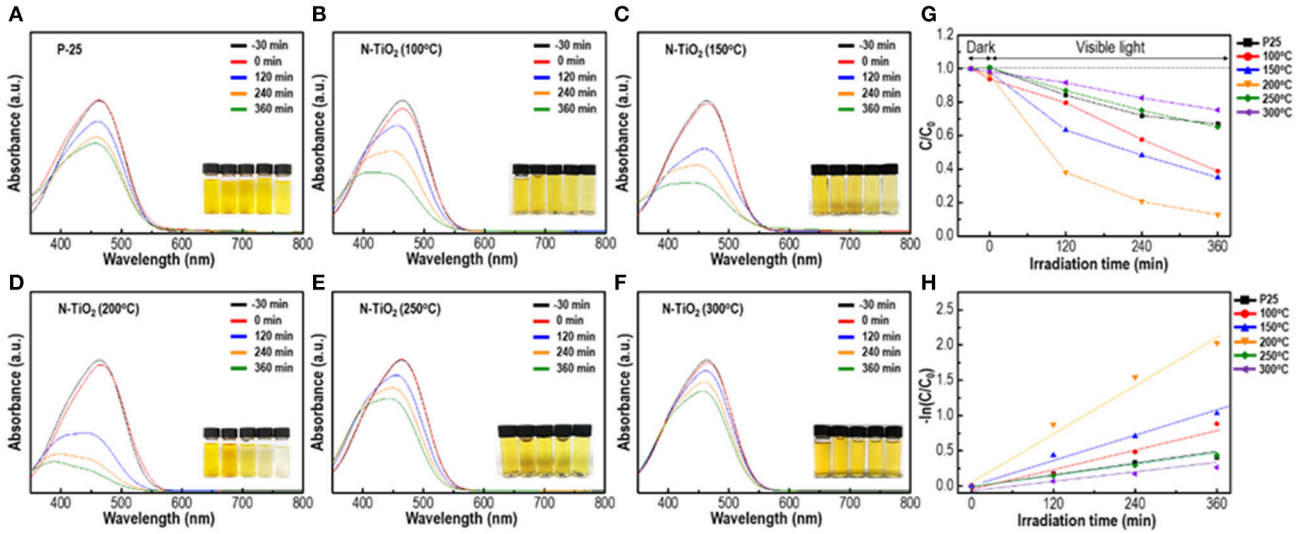

FIGURE 7 | Photocatalytic activity of N-TiO_2 within the visible region depending on different calcination temperature: **(A)** P-25, **(B)** 100°C, **(C)** 150°C, **(D)**200°C, **(E)** 250°C, **(F)** 300°C, **(G)** Photocatalytic efficiency, and **(H)** the plot of-ln(C_0/C).

et al., 2016). Not only N doping but also the Ti^{3+} donor contributed toward the absorption of light. Under visible light irradiation, nanoparticles excited and produced electron-hole pairs, which diffused into the particle surface. These electrons reduced Ti^{4+} into Ti^{3+} species that existed under the conduction band unless they were not trapped (Yang et al., 2010). However, prior studies proposed and certified that the N state above the valance band and Ti^{3+} that was produced by Ti^{4+} capturing electrons on the 1.2 eV conduction band that narrowed the band gap state could act as electron traps near the oxygen vacancy sites, reducing the electron-hole recombination duration time. Another parameter that affected the photodegradation efficiency was the crystallinity of the nanoparticles. It was already known that an amorphous-like layer of nanoparticles would occur due to its adsorption of water molecules on the particle surface. This would reduce the catalytic performance by masking interactions between particles and dye molecules. By removing the adsorbed species and increasing crystallinity, the photocatalytic properties could be enhanced (Yang et al., 2011). Thus, the conditions to obtain the highest photocatalytic properties within the visible light region should be optimized by adjusting the degree of crystallinity and N doping content (Jang et al., 2001; Zhoa et al., 2008; Wang et al., 2009). Following this approach, N-TiO_2 calcined at 100°C with a doping content of 0.52 at.% could be applied as a trapping agent; the photodegradation efficiency was reduced compared to the 200°C condition. Additionally, at lower calcination temperatures, physically embedded or adsorbed water molecules and applied electrolytes on the surface were crucial factors that limited active sites, motivating the reduction in degradation efficiency. At conditions >250°C, negligible N doping content was observed due to an unstable state amid a highly crystalline structure; the poor degradation properties compared to P25 indicated that N doping was passivated by oxidation and returning the material to its original anatase structure while widening the band gap, which would limit its contribution toward enhancement of the visible light region catalyst.

Photoluminescence Analysis From Various Calcination Temperatures

To evaluate the radiative recombination of excited electrons and holes, synthesized N-TiO_2 with 200°C calcined samples were analyzed via PL spectra under an excitation wavelength of 290 nm and compared to an undoped P-25 TiO_2 powder reference in **Figure 8**. Excited peaks in the spectra were observed at 390, 424, 441, and 452 nm indicating different emission sources. The peak at 390 nm could be attributed to the conduction to valence band energy state transition, peaks at 424 and 452 nm were signals from free excitations at the band edge and the excitation peak at 441 nm was due to localized self-trapped excitons (Jagadale et al., 2008; Kho et al., 2010; Ablat et al., 2014). In addition to the PL analysis, the intensity virtually decreased for the 200°C calcined sample, showing that the lifetimes of excited electrons and holes with regard to the N doped TiO_2 nanoparticles were greatly enhanced and contributed to decomposition reactions with organics until the electrons and holes recombined. These results coincided with the photocatalytic activity and XPS analysis showing that for temperatures >250°C, the N doping content was eliminated and the band gap recovered to its original value. Thus, photocatalytic activity would only occur within the UV region.

Growth Mechanism of N-TiO_2 Nanoparticles via Plasma Enhanced Electrolysis

To clarify the growth mechanism of the N-TiO_2 nanoparticles using plasma assisted electrolysis, a schematic diagram can be

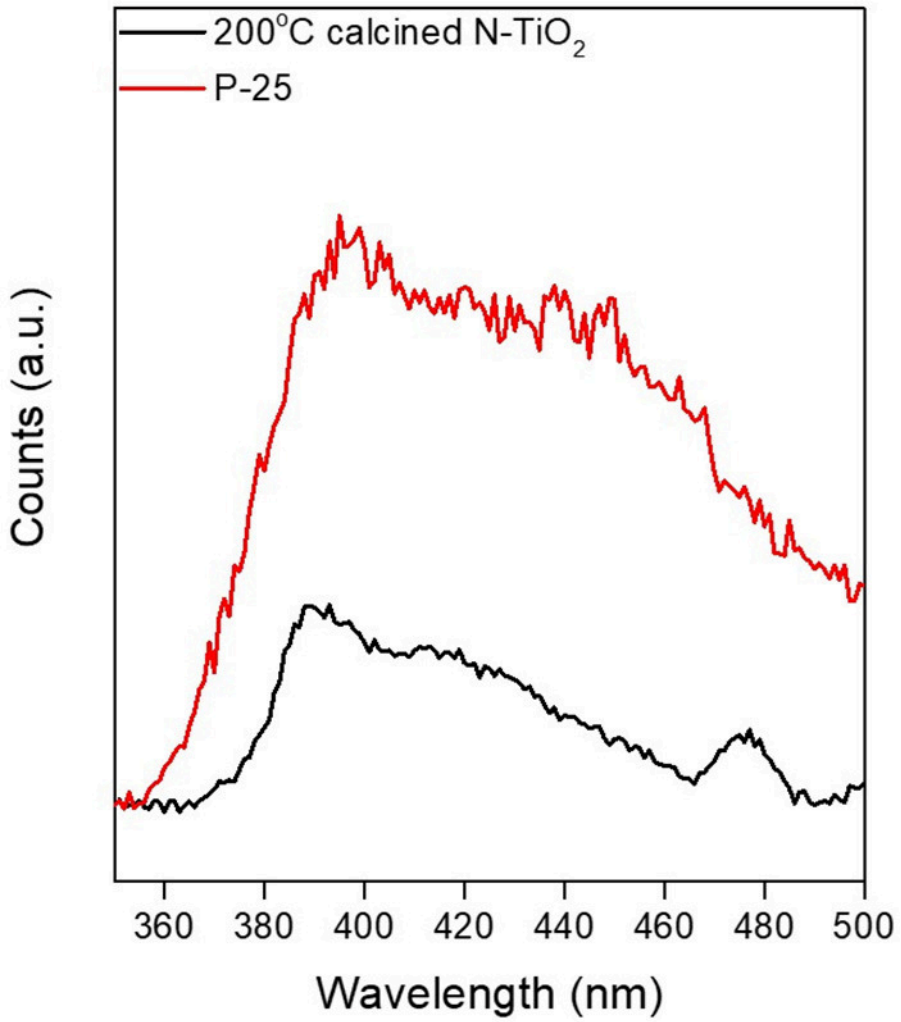

FIGURE 8 | PL spectra of P-25 TiO_2 and 200°C calcined 0.4 at.% N-TiO_2.

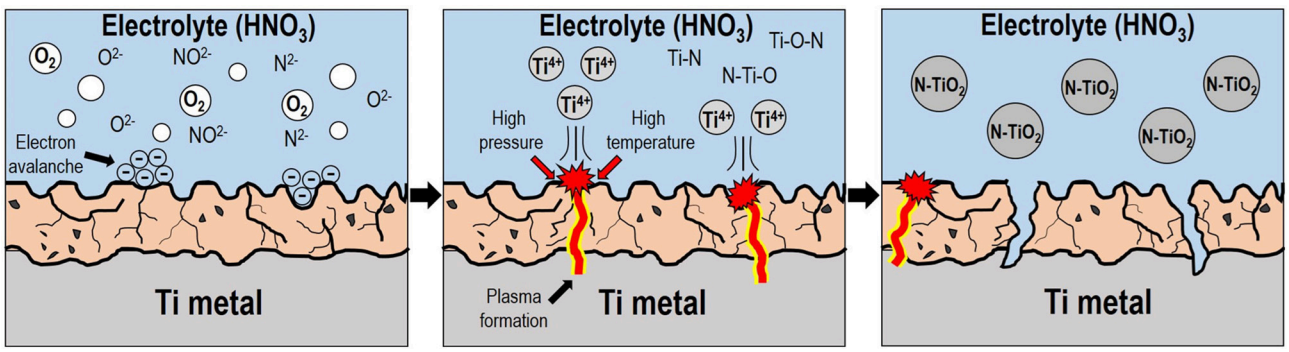

FIGURE 9 | Schematic diagram of the N-TiO_2 nanoparticle synthetic mechanism via plasma enhanced electrolysis.

seen in **Figure 9** with the following description: (1) During the initial stage, low voltages produced a porous thin TiO_2 oxide layer due to anodization during the pre-spark treatment period. (2) This increased the resistivity between the anode-electrolyte, forming an electric field strong enough to liberate and form as gas enveloped the anode surface and initially increased the applied

voltage. (3) High voltages greater than the breakdown voltage at the electron avalanche birthplace excited the electrolyte near the anode via ionization and dissociation, transforming gases into ions such as NO^{2-}, N^{2-}, and O^{2-}, which were subsequently localized onto the anode surface by applying considerable kinetic energy (Mikheev et al., 2015). (4) The ionized gaseous layer provided sufficient energy to initiate Joule heating, which entailed high temperatures and pressures, forming a plasma discharge within the gas envelope. Such arc plasma created Ti^{4+} metal cations from the outer surface of the anode into the electrolyte solution while the plasma gradually penetrated the inner part of the anode. (5) The metal cations then reacted with the as-prepared anionic gaseous species; the ionized cations initially reacted with N species from the ionization of nitric acid, a doping source of nitrogen, forming N-Ti-O bond structures within the Ti lattice through nucleation and growth mechanism; N-TiO_2 nanoparticles were subsequently produced and assisted by controlled temperature induced cooling processes (Cheng et al., 2012). Moreover, the scarcity of existing anions in solution could be attributed to the repression of particle formation; acid-based nanoparticle synthesis conditions would prevent agglomeration between particles.

CONCLUSIONS

Through the adoption of a novel synthetic method for amorphous N doped TiO_2 nanoparticles using plasma enhanced electrolysis, massive N-doped TiO_2 nanoparticles could be produced by merely supplying sufficient voltage to the anode, which was a metal source. This was because the synthetic phenomenon of the metal oxide nanoparticles occurred simultaneously via plasma generation with a rapid reaction.

Arc plasma formation was performed by applying a 500 V AC electric field to the nitric acid electrolyte. The particle morphology and size was verified from 12.1 to 24.7 nm relying on various nitric acid concentrations between the range of 5–15 mmol influenced by repulsive forces during nucleation. The N doping content and N-TiO_2 nanoparticle crystallinity could be controlled by varying the calcination conditions and completely transforming the amorphous structure to anatase, enabling the control of N doping content from 0.54 to 0.4 at.%. N-TiO_2 nanoparticles started to be synthesized just after applying voltage to the anode due to plasma generation, entailing a high temperature and pressure. The N-TiO_2 nanoparticles synthesized after calcination at 200°C featured 0.4 at.% of N doping content and exhibited the greatest MO degradation performance of 91% in the visible region, which could be attributed to a narrow band gap structure due to N doping; PL analysis also revealed the most delayed recombination rate as well (see **Figures 6**, **7**). Thus, this one-step metal-direct synthetic method via plasma generation demonstrated great potential for the novel and high-quality synthesis of N-doped metal oxide nanoparticles and could be scaled-up for industrial applications.

AUTHOR CONTRIBUTIONS

TK prepared in writing this paper work through experiment and data analysis. G-MG helped measuring photocatalytic activities of nanoparticles. H-BC helped and advised result of this paper and modified it as logical, YS helped searching for the related information about this paper. C-GL and Y-HC equally contributed to this manuscript and accepted responsibility for conduct of research and final approval.

ACKNOWLEDGMENTS

This study was supported by the Korea Institute of Energy Technology Evaluation and Planning (KETEP), which is funded by the Ministry of Trade, Industry and Energy of the Republic of Korea (No. 20152510101950), by the Nano●Material Technology Development Program through the National Research Foundation of Korea (NRF) funded by the Ministry of Science, ICT and Future Planning (No. 2016M3A7B4900044) and the Future Materials Discovery Program through the National Research Foundation of Korea (NRF) funded by the Ministry of Science, ICT & Future Planning (NRF-2016M3D1A1027836).

SUPPLEMENTARY MATERIAL

The Supplementary Material for this article can be found online at: https://www.frontiersin.org/articles/10.3389/fchem.2018.00458/full#supplementary-material

REFERENCES

Ablat, A., Wu, R., Jian, J., Jiang, X., Mamat, M., and Li, J. (2014). Room temperature ferromagnetism of N-doped TiO_2 nanowires. *Mater. Lett.* 132, 86–89. doi: 10.1016/j.matlet.2014.06.040

Alqadi, M. K., Abo Noqtah, O. A., Alzoubi, F. Y., Alzouby, J., and Aljarrah, K. (2014). PH effect on the aggregation of silver nanoparticles synthesized by chemical reduction. *Mater. Sci. Poland* 32, 107–111. doi: 10.2478/s13536-013-0166-9

Ansari, S. A., Khan, M. M., Ansari, M. O., and Cho, M. H. (2016). Nitrogen-doped titanium dioxide (N-doped TiO_2) for visible light photocatalysis. *New J. Chem.* 40, 3000–3009. doi: 10.1039/c5nj03478g

Aware, D. V., and Jadhav, S. S. (2015). Synthesis, characterization and photocatalytic applications of Zn-doped TiO_2 nanoparticles by sol–gel method. *Appl. Nanosci.* 6, 965–972. doi: 10.1007/s13204-015-0513-8

Ba-abbad, M. M., Kadhum, A. A. H., Mohamad, A. B., Takriff, M. S., and Sopian, K. (2012). Synthesis and catalytic activity of TiO_2 nanoparticles for photochemical oxidation of concentrated chlorophenols under direct solar radiation. *Int. J. Electrochem. Sci.* 7, 4871–4888.

Cao, Y., Tan, H., Shi, T., Tang, T., and Li, J. (2008). Preparation of Ag-doped TiO_2 nanoparticles for photocatalytic degradation of acetamiprid in water. *J. Chem. Tech. Biotech.* 83, 546–552. doi: 10.1002/jctb.1831

Caratto, V., Setti, L., Campodonico, S., Carnasciali, M. M., Botter, R., and Ferretti, M. (2012). Synthesis and characterization of nitrogen-doped TiO_2 nanoparticles prepared by sol–gel method. *J. Sol-Gel Sci. Technol.* 63, 16–22. doi: 10.1007/s10971-012-2756-0

Cheng, X., Yu, X., Xing, Z., and Wan, J. (2012). Enhanced photocatalytic activity of nitrogen doped TiO_2 anatase nano-particle under simulated sunlight irradiation. *Energy Proc.* 16, 598–605. doi: 10.1016/j.egypro.2012.01.096

Dong, H., Zeng, G., Tang, L., Fan, C., Zhang, C., He, X., et al. (2015). An overview on limitations of TiO_2-based particles for photocatalytic degradation of organic pollutants and the corresponding countermeasures. *Water Res.* 79, 128–146. doi: 10.1016/j.watres.2015.04.038

Dunnill, C. W., Ansari, Z., Kafizas, A., Perni, S., Morgan, D. J., and Wilson, M. (2011). Visible light photocatalysts—N-doped TiO_2 by sol–gel, enhanced with surface bound silver nanoparticle islands. *J. Mater. Chem.* 21, 11854–11861. doi: 10.1039/c1jm11557j

Galinska, A., and Walendziewski, J. (2005). Photocatalytic water splitting over Pt-TiO_2 in the presence of sacrificial reagents. *Energy Fuels* 19, 1143–1147. doi: 10.1021/ef0400619

Gao, Y., Feng, Y., Zhang, B., Zhang, F., Peng, X., and Liu, L. (2014). Double-N doping: a new discovery about N-doped TiO_2 applied in dye-sensitized solar cells. *RSC Adv.* 4, 16992–16998. doi: 10.1039/C4RA00053F

Jagadale, T. C., Takale, S. P., Sonawane, R. S., Joshi, H. M., Patil, S. I., and Kale, B. B. (2008). N-doped TiO_2 nanoparticle based visible light photocatalyst by modified peroxide sol-gel method. *J. Phys. Chem. C* 112, 14595–14602. doi: 10.1021/jp803567f

Jang, H. D., Kim, S. K., and Kim, S. J. (2001). Effect of particle size and phase composition of titanium dioxide nanoparticles on the photocatalytic properties. *J. Nanomat. Res.* 3, 141–147. doi: 10.1023/A:1017948330363

Kho, Y. K., Iwase, A., Teoh, W. Y., Madler, L., Kudo, A., and Amal, R. (2010). Photocatalytic H_2 evolution over TiO_2 nanoparticles. The synergistic effect of anatase and rutile. *J. Phys. Chem. C* 114, 2821–2829. doi: 10.1021/jp910810r

Kim, T. H., Eom, N. S. A., Kang, S.-O., and Choa, Y.-H. (2016). Plasma-assisted electrolytic synthesis of $In(OH)_3$ nanocubes for thermal transformation into In_2O_3 nanocubes with a controllable Sn content. *RSC Adv.* 6, 20337–20342. doi: 10.1039/c5ra25489b

Li, L., and Liu, C.-Y. (2009). Facile synthesis of anatase-brookite mixed-phase N-doped TiO_2 nanoparticles with high visible-light photocatalytic activity. *Euro. J. Inorg. Chem.* 25, 3727–3733. doi: 10.1002/ejic.200900369

Lin, Y., Li, D., Hu, J., Xiao, G., Wang, J., Li, W., et al. (2012). Highly efficient photocatalytic degradation of organic pollutants by PANI-modified TiO_2 composite. *J. Phys. Chem. C* 116, 5764–5772. doi: 10.1021/jp211222w

Liu, G., Sun, C., Yang, H. G., Smith, S. C., Wang, L., and Lu, G. Q. (2010). Nanosized anatase TiO_2 single crystals for enhanced photocatalytic activity. *Chem. Commun.* 46, 755–757. doi: 10.1039/b919895d

Mattioli, G., Bonapasta, A. A., Bovi, D., and Giannozzi, P. (2014). Photocatalytic and photovoltaic properties of TiO_2 nanoparticles investigated by Ab initio simulations. *J. Phys. Chem. C* 118, 29928–29942. doi: 10.1021/jp509830w

Mikheev, A. Y., Girn, A. V., Vakhteev, E. V., Alekseeva, E. G., and Ravodina, D. V. (2015). The formation of a surface layer during microarc oxidation of aluminum alloys. *IOP Conf. Ser. Mater. Sci. Eng.* 70:012002. doi: 10.1088/1757-899x/70/1/012002

Mohamed, M. A., Salleh, W. N. W., Jaafar, J., Ismail, A. F., and Nor, N. A. M. (2015). Photodegradation of phenol by n-doped TiO_2 anatase/rutile nanorods assembled microsphere under UV and visible light irradiation. *Mater. Chem. Phys.* 162, 113–123. doi: 10.1016/j.matchemphys.2015.05.033

Ni, M., Leung, M. K. H., Leung, D. Y. C., and Sumathy, K. (2007). A review and recent developments in photocatalytic water-splitting using TiO_2 for hydrogen production. *Renew. Sustain. Energy Rev.* 11, 401–425. doi: 10.1016/j.rser.2005.01.009

Scanlon, D. O., Dunnill, C. W., Buckeridge, J., Shevlin, S. A., Logsdail, A. J., and Woodley, S. M. (2013). Band alignment of rutile and anatase TiO_2. *Nat. Mater.* 12, 798–801. doi: 10.1038/nmat3697

Soares, G. B., Bravin, B., Vaz, C. M. P., and Ribeiro, C. (2011). Facile synthesis of N-doped TiO_2 nanoparticles by a modified polymeric precursor method and its photocatalytic properties. *Appl. Catal. B: Environ.* 106, 287–294. doi: 10.1016/j.apcatb.2011.05.018

Sun, S., Gao, P., Yang, Y., Yang, P., Chen, Y., and Wang, Y. (2016). N-doped TiO_2 nanobelts with coexposed (001) and (101) facets and their highly efficient visible-light-driven photocatalytic hydrogen production. *ACS Appl. Mater. Interfaces* 8, 18126–18131. doi: 10.1021/acsami.6b05244

Tang, J., Durrant, J. R., and Klug, D. R. (2008). Mechanism of photocatalytic water splitting in TiO_2. Reaction of water photoholes, importance of charge carrier dynamics, and evidence for four-hole chemistry. *J. Am. Chem. Soc.* 130, 13885–13891. doi: 10.1021/ja8034637

Vukoje, I., Kovac, T., Dzunuzovic, J., Dzunuzovic, E., Loncarevic, D., Ahrenkiel, S. P., et al. (2016). Photocatalytic ability of visible-light-responsive TiO_2 nanoparticles. *J. Phys. Chem. C* 120, 18560–18569. doi: 10.1021/acs.jpcc.6b04293

Wang, J., Tafen, D. N., Lewis, J. P., Hong, Z., Manivannan, A., And Zhi, M. (2009). Origin Of Photocatalytic Activity of nitrogen-doped TiO_2 nanobelts. *J. Amer. Chem. Soc.* 131, 12290–12297. doi: 10.1021/ja903781h

Wu, G., Nishikawa, T., Ohtani, B., and Chen, A. (2007). Synthesis and characterization of carbon-doped TiO_2 nanostructures with enhanced visible light response. *Chem. Mater.* 19, 4530–4537. doi: 10.1021/cm071244m

Wu, W. Y., Kung, W. Y., and Ting, J. M. (2011). Effect of pH values on the morphology of zinc oxide nanostructures and their photoluminescence spectra. *J. Amer. Ceram. Soc.* 94, 699–703. doi: 10.1111/j.1551-2916.2010.04146.x

Yang, G., Jiang, Z., Shi, H., Xiao, T., and Yan, Z. (2010). Preparation of highly visible-light active N-doped TiO_2 photocatalyst. *J. Mater. Chem.* 20, 5301. doi: 10.1039/c0jm00376j

Yang, L., Li, G., Hu, W., Zhao, M., Sun, L., and Zheng, J. (2011). Control over the crystallinity and defect chemistry of YVO_4 nanocrystals for optimum photocatalytic property. *Euro. J. Inorg. Chem.* 2011, 2211–2220. doi: 10.1002/ejic.201001341

Yu, H., Ye, L., Zhang, T., Zhou, H., and Zhao, T. (2017). Synthesis, characterization and immobilization of N-doped TiO_2 catalysts by a reformed polymeric precursor method. *RSC Adv.* 7, 15265–15271. doi: 10.1039/c6ra27187a

Yu, H., Zheng, X., Yin, Z., Tag, F., Fang, B., and Hou, K. (2007). Preparation of nitrogen-doped TiO_2 nanoparticle catalyst and its catalytic activity under visible light. *Chin. J. Chem. Eng.* 15, 802–807. doi: 10.1016/s1004-9541(08)60006-3

Zhao, Z., and Liu, Q. (2008). Mechanism of higher photocatalytic activity of anatase TiO_2 doped with nitrogen under visible-light irradiation from density functional theory calculation. *J. Phys. D Appl. Phys.* 41:025105. doi: 10.1088/0022-3727/41/2/025105

Zhoa, Y., Qiu, X., and Burda, C. (2008). The effects of sintering on the photocatalytic activity of n-doped TiO_2 nanoparticles. *Chem. Mater.* 20, 2629–2636. doi: 10.1021/cm703043j

Zhou, X., Peng, F., Wang, H., Yu, H., and Yang, J. (2011). Preparation of nitrogen doped TiO_2 photocatalyst by oxidation of titanium nitride with H_2O_2. *Mater. Res. Bull.* 46, 840–844. doi: 10.1016/j.materresbull.2011.02.029

Conflict of Interest Statement: The authors declare that the research was conducted in the absence of any commercial or financial relationships that could be construed as a potential conflict of interest.

frontiers in Chemistry

ORIGINAL RESEARCH
published: 24 July 2018
doi: 10.3389/fchem.2018.00313

Ti_4O_7/g-C_3N_4 for Visible Light Photocatalytic Oxidation of Hypophosphite: Effect of Mass Ratio of Ti_4O_7/g-C_3N_4

Wei Guan[1], *Zhenghua Zhang*[2*†], *Shichao Tian*[3*†] *and Jianwei Du*[1]

[1] South China Institute of Environmental Sciences, The Ministry of Environment Protection of PRC, Guangzhou, China, [2] Graduate School at Shenzhen, Research Institute of Environmental Engineering and Nano-Technology, Tsinghua University, Shenzhen, China, [3] Shenzhen Environmental Science and New Energy Technology Engineering Laboratory, Tsinghua-Berkeley Shenzhen Institute, Shenzhen, China

OPEN ACCESS

Edited by:
Fan Dong,
Chongqing Technology and Business University, China

Reviewed by:
Guohong Wang,
Hubei Normal University, China
Aihua Xu,
Wuhan Textile University, China
Shaowen Cao,
Wuhan University of Technology, China
Hongwei Huang,
China University of Geosciences, China

***Correspondence:**
Zhenghua Zhang
zhenghua.zhang@sz.tsinghua.edu.cn
Shichao Tian
18812672619@163.com

[†]*These authors have contributed equally to this work.*

Specialty section:
This article was submitted to Catalysis and Photocatalysis, a section of the journal Frontiers in Chemistry

Received: *07 May 2018*
Accepted: *09 July 2018*
Published: *24 July 2018*

Citation:
Guan W, Zhang Z, Tian S and Du J (2018) Ti_4O_7/g-C_3N_4 for Visible Light Photocatalytic Oxidation of Hypophosphite: Effect of Mass Ratio of Ti_4O_7/g-C_3N_4 Front. Chem. 6:313. doi: 10.3389/fchem.2018.00313

Hypophosphite wastewater treatment is still a critical issue in metallurgical processes and the oxidation of hypophosphite to phosphate followed by the precipitation of phosphate is an important strategy for hypophosphite wastewater treatment. Herein, Ti_4O_7/g-C_3N_4 photocatalysts with various mass ratios (Ti_4O_7 (m): g-C_3N_4 (m) = 0.5, 0.2, 0.1, and 0.05) were synthesized by a hydrolysis method and the effect of the mass ratio of Ti_4O_7 (m): g-C_3N_4 (m) on Ti_4O_7/g-C_3N_4 visible light photocatalytic oxidation of hypophosphite was evaluated. The as-prepared Ti_4O_7/g-C_3N_4 were characterized and confirmed by SEM, XPS, XRD and FTIR. Moreover, the specific surface area and the distribution of pore size of Ti_4O_7/g-C_3N_4 was also analyzed. Our results showed that Ti_4O_7/g-C_3N_4 exhibited remarkably improved photocatalytic performance on hypophosphite oxidation compared with g-C_3N_4 and meanwhile 1:2-Ti_4O_7/g-C_3N_4 with a mass ratio of 0.5 showed the best photocatalytic performance with the highest oxidation rate constant (17.7-fold and 91.0-fold higher than that of pure g-C_3N_4 and Ti_4O_7, respectively). The enhanced performance of photocatalytic oxidation of hypophosphite was ascribed to the heterojunction structure of Ti_4O_7/g-C_3N_4 with broader light absorption and significantly enhanced efficiency of the charge carrier (e^--h^+) generation and separation. Additionally, the generated $\cdot OH$ and $\cdot O_2^-$ radicals contributed to the hypophosphite oxidation during the photocatalytic system.

Keywords: photocatalysts, hypophosphite oxidation, graphitic carbon nitride, sub-stoichiometric titanium oxides, visible light irradiation

INTRODUCTION

Hypophosphite wastewater is produced in metallurgical processes where hypophosphite is a widely used reducing reagent for chemical nickel deposition (Gan et al., 2007; Huang et al., 2009). The discharge of hypophosphite wastewater may result in eutrophication and therefore the further treatment is required (Piveteau et al., 2017; Tian et al., 2017). Coagulants such as Fe have been widely used for phosphorus removal (Shih et al., 2013), however, the hypophosphite precipitants are not stable due to the high solubility constant (Zhao et al., 2017). As such, the pre-oxidation of hypophosphite to phosphate is very important for hypophosphite wastewater treatment so as to facilitate the following precipitation of phosphate in the form of insoluble salts precipitates.

Photocatalysis is considered to be a useful technology for water treatment with advantages of energy-free by using solar energy and high oxidation efficiency of pollutants by hydroxyl radicals (·OH) and superoxide radicals ($\cdot O_2^-$) generated during the photocatalytic process (Hao et al., 2017). The most commonly used TiO_2 photocatalyst, however, is greatly limited in wide applications especially under visible light or sunlight due to its main drawback of wide band gap (3.2 eV) (Hao et al., 2016; Ma et al., 2018). Therefore, photocatalysts with wide range of response wavelength as well as good photogenerated charge separation properties are urgently required for photocatalytic applications.

Recently, graphite-like carbon nitride ($g\text{-}C_3N_4$) has attracted lots of attentions due to its advantages including small band gap of 2.73 eV, robust chemical stability over a wide pH range of 0–14 (Zhang et al., 2014; Li et al., 2016a,b). Nevertheless, limitations including low surface area and poor photogenerated charge separation properties still hinder the photocatalytic applications of $g\text{-}C_3N_4$ (Shao et al., 2017). Preparation of $g\text{-}C_3N_4$-based heterojunction is an alternative pathway to facilitate the enhancement of charge separation and photocatalytic performance (Masih et al., 2017). For instance, photocatalysts with *p–n* junction exhibited excellent photocatalytic performance in environmental and energy applications (Huang et al., 2015a,b, 2016; Zhang et al., 2018).

Magnéli phase titanium suboxides (Ti_nO_{2n-1}) are substoichiometric titanium oxides, where n is an integer between 4 and 10 (i.e., 4, 5, 6, and 8) (Zaky and Chaplin, 2014). Among various compositions of Ti_nO_{2n-1}, Ti_4O_7 has the properties of best conductivity (1,500 S cm^{-1}) and the robust resistance to aggressive chemical conditions (Ganiyu et al., 2016). Construction of $g\text{-}C_3N_4/Ti_4O_7$ heterojunction significantly improved the photocatalytic performance as a result of the effective enhancement of charge separation was reported in our previous work (Guan et al., 2018). However, the effect of the mass ratio of Ti_4O_7 (m): $g\text{-}C_3N_4$ (m) of the $g\text{-}C_3N_4/Ti_4O_7$ heterojunction on photocatalytic performance is still unknown. In this study, the effect of the mass ratio of $Ti_4O_7/g\text{-}C_3N_4$ (Ti_4O_7 (m): $g\text{-}C_3N_4$ (m) = 0.5, 0.2, 0.1 and 0.05) on photocatalytic oxidation of hypophosphite was evaluated in view of the photocatalytic performance, optical and electrochemical properties as well as the contributions of ·OH and $\cdot O_2^-$ radicals generated during the photocatalytic process. Our results indicated that $Ti_4O_7/g\text{-}C_3N_4$ with a mass ratio of 0.5 showed the highest rate constant of photocatalytic oxidation of hypophosphite (17.7-fold and 91.0-fold higher than that of pure $g\text{-}C_3N_4$ and Ti_4O_7, respectively).

MATERIALS AND METHODS

Chemicals

The reagents used for the preparation and performance characterization of $g\text{-}C_3N_4/Ti_4O_7$ were analytical grade and included sub-stoichiometric titanium oxide, melamine, urea, sodium hypophosphite, sodium sulfate, isopropanol, sodium hydroxide, sulfuric acid. All chemicals were bought from Sinopharm Chemical Reagent Co., Ltd. (Beijing, China). In addition, all solutions were prepared using freshly prepared Milli-Q water (Millipore, 18.2 MΩ cm).

Preparation of $Ti_4O_7/g\text{-}C_3N_4$ Photocatalysts

Graphite-like carbon nitride was prepared first using a liquid-based growth method (Sun et al., 2018). Then, $g\text{-}C_3N_4$ (2 g) and Ti_4O_7 (1, 0.4, 0.2, 0.1 g) were well mixed in the 0.1 mol/L NaOH solution (100 mL) using ultrasonication following by the annealing procedure at 160°C for 20 h. Subsequently, the as-prepared $g\text{-}C_3N_4/Ti_4O_7$ with various mass ratios (Ti_4O_7 (m): $g\text{-}C_3N_4$ (m) = 0.5, 0.2, 0.1, and 0.05) were dried at 60°C for 12 h before usage and noted as 1:2-$Ti_4O_7/g\text{-}C_3N_4$, 1:5-$Ti_4O_7/g\text{-}C_3N_4$, 1:10-$Ti_4O_7/g\text{-}C_3N_4$ and 1:20-$Ti_4O_7/g\text{-}C_3N_4$, respectively.

Analysis and Test Methods

The as-prepared $g\text{-}C_3N_4/Ti_4O_7$ were characterized by scanning electron microscopy (SEM) (JEOL JSM-6701F), X-ray photoelectron spectroscopy (XPS) (Phi Quantern instrument with C 1s peak (284.8 eV) as the calibrated reference), X-ray diffraction (XRD) (model D/max RA, Rigaku Co., Japan), and fourier transforms infrared spectroscopy spectra (FTIR) (Bruker Tensor-27). The specific surface area and the pore size distribution of the as-prepared $g\text{-}C_3N_4/Ti_4O_7$ were calculated by Brunauer-Emmett-Teller (BET) equation and Barrett-Joyner-Halenda (BJH) method according to the N_2 adsorption/desorption isotherms. The optical and electrochemical properties of the as-prepared $g\text{-}C_3N_4/Ti_4O_7$ were evaluated by Ultraviolet-visible diffraction spectra (UV-vis DRS) (UV-2450, Shimadzu, Japan) and CHI 660B electrochemical system in view of photocurrent (PC), cyclic voltammetry (CV) and electrochemical impedance spectroscopy (EIS). The contributions of ·OH and $\cdot O_2^-$ radicals generated during the visible light photocatalytic process were identified by comparing the efficiencies of hypophosphite oxidation in the absence and presence of isopropanol (IPA) and N_2 purging.

Analysis of Photocatalytic Performance

The photocatalytic performance of $g\text{-}C_3N_4/Ti_4O_7$ was characterized by photocatalytic oxidation of hypophosphite with the concentration of hypophosphite measured by ion chromatography using a 732 IC detector. A metal-halide lamp (35 W, Philips) with the light strength of ∼5 mW cm^{-2} was used as the light source and a UV-cutoff filter of 420 nm was used to provide the visible light with the wavelength over 420 nm. Before the photocatalytic experiments, $g\text{-}C_3N_4/Ti_4O_7$ with various mass ratios (10 mg) dispersed in 100 mg L^{-1} hypophosphite aqueous solution (100 mL) were continuously stirred for 30 min in the dark to achieve the adsorption–desorption equilibrium. After that, the visible light photocatalytic oxidation of hypophosphite was conducted with the above solutions exposing to the visible light irradiation and sampling conducted at 1 h intervals over

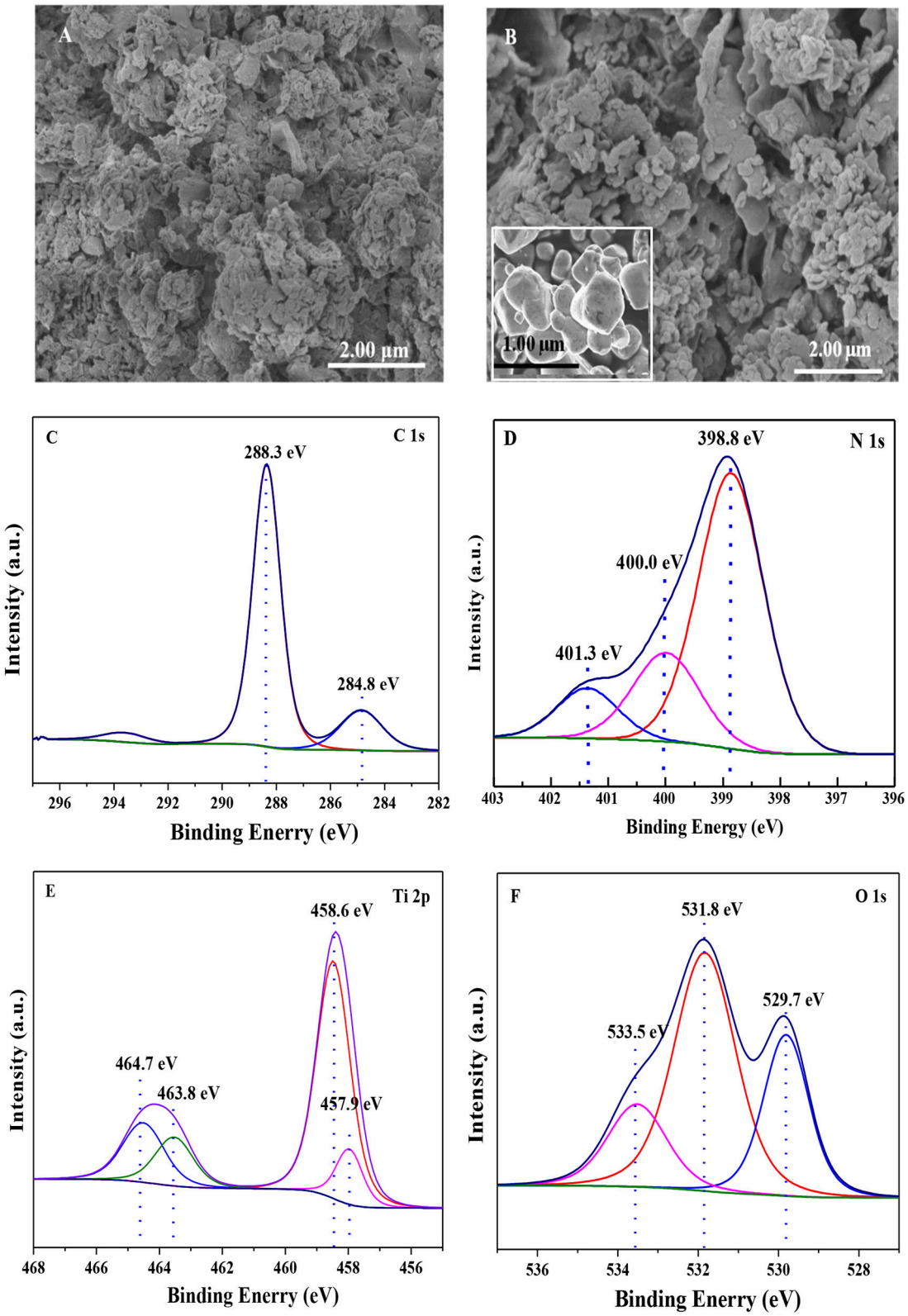

FIGURE 1 | The SEM images of **(A)** g-C_3N_4, **(B)** Ti_4O_7/g-C_3N_4 photocatalysts; and XPS spectrum of **(C)** C 1s, **(D)** N 1s, **(E)** Ti 2p, **(F)** O 1s of Ti_4O_7/g-C_3N_4 photocatalyst.

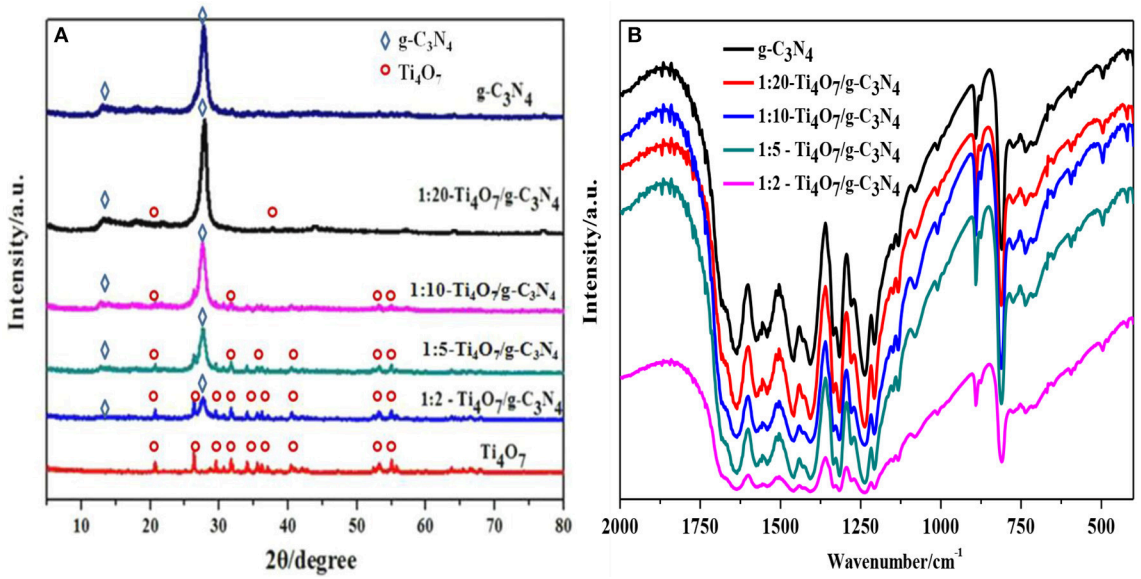

FIGURE 2 | Structure and morphology analysis of g-C_3N_4 and Ti_4O_7/g-C_3N_4 photocatalysts: **(A)** XRD patterns analysis; **(B)** FTIR spectrometer analysis.

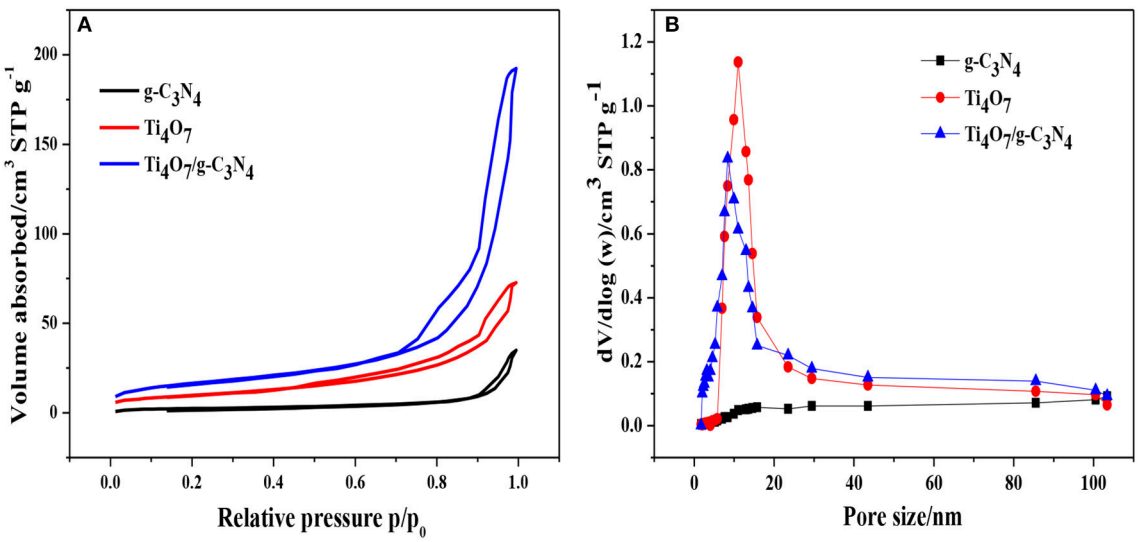

FIGURE 3 | (A) N_2 adsorption-desorption isotherms and **(B)** pore size distribution of g-C_3N_4, pure Ti_4O_7 and 1:2-Ti_4O_7/g-C_3N_4 photocatalysts.

6 h experimental period. More detailed information about the photocatalytic experiment can be found in our most recent paper (Guan et al., 2018). The oxidation efficiency of hypophosphite (η) was calculated using the following equation (Guan et al., 2017):

$$\eta = \frac{C_0 - C_t}{C_0} \times 100\% \quad (1)$$

where C_0 and C_t represent the concentrations of hypophosphite at initial and given time, respectively.

RESULTS AND DISCUSSION

Materials Characterization

The SEM images of pure g-C_3N_4 and Ti_4O_7/g-C_3N_4 photocatalysts were shown in **Figure 1** that g-C_3N_4 had a sheet-like structure (**Figure 1A**) and spheroidal Ti_4O_7 crystals were deposited on the surface of C_3N_4 (**Figure 1B**). The corresponding XPS high resolution spectra of Ti_4O_7/g-C_3N_4 were analyzed as shown in **Figure 1**. There were two components for the XPS spectra of C 1s core level (**Figure 1C**), the standard reference carbon (284.8 eV) and the sp^2 bonded C in N=C(–N)$_2$ (288.3 eV) (Jo and Natarajan, 2015). With regard to the N 1s

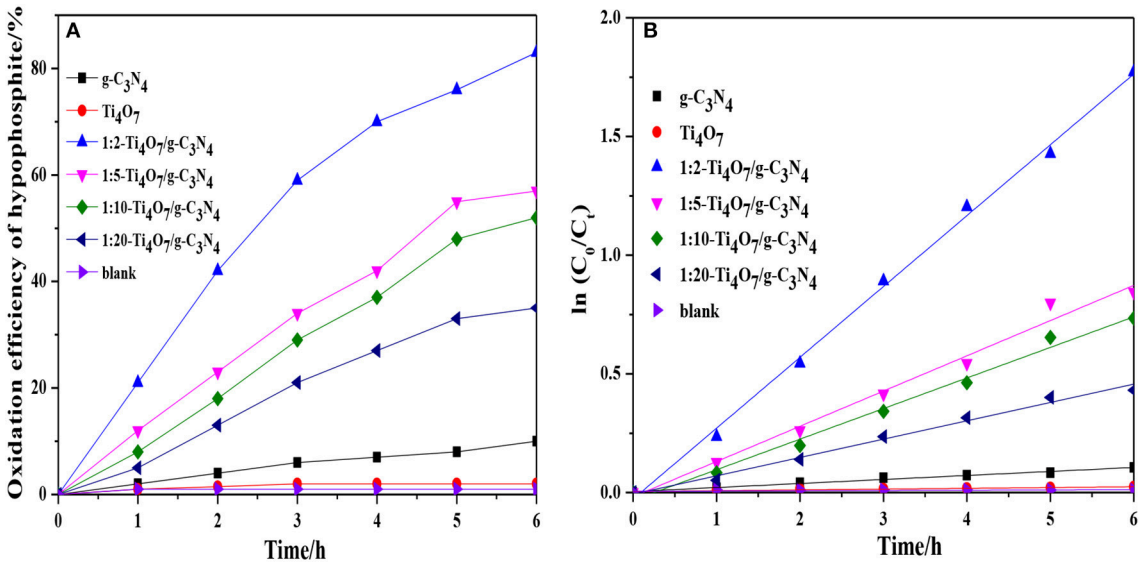

FIGURE 4 | (A) The oxidation efficiency of hypophosphite for different photocatalysts; **(B)** Plot of $\ln(C_0/C_t)$ against reaction time for the catalytic oxidation of hypophosphite using different photocatalysts.

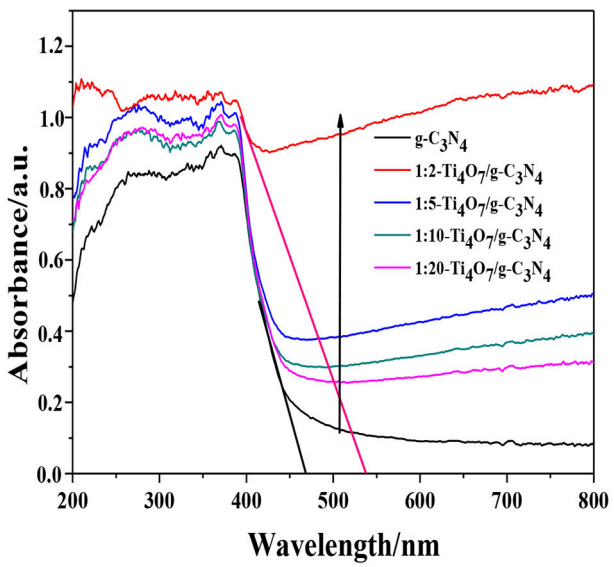

FIGURE 5 | UV–vis DRS spectra of different photocatalysts.

spectra, there were three peaks (**Figure 1D**), the main peak at 398.8 eV assigned to sp^2 nitrogen (C=N–C) involved in triazine rings, the peak at 400.0 eV originated from the tertiary nitrogen bonded to carbon atoms in the form of N–$(C)_3$ (Wu et al., 2013) and the peak at 401.3 eV ascribed to amino functions (C–N–H) (Gao et al., 2014). These assignments of C 1s and N 1s were agreed well with the XPS results of g-C_3N_4 reported previously. Meanwhile, Ti_4O_7 is a mixed-valence compound with two evenly occupied Ti^{4+} ($3d^0$) and Ti^{3+} ($3d^1$) configurations. Four peaks were observed for Ti 2p spectra (**Figure 1E**) that two broad peaks at 458.6 eV and 464.7 eV were respectively assigned to Ti $2p_{1/2}$ and Ti $2p_{3/2}$ peaks of Ti^{4+}, and another two peaks at 457.9 eV and 463.8 eV were assigned to Ti^{3+} (Zeng et al., 2017). In terms of the O 1s spectra, three peaks were observed (**Figure 1F**) that the peak at 533.5 eV was assigned to the C–O functional groups, and the peaks at 531.8 and 529.7 eV were ascribed to the OH–Ti and O–Ti bonds (Li et al., 2017). The XPS results confirmed the presence of Ti_4O_7 on the surface of g-C_3N_4 with covalent bonds.

The XRD phase structures of Ti_4O_7/g-C_3N_4 photocatalysts with various mass ratios were shown in **Figure 2A**. Peaks at 13.10° and 27.40° were indexed as (1 0 0) plane of tri-s-triazine units and (0 0 2) plane of the conjugated aromatic system of g-C_3N_4, respectively (Liang and Zhu, 2016). Meanwhile, major peaks of Ti_4O_7 including 20.7, 26.3, 29.5, 31.7, 34.0, 36.3, 40.5, 53.1, 55.0, 63.8, and 66.4° were also found (Guo et al., 2016). With increase of the mass ratio of Ti_4O_7 (m): g-C_3N_4 (m), the intensity of the Ti_4O_7 peaks became stronger while that of the C_3N_4 peaks became weaker. Furthermore, Ti_4O_7/g-C_3N_4 especially 1:2-Ti_4O_7/g-C_3N_4 (mass ratio of Ti_4O_7/g-C_3N_4 of 0.5) matched well with the reference of pure Ti_4O_7 and g-C_3N_4, indicating that the main structures of Ti_4O_7 and g-C_3N_4 were not destroyed during the synthesis process of Ti_4O_7/g-C_3N_4.

The as-prepared Ti_4O_7/g-C_3N_4 photocatalysts with various mass ratios were further characterized by FTIR as shown in **Figure 2B**. Typical absorption peaks of 1,230–1,630 cm^{-1} were attributed to tri-s-triazine ring moieties of g-C_3N_4. For example, the absorption peaks of 1,638 and 1,570 cm^{-1} were related to C=N stretching, and the peaks of 1,474, 1,410, 1,322, 1,241 cm^{-1} were attributed to C–N stretching. Meanwhile, the sharp peak of 810 cm^{-1} was due to the bending vibration of heptazine rings, indicating that the heptazine units might exist in C_3N_4 (Hatamie et al., 2018). With increase of the mass ratio of Ti_4O_7/g-C_3N_4, the absorption intensity related to the vibrational bands

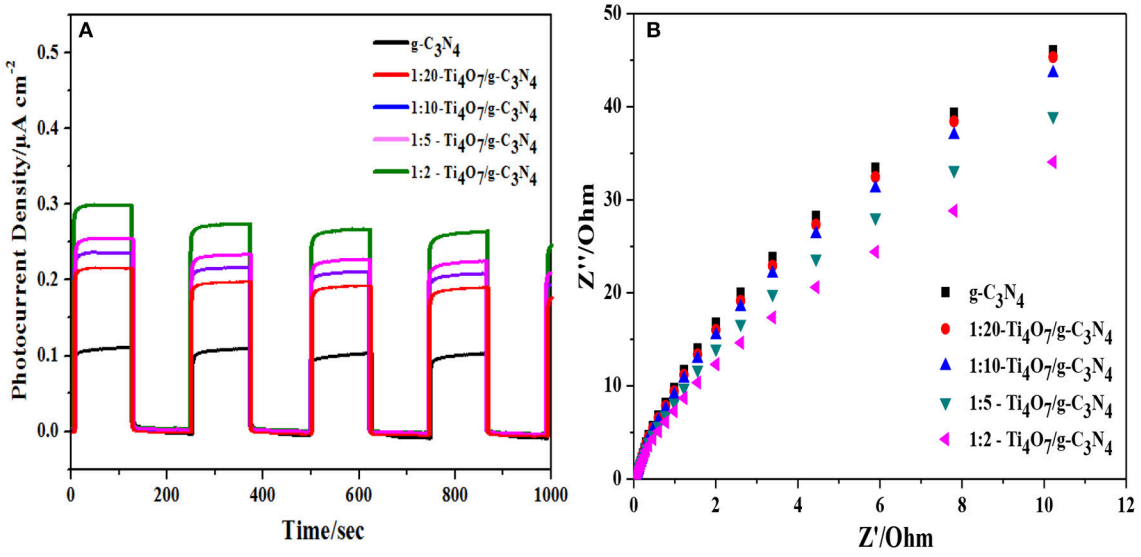

FIGURE 6 | Electrochemical properties analysis: **(A)** photocurrent density and **(B)** EIS Nyquist plots of different photocatalysts.

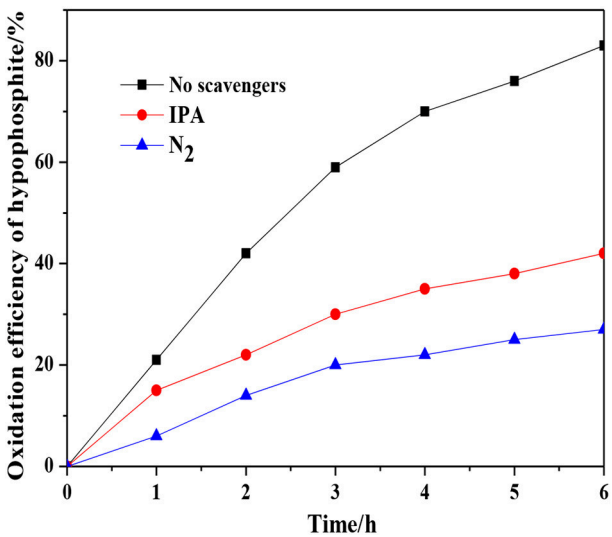

FIGURE 7 | Effect of radical scavengers on the photocatalytic oxidation of hypophosphite by the 1:2-Ti_4O_7/g-C_3N_4 photocatalyst.

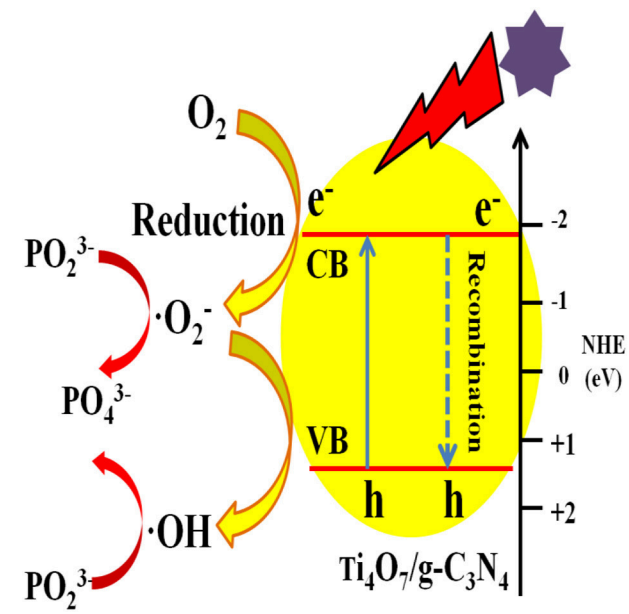

FIGURE 8 | Schematic of the mechanism of photocatalytic oxidation of hypophosphite by Ti_4O_7/g-C_3N_4 photocatalysts.

of g-C_3N_4 became weaker. The presence of Ti_4O_7 in Ti_4O_7/g-C_3N_4 restricted the evolution trend of g-C_3N_4 and thus alleviated the severe stacking of aromatic units of g-C_3N_4. Additionally, the delocalized π-π conjugated electronic system of g-C_3N_4 facilitated the transfer of photogenerated electron-hole pairs during the photocatalytic process (Jourshabani et al., 2018).

The nitrogen adsorption-desorption isotherms and pore size distribution of pure Ti_4O_7, g-C_3N_4 and 1:2-Ti_4O_7/g-C_3N_4 photocatalysts were shown in **Figure 3**. The specific surface area calculated according to **Figure 3A** was 116.0, 56.5, and 174.0 $m^2 \cdot g^{-1}$ for Ti_4O_7, g-C_3N_4 and 1:2-Ti_4O_7/g-C_3N_4, respectively. Generally, a catalyst with larger surface area could offer more active sites for adsorption and photodegradation toward organic pollutants, resulting in an enhanced photodecomposition activity (Dong et al., 2015). As such, compared with pure Ti_4O_7 and g-C_3N_4, 1:2-Ti_4O_7/g-C_3N_4 with larger specific surface area would facilitate photocatalytic oxidation of hypophosphite. Moreover, the pore size distribution of 1:2-Ti_4O_7/g-C_3N_4 was between 5

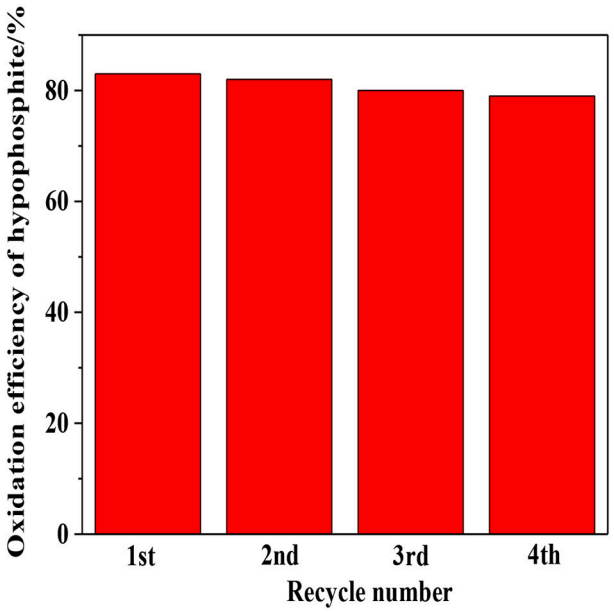

FIGURE 9 | The stability analysis of the 1:2-Ti_4O_7/g-C_3N_4 photocatalyst.

and 15 nm and that of pure Ti_4O_7 was mainly in the range of 10–25 nm, while no obvious mesopores were observed for g-C_3N_4 (**Figure 3B**).

Photocatalytic Performance Analysis

The photocatalytic performance of different photocatalysts was analyzed and compared as shown in **Figure 4A**. Ti_4O_7/g-C_3N_4 exhibited the significantly improved efficiency in hypophosphite oxidation under visible light irradiation ($\lambda > 420$ nm) in comparison to the pure g-C_3N_4 and Ti_4O_7. Additionally, the oxidation efficiency of hypophosphite was increased with increase of the mass ratio of Ti_4O_7/g-C_3N_4 and 1:2-Ti_4O_7/g-C_3N_4 illustrated the best photocatalytic performance with the highest oxidation efficiency of 83.6%. Furthermore, the photocatalytic oxidation reaction of hypophosphite was well fitted by pseudo first-order kinetic ($R^2 > 0.95$) as shown in **Figure 4B** and the rate constant of 1:2-Ti_4O_7/g-C_3N_4 was 17.7-fold and 91.0-fold higher than that of pure g-C_3N_4 and Ti_4O_7, respectively. The low efficiency of photocatalytic oxidation of hypophosphite for pure g-C_3N_4 was possibly because of the rapid combination of electron-hole pairs (Yan et al., 2018). Similarly, the photocatalytic performance of pure Ti_4O_7 was extremely limited herein, which was mainly due to the wide band gap of 2.9 eV of pure Ti_4O_7 (Maragatha et al., 2017). Nevertheless, the efficiency of photocatalytic oxidation of hypophosphite was remarkably improved especially for 1:2-Ti_4O_7/g-C_3N_4 possibly as a result of the Ti_4O_7/g-C_3N_4 heterojunction with effectively increased recombination lifetime of electron-hole pairs and better charge transfer during the photocatalytic process, which was discussed in the following parts.

Optical Properties Analysis

Generally, the band gap of a semiconductor is related to its photocatalytic performance, because it determines the absorption properties of the incident photon, the recombination lifetime of the electron-hole pairs and transfer of charge carriers. As shown in **Figure 5**, Ti_4O_7/g-C_3N_4 showed a distinct red-shift in comparison to pure g-C_3N_4 in the UV–vis diffuse reflectance spectra. Moreover, the absorption intensities ranging from 450 to 800 nm gradually strengthened with increase of the mass ratio of Ti_4O_7 (m): g-C_3N_4 (m), indicating that the Ti_4O_7/g-C_3N_4 heterojunction with good interaction between Ti_4O_7 and g-C_3N_4 facilitated the enhancement of visible-light harvesting (Chang et al., 2018). The band gap of Ti_4O_7/g-C_3N_4 was determined such that (Ai et al., 2018):

$$(\alpha h\nu)^2 = A(h\nu - E_g) \quad (2)$$

where α is the optical absorption coefficient; h is the Plank's constant; ν is the photonic frequency; A is the proportionality constant; E_g is the band gap.

The band gap followed the order: 1:2-Ti_4O_7/g-C_3N_4 (2.07 eV) < 1:5-Ti_4O_7/g-C_3N_4 (2.25 eV) < 1:10-Ti_4O_7/g-C_3N_4 (2.33 eV) < 1:20-Ti_4O_7/g-C_3N_4 (2.43 eV) < pure g-C_3N_4 (2.70 eV). As such, the narrowed band gap of Ti_4O_7/g-C_3N_4 would effectively enhance the photoabsorption efficiency, which thus contributed to the improved efficiency of photocatalytic oxidation of hypophosphite as shown in **Figure 4**.

Electrochemical Properties Analysis

CV and EIS results can indicate the combination efficiency of electron-hole pairs during the photocatalytic process. As shown in **Figure 6A**, the transient photoelectrochemical response current density of Ti_4O_7/g-C_3N_4 increased with the increase of the mass ratio of Ti_4O_7/g-C_3N_4. 1:2-Ti_4O_7/g-C_3N_4 had the highest photocurrent density of 0.30 μA cm^{-2}, while the photocurrent density for pure g-C_3N_4 was only 0.10 μA cm^{-2}. The enlarged photocurrent density of Ti_4O_7/g-C_3N_4 suggested the more efficient charge carrier (e^--h^+) generation on the Ti_4O_7/g-C_3N_4 surface (Liu et al., 2017). Herein, the electrons in the valence band of g-C_3N_4 were excited upon visible light irradiation and then migrated to the conduction band of Ti_4O_7 with effectively enhanced efficiency of the charge carrier (e^--h^+) generation and separation (Samanta and Srivastava, 2017), which improved the photocatalytic performance as indicated in **Figure 4**. In addition, the photoelectrochemical response current density of Ti_4O_7/g-C_3N_4 switched reversibly and was unchanged after repetitive ON/OFF illumination cycles, indicating the good photoelectrochemical stability of Ti_4O_7/g-C_3N_4.

Charge transfer of photocatalysts is another very important factor determining the photocatalytic performance (Kang et al., 2016). EIS was applied to analyze the photogenerated electron transfer process of Ti_4O_7/g-C_3N_4. As shown in **Figure 6B**, the arc radius decreased gradually with increase of the mass ratio of Ti_4O_7/g-C_3N_4 and the arc radius was lowest for 1:2-Ti_4O_7/g-C_3N_4. It is well known that the radius of Nyquist circle is related to the interfacial charge transfer that the smaller radius of Nyquist circle indicates a faster interfacial charge transfer and

lower recombination rate of electron and hole (Guo et al., 2017). Herein, the decreased arc radius of $Ti_4O_7/g\text{-}C_3N_4$ indicated that 1:2-$Ti_4O_7/g\text{-}C_3N_4$ in comparison to pure $g\text{-}C_3N_4$ would also facilitate the photocatalytic oxidation of hypophosphite as evident in **Figure 4**.

Proposed Mechanism

Reactive oxygen species (ROS) including $\cdot O_2^-$ and ·OH would be generated during the photocatalytic system (Huang et al., 2017a,b). Herein, the contributions of ·OH and $\cdot O_2^-$ to the photocatalytic oxidation of hypophosphite were analyzed by evaluation of the photocatalytic oxidation efficiency of hypophosphite in the presence of isopropanol (IPA) acting as the scavenger of ·OH (Tian et al., 2015) and N_2 purging applied to reduce the superoxide $\cdot O_2^-$ radicals (Zhang et al., 2017). As shown in **Figure 7**, the oxidation efficiency of hypophosphite was decreased to 42 and 27% in the presence of IPA and N_2, respectively. In contrast, that value was 83% without radical scavengers. These results indicated that ·OH and $\cdot O_2^-$ radicals significantly contributed to the photocatalytic oxidation of hypophosphite and other radicals such as singlet oxygen ($^1O_2$) and peroxyl ($RO_2\cdot$) may also make a contribution as evident by the lowest efficiency of 27% rather than 0% (Huang et al., 2017a).

The photocatalytic mechanism of $Ti_4O_7/g\text{-}C_3N_4$ was proposed as shown in **Figure 8**. Under visible light irradiation, electrons in the valence band of $g\text{-}C_3N_4$ were excited and then the excited electrons migrated to the conduction band of Ti_4O_7 through the heterojunction surface of $Ti_4O_7/g\text{-}C_3N_4$ with the generation of holes in the valence band of $g\text{-}C_3N_4$ (Zhu et al., 2018). The electrons on the surface of Ti_4O_7 could easily react with O_2 adsorbed on the $Ti_4O_7/g\text{-}C_3N_4$ surface to generate $\cdot O_2^-$ radicals for hypophosphite oxidation. Meanwhile, the active ·OH radicals with high redox potential were generated through $\cdot O_2^-$ radicals, which further facilitated the oxidation of hypophosphite (Nosaka and Nosaka, 2017; Guan et al., 2018). Therefore, it can be concluded that the oxidation of hypophosphite was mainly ascribed to ·OH and $\cdot O_2^-$ radicals generated during the photocatalytic process as shown in **Figure 8**.

Analysis of Stability

The stability of photocatalyst is another vital consideration to evaluate the photocatalytic performance. As shown in **Figure 9**, relatively robust reusability was exhibited by 1:2-$Ti_4O_7/g\text{-}C_3N_4$ photocatalyst that the efficiency of photocatalytic oxidation of hypophosphite was almost stable in the range of 79–84% after four repetitive experiments. The slight decrease of oxidation efficiency was possibly due to the inevitable mass loss of photocatalyst during the recycling process.

CONCLUSION

In this work, $Ti_4O_7/g\text{-}C_3N_4$ with various mass ratios (Ti_4O_7 (m): $g\text{-}C_3N_4$ (m) = 0.5, 0.2, 0.1, and 0.05) were synthesized by a hydrolysis method and the effect of the mass ratio of $Ti_4O_7/g\text{-}C_3N_4$ on $Ti_4O_7/g\text{-}C_3N_4$ visible light photocatalytic oxidation of hypophosphite was evaluated. $Ti_4O_7/g\text{-}C_3N_4$ exhibited remarkably improved photocatalytic performance on hypophosphite oxidation in comparison to pure $g\text{-}C_3N_4$ and 1:2-$Ti_4O_7/g\text{-}C_3N_4$ with a mass ratio of 0.5 showed the best photocatalytic performance with the highest oxidation rate constant of photocatalytic (17.7-fold and 91.0-fold higher than that of pure $g\text{-}C_3N_4$ and Ti_4O_7, respectively). The heterojunction structure of $Ti_4O_7/g\text{-}C_3N_4$ with broader light absorption significantly enhanced the efficiency of the charge carrier (e^--h^+) generation and separation. ·OH and $\cdot O_2^-$ radicals generated during the photocatalytic process were the main radicals contributing to the oxidation of hypophosphite.

AUTHOR CONTRIBUTIONS

WG: experiment. ZZ: paper writing. ST: data analysis. JD: sample analysis.

FUNDING

This work was supported by National Natural Science Foundation of China (No. 51608086); Science and Technology Planning Project of Guangdong Province (2017A050506032); Science and Technology Project from Chongqing (CSTC2015JCYJA20027); Chongqing Key Laboratory of Environmental Materials and Remediation Technology, Chongqing University of Arts and Sciences (CKE1407); Scientific Research Foundation of Chongqing University of Arts and Sciences (R2014CH08).

REFERENCES

Ai, Z. Z., Zhao, G., Zhong, Y. Y., Shao, Y. L., Huang, B. B., Wu, Y. Z., et al. (2018). Phase junction CdS: High efficient and stable photocatalyst for hydrogen generation. *Appl. Catal. B: Environ.* 221, 179–186. doi: 10.1016/j.apcatb.2017.09.002

Chang, F., Zheng, J. J., Wang, X. F., Xu, Q., Deng, B. Q., Hu, X. F., et al. (2018). Heterojuncted non-metal binary composites silicon carbide/$g\text{-}C_3N_4$ with enhanced photocatalytic performance. *Mat. Sci. Semicon. Proc.* 75, 183–192. doi: 10.1016/j.mssp.2017.11.043

Dong, G. H., Ho, W. K., Li, Y. H., and Zhang, L. Z. (2015). Facile synthesis of porous graphene-like carbon nitride ($C_6N_9H_3$) with excellent photocatalytic activity for NO removal. *Appl. Catal. B: Environ.* 174–175, 477–485. doi: 10.1016/j.apcatb.2015.03.035

Gan, X. P., Wu, Y. T., Liu, L., Shen, B., and Hu, W. B. (2007). Electroless copper plating on PET fabrics using hypophosphite as reducing agent. *Surf. Coat. Tech.* 201, 7018–7023. doi: 10.1016/j.surfcoat.2007.01.006

Ganiyu, S. O., Oturan, N., Raffy, S., Cretin, M., Esmilaire, R., van Hullebusch, E. et al. (2016). Sub-stoichiometric titanium oxide (Ti_4O_7) as a suitable ceramic anode for electrooxidation of organic pollutants: a case study of kinetics, mineralization and toxicity assessment of amoxicillin. *Water Res.* 106, 171–182. doi: 10.1016/j.watres.2016.09.056

Gao, D. Q., Xu, Q., Zhang, J., Yang, Z. L., Si, M. S., Yan, Z. J., et al. (2014). Defect-related ferromagnetism in ultrathin metal-free $g\text{-}C_3N_4$ nanosheets. *Nanoscale* 6, 2577–2581. doi: 10.1039/c3nr04743a

Guan, W., Sun, G. G., Yin, L., Zhang, Z. H., and Tian, S. C. (2018). $Ti_4O_7/g\text{-}C_3N_4$ visible light photocatalytic performance on hypophosphite oxidation: effect of annealing temperature. *Front. Chem.* 6:37. doi: 10.3389/fchem.2018.00037

Guan, W., Tian, S. C., Cao, D., Chen, Y. T., and Zhao, X. (2017). Electrooxidation of nickel-ammonia complexes and simultaneous electrodeposition recovery of nickel from practical nickel-electroplating rinse wastewater. *Electrochim. Acta* 246, 1230–1236. doi: 10.1016/j.electacta.2017.06.121

Guo, L., Jing, Y., and Chaplin, B. P. (2016). Development and characterization of ultrafiltration TiO_2 magnéli phase reactive electrochemical membranes. *Environ. Sci. Technol.* 50, 1428–1436. doi: 10.1021/acs.est.5b04366

Guo, W., Wang, J. Y., Fan, C., Chen, Z., Liu, P., Zhu, D. J., et al. (2017). Synthesis of carbon self-repairing porous g-C_3N_4 nanosheets/$NiCo_2S_4$ nanoparticles hybrid composite as high-performance electrode materials for supercapacitors. *Electrochim. Acta* 253, 68–77. doi: 10.1016/j.electacta.2017.09.025

Hao, R. R., Wang, G. H., Jiang, C. J., Tang, H., and Xu, Q. C. (2017). *In situ* hydrothermal synthesis of g-C_3N_4/TiO_2 heterojunction photocatalysts with high specific surface area for rhodamine B degradation. *Appl. Surf. Sci.* 411, 400–410. doi: 10.1016/j.apsusc.2017.03.197

Hao, R. R., Wang, G. H., Tang, H., Sun, L. L., Xu, C., and Han, D. Y. (2016). Template-free preparation of macro/mesoporous g-C_3N_4/TiO_2 heterojunction photocatalysts with enhanced visible light photocatalytic activity. *Appl. Catal. B: Environ.* 187, 47–58. doi: 10.1016/j.apcatb.2016.01.026

Hatamie, A., Marahel, F., and Sharifat, A. (2018). Green synthesis of graphitic carbon nitride nanosheet (g-C_3N_4) and using it as a label-free fluorosensor for detection of metronidazole via quenching of the fluorescence. *Talanta* 176, 518–525. doi: 10.1016/j.talanta.2017.08.059

Huang, H. W., Han, X., Li, X. W., Wang, S. C., Chu, P. K., and Zhang, Y. H. (2015a). Fabrication of multiple heterojunctions with tunable visible-light-active photocatalytic reactivity in BiOBr–BiOI full-range composites based on microstructure modulation and band structures. *ACS Appl. Mater. Interfaces* 7, 482–492. doi: 10.1021/am5065409

Huang, H. W., He, Y., Du, X., Chu, P. K., and Zhang, Y. H. (2015b). A general and facile approach to heterostructured core/shell $BiVO_4$/BiOI *p-n* junction: room-temperature *in situ* assembly and highly boosted visible-light photocatalysis. *ACS Sustainable Chem. Eng.* 3, 3262–3273. doi: 10.1021/acssuschemeng.5b01038

Huang, H. W., Tu, S. C., Zeng, C., Zhang, T. R., Reshak, A. H., and Zhang, Y. H. (2017a). Macroscopic polarization enhancement promoting photo- and piezoelectric-induced charge separation and molecular oxygen activation. *Angew. Chem. Int. Ed.* 56, 11860–11864. doi: 10.1002/anie.201706549

Huang, H. W., Xiao, K., He, Y., Zhang, T. R., Dong, F., Du, X., et al. (2016). *In situ* assembly of BiOI@$Bi_{12}O_{17}Cl_2$ *p-n* junction: charge induced unique front-lateral surfaces coupling heterostructure with high exposure of BiOI {001} active facets for robust and nonselective photocatalysis. *Appl. Catal. B: Environ.* 199, 75–86. doi: 10.1016/j.apcatb.2016.06.020

Huang, H. W., Xiao, K., Tian, N., Dong, F., Zhang, T. R., Du, X., et al. (2017b). Template-free precursor-surface-etching route to porous, thin g-C_3N_4 nanosheets for enhancing photocatalytic reduction and oxidation activity. *J. Mater. Chem. A* 5, 17452–17463. doi: 10.1039/c7ta04639a

Huang, Y. H., Su, H. T., and Lin, L. W. (2009). Removal of citrate and hypophosphite binary components using fenton, photo-fenton and electro-fenton processes. *J. Environ. Sci.* 21, 35–40. doi: 10.1016/S1001-0742(09)60008-5

Jo, W. K., and Natarajan, T. S. (2015). Influence of TiO_2 morphology on the photocatalytic efficiency of direct Z-scheme g-C_3N_4/TiO_2 photocatalysts for isoniazid degradation. *Chem. Eng. J.* 281, 549–565. doi: 10.1016/j.cej.2015.06.120

Jourshabani, M., Shariatinia, Z., and Badiei, A. (2018). Synthesis and characterization of novel Sm_2O_3/S-doped g-C_3N_4 nanocomposites with enhanced photocatalytic activities under visible light irradiation. *Appl. Surf. Sci.* 427, 375–387. doi: 10.1016/j.apsusc.2017.08.051

Kang, K., Watanabe, S., Broch, K., Sepe, A., Brown, A., Nasrallah, I., et al. (2016). 2D coherent charge transport in highly ordered conducting polymers doped by solid state diffusion. *Nat. Mater.* 15, 896–902. doi: 10.1038/NMAT4634

Li, Y. A., Wang, M. Q., Bao, S. J., Lu, S. Y., Xu, M. W., Long, D. B., et al. (2016b). Tuning and thermal exfoliation graphene-like carbon nitride nanosheets for superior photocatalytic activity. *Ceram. Int.* 42, 18521–18528. doi: 10.1016/j.ceramint.2016.08.190

Li, Y., Zhang, C., Shuai, D. M., Naraginti, S., Wang, D. W., and Zhang, W. L. (2016a). Visible-light-driven photocatalytic inactivation of MS2 by metal-free g-C_3N_4: virucidal performance and mechanism. *Water Res.* 106, 249–258. doi: 10.1016/j.watres.2016.10.009

Li, Z. Q., Qi, M. Y., Tu, C. Y., Wang, W. P., Chen, J. R., and Wang, A. J. (2017). Highly efficient removal of chlorotetracycline from aqueous solution using graphene oxide/TiO_2 composite: properties and mechanism. *Appl. Surf. Sci.* 425, 765–775. doi: 10.1016/j.apsusc.2017.07.027

Liang, F. F., and Zhu, Y. F. (2016). Enhancement of mineralization ability for phenol via synergetic effect of photoelectrocatalysis of g-C_3N_4 film. *Appl. Catal. B: Environ.* 180, 324–329. doi: 10.1016/j.apcatb.2015.05.009

Liu, Q., Chen, T. X., Guo, Y. R., Zhang, Z. G., and Fang, X. M. (2017). Grafting Fe(III) species on carbon nanodots/Fe-doped g-C_3N_4 via interfacial charge transfer effect for highly improved photocatalytic performance. *Appl. Catal. B: Environ.* 205, 173–181. doi: 10.1016/j.apcatb.2016.12.028

Ma, L. N., Wang, G. H., Jiang, C. J., Bao, H. L., and Xu, Q. C. (2018). Synthesis of core-shell TiO_2@g-C_3N_4 hollow microspheres for efficient photocatalytic degradation of rhodamine B under visible light. *Appl. Surf. Sci.* 430, 263–272. doi: 10.1016/j.apsusc.2017.07.282

Maragatha, J., Rani, C., Rajendran, S., and Karuppuchamy, S. (2017). Microwave synthesis of nitrogen doped Ti_4O_7 for photocatalytic applications. *Physica. E* 93, 78–82. doi: 10.1016/j.physe.2017.05.020

Masih, D., Ma, Y. Y., and Rohani, S. (2017). Graphitic C_3N_4 based noble-metal-free photocatalyst systems: a review. *Appl. Catal. B: Environ.* 206, 556–588. doi: 10.1016/j.apcatb.2017.01.061

Nosaka, Y., and Nosaka, A. Y. (2017). Generation and detection of reactive oxygen species in photocatalysis. *Chem. Rev.* 117, 11302–11336. doi: 10.1021/acs.chemrev.7b00161

Piveteau, S., Picard, S., Dabert, P., and Daumer, M. L. (2017). Dissolution of particulate phosphorus in pig slurry through biological acidification: a critical step for maximum phosphorus recovery as struvite. *Water Res.* 124, 693–701. doi: 10.1016/j.watres.2017.08.017

Samanta, S., and Srivastava, R. (2017). Thermal catalysis vs. photocatalysis: a case study with $FeVO_4$/g-C_3N_4 nanocomposites for the efficient activation of aromatic and benzylic CH bonds to oxygenated products. *Appl. Catal. B: Environ.* 218, 621–636. doi: 10.1016/j.apcatb.2017.06.043

Shao, H. X., Zhao, X., Wang, Y. B., Mao, R., Wang, Y., Qiao, M., et al. (2017). Synergetic activation of peroxymonosulfate by Co_3O_4 modified g-C_3N_4 for enhanced degradation of diclofenac sodium under visible light irradiation. *Appl. Catal. B: Environ.* 218, 810–818. doi: 10.1016/j.apcatb.2017.07.016

Shih, Y. J., Lin, C. P., and Huang, Y. H. (2013). Application of fered-fenton and chemical precipitation process for the treatment of electroless nickel plating wastewater. *Sep. Purif. Technol.* 104, 100–105. doi: 10.1016/j.seppur.2012.11.025

Sun, X., Jiang, D., Zhang, L., and Wang, W. Z. (2018). Alkaline modified g-C_3N_4 photocatalyst for high selective oxide coupling of benzyl alcohol to benzoin. *Appl. Catal. B: Environ.* 220, 553–560. doi: 10.1016/j.apcatb.2017.08.057

Tian, Q., Zhuang, L. J., Ong, S. K., Wang, Q., Wang, K. W., Xie, X. H., et al. (2017). Phosphorus (P) recovery coupled with increasing influent ammonium facilitated intracellular carbon source storage and simultaneous aerobic phosphorus & nitrogen removal. *Water Res.* 119, 267–275. doi: 10.1016/j.watres.2017.02.050

Tian, S. C., Li, Y. B., and Zhao, X. (2015). Cyanide removal with a copper/active carbon fiber cathode via a combined oxidation of a fenton-like reaction and *in situ* generated copper oxides at anode. *Electrochim. Acta* 180, 746–755. doi: 10.1016/j.electacta.2015.09.006

Wu, G. S., Thind, S. S., Wen, J. L., Yan, K., and Chen, A. C. (2013). A novel nanoporous α-C_3N_4 photocatalyst with superior high visible light activity. *Appl. Catal. B: Environ.* 142–143, 590–597. doi: 10.1016/j.apcatb.2013.05.070

Yan, X. X., Jia, Z. Y., Che, H. B., Chen, S. Q., Hu, P., Wang, J. S., et al. (2018). A selective ion replacement strategy for the synthesis of copper doped carbon nitride nanotubes with improved photocatalytic hydrogen evolution. *Appl. Catal. B: Environ.* 234, 19–25. doi: 10.1016/j.apcatb.2018.04.020

Zaky, A. M., and Chaplin, B. P. (2014). Mechanism of *p*-substituted phenol oxidation at a Ti_4O_7 reactive electrochemical membrane. *Environ. Sci. Technol.* 48, 5857–5867. doi: 10.1021/es5010472

Zeng, X. K., Wang, Z. Y., Wang, G., Gengenbach, T. R., McCarthy, D. T., Deletic, A., et al. (2017). Highly dispersed TiO_2 nanocrystals and WO_3 nanorods

on reduced graphene oxide: Z-scheme photocatalysis system for accelerated photocatalytic water disinfection. *Appl. Catal. B: Environ.* 218, 163–173. doi: 10.1016/j.apcatb.2017.06.055

Zhang, F. W., Wen, Q. J., Hong, M. Z., Zhuang, Z. Y., and Yu, Y. (2017). Efficient and sustainable metal-free GR/C_3N_4/CDots ternary heterostructrues for versatile visible-light-driven photoredox applications: toward synergistic interaction of carbon materials. *Chem. Eng. J.* 307, 593–603. doi: 10.1016/j.cej.2016.08.120

Zhang, L. P., Wang, G. H., Xiong, Z. Z., Tang, H., and Jiang, C. J. (2018). Fabrication of flower-like direct Z-scheme β-Bi_2O_3/g-C_3N_4 photocatalyst with enhanced visible light photoactivity for rhodamine B degradation. *Appl. Surf. Sci.* 436, 162–171. doi: 10.1016/j.apsusc.2017.11.280

Zhang, X. S., Hu, J. Y., and Jiang, H. (2014). Facile modification of a graphitic carbon nitride catalyst to improve its photoreactivity under visible light irradiation. *Chem. Eng. J.* 256, 230–237. doi: 10.1016/j.cej.2014.07.012

Zhao, Z. L., Dong, W. Y., Wang, H. J., Chen, G. H., Wang, W., Liu, Z. K., et al. (2017). Advanced oxidation removal of hypophosphite by O_3/H_2O_2 combined with sequential Fe(II) catalytic process. *Chemosphere* 180, 48–56. doi: 10.1016/j.chemosphere.2017.04.003

Zhu, Z., Huo, P. W., Lu, Z. Y., Yan, Y. S., Liu, Z., Shi, W. D., et al. (2018). Fabrication of magnetically recoverable photocatalysts using g-C_3N_4 for effective separation of charge carriers through like-Z-scheme mechanism with Fe_3O_4 mediator. *Chem. Eng. J.* 331, 615–625. doi: 10.1016/j.cej.2017.08.131

Conflict of Interest Statement: The authors declare that the research was conducted in the absence of any commercial or financial relationships that could be construed as a potential conflict of interest.

frontiers in Chemistry

ORIGINAL RESEARCH
published: 12 June 2018
doi: 10.3389/fchem.2018.00219

High Efficient Visible-Light Photocatalytic Performance of Cu/ZnO/rGO Nanocomposite for Decomposing of Aqueous Ammonia and Treatment of Domestic Wastewater

Shiying He[1], *Pengfu Hou*[1], *Evangelos Petropoulos*[2], *Yanfang Feng*[1], *Yingliang Yu*[1], *Lihong Xue*[1] *and Linzhang Yang*[1]*

[1] Institute of Agricultural Resources and Environment, Jiangsu Academy of Agricultural Sciences, Nanjing, China, [2] School of Engineering, Newcastle University, Newcastle upon Tyne, United Kingdom

OPEN ACCESS

Edited by:
Fan Dong,
Chongqing Technology and Business University, China

Reviewed by:
Zhihua Xu,
Jianghan University, China
Guohong Wang,
Hubei Normal University, China

***Correspondence:**
Linzhang Yang
lzyang@issas.ac.cn

Specialty section:
This article was submitted to Catalysis and Photocatalysis, a section of the journal Frontiers in Chemistry

Received: 04 April 2018
Accepted: 28 May 2018
Published: 12 June 2018

Citation:
He S, Hou P, Petropoulos E, Feng Y, Yu Y, Xue L and Yang L (2018) High Efficient Visible-Light Photocatalytic Performance of Cu/ZnO/rGO Nanocomposite for Decomposing of Aqueous Ammonia and Treatment of Domestic Wastewater. Front. Chem. 6:219. doi: 10.3389/fchem.2018.00219

Photocatalytic removal of ammonium-nitrogen (NH_4^+-N) from water using solar energy is an approach of high interest and applicability due to the convenience in application. ZnO has a great potential in photocatalytic decomposition of NH_4^+-N and conversion of this nutrient to under visible light irradiations. However the applicability of pristine ZnO though is limited due to its reduced capacity to utilize light from natural light. Herein, we report a two-step ZnO-modified strategy (Cu-doped ZnO nanoparticles, immobilized on reduced graphene oxide (rGO) sheets) for the promotion of photocatalytic degradation of NH_4^+-N under visible light. UV-Vis spectra showed that the Cu/ZnO/rGO can be highly efficient in the utilization of photons from the visible region. Hence, Cu/ZnO/rGO managed to demonstrate adequate photocatalytic activity and effective NH_4^+-N removal from water under visible light compared to single ZnO. Specifically, up to 83.1% of NH_4^+-N (initial concentration 50 mg·L^{-1}, catalyst dosage 2 g·L^{-1}, pH 10) was removed within 2 h retention time under Xe lamp irradiation. From the catalysis, the major by-product was N_2. The high ammonia degradation efficiency from the ZnO/Cu/rGO is attributed to the improvement of the reactive oxygen species (ROSs) production efficiency and the further activation of the interfacial catalytic sites. This study also demonstrated that such nanocomposite is a recyclable agent. Its NH_4^+-N removal capacity remained effective even after five batch cycles. In addition, Cu/ZnO/rGO was applied to treat real domestic wastewater, and it was found that chemical oxygen demand (COD), total nitrogen (TN) and total phosphorus (TP) removal efficiencies can reach 84.3, 80.7, and 90.3%, respectively. Thus, Cu/ZnO/rGO in the presence of solar light can be a promising photocatalyst in the field of wastewater treatment.

Keywords: ZnO, graphene oxide, nanocomposite, photocatalysis, ammonia-nitrogen removal, water treatment

INTRODUCTION

Accumulation of ammonia nitrogen (NH_4^+-N) to aqueous ecosystems, as a result of the rapid agricultural and industrial development (Kirkpatrick et al., 2014; Li et al., 2014), severely impacts the aquatic ecosystems due to eutrophication. Specifically, increased presence of ammoniacal compounds in water leads to cyanobacteria blooms harmful to various aquatic species due to their competitive behavior for respiration (Hued et al., 2006). Furthermore, the ammoniacal oxidative forms (NO_2^-, NO_3^-) are harmful to human health (Sun et al., 2012). Numerous techniques have been developed to treat ammonia-rich wastewater including biological processing (Li et al., 2016), constructed wetlands (Wang et al., 2016), adsorption (Halim et al., 2010), chemical oxidation (Kurniawan et al., 2006), and photocatalytic processes (Meeroff et al., 2012). Among these, photocatalytic removal of aqueous NH_4^+-N has been extensively investigated due to its high efficiency, low cost, and the absence of secondary pollutants (Nemoto et al., 2007; Yuzawa et al., 2012).

Semiconductor photocatalysts such as TiO_2, ZnO, g-C_3N_4, and Bi_2O_3 have attracted enormous research interest in environmental pollution in contiguous years (Hao et al., 2017; Ma et al., 2018; Zhang et al., 2018). Among various semiconductor photocatalysts, ZnO is considered as one of the most promising photocatalysts for solar energy conversion and photodegradation of pollutants. Its advantages are the high oxidative capacity, low toxicity, high abundance at low cost, and optical stabilities (Daneshvar et al., 2007b; Kuriakose et al., 2015; Akir et al., 2017). When ZnO is illuminated with UV light an electron (e^-) excites from the valence band (VB) to the conduction band (CB) leaving a hole (h^+) in the VB, generating electron-hole pairs (Equation 1) (Lee et al., 2016). Holes are powerful oxidants that can be excited to split water molecules producing hydroxyl radicals (•OH) (Equation 2), whereas electrons can act as O_2 reductants for hydroxyl radicals (•OH) formation (Equations 3, 4) (Lee et al., 2016). Both •OH and holes could oxidize ammonia to nitrogen gas (Reaction Scheme I) and/or to nitrate (Reaction Scheme II) (Altomare et al., 2012). Reaction Scheme I is the ideal path for ammonia conversion due to the production of harmless N_2 and H_2 gases. The production of H_2 also highlights the capacity of this photocatalytic process for carbon neutral/positive "waste" water treatment and/or bio-refinement.

$$ZnO + h\nu \rightarrow ZnO\left(e_{cb}{}^- + h_{vb}{}^+\right) \quad (1)$$

$$h^+ + H_2O \rightarrow H^+ + \cdot OH \quad (2)$$

$$O_2 + e^- + H^+ \rightarrow H_2O_2 \quad (3)$$

$$H_2O_2 + e^- \rightarrow \cdot OH + OH^- \quad (4)$$

Reaction Scheme I:

$$NH_4 + \cdot OH \rightarrow \cdot NH_2 + H_2O \quad (5)$$

$$\cdot NH_2 + \cdot OH \rightarrow NH + H_2O(or\ H^+) \quad (6)$$

$$NH + \cdot OH \rightarrow N + H_2O(or\ H^+) \quad (7)$$

$$NH_x + NH_y \rightarrow N_2H_{x+y}\ (x, y = 0, 1, 2) \quad (8)$$

$$N_2H_{x+y} + (x+y)\,h^+ \rightarrow N_2 + (x+y)H^2(N_2\ formation) \quad (9)$$

Reaction Scheme II:

$$NH_3 + OH^{\cdot} \rightarrow NH_2OH + H^+ \quad (10)$$

$$NH_2OH + OH^{\cdot} \rightarrow NO_2^- \rightarrow NO_3^- \quad (11)$$

The applicability of pristine ZnO for photocatalysis purposes is limited due to the reduced light utilization from natural light (∼4% of the solar spectrum) as a result of its wide band gap (3.37 eV). Moreover, the photocatalytic efficiency of ZnO is often hindered by the fast charge recombination of the photoinduced electron-hole pairs (h^+/e^-) and the lack of active sites on the catalyst surface (Daneshvar et al., 2007a; Akir et al., 2017). Thus, development of efficient procedures to overcome these bottlenecks and promote the light absorption from the visible-light region is essential. Numerous studies have tried to develop a low-cost, highly-active, and easily recycled photocatalysts. Various approaches were employed to achieve that including doping of cations and anions, creating oxygen vacancies, semiconductor coupling, and combining with carbon materials (Hao et al., 2016; Lee et al., 2016; Qi et al., 2017; Lu et al., 2018). Additions of Cu^{2+} have been reported as a promising method to decrease the band gap (Kuriakose et al., 2015; Yildirim et al., 2016). Copper ions have the similar ionic radii (0.73 Å) to the ionic radii of Zn (0.74 Å), which can easily form extra impurities at the ZnO lattice and add a localized electronic energy level within the band gap. The dopant energy level is temporally located below the CB, which subsequently facilitates electron trapping and inhibits the recombination of the h^+/e^- pairs. It is observed that the photocatalytic efficiency and the absorption in visible-light enhances with Cu^{2+} doping (Sharma et al., 2017).

Regardless the potential benefits of the Cu doped ZnO, its efficiency as a visible-light photocatalyst is yet limited. Reports have shown that addition of carbon materials (such as carbon nanotubes, graphene, amorphous carbon) could improve the stability and photocatalytic performance of ZnO, not only by enhancing charge separation, but also by extending its optical absorption to the visible light range. Graphene oxide (GO) [two-dimensional (2D) carbon nanostructure] is a promising additive as it possesses high electron mobility (exceeding 2,000 cm^2/V), good optical transparency, high surface area (2,600 $m^2\ g^{-1}$) (Bolotin et al., 2008; Jang et al., 2013) and contains series of reactive oxygen functional groups on their surface (e.g., carboxylic acid, hydroxyl, and epoxide groups) (Akir et al., 2017). All these properties make GO one of the most desirable materials for photocatalyst support (Sun et al., 2015). ZnO/GO

composite has been previously fabricated using hydrothermal and electrochemical methods with improved photodegradation performance under visible light irradiation. The 2D GO acts both as an electron-acceptor as well as an electron-transport material that manipulates the charge transfer across the ZnO-graphene interface. The electrons transfer from the ZnO conduction band to the GO energy level can reside there for longer periods (Zhao et al., 2017). This phenomenon results in effective separation of the photo-generated carriers that often inhibit the h^+/e^- recombination and in their absence the photocatalytic activity of ZnO can be drastically enhanced (Hsieh and Ting, 2018).

Many studies demonstrated improved ZnO photocatalytic performance by either doping or via GO addition for the enhancement of light absorption and recombination reduction. Therefore, combining the advantage of Cu doping with those of graphene support, Cu/ZnO/rGO nanocomposite could in theory promote visible-light-driven photocatalysis. Thus far, our knowledge on applications of Cu/ZnO/rGO composite for catalysis is limited, especially in the case of nutrient treatment from water. To shed further light on this field we fabricated a Cu/ZnO/rGO nanocomposite to investigate the photocatalytic activity of this specific nanocomposite to ammonia decomposition. Its practical application in the treatment of real domestic wastewater was also evaluated.

MATERIALS AND METHODS

Synthesis of Cu/ZnO/rGO Photocatalyst

Cu/ZnO/rGO nanocomposite was prepared via a two-step hydrothermal method. Zinc acetate hydrate (50 mL, 0.34 M), copper nitrate hydrate (50 mL, 0.015 M) and sodium oxalate (40 mL, 0.5 M) were mixed (magnetic stirrer) at room temperature until homogeneity was achieved. KOH (20 mL, 1 M) was then added drop wise. After stirring for 2 h a homogeneous white solution was obtained (200 mL), sealed and sterilized (autoclave, with a filling fraction of 0.8 and kept at 120°C for 10 h). The white precipitate was formed, collected by filtration and washed with DI water and ethanol (in turn, three and two times respectively) to remove residues. The resultant Cu/ZnO nanostructure was dried in an oven at 80°C and then left on air for 12 h. 25 mg of GO powder was added to 50 mL deionized (DI) water under ultrasonic dispersion for 30 min. 0.4 g Cu/ ZnO (as synthesized) and 30 mL DI water were added to the GO solution and sonicated for 30 min. The mixture was transferred to a 100 mL Teflon liner and kept at 160°C for 12 h (sterilization). The white color of Cu/ZnO changed to dark gray. Meanwhile, GO were thermally reduced after the hydrothermal process, the gray precipitate was filtered and washed several times with DI water and ethanol separately. The final product (Cu/ZnO/rGO photocatalyst) (4 mol% of Cu and 6 mass% of rGO) was left in an oven at 70°C for 10 h. Pure ZnO nanostructures were synthesized using the same procedure without addition of copper nitrate hydrate as controls.

Characterization of Cu/ZnO/rGO Photocatalyst

The morphology of the nanostructured samples was characterized by field emission gun scanning electron microscopy (FESEM, JEOL, JSM-5610LV) and transmission electron microscopy (TEM, JEOL, JEM-200CX). The crystal structure of the as-synthesized Cu/ZnO/rGO was determined by X-ray diffractometer (XRD, Bruker, D8 ADVANCE) using high-intensity Cu Karadiation (k = 1.54051 Å) at an accelerating voltage of 40 kV and emission current of 30 mA. The spectrum was recorded from the region of 2θ (20–80°). UV-visible spectroscopy was used to evaluate the optical absorption in the range 300–850 nm (UV-Vis spectrophotometer, Evolution 220). X-ray photoelectron spectroscopy (XPS, ThermoFisher Scientific ESCALAB250Xi) was used to analyze the surface chemical state.

Photocatalytic Removal of Aqueous NH_4^+-N

The photocatalytic removal of aqueous ammonia was performed in a cylindrical quartz batch photoreactor. A certain dose of photocatalyst was suspended in 100 mL NH_4Cl aqueous solution. Prior to photocatalytic process, adsorption of ammonia in darkness for 30 min was performed to achieve adsorption equilibrium. The reaction solution was then irradiated under light illumination for 2 h under the xenon lamp (120 W, light with wavelengths 400–700 nm, visible light region). The high-pressure Hg lamp (125 W, with a peak light intensity at 254 nm, UV light region) was used to compare the NH_4^+-N removal efficiency of photocatalysts under different light sources. The distance between light source and photoreactor was set as 10 cm. The reaction solution was supplied with oxygen via bubbling (150 mL/min flow rate) to develop a consistent amount of dissolve oxygen. For comparison, a blank control without photocatalyst was also evaluated to quantify NH_4^+-N volatilization.

In this study, the effect of operational parameters including initial ammonia concentration, initial pH and Cu/ZnO/rGO dosage on the photocatalytic degradation efficiency were investigated. For the evaluation of the initial pH, the photocatalytic oxidation of aqueous NH_4^+-N at different pH (4, 7, 9, 10, and 11) was performed by adding 2 g photocatalyst to 100 mL aqueous ammonia solution (50 mg/L). The pH was adjusted to desired values (4, 7, 9, 10, and 11) by an addition HCl or KOH solutions. To evaluate the impact of catalyst excess, different amounts of Cu/ZnO/rGO (0.2, 0.5, 1, 2, and 3 g/L) were dispersed in 100 mL aqueous ammonia solution (50 mg/L), the solution pH was adjusted to 10. The effect of the initial ammonia concentration (10, 30, 50, 70, and 100 mg/L) on the photocatalytic degradation of ammonia was investigated at 2 g/L of the photocatalyst and initial pH 10. All trials were performed at room temperature (25°C) using constant magnetic stirring, the illumination time was up to 2 h. A volume of 1 mL of the treated solution was sampled every 30 min and then immediately centrifuged at 8,000 rpm for 10 min to remove photocatalyst-originated particles prior analysis. The concentrations of NH_4^+-N, NO_3^--N, and NO_2^--N in the supernatant were measured via flow injection analysis on a Skalar San++ System (Skalar Co., The Netherlands). For the catalyst

stability test, leaching of Cu^{2+} and Zn^{2+} ions in the supernatant were analyzed by inductively coupled plasma mass spectroscopy (ICP-MS) (Thermo Scientific, Waltham, MA). To examine reusability of Cu/ZnO/rGO, the photocatalyst was recovered by centrifugation and washed with DI water prior re-application. The consecutive photocatalytic experiments were conducted for five runs. All trials were conducted in triplicate. And the data were expressed as the means with standard deviation (SD). The significance of the difference between the treatments means was assessed by Tukey's multiple range tests. Differences at $P < 0.05$ were considered statistically significant.

Treatment of Real Domestic Wastewater by Cu/ZnO/rGO

The real wastewater used in the present study was collected from a manhole shaft in the residential area of Jiangsu Academy of Agricultural Sciences. The general characteristics of the wastewater were as follows: NH_4^+-N: 43.5 ± 0.76 mg/L; total nitrogen (TN): 47.6 ± 0.95 mg/L; total phosphorus (TP): 5.44 ± 0.36 mg/L and chemical oxygen demand (COD): 68.5 ± 1.2 mg/L. It is suggested that nitrogen mainly exists as NH_4^+-N. Cu/ZnO/rGO nanocomposite (2 g·L^{-1}) was added to 100 mL wastewater in the photoreactor. Its performance in the simultaneous removal of P, COD, and N (NH_4^+-N and TN) was evaluated in this investigation. After visible light illumination for 2 h, aqueous samples were analyzed three times. COD was measured using a COD analyzer (DR1010 COD, HACH, China). N (NH_4^+-N and TN) and P were analyzed on a Skalar San++ System (Skalar Co., The Netherlands).

RESULTS AND DISCUSSION

Characterization of Photocatalysts

Figures 1, **2** show the morphology of the as-synthesized pure ZnO, Cu/ZnO, and Cu/ZnO/rGO nanostructures (SEM, TEM). It is observed that pure ZnO exhibits nanosheet-like structure with a rough surface and irregular shape (**Figures 1A**, **2A**). The images reveals that numerous ZnO nanosheets (about 50–100 nm) aggregated and assembled flower-like microsphere structures (with the size ranging from 500 nm to 1 μm). The morphology and size considerably changed by the addition of Cu^{2+}. Different morphologies of these Cu/ZnO nanostructures including nanospheres, nanorods and nanosheets were observed (**Figures 1C**, **2B**). Cu doping also reduced the agglomeration of ZnO. The average nanostructures size decreased (about 10–60 nm) when Cu^{2+} was incorporated to the ZnO matrix. These variations in morphology and size can be attributed to potential changes in the ZnO nucleation and growth process. The decrease in the average size of Cu/ZnO implies that the overall growth rate decreased in all dimensions for the treatment with Cu^{2+} doping. Since the ionic radii of Cu^{2+} ions is different from that of Zn^{2+}, the presence of Cu^{2+} ions in the precursor solution induces a thermodynamic barrier that hinders the ZnO nucleation rate and impedes Zn species from adsorption for further growth. Therefore, the further nanostructure growth at all ZnO dimensions decreases. It has been reported that doping ZnO with Ce and Cu ions can form Zn–Ce–Cu–O in the crystal lattice and decrease the size of the nanoparticles (Mary et al., 2015). The smaller particles can provide with increased reactive sites promoting photocatalysis. Smaller particles have the tendency to

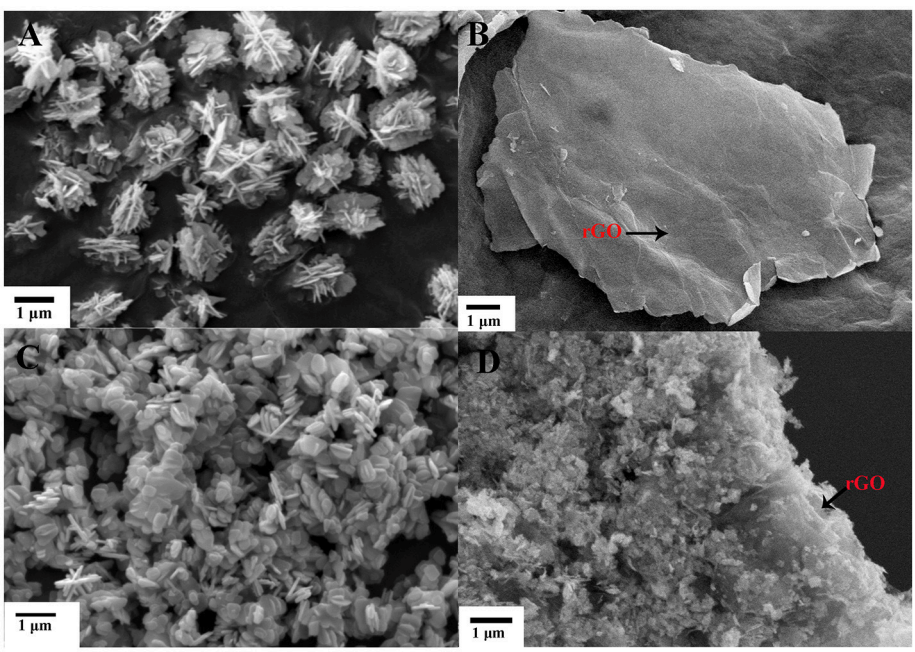

FIGURE 1 | SEM images of **(A)** ZnO, **(B)** GO, **(C)** Cu/ZnO, and **(D)** Cu/ZnO/rGO nanocomposite.

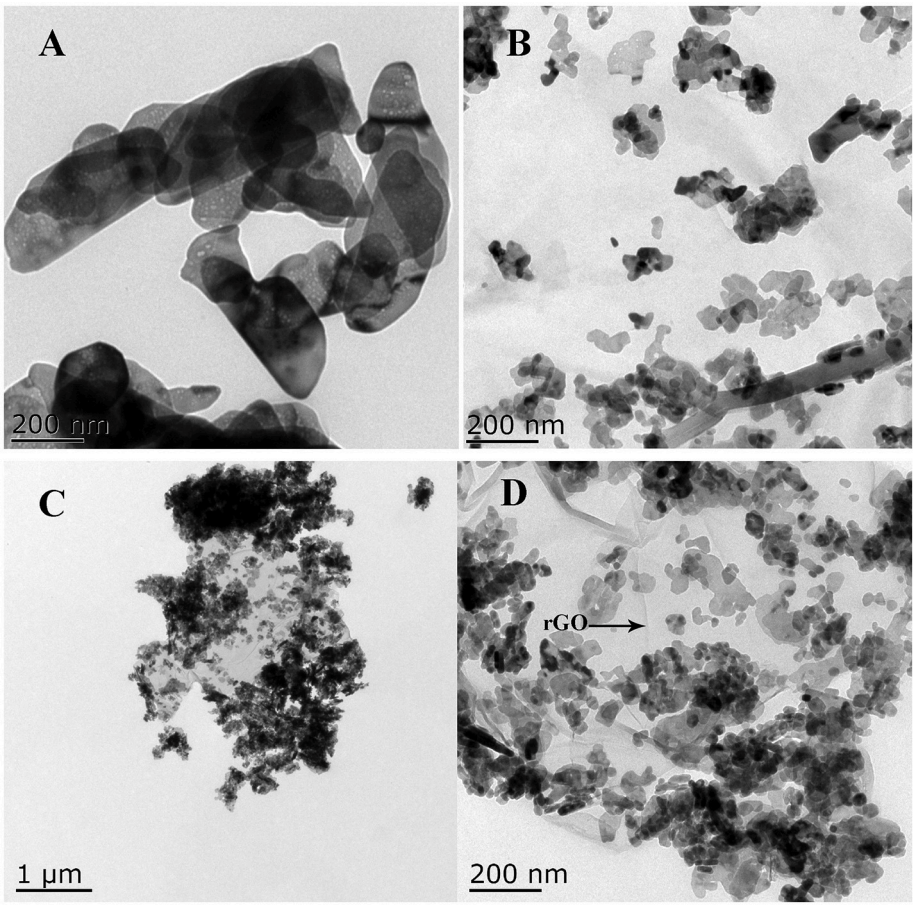

FIGURE 2 | TEM images of **(A)** ZnO, **(B)** Cu/ZnO, **(C)** Cu/ZnO/rGO, and **(D)** enlarged image of Cu/ZnO/rGO.

interact with nanoparticles, resulting to irregular shapes (Mary et al., 2015).

With the incorporation of rGO, the close interfacial connection between ZnO and rGO became well-defined. SEM and TEM images showed the formation of Cu/ZnO/rGO nanocomposite ranging from sub-micrometers to several micrometers (**Figures 1D**, **2C,D**). The well-defined Cu/ZnO nanostructure anchors on the surface of rGO sheets, illustrating the excellent adhesion between rGO and Cu/ZnO nanostructures. It is evident that rGO effectively inhibits ZnO agglomeration. This close contact between rGO and ZnO is beneficial to the effective photo-generated charge transfer, effectively inhibiting the e^-/h^+ pair recombination, which is favorable for photocatalytic reaction. It was also observed that the morphology and the size range of the anchored ZnO nanostructures are not affected by the addition of the hydrothermally produced rGO. rGO acts as an ideal support for semiconductors due to its unique two dimensional structure, high electron conductivity and mobility, high surface area, and excellent chemical stability. It is also reported that rGO has a series of oxygen functional moieties, including hydroxyl, and epoxy groups on its panels as well as carboxyl and carbonyl groups at its edges (Fu et al., 2011). The presence of the functional groups on the surface of rGO acts as anchoring sites for ZnO nanoparticles and prevents from nanopaticles agglomeration (Najafi et al., 2017).

The crystal structural parameters of the synthesized ZnO, Cu/ZnO and Cu/ZnO/rGO nanostructures (**Figure 3A**) showed that all samples have almost identical patterns. The diffraction peaks exhibit a single phase hexagonal wurtzite structure without any impurities indicating Cu^{2+} and rGO do not change the crystalline structure of ZnO. The diffraction peaks (at 2θ = 31.8, 34.3, 36.1, 47.6, 56.6, 62.8, 68, and 69.1° Corresponding to the (100), (002), (101), (102), (110), (103), (200), and (112) planes) well match with the hexagonal wurtzite structure of crystalline ZnO (00-036-1415). The sharp and intense peaks in all samples indicate high single crystallinity. No additional peak from copper or its complex oxides was detected in the recorded patterns within the detection limits. This indicates that the doping does not alter the original structure by adding an additional phase. Decreased diffraction peak intensities were observed in Cu/ZnO and Cu/ZnO/rGO due to the substitution of Cu ion by ZnO crystal lattice at the Zn^{2+} sites. This replacement can be attributed to the fact that ionic radii (0.73 Å) of Cu^{2+} is

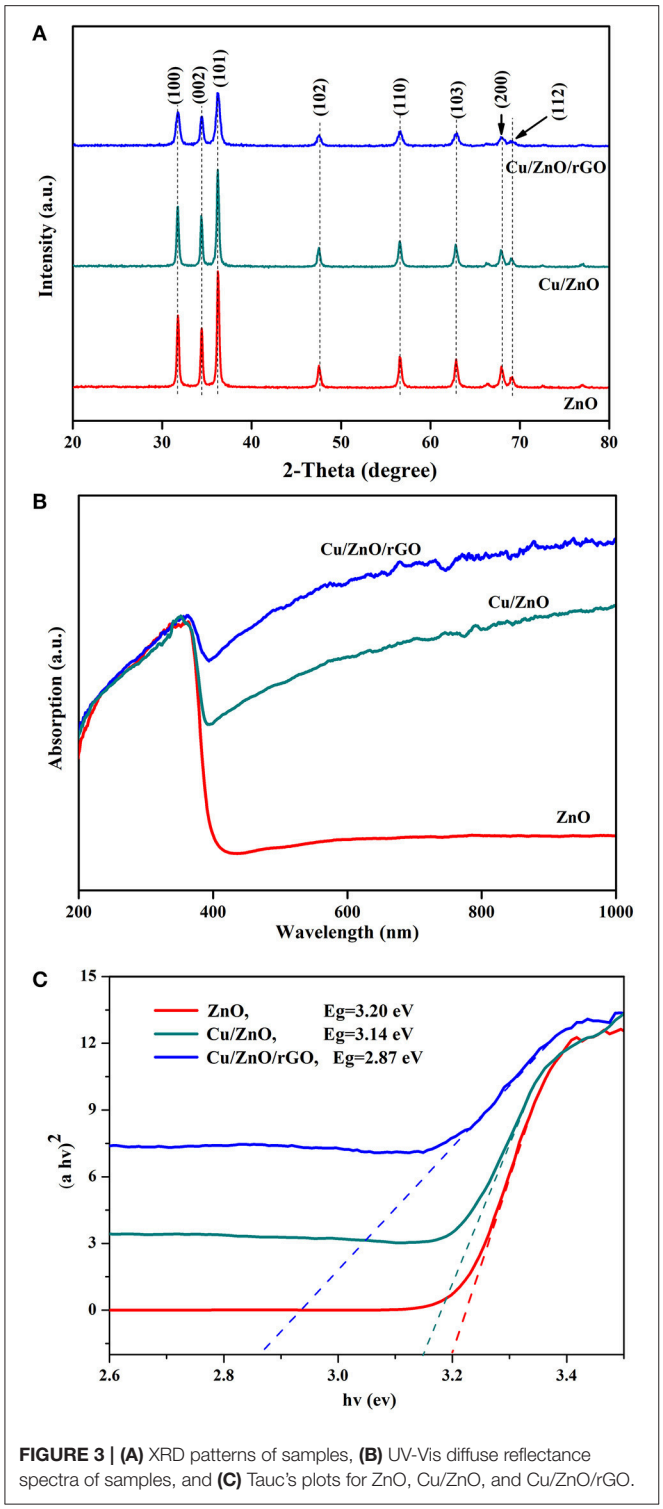

FIGURE 3 | (A) XRD patterns of samples, **(B)** UV-Vis diffuse reflectance spectra of samples, and **(C)** Tauc's plots for ZnO, Cu/ZnO, and Cu/ZnO/rGO.

close to that of Zn^{2+} (0.74 Å) (Meshram et al., 2016). It is difficult to see the rGO peaks in Cu/ZnO/rGO which may be due to the low content of rGO as well as the variation of the stacking mode of r caused by the incorporation of the ZnO nanostructures.

The internal changes of the synthesized nanocomposite samples are also reflected at their light absorption, based on UV–Vis diffuse reflectance spectra (**Figure 3B**). Pure ZnO shows a strong absorption peak at ≈360 nm (typical band-to-band transition characteristics of the wurtzite hexagonal ZnO) (Zhao et al., 2017). No apparent absorption was observed in the visible light region. It is known that ZnO consists of O *2p* orbital of valence band (VB) and Zn *4s* orbital of conduction band (CB). The distance between the VB (O 2p) and the CB (Zn 4s) of pure ZnO is ∼3.2 eV, hence, it can absorb a major part of UV light (Xia et al., 2014; Lee et al., 2016). When Cu^{2+} ions are doped to the ZnO, an additional broad absorption peak in the visible light (range 500–800 nm) was observed due to a reduction in the band gap. The optical absorption measurement supports the Cu substitution in the ZnO lattice. As an impurity in the ZnO lattice, the localized *d*-electrons of Cu^{2+} ions narrow the ZnO VB and CB gap by forming strong Cu (*3d*)-O (*2p*) and Cu (*3d*)-Zn (*4s*) bonds (Xia et al., 2014). Furthermore, with the addition of rGO, the adsorption in the visible light region is enhanced compared to pure ZnO and Cu/ZnO nanostructures. rGO is a zero-gap semiconductor, the interaction of ZnO with rGO can generate an electronic energy level below the CB of ZnO (Bolotin et al., 2008). Thus, the Cu/ZnO/rGO nanocomposite requires decreased band gap energy and an increased light absorption. Moreover, the increased absorption in the visible light is also ascribed to the black body properties of rGO sheets. The white color of ZnO changed to dark gray after rGO introduction, indicating that the addition of rGO leads to an enhancement of background absorption in the visible light region (for Cu/ZnO/rGO nanocomposite). The band gaps of the as-prepared photocatalysts were calculated using the following formula for near-edge optical absorption of semiconductors:

$$\left(\frac{\alpha h\nu}{A}\right)^{2} = \left(h\nu - Eg\right) \tag{12}$$

Where α is the absorption coefficient, $h\nu$ is the photon energy, A is a constant. **Figure 3C** shows the plot of $(\alpha h\nu)^2$ vs. $h\nu$. The calculated *Eg* values are 3.20, 3.14, and 2.87 eV for ZnO, Cu/ZnO and Cu/ZnO/rGO, respectively. It can be clearly seen that Cu/ZnO/rGO composite has the lowest band gap value (2.87 eV), which is beneficial for the absorption of the visible light absorption.

The full scan XPS spectrum and high-resolution XPS spectra of Zn 2p, Cu 2p, and O 1s were carried out to clarify the elemental composition and chemical state of the as-synthesized Cu/ZnO/rGO nanocomposite. It is obvious from the **Figure 4A** that the detected peaks were assigned to Zn, Cu, O, and C. As also shown in **Figure 4B**, the intense character peaks centered at 1,022.62 eV (Zn 2p3/2) and 1,048.42 eV (Zn 2p1/2). This clearly indicates the oxidation state of Zn atoms. The Cu 2p binding energies of the as-prepared samples were 932.15 eV (Cu 2p3/2 and 952.36 eV (Cu 2p1/2) (**Figure 4C**), respectively, which also proved the oxidation state of Cu atoms in the Cu/ZnO/rGO. From O 1s spectra (**Figure 4D**), it was observed that the two peaks belonging to Zn-O, and O-H bonding located at 530.69 and 532.51 eV, respectively.

Combining the results from XRD spectroscopy, SEM, TEM images, UV-Vis, and XPS analyses, the Cu/ZnO/rGO

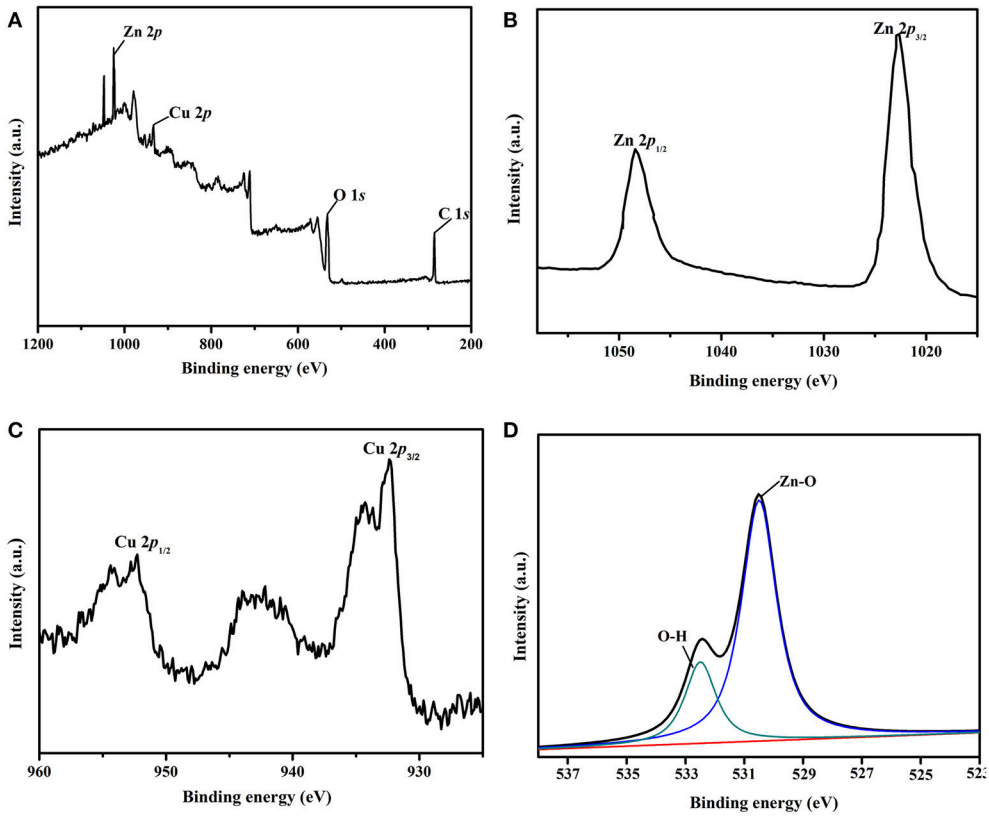

FIGURE 4 | (A) XPS spectrum of Cu/ZnO/rGO, **(B)** high-resolution spectrum of the Zn 2p region, **(C)** high-resolution spectrum of the Cu 2p region, and **(D)** and high-resolution spectrum of the O 1s region.

nanocomposite possesses a smaller and better-dispersed ZnO on rGO with notably enhanced absorption in the visible light region. This suggests the theoretically, at least, improvement of the visible-light photocatalytic activity for aqueous ammonia removal in wastewater.

Photocatalytic Removal of NH_4^+-N With Cu/ZnO/rGO Under UV And Visible Light

The aim of this study is to develop a new photocatalyst for aqueous ammonia degradation under visible light. The photocatalytic activities of the as synthesized photocatalysts were compared under a xenon (400 nm cutoff filter, visible light region) and Hg lamp (UV light region). Controls without photocatalysts showed that the concentration of aqueous NH_4^+-N reduces by 10% (**Figure 5**), indicating the volatilization is not the major contributor in the NH_4^+-N removal process. All the photocatalysts (pure ZnO, Cu/ZnO, and Cu/ZnO/rGO) exhibited good photocatalytic activities for NH_4-N treatment in the UV light region. As shown in **Figure 5**, the removal efficiency under UV light with ZnO, Cu/ZnO, and Cu/ZnO/rGO were 55.6, 64.5, and 79.2% respectively. Pure ZnO nanoparticles showed negligible photocatalytic activity on ammonia under visible-light, which is due to the large band gap of ZnO and the lack of absorption in the visible region. It is also observed that the

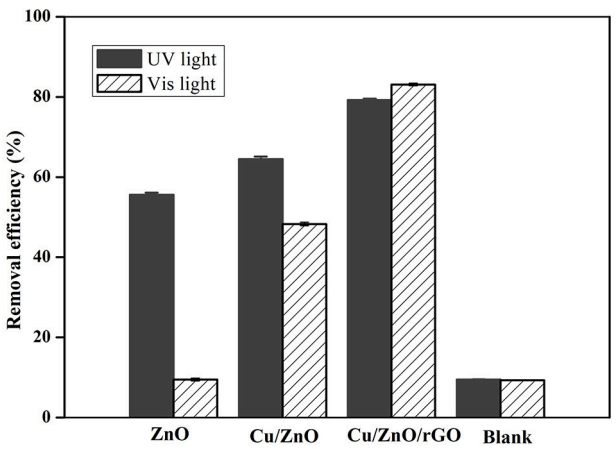

FIGURE 5 | Photocatalytic removal efficiency of NH_4^+-N under UV and Vis irradiation with no catalyst (blank), ZnO, Cu/ZnO, and Cu/ZnO/rGO.

Cu doped ZnO nanocomposite exhibits higher photocatalytic activities than pure ZnO, especially in the visible light region. In the photocatalytic process, the photo-generated holes in the VB and the electrons from the CB could participate in

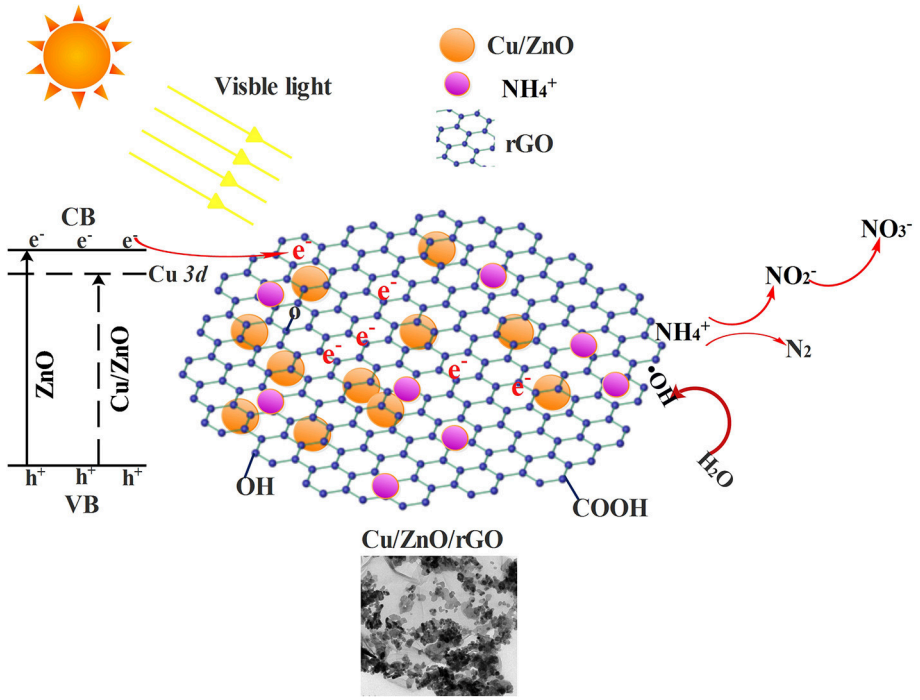

FIGURE 6 | Potential reaction mechanism for NH_4^+-N photo degradation via Cu/ZnO/rGO.

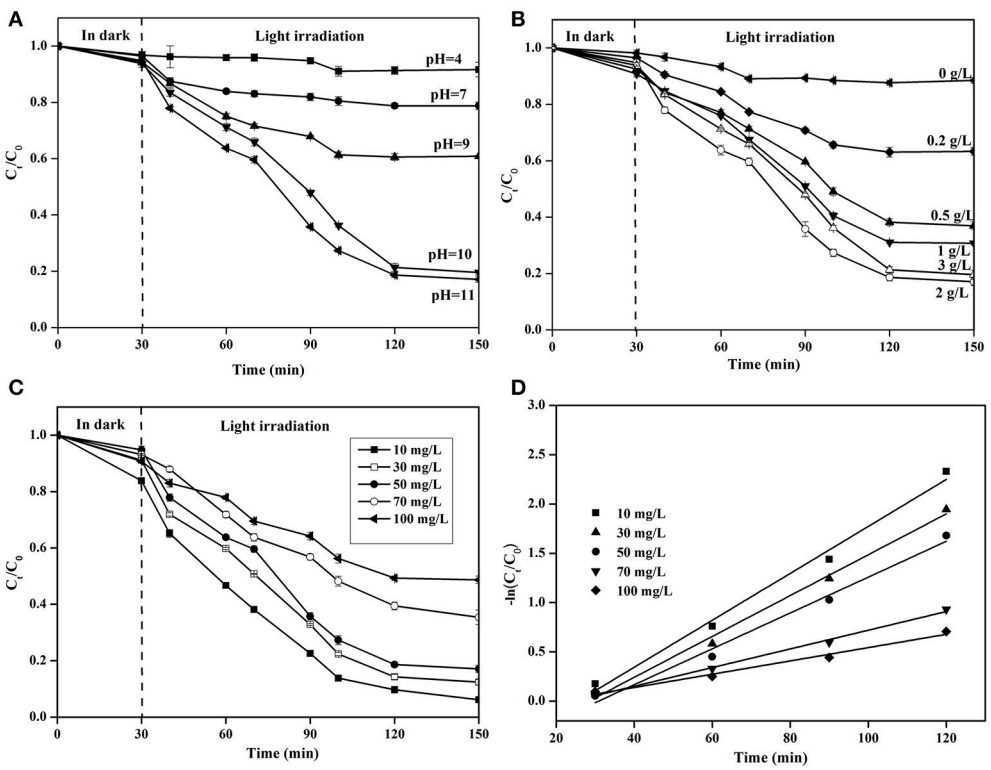

FIGURE 7 | Photocatalytic NH_4^+-N removal efficiency **(A)** at different pH, **(B)** at various Cu/ZnO/rGO dosages, and **(C)** at various NH_4^+-N concentrations, **(D)** overall photocatalysis reaction kinetics.

the oxidation of aqueous NH_4^+-N (Yuzawa et al., 2012). From literature, dopant ions incorporated in the ZnO matrix can modify the energy band of ZnO by creating new electron energy levels within the bandgap (Xia et al., 2014; Sharma et al., 2017). The photo-generated electrons could easily transfer from the CB of ZnO to the localized dopant energy levels and get trapped by the dopant ions. In the meantime, the photo-generated holes were left in the VB of ZnO and migrated to the catalyst surfaces. Therefore, the recombination of the electron and the hole could be inhibited. The excited electrons and holes subsequently could produce more reactive oxygen species (ROSs, mainly •OH and $\bullet O_2^-$ radicals) to degrade ammonia, resulting in the improved photocatalytic activity under visible light. The decrease in the particles size will increase the specific surface area and provide with larger active surface, which consequently would lead to a higher interfacial charge carrier transfer for photocatalysis. Cu ions doped with ZnO or TiO_2 have also been reported capable to enhance the methyl orange, phenol and humic substances degradation efficiency (Maleki et al., 2015; Zhang et al., 2015; Meshram et al., 2016).

The NH_4^+-N removal efficiency was substantially enhanced with rGO supporting. It is obvious that Cu/ZnO/rGO composite catalysts exhibited the highest photocatalytic degradation efficiency, with removal efficiency of 79.2% in UV light and 83.1% under visible light irradiation. The influence of rGO at the photocatalytic ammonia removal enhancement can be explained as follows: (i) In the Cu/ZnO/rGO composite, ZnO is one of the most efficient electron donors while rGO is a relatively effective electron acceptor. Irradiated with visible photon energy, photo-excited electrons and holes from ZnO were extracted by the rGO bridges through interfacial interactions. The high conductivity of rGO sheets enables quick charge transfer prolonging the charge carriers life-time, suppressing the h^+/e^- recombination (Zhao et al., 2017). These interactions can effectively enhance the generation of active radical species under photo irradiation which are eventually responsible for the photocatalytic decomposition of ammonia. (ii) From the obtained results, rGO nanosheets have the ability for ammonia adsorption due to their larger specific surface areas and functional oxygen groups. rGO could also prevent ZnO agglomeration enhancing the adsorption of ammonia molecules. The ammonia molecules adsorbed on photocatalyst are more favorable to interact with the ROSs than those in the solution form. (iii) Moreover, the high optical transparency of rGO facilitates light harvesting and subsequently enhances the power conversion efficiency. Furthermore, increase of the rGO concentration over 6% mass adversely affects the NH_4^+-N removal efficiency (Figure S1). The reduced efficiency is most likely caused by rGO overloading. The excessive rGO could act as a block restricting the light absorption of ZnO and encouraging the electron hole recombination. Similar behavior on the effect of rGO dosage has been reported previously, where rGO overloading caused a negative influence over the catalytic performance (Ranjith et al., 2017).

In conclusion, combined with Cu doping and rGO supporting, photocatalytic activity of ZnO under visible-light irradiation is enhanced. A possible reaction mechanism and the photodegradation process are illustrated in **Figure 6**.

pH is an vital parameter in photocatalytic reactions (Shibuya et al., 2015). For the investigation of the photocatalytic NH_4^+-N removal with Cu/ZnO/rGO at various pH (4.0 to11.0), the

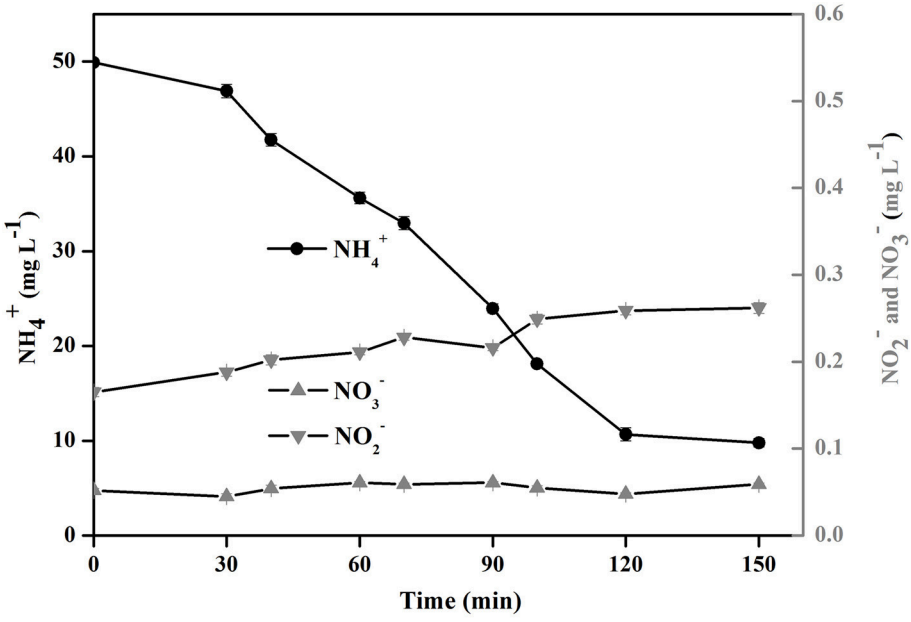

FIGURE 8 | Fate of NH_4^+-N, NO_2^--N, and NO_3^--N using Cu/ZnO/rGO for the photocatalytic oxidation of ammonia.

catalyst and the ammonia solution were kept in dark for 30 min then excited under light illumination for 2 h. The decrease of NH_4^+-N in the dark was less than 10%, and the reduction related to the physicochemical adsorption property of the photocalysts. From **Figure 7A**, Cu/ZnO/rGO demonstrated higher NH_4^+-N removal efficiency in alkaline conditions rather than in neutral or acidic ones. The concentration of NH_4^+-N remained unchanged at pH 4. The NH_4^+-N removal efficiency increased as per pH rising and reached the maximum at a pH >10. This is explained by the fact that pH influences not only the existing forms of the NH_4^+-N in solution but also the photocatalyst's surface charge properties (Shibuya et al., 2015). Firstly, ionized ammonium (NH_4^+) and un-ionized ammonia (NH_3) are the main types of ammonia nitrogen (at equilibrium in water with a pKa of 9.26). It has been reported that NH_4^+ could not be oxidized by the VB holes (h_{VB}^+) or hydroxyl radicals (·OH). (Lee et al., 2002). When the solution pH is higher than 9.26, the dominant species of aqueous ammonia is NH_3. The proportion of NH_4^+ is reversely proportional with the solution pH when < 9.26 (Sun et al., 2015). Thus, ammonia degradation efficiency decreases in neutral or acidic solutions. When the solution pH dropped to 7, almost all aqueous ammonia was in the form of NH_4^+, and impossible to be photocatalytically oxidized. Secondly, the number of hydroxide groups (OH^-) increases with the pH increase, and more hydroxyl radical (·OH) can be generated by Cu/ZnO/rGO, resulting in the promotion of the NH_4^+-N removal efficiency. Thirdly, the surface of Cu/ZnO/rGO catalysts is maintained positively charged in acidic conditions, a condition unfavorable for the adsorption of ammonium molecules at the catalyst surface. Moreover, the space steric hindrance of NH_3 is smaller than the one of NH_4^+, which is more conducive to the reaction of NH_3 with ·OH (Luo et al., 2015). This finding is aligned with the theoretical relationship between pH and ammonia photocatalysis (Wang et al., 2014; Shibuya et al., 2015).

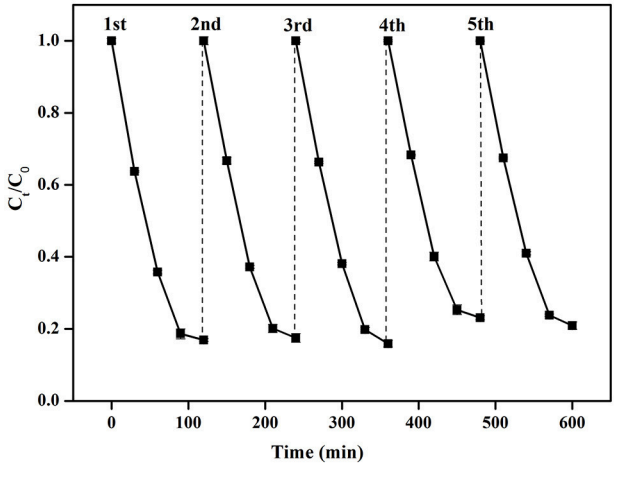

FIGURE 9 | Repeated photocatalytic oxidation of NH_4^+-N by Cu/ZnO/rGO.

TABLE 1 | Comparison of ammonia removal efficiency (%) using various photocatalysts.

Photocatalysts	Light	Removal efficiency (%)	Main products	Time(h)	Ref.
TiO_2/perlite	UV	68	N_2	3	Shavisi et al., 2014
Pd/N/ TiO_2	Vis	80	N_2	2	Sun et al., 2015
La/Fe/ TiO_2	UV	64.6	NO_3^-, NO_2^-, N_2	5	Luo et al., 2015
$ZnFe_2O_4$/rGO	Vis	92.3	N_2	4	Liu et al., 2017
SL g-C_3N_4	UV	80	NO_3^-	6	Wang et al., 2014
TiO_2-ZnO/LECA	Vis	95.2	/	3	Mohammadi et al., 2016
Cu/ZnO/rGO	Vis	83.2	N_2	2	This work

The optimum amount of catalysts is essential for effective photocatalytic removal of ammonia. **Figure 7B** shows the effect of Cu/ZnO/rGO dosage on photocatalytic performance under visible light. Increasing catalyst dosage from 0.2 to 2 g/L, ammonia degradation increases from 31.5 to 83.2% respectively. When the photocatalyst dosage is kept low, the production of ROSs is limited. Dosage increase could offer with more accessible active sites to be exposed to light irradiation and generate more ROSs leading to the enhanced photocatalytic activity. Further increase in the amount of Cu/ZnO/rGO (3 g/L) leads to a removal efficiency reduction. This is attributed to the excessive amount of photocatalysts that could reduce light transmittance and decrease the light penetration. Moreover, a large amount of catalysts could form larger agglomerates and consequently decrease the active catalyst surface. Therefore, a Cu/ZnO/rGO overdose limits photocatalytic performance. The optimal concentration of Cu/ZnO/rGO in the trial was found 2 g/L.

The initial ammonium concentration has a profound impact on the removal rate. As shown on **Figure 7C**, at high initial NH_4^+-N concentration a significant decrease ($P < 0.05$) in the rate of ammonium degradation was observed. This is due to the relationship of the rate of ammonia photo-degradation to the availability of catalytic sites on the catalyst surface that dictates the formation of ·OH. At this study, the amount of Cu/ZnO/rGO was kept constant, thus the high initial ammonia concentration could occupy a greater number of Cu/ZnO/rGO active sites available for degradation in the presence of excessive "influent" concentration. Thus, the formation of ·OH on the catalyst surface was inhibited. This results in decreased removal rates and subsequently to longer retention times to complete degradation. **Figure 7C** indicates that the percentage of degradation varies from 89.2 to 45.0% for 10–100 mg/L respectively. The kinetic studies of the photocatalytic degradation of ammonia using Cu/ZnO/rGO at different initial concentrations were also investigated using the pseudo-first-order kinetic reaction:

$$\ln\left\{\frac{C_0}{C}\right\} = Kt \tag{13}$$

Where K (min^{-1}) is the first-order rate constant, which is calculated from the slope of ln (C_0/C) vs. t plots, t is the irradiation time, C_0 is the initial NH_4^+-N concentration at the beginning of the photocatalytic reaction, C is the NH_4^+-N concentration at different irradiation time. A linear relationship between the ln (C_0/C) and t (**Figure 7D**) shows that the rate constant values K (min^{-1}) decreases with increased ammonia concentration. The values of rate constants for 10, 30, 50, 70, and 100 mg/L of NH_4^+-N are estimated to be 0.0238 min^{-1}, 0.02073 min^{-1}, 0.01819 min^{-1}, 0.00947 min^{-1}, and 0.00647 min^{-1}, respectively.

As shown in Reaction Schemes I and II, nitrogen gas (N_2), nitrite (NO_2^--N), and nitrate (NO_3^--N) are the plausible by-products of the photocatalytic removal of aqueous NH_4^+-N. To further confirm the mechanism of the NH_4^+-N oxidation with Cu/ZnO/rGO the fate of the inorganic N atoms (including NH_4^+-N, NO_2^--N, and NO_3^--N) during the process were quantified. **Figure 8** shows that concentration of aqueous NH_4^+-N decreased from 50 mg/L to 8.5 mg/L after 2 h treatment. During the degradation process, only minor amounts of NO_3^--N (0.43 mg/L) and NO_2^--N (0.262 mg/L) were detected. Considering the weak volatilization of aqueous NH_4^+-N (about 4.8 mg/ L, control experiment without catalyst) it is proposed that ∼70% of NH_4^+-N is converted to N_2 according to the N-mass balance. The formation of nontoxic N_2 is an advantage of the specific process.

The stability of a photocatalyst is a crucial parameter for the evaluation of an agent as per its practical application. The stability of Cu/ZnO/rGO was evaluated by a successive cyclic experiment performed using 200 mg Cu/ZnO/rGO in 100 mL ammonia solution with an initial concentration of approximately 50 $mg{\cdot}L^{-1}$ under visible light irradiation. **Figure 9** shows that the photocatalyst did not exhibit any obvious loss of activity, and high NH_4^+-N efficiency of Cu/ZnO/rGO was maintained even after five successive trials. Specifically, the photocatalytic was reduced by up to ∼0.6%. Therefore, Cu/ZnO/rGO nanocomposite has a stable photocatalytic activity with a relatively satisfactory recyclability and reusability. The release of the Zn^{2+} and Cu^{2+} ions from the Cu/ZnO/rGO photocatalysts was also measured via ICP. The results pointed that Zn^{2+} and Cu^{2+} ions were not detected at any of the five-cycles. Moreover, the XRD analysis revealed that the structure of Cu/ZnO/rGO remained the same before and after the photocatalysis (Figure S2). The above indicate the good degree of stability of the Cu/ZnO/rGO underlying its high potential in practical applications.

In addition, we also compare our NH_4^+-N removal efficiency with some of the related literatures, it is shown that Cu/ZnO/rGO has similar NH_4^+-N removal efficiency with that of the reported catalysts (**Table 1**). The advantage of our investigation is that the removal efficiency was achieved within 2 h retention time. The short retention time dictates the size of the tank in water and wastewater treatment engineering. Subsequently the effective catalysts can reduce the capital cost of these applications paving the path toward sustainable treatment.

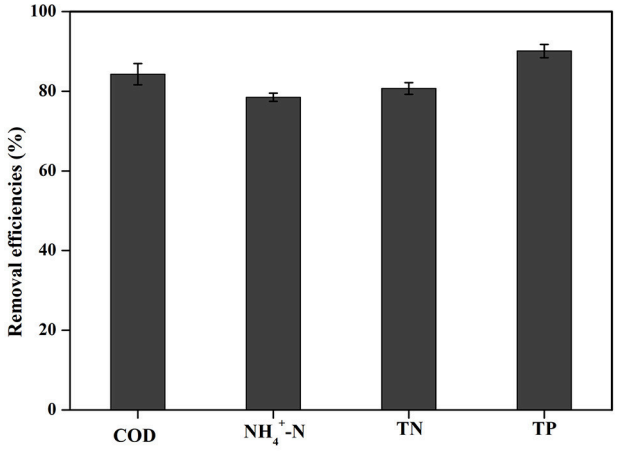

FIGURE 10 | Treatment of real domestic wastewater by Cu/ZnO/rGO (COD, NH_4^+-N, TN, and TP removal efficiencies).

The COD, N, and P Changes of Actual Domestic Wastewater

The applicability of Cu/ZnO/rGO nanocomposite in real domestic wastewater was also investigated. Our study clearly shows that Cu/ZnO/rGO exhibit highly efficient simultaneous removal of COD, N, and P (**Figure 10**). After treating wastewater with Cu/ZnO/rGO, the concentrations of COD were reduced by 57.7 mg/L (removal efficiency: 84.3%) by photocatalytic degradation. The removal efficiency of NH_4^+-N and TN were 78.5 and 80.7%, respectively. In addition, the concentration of TP decreased from 5.44 to 0.53 mg/L (removal efficiency: 90.3%). Based on these findings, it is clear that Cu/ZnO/rGO nanocomposite is an ideal agent for real wastewater treatment.

CONCLUSIONS

In summary, Cu-doped ZnO/rGO nanocomposite was sufficiently prepared via a two-step hydrothermal method. The incorporation of Cu ions and rGO with ZnO broadened the response of the photocatalyst to visible light. The fabricated Cu/ZnO/rGO showed higher ammonia removal efficiency (>80%) than the pure ZnO under visible-light irradiation, and the major oxidation product was N_2. The facile modification of ZnO by Cu ions and rGO can improve the ROSs production efficiency and further activate the interfacial catalytic sites, which account for the higher degradation efficiency. This study demonstrates that Cu/ZnO/rGO composite is a promising alternative for NH_4^+-N removal and real domestic wastewater treatment with effective application of solar energy. Further work is now underway to combine the Cu/ZnO/rGO nanocomposite with a suitable reactor to degrade pollutants for the water treatment in practice.

AUTHOR CONTRIBUTIONS

SH, LX, and LY designed and conducted the experiments. PH, YF, and YY analyzed the data. SH, EP and LY wrote the paper.

ACKNOWLEDGMENTS

This work was supported by grants from the National Key Research and Development Program of China (2017YFD0800101), National Natural Science Foundation of China (grant numbers 41771295, 41601319, 41501320), and Jiangsu Provincial six top talent peak projects (NY-054).

SUPPLEMENTARY MATERIAL

The Supplementary Material for this article can be found online at: https://www.frontiersin.org/articles/10.3389/fchem.2018.00219/full#supplementary-material

REFERENCES

Akir, S., Hamdi, A., Addad, A., Coffinier, Y., Boukherroub, and, R., and Omrani, A. D. (2017). Facile synthesis of carbon-ZnO nanocomposite with enhanced visible light photocatalytic performance. *Appl. Surf. Sci.* 400, 461–470. doi: 10.1016/j.apsusc.2016.12.212

Altomare, M., Chiarello, G. L., Costa, A., Guarino, M., and Selli, E. (2012). Photocatalytic abatement of ammonia in nitrogen-containing effluents. *Chem. Eng. J.* 191, 394–401. doi: 10.1016/j.cej.2012.03.037

Bolotin, K. I., Sikes, K. J., Jiang, Z., Klima, M., Fudenberg, G., Hone, J., et al. (2008). Ultrahigh electron mobility in suspended graphene. *Solid State Commun.* 146, 351–355. doi: 10.1016/j.ssc.2008.02.024

Daneshvar, N., Aber, S., Dorraji, M. S. S., Khataee, A. R., and Rasoulifard, M. H. (2007a). Photocatalytic degradation of the insecticide diazinon in the presence of prepared nanocrystalline ZnO powders under irradiation of UV-C light. *Sep. Purif. Technol.* 58, 91–98. doi: 10.1016/j.seppur.2007.07.016

Daneshvar, N., Rasoulifard, M. H., Khataee, A. R., and Hosseinzadeh, F. (2007b). Removal of CI Acid Orange 7 from aqueous solution by UV irradiation in the presence of ZnO nanopowder. *J. Hazard. Mater.* 143, 95–101. doi: 10.1016/j.jhazmat.2006.08.072

Fu, Y. S., Sun, X. Q., and Wang, X. (2011). $BiVO_4$-graphene catalyst and its high photocatalytic performance under visible light irradiation. *Mater. Chem. Phys.* 131, 325–330. doi: 10.1016/j.matchemphys.2011.09.049

Halim, A. A., Aziz, H. A., Johari, M. A., Ariffin, K. S., and Adlan, M. N. (2010). Ammoniacal nitrogen and COD removal from semi-aerobic landfill leachate using a composite adsorbent: fixed bed column adsorption performance. *J. Hazard. Mater.* 175, 960–964. doi: 10.1016/j.jhazmat.2009.10.103

Hao, R. R., Wang, G. H., Jiang, C. J., Tang, H., and Xu, Q. C. (2017). *In situ* hydrothermal synthesis of g-C_3N_4/TiO_2 heterojunction photocatalysts with high specific surface area for Rhodamine B degradation. *Appl. Surf. Sci.* 411, 400–410. doi: 10.1016/j.apsusc.2017.03.197

Hao, R. R., Wang, G. H., Tang, H., Sun, L. L., Xu, C., and Han, D. Y. (2016). Template-free preparation of macro/mesoporous g-C_3N_4/TiO_2 heterojunction photocatalysts with enhanced visible light photocatalytic activity. *Appl. Catal. B* 187, 47–58. doi: 10.1016/j.apcatb.2016.01.026

Hsieh, S. H., and Ting, J. M. (2018). Characterization and photocatalytic performance of ternary Cu-doped ZnO/Graphene materials. *Appl. Surf. Sci.* 427, 465–475. doi: 10.1016/j.apsusc.2017.06.176

Hued, A. C., Caruso, M. N., Wunderlin, D. A., and Bistoni, M. A. (2006). Field and *in vitro* evaluation of ammonia toxicity on native fish species of the central region of Argentina. *B Environ. Contam. Tox.* 76, 984–991. doi: 10.1007/s00128-006-1015-x

Jang, M. S., Kim, H., Son, Y. W., Atwater, H. A., and Goddard, W. A. (2013). Graphene field effect transistor without an energy gap. *Proc. Natl. Acad. Sci. U.S.A.* 110, 8786–8789. doi: 10.1073/pnas.1305416110

Kirkpatrick, B., Kohler, K., Byrne, M., Fleming, L. E., Scheller, K., Reich, A., et al. (2014). Human responses to Florida red tides: Policy awareness and adherence to local fertilizer ordinances. *Sci. Total Environ.* 493, 898–909. doi: 10.1016/j.scitotenv.2014.06.083

Kuriakose, S., Satpati, B., and Mohapatra, S. (2015). Highly efficient photocatalytic degradation of organic dyes by Cu doped ZnO nanostructures. *Phys. Chem. Chem. Phys.* 17, 25172–25181. doi: 10.1039/C5CP01681A

Kurniawan, T. A., Lo, W. H., and Chan, G. Y. S. (2006). Radicals-catalyzed oxidation reactions for degradation of recalcitrant compounds from landfill leachate. *Chem. Eng. J.* 125, 35–57. doi: 10.1016/j.cej.2006.07.006

Lee, J., Park, H., and Choi, W. (2002). Selective photocatalytic oxidation of NH_3 to N_2 on plantation TiO_2 in water. *Environ. Sci. Technol.* 36, 5462–5468. doi: 10.1021/es025930s

Lee, K. M., Lai, C. W., Ngai, K. S., and Juan, J. C. (2016). Recent developments of zinc oxide based photocatalyst in water treatment technology: a review. *Water Res.* 88, 428–448. doi: 10.1016/j.watres.2015.09.045

Li, H. M., Tang, H. J., Shi, X. Y., Zhang, C. S., and Wang, X. L. (2014). Increased nutrient loads from the Changjiang (Yangtze) river have led to increased harmful algal blooms. *Harmful Algae* 39, 92–101. doi: 10.1016/j.hal.2014.07.002

Li, R., Morrison, L., Collins, G., Li, A., and Zhan, X. (2016). Simultaneous nitrate and phosphate removal from wastewater lacking organic matter through microbial oxidation of pyrrhotite coupled to nitrate reduction. *Water Res.* 96, 32–41. doi: 10.1016/j.watres.2016.03.034

Liu, S. Q., Zhu, X. L., Zhou, Y., Meng, Z. D., Chen, Z. G., Liu, C. B., et al. (2017). Smart photocatalytic removal of ammonia through molecular recognition of zinc ferrite/reduced graphene oxide hybrid catalyst under visible-light irradiation. *Catal. Sci. Technol.* 7, 3210–3219. doi: 10.1039/C7CY00797C

Lu, L. Y., Wang, G. H., Zou, M., Wang, J., and Li, J. (2018). Effects of calcining temperature on formation of hierarchical TiO_2/g-C_3N_4 hybrids as an effective Z-scheme heterojunction photocatalyst. *Appl. Surf. Sci.* 441, 1012–1023. doi: 10.1016/j.apsusc.2018.02.080

Luo, X. P., Chen, C. F., Yang, J., Wang, J. Y., Yan, Q., Shi, H. Q., et al. (2015). Characterization of La/Fe/TiO_2 and its photocatalytic performance in ammonia nitrogen wastewater. *Int. J. Env. Res.* 12, 14626–14639. doi: 10.3390/ijerph121114626

Ma, L. N., Wang, G. H., Jiang, C. J., Bao, H. L., and Xu, Q. C. (2018). Synthesis of core-shell TiO_2@g-C_3N_4 hollow microspheres for efficient photocatalytic degradation of rhodamine B under visible light. *Appl. Surf. Sci.* 430, 263–272. doi: 10.1016/j.apsusc.2017.07.282

Maleki, A., Safari, M., Shahmoradi, B., Zandsalimi, Y., Daraei, H., and Gharibi, F. (2015). Photocatalytic degradation of humic substances in aqueous solution using Cu-doped ZnO nanoparticles under natural sunlight irradiation. *Environ. Sci. Pollut. R.* 22, 16875–16880. doi: 10.1007/s11356-015-4915-7

Mary, J. A., Vijaya, J. J., Bououdina, M., Kennedy, L. J., Dai, J. H., and Song, Y. (2015). Effect of Ce and Cu co-doping on the structural, morphological, and optical properties of ZnO nanocrystals and first principle investigation of their stability and magnetic properties. *Physica Low Dimen. Syst. Nanostruct.* 66, 209–220. doi: 10.1016/j.physe.2014.10.019

Meeroff, D. E., Bloetscher, F., Reddy, D. V., Gasnier, F., Jain, S., McBarnette, A., et al. (2012). Application of photochemical technologies for treatment of landfill leachate. *J. Hazard. Mater.* 209, 299–307. doi: 10.1016/j.jhazmat.2012.01.028

Meshram, S. P., Adhyapak, P. V., Amalnerkar, D. P., and Mulla, I. S. (2016). Cu doped ZnO microballs as effective sunlight driven photocatalyst. *Ceram. Int.* 42, 7482–7489. doi: 10.1016/j.ceramint.2016.01.154

Mohammadi, Z., Sharifnia, S., and Shavisi, Y. (2016). Photocatalytic degradation of aqueous ammonia by using TiO_2-ZnO/LECA hybrid photocatalyst. *Mater. Chem. Phys.* 184, 110–117. doi: 10.1016/j.matchemphys.2016.09.031

Najafi, M., Kermanpur, A., Rahimipour, M. R., and Najafizadeh, A. (2017). Effect of TiO_2 morphology on structure of TiO_2-graphene oxide nanocomposite

synthesized via a one-step hydrothermal method. *J. Alloy. Compd.* 722, 272–277. doi: 10.1016/j.jallcom.2017.06.001

Nemoto, J., Gokan, N., Ueno, H., and Kaneko, M. (2007). Photodecomposition of ammonia to dinitrogen and dihydrogen on platinized TiO_2 nanoparticules in an aqueous solution. *J. Photoch. Photobio. A* 185, 295–300. doi: 10.1016/j.jphotochem.2006.06.024

Qi, K. Z., Cheng, B., Yu, J. G., and Ho, W. K. (2017). Review on the improvement of the photocatalytic and antibacterial activities of ZnO. *J. Alloy. Comp.* 727, 792–820. doi: 10.1016/j.jallcom.2017.08.142

Ranjith, K. S., Manivel, P., Rajendrakumar, R. T., and Uyar, T. (2017). Multifunctional ZnO nanorod-reduced graphene oxide hybrids nanocomposites for effective water remediation: effective sunlight driven degradation of organic dyes and rapid heavy metal adsorption. *Chem. Eng. J.* 325, 588–600. doi: 10.1016/j.cej.2017.05.105

Sharma, A., Varshney, M., Shin, H. J., Lee, B. H., Chae, K. H., and Won, S. O. (2017). Effect of Cu insertion on structural, local electronic/atomic structure and photocatalyst properties of TiO_2, ZnO and $Ni(OH)_2$ nanostructures: XANES-EXAFS study. *Mater. Chem. Phys.* 191, 129–144. doi: 10.1016/j.matchemphys.2017.01.008

Shavisi, Y., Sharifnia, S., Hosseini, S. N., and Khadivi, M. A. (2014). Application of TiO_2/perlite photocatalysis for degradation of ammonia in wastewater. *J. Ind. Eng. Chem.* 20, 278–283. doi: 10.1016/j.jiec.2013.03.037

Shibuya, S., Sekine, Y., and Mikami, I. (2015). Influence of pH and pH adjustment conditions on photocatalytic oxidation of aqueous ammonia under airflow over Pt-loaded TiO_2. *Appl. Catal. A-Gen.* 496, 73–78. doi: 10.1016/j.apcata.2015.02.024

Sun, D. C., Sun, W. Z., Yang, W. Y., Li, Q., and Shang, J. K. (2015). Efficient photocatalytic removal of aqueous NH_4^+-NH_3 by palladium-modified nitrogen-doped titanium oxide nanoparticles under visible light illumination, even in weak alkaline solutions. *Chem. Eng. J.* 264, 728–734. doi: 10.1016/j.cej.2014.12.012

Sun, H. J., Lü, K., Minter, E. J., Chen, Y. F., Yang, Z., and Montagnes, D. J. S. (2012). Combined effects of ammonia and microcystin on survival, growth, antioxidant responses, and lipid peroxidation of bighead carp Hypophthalmythys nobilis larvae. *J. Hazard. Mater.* 221, 213–219. doi: 10.1016/j.jhazmat.2012.04.036

Sun, L. L., Wang, G. H., Hao, R. R., Han, D. Y., and Cao, S. (2015). Solvothermal fabrication and enhanced visible light photocatalytic activity of Cu_2O-reduced graphene oxide composite microspheres for photodegradation of Rhodamine B. *Appl. Surf. Sci.* 358, 91–99. doi: 10.1016/j.apsusc.2015.08.128

Wang, H., Su, Y., Zhao, H. X., Yu, H. T., Chen, S., Zhang, Y. B., et al. (2014). Photocatalytic oxidation of aqueous ammonia using atomic single layer graphitic-C_3N_4. *Environ. Sci. Technol.* 48, 11984–11990. doi: 10.1021/es503073z

Wang, W., Ding, Y., Wang, Y. H., Song, X. S., Ambrose, R. F., Ullman, J. L., et al. (2016). Treatment of rich ammonia nitrogen wastewater with polyvinyl alcohol immobilized nitrifier biofortified constructed wetlands. *Ecol. Eng.* 94, 7–11. doi: 10.1016/j.ecoleng.2016.05.078

Xia, C. H., Wang, F., and Hu, C. L. (2014). Theoretical and experimental studies on electronic structure and optical properties of Cu-doped ZnO. *J. Alloy. Comp.* 589, 604–608. doi: 10.1016/j.jallcom.2013.11.066

Yildirim, O. A., Arslan, H., and Sonmezoglu, S. (2016). Facile synthesis of cobalt-doped zinc oxide thin films for highly efficient visible light photocatalysts. *Appl. Surf. Sci.* 390, 111–121. doi: 10.1016/j.apsusc.2016.08.069

Yuzawa, H., Mori, T., Itoh, H., and Yoshida, H. (2012). Reaction mechanism of ammonia decompositon to nitrogen and hydrogen over metal loaded titanium oxide photocatalyst. *J. Phys. Chem. C* 116, 4126–4136. doi: 10.1021/jp209795t

Zhang, H., Guo, L. H., Wang, D. B., Zhao, L. X., and Wan, B. (2015). Light-induced efficient molecular oxygen activation on a Cu(II)-grafted TiO_2/graphene photocatalyst for phenol degradation. *ACS Appl. Mater. Inter.* 7, 1816–1823. doi: 10.1021/am507483q

Zhang, L. P., Wang, G. H., Xiong, Z. Z., Tang, H., and Jiang, C. J. (2018). Fabrication of flower-like direct Z-scheme beta-Bi_2O_3/g-C_3N_4 photocatalyst with enhanced visible light photoactivity for Rhodamine B degradation. *Appl. Surf. Sci.* 436, 162–171. doi: 10.1016/j.apsusc.2017.11.280

Zhao, Y. T., Liu, L., Cui, T. T., Tong, G. X., and Wu, W. H. (2017). Enhanced photocatalytic properties of ZnO/reduced graphene oxide sheets (rGO) composites with controllable morphology and composition. *Appl. Surf. Sci.* 412, 58–68. doi: 10.1016/j.apsusc.2017.03.207

Conflict of Interest Statement: The authors declare that the research was conducted in the absence of any commercial or financial relationships that could be construed as a potential conflict of interest.

frontiers in Chemistry

ORIGINAL RESEARCH
published: 18 May 2018
doi: 10.3389/fchem.2018.00175

Photocatalytic Oxidation of Acetone Over High Thermally Stable TiO_2 Nanosheets With Exposed (001) Facets

Ting Shi[1], Youyu Duan[1], Kangle Lv[1], Zhao Hu[1], Qin Li[1], Mei Li[1]* and Xiaofang Li[1,2]*

[1] Key Laboratory of Catalysis and Materials Science of the State Ethnic Affairs Commission & Ministry of Education, Hubei Province, College of Resources and Environmental Science, South-Central University for Nationalities, Wuhan, China,
[2] College of Chemistry and Chemical Engineering, Wuhan University of Science and Technology, Wuhan, China

Anatase TiO_2 (A-TiO_2) usually exhibits superior photocatalytic activity than rutile TiO_2 (R-TiO_2). However, the phase transformation from A-TiO_2 to R-TiO_2 will inevitably happens when the calcination temperature is up to 600°C, which hampers the practical applications of TiO_2 photocatalysis in hyperthermal situations. In this paper, high energy faceted TiO_2 nanosheets (TiO_2-NSs) with super thermal stability was prepared by calcination of $TiOF_2$ cubes. With increase in the calcination temperature from 300 to 600°C, $TiOF_2$ transforms into TiO_2 hollow nanoboxes (TiO_2-HNBs) assembly from TiO_2-NSs via Ostwald Rippening process. Almost all of the TiO_2-HNBs are disassembled into discrete TiO_2-NSs when calcination temperature is higher than 700°C. Phase transformation from A-TiO_2 to R-TiO_2 begins at 1000°C. Only when the calcination temperature is higher than 1200°C can all the TiO_2-NSs transforms into R-TiO_2. The 500°C-calcined sample (T500) exhibits the highest photoreactivity toward acetone oxidation possibly because of the production of high energy TiO_2-NSs with exposed high energy (001) facets and the surface adsorbed fluorine. Surface oxygen vacancy, due to the heat-induced removal of surface adsorbed fluoride ions, is responsible for the high thermal stability of TiO_2-NSs which are prepared by calcination of $TiOF_2$ cubes.

Keywords: TiO_2, photocatalytic degradation, acetone, fluorine, oxygen vacancy

OPEN ACCESS

Edited by:
Fan Dong,
Chongqing Technology and Business University, China

Reviewed by:
Xin Li,
South China Agricultural University, China
Shiyong Sun,
Southwest University of Science and Technology, China

****Correspondence:***
Kangle Lv
lvkangle@mail.scuec.edu.cn
Mei Li
limei@mail.scuec.edu.cn

Specialty section:
This article was submitted to Catalysis and Photocatalysis, a section of the journal Frontiers in Chemistry

Received: *07 April 2018*
Accepted: *30 April 2018*
Published: *18 May 2018*

Citation:
Shi T, Duan Y, Lv K, Hu Z, Li Q, Li M and Li X (2018) Photocatalytic Oxidation of Acetone Over High Thermally Stable TiO_2 Nanosheets With Exposed (001) Facets. Front. Chem. 6:175. doi: 10.3389/fchem.2018.00175

INTRODUCTION

Semiconductor photocatalysis has attracted much attention due to its potential applications such as water (Regmi et al., 2018; Xu et al., 2018) and air purification (Wen et al., 2015; Cui et al., 2017; Li et al., 2017a; Qi et al., 2017) and water splitting for clean H_2 energy (Cheng et al., 2018) due to its peculiar chemical and physical properties. As a typical semiconductor photocatalyst, anatase TiO_2 (A-TiO_2) usually shows excellent photocatalytic activity. However, it usually transforms into poor photoreactive rutile TiO_2 (R-TiO_2) when calcination temperature is higher than about 600°C, which hampers the practical applications of A-TiO_2 in hyperthermal situations (Lv et al., 2011; Liang et al., 2017). For example, the temperature of some industrial waste gases after burning can be as high as 900–1000°C, which makes the photocatalytic oxidation technology lose its power due to the phase transformation of A-TiO_2 at such high temperature. There are many photocatalytically active stable TiO_2-coated ceramic materials which are used for the control of organic contaminants,

including sanitary wares, bathroom tiles and self-cleaning glass. They require high processing temperatures and therefore need excellent stability at high temperature (Periyat et al., 2009). Thus, exploration of thermally stable TiO_2 photocatalyst is very important but this question remains unsolved.

As one of volatile organic compounds (VOCs), acetone is a widely used solvent especially in chemical plant. The emission of acetone can not only cause the problems to global environment, but also bring harms to human health (Zhu et al., 2016). When the concentration of acetone vapor is higher than 500 ppm, it can irritate eyes and discomfort respiratory system (Li et al., 2018). So, it is of great importance to explore an efficient method to decompose of acetone. Because semiconductor photocatalysis is considered as an environmentally benign way, it is no doubt very promising for VOCs removal under normal conditions.

It is generally accepted that the quantum efficiency of photocatalysis is highly related to the physical properties of TiO_2 such as crystal structure, relative crystallinity, size of the particle, and specific surface area (Xu et al., 2007; Lan et al., 2015; Wang et al., 2015, 2016; Wen et al., 2015; Li et al., 2016; Sajan et al., 2016; Liang et al., 2017; Xia et al., 2017; Lin et al., 2018a,b). Recently, growing interesting has been devoted to the synthesis of TiO_2 nanocrystals with exposed high energy {001} facets by surface fluorination of TiO_2 to reduce the surface energy (Yang et al., 2008, 2009; Chen et al., 2010; Yu et al., 2014; Sajan et al., 2016; Liang et al., 2017). On considering that $TiOF_2$ cubes are fluorine-containing materials, they prefer to transform into high energy TiO_2 nanocrystals during calcination. After the removal of surface adsorbed fluorine ions at high temperature, the formed oxygen vacancy (OV) on the surface of the photocatalyst will prevent the fusion of neighboring A-TiO_2 nanocrystals, which is believed to improve the thermal stability of TiO_2 nanocrystals. Herein, we systematically studied the dependence of the structure and photocatalytic activity of $TiOF_2$ cubes on the calcination temperature. Acetone was selected as the targeted VOCs to evaluate the photoreactivity of the as-prepared photocatalyst.

EXPERIMENTAL SECTION

Synthesis

Precursor $TiOF_2$ was synthesized through the solvothermal reaction of Tetrabutyl titanium (TBT), acetic acid (HAc) and hydrofluoric acid (HF) (Huang et al., 2013). Typically, 20.0 g of TBT was dropwise added into the mixed solution containing 6.4 ml of HF (47 wt%) and 40.0 ml of HAc under magnetic stirring. The resulted white suspensions were transferred to an autoclave with volume of 100 ml, which was then kept at 200°C for 2 h. The white deposition was collected and washed with ethanol and distilled water until the filtrate is neutral (pH7). After oven dry at 80°C, we obtained the precursor $TiOF_2$.

Precursor $TiOF_2$ was then calcined at certain temperature (300-1200°C) for 2 h by keeping the same heating rate (5°C min^{-1}). The obtained photocatalyst is denoted as Tx (**Table 1**), where x is the calcination temperature. For example, T500 is that the photocatalyst which was prepared by calcination of the precursor $TiOF_2$ at 500°C for 2 h.

TABLE 1 | Physical property of the photocatalyst.

Sample	Calcination temperature (°C)	Phase structure[a]	S_{BET}[b] (m^2g^{-1})
T300	300	$TiOF_2$	5.7
T400	400	$TiOF_2$/A-TiO_2	6.4
T500	500	$TiOF_2$/A-TiO_2	5.6
T600	600	A-TiO_2	3.2
T700	700	A-TiO_2	2.4
T800	800	A-TiO_2	2.0
T900	900	A-TiO_2	2.0
T1000	1000	A-TiO_2/R-TiO_2	1.3
T1100	1100	A-TiO_2/R-TiO_2	1.2
T1200	1200	R-TiO_2	0.4

[a] *A-TiO_2 and R-TiO_2 represent anatase TiO_2 and rutile TiO_2, respectively.*
[b] *The BET surface area is determined by a multipoint BET method using the adsorption data in the relative pressure (P/P_0) range from 0.05 to 0.3.*

Characterization

XRD patterns of the photocatalysts were performed on a X-ray diffractometer (D8- advance, Bruker Co., German), and the scan rate of Cu K*a* radiation keeps 0.02° 2θ s^{-1}, using an accelerated voltage and applied current of 15 kV and 20 mA, respectively. We observe the morphology of the prepared photocatalyst by an FESEM with an acceleration voltage of 20 kV (Hitach, Japan) and a TEM (Tecnai G20, USA) using an acceleration voltage of 200 kV, respectively. The optical property of the photocatalyst was measured by a spectrophotometer (UV-2550, Shimadzu, Japan) from 200 to 800 nm using $BaSO_4$ as background. FTIR was obtained on a infrared spectrometer (NeXUS 470) using the KBr pellet technique. XPS was recorded using monochromatic Al-Ka radiation under vacuum at 2×10^{-6} Pa on a photoelectron spectrometer (VG Multilab 2000). The C1s peak at 284.8 eV originated from the surface adventitious carbon is used to reference all the binding energies. EPR signal of the photocatalyst was recorded in an EPR spectrometer (JES-FA 200, JEOL) at room temperature (frequency of 100 kHz and microwave power of 0.99 mW). Nitrogen sorption isotherm was measured on an ASAP 2020 nitrogen adsorption equipment (Micromeritics, USA). Before investigating the surface areas of the photocatalysts, all samples were degassed firstly at 200°C.

Photoelectrochemical Measurements

We use CHI760e as electrochemical workstation (Shanghai, China) to measure the transient photocurrent, EIS Nyquist plots and Mott-Schottky plots in a standard there-electrode system, where Pt wire was used as the counter electrode, and the prepared samples and Ag/AgCl in saturated KCl were used as the working and reference electrode, respectively. During the measurement, 0.4 M Na_2SO_4 was used as electrolyte solution. In the Mott-Schottky measurement, direct current potential polarization was kept at a fixed frequency, and the working electrode was prepared on a glassy carbon electrode. Before the test of photocurrent, 50 mg photocatalysts and 30 μL Nafion were dispersed into 1 mL water/absolute ethanol mixed solvent (v/v = 1/1), and then the mixed aqueous solution was dispersed uniformly

through ultrasound to form a homogeneous catalyst colloid. The ITO/TiO_2 electrode was prepared using the as-prepared photocatalyst colloid as precursor by a drip coating method. The light source is a 3W LED lamp (Shenzhen LAMPLIC, China) emitted mainly at 365 nm. The intensity for the lamp at working distance is measured to be 0.41 W/cm^2.

Evaluation of the Photocatalytic Activity

Photocatalytic oxidation of gasous acetone was used to evaluate the photocatalytic activity of the photocatalyst, which was performed in a 15 L reactor at ambient temperature under UV light irradiation. 0.3 g of the powder was firstly dispersed in 30 mL of double distilled water by sonicating treatment for 5 min. The obtained suspensions were then evenly transferred into three glass dishes in diameters of about 7.0 cm. After drying at 80°C for about 2 h, the dishes that have been coated with a layer of the photocatalyst were placed in the reactor, and then 10 uL of acetone was injected into the reactor by a microsyringe. The vaporated acetone then begins to adsorb on the surface of the photocatalyst. Thirty minutes later, the adsorption–desorption equilibrium of acetone can be established. The photocatalytic oxidation of acetone begins after turning on the UV light, which is 5 cm above the dishes. The concentrations of acetone and the produced carbon dioxide in the reactor were determined online with a Photoacoustic IR Multigas Monitor (Model 1412, INNOVA). Before irradiation, the initial concentration of acetone after the adsorption equilibrium was about 300 ppm, which almost keeps unchanged for about 5 min before lighting a UV lamp (15W@365 nm).

RESULTS AND DISCUSSION

Effect of Calcination Temperature on Phase Structure

Phase structure of the photocatalyst is important to the photoreactivity. Therefore, we used XRD to study the phase evolution of the photocatalyst during calcination. From **Figure 1**, a broad peak centering at $2\theta = 23.4°$, which corresponds to the (100) plane diffraction of $TiOF_2$, was observed for the prepared precursor, and no any peak of TiO_2 phases (A-TiO_2 and R-TiO_2) exists, indicating the successful synthesis of $TiOF_2$(Huang et al., 2013). After calcination at 300°C for 2 h, the phase struccture of the sample (T300) almost keeps unchanged. With increase in the calcination temperature to 400°C, the peak intensity for $TiOF_2$ decreases. Simultaneously, a small peak at $2\theta = 25.3°$, which corresponds to the (101) plane diffraction of A-TiO_2, can be observed for T400 sample, indicating that phase transformation from $TiOF_2$ to anatase begins. This phase transformation becomes obvious after calcination of $TiOF_2$ at 500°C, and the prepared $TiOF_2$ totally transforms into anatase TiO_2 at 600°C.

It is proposed that the reaction for the heat-induced phase transformation from $TiOF_2$ to TiO_2 is as follows (Equation 1) (Zhao et al., 2018).

$$2TiOF_2 + \text{heat} \rightarrow TiO_2 + TiF_4\uparrow \quad (1)$$

Further increase in the calcination from 600 to 900°C, the peak intensity of A-TiO_2 increases, indicating the enhanced crystallization. Meanwhile, the narrowing of the width for the (101) plane diffraction peak indicates the increase of A-TiO_2 crystallite size. The peak intensity for the (101) peak of anatase TiO_2 begins to decrease at calcination temperature of 1000°C, which is a sign of anatase-to-rutile phase transfermation. The formation of rutile phase is confirmed from the XRD pattern of the T1100 sample due to the formation of a small peak at $2\theta = 27.3°$, which corresponds to the (110) plane diffraction of R-TiO_2. Only when the calcination temperature reaches 1200°C can all of the A-TiO_2 transform into R-TiO_2.

Usually, A-TiO_2 nanocrystals begin transform into R-TiO_2 at about 600°C. However, in the present study, the temperature for anatase-to-rutile transformation is as high as 1100°C, which indicates that these samples are promising to be used in hyperthermal situations.

Evolution of the Morphology

The SEM images of the precursor $TiOF_2$ is shown in **Figure 2**. It can be clearly observed that these $TiOF_2$ nanoparticles are in cubic shape and relatively monodispersed (**Figure 2a**), which is consistent with the reported literatures (Chen et al., 2012; Wang

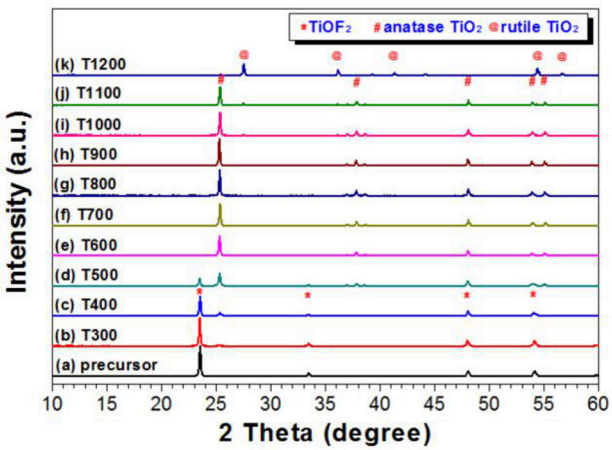

FIGURE 1 | XRD patterns of the photocatalysts calcined at different temperatures.

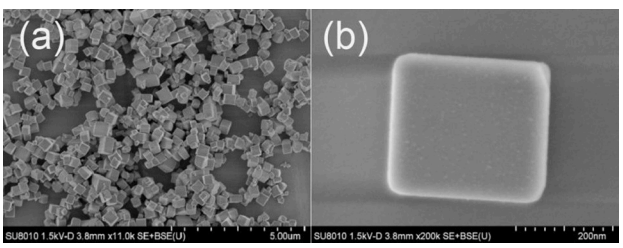

FIGURE 2 | SEM images of the precursor $TiOF_2$ at low **(a)** and high magnification **(b)**.

et al., 2012). From the high resolution SEM image shown in **Figure 2b**, we can estimate that the sidelength of the $TiOF_2$ cube is about 250 nm.

After calcination of the precursor $TiOF_2$ at 300°C, the morphology of the resulted sample (T300) almost keeps unchanged (SEM image not shown here). However, some nanoboxes with hollow interiors can be clearly seen from the SEM image of T400 sample (**Figure 3a**). These anatase TiO_2 hollow nanoboxes (TiO_2-HNBs) assemble from TiO_2 nanosheets (TiO_2-NSs) with exposed high energy (001) facets (Wen et al., 2011). The thickness of the TiO_2-NSs is about 30 nm. It has been proven that high energy TiO_2 nanosheets with exposed (001) facets can be prepared by using fluoride ions as shape-directing reagent (Yang et al., 2008; Lv et al., 2012). Then, it is not hard to understand the formation of high energy TiO_2-NSs during calcination of $TiOF_2$, a kind of fluorine-containing materials.

Since the sidelength of the obtained TiO_2-HNBs is similar as these precursor $TiOF_2$ cube, it is proposed that the formation of TiO_2-HNBs assembly from TiO_2-NSs is through a Ostwald Rippening process (Lou et al., 2008; Huang et al., 2013).

After calcination at 500°C, most of the $TiOF_2$ cubes transform into TiO_2-HNBs (**Figure 3c**). **Figure 3d** shows an enlarged SEM image of a broken TiO_2 hollow nanobox, from which we can see that the thickness of the TiO_2 nanosheet increases to about 50 nm, much thicker than that of T400 sample.

The structure of TiO_2-HNBs was further confirmed by the corresponding TEM image of T500 sample (**Figure 4a**), from which we can observe the presence of some erected TiO_2-NSs and a $TiOF_2$ cube that has not totally transformed into anatase TiO_2. This is consistent with the corresponding XRD characterization result (**Figure 1d**). From the side view HRTEM image of a discrete TiO_2-NS (**Figure 4b**), we can clearly see the lattice spacing of 0.235 nm that parallels to the top and bottom facets, which corresponds to the (001) planes of A-TiO_2 (Han et al., 2009). This confirms that the obtained TiO_2-HNBs are assembly from high energy TiO_2-NSs with exposed (001) facets (Wang et al., 2010).

When the calcination temperature increases to 600°C, we can see that almost all of the TiO_2-HNBs decompose into discrete TiO_2-NSs (**Figure 3e**). From the truncated biypramidal shape of a TiO_2 nanocrystals (**Figure 3f**), we can estimate that the thickness of the TiO_2-NSs is about 100 nm (T600 sample), which increases to ca. 150 nm for T700 sample (**Figures 3g,h**). Even calcined at 1100°C, some TiO_2 nanosheets still keep bipyramidal shape (decahedron) with exposed (001) and (101) facets (**Figures 3i,j**), further indicating the thermal stability of high energy TiO_2-NSs.

The bipyramidal shapes of TiO_2 nanostructures disappear (**Figures 3k,l**) when calcination of $TiOF_2$ cubes at 1200°C. This can be explained by the sintering of the sample due to phase transformation from A-TiO_2 to R-TiO_2 (**Figure 1**).

By comparing the morphologies of TiO_2-NSs from **Figure 3**, we can clearly see that heat treatment of $TiOF_2$ cubes only results in the growth of TiO_2 nanosheet along (001) direction. **Scheme 1** illustrates the morphology evolution and phase transformation of $TiOF_2$ cube during calcination.

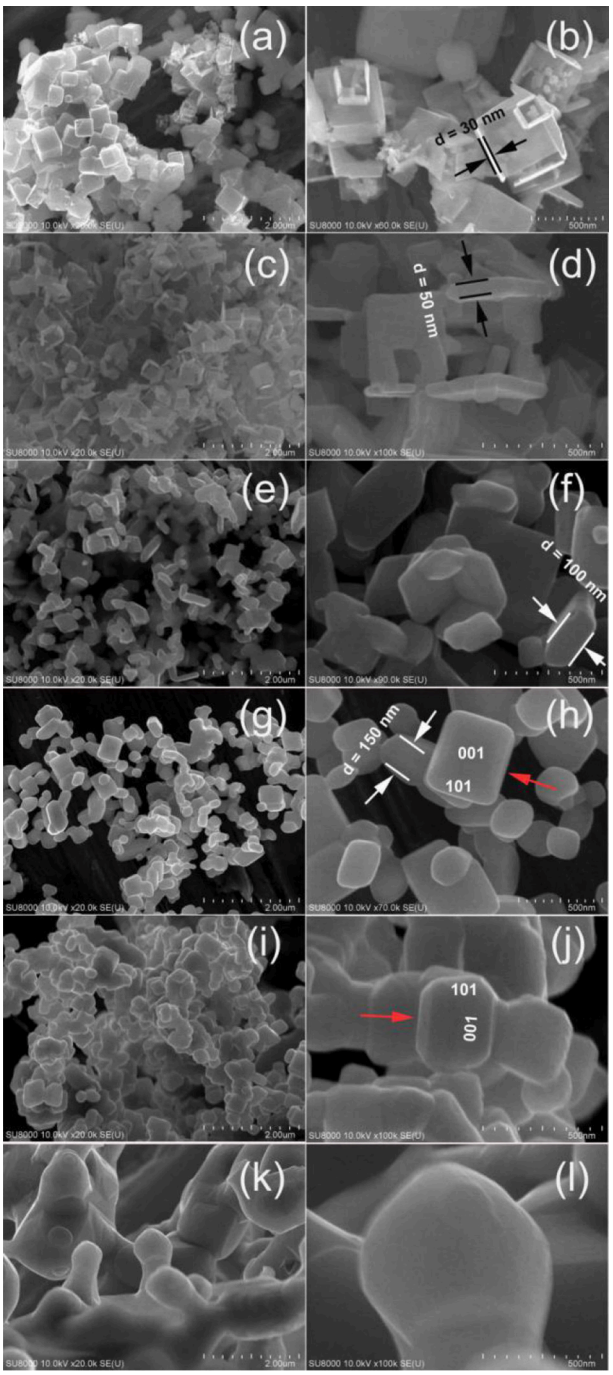

FIGURE 3 | Comparison of the SEM images for T400 **(a,b)**, T500 **(c,d)**, T600 **(e,f)**, T700 **(g,h)**, T1100 **(i,j),** and T1200 **(k,l)** samples.

Uv-vis Absorption and FTIR Spectra

Light-harvesting ability plays a very important role on the photoreactivity of the photocatalyst (Li et al., 2017b). Therefore, we compared the UV-vis absorption spectra of the samples. It can be seen that from **Figure 5** that, when calcination temperature is below 1100°C, all samples possess similar absorption spectra

(**Figure 5**). The onset of the UV-vis absorption spectrum for T400 sample is at 389 nm, corresponding to a bangap of 3.19 eV. However, the absorption edge was obviously red-shifted for T1200 sample. The onset of the spectrum for T1200 sample begins at 424 nm, corresponding to a bandgap of 2.92 eV, which can be ascribed to the phase transformation (**Figure 1**).

Figure 6 compares the FTIR spectra of the photocatalysts treated at different calcination temperature. From which, it can be seen that all samples exhibit strong absorption peaks cenerting at about 3,427, 1,628, 1,403, and 554 cm^{-1}. The peaks of 3,427 and 1,628 cm^{-1} originate from the -OH groups/H_2O due to the adsorption of moisture from the air, while the peaks centering at about 1403 and 554 cm^{-1} originate from the vibration of

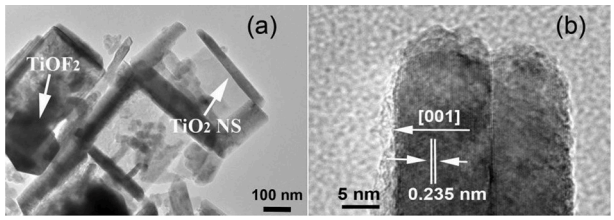

FIGURE 4 | TEM image **(a)** and high-resolution TEM image **(b)** of T500 sample, arrows in **(a)** indicating the presence of $TiOF_2$ cube and TiO_2 nanosheet (TiO_2-NS).

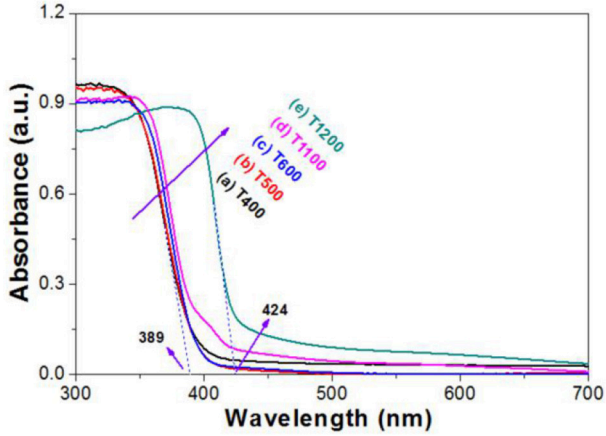

FIGURE 5 | UV-vis absorption spectra of the photocatalysts.

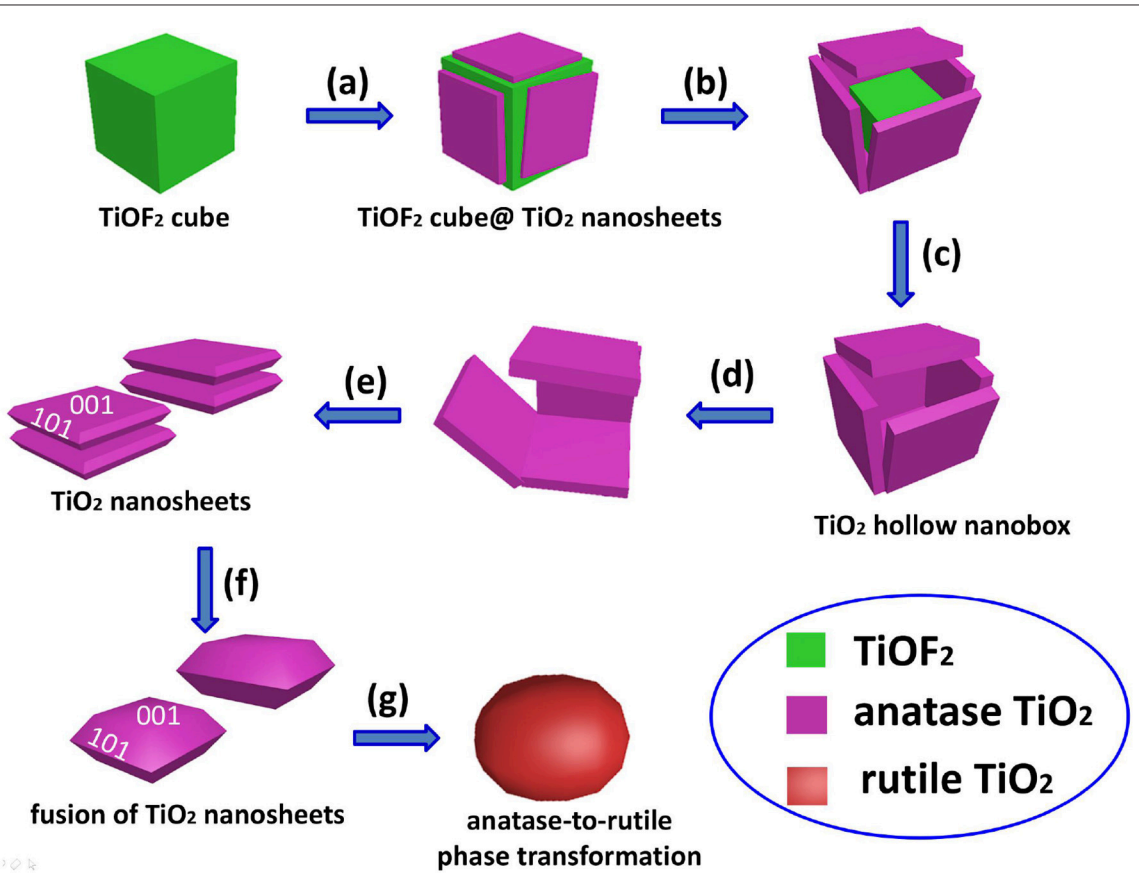

SCHEME 1 | Morphology evolution and phase transformation of $TiOF_2$ cube during calcination at different temperatures: **(a)** 300°C, **(b)** 400°C, **(c)** 500°C, **(d)** 600°C, **(e)** 700°C, **(f)** 1100°C, and **(g)** 1200°C.

Ti-O and O-Ti-O. Carefully view shows that there is a strong absorption peak at 978 cm^{-1}, which decreases with increasing in the calcination temperature. This peak was attributed to the vibration of Ti-F bond of $TiOF_2$. When calcination temperature increases to 600°C, the vibration of Ti-F disappears because of the complete phase transformation of $TiOF_2$-to-anatase TiO_2 (**Figure 1**; Zhao et al., 2018).

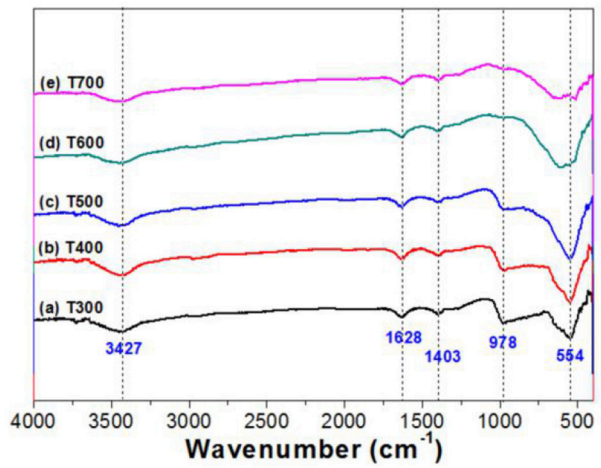

FIGURE 6 | FTIR spectra of the photocatalysts.

Analysis of XPS Spectrum

Figure 7A compares the XPS survey spectra of photocatalysts for T400, T500, and T600 photocatalysts. From which, it can be observed that the XPS spectra are similar. All these samples contain titanium (Ti), oxygen (O), fluorine (F), and carbon (C) elements. The C element originates from the adventitious hydrocarbon from the XPS instrument itself. We can also be clearly see that the peak intensity of F element tends to decrease with increasing the calcination temperature from 400 to 600°C. The atomic ratios of F:Ti were determined to be 1.19 for T400 sample, 0.50 for T500 sample, and 0.17 for T600 sample, respectively. The steady decrease in F content with increase in the calcination is because of the $TiOF_2$ to A-TiO_2 phase transformation (**Figure 1** and Equation 1), and the removal of adsorbed fluoride ions on the surface of A-TiO_2.

Figures 7B,C show the high resolution XPS spectra in Ti 2p and O 1s regions, respectively. It can be seen that, both the binding energies for Ti 2p and O 1s of the samples steady decrease with increasing the calcination temperature. This is attributed to the $TiOF_2$-to-TiO_2 phase transformation (**Figure 1** and Equation 1), and the formation of oxygen vacancy due to

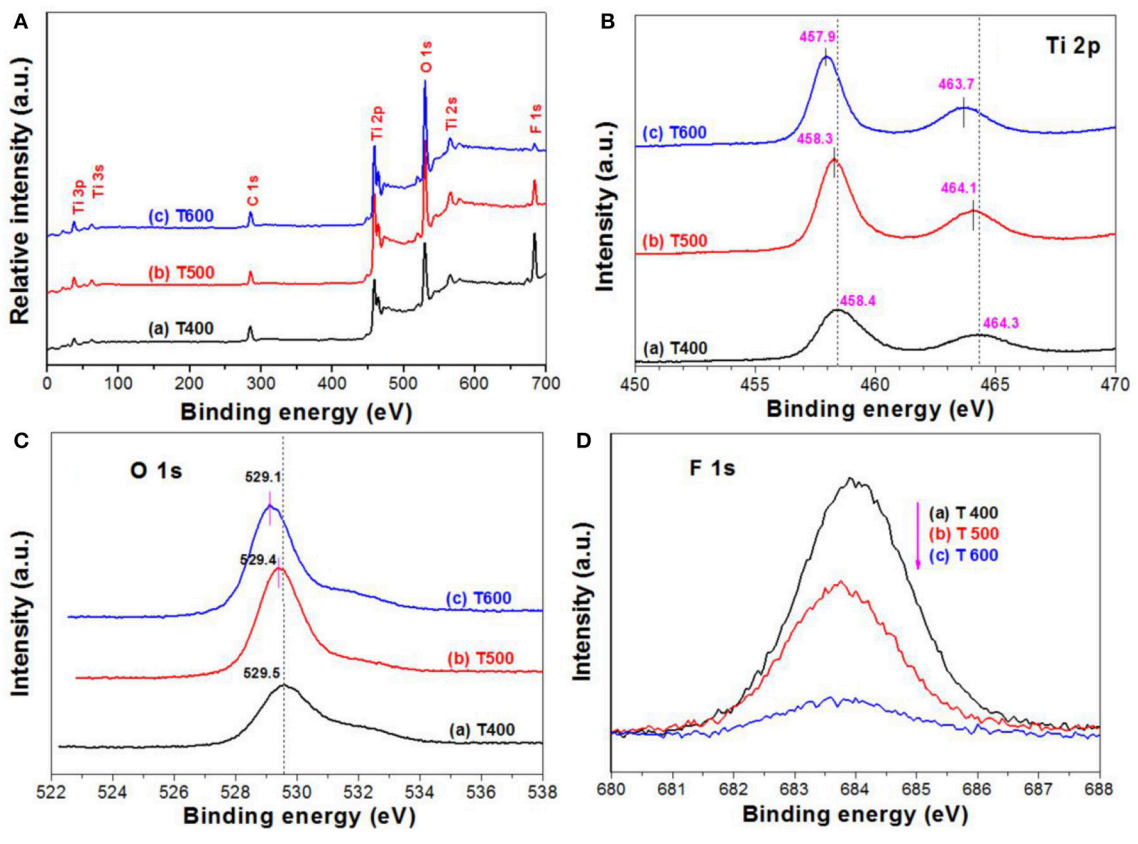

FIGURE 7 | XPS survey spectra of the photocatalysts **(A)**, and the corresponding high resolution XPS spectra in Ti 2p **(B)**, O 1s **(C),** and F 1s **(D)** regions, respectively.

the removal of surface adsorbed fluoride ions over TiO_2 upon calcination (Lv et al., 2011). It has been accepted that almost all of the fluoride ions adsorbed on the surface of high energy TiO_2 nanosheets can be removed after calcination at 500°C.

The F 1s binding energy peak centering at about 684 eV (**Figure 7D**) is designated to the surface fluoride (Ti-F). No peak with binding energy of about 688.5 eV, corresponding to the lattice F^- of TiO_2, is found in all the photocatalysts, indicating that calcination of $TiOF_2$ cannot results in the doping of fluorine into anatase TiO_2 (Yu et al., 2002). We can also clearly see that the peak intensity of F 1s steady decreases with increasing the calcination temperature, this can be attributed to the heat-induced phase transformation from $TiOF_2$ to A-TiO_2 and the desorption of surface adsorbed fluoride ions (Yang et al., 2008).

Photocatalytic Oxidation of Acetone

Photocatalytic oxidation of acetone was used to monitor the photoreactivity of the prepared photocatalyst. The reaction for the photocatalytic oxidation of acetone is as follows (Equation 2).

$$(CH_3)_2CO + 4O_2 = 3CO_2 + 3H_2O \quad (2)$$

Figure 8A compares the relative photoreactivity of the photocatalyst by calculation the decomposed acetone within 2 h. It was found that the photocatalytic activity of the precursor $TiOF_2$ can be neglected (only 4.0 ppm acetone was decomposed). The poor photocatalytic activity of $TiOF_2$ is possibly due to its easy recombination of photo-generated carriers.

The photocatalytic activity of the photocatalyst increases with increase in the calcination temperature from 300°C (12.8 ppm) to 500°C (102.5 ppm), which is due to the production of A-TiO_2. When further increase in the heat temperature from 600°C (94.6 ppm) to 1100°C (25.4 ppm), the photocatalytic activity of the photocatalyst steady decreases, possibly due to the decreased specific surface area (**Table 1**). Only 5.9 ppm of acetone was found to decompose when T1200 sample is used as photocatalyst. This is because of the complete A-TiO_2 to R-TiO_2 phase transformation (**Figure 1**) and smallest BET surface area (0.4 m^2g^{-1}).

Reusability of the photocatalyst is also important from the viewpoint of the practical applications (Liu et al., 2010). Therefore, we monitored the recycling use of T500 sample for 5 times in acetone oxidation (**Figure 8B**). It can be seen that no obvious reactivity decrease was observed for T500 sample even continual use for 5 times, indicating that T500 sample is potential to be used in practical applications.

Mechanism

The value of photocurrent is usually used to evaluate the ability to generate and transfer of charge carriers for illuminated semiconductor photocatalyst (Cheng et al., 2018; Huang et al., 2018). The photocurrent of the prepared photocatalyst was therefore tested for several on-off cycles (**Figure 9**). It can be

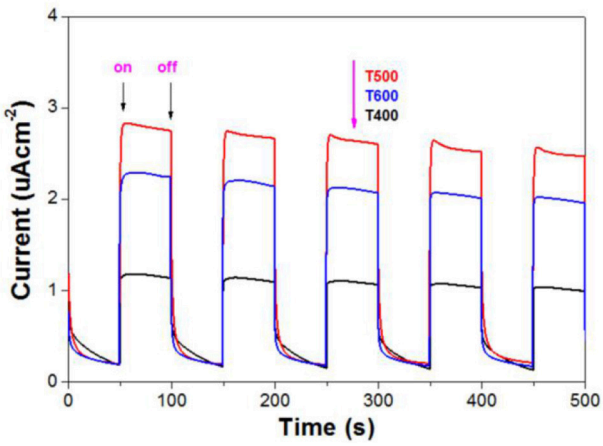

FIGURE 9 | Photocurrents of the photocatalysts.

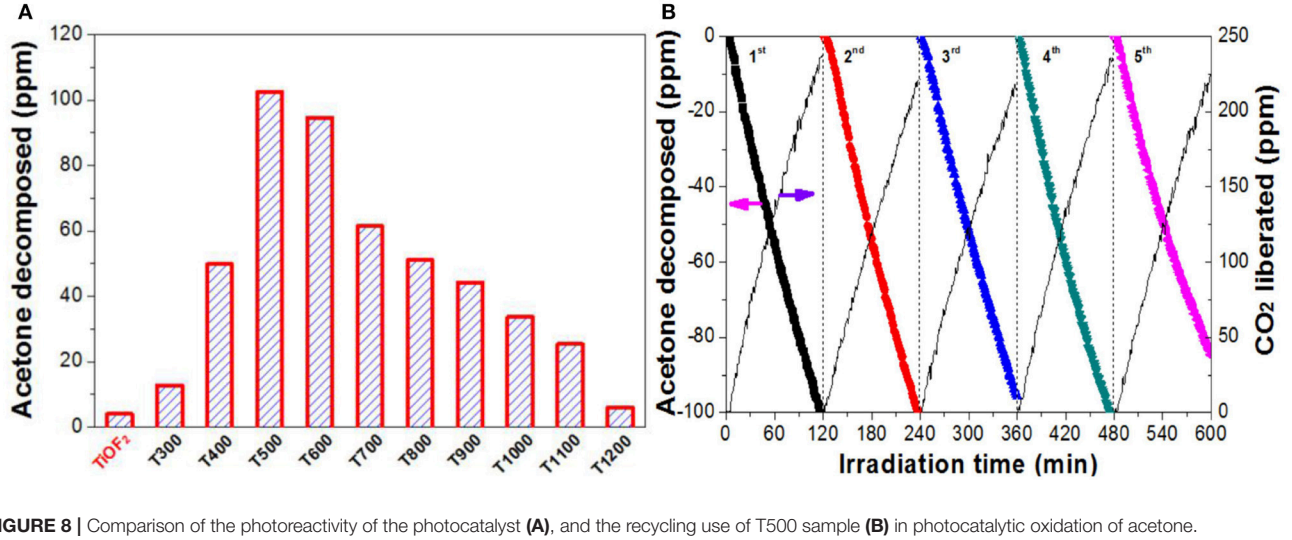

FIGURE 8 | Comparison of the photoreactivity of the photocatalyst **(A)**, and the recycling use of T500 sample **(B)** in photocatalytic oxidation of acetone.

seen that, when irradiation of the TiO_2 film electrodes, obvious prompt photocurrent signals are produced, which exhibit good reproducibility. When the lamp is turned off, the photocurrent value for all the TiO_2 film electrodes are instantaneously close to zero. We can also see, with increasing the calcination temperature from 400 to 600°C, the photocurrent of the photocatalyst increases first and then decreases. The photocurrent of T500 sample is the as high as 2.8 uAcm^{-2}, which is much higher than that of T400 (1.1 uAcm^{-2}) and T600 (2.3 uAcm^{-2}) samples. The photoreactivity of semiconductor photocatalyst is closely related to the efficiency of the separation of the photo-generated electron-hole pairs (Fu et al., 2008). So it is safe to predict that the photoreactivity of T500 is higher than that of T400 and T600 samples, which keeps in line with the experimental results (**Figure 8**).

It has been accepted that fluoride ions show strong affinity to titanium (Equation 3), and the photoreactivity of TiO_2 nanocrystals can be obviously improved after the introduction of surface fluorination (Minero et al., 2000; Xu et al., 2007; Cheng et al., 2008). According to the study of Yu et al., the difference in surface energy makes the photo-generated electrons and holes migrate to (101) and (001) facets, respectively (Yu et al., 2014). The CB electrons aggregated in (101) facets are captured by surface adsorbed oxygen to produce super oxygen radicals ($O_2^{\cdot-}$), while the VB holes aggregated on the (001)facets are transfer into hydroxyl radicals (·OH). Both $O_2^{\cdot-}$ and ·OH are important reactive oxygen species (ROSs) for the degradation of organics. When compared with pristine TiO_2, surface fluorination of TiO_2 changes the state of the formed hydroxyl radicals from surface bounded ·OH radicals (Equation 6) to mobile ·OH radicals ($\cdot OH_{free}$). This is because the displacement of fluoride to surface OH^- groups (Equation 3) induces the direct oxidization solvent water by holes (Equation 7).

$$\equiv Ti - OH + F^- \rightarrow \equiv Ti - F + OH^- \quad (3)$$

$$TiO_2 + hv \rightarrow TiO_2\,(h^+ \cdots e^-) \quad (4)$$

$$O_2 + e^- \rightarrow O_2^{\cdot-} \quad (5)$$

$$\equiv Ti - OH + h^+ \rightarrow \equiv Ti\cdots OH \quad (6)$$

$$\equiv Ti - F + H_2O + h^+ \rightarrow \equiv Ti - F + \cdot OH_{free} \quad (7)$$

As free ·OH radical are more active than surface bounded ·OH radicals, the oxidation of acetone into CO_2 and H_2O is greatly enhanced due to the attacks of super oxygen radicals and free ·OH radicals (Equation 8). The proposed mechanism for the enhanced photoreactivity of surface fluorinated TiO_2 nanosheet toward acetone oxidation is shown in **Scheme 2**.

$$C_3H_6O + O_2^{\cdot-}/\cdot OH_{free} \rightarrow CO_2 + H_2O \quad (8)$$

Recently, significantly growing interest has been devoted to studying of hierarchical nanostructures due to their unique properties and widespread potential applications (Lou et al., 2008). For example, when compared with solid spheres, TiO_2 hollow spheres usually shows much higher photocatalytic activity mainly because they possess better light-harvesting ability (Li et al., 2009). In the present study, the hierarchically structured

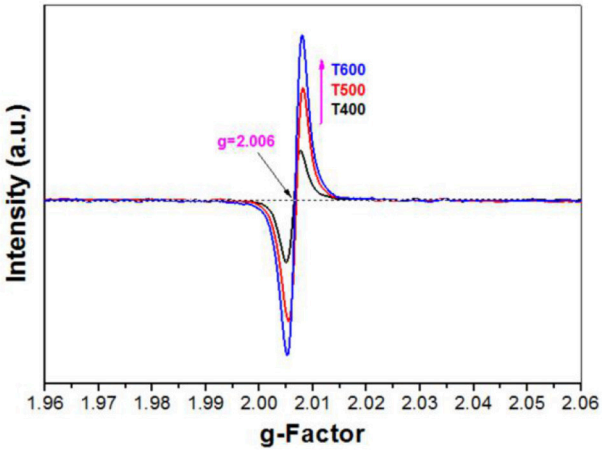

FIGURE 10 | EPR spectra of the photocatalysts.

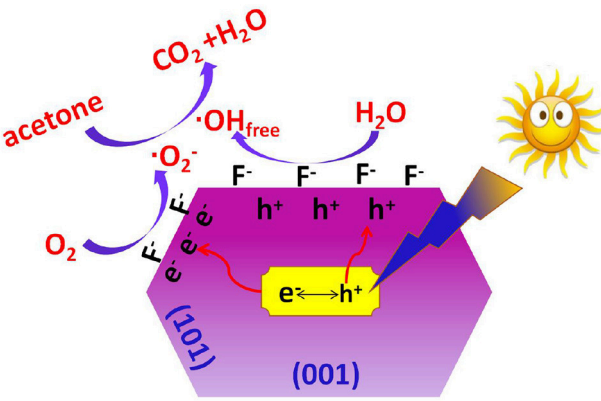

SCHEME 2 | Proposed mechanism for the enhanced photocatalytic activity of surface fluorinated TiO2 nanosheets with exposed high energy (001) facets toward acetone oxidation.

T500 sample, that is TiO_2 hollow nanobox assembly from TiO_2 nanosheets should also benefit the use of light (**Figure 5**), enhancing the photoreactivity.

However, the photoreactivity of TiO_2-NSs steady decrease with increase in the calcination temperature from 500 to 1100°C due to the collapse of the hierarchical TiO_2 hollow nanobox and the removal of surface adsorbed fluorine, leaving surface oxygen vacancy (**Figure 8**; Cheng et al., 2018).

$$\equiv Ti - F + heat \rightarrow \equiv Ti - \square \quad (9)$$

The formation of surface oxygen vacancy was proved by electron paramagnetic resonance (EPR) technique. It was found that the signal intensity for oxygen vacancy of the photocatalyst increases with increase in the calcination temperature from 400 to 600°C (**Figure 10**) due to the heat-induced desorption of

surface adsorbed fluoride ions (Equation 9).

$$\equiv \mathrm{Ti-OH} + \mathrm{HO-Ti} \equiv \rightarrow \equiv \mathrm{Ti-O-Ti} \equiv + \mathrm{H_2O} \quad (10)$$

$$\equiv \mathrm{Ti-\square} + \mathrm{\square - Ti} \equiv \rightarrow \text{ no reaction} \quad (11)$$

It was believed that only when the crystalline size of the nanocrystal is larger than a critical size can phase transformation begin (Padmanabhan et al., 2007; Periyat et al., 2008, 2009). Therefore, the growth of TiO_2 nanocrystal is a prerequisite before the phase transformation of A-TiO_2 to R-TiO_2. The growth of pristine TiO_2 nanocrystal is relatively easy by formation of =Ti-O-Ti= chain between two neighboring TiO_2 nanoparticles (Equation 10). However, the growth of the =Ti-O-Ti= chain is prevented due to the formation of surface oxygen vacancy (Equation 11). Only when the lattice oxygen is diffused from the bulk to the surface of TiO_2 nanosheet with oxygen vacancy at high temperaure can the fusion of neighboring TiO_2-NSs become possible (Lv et al., 2011). Therefore, it is not hard to understand the super thermal stability of TiO_2-NSs prepared by calcination of $TiOF_2$ cubes.

After the removal of surface adsorbed fluoride ions by calcination, these TiO_2-NSs prefer to aggregate and grow along (001) direction to reduce the high surface energy (Lv et al., 2011). Then we can clearly observe the steady increase in the thickness of TiO_2-NSs (**Figure 3**).

CONCLUSIONS

TiO_2 nanosheets with high thermal stability were prepared by calcination of $TiOF_2$ cubes. The anatase-to-rutile phase transformation temperature reaches as high as 1100°C. 500°C-calcined sample shows the highest photoreactivity toward acetone oxidation due to the surface fluorination. The high thermal stability of TiO_2 nanosheets is ascribed to the introduction of surface oxygen vacancy after removal of the surface adsorbed fluoride ions, which prevents the growth of TiO_2 nanosheets. The present study provide a novel way in design of thermally stable materials.

AUTHOR CONTRIBUTIONS

TS and YD performed the experiments. KL planned the project, designed the experiments, and wrote the manuscript. ZH, QL and XL assisted in the analysis and interpretation of the data. ML revised the manuscript.

ACKNOWLEDGMENTS

This work was supported by the National Natural Science Foundation of China (51672312, 21571192 and 21373275), the Science and Technology Program of Wuhan (2016010101010018) and Fundamental Research Funds for the Central Universities, South-Central University for Nationalities (CZT18016).

REFERENCES

Chen, J. S., Tan, Y. L., Li, C. M., Cheah, Y. L., Luan, D., Madhavi, S., et al. (2010). Constructing hierarchical spheres from large ultrathin anatase TiO_2 nanosheets with nearly 100% exposed (001) facets for fast reversible lithium storage. *J. Am. Chem. Soc.* 132, 6124–6130. doi: 10.1021/ja100102y

Chen, L., Shen, L. F., Nie, P., Zhang, X. G., and Li, H. S. (2012). Facile hydrothermal synthesis of single crystalline $TiOF_2$ nanocubes and their phase transitions to TiO_2 hollow nanocages as anode materials for lithium-ion battery. *Electrochim. Acta* 62, 408–415. doi: 10.1016/j.electacta.2011.12.058

Cheng, J. S., Hu, Z., Lv, K. L., Wu, X. F., Li, Q., Li, Y. H., et al. (2018). Drastic promoting the visible photoreactivity of layered carbon nitride by polymerization of dicyandiamide at high pressure. *Appl. Catal. B* 232, 330–339. doi: 10.1016/j.apcatb.2018.03.066

Cheng, X. F., Leng, W. H., Liu, D. P., Xu, Y. M., Zhang, J. Q., and Cao, C. N. (2008). Electrochemical preparation and characterization of surface-fluorinated TiO_2 nanoporous film and its enhanced photoelectrochemical and photocatalytic properties. *J. Phys. Chem. C* 112, 8725–8734. doi: 10.1021/jp7097476

Cui, W., Li, J. Y., Cen, W. L., Sun, Y. J., Lee, S. C., and Dong, F. (2017). Steering the interlayer energy barrier and charge flow via bioriented transportation channels in g-C3N4: enhanced photocatalysis and reaction mechanism. *J. Catal.* 352, 351–360. doi: 10.1016/j.jcat.2017.05.017

Fu, H. B., Xu, T. G., Zhu, S. B., and Zhu, Y. F. (2008). Photocorrosion inhibition and enhancement of photocatalytic activity for ZnO via hybridization with C_{60}. *Environ. Sci. Technol.* 42, 8064–8069. doi: 10.1021/es801484x

Han, X. G., Kuang, Q., Jin, M. S., Xie, Z. X., and Zheng, L. S. (2009). Synthesis of titania nanosheets with a high percentage of exposed (001) facets and related photocatalytic properties. *J. Am. Chem. Soc.* 131, 3152–3153. doi: 10.1021/ja8092373

Huang, T. T., Li, Y. H., Wu, X. F., Lv, K. L., Li, Q., Li, M., et al. (2018). In-situ transformation of Bi_2WO_6 to highly photoreactive Bi_2WO_6@Bi_2S_3 nanoplate *via* ion exchange. *Chin. J. Catal.* 39, 718–727. doi: 10.1016/S1872-2067(17)62913-9

Huang, Z. A., Wang, Z. Y., Lv, K. L., Zheng, Y., and Deng, K. J. (2013). Transformation of $TiOF_2$ cube to a hollow nanobox assembly from anatase TiO_2 nanosheets with exposed {001} facets via solvothermal strategy. *ACS Appl. Mater. Interfaces* 5, 8663–8669. doi: 10.1021/am4023048

Lan, J. F., Wu, X. F., Lv, K. L., Si, L. L., and Deng, K. J. (2015). Fabrication of TiO_2 hollow microspheres using $K_3PW_{12}O_{40}$ as template. *Chin. J. Catal.* 36, 2237–2243. doi: 10.1016/S1872-2067(15)60987-1

Li, X. F., Lv, K. L., Deng, K. J., Tang, J. F., Su, R., Sun, J., et al. (2009). Synthesis and characterization of ZnO and TiO_2 hollow spheres with enhanced photoreactivity. *Mater. Sci. Eng. B* 158, 40–47. doi: 10.1016/j.mseb.2008.12.036

Li, X., Yu, J. G., and Jaroniec, M. (2016). Hierarchical photocatalysts. *Chem. Soc. Rev.* 45, 2603–2636. doi: 10.1039/C5CS00838G

Li, Y. H., Lv, K. L., Ho, W. K., Dong, F., Wu, X. F., and Xia, Y. (2017a). Hybridization of rutile TiO_2 ($rTiO_2$) with g-C_3N_4 quantum dots (CN QDs): an efficient visible-light-driven Z-scheme hybridized photocatalyst. *Appl. Catal. B* 202, 611–619. doi: 10.1016/j.apcatb.2016.09.055

Li, Y. H., Lv, K. L., Ho, W. K., Zhao, Z. W., and Yu, H. (2017b). Enhanced visible-light photo-oxidation of nitric oxide using bismuth-coupled graphitic carbon nitride composite heterostructures. *Chin. J. Catal.* 38, 321–329. doi: 10.1016/S1872-2067(16)62573-1

Li, Y. H., Wu, X. F., Ho, W. K., Lv, K. L., Li, Q., Li, M., et al. (2018). Graphene-induced formation of visible-light-responsive SnO_2-Zn_2SnO_4 Z-scheme photocatalyst with surface vacancy for the enhanced photoreactivity towards NO and acetone oxidation. *Chem. Eng. J.* 336, 200–210. doi: 10.1016/j.cej.2017.11.045

Liang, L., Li, K. N., Lv, K. L., Ho, W. K., and Duan, Y. Y. (2017). Highly photoreactive TiO_2 hollow microspheres with super thermal stability for acetone oxidation. *Chin. J. Catal.* 38, 2085–2093. doi: 10.1016/S1872-2067(17)62952-8

Lin, S., Sun, S. Y., Shen, K. X., Tan, D. Y., Zhang, H. P., Dong, F. Q., et al. (2018a). Photocatalytic microreactors based on nano TiO2-containing clay colloidosomes. *Appl. Clay Sci.* doi: 10.1016/j.clay.2017.08.022. [Epub ahead of print].

Lin, S., Sun, S. Y., Wang, K., Shen, K. X., Ma, B. B., Ren, Y. Q., et al. (2018b). Bioinspired design of alcohol dehydrogenase@nano TiO_2 microreactors for sustainable cycling of NAD^+/NADH coenzyme. *Nanomaterials* 8, 1–9. doi: 10.3390/nano8020127

Liu, Y., Chen, L. F., Hu, J. C., Li, J. L., and Richards, R. (2010). TiO_2 nanoflakes modified with gold nanoparticles as photocatalysts with high activity and durability under near UV irradiation. *J. Phys. Chem. C* 114, 1641–1645. doi: 10.1021/jp910500c

Lou, X. W., Archer, L. A., and Yang, Z. C. (2008). Hollow micro-/nanostructures: synthesis and applications. *Adv. Mater. Weinheim.* 20, 3987–4019. doi: 10.1002/adma.200800854

Lv, K. L., Cheng, B., Yu, J. G., and Liu, G. (2012). Fluorine ions-mediated morphology control of anatase TiO_2 with enhanced photocatalytic activity. *Phys. Chem. Chem. Phys.* 14, 5349–5362. doi: 10.1039/c2cp23461k

Lv, K. L., Xiang, Q. J., and Yu, J. G. (2011). Effect of calcination temperature on morphology and photocatalytic activity of anatase TiO_2 nanosheets with exposed {001} facets. *Appl. Catal. B.* 104, 275–281. doi: 10.1016/j.apcatb.2011.03.019

Minero, C., Mariella, G., Maurino, V., and Pelizzetti, E. (2000). Photocatalytic transformation of organic compounds in the presence of inorganic anions. 1. Hydroxyl-mediated and direct electron-transfer reactions of phenol on a titanium dioxide-fluoride system. *Langmuir.* 16, 2632–2641. doi: 10.1021/la9903301

Padmanabhan, S. C., Pillai, S. C., Colreavy, J., Balakrishnan, S., McCormack, D. E., Perova, T. S., et al. (2007). A simple sol-gel processing for the development of high-temperature stable photoactive anatase titania. *Chem. Mater.* 19, 4474–4481. doi: 10.1021/cm070980n

Periyat, P., McCormack, D. E., Hinder, S. J., and Pillai, S. C. (2009). One-pot synthesis of anionic (nitrogen) and cationic (sulfur) codoped high-temperature stable, visible light active, anatase photocatalysts. *J. Phys. Chem. C* 113, 3246–3253. doi: 10.1021/jp808444y

Periyat, P., Pillai, S. C., McCormack, D. E., Colreavy, J. C., and Hinder, S. J. (2008). Improved high-temperature stability and sun-light-driven photocatalytic activity of sulfur-doped anatase TiO_2. *J. Phys. Chem. C* 112, 7644–7652. doi: 10.1021/jp0774847

Qi, K. Z., Cheng, B., Yu, J. G., and Ho, W. K. (2017). A review on TiO_2-based Z-scheme photocatalysts. *Chin. J. Catal.* 38, 1936–1955. doi: 10.1016/S1872-2067(17)62962-0

Regmi, C., Joshi, B., Ray, S. K., Gyawali, G., and Pandey, R. P. (2018). Understanding mechanism of photocatalytic microbial decontamination of environmental wastewater. *Front. Chem.* 6:33. doi: 10.3389/fchem.2018.00033

Sajan, C. P., Wageh, S., Al-Ghamdi, A. A., Yu, J. G., and Cao, S. W. (2016). TiO_2 nanosheets with exposed {001} facets for photocatalytic applications. *Nano Res.* 9, 3–27. doi: 10.1007/s12274-015-0919-3

Wang, Q., Qin, Z. N., Chen, J., Ren, B. S., Chen, Q. F., Guo, Y. C., et al. (2016). Green synthesis of nickel species *in situ* modified hollow microsphere TiO_2 with enhanced photocatalytic activity. *Appl. Surf. Sci.* 364, 1–8. doi: 10.1016/j.apsusc.2015.12.033

Wang, X. F., Yu, R., Wang, K., Yang, G. Q., and Yu, H. G. (2015). Facile template-induced synthesis of Ag-modified TiO_2 hollow octahedra with high photocatalytic activity. *Chin. J. Catal.* 36, 2211–2218. doi: 10.1016/S1872-2067(15)60978-0

Wang, Z. Y., Huang, B. B., Dai, Y., Zhang, X. Y., Qin, X. Y., Li, Z., et al. (2012). Topotactic transformation of single-crystalline $TiOF_2$ nanocubes to ordered arranged 3D hierarchical TiO_2 nanoboxes. *CrystEngComm* 14, 4578–4581. doi: 10.1039/C2CE25271F

Wang, Z. Y., Lv, K. L., Wang, G. H., Deng, K. J., and Tang, D. G. (2010). Study on the shape control and photocatalytic activity of high-energy anatase titania. *Appl. Catal. B* 100, 378–385. doi: 10.1016/j.apcatb.2010.08.014

Wen, C. Z., Hu, Q. H., Guo, Y. N., Gong, X. Q., Qiao, S. Z., and Yang, H. G. (2011). From titanium oxydifluoride ($TiOF_2$) to titania (TiO_2): phase transition and non-metal doping with enhanced photocatalytic hydrogen (H_2) evolution properties. *Chem. Commun.* 47, 6138–6140. doi: 10.1039/c1cc10851d

Wen, J. Q., Li, X., Liu, W., Fang, Y. P., Xie, J., and Xu, Y. H. (2015). Photocatalysis fundamentals and surface modification of TiO_2 nanomaterials. *Chin. J. Catal.* 36, 2049–2070. doi: 10.1016/S1872-2067(15)60999-8

Xia, Y., Li, Q., Lv, K. L., and Li, M. (2017). Heterojunction construction between TiO_2 hollowsphere and $ZnIn_2S_4$ flower for photocatalysis application. *Appl. Surf. Sci.* 398, 81–88. doi: 10.1016/j.apsusc.2016.12.006

Xu, X., Sun, Y. F., Fan, Z. H., Zhao, D. Q., Xiong, S. M., Zhang, B. Y., et al. (2018). Mechanisms for·O_2^- and·OH production on flowerlike $BiVO_4$ photocatalysis based on electron spin resonance. *Frontier in Chem.* 6:64. doi: 10.3389/fchem.2018.00064

Xu, Y. M., Lv, K. L., Xiong, Z. G., Leng, W. H., Liu, W. P. D., and Xue, X. J. (2007). Rate enhancement and rate inhibition of phenol degradation over irradiated anatase and rutile TiO_2 on the addition of NaF: new insight into the mechanism. *J. Phys. Chem. C* 111, 19024–19032. doi: 10.1021/jp076364w

Yang, H. G., Liu, G., Qiao, S. Z., Sun, C. H., Jin, Y. G., Smith, S. C., et al. (2009). Solvothermal synthesis and photoreactivity of anatase TiO_2 nanosheets with dominant {001} facets. *J. Am. Chem. Soc.* 131 4078–4083. doi: 10.1021/ja808790p

Yang, H. G., Sun, C. H., Qiao, S. Z., Zou, J., Liu, G., Smith, S. C., et al. (2008). Anatase TiO_2 single crystals with a large percentage of reactive facets. *Nature* 453, 638–641. doi: 10.1038/nature06964

Yu, J. C., Yu, J. G., Ho, W. K., Jiang, Z. T., and Zhang, L. Z. (2002). Effects of F^- doping on the photocatalytic activity and microstructures of nanocrystalline TiO_2 powders. *Chem. Mater.* 14, 3808–3816. doi: 10.1021/cm020027c

Yu, J. G., Low, J. X., Xiao, W., Zhou, P., and Jaroniec, M. (2014). Enhanced photocatalytic CO_2-reduction activity of anatase TiO_2 by coexposed {001} and {101} facets. *J. Am. Chem. Soc.* 136, 8839–8842. doi: 10.1021/ja5044787

Zhao, X., Du, Y. T., Zhang, C. J., Tian, L. J., Li, X. F., Deng, K. J., et al. (2018). Enhanced visible photocatalytic activity of TiO_2 hollow boxes modified by methionine for RhB degradation and NO oxidation. *Chin. J. Catal.* 39, 736–746. doi: 10.1016/S1872-2067(18)63039-6

Zhu, X. B., Tu, X., Mei, D. H., Zheng, C. H., Zhou, J. S., Gao, X., et al. (2016). Investigation of hybrid plasma-catalytic removal of acetone over CuO/g-Al_2O_3 catalysts using response surface method. *Chemosphere* 155, 9–17. doi: 10.1016/j.chemosphere.2016.03.114

Conflict of Interest Statement: The authors declare that the research was conducted in the absence of any commercial or financial relationships that could be construed as a potential conflict of interest.

frontiers in Chemistry

ORIGINAL RESEARCH
published: 18 May 2018
doi: 10.3389/fchem.2018.00156

Compressible and Recyclable Monolithic g-C_3N_4/Melamine Sponge: A Facile Ultrasonic-Coating Approach and Enhanced Visible-Light Photocatalytic Activity

Ye Yang[1,2], *Qian Zhang*[1]*, *Ruiyang Zhang*[1], *Tao Ran*[1], *Wenchao Wan*[1] and *Ying Zhou*[1,2]*

[1] The Center of New Energy Materials and Technology, School of Materials Science and Engineering, Southwest Petroleum University, Chengdu, China, [2] State Key Laboratory of Oil and Gas Reservoir Geology and Exploitation, Southwest Petroleum University, Chengdu, China

OPEN ACCESS

Edited by:
Fan Dong,
Chongqing Technology and Business University, China

Reviewed by:
Liwu Zhang,
Fudan University, China
Hongwei Huang,
China University of Geosciences, China

***Correspondence:**
Qian Zhang
zhangqian@swpu.edu.cn
Ying Zhou
yzhou@swpu.edu.cn

Specialty section:
This article was submitted to Catalysis and Photocatalysis, a section of the journal Frontiers in Chemistry

Received: 02 March 2018
Accepted: 19 April 2018
Published: 18 May 2018

Citation:
Yang Y, Zhang Q, Zhang R, Ran T, Wan W and Zhou Y (2018) Compressible and Recyclable Monolithic g-C_3N_4/Melamine Sponge: A Facile Ultrasonic-Coating Approach and Enhanced Visible-Light Photocatalytic Activity. Front. Chem. 6:156. doi: 10.3389/fchem.2018.00156

Powdery photocatalysts seriously restrict their practical application due to the difficult recycle and low photocatalytic activity. In this work, a monolithic g-C_3N_4/melamine sponge (g-C_3N_4/MS) was successfully fabricated by a cost-effective ultrasonic-coating route, which is easy to achieve the uniform dispersion and firm loading of g-C_3N_4 on MS skeleton. The monolithic g-C_3N_4/MS entirely inherits the porous structure of MS and results in a larger specific surface area (SSA) than its powdery counterpart. Benefit from this monolithic structure, g-C_3N_4/MS gains more exposed active sites, enhanced visible-light absorption and separation of photogenerated carriers, thus achieving noticeable photocatalytic activity on nitric oxide (NO) removal and CO_2 reduction. Specifically, NO removal ratio is as high as 78.6% which is 4.5 times higher than that of the powdery g-C_3N_4, and yield rate of CO and CH_4 attains 7.48 and 3.93 μmol g^{-1} h^{-1}. Importantly, the features of low-density, high porosity, good elasticity, and firmness, not only endow g-C_3N_4/MS with flexibility in various environmental applications, but also make it easy to recycle and stable for long-time application. Our work provides a feasible approach to fabricate novel monolithic photocatalysts with large-scale production and application.

Keywords: g-C_3N_4/melamine sponge, photocatalysis, NO removal, monolith, visible light

INTRODUCTION

Semiconductor photocatalysis is one of the promising strategies for pollutants abatement (Maggos et al., 2007; Huang et al., 2013, 2016; Zhao et al., 2015) and has attracted intense investigation in the past decades. Up to now, hundreds of semiconductors have been explored and applied in the field of environmental remediation (Liu et al., 2008; Hossain and Mukherjee, 2013; Huang et al., 2015a, 2017a; Zhou et al., 2016). However, only a few of them have been considered as potential candidates for practical application in view of their nontoxic, suitable band gap, band edge energy, good stability and earth-abundant source. g-C_3N_4 is one of those semiconductors, which possesses graphene-like structure and constituted mainly by carbon and nitrogen. Since g-C_3N_4 was first reported to photocatalytic water splitting

by Wang et.al (Wang et al., 2009), it quickly becomes a hot material in photocatalysis. Afterwards, g-C_3N_4 has already been applied in various reactions such as CO_2 photoreduction, NO removal, and dye degradation (Yan et al., 2009; Dong et al., 2014a; Sun H. et al., 2017). However, extensive studies revealed that g-C_3N_4 suffers from fast photo-generated carriers recombination, limited visible-light absorption, and low surface area. Various strategies have been carried out to overcome these intrinsic drawbacks of g-C_3N_4, such as elemental doping, composite with other materials and morphology control synthesis, etc. (Liu et al., 2010; Zhao et al., 2012; Hou et al., 2014; Cheng et al., 2015; Han Q. et al., 2015; Li et al., 2017; Yang et al., 2017). Besides above disadvantages, as a potential photocatalyst for practical application, g-C_3N_4 is also hindered by difficult recycle originating from particle heavy loss during its complicated recovery process, inefficient utilization of active sites and light energy resulting from particle aggregation. Comparison with the intrinsic drawbacks of g-C_3N_4, these problems are vital to achieve successful application of photocatalyst on actual environmental issues, but they are rarely studied and generally beyond the aforementioned strategies to overcome.

Recently, monolithic or integrated photocatalysts are found to be a plausible way to solve the practical application problem of photocatalyst (Cheng et al., 2016; Wan et al., 2018). The so-called monolithic photocatalyst usually consists of two parts, one is a macroscopical support with porous three-dimensional (3D) skeleton, and the other is the loaded photocatalyst particles. After integrating powdery catalysts on its support, their recycling becomes easy to achieve by a tweezer (Liu W. J. et al., 2015; Tang et al., 2017). Meanwhile, the 3D porous structure of support gives the powdery catalysts a high dispersion and exposes more active sites by avoiding particles agglomeration. Moreover, this structure also benefits light energy harvest and transportation of liquid or gas pollutants. Until now, graphene aerogels are the most studied monolithic photocatalyst supports because of their inherent large surface area, high porosity and low density. We have fabricated monolithic C_3N_4/graphene oxide aerogel (GOA) in our previous work and found obvious activity enhancement (Wan et al., 2016), which is in line with the results from other monolithic photocatalyst/graphene aerogels (Fan et al., 2015; Cui et al., 2017; Wang et al., 2017). However, the intrinsic brittleness and weak firmness of aerogels make it easy to break into pieces during mechanical deformation, which seriously restrict its potential in practical application. Other firm supports, such as carbon foam and Al_2O_3 ceramic foam with hard 3D framework, are also selected to fabricate monolithic photocatalyst (Dong et al., 2014b; Lin et al., 2016). Nevertheless, it is very difficult to achieve uniform loading by directly mixing photocatalyst with these hard supports. To overcome this problem, special strategies with high cost and energy consumption, like *in-situ* immobilizing approach and laser ablating deposition (Liang et al., 2015; Lin et al., 2016), are used to achieve the good catalyst dispersion. The sophisticated preparation method severely limits the hard supports to be extensively utilized in fabrication of monolithic photocatalyst. Based on the above considerations, the proper support remains an obstacle for the practical application of monolithic photocatalyst. Lately, melamine sponge (MS), a cheap commercial polymer foam which is widely used as kitchen and construction materials, is successfully used for oil-water separation by integrating with graphene (Liu T. T. et al., 2015; Zhao et al., 2016). The fabricated graphene/MS exhibits low-density, high porosity and high elasticity inherited from MS, which exactly match the support characteristics of the monolithic photocatalyst. Importantly, the good elasticity makes MS more ductile and avoids the drawbacks of brittle and hard materials. Therefore, MS is a potential alternative and selected as the support for monolithic photocatalyst fabrication.

Herein, we prepare a monolithic g-C_3N_4/MS by a facile ultrasonic-coating method at room temperature, which is very easy to achieve mass production. The monolithic structure endows g-C_3N_4/MS with enhanced light harvest and more exposed active sites, ensuring its good photocatalytic activity. Importantly, the as-prepared monolithic photocatalyst exhibits low-density, high porosity, high elasticity and good firmness, which not only make it flexible in various environmental applications including NO removal, and CO_2 photoreduction, but also make it easy to recycle and suitable for practical application. Overall, our results provide a novel strategy to develop monolithic photocatlyst for practical application with large-scale production.

EXPERIMENTAL

Synthesis of g-C_3N_4

The polymeric g-C_3N_4 was prepared by pyrolysis of urea (Liu et al., 2011). In a typical process, 15 g urea was added into an alumina crucible with a cover and then heated to 550°C in a muffle furnace for 1 h with a heating rate of about 55°C min^{-1}. After cool down to room temperature, the final yellow agglomerates were the pristine g-C_3N_4 and subsequently ground into powder for further use.

Preparation of Monolithic g-C_3N_4/MS

For the preparation of monolithic g-C_3N_4/MS, 2.5 g g-C_3N_4 powder was dispersed in 500 mL water and sonicated for 1 h to form a g-C_3N_4 suspension. MS was cut into suitable size and washed with deionized water and alcohol in order, then dried at room temperature. Next, the clean MS was immersed into g-C_3N_4 suspension for 30 min, and then squeezed out the excess solution. After that, the sample was transferred into a culture dish and freeze-dried (−70°C pre-freezing) for 48 h to obtain g-C_3N_4/MS. For comparison, powdery g-C_3N_4 without MS was processed through the same procedures and denoted as sonicated g-C_3N_4. To obtain the best photocatalytic activity of monolithic g-C_3N_4/MS, we finely investigated the effect of g-C_3N_4 suspension concentration (3 mg mL^{-1}-40 mg mL^{-1}) and MS thickness (0.5–2.5 cm). The sizes of monolithic g-C_3N_4/MS varied with different experiments and were stated at their first appearance in the text.

Characterization

Powder X-ray diffraction (PXRD) was performed on a PANalytical X'pert diffractometer with a Cu Ka radiation. Transmission electron microscopy (TEM) was performed on

a FEI tecnai G2 F30 microscope operated at 200 kV. The morphology of g-C_3N_4/MS was observed through scanning electron microscopy (SEM) on a ZEISS EVO MA15 microscopy. The Fourier transform infrared (FT-IR) spectra were measured using a Nicolet 6700 spectrometer on samples embedded in KBr pellets. UV-vis diffuse reflectance spectrum (DRS) data were recorded on a Shimadzu UV-2600 spectrophotometer. Photoluminescence spectra were recorded on F-7000 FL spectrofluorometer with an excitation wavelength at 320 nm. X-ray photoelectron spectroscopy (XPS) was performed by using a Thermo Scientific Escalab 250Xi spectrometer. The specific surface area (SSA) was determined via using methylene blue (MB) adsorption method on a UV-vis spectrophotometer (UV-5100, Anhui Wanyi; Tran et al., 2015), the SSA of g-C_3N_4 and g-C_3N_4/MS were calculated by the following equation:

$$SSA = \frac{N_A A_{MB}(C_0 - C_e)V}{M_{MB} m_s}$$

Where N_A represents Avogadro's constant (6.02×10^{23} mol^{-1}), A_{MB} represents the covered area of per MB molecule (typically assumed to be 1.35 nm^2), C_o and C_e are the initial and equilibrium concentrations of MB, V is the volume of MB solution, M_{MB} is the relative molecular mass of MB, and m_s is the mass of the sample.

Evaluation of Photocatalytic Activity

The photocatalytic activity of g-C_3N_4/MS was evaluated in both gaseous systems. Photocatalytic removal of NO at ppb level was previously reported in details (Zhang et al., 2014). Typically, A 150 W metal halide lamp with a visible light filter (>420 nm) was employed to operate the experiment. A piece of g-C_3N_4/MS was put into the reactor for photocatalytic activity test. The light intensity is 35.88 mW cm^{-2} measured by a light intensity meter. The initial concentration of NO was diluted to 500 ppb by drying air. The flow rates of dry air and NO are set at 2 L min^{-1} and 9.5 mL min^{-1}, respectively. The formula of degradation rate of NO was counted by the following equation:

$$\omega\,(\%) = \frac{[C\,(NO_X) - C\,(NO) - C_0(NO_2)}{C\,(NO_X)} \times 100\%$$

Where C (NO_x) represents the concentration of total nitric oxide (NO_2 and NO), while C_0 is the initial concentration of NO_2 when reaching the adsorption-desorption equilibrium.

The photocatalytic reduction of CO_2 was performed in a 380 mL home-made reactor at ambient temperature and pressure. A 300 W Xe lamp was used as a light source and positioned 8 cm above the photocatalytic reactor. In a typical test, a plastic beaker with 20 mL deionized water was deposited at the bottom of the reactor, and a culture dish with 100 mg g-C_3N_4 powder or g-C_3N_4/MS (38.5 cm^2) was placed on the plastic beaker. Before irradiation, the reactor was sealed and vacuumed by a pump, then removed air by blowing argon for 15 min. Subsequently, 1 mL CO_2 was injected into the reactor. After 4 h irradiation, 1 mL of gas was taken out from the reactor and analyzed by using a gas chromatograph (Techcomp GC7900) equipped with a flame ionized detector (FID) and a thermal conductivity detector (TCD). CO and CH_4 were analyzed by the FID, and H_2 was analyzed by TCD.

RESULTS AND DISCUSSION

Fabrication and Physical Properties of g-C_3N_4/MS

The general preparation approach of g-C_3N_4/MS was illustrated in **Figure 1A**. Direct mixture of powdery g-C_3N_4 and MS is hard to gain a monolithic g-C_3N_4/MS with good particle dispersion and well contact between particle and MS skeleton. Therefore, the g-C_3N_4 powder was firstly added into water and sonicated for 30 min to form uniform suspension, which make the particle diffusion easy and fast in the porous structure of MS. Then, the pretreated MS was immersed into this suspension through dipping and squeezing procedures until MS was fully covered by g-C_3N_4 particles. Finally, followed by a conventional freezing-drying process, the monolithic g-C_3N_4/MS was obtained. Obviously, no large particles were observed on the cross-section photo in **Figure 1A**, indicating that the g-C_3N_4 powder was uniformly coated on MS skeleton. For comparison, we also dipped MS in a saturated solution of urea, which is the g-C_3N_4 precursor. After removing the water by freeze-drying, we attempted to fabricate the monolithic g-C_3N_4/MS by *in-situ* immobilizing approach at 550°C. However, the obtained monolithic composite became very fragile due to the carbonization of MS skeleton. Moreover, the g-C_3N_4 powder gathered on the composite surface with an inhomogeneous dispersion (Figure S1). The failed trial illustrated the mild ultrasonic-coating approach is superior to other methods for monolithic g-C_3N_4/MS fabrication. Importantly, the facile ultrasonic-coating approach developed here is also adapted to other porous supports, such as nickel foam, Al_2O_3 ceramic foam, glass fiber and polyester fiber, and the corresponding monolithic products of g-C_3N_4 are shown in Figure S2.

Physical properties of materials are pivotal to their practical application. As shown in **Figure 1B**, the monolithic g-C_3N_4/MS has an ultra-low density (11.5 mg cm^{-3}), which can stay on dog tail grass and remarkably lighter than that of reported BiOBr/reduced GOA (50 mg cm^{-3}) (Liu W. J. et al., 2015), TiO_2/graphene aerogel (19 mg cm^{-3}) (Qiu et al., 2014), and MoS_2/reduced GOA (56.1 mg cm^{-3}) (Zhang R. Y. et al., 2017). Moreover, SSA of g-C_3N_4/MS (7.6 m^2 g^{-1}) is much more larger than that of the pristine g-C_3N_4 (0.9 m^2 g^{-1}), which not only offer more active sites but also have larger absorption capacity than its powdery counterpart. In addition, facile modification of shapes and sizes endows g-C_3N_4/MS with a good flexibility to handle different situations in practical application (**Figures 1C,D**). More importantly, the g-C_3N_4/MS presents excellent elasticity. As revealed in **Figure 1E**, the g-C_3N_4/MS can instantaneously recover and maintain its integrity after removing of the heavy loading (410 g counterweight), suggesting that g-C_3N_4/MS possesses enough mechanical strength to deal with intricate operation in environmental abatement. To further ensure the firmness of g-C_3N_4 on MS skeletons, a test is carried

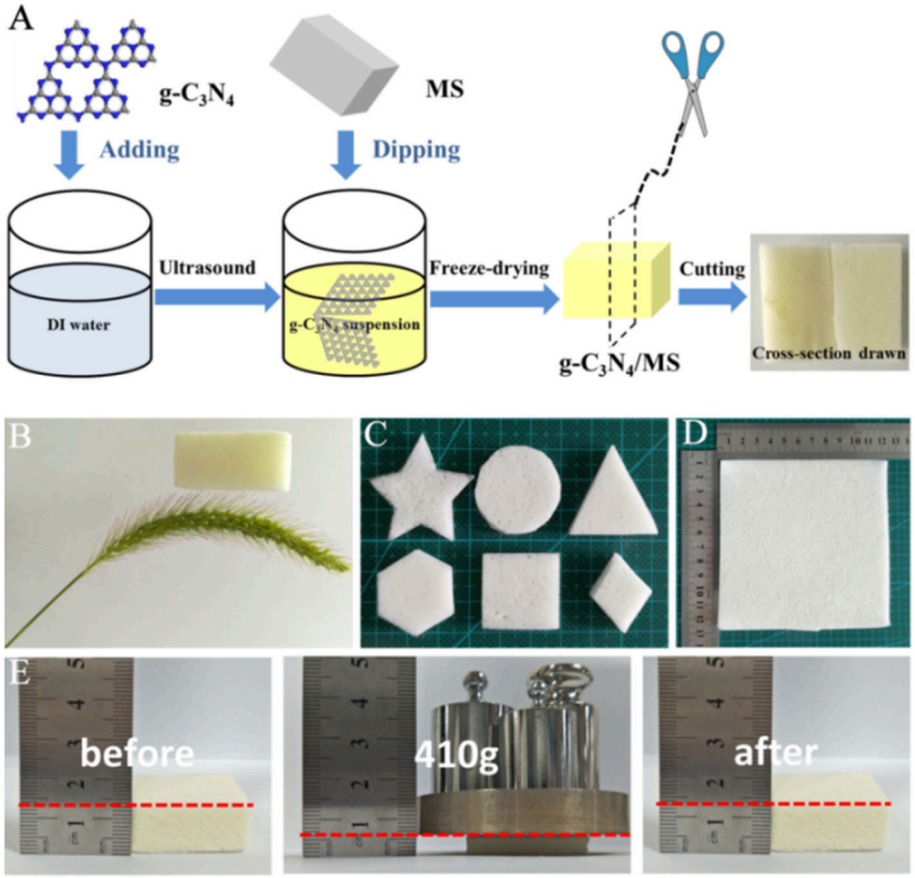

FIGURE 1 | (A) Preparation process of g-C_3N_4/MS photocatalyst; **(B)** Ultra-light g-C_3N_4/MS resting on dog tail grass; **(C)** g-C_3N_4/MS with various shapes; **(D)** g-C_3N_4/MS with large area (12.0 × 12.0 × 0.5 cm^3); **(E)** Mechanical property of g-C_3N_4/MS.

out by blowing the g-C_3N_4/MS with a strong airflow for 12 h, the detailed simulation device diagram is shown in Figure S3a. The dropping g-C_3N_4 powder from g-C_3N_4/MS is collected and weighted up. The final weight loss is less than 7.60 mg, which account for 1.15% of g-C_3N_4 loaded on MS skeletons (Figure S3b). The above result demonstrates that g-C_3N_4 is firmly distributed on MS even under extreme work condition, which is pivotal to the recycle in practical application.

Photocatalytic Activity

Benefit from the characteristics of low-density, high porosity and good elasticity, the monolithic g-C_3N_4/MS can be used to removal gaseous pollutants. Therefore, two different photocatalysis applications including NO removal, dye degradation, and CO_2 photoreduction, are selected to test the photocatalytic activity of the as-prepared monolithic g-C_3N_4/MS. NO, a typical air contaminants, mostly produced from the combustion of fossil fuels and the emission of vehicle exhaust, can cause a series of atmosphere pollution problems such as acid rain, photochemical smog and haze (Wang et al., 2016). Photo-oxidation technique is considered an alternative to remove NO at low concentration (Zhou et al., 2014). Therefore, the g-C_3N_4/MS samples are firstly investigated by NO removal at the indoor ppb level. **Figure 2A** shows the effect of g-C_3N_4 concentration on NO photo-removal ratio occurring on g-C_3N_4/MS. Notably, the MS coated with 5 mg mL^{-1} suspension achieves the highest removal ratio of 45% within 30 min. As the concentration of g-C_3N_4 suspension less than 5 mg mL^{-1}, the photocatalytic activity of g-C_3N_4/MS gradually enhanced with the increased concentration of g-C_3N_4 suspension. With a concentration higher than 5 mg mL^{-1}, the photocatalytic activity of the g-C_3N_4/MS slightly decreased, attributing to agglomeration of the excessive g-C_3N_4 which not only hinder the NO transport by blocking pore channels in MS, but also cause a reduced light transmittance. Moreover, the thicknesses of MS have also been investigated, which is closely associated with the light utilization. Benefit from the good transparence of MS, the activity of g-C_3N_4/MS enhanced along with increased MS thickness in **Figure 2B**, but the corresponding best unit mass rate constant (0.868 min^{-1} g^{-1}) of NO removal is belong to g-C_3N_4/MS with 0.5 cm thickness (As shown in Figure S4). Based on above results, the optimal concentration and thickness were fixed at 5 mg mL^{-1} and 0.5 cm, respectively.

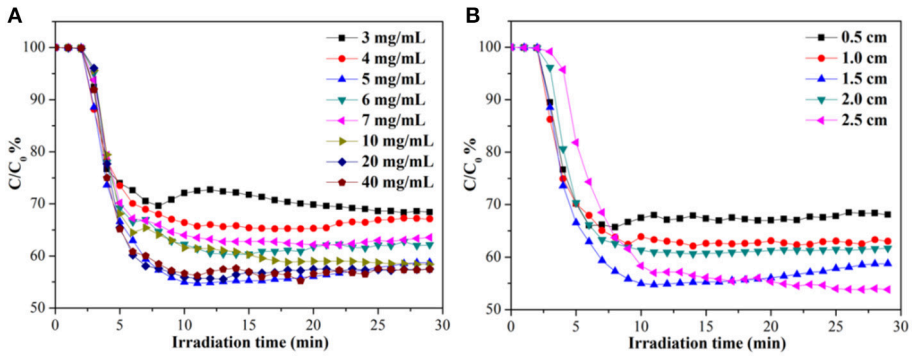

FIGURE 2 | Photocatalytic NO removal ratios in presence of g-C_3N_4/MS fabricated with **(A)** different concentrations and **(B)** different thicknesses under visible light irradiation.

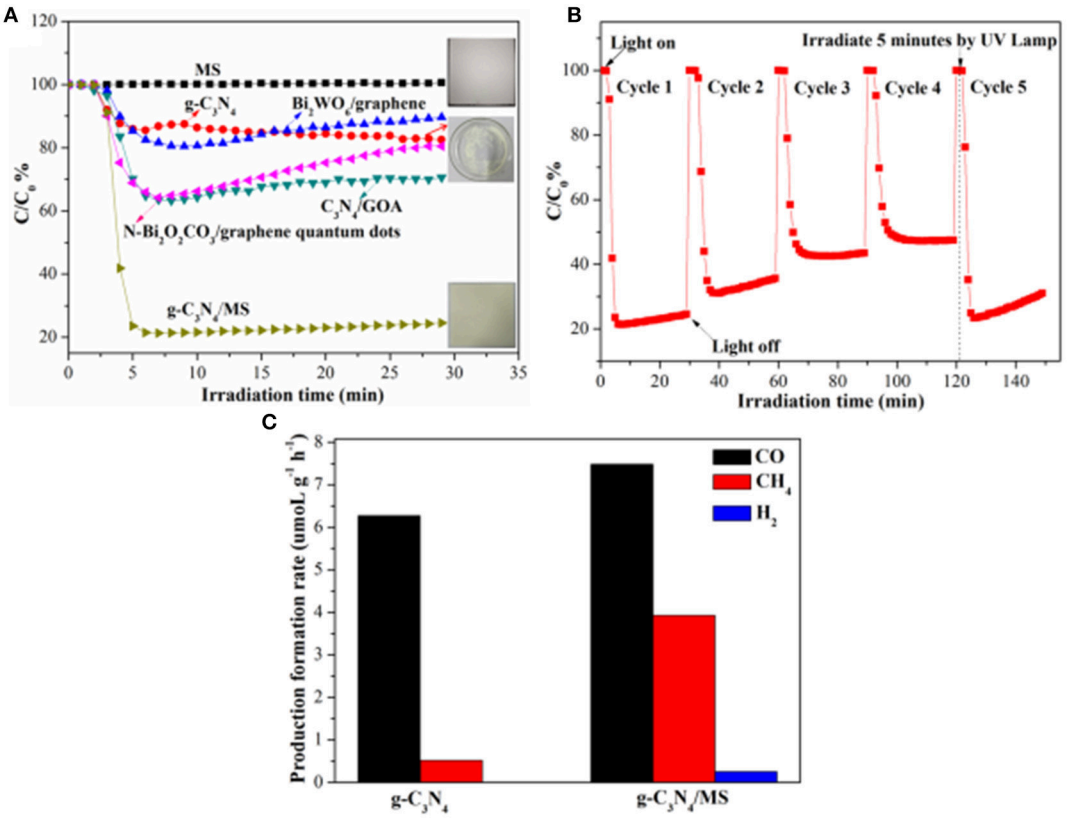

FIGURE 3 | Photocatalytic activity of g-C_3N_4/MS under visible-light irradiation: **(A)** NO removal ratios of different samples; **(B)** Photocatalytic recycling test on large area g-C_3N_4/MS; **(C)** Production rate of CO, CH_4 and H_2 on g-C_3N_4, g-C_3N_4/MS respectively in photocatalytic CO_2 reduction under UV-Vis light irradiation.

The fabrication and utilization of monolithic photocatalysts with large area on macro-scale is significant to their practical application. Therefore, a monolithic g-C_3N_4/MS with area of 12.0 × 12.0 cm^2 is prepared for further test of NO removal under visible-light illumination (**Figure 3A**). For comparison, the NO removal on powdery g-C_3N_4 and pristine MS are also performed under the same conditions, respectively. Surprisingly, monolithic g-C_3N_4/MS presents the highest NO removal ratio of 78.6% in initial 5 min which is about 4.5 times higher than that of powdery g-C_3N_4 (17.6%), while no NO removal occurs on the pristine MS. After initial 5 min, NO removal ratio of g-C_3N_4/MS tends to be steady, which could be interpreted as partial active sites replaced by adsorptive NO_3^- or NO (Ai et al., 2009; Huang et al., 2010; Liu et al., 2017) and finally reached an adsorption and desorption equilibrium of these oxynitrides. Moreover, comparison with other photocatalysts in our previous work, large area g-C_3N_4/MS exhibits optimum activity (78.6%), which is approximate 4.25, 2.25 and 2.32 times higher than

that of Bi_2WO_6/graphene (Zhou et al., 2014), C_3N_4/GOA (GOA) (Wan et al., 2016), and N-$Bi_2O_2CO_3$/graphene quantum dots (Liu et al., 2017), respectively. Notably, the fraction of generated NO_2 is lower than 5.4% over all our samples (as shown in Figure S5a), indicating those samples selectively oxidize NO to NO_3^- rather than NO_2. Based on above results, the g-C_3N_4/MS with large area shows obviously enhanced photocatalytic activity than its powdery counterpart, indicating the monolithic photocatalyst is an effective strategy to solve the problems encountered by powdery photocatalysts in large-scale application.

The stability and recyclability of photocatalysts are also important to their practical applications (Hu et al., 2017). Here, we carried out cycle and long-time tests to further evaluate the performance of the monolithic g-C_3N_4/MS. The result of cycle test is listed in **Figure 3B**. It can be seen that the NO removal ratio of g-C_3N_4/MS dropped quickly during the first two cycles. After that, the NO removal ratio approached to stabilization within third cycle and slightly decreased with incremental cycle-index, which attributed to temporary absorption equilibrium of oxynitrides (NO, NO_3^-) in third cycle and their continuous accumulation on g-C_3N_4/MS. Fortunately, after UV lamp irradiation for 5 min, the adsorbed oxynitrides are desorbed and results in an immediate recovery of sample activity (**Figure 3B**). Furthermore, result of long-time test is displayed in Figure S5b. The g-C_3N_4/MS can achieve a stable catalytic performance after 1 h and keep a relatively high activity in the 2 h test interval. All above results confirm that the large area g-C_3N_4/MS has a superior recyclability and stability for NO removal, confirming its potential in practical application.

Apart from the photo-oxidation availability, the monolithic g-C_3N_4/MS also exhibits good ability of CO_2 photoreduction. CO_2 is the main greenhouse gas that generation from human activity and the combustion of fossil fuels which is responsible for global warming (Norby and Luo, 2004). As displayed in **Figure 3C**, the g-C_3N_4/MS shows higher photocatalytic activity (7.48 μmol g^{-1} h^{-1} CO, 3.93 μmol g^{-1} h^{-1} CH_4 and 0.26 μmol g^{-1} h^{-1} H_2) than that of powdery g-C_3N_4 (6.27 μmol g^{-1} h^{-1} CO, 0.52 μmol g^{-1} h^{-1} CH_4 and 0 μmol g^{-1} h^{-1} H_2). Notably, yield of CO is higher than that of CH_4 on both two samples, because the conversion from CO_2 to CO is 4-electron process, whereas that from CO_2 to CH_4 is 8-electrons process, obviously, the former is easier than the latter which can account for higher yield of CO. No H_2 generated on g-C_3N_4 and traced H_2 appeared on g-C_3N_4/MS indicate that all samples have high selectivity for CO_2 reduction rather than H_2 reduction.

In view of above results of NO removal, and CO_2 photoreduction, the monolithic g-C_3N_4/MS does show practical potential in various applications and enhanced photocatalytic activity than its powdery counterpart. The large SAA must be responsible for this activity enhancement. However, to get a deep insight into the reasons of the improved performance, more investigations further carried out on the monolithic g-C_3N_4/MS.

Structure and Morphology

The PXRD patterns of MS, g-C_3N_4/MS, sonicated g-C_3N_4 and g-C_3N_4 are displayed in **Figure 4**. The peaks at ca. 13.1 and 27.3° can be assigned to (100) and (002) crystal planes of g-C_3N_4, respectively (Gholipour et al., 2016). Obviously, the PXRD patterns of g-C_3N_4 are consistent before and after ultrasonic process, confirming the crystal structure of g-C_3N_4 is very stable. Moreover, no difference is found in the PXRD patterns of g-C_3N_4/MS and MS, indicating the g-C_3N_4 particles are uniformly dispersed on the porous framework of MS rather than aggregated on its surface.

To reveal the microstructure and morphology of samples, TEM and SEM were conducted as shown in **Figure 5**. The TEM images of g-C_3N_4 and sonicated g-C_3N_4 show similar thin nano-flake structure with some mesopores (**Figures 5A,B**), which derived from gases releasing such as NH_3 and CO_2 during the pyrolysis of urea (Mao et al., 2013). Combination with PXRD results, it is sure no noticeable change appeared on the structure and morphology of g-C_3N_4 before and after the ultrasonic. In **Figure 5C**, the SEM image of MS reveals an interconnected 3D network structure with abundant open-cell pores, which not only offer sufficient channels for reactant transport, but also offer enough locations for photocatalyst particle dispersion. It is notable that the g-C_3N_4 was successfully coated on the smooth skeleton of MS according to the g-C_3N_4/MS image in **Figure 5D**. Based on the analysis of structure and morphology, the uniform dispersion of g-C_3N_4 achieves in monolithic g-C_3N_4/MS, confirming the feasibility of our coating strategy.

Figure 6 shows the FT-IR spectra of g-C_3N_4, g-C_3N_4/MS and MS. The spectrum of g-C_3N_4 displays typical peaks at 3000-3600 cm^{-1}, 1200-1700 cm^{-1}, and 811 cm^{-1}, which are ascribed to the vibrational absorption of N-H and O-H, CN heterocycles and triazine unit (Kang et al., 2015; Wei et al., 2016; Sun Z. X. et al., 2017). Moreover, in the spectrum of MS, the prominent

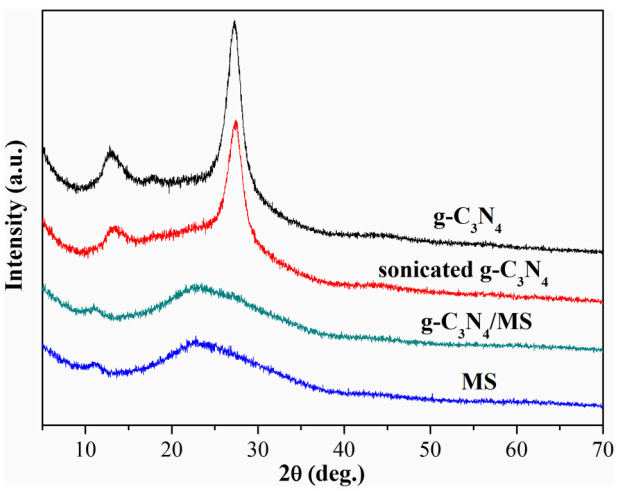

FIGURE 4 | PXRD patterns of g-C_3N_4, sonicated g-C_3N_4, g-C_3N_4/MS and MS.

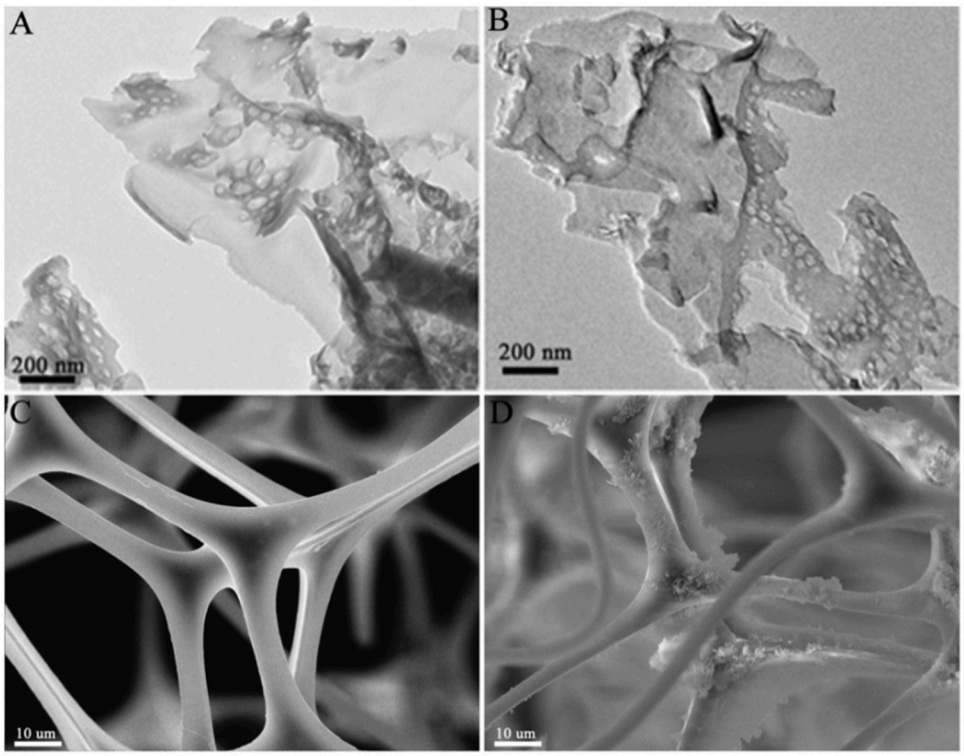

FIGURE 5 | TEM images of samples: **(A)** g-C_3N_4; **(B)** sonicated g-C_3N_4. SEM images of samples: **(C)** MS; **(D)** g-C_3N_4/MS.

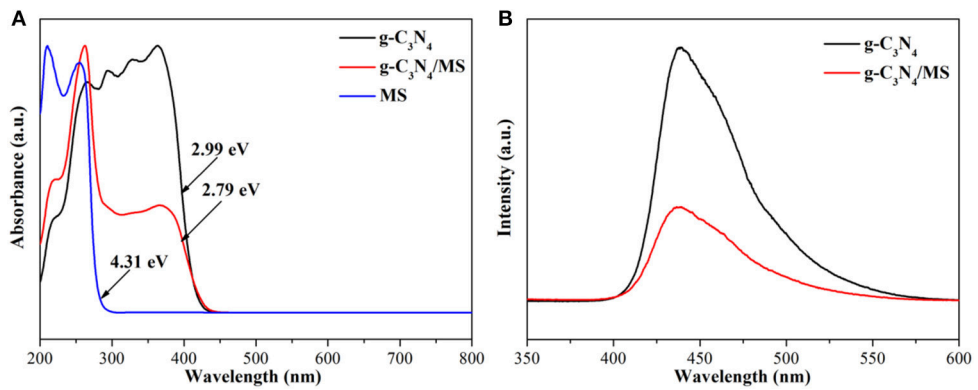

FIGURE 7 | (A) UV-vis DRS of g-C3N4, g-C3N4/MS and MS; **(B)** PL spectra of g-C3N4, g-C3N4/MS.

peaks located at 808, 1154, 1545, and 3422 cm^{-1}, attributing to triazine ring bending, C-O stretching, C=N stretching and N-H stretching, while peaks centered at 988, 1329, and 1466 cm^{-1} corresponding to C-H bending vibrations (Pham and Dickerson, 2014; Zhang W. B. et al., 2017). Particularly, a new peak and an intensive peak appeared at 1334 cm^{-1} and 813 cm^{-1} in g-C_3N_4/MS spectrum, indicating a weak chemical interaction exists between g-C_3N_4 and MS skeletons. The above results reveal both van der waals and chemical interactions between g-C_3N_4 and MS, which explain the good firmness of monolithic g-C_3N_4/MS.

Band Structure and Photocatalytic Mechanism

The band gap of MS, g-C_3N_4 and g-C_3N_4/MS were determined by the results of UV-vis DRS in **Figure 7A**. Obviously, g-C_3N_4 absorption is located in visible region with a calculated band gap of 2.99 eV, while MS shows only UV light absorption with a wide band gap of 4.31 eV. Moreover, the DRS profile of the g-C_3N_4/MS exhibits a mechanical combination of the absorption features of the g-C_3N_4 and MS alone. Importantly, visible-light absorption of g-C_3N_4/MS gets a slight enhancement (2.79 eV), which may be attributed to the light multistage

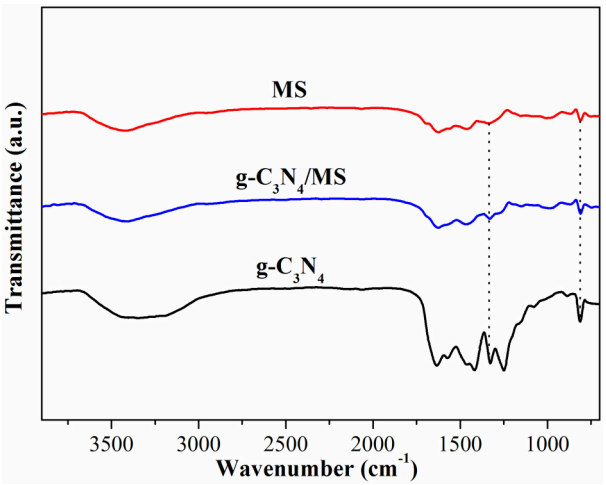

FIGURE 6 | FTIR spectra of g-C3N4, g-C3N4/MS and MS.

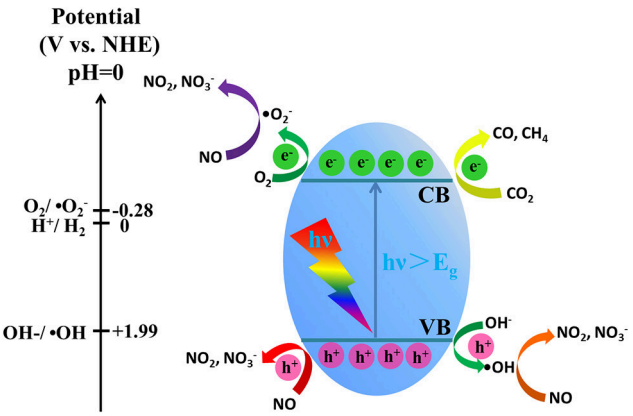

FIGURE 8 | Schematic illustration of the photocatalytic process over the g-C3N4/MS.

refraction and reflection on the MS framework (Dong et al., 2014b). In addition, the g-C_3N_4/MS not only enhances the light absorption, but also significantly suppresses the recombination of photo-generated carriers according to photoluminescence (PL) spectra in **Figure 7B**, which accounts for the enhancement of photocatalytic activity.

According to the above UV-vis DRS analysis (**Figure 7A**) and the XPS valence band spectrum (Figure S6), the band structure of g-C_3N_4/MS is proposed in **Figure 8** with VB edge and CB edge located at 2.01 and −0.98 eV, respectively. As shown in **Figure 8**, the potential of VB holes (h^+) is slight positive than OH^-/OH (1.99 eV), while the potential of CB electron (e^-) is much negative than that of O_2/O_2^- (−0.28 eV). Therefore, the photogenerated holes can directly oxidize OH^- to OH, and the photogenerated electrons can reduce easily O_2 to O_2^-. It is well known that OH and O_2^- usually have strong oxidative ability and play the key role in photocatalytic oxidation reaction (Huang et al., 2015b,c, 2017b). Moreover, in consideration of the oxidation potentials of NO_2/NO (1.03 eV), HNO_2/NO (0.99 eV), HNO_3/NO (0.94 eV) (Wan et al., 2016), all OH, O_2^- and hole generated on g-C_3N_4/MS are able to remove NO. In addition, the reduction potentials of E (CO_2/CH_4), E (CO_2/CO) and E (H_2O/H_2) were located at −0.24, −0.52, and −0.41 eV, respectively (Yu et al., 2014; Han B. et al., 2015). Comparison with CB potential (−0.98 eV), the photogenerated electron is capable of reducing CO_2 on g-C_3N_4/MS. Based on above analyses and the results in photocatalytic activity part, the possible photocatalytic mechanism are simply illustrated in **Figure 8**. In short, there are three main pathways for NO removal, involving three different active oxidation species (OH, O_2^- and h^+), while there is one pathway for CO_2 photoreduction, involving only one active species (e^-).

CONCLUSIONS

In summary, a novel monolithic g-C_3N_4/MS was fabricated by a facile ultrasonic-coating method. This monolithic g-C_3N_4/MS possesses a uniform dispersion of g-C_3N_4 and large SSA, which not only facilitate exposing more active sites of g-C_3N_4 but also enhancing the visible-light absorption. Consequently, monolithic g-C_3N_4/MS shows obviously improved visible-light photocatalytic activity. The PL detection further reveals that enhanced separation of photogenerated carriers is also responsible for the activity enhancement. More importantly, the characteristics of low-density and high porosity allow the monolithic g-C_3N_4/MS to be applied in various environmental issues, while the high elasticity, good firmness, and mechanical strength give it noticeable recyclability and stability, confirming its feasibility for practical application. All in all, in this work, we fabricated a monolithic g-C_3N_4/MS with enhanced photocatalytic activity which can be easy to achieve large-scale production for practical photocatalysis application. Our results provide a low-cost and mild method for mass production of new monolithic photocatalysts.

AUTHOR CONTRIBUTIONS

YY: Partly designed the experiments and wrote the manuscript; RZ, TR, and WW: Assisted in the analysis and interpretation of the data; YZ and QZ: Proposed the project, designed the experiment, and wrote the manuscript.

ACKNOWLEDGMENTS

We gratefully acknowledge financial support from the Sichuan Provincial International Cooperation Project (2017HH0030), National Natural Science Foundation of China (21403172) and the Innovative Research Team of Sichuan Province (2016TD0011).

SUPPLEMENTARY MATERIAL

The Supplementary Material for this article can be found online at: https://www.frontiersin.org/articles/10.3389/fchem.2018.00156/full#supplementary-material

REFERENCES

Ai, Z. H., Ho, W. K., Lee, S. C., and Zhang, L. Z. (2009). Efficient photocatalytic removal of NO in indoor air with hierarchical bismuth oxybromide nanoplate microspheres under visible light. *Environ. Sci. Technol.* 43, 4143–4150. doi: 10.1021/es9004366

Cheng, F. X., Wang, H. N., and Dong, X. P. (2015). The amphoteric properties of g-C_3N_4 nanosheets and fabrication of their relevant heterostructure photocatalysts by an electrostatic re-assembly route. *Chem. Commun.* 51, 7176–7179. doi: 10.1039/C5CC01035G

Cheng, W., Rechberger, F., and Niederberger, M. (2016). From 1D to 3D–macroscopic nanowire aerogel monoliths. *Nanoscale* 8, 14074–14077. doi: 10.1039/C6NR04429H

Cui, C., Li, S., Qiu, Y. W., Hu, H. H., Li, X. Y., and Li, C. R. (2017). Fast assembly of Ag_3PO_4 nanoparticles within three-dimensional graphene aerogels for efficient photocatalytic oxygen evolution from water splitting under visible light. *Appl. Catal. B Environ.* 200, 666–672. doi: 10.1016/j.apcatb.2016.07.056

Dong, F., Ou, M. Y., Jiang, Y. K., Guo, S., and Wu, Z. B. (2014a). Efficient and durable visible light photocatalytic performance of porous carbon nitride nanosheets for air purification. *Ind. Eng. Chem. Res.* 53, 2318–2330. doi: 10.1021/ie4038104

Dong, F., Wang, Z. Y., Li, Y. H., Ho, W. K., and Lee, S. C. (2014b). Immobilization of polymeric g-C_3N_4 on structured ceramic foam for efficient visible light photocatalytic air purification with real indoor illumination. *Environ. Sci. Technol.* 48, 10345–10353. doi: 10.1021/es502290f

Fan, Y., Ma, W., Han, D., Gan, S., Dong, X., and Niu, L. (2015). Convenient recycling of 3D AgX/graphene aerogels (X= Br, Cl) for efficient photocatalytic degradation of water pollutants. *Adv. Mater.* 27, 3767–3773. doi: 10.1002/adma.201500391

Gholipour, M. R., Béland, F., and Do, T. O. (2016). Post-calcined carbon nitride nanosheets as an efficient photocatalyst for hydrogen production under visible light irradiation. *ACS Sustain. Chem. Eng.* 5, 213–220. doi: 10.1021/acssuschemeng.6b01282

Han, B., Wei, W., Chang, L., Cheng, P. F., and Hu, Y. H. (2015). Efficient visible light photocatalytic CO_2 reforming of CH_4. *ACS Catal.* 6, 494–497. doi: 10.1021/acscatal.5b02653

Han, Q., Wang, B., Zhao, Y., Hu, C., and Qu, L. (2015). A Graphitic-C_3N_4"Seaweed" architecture for enhanced hydrogen evolution. *Angew. Chem. Int. Ed.* 54, 11433–11437. doi: 10.1002/anie.201504985

Hossain, S. T., and Mukherjee, S. K. (2013). Toxicity of cadmium sulfide (CdS) nanoparticles against *Escherichia coli* and HeLa cells. *J. Hazard. Mater.* 260, 1073–1082. doi: 10.1016/j.jhazmat.2013.07.005

Hou, Y., Zuo, F., Dagg, A. P., Liu, J. K., and Feng, P. Y. (2014). Branched WO_3 nanosheet array with layered C_3N_4 heterojunctions and CoOx nanoparticles asa flexible photoanode for efficient photoelectrochemical water oxidation. *Adv. Mater.* 26, 5043–5049. doi: 10.1002/adma.201401032

Hu, J. D., Chen, D. Y., Li, N. J., Xu, Q. F., Li, H., He, J. H., et al. (2017). *In situ* fabrication of $Bi_2O_2CO_3/MoS_2$ on carbon nanofibers for efficient photocatalytic removal of NO under visible-light irradiation. *Appl. Catal. B Environ.* 217, 224–231. doi: 10.1016/j.apcatb.2017.05.088

Huang, H. W., Han, X., Li, X., Wang, S., Chu, P. K., and Zhang, Y. (2015a). Fabrication of multiple heterojunctions with tunable visible-light-active photocatalytic reactivity in BiOBr–BiOI full-range composites based on microstructure modulation and band structures. *ACS Appl. Mater. Interfaces* 7, 482–492. doi: 10.1021/am5065409

Huang, H. W., He, Y., Lin, Z. S., Kang, L., and Zhang, Y. H. (2013). Two novel Bi-based borate photocatalysts: crystal structure, electronic structure, photoelectrochemical properties, and photocatalytic activity under simulated solar light irradiation. *J. Phys. Chem. C* 117, 22986–22994. doi: 10.1021/jp4084184

Huang, H. W., He, Y., Li, X. W., Li, M., Zeng, C., Dong, F., et al. (2015b). $Bi_2O_2(OH)(NO_3)$ as a desirable $[Bi_2O_2]^{2+}$ layered photocatalyst: strong intrinsic polarity, rational band structure and {001} active facets co-beneficial for robust photooxidation capability. *J. Mater. Chem. A* 3, 24547–24556. doi: 10.1039/C5TA07655B

Huang, H. W., Li, X. W., Wang, J. J., Dong, F., Chu, P. K., Zhang, T. R., et al. (2015c). Anionic group self-doping as a promising strategy: band-gap engineering and multi-functional applications of high-performance CO_3^{2-} doped $Bi_2O_2CO_3$. *ACS Catal.* 5, 4094–4103. doi: 10.1021/acscatal.5b00444

Huang, H. W., Xiao, K., He, Y., Zhang, T. R., Dong, F., Du, X., et al. (2016). *In situ* assembly of $BiOI@Bi_{12}O_{17}Cl_2$ p-n junction: charge induced unique front-lateral surfaces coupling heterostructure with high exposure of BiOI {001} active facets for robust and nonselective photocatalysis. *Appl. Catal. B Environ.* 199, 75–86. doi: 10.1016/j.apcatb.2016.06.020

Huang, H. W., Tu, S. C., Zeng, C., Zhang, T. R., Reshak, A. H., and Zhang, Y. H. (2017a). Macroscopic polarization enhancement promoting photo$^-$ and piezoelectric$^-$ induced charge separation and molecular oxygen activation. *Angew. Chem.* 39, 12022–12026. doi: 10.1002/ange.201706549

Huang, H. W., Xiao, K., Zhang, T. R., Dong, F., and Zhang, Y. H. (2017b). Rational design on 3D hierarchical bismuth oxyiodides via *in situ* self-template phase transformation and phase-junction construction for optimizing photocatalysis against diverse contaminants. *Appl. Catal. B Environ.* 203, 879–888. doi: 10.1016/j.apcatb.2016.10.082

Huang, Y., Ai, Z. H., Ho, W. K., Chen, M. J., and Lee, S. C. (2010). Ultrasonic spray pyrolysis synthesis of porous Bi_2WO_6 microspheres and their visible-light-induced photocatalytic removal of NO. *J. Phys. Chem. C* 114, 6342–6349. doi: 10.1021/jp912201h

Kang, S. F., Fang, Y., Huang, Y. K., Cui, L. F., Wang, Y. Z., Qin, H. F., et al. (2015). Critical influence of g-C_3N_4 self-assembly coating on the photocatalytic activity and stability of Ag/AgCl microspheres under visible light. *Appl. Catal. B Environ.* 168, 472–482. doi: 10.1016/j.apcatb.2015.01.002

Li, P. H., Wang, F., Wei, S. Q., Li, X. Y., and Zhou, Y. (2017). Mechanistic insights into CO_2 reduction on Cu/Mo-loaded two-dimensional g-C_3N_4 (001). *Phys. Chem. Chem. Phys.* 19, 4405–4410. doi: 10.1039/C6CP08409E

Liang, Q., Li, Z., Yu, X., Huang, Z. H., Kang, F., and Yang, Q. H. (2015). Macroscopic 3D porous graphitic carbon nitride monolith for enhanced photocatalytic hydrogen evolution. *Adv. Mater.* 27, 4634–4639. doi: 10.1002/adma.201502057

Lin, Z. Y., Li, J. L., Zheng, Z. Q., Li, L. H., Yu, L. L., Wang, C. X., et al. (2016). A floating sheet for efficient photocatalytic water splitting. *Adv. Energy Mater.* 6:1600510. doi: 10.1002/aenm.201600510

Liu, G., Niu, P., Sun, C. H., Smith, S. C., Chen, Z. G., Lu, G. Q., et al. (2010). Unique electronic structure induced high photoreactivity of sulfur-doped graphitic C_3N_4. *J. Am. Chem. Soc.* 132, 11642–11648. doi: 10.1021/ja103798k

Liu, G., Zhao, Y. N., Sun, C. H., Li, F., Lu, G. Q., and Cheng, H. M. (2008). Synergistic effects of B/N doping on the visible-light photocatalytic activity of mesoporous TiO_2. *Angew. Chem. Int. Ed.* 47, 4516–4520. doi: 10.1002/anie.200705633

Liu, J. H., Zhang, T. K., Wang, Z. C., Dawson, G., and Chen, W. (2011). Simple pyrolysis of urea into graphitic carbon nitride with recyclable adsorption and photocatalytic activity. *J. Mater. Chem.* 21, 14398–14401. doi: 10.1039/c1jm12620b

Liu, T. T., Zhao, G. Z., Zhang, W. H., Chi, H. J., Hou, C. L., and Sun, Y. Y. (2015). The preparation of superhydrophobic graphene/melamine composite sponge applied in treatment of oil pollution. *J. Porous Mater.* 22, 1573–1580. doi: 10.1007/s10934-015-0040-8

Liu, W. J., Cai, J. Y., and Li, Z. H. (2015). Self-assembly of semiconductor nanoparticles/reduced graphene oxide (RGO) composite aerogels for enhanced photocatalytic performance and facile recycling in aqueous photocatalysis. *ACS Sustain. Chem. Eng.* 3, 277–282. doi: 10.1021/sc5006473

Liu, Y., Yu, S., Zhao, Z. Y., Dong, F., Dong, X. A., and Zhou, Y. (2017). N-Doped $Bi_2O_2CO_3$/graphene quantum dot composite photocatalyst: enhanced visible-light photocatalytic no oxidation and in situ drifts studies. *J. Phys. Chem. C* 121, 12168–12177. doi: 10.1021/acs.jpcc.7b02285

Maggos, T., Bartzis, J. G., Leva, P., and Kotzias, D. (2007). Application of photocatalytic technology for NOx removal. *Appl. Phys. A* 89, 81–84. doi: 10.1007/s00339-007-4033-6

Mao, J., Peng, T. Y., Zhang, X. H., Li, K., Ye, L. Q., and Zan, L. (2013). Effect of graphitic carbon nitride microstructures on the activity and selectivity of photocatalytic CO_2 reduction under visible light. *Catal. Sci. Technol.* 3, 1253–1260. doi: 10.1039/c3cy20822b

Norby, R. J., and Luo, Y. Q. (2004). Evaluating ecosystem responses to rising atmospheric CO_2 and global warming in a multi-factor world. *New Phytol.* 162, 281–293. doi: 10.1111/j.1469-8137.2004.01047.x

Pham, V. H., and Dickerson, J. H. (2014). Superhydrophobic silanized melamine sponges as high efficiency oil absorbent materials. *ACS Appl. Mater. Interfaces* 6, 14181–14188. doi: 10.1021/am503503m

Qiu, B. C., Xing, M. Y., and Zhang, J. L. (2014). Mesoporous TiO_2 nanocrystals grown in situ on graphene aerogels for high photocatalysis and lithium-ion batteries. *J. Am. Chem. Soc.* 136, 5852–5855. doi: 10.1021/ja500873u

Sun, H., Zhou, X. Z., Zhang, H. Z., and Tu, W. X. (2017). An efficient exfoliationmethod to obtain graphitic carbon nitride nanosheets with superior visible-light photocatalytic activity. *Int. J. Hydrogen Energy* 42, 7930–7937. doi: 10.1016/j.ijhydene.2016.12.080

Sun, Z. X., Fischer, J. M. T. A., Li, Q., Hu, J., Tang, Q. J., Wang, H. Q., et al. (2017). Enhanced CO_2 photocatalytic reduction on alkali-decorated graphitic carbon nitride. *Appl. Catal. B Environ.* 216, 146–155. doi: 10.1016/j.apcatb.2017.05.064

Tang, L., Jia, C. T., Xue, Y. C., Li, L., Wang, A. Q., Xu, G., et al. (2017). Fabrication of compressible and recyclable macroscopic g-C_3N_4/GO aerogel hybrids for visible-light harvesting: a promising strategy for water remediation. *Appl. Catal. B Environ.* 219, 241–248. doi: 10.1016/j.apcatb.2017.07.053

Tran, D. N. H., Kabiri, S., Sim, T. R., and Losic, D. (2015). Selective adsorption of oil-water mixtures using polydimethylsiloxane (PDMS)-graphene sponges. *Environ. Sci. Water Res. Technol.* 1, 298–305. doi: 10.1039/C5EW00035A

Wan, W. C., Yu, S., Dong, F., Zhang, Q., and Zhou, Y. (2016). Efficient C_3N_4/graphene oxide macroscopic aerogel visible-light photocatalyst. *J. Mater. Chem. A* 4, 7823–7829. doi: 10.1039/C6TA01804A

Wan, W. C., Zhang, R. Y., Ma, M. Z., and Zhou, Y. (2018). Monolithic aerogel photocatalysts: a review. *J. Mater. Chem. A* 6, 754–775. doi: 10.1039/C7TA09227J

Wang, X., Maeda, K., Thomas, A., Takanabe, K., Xin, G., Carlsson, J. M., et al. (2009). A metal-free polymeric photocatalyst for hydrogen production from water under visible light. *Nat. Mater.* 8, 76–80. doi: 10.1038/nmat2317

Wang, X., Liang, Y. H., An, W. J., Hu, J. S., Zhu, Y. F., and Cui, W. Q. (2017). Removal of chromium (VI) by a self-regenerating and metal free g-C_3N_4/graphene hydrogel system via the synergy of adsorption and photo-catalysis under visible light. *Appl. Catal. B Environ.* 219, 53–62. doi: 10.1016/j.apcatb.2017.07.008

Wang, Y. L., Cui, X. B., Yang, Q. Y., Liu, J., Gao, Y., Sun, P., et al. (2016). Preparation of Ag-loaded mesoporous WO_3 and its enhanced NO_2 sensing performance. *Sensors Actuat. B* 225, 544–552. doi: 10.1016/j.snb.2015.11.065

Wei, H. T., Zhang, Q., Zhang, Y. C., Yang, Z. J., Zhu, A. P., and Dionysiou, D. D. (2016). Enhancement of the Cr (VI) adsorption and photocatalytic reduction activity of g-C_3N_4 by hydrothermal treatment in HNO_3 aqueous solution[J]. *Appl. Catal. A General* 521, 9–18. doi: 10.1016/j.apcata.2015.11.005

Yan, S. C., Li, Z. S., and Zou, Z. G. (2009). Photodegradation performance of g-C_3N_4 fabricated by directly heating melamine. *Langmuir* 25, 10397–10401. doi: 10.1021/la900923z

Yang, L. Q., Huang, J. F., Shi, L., Gao, L. Y., Yu, Q., Jie, Y. N., et al. (2017). A surface modification resultant thermally oxidized porous g-C_3N_4 with enhanced photocatalytic hydrogen production. *Appl. Catal. B Environ.* 204, 335–345. doi: 10.1016/j.apcatb.2016.11.047

Yu, J. G., Jin, J., Cheng, B., and Jaroniec, M. (2014). A noble metal-free reduced graphene oxide-CdS nanorod composite for the enhanced visible-light photocatalytic reduction of CO_2 to solar fuel. *J. Mater. Chem. A* 2, 3407–3416. doi: 10.1039/c3ta14493c

Zhang, Q., Zhou, Y., Wang, F., Dong, F., Li, W., Li, H. M., et al. (2014). From semiconductors to semimetals: bismuth as a photocatalyst for NO oxidation in air. *J. Mater. Chem. A* 2, 11065–11072. doi: 10.1039/C4TA01339E

Zhang, R. Y., Wan, W. C., Li, D. W., Dong, F., and Zhou, Y. (2017). Three-dimensional MoS_2/reduced graphene oxide aerogel as a macroscopic visible-light photocatalyst. *Chin. J. Catal.* 38, 313–320. doi: 10.1016/S1872-2067(16)62568-8

Zhang, W. B., Zhai, X. L., Xiang, T. H., Zhou, M., Zang, D. L., Gao, Z. X., et al. (2017). Superhydrophobic melamine sponge with excellent surface selectivity and fire retardancy for oil absorption. *J. Mater. Sci.* 52, 73–85. doi: 10.1007/s10853-016-0235-7

Zhao, J., Guo, Q. J., Wang, X., Xie, H. L., and Chen, Y. Z. (2016). Recycle and reusable melamine sponge coated by graphene for highly efficient oil-absorption. *Colloid Surface A* 488, 93–99. doi: 10.1016/j.colsurfa.2015.09.048

Zhao, S. S., Chen, S., Yu, H. T., and Quan, X. (2012). g-C_3N_4/TiO_2 hybrid photocatalyst with wide absorption wavelength range and effective photogenerated charge separation. *Sep. Purif. Technol.* 99, 50–54. doi: 10.1016/j.seppur.2012.08.024

Zhao, Z., Sun, Y., and Dong, F. (2015). Graphitic carbon nitride based nanocomposites: a review. *Nanoscale* 7, 15–37. doi: 10.1039/C4NR03008G

Zhou, Y., Zhang, X. J., Zhang, Q., Dong, F., Wang, F., and Xiong, Z. (2014). Role of graphene on the band structure and interfacial interaction of Bi_2WO_6/graphene composites with enhanced photocatalytic oxidation of NO. *J. Mater. Chem. A* 2, 16623–16631. doi: 10.1039/C4TA03762F

Zhou, Y., Zhao, Z. Y., Wang, F., Cao, K., Doronkin, D. E., Dong, F., et al. (2016). Facile synthesis of surface N-doped $Bi_2O_2CO_3$: origin of visible light photocatalytic activity and in situ DRIFTS studies. *J. Hazard. Mater.* 307, 163–172. doi: 10.1016/j.jhazmat.2015.12.072

Conflict of Interest Statement: The authors declare that the research was conducted in the absence of any commercial or financial relationships that could be construed as a potential conflict of interest.

frontiers in Chemistry

ORIGINAL RESEARCH
published: 18 April 2018
doi: 10.3389/fchem.2018.00123

Insights Into Highly Improved Solar-Driven Photocatalytic Oxygen Evolution Over Integrated Ag_3PO_4/MoS_2 Heterostructures

Xingkai Cui[1], Xiaofei Yang[1,2,3], Xiaozhai Xian[1], Lin Tian[1], Hua Tang[1] and Qinqin Liu[1]**

[1] School of Materials Science and Engineering, Jiangsu University, Zhenjiang, China, [2] College of Science, Nanjing Forestry University, Nanjing, China, [3] State Key Laboratory of Photocatalysis on Energy and Environment, Fuzhou University, Fuzhou, China

OPEN ACCESS

Edited by:
Fan Dong,
Chongqing Technology and Business University, China

Reviewed by:
Kangle Lv,
South-Central University for Nationalities, China
Yanhui Ao,
Hohai University, China
Shichao Tian,
Research Institute of Tsinghua University in Shenzhen, China

***Correspondence:**
Xiaofei Yang
xiaofei_yang1980@163.com;
xiaofei.yang@njfu.edu.cn
Qinqin Liu
liu_qin_qin@126.com

Specialty section:
This article was submitted to Catalysis and Photocatalysis, a section of the journal Frontiers in Chemistry

Received: 13 March 2018
Accepted: 03 April 2018
Published: 18 April 2018

Citation:
Cui X, Yang X, Xian X, Tian L, Tang H and Liu Q (2018) Insights Into Highly Improved Solar-Driven Photocatalytic Oxygen Evolution Over Integrated Ag_3PO_4/MoS_2 Heterostructures Front. Chem. 6:123. doi: 10.3389/fchem.2018.00123

Oxygen evolution has been considered as the rate-determining step in photocatalytic water splitting due to its sluggish four-electron half-reaction rate, the development of oxygen-evolving photocatalysts with well-defined morphologies and superior interfacial contact is highly important for achieving high-performance solar water splitting. Herein, we report the fabrication of Ag_3PO_4/MoS_2 nanocomposites and, for the first time, their use in photocatalytic water splitting into oxygen under LED light illumination. Ag_3PO_4 nanoparticles were found to be anchored evenly on the surface of MoS_2 nanosheets, confirming an efficient hybridization of two semiconductor materials. A maximum oxygen-generating rate of 201.6 $\mu mol \cdot L^{-1} \cdot g^{-1} \cdot h^{-1}$ was determined when 200 mg MoS_2 nanosheets were incorporated into Ag_3PO_4 nanoparticles, which is around 5 times higher than that of bulk Ag_3PO_4. Obvious enhancements in light-harvesting property, as well as electron-hole separation and charge transportation are revealed by the combination of different characterizations. ESR analysis verified that more active oxygen-containing radicals generate over illuminated Ag_3PO_4/MoS_2 composite photocatalysts rather than irradiated Ag_3PO_4. The improvement in oxygen evolution performance of Ag_3PO_4/MoS_2 composite photocatalysts is ascribed to wide spectra response in the visible-light region, more efficient charge separation, and enhanced oxidation capacity in the valence band (VB). This study provides new insights into the design and development of novel composite photocatalytic materials for solar-to-fuel conversion.

Keywords: Ag_3PO_4, MoS_2, composite photocatalyst, oxygen evolution, water splitting, Z-scheme

INTRODUCTION

Inspired by natural photosynthesis, the construction of visible-light-responsive functional semiconducting materials for highly efficient photocatalytic water splitting and reduction of CO_2 has drawn considerable attention over the past few years (Maeda and Domen, 2010; Mikkelsen et al., 2010; Takanabe, 2017; Zheng et al., 2017). Especially, water splitting into hydrogen and oxygen has been intensively investigated due to the nature of clean and sustainable solar-to-fuel conversion. Compared with the hydrogen evolution reaction (HER), four-electron water oxidation process is more difficult to be fulfilled since a higher potential more than 1.23 eV is required

(Kudo and Miseki, 2009), mostly an overpotential is also required. Thus, oxygen evolution is considered as the rate-determining step in photocatalytic overall water splitting process. So far only few semiconductors such as WO_3, $BiVO_4$, have been employed as photocatalysts for oxygen production from water splitting (Xin et al., 2009; Wu et al., 2016; Zeng et al., 2017; He et al., 2018). Due to the limitations of band structures and light-harvesting properties in the visible light region, the utilization of sing-component semiconductors as catalysts for oxygen evolution has encountered serious difficulties, the design and development of novel composite materials for solar-driven photocatalytic water splitting are highly desirable.

Since the pioneer work of silver phosphate (Ag_3PO_4) semiconductor for photocatalytic applications in 2010 (Yi et al., 2010). Many efforts have been devoted to synthesize Ag_3PO_4 photocatalysts with different nanostructures and a variety of Ag_3PO_4-based composite photocatalytic materials for energy and environmental applications (Bi et al., 2012; Wang et al., 2012; Hu et al., 2013; Cao et al., 2017). Nanostructure engineering of pristine Ag_3PO_4 and hybridization of Ag_3PO_4 with other semiconductors have been proven to offer superior advantages in light absorption, electron-hole separation and charge transportation, resulting in the enhancement in the photocatalytic activity (Yang et al., 2015b; Lv et al., 2016; Wang et al., 2017; Zhou et al., 2018). The key to synthesizing highly efficient Ag_3PO_4-based composite photocatalysts lies in screening promising candidates with matched band structures and constructing heterojunctions with optimal morphologies and interfaces, where favorable visible light utilization and tandem charge transfer pathway should be taken into consideration. The past decades have witnessed the use of molybdenum disulfide (MoS_2), a 2D lamellar material with excellent conductive property, as electrocatalysts and photocatalysts for applications in electrochemical and solar-to-fuel conversion (Xiang et al., 2012; Dai et al., 2017; Yang et al., 2017). It was confirmed that the combination of MoS_2 with functional semiconductors enabled obvious enhancements in both photocatalytic and electrocatalytic hydrogen production activity (Sun et al., 2016; Zhang et al., 2016; Iqbal et al., 2017; Yuan et al., 2017). The hybridization of MoS_2 with Ag_3PO_4 to produce MoS_2/Ag_3PO_4 composite materials has been primarily explored, however the application is restricted to the photodegradation of different kinds of organic pollutants (Wang L. et al., 2015; Wang P. F. et al., 2015; Gyawali and Lee, 2016; Li et al., 2016; Zhu et al., 2016; Wan et al., 2017), the employment of MoS_2/Ag_3PO_4 nanocomposites as photocatalysts for solar-light-driven oxygen evolution from water splitting has not yet been explored.

Most recently, we reported the *in-situ* deposition of Ag_3PO_4 on graphitic carbon nitride (g-C_3N_4) nanostructures for highly efficient Z-scheme oxygen evolution from water splitting (Yang et al., 2015a,c; Cui et al., 2018; Tian et al., 2018). In consideration of the matched band structures of bulk Ag_3PO_4 and MoS_2 materials for redox reactions, in this work, we demonstrate the hybridization of oxygen-producing photocatalyst Ag_3PO_4 with few-layered, two-dimensional MoS_2 nanosheets, and the use of Ag_3PO_4/MoS_2 nanocomposites for photocatalytic water oxidation under LED illumination. As-prepared hybrid materials exhibit well-organized nanostructures, in which sheet-like MoS_2 materials provide sufficient active sites for the deposition of Ag_3PO_4 nanoparticles. It is for the first time that oxygen evolution performance over the obtained Ag_3PO_4/MoS_2 composite photocatalysts has been evaluated, moreover, the effects of highly conductive MoS_2 materials on visible light utilization, electron-hole separation and water oxidation efficiency are systematically revealed.

EXPERIMENTAL

Preparation

MoS_2 nanosheets were fabricated by the ultrasonic stripping of commercially available MoS_2 materials. In a typical synthesis of Ag_3PO_4/MoS_2 nanocomposites, different amounts of sheet-like MoS_2 (50, 100, 200, 300 mg) were added into 90 mL H_2O, respectively, followed by the ultrasonic treatment for 3 h. Next, 30 mL of $AgNO_3$ (18 mmol, 3.06 g) aqueous solution was added dropwise into the MoS_2 suspension, and stirred for further 12 h. And then 30 mL of Na_3PO_4 (6 mmol, 2.28 g) aqueous solution was added slowly into the above mixture, followed by continuous stirring for 3 h. After high-speed centrifugation, solid products were washed with deionized water and ethanol repeatedly, and dried at 60°C for 12 h. The final products were collected and are denoted as AM-50, AM-100, AM-200, and AM-300.

Characterizations

X-ray diffraction (XRD) was measured using Cu Kα radiation with the 2θ range from 5 to 80° at a scan rate of 5° min^{-1} on D/MAX2500PC. Raman spectra were recorded by Thermo Scientific™ DXR spectrometer operating at 532 nm. X-ray photoelectron spectroscopy (XPS) was evaluated by Perkin-Elmer PHI 5000C. The field-emission scanning electron microscopy (FE-SEM) was performed on JSM-7001F. The Ultraviolet-visible diffuse reflectance spectrophotometer (UV-vis DRS) on UV2450 from 200 to 800 nm with $BaSO_4$ as reference standard. Photoluminescence (PL) emission measurements were carried out by a QuantaMaster™ 40 with an excitation wavelength of 420 nm. The electron spin resonance (ESR) measurements were recorded on a JES FA200 Spectrometer using the 5, 5-dimethyl-1-pyrroline-N-oxide (DMPO) as the radical capture reagent.

Photocatalytic Measurements

The efficiency of photocatalytic oxygen evolution was monitored by *in-situ* oxygen sensor in a sealed system connected with a circulation system. Before the measurement, oxygen-free and air-saturated water were used to calibrate the oxygen probe with temperature compensation. For the measurement of oxygen evolution, 0.3 g of the photocatalyst powder was added into $AgNO_3$ aqueous solution (100 mL, 10 g/L), followed by an ultrasonic treatment for 5 min.

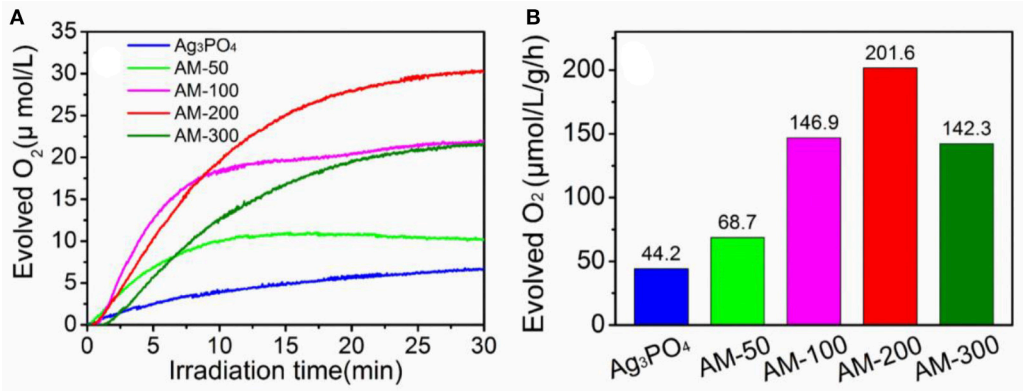

FIGURE 1 | Oxygen-evolving concentrations **(A)** and rates **(B)** over different photocatalysts under LED illumination.

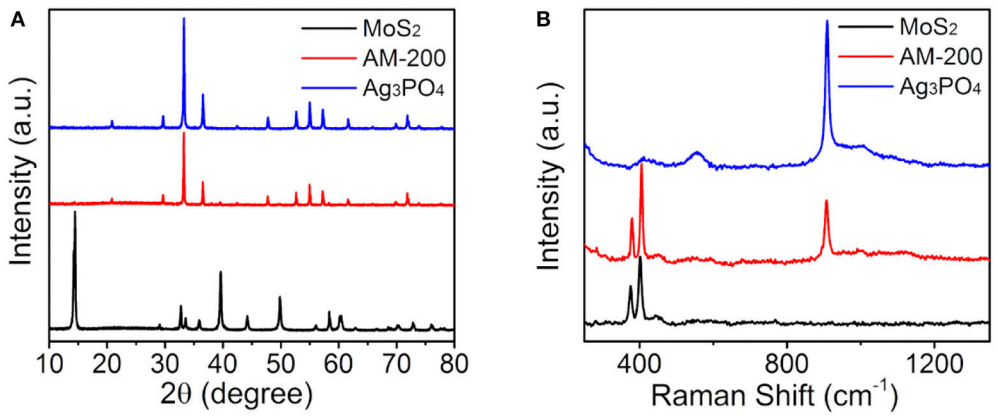

FIGURE 2 | XRD patterns **(A)** and Raman spectra **(B)** of pure Ag_3PO_4, MoS_2, and the composite AM-200.

RESULTS AND DISCUSSION

Photocatalytic oxygen evolution from water splitting over pure Ag_3PO_4 and Ag_3PO_4/MoS_2 composites with different mass ratios were evaluated, and the results are presented in **Figure 1**. It can be observed (**Figure 1A**) that the amount of evolved oxygen increases gradually when 50 and 100 mg MoS_2 were employed, the highest concentration of produced oxygen was recorded when the content of MoS_2 was increased to 200 mg. Further increase in the MoS_2 content from 200 to 300 mg in the Ag_3PO_4/MoS_2 composite resulted in the deterioration in the oxygen-generating performance. Notably all the composites showed improved oxygen-evolving performance than bulk Ag_3PO_4 material. The oxygen-evolving rates of as-prepared samples under LED illumination are further quantified and shown in **Figure 1B**. When 200 mg MoS_2 was introduced to hybridize with Ag_3PO_4, an optimal oxygen-generating rate of 201.6 $\mu mol \cdot L^{-1} \cdot g^{-1} \cdot h^{-1}$ was determined, which is about 4.5 times higher than that of pure Ag_3PO_4. It can be concluded from the oxygen evolution performance that a proper addition of MoS_2 may promote the water oxidation efficiency, while the use of more than 200 mg of MoS_2 is found to show negative effects on the oxygen evolution performance. For simplicity, only the composite AM-200 with the best oxygen-producing efficiency is chosen for comparisons with two starting materials in the following sections.

Following the evaluation of photocatalytic oxygen evolution performance, phase structures of the AM-200 composite were confirmed by XRD patterns (**Figure 2A**). Diffraction peaks (black line) appearing in 14.32, 32.62, 33.44, 35,82, 39.48, 44,1, 49.72, 58.24, 60.32, and 72.72° can be assigned to the (002), (100), (101), (102), (103), (006), (105), (110), (008), and (203) planes of hexagonal MoS_2 (JCPDS No. 37-1492). And the characteristic peaks (blue line) located at 20.96, 29.78, 33.38, 36.66, 47.86, 52.76, 55.1, 57.34, 61.72, and 73.94° correspond to planes (110), (200), (210), (211), (310), (222), (320), (321), (400), and (332) of bulk Ag_3PO_4 (JCPDS No. 06-0505), respectively. No obvious difference can be observed in characteristic diffraction peaks of bulk Ag_3PO_4 and Ag_3PO_4/MoS_2 composite (AM-200), presumably due to a relatively weaker diffraction intensity of MoS_2. The molecular structures of pure MoS_2, bulk Ag_3PO_4 and the Ag_3PO_4/MoS_2 composite AM-200 were further characterized

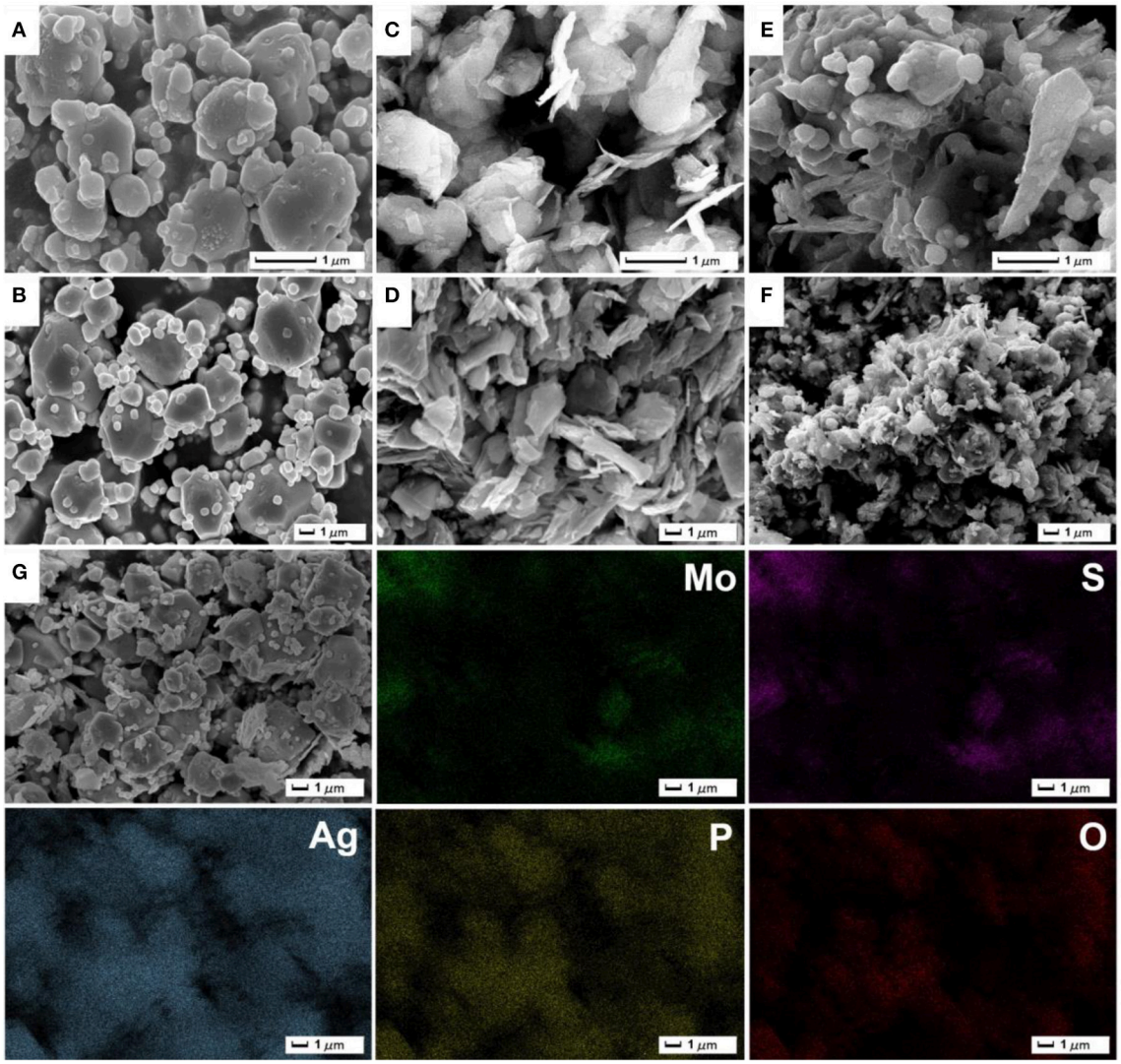

FIGURE 3 | Low-magnification **(A,C,E)** and high-magnification **(B,D,F)** SEM images of pure Ag_3PO_4 **(A,B),** MoS_2 **(C,D)** as well as the composite AM-200 **(E,F)**; EDS element mapping images of AM-200 **(G)**.

by Raman spectra (**Figure 2B**). In the spectrum of Ag_3PO_4, a sharp absorption peak at 908.5 cm^{-1} can be attributed to the motion of terminal oxygen bond vibration in phosphate chains. The peak at 1002.4 cm^{-1} is ascribed to the asymmetric stretching vibrations of O–P–O bonds in $[PO_4]$ clusters. The broad peak located at 554.4 cm^{-1} arises from the asymmetric stretch of P–O–P bonds, while the peak centered at 406.1 cm^{-1} corresponds to the symmetric bending vibration modes related to $[PO_4]$ clusters (Botelho et al., 2015). For pure MoS_2, characteristic Raman shifts located at 375.8 and 402.1 cm^{-1} are assigned to the E_{2g} and A_{1g} modes, while the peak appearing at 446.2 cm^{-1} is suggested to come from the interaction of the longitudinal acoustic phonon and Raman inactive A_{2u} modes (Koroteev et al., 2011; Lukowski et al., 2013). All characteristic peaks of both Ag_3PO_4 and MoS_2 were detected in Raman spectrum of the Ag_3PO_4/MoS_2 composite AM-200, indicating a complete hybridization of Ag_3PO_4 with MoS_2.

The morphologies of as-prepared samples were recorded by SEM images (**Figure 3**). From **Figures 3A,B**, as-synthesized Ag_3PO_4 products present an irregular polyhedron structure with the size of about 1–3 μm, and a few of small particles are distributed around large particles. SEM images of ultrasonic-treated MoS_2 material (**Figures 3C,D**) shows that stripped MoS_2 exhibit a thin sheet-like nanostructure. The stripped MoS_2 layer-like material has a certain accumulation and parts of MoS_2 materials have not been stripped into pieces. The Ag_3PO_4/MoS_2 composite AM-200 was synthesized by the *in-situ* deposition of Ag_3PO_4 nanoparticles on the surface of MoS_2 nanosheets via electrostatically driven self-assembly. As displayed in **Figures 3E,F**, the Ag_3PO_4 particles are uniformly distributed on the MoS_2 nanosheets without obvious agglomeration. It can

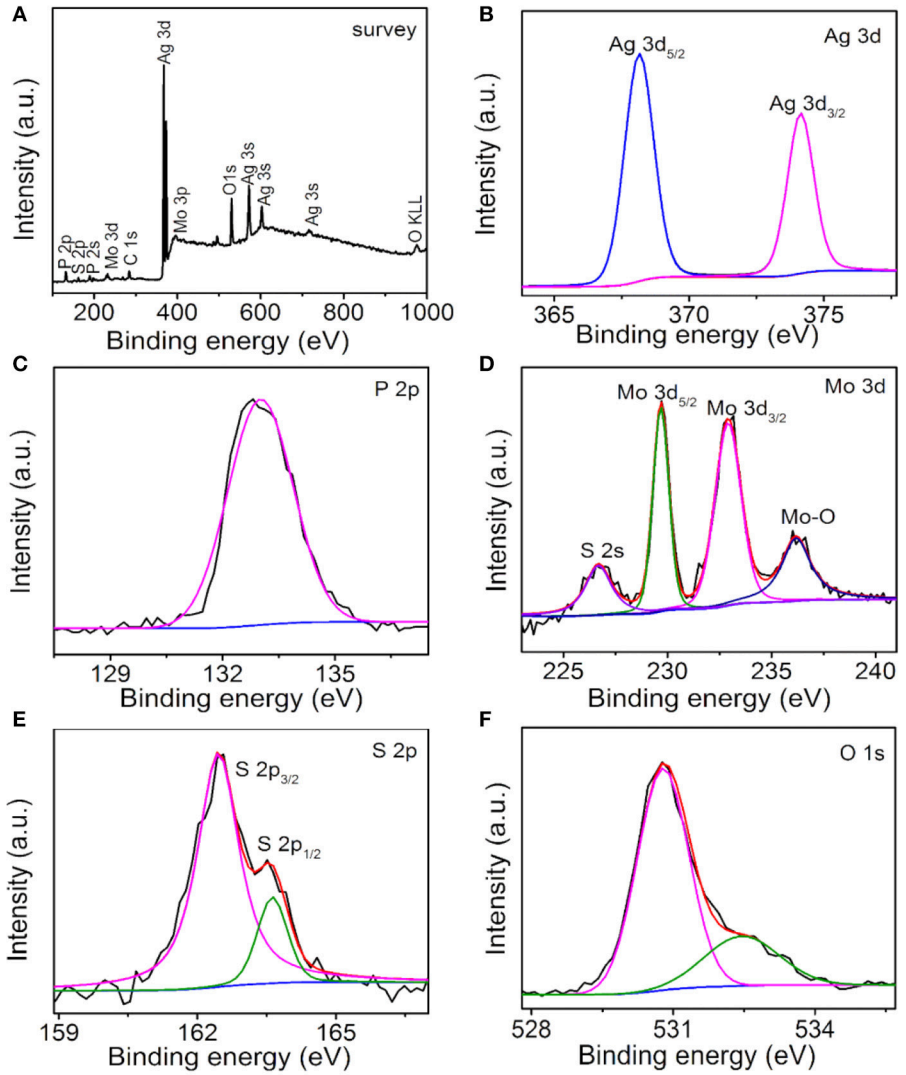

FIGURE 4 | XPS spectra of AM-200: Survey **(A)**, Ag 3d **(B)**, P 2p **(C)**, Mo 3d **(D)**, S 2p **(E),** and O 1s **(F)**.

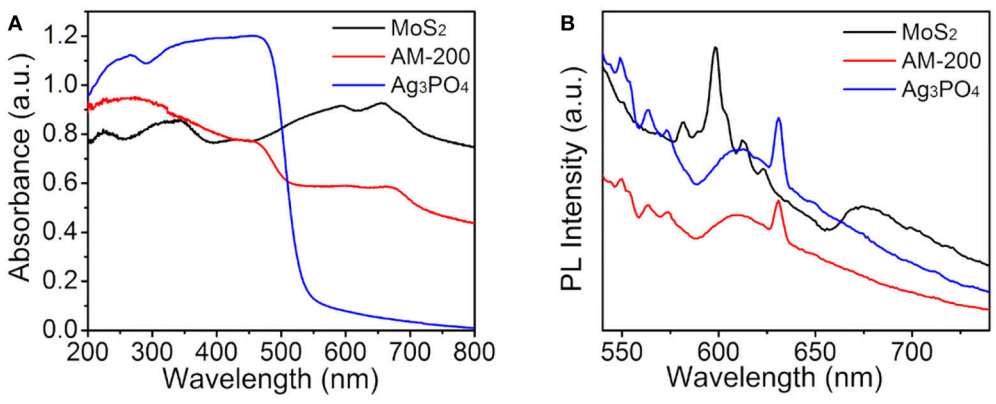

FIGURE 5 | UV-vis DRS **(A)** and PL spectra **(B)** of pure Ag_3PO_4, MoS_2 and the composite AM-200.

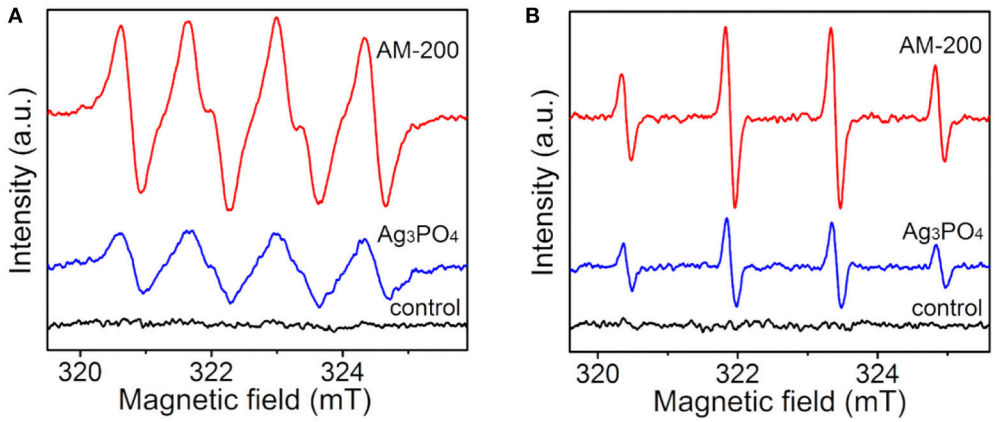

FIGURE 6 | ESR spectra of radical adducts trapped by DMPO in methanol **(A)** and aqueous **(B)** dispersions of Ag_3PO_4 and AM-200 under light irradiation.

be observed that the particle size of Ag_3PO_4 in AM-200 decreases slightly and is more uniform when a certain amount of MoS_2 were hybridized with Ag_3PO_4, suggesting that the addition of MoS_2 nanosheets have an effect on the particle size of Ag_3PO_4. The EDS element mapping images of AM-200 suggest that Mo, S, Ag, P, and O elements are homogeneously distributed, confirming the complete hybridization of Ag_3PO_4 particles and MoS_2 nanosheets.

The surface chemical compositions and states of the Ag_3PO_4/MoS_2 composite AM-200 were investigated by XPS characterization, the results are shown in **Figure 4**. Ag, P, O, Mo, S, and C elements can be detected in the survey spectrum (**Figure 4A**) of as-prepared composite AM-200. The existence of C 1s peak is may due to the adventitious carbon on the surface of sample. In the high resolution spectrum of Ag 3d (**Figure 4B**), two peaks at 368.1 and 374.2 eV can be assigned to the Ag $3d_{5/2}$ and Ag $3d_{3/2}$, respectively. The broad peak in the P 2p spectrum (**Figure 4C**) located at 133.0 eV originates from the P^{5+} in the Ag_3PO_4. The high resolution spectrum of Mo 3d is displayed in **Figure 4D**, the peaks at 226.7, 229.7, 232.9, and 236.2 eV can be ascribed to the S 2s, Mo $3d_{5/2}$, Mo $3d_{3/2}$, and Mo-O binding, respectively. Particularly, the first three binding energies indicated that S and Mo elements in the MoS_2 are found in the form of S^{2-} and Mo^{4+}, respectively, and the last one might result from the exposed Mo atoms during the exfoliation process combining with the O of Ag_3PO_4 (Wan et al., 2017). The S 2p XPS spectrum (**Figure 4E**) can be divided into two peaks centered at 162.5 and 163.6 eV, respectively, corresponding to the S $2p_{3/2}$ and S $2p_{1/2}$ in the MoS_2. The spectrum of O 1s (**Figure 4F**) can be fitted into two peaks located at 530.8 and 532.5 eV, originating from the O^{2-} in the Ag_3PO_4 and the hydroxyl group, respectively.

It is well-known that the utilization of visible light is one of key factors affecting the activity of a photocatalyst, therefore, the light-harvesting properties of all samples were measured by UV-vis DRS ranging from 200 to 800 nm and the absorption spectra are presented in **Figure 5A**. It can be seen that pure Ag_3PO_4 has a clear absorption edge around 530 nm, and black MoS_2 material reveals full-spectrum absorption in the range of 200–800 nm. The light absorption intensity of Ag_3PO_4/MoS_2 composite AM-200 in the wavelength range of 500–800 nm was increased when a certain amount of MoS_2 (200 mg) were employed to hybridize with Ag_3PO_4, implying that the integration of MoS_2 with Ag_3PO_4 favors a more efficient utilization of visible light. In addition to the light absorption, the separation of photoinduced electron-hole pairs is also believed to play a predominant role in determining the photocatalytic activity, thus the recombination of photogenerated charge carrier for the as-synthesized samples was analyzed by PL spectroscopy measurements. **Figure 5B** reveals Ag_3PO_4 has a strong excitation peak around 630 nm, stemming from the recombination of electrons and holes. After the addition of MoS_2, the Ag_3PO_4/MoS_2 composite AM-200 presented a similar position of excitation peak with Ag_3PO_4, and the PL emission intensity of AM-200 was weaker than those of pure MoS_2 and Ag_3PO_4, suggesting that the recombination efficiency of photoexcited charge carriers in the Ag_3PO_4/MoS_2 composite AM-200 has been effectively suppressed when the heterostructured composite was formed. A slower recombination rate of photogenerated electron-hole pairs boosts the enhancement in the photocatalytic performance.

To further determine the influence of the redox capacity of samples on the photocatalytic activity, as well as to investigate the mechanism behind the enhanced photocatalytic oxygen evolution from water splitting, the ESR measurement was carried out to confirm active radicals *in-situ* formed under light illumination. It can be observed in **Figure 6A** that no obvious peak was detected in dark. Under illumination, several strong peaks arising from DMPO-captured radicals can be detected in methanol dispersion for both pure Ag_3PO_4 and the Ag_3PO_4/MoS_2 composite AM-200, typical peaks are assigned to the spin adducts (DMPO-$O_2^{\bullet-}$). Compared with signals derived from pure Ag_3PO_4, higher signal intensities of DMPO-captured superoxide radicals were observed in the methanol dispersion of AM-200. It is shown in **Figure 6B** that no radical signal was detected in dark. A typical intensity ratio of 1:2:2:1 was determined from the spin adducts in aqueous dispersions of

both Ag_3PO_4 and AM-200 under light irradiation, representing the generation of the spin adducts (DMPO-•OH). Similarly, the intensity of radical signal for AM-200 increased largely comparable to that of Ag_3PO_4.On the basis of the above results, it is concluded that higher intensities of both photo-induced $O_2^{\bullet-}$ and •OH were recorded when a proper amount of MoS_2 was employed.

Furthermore, the band edge positions of valence band (VB) and conduction band (CB) also have an important effect on the redox catalytic capability, which can be deduced by the following formula (Li et al., 2016):

$$E_{VB} = \chi - E_e + 0.5E_g$$
$$E_{CB} = E_{VB} - E_g$$

Where E_{CB} and E_{VB} represent the CB and VB edge potentials, respectively; χ is the electro-negativity of the semiconductor, which is the geometric mean of the electro-negativities of the constituent atoms, and χ-values for Ag_3PO_4 and MoS_2 are 5.96 and 5.32 eV (Wan et al., 2017), respectively. E_e is about 4.5 eV, representing the free electron energy on the hydrogen scale. E_g was the band gap energy of the semiconductor, and E_g-values for Ag_3PO_4 and MoS_2 are about 2.45 and 1.9 eV (Yang et al., 2015c; Li et al., 2016), respectively. According to the calculation, the E_{VB}-values of Ag_3PO_4 and MoS_2 are about 2.69 and 1.77 eV, the top of which for both Ag_3PO_4 and MoS_2 is more positive than the redox potential of O_2/H_2O (1.23 eV) (Xie et al., 2013), theoretically both two semiconductors are able to split water into oxygen. However, overpotential is generally required for practical water splitting, in this study, Ag_3PO_4 acts as the oxygen-evolving catalyst for solar-driven water splitting due to its more positive potential higher than that for water oxidation. Subsequently E_{CB} positions of Ag_3PO_4 and MoS_2 are determined to be 0.24 and −0.13 eV, respectively. Therefore, the enhanced photocatalytic oxygen-generating performance over the Ag_3PO_4/MoS_2 composite photocatalyst could be explained as follows: first, the electrons in the VB of Ag_3PO_4 could be initially excited into CB, and subsequently, may recombine with the holes in the VB of MoS_2 via a possible Z-scheme configuration. Thus, more efficient electron-hole separations and charge transporatation occur in the illuminated hybrid materials due to the existence of highly conductive MoS_2 sheets and possible Z-scheme pathway for electron transfer. The electron-hole recombination on the surface of Ag_3PO_4 can be suppressed, as a result, active holes left on the VB position of Ag_3PO_4 may oxidize water into oxygen effectively, leading to highly efficient oxygen evolution performance over the Ag_3PO_4/MoS_2 composite photocatalysts.

CONCLUSIONS

In conclusion, effective Ag_3PO_4/MoS_2 composite photocatalysts were successfully fabricated by combining ion-exchange process and electrostatic assembly of Ag_3PO_4 nanoparticles on the surface of MoS_2 nanosheets. The Ag_3PO_4/MoS_2 hybrid materials demonstrated superior interfacial contact and wide-spectrum light-harvesting property in the visible light region. When employed as the catalyst for photocatalytic water splitting, it exhibited highly improved oxygen evolution performance than bulk Ag_3PO_4 under LED irradiation. The oxygen-evolving rate of the optimal Ag_3PO_4/MoS_2 composite (AM-200) is nearly five times faster than pure Ag_3PO_4. The combined characterizations and theoretical analysis on band structures suggest that the enhanced water oxidation efficiency is attributed to remarkable response to visible light, more efficient charge transportation and possibly specific Z-scheme pathway derived from matched band positions. The finding in this work offers a great opportunity in designing and synthesizing novel composite photocatalytic materials for applications in solar energy conversion, allowing us to develop an understanding of the fundamental mechanisms of Ag_3PO_4-based composite photocatalytic materials.

AUTHOR CONTRIBUTIONS

XY and QL: designed the project, guided the study, and polished the manuscript; XC, XX, and LT: conducted the experiments and characterized the samples; HT: revised the manuscript.

ACKNOWLEDGMENTS

This work was supported by the National Natural Science Foundation of China (51672113), Six Talent Peaks Project in Jiangsu Province (2015-XCL-026), Natural Science Foundation of Jiangsu Province (BK20171299), State Key Laboratory of Photocatalysis on Energy and Environment (SKLPEE-KF201705), Fuzhou University, Postgraduate Research & Practice Innovation Program of Jiangsu Province (SJZZ16_0192), and State Key Laboratory of Advanced Technology for Materials Synthesis and Processing (2016-KF-10), Wuhan University of Technology.

REFERENCES

Bi, Y. P., Hu, H. Y., Ouyang, S. X., Jiao, Z. B., Lu, G. X., and Ye, J. H. (2012). Selective growth of metallic Ag nanocrystals on Ag_3PO_4 submicro-cubes for photocatalytic applications. *Chem. Eur. J.* 18, 14272–14275. doi: 10.1002/chem.201201435

Botelho, G., Sczancoski, J. C., Andres, J., Gracia, L., and Longo, E. (2015). Experimental and theoretical study on the structure, optical properties, and growth of metallic silver nanostructures in Ag_3PO_4. *J. Phys. Chem. C* 119, 6293–6306. doi: 10.1021/jp512111v

Cao, Q., Yu, J., Yuan, K., Zhong, M., and Delaunay, J. J. (2017). Facile and large-area preparation of porous Ag_3PO_4 photoanodes for enhanced photoelectrochemical water oxidation. *ACS Appl. Mater. Interfaces* 9, 19507–19512. doi: 10.1021/acsami.7b03098

Cui, X. K., Tian, L., Xian, X. Z., Tang, H., and Yang, X. F. (2018). Solar photocatalytic water oxidation over Ag_3PO_4/g-C_3N_4 composite materials mediated by metallic Ag and graphene. *Appl. Surf. Sci.* 430, 108–115. doi: 10.1016/j.apsusc.2017.07.290

Dai, W. L., Yu, J. J., Deng, Y. Q., Hu, X., Wang, T. Y., and Luo, X. B. (2017). Facile synthesis of MoS_2/Bi_2WO_6 nanocomposites for enhanced CO_2

photoreduction activity under visible light irradiation. *Appl. Surf. Sci.* 403, 230–239. doi: 10.1016/j.apsusc.2017.01.171

Gyawali, G., and Lee, S. W. (2016). Microwave hydrothermal synthesis and characterization of Ag_3PO_4/MoS_2 composite photocatalyst. *J. Nanosci. Nanotechnol.* 16, 11158–11163. doi: 10.1166/jnn.2016.13471

He, Y., Li, L., Fan, W. G., Zhang, C. X., and Leung, M. K. H. (2018). A novel and facile solvothermal-and-hydrothermal method for synthesis of uniform $BiVO_4$ film with high photoelectrochemical performance. *J. Alloys Compd.* 732, 593–602. doi: 10.1016/j.jallcom.2017.10.153

Hu, H. Y., Jiao, Z. B., Yu, H. C., Lu, G. X., Ye, J. H., and Bi, Y. P. (2013). Facile synthesis of tetrahedral Ag_3PO_4 submicro-crystals with enhanced photocatalytic properties. *J. Mater. Chem. A* 1, 2387–2390. doi: 10.1039/c2ta01151d

Iqbal, S., Pan, Z. W., and Zhou, K. B. (2017). Enhanced photocatalytic hydrogen evolution from in situ formation of few-layered MoS_2/CdS nanosheet-based van der Waals heterostructures. *Nanoscale* 9, 6638–6642. doi: 10.1039/C7NR01705G

Koroteev, V. O., Bulusheva, L. G., Asanov, I. P., Shlyakhova, E. V., Vyalikh, D. V., and Okotrub, A. V. (2011). Charge transfer in the MoS_2/Carbon nanotube composite. *J. Phys. Chem. C* 115, 21199–21204. doi: 10.1021/jp205939e

Kudo, A., and Miseki, Y. (2009). Heterogeneous photocatalyst materials for water splitting. *Chem. Soc. Rev.* 38, 253–278. doi: 10.1039/B800489G

Li, S. P., Gu, X. Q., Zhao, Y. L., Qiang, Y. H., Zhang, S., and Sui, M. R. (2016). Enhanced visible-light photocatalytic activity and stability by incorporating a small amount of MoS_2 into Ag_3PO_4 microcrystals. *J. Mater. Sci. Mater. Electron.* 27, 386–392. doi: 10.1007/s10854-015-3765-x

Lukowski, M. A., Daniel, A. S., Meng, F., Forticaux, A., Li, L. S., and Jin, S. (2013). Enhanced hydrogen evolution catalysis from chemically exfoliated metallic MoS_2 nanosheets. *J. Am. Chem. Soc.* 135, 10274–10277. doi: 10.1021/ja404523s

Lv, J. L., Dai, K., Lu, L. H., Geng, L., Liang, C. H., and Zhu, G. P. (2016). Cu/Ag/Ag_3PO_4 ternary composite: a hybrid alloy-semiconductor heterojunction structure with visible light photocatalytic properties. *J. Alloys Compd.* 682, 778–784. doi: 10.1016/j.jallcom.2016.04.313

Maeda, K., and Domen, K. (2010). Photocatalytic water splitting: recent progress and future challenges. *J. Phys. Chem. Lett.* 1, 2655–2661. doi: 10.1021/jz1007966

Mikkelsen, M., Jorgensen, M., and Krebs, F. C. (2010). The teraton challenge. A review of fixation and transformation of carbon dioxide. *Energy Environ. Sci.* 3, 43–81. doi: 10.1039/B912904A

Sun, M. X., Wang, Y., Fang, Y. L., Sun, S. F., and Yu, Z. S. (2016). Construction of MoS_2/CdS/TiO_2 ternary composites with enhanced photocatalytic activity and stability. *J. Alloys Compd.* 684, 335–341. doi: 10.1016/j.jallcom.2016.05.189

Takanabe, K. (2017). Photocatalytic water splitting: quantitative approaches toward photocatalyst by design. *ACS Catal.* 7, 8006–8022. doi: 10.1021/acscatal.7b02662

Tian, L., Xian, X. Z., Cui, X. K., Tang, H., and Yang, X. F. (2018). Fabrication of modified g-C_3N_4 nanorod/Ag_3PO_4 nanocomposites for solar-driven photocatalytic oxygen evolution from water splitting. *Appl. Surf. Sci.* 430, 301–308. doi: 10.1016/j.apsusc.2017.07.185

Wan, J., Du, X., Liu, E. Z., Hu, Y., Fan, J., and Hu, X. Y. (2017). Z-scheme visible-light-driven Ag_3PO_4 nanoparticle@MoS_2 quantum dot/few-layered MoS_2 nanosheet heterostructures with high efficiency and stability for photocatalytic selective oxidation. *J. Catal.* 345, 281–294. doi: 10.1016/j.jcat.2016.11.013

Wang, L., Chai, Y. Y., Ren, J., Ding, J., Liu, Q. Q., and Dai, W. L. (2015). Ag_3PO_4 nanoparticles loaded on 3D flower-like spherical MoS_2: a highly efficient hierarchical heterojunction photocatalyst. *Dalton Trans.* 44, 14625–14634. doi: 10.1039/C5DT01961C

Wang, P. F., Shi, P. H., Hong, Y. C., Zhou, X. J., and Yao, W. F. (2015). Facile deposition of Ag_3PO_4 on graphene-like MoS_2 nanosheets for highly efficient photocatalysis. *Mater. Res. Bull.* 62, 24–29. doi: 10.1016/j.materresbull.2014.10.016

Wang, P., Xu, S., Xia, Y., Wang, X., Yu, H., and Yu, J. (2017). Synergistic effect of CoPi-hole and Cu(II)-electron cocatalysts for enhanced photocatalytic activity and photoinduced stability of Ag_3PO_4. *Phys. Chem. Chem. Phys.* 19, 10309–10316. doi: 10.1039/C7CP01043E

Wang, W., Cheng, B., Yu, J., Liu, G., and Fan, W. (2012). Visible-light photocatalytic activity and deactivation mechanism of Ag_3PO_4 spherical particles. *Chem. Asian J.* 7, 1902–1908. doi: 10.1002/asia.201200197

Wu, Q. F., Bao, S. Y., Tian, B. Z., Xiao, Y. F., and Zhang, J. L. (2016). Double-diffusion-based synthesis of $BiVO_4$ mesoporous single crystals with enhanced photocatalytic activity for oxygen evolution. *Chem. Commun.* 52, 7478–7481. doi: 10.1039/C6CC02737G

Xiang, Q. J., Yu, J. G., and Jaroniec, M. (2012). Synergetic effect of MoS_2 and graphene as cocatalysts for enhanced photocatalytic H_2 production activity of TiO_2 nanoparticles. *J. Am. Chem. Soc.* 134, 6575–6578. doi: 10.1021/ja302846n

Xie, G., Zhang, K., Guo, B., Liu, Q., Fang, L., and Gong, J. R. (2013). Graphene-based materials for hydrogen generation from light-driven water splitting. *Adv. Mater.* 25, 3820–3839. doi: 10.1002/adma.201301207

Xin, G., Guo, W., and Ma, T. L. (2009). Effect of annealing temperature on the photocatalytic activity of WO_3 for O_2 evolution. *Appl. Surf. Sci.* 256, 165–169. doi: 10.1016/j.apsusc.2009.07.102

Yang, L., Guo, S. H., and Li, X. H. (2017). Au nanoparticles@MoS_2 core-shell structures with moderate MoS_2 coverage for efficient photocatalytic water splitting. *J. Alloys Compd.* 706, 82–88. doi: 10.1016/j.jallcom.2017.02.240

Yang, X. F., Chen, Z. P., Xu, J. S., Tang, H., Chen, K. M., and Jiang, Y. (2015a). Tuning the morphology of g-C_3N_4 for improvement of Z-scheme photocatalytic water oxidation. *ACS Appl. Mater. Interfaces* 7, 15285–15293. doi: 10.1021/acsami.5b02649

Yang, X. F., Qin, J. L., Jiang, Y., Chen, K. M., Yan, X. H., Zhang, D., et al. (2015b). Fabrication of P25/Ag_3PO_4/graphene oxide heterostructures for enhanced solar photocatalytic degradation of organic pollutants and bacteria. *Appl. Catal. B Environ.* 166, 231–240. doi: 10.1016/j.apcatb.2014.11.028

Yang, X., Tang, H., Xu, J., Antonietti, M., and Shalom, M. (2015c). Silver phosphate/graphitic carbon nitride as an efficient photocatalytic tandem system for oxygen evolution. *ChemSusChem* 8, 1350–1358. doi: 10.1002/cssc.201403168

Yi, Z., Ye, J. , Kikugawa, N., Kako, T., Ouyang, S. X., Stuart-Williams, H., et al. (2010). An orthophosphate semiconductor with photooxidation properties under visible-light irradiation. *Nat. Mater.* 9, 559–564. doi: 10.1038/nmat2780

Yuan, Y. J., Chen, D. Q., Yang, S. H., Yang, L. X., Wang, J. J., Cao, D. P., et al. (2017). Constructing noble-metal-free Z-scheme photocatalytic overall water splitting systems using MoS_2 nanosheet modified CdS as a H_2 evolution photocatalyst. *J. Mater. Chem. A* 5, 21205–21213. doi: 10.1039/C7TA06644A

Zeng, Q. Y., Li, J. H., Li, L. S., Bai, J., Xia, L. G., and Zhou, B. X. (2017). Synthesis of $WO_3/BiVO_4$ photoanode using a reaction of bismuth nitrate with peroxovanadate on WO_3 film for efficient photoelectrocatalytic water splitting and organic pollutant degradation. *Appl. Catal. B Environ.* 217, 21–29. doi: 10.1016/j.apcatb.2017.05.072

Zhang, J., Huang, L. H., Lu, Z. D., Jin, Z. L., Wang, X. Y., Xu, G. L., et al. (2016). Crystal face regulating MoS_2/TiO_2(001) heterostructure for high photocatalytic activity. *J. Alloys Compd.* 688, 840–848. doi: 10.1016/j.jallcom.2016.07.263

Zheng, Y., Zhang, W. Q., Li, Y. F., Chen, J., Yu, B., Wang, J. C., et al. (2017). Energy related CO_2 conversion and utilization: advanced materials/nanomaterials, reaction mechanisms and technologies. *Nano Energy* 40, 512–539. doi: 10.1016/j.nanoen.2017.08.049

Zhou, T. H., Zhang, G. Z., Ma, P. J., Qiu, X. L., Zhang, H. W., Yang, H., et al. (2018). Efficient degradation of rhodamine B with magnetically separable Ag_3PO_4@$MgFe_2O_4$ composites under visible irradiation. *J. Alloys Compd.* 735, 1277–1290. doi: 10.1016/j.jallcom.2017.11.245

Zhu, C. S., Zhang, L., Jiang, B., Zheng, J. T., Hu, P., Li, S. J., et al. (2016). Fabrication of Z-scheme Ag_3PO_4/MoS_2 composites with enhanced photocatalytic activity and stability for organic pollutant degradation. *Appl. Surf. Sci.* 377, 99–108. doi: 10.1016/j.apsusc.2016.03.143

Conflict of Interest Statement: The authors declare that the research was conducted in the absence of any commercial or financial relationships that could be construed as a potential conflict of interest.

frontiers in Chemistry

ORIGINAL RESEARCH
published: 26 March 2018
doi: 10.3389/fchem.2018.00064

Mechanisms for $\cdot O_2^-$ and ·OH Production on Flowerlike $BiVO_4$ Photocatalysis Based on Electron Spin Resonance

Xuan Xu[1,2], *Yaofang Sun*[1,2], *Zihong Fan*[3], *Deqiang Zhao*[1,2], *Shimin Xiong*[1,2], *Bingyao Zhang*[1,2], *Shiyu Zhou*[1,2] *and Guotao Liu*[1,2]*

[1] *Key Laboratory of Three Gorges Reservoir Region's Eco-Environment, Ministry of Education, Chongqing University, Chongqing, China,* [2] *National Centre for International Research of Low-Carbon and Green Buildings, Chongqing University, Chongqing, China,* [3] *College of Environmental and Resources, Chongqing Technology and Business University, Chongqing, China*

Many studies have focused on the use of $BiVO_4$ as a photocatalyst, but few have investigated the production of free radicals during the photocatalytic process. Following synthesis of flowerlike $BiVO_4$ and characterization by X-ray diffraction (XRD), Raman spectroscopy, Scanning electron microscopy (SEM) Scanning electron microscopy (EDX), UV-Vis and XPS, we successfully prepared $BiVO_4$. Then we used electron spin resonance (ESR) to determine the production and degradation of individual active free radicals, including the superoxide radical ($\cdot O_2^-$) and the hydroxyl radical (·OH). In the first experiment, we used ESR to detect the signals of free radicals ($\cdot O_2^-$ and ·OH) under varying oxygen conditions. The results shown that in addition to production by $\cdot O_2^-$, ·OH could also be produced by oxidation of h^+ to OH^-. In the next experiment, we detected ·OH under varying pH to identify the result of the first experiment, and found that signal intensities increased with increasing pH, indicating the mechanism for ·OH production. Finally, we conducted a trapping experiment to examine free radical degradation mechanisms. We identified ·OH and h^+ as the main active free radicals and showed the complete production about ·OH. These results improve current knowledge of free radical production mechanisms, which can be used to enhance the photocatalytic performance of $BiVO_4$.

Keywords: electron spin resonance (ESR), degradation mechanism, bismuth vanadate ($BiVO_4$), superoxide radical ($\cdot O_2^-$), hydroxyl radical (·OH)

OPEN ACCESS

Edited by:
Fan Dong,
Chongqing Technology and Business University, China

Reviewed by:
Fatwa Abdi,
Helmholtz-Zentrum Berlin für Materialien und Energie, Germany
Alessandro Di Mauro,
Istituto per la Microelettronica e Microsistemi (CNR), Italy
Liqun Ye,
Nanyang Normal University, China

***Correspondence:**
Guotao Liu
liu-guotao@163.com

Specialty section:
This article was submitted to Catalysis and Photocatalysis, a section of the journal Frontiers in Chemistry

Received: *19 October 2017*
Accepted: *27 February 2018*
Published: *26 March 2018*

Citation:
Xu X, Sun Y, Fan Z, Zhao D, Xiong S, Zhang B, Zhou S and Liu G (2018) Mechanisms for $\cdot O_2^-$ and ·OH Production on Flowerlike $BiVO_4$ Photocatalysis Based on Electron Spin Resonance. Front. Chem. 6:64. doi: 10.3389/fchem.2018.00064

INTRODUCTION

The development of modern society and global economy has led to a series of environmental problems. The public's awareness of environmental issues has gradually increased with the growing realization that the environment requires continuous protection in order to sustain life (Zhang et al., 2010). Related to this area of thought is the utilization of solar energy. The development of photocatalytic semiconductors for organic pollutant degradation in wastewater has become a challenging research topic (Zhang et al., 2015). Many studies are now focusing on the photocatalytic decomposition of wastewater and degradation of organic pollutants under visible light irradiation

(Long et al., 2006). Since the discovery of photo-induced decomposition of water by TiO_2 electrodes (Inoue et al., 1979), semiconductor-based photocatalysis has attracted extensive interest and the properties of several photocatalytic materials, such as TiO_2 and ZnO, have been investigated. The development of visible-light-driven photocatalysts involves two strategies (Long et al., 2006): modification of TiO_2 and exploitation of novel semiconductor materials. Many studies have reported that TiO_2 is a promising material for Surface Enhanced Raman Scattering (SERS) owning to its high refractive index, versatility in terms of surface functionalization, and synergistic coupling with plasmonic nanoparticles (Xu et al., 2017). In addition, TiO_2 has many advantages that are beneficial to photocatalytic reactions, such as extraordinary chemical stability, low cost, and small environmental impact (Inoue et al., 1979). However, it also has some limitations, such as a low quantum efficiency and wide band-gap (3.2 eV); therefore, TiO_2-based photocatalytic reactions can only occur under ultraviolet irradiation (Zhang et al., 1998; Ren et al., 2012; Wang et al., 2014). Bismuth vanadate ($BiVO_4$), a promising photocatalyst, has received considerable attention because of its high absorption of visible light (VL), and VL accounts for over 50% of total sunlight (Xu et al., 2016). Due to its non-toxicity, environmentally friendly $BiVO_4$-based paints have recently replaced paints containing toxic pigments, such as lead chromate ($PbCrO_4$) and cadmium sulfide (CdS) (Nalbandian et al., 2015). As a new VL-active photocatalyst, $BiVO_4$ occurs in three main crystal forms: monoclinic scheelite, tetragonal zircon, and tetragonal scheelite structures. Monoclinic scheelite and tetragonal scheelite possess similar scheelite crystalline structures (Shan et al., 2014). Compared with the other two phases, the monoclinic scheelite phase of $BiVO_4$ exhibits much higher photocatalytic activity under visible light, as illustrated by extensive photocatalytic research (Xu et al., 2016). With the rise of $BiVO_4$ applications, various methods for the synthesis of $BiVO_4$ photocatalysts have been proposed (Zhao et al., 2016). In addition, many researchers have focused on modifying $BiVO_4$ to inhibit the recombination of electron carriers and improve its photocatalytic absorption efficiency (Kohtani et al., 2005; Xu et al., 2008; Wang et al., 2015; Zhang et al., 2016; Zhao et al., 2016).

Though many studies have focused on the modification of $BiVO_4$ and its photocatalytic properties, there are few published investigations on its photocatalytic mechanism. According to published literatures (Hashimoto et al., 2005; Lam et al., 2014), the main active free radicals that take part in the photocatalytic system include the hydroxyl radical (·OH), the superoxide radical ($\cdot O_2^-$), and the hole (h^+). Among these active free radicals, ·OH is mainly generated by oxidation of h^+ to water or via a series of reactions involving $\cdot O_2^-$. The main activate free radicals that affecting the degradation of photocatalytic materials in different photocatalytic systems vary, although they typically include one of the three above-mentioned radicals. Previous research has focused on the direct effects that photocatalytic materials exert on pollutant degradation, and reaction mechanisms typically are based on trapping experiments (Xu et al., 2016). However, there is limited research on identification of the main active free radicals using various methods, and the mechanisms of ·OH and $\cdot O_2^-$ generation are unclear (Ge et al., 2012b). Some studies on $BiVO_4$ have reported the reduction of oxygen by electrons as a mechanism for the generation of $\cdot O_2^-$, however no experiments have been conducted to confirm this conclusion. Furthermore, some studies have reported conflicting conclusions on free radical reaction mechanisms, indicating that ·OH can be generated by $\cdot O_2^-$ but not by h^+ (Cheng et al., 2012). Thus, it is unclear whether ·OH can be generated by h^+, and further research is necessary to clarify the mechanisms of free radical reactions.

Spin trapping in conjunction with electron spin resonance (ESR) has been widely used for the indirect detection of short-lived radicals (Ming et al., 2014). Spin trapping compounds are used to convert short-lived radicals into relatively longer-lived radical products, spin adducts, which can be easily detected by ESR (Castellanos et al., 2001; Kubo et al., 2012). This is a very intuitive method to detect the presence of unpaired electrons, such as free radicals, transition metals, electron holes, etc.

The aim of this study was to clarify the recent controversy regarding the formation mechanism of ·OH, particularly whether it can be generated by $\cdot O_2^-$ or h^+. In addition to the synthesis and characterization of $BiVO_4$, we investigated its photocatalytic degradation mechanism with regard to the formation of ·OH. We used ESR to determine individual active free radicals, including $\cdot O_2^-$ and ·OH. According to the results, oxygen plays multiple roles in this mechanism and primarily determines the pathway by which these two active free radicals are generated. We further investigated the main radicals participating in the photocatalytic process by changing the pH of the reaction system. Finally, a trapping experiment was conducted and the photocatalytic mechanism of $BiVO_4$ was discussed in detail.

EXPERIMENTAL METHODS

Reagents, Preparation, and Characterization of Materials

Reagents

Pure chemicals of analytical grade were used without further purification. Sodium hydroxide (NaOH), ammonium metavanadate (NH_4VO_3), and silver nitrate ($AgNO_3$) were purchased from the Chongqing Chuandong Chemical Company. Bismuth nitrate ($Bi(NO_3)_3 \cdot 5H_2O$) and nitric acid (HNO_3) were obtained from the Chengdu Area of the Industrial Development Zone (Xinde Mulan). Dimethyl pyridine N-oxide (DMPO), absolute ethyl alcohol (C_2H_5OH), and isopropanol (IPA) were acquired from the Industrial Development Zone, Mulan Town, Xindu District of Chengdu. Sodium oxalate ($Na_2C_2O_4$), commercial Titania (P25) and L- cysteine were bought from the Sinopharm Chemical Reagent Co, Ltd, and p-benzoquin-one (PBQ) was obtained from the Chengdu Kelong Chemical Reagent Factory.

Synthesis of Flowerlike $BiVO_4$

To synthesize flowerlike $BiVO_4$, 0.072 g L-cysteine was dissolved in 4 ml of 4 mol/l HNO_3 and the mixture was stirred for 30 min, then 2 mmol of $Bi(NO_3)_3 \cdot 5H_2O$ was dissolved in the mixture and was stirred for 30 min, resulting in solution A. Next, 2 mmol

NH_4VO_3 was dissolved in 4 ml of 2 mol·L^{-1} NaOH, resulting in solution B. Solutions A and B were mixed together and 50 ml distilled water was added in it, while regulating the pH (2.5), and the mixture was ultrasonically dispersed for 30 min. The mixture was then transferred to a reaction vessel and allowed to react at 180°C for 16 h. Finally, the system was naturally cooled to room temperature and washed with absolute ethanol followed by distilled water about six times. The final product was dried under a vacuum overnight at 60°C for 6 h.

Characterization

The crystalline structures of all samples were characterized by X-ray diffraction (XRD) using a Rigaku D/Max-rB diffractometer with Cu Ka radiation. Scanning electron microscopy (SEM) images were acquired with a Zeiss AURIGA field emission microscope (electron high tension (EHT) = 5 kV, work distance (WD) = 8.8 nm; Zeiss, Oberkochen, Germany). The surface chemical environment was analyzed by XPS on a PHI5000 VersaProbe system with monochromatic Al Kα X-rays. Energy dispersive X-ray (EDX) images were acquired with an EDX-100A-4. UV-Vis DRS was performed with a Hitachi U-3010 UV-Vis spectrometer. ESR analyses were performed using a JES FA200 X-band ESR spectrometer operating in the X-band at 0.907 GHz and 0.998 mW.

Photocatalytic Degradation Experiment

The photocatalytic activity of $BiVO_4$ was assessed by evaluating the degree of photodegradation of Rhodamine B (RhB) solution under visible light at room temperature. In each experiment, 0.10 g of catalyst was added to an aqueous RhB solution (300 ml, 5 mg·L^{-1}), and the mixture was magnetically stirred for 30 min in the dark to achieve high dispersion and adsorption–desorption equilibrium between the dye and catalyst. Then, the solution was placed in a 500 mL beaker and positioned 350 mm away from the visible light source. Samples were collected after every 2 h of irradiation, and then centrifuged at 12000 rpm to remove the catalyst powder. The concentration of the remaining dye was monitored by measuring the absorbance of the solution at 552 nm. For comparison, control experiments were performed using P25 as a catalyst under the same conditions. At the same time, we did the repeated test.

Mechanisms for $\cdot O_2^-$ and ·OH Production

ESR Experiment

The ESR experiment was primarily focused on the analysis of ·OH and $\cdot O_2^-$. In the case of ·OH, the whole test was performed in aqueous solution. First, 5 mg of $BiVO_4$ was weighed and dispersed in 5 mL water via ultrasound for 20 min; then, argon was bubbled through the solution for 20 min to strip oxygen from the solution; DMPO (100 mM) solution (also bubbled with argon to remove oxygen) was used for hybrid acquisition under visible light. Simultaneously, the same experiment was performed in the presence of oxygen as a control.

There were some differences in the O_2^- experiment. First, 5 mg of $BiVO_4$ was weighed and dispersed in methanol along with a capturing agent, DMPO (100 mM). The solution was then deoxygenated with argon as before, and the test was conducted under visible light. Again, the same experiment was conducted under aerobic conditions as a control. All tests were conducted under neutral conditions (pH = 7).

We also analyzed the DMPO spin-trapping ESR spectra of $BiVO_4$ in an aqueous dispersion for DMPO–·OH (1:2:2:1) (Zhou et al., 2012) and in a methanol dispersion for DMPO–$\cdot O_2^-$. The characteristic peaks of DMPO–·OH and DMPO–$\cdot O_2^-$ respectively indicated the production of ·OH and $\cdot O_2^-$ species in the samples.

To identify whether h^+ can generate ·OH, we conducted the above ·OH experiment under varying oxygen levels, and then under varying pH (pH = 5, 9, 7, 11).

Trapping Experiment

The method of trapping experiment is the same to photocatalytic degradation experiment, what different is the addition of scavengers. In these experiments, we used PBQ (0.1 mmol), IPA (0.1 mol·L^{-1}), $AgNO_3$ (0.1 mmol), and $Na_2C_2O_4$ (0.1 mmol) as $\cdot O_2^-$, ·OH, electron, and h^+ scavengers, respectively (Chen et al., 2013). In each experiment, 0.10 g of catalyst was added to an aqueous RhB solution (300 ml, 5 mg·L^{-1}), and the mixture was magnetically stirred for 30 min in the dark to achieve high dispersion and adsorption–desorption equilibrium between the dye and catalyst. Then, the solution was placed in a 500 mL beaker and positioned 350 mm away from the visible light source. Samples were collected after every 2 h of irradiation, and then centrifuged at 12,000 rpm to remove the catalyst powder. The concentration of the remaining dye was monitored by measuring the absorbance of the solution at 552 nm. For comparison, control experiments were performed using $BiVO_4$ as a catalyst, or without any catalyst, under the same conditions.

RESULTS AND DISCUSSION

Sample Composition and Morphology

X-ray diffraction enables the qualitative analysis and phase identification of a compound. Additionally this analytical technique facilitates determination of crystalline structures (regardless of symmetry measurements, etc.). From the XRD spectrum, the crystalline structure, lattice parameters, and defects (dislocations, etc.) can be determined (Zhang et al., 2006). As seen in **Figure 1A**, the diffraction peaks of the sample agree well with those for the standard monoclinic $BiVO_4$ (JCPDS No. 83–1697), indicating that the material consists of a single phase. Other authors have obtained similar XRD patterns of $BiVO_4$ (Zhang et al., 2010; Jiang et al., 2012), suggesting that highly monoclinic scheelite $BiVO_4$ was obtained.

Raman spectroscopy is commonly used to determine the structure of prepared $BiVO_4$ together with XRD, and we further examined the prepared $BiVO_4$ structure with this technique. Based on band component analysis of the Raman and IR spectra (Hardcastle et al., 1991; Gotić et al., 2005; Zhang and Zhang, 2009), we identified Raman bands at 146, 210, 324, 698, and 853 cm^{-1} (**Figure 1B**). The Raman bands of the prepared $BiVO_4$ are quite distinctive and sharp. The band with the highest intensity (853 cm^{-1}) was assigned to ν_s (V–O) (Zhang and Zhang, 2009), and the weak shoulder at 698 cm^{-1}

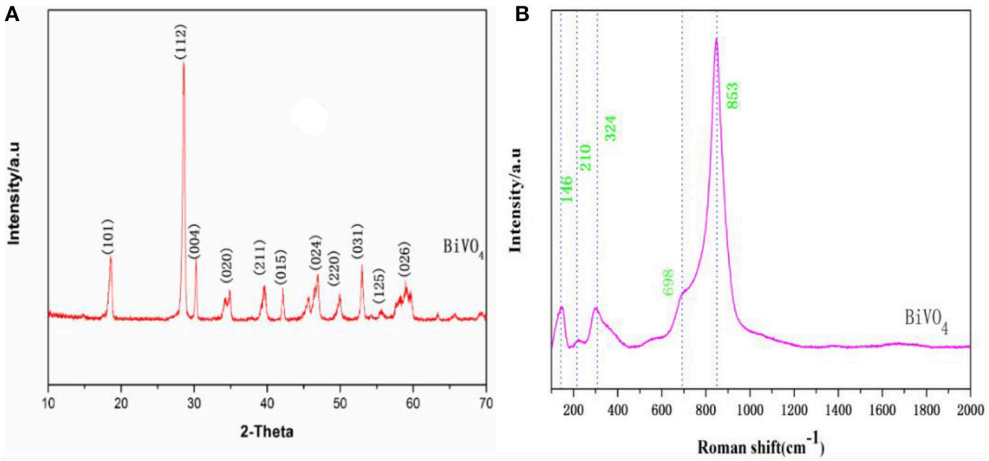

FIGURE 1 | (A) XRD patterns of $BiVO_4$ **(B)** Raman spectra of $BiVO_4$.

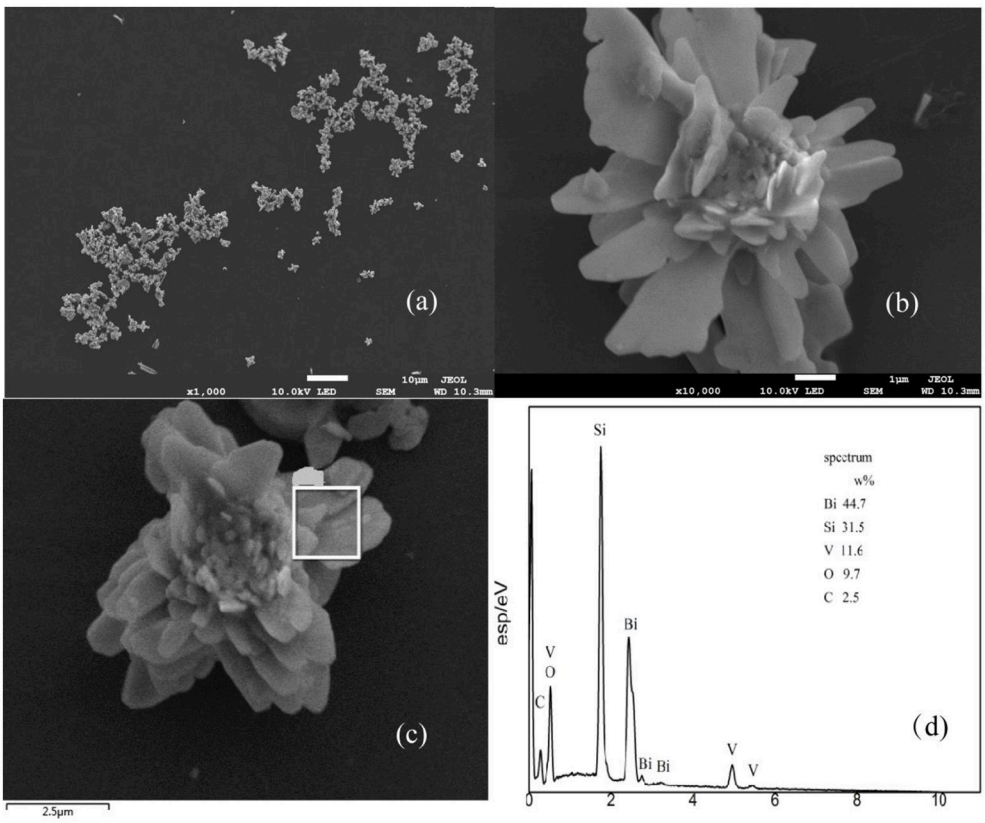

FIGURE 2 | SEM of $BiVO_4$ **(a,b)**, and EDX spectra with the corresponding EDX elemental mapping results **(c,d)**.

was assigned to ν_{as} (V–O) (Ye et al., 2012). Medium intensity bands were observed at 324 and 146 cm^{-1}. External vibrational modes (rotation/translation) are visible at 210 cm^{-1} (Jiang et al., 2012). These values correspond to the typical vibrations of monoclinic $BiVO_4$, although there are minor differences in some parts of the spectrum due to the fact that Raman band positions are sensitive to short-range order, whereas band widths are more sensitive to the degree of crystallinity, defects, disorders, particle size, and/or aggregation of particles (Gotić et al., 2005).

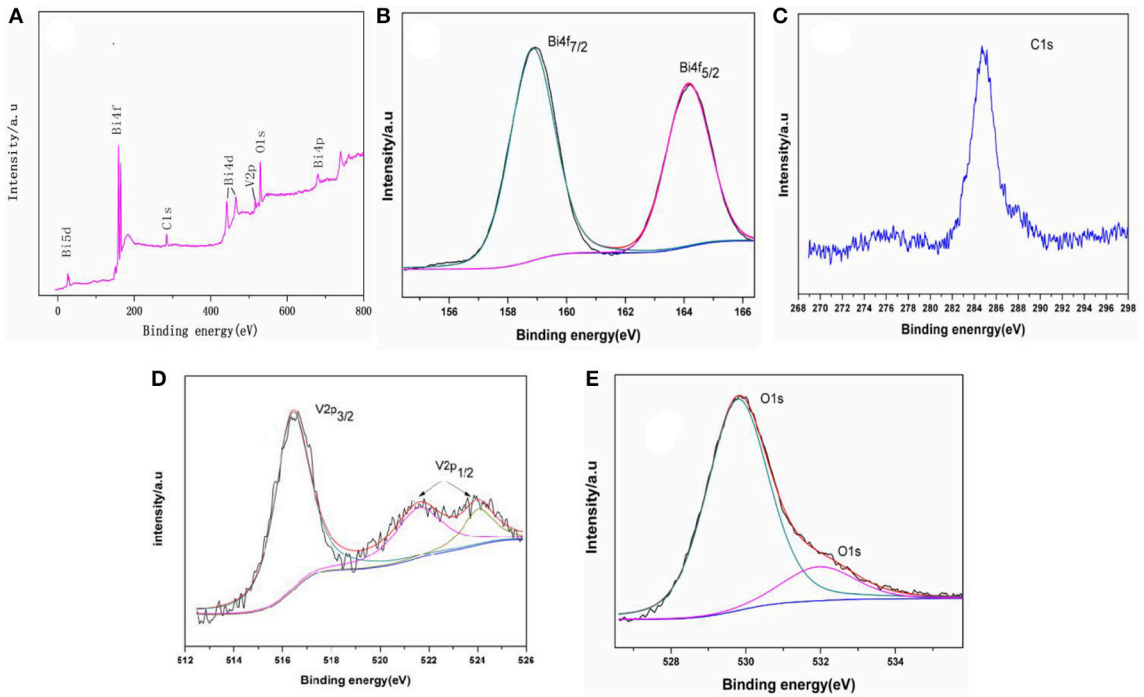

FIGURE 3 | XPS of the samples: **(A)** survey spectra, **(B)** Bi4f5/2 and Bi4f7/2 peaks **(C)** C1s peaks, **(D)** V2p3/2 and V2p1/2, and **(E)** O1s peaks.

The sizes and morphologies of the prepared samples were examined by SEM (**Figures 2a,b**). The shape of the material is similar to that of the flower, and each of the slices about the sample was about 2–5 μm. Based on the EDX results shown in **Figures 2c,d**, it can be concluded that the components of the material mainly include V, Bi, O, and Si (Si signals come from the conductive adhesives used in the EDX measurement). These results show the exact composition of the material and are in good agreement with the XPS results (**Figure 3**).

XPS was used to examine the chemical states of elements in the photocatalytic material. **Figure 3A** shows the full spectra of $BiVO_4$ in the range of 0–800 eV. The survey spectrum shows that the composite contains Bi, O, V, and C. As is reported in some papers (Long et al., 2006; Xu et al., 2016), the form of the Bi is Bi^{3+} in the compound $BiVO_4$ and the binding energies for Bi 4f7/2 and Bi4f5/2 are 158.8 and 163.4 eV, respectively (**Figure 3B**). **Figure 3C** shows the binding energy of C. The peaks at binding energies of 516.4 eV (V2p3/2), 522.0 eV (V2p1/2), and 524.2 eV (V2p1/2) are visible in **Figure 3D**. The peaks at binding energying of 516.4 eV (V2p3/2) and 524.2 eV (V2p1/2) indicate the V species in the composite is V^{5+} (Long et al., 2006; Xu et al., 2016; Zhao et al., 2016). And the peak at binding energying of 522.0 eV also represent the element of V (V2p1/2), which means there are some impurities when preparation (Zhao et al., 2016). The three peaks (**Figure 3D**) all represent V2p, and you can find the same peaks of V in other paper (Jia et al., 2012; Ota et al., 2014). Finally, **Figure 3E** shows the binding energy of O. Together, these data indicate that the tested sample consists of $BiVO_4$ microspheres as the same as other paper although there contains some impurities when preparation (Zhou et al., 2011; Xu et al., 2016).

Optical Properties and Degradation Properties

Optical absorption properties are key characteristics for a catalyst's photocatalytic activity (Hardcastle et al., 1991). The absorption of visible light by a photocatalyst is mainly due to band-gap transition. To investigate photocatalytic properties, the range of the photocatalyst's absorption wavelength within that of natural light must first be determined. **Figure 4A** shows the UV-Visible absorption spectra of the obtained $BiVO_4$ product, which exhibits strong absorption in both the visible and UV range, indicating its potential as a good photocatalyst for sunlight-driven applications.

As is known to us, energy band structures of a semiconductor continue to be important in determining its photocatalytic activity. And the relationship of absorbance and incident photon energy can be described by the following equation (Cheng et al., 2012):

$$\alpha h\nu = [A(h\nu - Eg)^{\frac{1}{2}}$$

Where α, ν, and A are the absorption coefficient, light frequency, and proportionality constant, respectively. The band-gap energy (there means direct band-gap), E_g, of the obtained photocatalyst can be estimated from a plot depicting $(\alpha h\nu)^2$ vs. hν (Cheng et al., 2012; Xu et al., 2016; Zhao et al., 2016). According to the data and corresponding theoretical calculations, the band-gap energies of

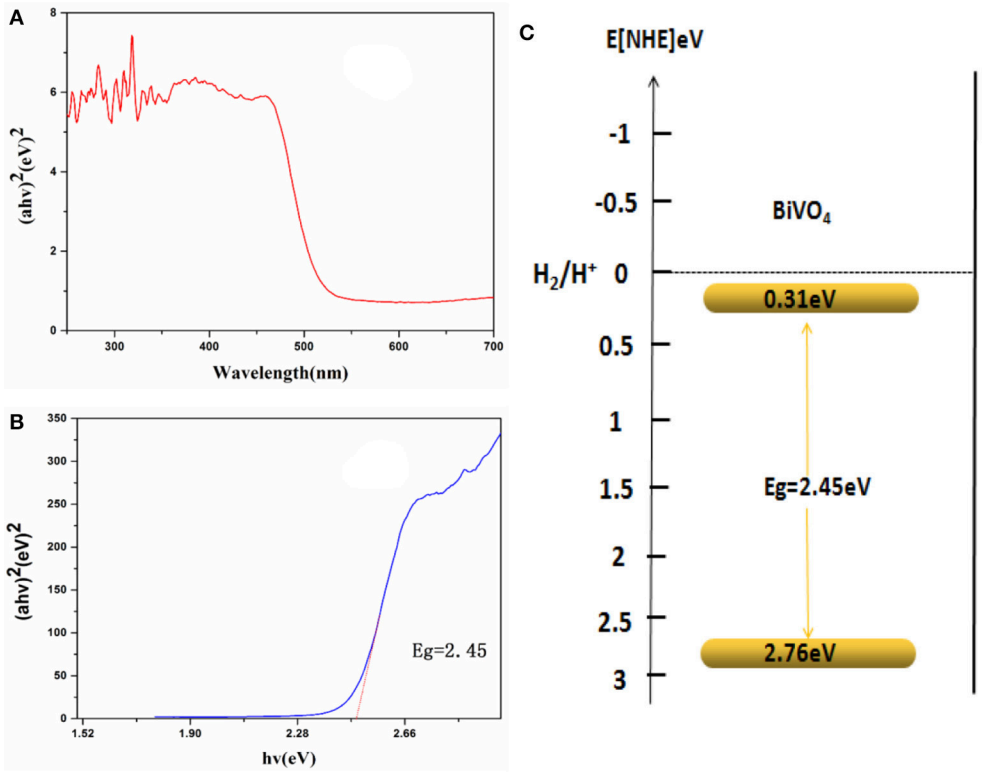

FIGURE 4 | (A) UV-Vis DRS spectra. **(B)** Relationship between $(\alpha h\nu)^2$ and the photon energy ($h\nu$) of the as-synthesized $BiVO_4$ **(C)** Schematic illustration of the band gap structure of $BiVO_4$.

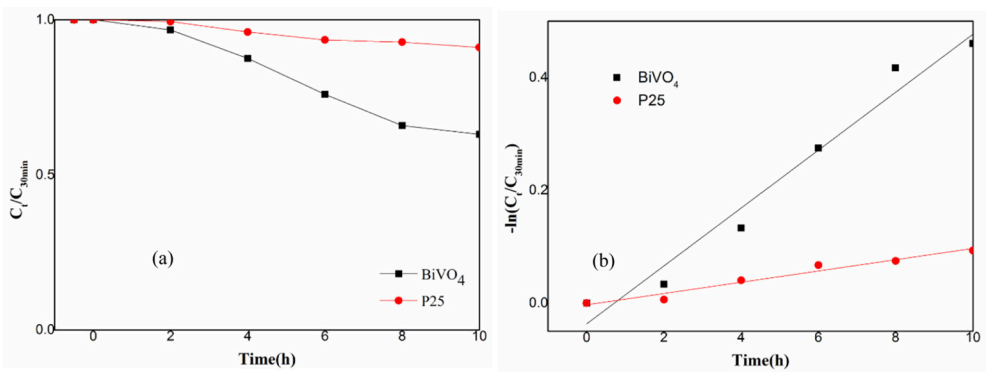

FIGURE 5 | (a) Photocatalytic degradation of RhB over $BiVO_4$ and P25; **(b)** First order kinetic fitting of Photocatalytic degradation of RhB over $BiVO_4$ and P25.

$BiVO_4$ were estimated to be about 2.45 eV as shown in **Figure 4B**. For a semiconductor, the CBM and VBM can be calculated according to the following empirical equation (Ye et al., 2012): $E_{CBM} = \chi - Ee - 0.5E_g$, where E_{CBM} is the CBM edge potential; χ is the electronegativity of the semiconductor (6.04 for $BiVO_4$) (Long et al., 2006); Ee is the energy of free electrons (about 4.5 eV); and E_g is the band-gap energy of the semiconductor (2.45 eV, as estimated previously). According to the equation $E_{VBM} = E_{CBM} + Eg$, the value of E_{CBM} is 0.31 eV and E_{VBM} is 2.76 eV. Similar results were also reported by Long et al (Long et al., 2006). What's more, the value of E_{CBM} and E_{VBM} are different owning to different test or different calculation method in different papers although the band-gap energy is very similar (Zhang et al., 1998; Long et al., 2006). A schematic illustration of the band-gap structure of $BiVO_4$ is shown in **Figure 4C**.

This paper also tested the photocatalytic efficiency of P25 and $BiVO_4$ and the result was shown in **Figure 5**. The **Figure 5A** experimental results showed that the efficiency of P25 was

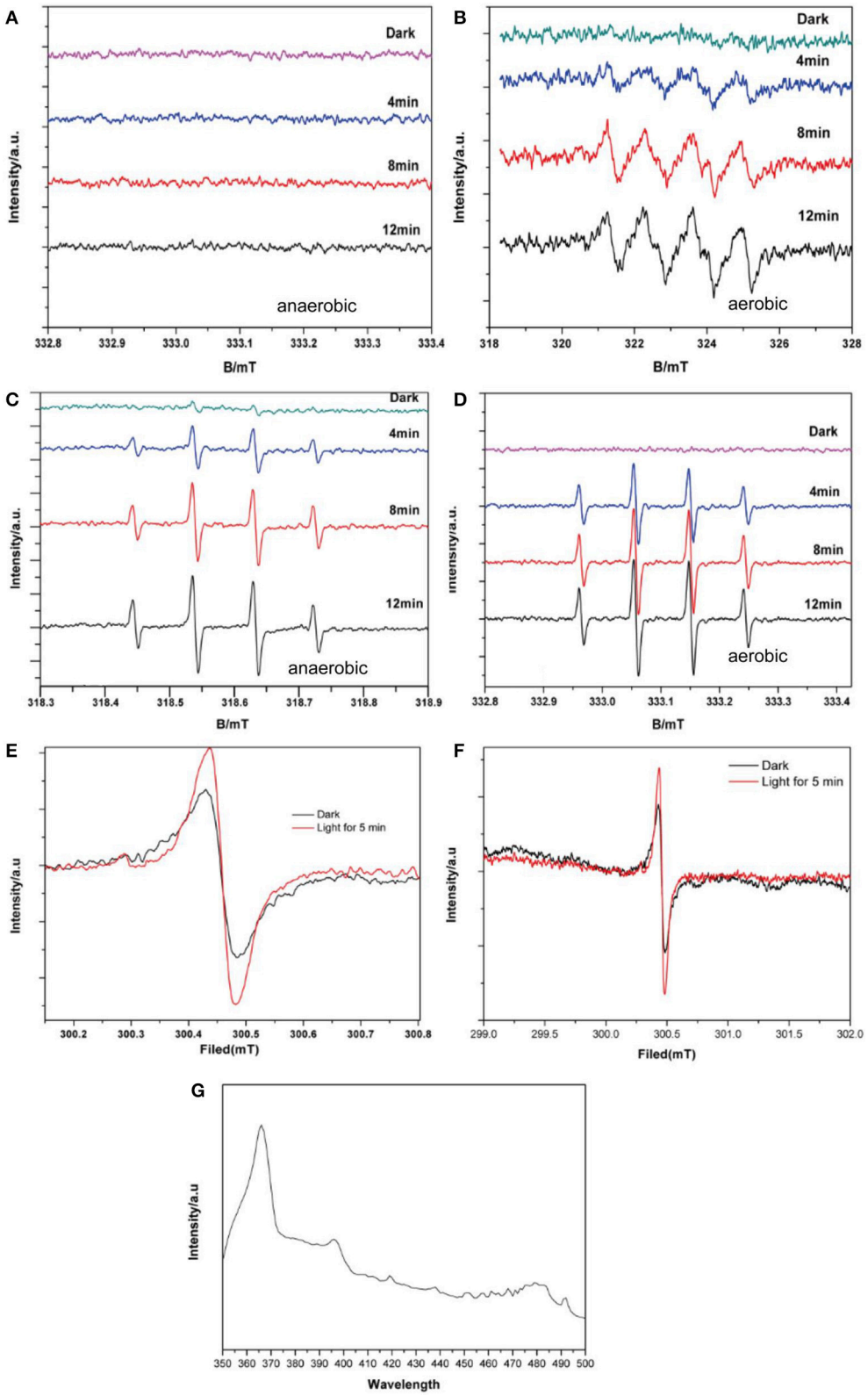

FIGURE 6 | DMPO spin-trapping ESR spectra under visible light for **(A)** DMPO–·O_2^- with $BiVO_4$, without O_2 **(B)** DMPO–·O_2^- with $BiVO_4$, with O_2 **(C)** DMPO–·OH with $BiVO_4$, without O_2 **(D)** DMPO–·OH with $BiVO_4$, with O_2 **(E)** ESR spectra of $BiVO_4$ recorded in the dark and under illumination for 5 min **(F)** magnified ESR spectra of $BiVO_4$ **(G)** PL spectra of $BiVO_4$.

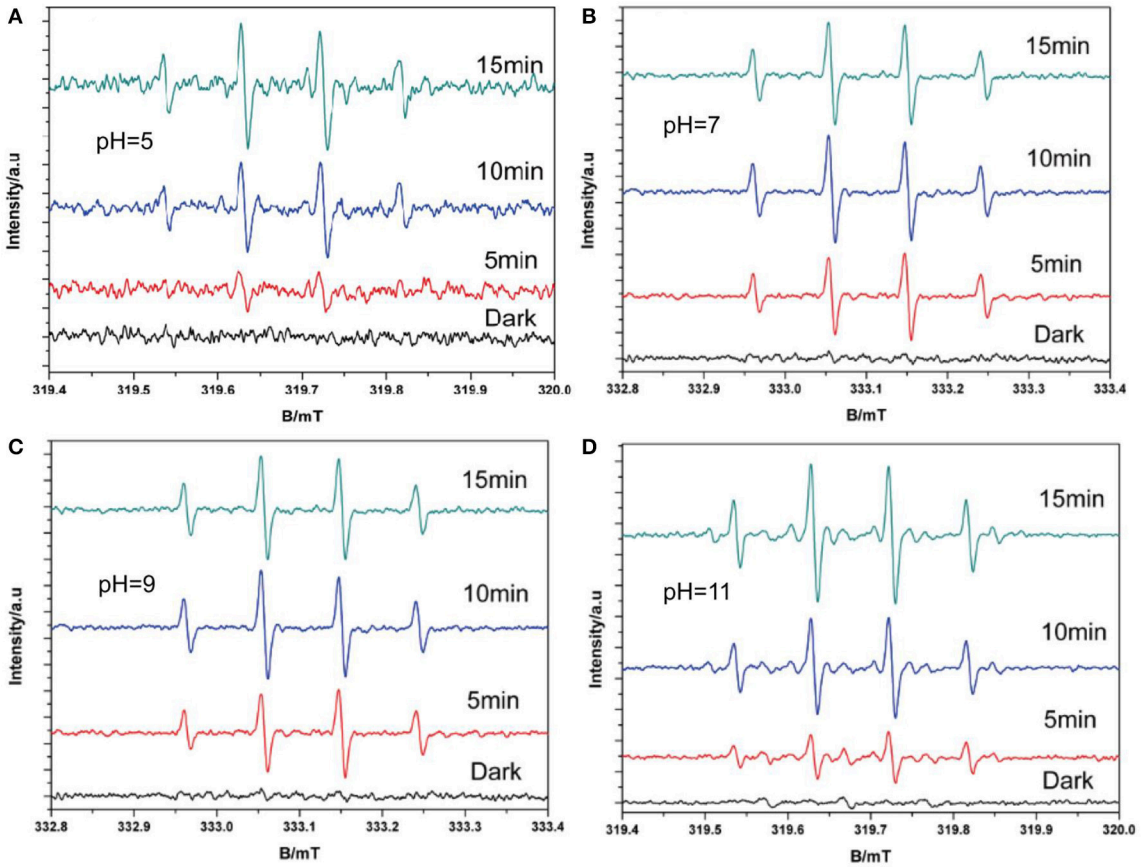

FIGURE 7 | DMPO–·OH with O_2 spin-trapping ESR spectra under visible light in and varying pH (**A** pH = 5; **B** pH = 7; **C** pH = 9; **D** pH = 11).

9%, while the efficiency of $BiVO_4$ was 37%. The **Figure 5B** was the first order kinetic fitting of the degradation result, both of these results indicated a better efficiency of RhB degradation in the presence of $BiVO_4$ compared to the P25, and this exactly represented a good degradation property of $BiVO_4$.

Mechanisms for $\cdot O_2^-$ and ·OH Production

ESR Analysis

Based on the ESR results as shown in **Figures 6A,B**, signals with intensities corresponding to the characteristic peaks of DMPO–$\cdot O_2^-$ adducts were observed when the reaction was performed under visible light irradiation, but not when the reaction was performed in the dark. The peak intensities further increased with increased irradiation time. Furthermore, DMPO–$\cdot O_2^-$ signals were observed under aerobic conditions (**Figure 6B**) but not under anaerobic conditions (**Figure 6A**). This is consistent with the production mechanism of $\cdot O_2^-$ via O_2, as previously reported (Ge et al., 2012b; Ye et al., 2012). Although there still were some studies mentioned no $\cdot O_2^-$ contained in the degradation system of $BiVO_4$ (Ge et al., 2012a; Lopes et al., 2015). As shown in **Figures 6C,D**, DMPO–·OH was observed under both aerobic and anaerobic conditions, respectively, and the signal intensity was stronger in the aerobic case. These results demonstrate the validity of both aerobic and anaerobic pathways for the production of ·OH. In the first pathway, oxygen, which is an effective electron acceptor, absorbed on the catalyst surface is the main capturing agent targeting photogenerated electrons and can oxidize the hydroxylated products to produce ·OH. The h^+ produced by the photocatalyst can then oxidize OH^- in water to produce ·OH, representing the second possible path. However there is no report for the identification of this phenomenon. The experimental results verified the validity of first path, and to ensure the possibility of the second path, we performed an experiment in which the pH was varied.

The ESR spectrum of $BiVO_4$ is shown in **Figures 6E,F** reveals a magnified section of the same spectrum to provide more detail. These confirm the separation of electron–hole pairs in the $BiVO_4$ and provide evidence for the existence of ·OH (Yang et al., 2015). The signal intensity of the 300.5 mT peak (g = 2.002) is evidently strong (**Figure 6E**) in comparison with the peak for the same sample in darkness, indicating the presence of h^+. In order to further for the explanation about the recombination of electron–hole pairs, we did the photoluminescence (PL) test. PL spectra can reveal the movement, transfer and recombination of photoelectron-hole pairs. It's an effective means to characterize the separation

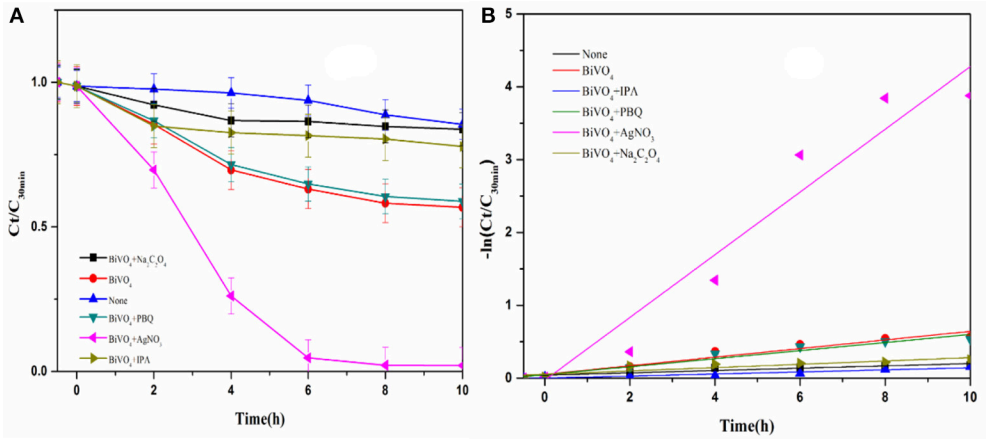

FIGURE 8 | (A) Photocatalytic degradation of RhB over $BiVO_4$ in the presence of scavengers; **(B)** First order kinetic fitting of Photocatalytic degradation of RhB over $BiVO_4$.

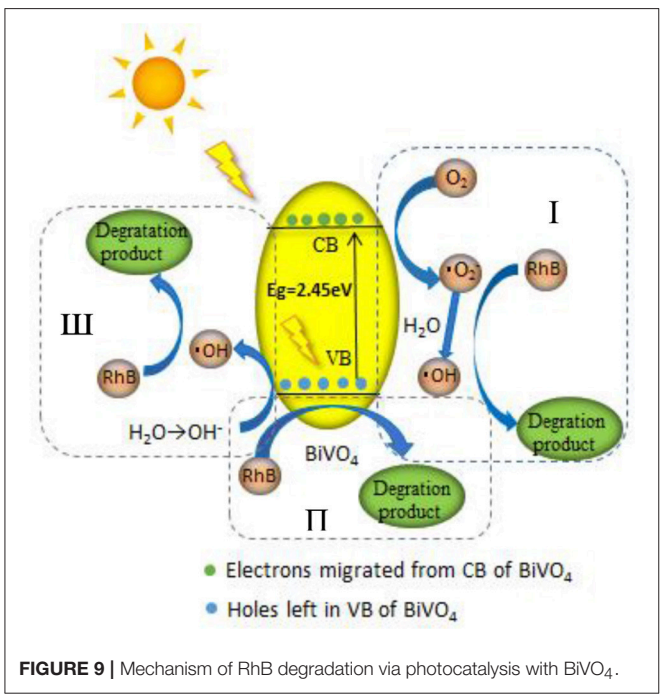

FIGURE 9 | Mechanism of RhB degradation via photocatalysis with $BiVO_4$.

efficiency of semiconductors. In general, the lower the intensity of the emission peak in the PL spectrum, the higher the efficiency of the electron and hole separation in the semiconductor and the higher the photocatalytic activity of the photocatalyst (Gao et al., 2014). From the PL result shown in **Figure 6G** shows the PL spectra of $BiVO_4$ under the excitation wavelength of 325 nm, we can find the strong peak under 367 nm, which means the existence about recombination of electron–hole pairs (Zhao et al., 2017).

According to the results of the pH experiment (**Figure 7**), the DMPO–·OH signal increased with increasing pH between 5 and 9, which could be found from the signal intensity under 5 min light; however, no obvious increase was observed when the pH increased to 11. This is because more ·OH radicals are produced under alkaline conditions than under acidic or neutral conditions. However, increased alkalinity may also alter the charge of the catalyst surface, thus affecting the production of hydroxyl radicals, which explains the lack of an increase at pH = 11 (Wang et al., 2011). These results confirm the validity of the second path, indicating that ·OH can be produced by the oxidation of h^+ for OH^-. Together, the ESR results explain the complete production of ·OH. The trapping experiment was performed to determine the main pathway for ·OH generation.

Scavengers Study

The photocatalytic activities of the samples were evaluated by analyzing the degradation of RhB under visible light irradiation. The effect of $BiVO_4$ on RhB degradation was obvious when compared to the result without any catalyst (**Figure 8**). The experimental results indicate complete inhibition of RhB degradation in the presence of IPA, suggesting that ·OH is the main reactive species contributing to the photocatalytic degradation of RhB over $BiVO_4$. $\cdot O_2^-$ also influenced the photocatalytic degradation of RhB, but the effect was less obvious than that of ·OH. As is known to us, the h^+ and e^- are the original active species in the degradation system. The presence of $AgNO_3$ captured e^- and reduced the recombination of h^+ and e^-, as a result it increased the effect of h^+. At the same time, the h^+ could further generate ·OH, which promoted the degradation of RhB. Because the ·OH was also the production of hole, we concluded that h^+ also plays an important role, and similar results were also reported by Zhou et al (Xu et al., 2017). What's more, we found obviously decrease on the addition of $Na_2C_2O_4$. The capture of h^+ meant there was no any hole and·OH in the degradation system, thus the degradation effect obviously decreased. As a result, we concluded the importance of hole. And its importance was further confirmed by the slight enhancement of RhB degradation after the addition of $Na_2C_2O_4$ to capture the photogenerated

hole. Furthermore, the addition of $AgNO_3$ enhanced the degradation effect, which also demonstrates the strong influence of electron–hole recombination on the degradation process. These results demonstrate that h^+ can directly degrade RhB, and therefore it plays a significant role in the system, as indicted by the second pathway. In addition, ·OH is mainly generated by h^+.

Elucidate the Mechanism

We proposed a reaction mechanism based on the results of the experiments described above (**Figure 9**). First, the adsorbed RhB is photo-activated by visible light, so that electrons can transfer from the singlet excited RhB (RhB*) to the CB of $BiVO_4$, leaving h^+ in the VB. Then, the electrons in the CB react with O_2, resulting in the production of $\cdot O_2^-$ and ·OH radicals, as illustrated in process I (**Figure 9**). However, this degradation process is our speculation based on references and the ESR experiment. We cannot ignore the indirect effect of the $\cdot O_2^-$ on the degradation of RhB owning to its little effect on the production of ·OH based on the trapping experiment result, and this process is not the main degradation mechanism. The O_2^- is perhaps only participating in a side reaction or maybe can further generate ·OH for the degradation. And the evidence for this process still requires further study. At the same time, h^+ in VB can oxidize the OH^- produced by ionization of water to ·OH, which is the main active free radical for RhB degradation, as shown in process III (**Figure 9**). Finally, the $\cdot O_2^-$ and ·OH degrade RhB^+ and RhB, indicating the major role of ·OH in the degradation system. At the same time, the h^+ can also degrade RhB^+ and RhB directly (which can be concluded from the trapping experiment result), as demonstrated in process II (**Figure 9**). However, the proportion of RhB degraded by this process is minor. So we conclude that there are three processes in the degradation system, the main mechanism is the process III, the process II occur very minor and the process I is the speculation based on our experiment result. Further study would be done for the process I. The entire sequence is summarized in the following reactions:

$$BiVO_4 + h\nu \rightarrow h^+ + e^- \quad \text{(R1)}$$

$$O_2 + e^- + H^+ \rightarrow H_2O_2 \quad \text{(R2)}$$

$$H_2O_2 + e^- \rightarrow \cdot O_2^- + OH^- \quad \text{(R3)}$$

$$\cdot O_2^- + H_2O \rightarrow \cdot OH + OH^- \quad \text{(R4)}$$

$$h^+ + OH^- \rightarrow \cdot OH \quad \text{(R5)}$$

$$h^+ + \cdot O_2^- + \cdot OH + RhB \rightarrow \text{Degration product} \quad \text{(R6)}$$

The mechanism and reactions for flowerlike $BiVO_4$ photocatalysis described in this study are the same as those from described in previous research (Liu et al., 2006; Li, 2012; Wei et al., 2013), which are generally accepted as true (Han et al., 2003; Cruz and Pérez, 2010; Tian et al., 2014; Aguilera-Ruiz et al., 2015; Gao et al., 2015). The difference between this study and others is that ESR identifies the production of $\cdot O_2^-$ and provides a direct analysis of the pathways for the production of ·OH radicals, as shown in R4 and R5. These results indicate that h^+ can also produce ·OH, a result which has not been identified in previous research (Lam et al., 2014); thus, h^+ plays an important role in the degradation system by mainly producing ·OH. This result makes it a little more clearly about the production of ·OH in the complete photocatalytic system, of which is one of the most effective active free radicals.

CONCLUSION

In summary, we successfully prepared flowerlike $BiVO_4$ and characterized the resulting samples using a variety of analytical methods to thoroughly investigate their morphologies and compositions. After the well synthesis of material, we compared the photocatalytic activity of $BiVO_4$ to P25 and the result shown a well degradation property of $BiVO_4$. Based on the ESR experiment, we found the main free radicals in the reaction system and concluded the production of them by changing test conditions and trapping experiment. The mechanism for RhB degradation via $BiVO_4$ photocatalysis was successfully elucidated by these experiments mentioned earlier. The main active free radicals in the reaction system are h^+ and ·OH. For the production of ·OH, in addition to production by $\cdot O_2^-$, it can also be produced by oxidation of h^+ to OH^-, which is the main pathway for ·OH generation. However, we cannot ignore the indirect effect of the $\cdot O_2^-$ on the degradation of RhB owning to its little effect on the production of ·OH based on the trapping experiment result. Weather the $\cdot O_2^-$ can further generate OH still require further future study .More ·OH will be generated if there is more OH^- in the degradation system. At the same time, future research should further elucidate the degradation system by conducting experiments under varying pH. This new insight into radical production can be used in tandem with further experimental investigation to help improve photocatalyst performance.

AUTHOR CONTRIBUTIONS

XX, YS, and ZF: conceived of the study and designed the experiments; YS, SZ, and SX: performed the experiments; YS, DZ, and BZ: analyzed the data; GL: contributed reagents, materials, and analysis tools; YS wrote the paper.

ACKNOWLEDGMENTS

Financial support from the Science and Technology Innovation Special Projects of Social Undertakings and Livelihood Support, Chongqing (cstc2016shmszx20009), the Chongqing Research Program of Basic Research and Frontier Technology (cstc2015jcyjA20013, cstc2017jcyjBX0080), and the 111 Project (B13041) are gratefully acknowledged.

REFERENCES

Aguilera-Ruiz, E., García-Pérez, U. M., de la Garza-Galván, M., Zambrano-Robledo, P., Bermúdez-Reyes, B, and Peral, J. (2015). Efficiency of $Cu_2O/BiVO_4$, particles prepared with a new soft procedure on the degradation of dyes under visible-light irradiation. *Appl. Sur. Sci.* 328, 361–367. doi: 10.1016/j.apsusc.2014.12.059

Castellanos, M. M., Reyman, D., Sieiro, C., and Calle, P. (2001). ESR-spin trapping study on the sonochemistry of liquids in the presence of oxygen. Evidence for the superoxide radical anion formation. *Ultrason. Sonochem.* 8, 17–22. doi: 10.1016/S1350-4177(99)00047-4

Chen, L., Huang, R., Xiong, M., Yuan, Q., He, J., Jia, J., et al., (2013). room-temperature synthesis of flower-like BiOX (X-Cl, Br, I) hierarchical structures and their visible-light photocatalytic activity. *Inorg. Chem.* 52, 11118–11125. doi: 10.1021/ic401349j

Cheng, B., Wang, W. G., Shi, L., Zhang, J., Ran, J. R., and Yu, H. G. (2012). Template-free hydrothermal synthesis of monoclinic hollow microspheres and their enhanced visible-light photocatalytic activity. *Int. J. Photoener.* 0.1, 121–129. doi: 10.1155/2012/797968

Cruz, M. D. L., and Pérez, U. M. G. (2010). Photocatalytic properties of $BiVO_4$, prepared by the co-precipitation method: degradation of rhodamine B and possible reaction mechanisms under visible irradiation[J]. *Mater. Res. Bull.* 45, 135–141. doi: 10.1016/j.materresbull.2009.09.029

Gao, W., Wang, M., Ran, C., Yao, X., Yang, H., Liu, J., et al. (2014). One-pot synthesis of Ag/r-GO/TiO_2 nanocomposites with high solar absorption and enhanced anti-recombination in photocatalytic applications. *Nanoscale* 6, 5498–5508. doi: 10.1039/c3nr05466g

Gao, X. M., Wang, Z. H., Fu, F., and Li, W. H. (2015). Effects of pH on the hierarchical structures and photocatalytic performance of Cu-doped $BiVO_4$, prepared via the hydrothermal method. *Mat. Sci. Semicon. Proc.* 35, 197–206. doi: 10.1016/j.mssp.2015.03.012

Ge, M., Liu, L., Chen, W., and Zhou, Z. (2012a). Sunlight-driven degradation of Rhodamine B by peanut-shaped porous $BiVO_4$ nanostructures in the H_2O_2-containing system. *Crystengcomm* 14, 1038–1044. doi: 10.1039/C1CE06264F

Ge, M., Zhu, N., Zhao, Y., Li, J., and Liu, L. (2012b). Sunlight-Assisted Degradation of Dye Pollutants in Ag_3PO_4 Suspension. *Ind. Eng. Chem. Res.* 51, 5167–5173. doi: 10.1021/ie202864n

Gotić, M., Musić, S., Ivanda, M., Šoufek, M., and Popović, S. (2005). Synthesis and characterisation of bismuth(III) vanadate. *J. Mol. Str.* 744, 535–540. doi: 10.1016/j.molstruc.2004.10.075

Han, S. T., Xi, H. L., Shi, R. X., Fu, X. Z., and Wang, X. X. (2003). Prospect and progress in the semiconductor photocatalysis. *Chin. J. Chem. Phys.* 16, 339–349. doi: 10.1088/1674-0068/16/5/339-349

Hardcastle, F. D., Wachs, I. E., Eckert, H., and Jefferson, D. A. (1991). Vanadium(V) environments in bismuth vanadates: a structural investigation using Raman spectroscopy and solid state 51 V NMR. *J. Solid State Chem.* 90, 194–210.. doi: 10.1016/0022-4596(91)90135-5

Hashimoto, K., Irie, H., and Fujishima, A. (2005). TiO_2 photocatalysis: a historical overview and future prospects. *Jpn. J. Appl. Phys.* 44, 8269–8285. doi: 10.1143/JJAP.44.8269

Inoue, T., Fujishima, A., Konishi, S., and Honda, K. (1979). Photoelectrocatalytic reduction of carbon dioxide in aqueous suspensions of semiconductor powders. *Nature* 277, 637–638. doi: 10.1038/277637a0

Jia, Q., Iwashina, K., and Kudo, A. (2012). Facile fabrication of an efficient $BiVO_4$ thin film electrode for water splitting under visible light irradiation. *Proc. Natl. Acad. Sci. U.S.A.* 109, 11564–11569. doi: 10.1073/pnas.1204623109

Jiang, H., Dai, H., Meng, X., Zhang, L., Deng, J., Liu, Y., et al. (2012). Hydrothermal fabrication and visible-light-driven photocatalytic properties of bismuth vanadate with multiple morphologies and/or porous structures for Methyl Orange degradation. *J. E. Sci.* 24, 449–457 doi: 10.1016/S1001-0742(11)60793-6

Kohtani, S., Tomohiro, M., Tokumura, K., and Nakagaki, R. (2005). Photooxidation reactions of polycyclic aromatic hydrocarbons over pure and Ag-loaded $BiVO_4$, photocatalysts. *Appl. Catal. B Environ.* 58, 265–272. doi: 10.1016/j.apcatb.2004.12.007

Kubo, M., Sekiguchi, K., Shibasaki-Kitakawa, N., and Yonemoto, T. (2012). Kinetic model for formation of DMPO-OH in water under ultrasonic irradiation using EPR spin trapping method. *Resh. Chem. Interm.* 38, 2191–2204. doi: 10.1007/s11164-012-0536-7

Lam, S. M., Sin, J. C., Abdullah, A. Z., and Mohamed, A. R. (2014). Photocatalytic TiO_2/carbon nanotube nanocomposites for environmental applications: an overview and recent developments. *Fuller Nanotub Car N.* 22, 471–509. doi: 10.1080/1536383X.2012.690458

Li, G. (2012). Production and contribution of hydroxyl radicals in photocatalytic oxidation process. *Chin. J. Environ. Eng.* 6, 3388–3392.

Liu, H., Ye, X., Lian, Z., Wen, Y., and Shangguan, W. (2006). Experimental study of photocatalytic oxidation of formaldehyde and its by-products. *Res. Chem. Interm.* 32, 3219–3216. doi: 10.1163/156856706775012978

Long, M., Cai, W. M., Cai, J., Zhou, B. X., Chai, X. Y., and Wu, Y. H. (2006). Efficient photocatalytic degradation of phenol over Co_3O_4 /$BiVO_4$, composite under visible light irradiation. *J. Phys. Chem. B.* 110, 20211–202166. doi: 10.1021/jp063441z

Lopes, O. F., Carvalho, K. T. G., Macedo, G. K., de Mendonça, V. R., Avansi, W. Jr., and Ribeiro, C. (2015). Synthesis of $BiVO_4$ via oxidant peroxo-method: insights into the photocatalytic performance and degradation mechanism of pollutants. *New J. Chem.* 39, 6231–6237. doi: 10.1039/C5NJ00984G

Ming, G., Tan, M. M., and Cui, G. H. (2014). Synthesis of $Ag_3PO_4/BiVO_4$ composite photocatalyst and its photocatalytic degradation of dyes under visible light irradiation. *Acta Phys. Chim. Sin.* 30, 2107–2112. doi: 10.3866/PKU.WHXB201409041

Nalbandian, M. J., Zhang, M., Sanchez, J., Y.-,Choa, H., Cwiertny, D. M., and Myung, N. V. (2015). Synthesis and optimization of $BiVO_4$, and co-catalyzed $BiVO_4$, nanofibers for visible light-activated photocatalytic degradation of aquatic micropollutants. *J. Mol. Catal. A. Chem.* 404–405, 18–26. doi: 10.1016/j.molcata.2015.04.003

Ota, T., Arimoto, K., Tsujimoto, A., Watanabe, J., and Ikeda, Y. (2014). Preparation of inorganic yellow transparent film, using organometallic compounds as raw materials. *Shikizai Kyokaishi* 87, 306–310. doi: 10.4011/shikizai.87.306

Ren, L., Qi, X., Liu, Y. D., Huang, Z., Wei, X., Li, J., et al. (2012). Upconversion-P25-graphene composite as an advanced sunlight driven photocatalytic hybrid material. *J. Mater. Chem.* 22, 11765–11771. doi: 10.1039/c2jm 30457k

Shan, L. W., Mi, J. B., Dong, L. M., Han, Z. D., and Liu, B. (2014). Enhanced photocatalytic properties of silver oxide loaded bismuth vanadate. *Chin. J. Chem. Eng.* 22, 909–913. doi: 10.1016/j.cjche.2014.06.015

Tian, Y., Chang, B., Lu, J., Fu, J., Xi, F., and Dong, X. (2014). Hydrothermal synthesis of graphitic carbon nitride-Bi_2WO_6 heterojunctions with enhanced visible light photocatalytic activities. *Powder Technol.* 267, 126–133. doi: 10.1016/j.powtec.2014.07.021

Wang, M., Niu, C., Liu, J., Wang, Q., Yang, C., and Zheng, H. (2015). Effective visible light-active nitrogen and samarium co-doped $BiVO_4$ for the degradation of organic pollutants. *J. Alloy Compd.* 648, 1109–1115. doi: 10.1016/j.jallcom.2015.05.115

Wang, Y., He, Y. M., Lai, Q. H., and Fan, M. H. (2014). Review of the progress in preparing nanoTiO_2:Animportant environmental engineering material. *J. Environ. Sci. China* 26, 2139–2177. doi: 10.1016/j.jes.2014.09.023

Wang, Z. H., Ma, W. H., Chen, C. C., Ji, H. W., and Zhao, J. C. (2011). Probing paramagnetic species in titania-based heterogeneous photocatalysis by electron spin resonance (ESR) spectroscopy-A mini review. *Chem. Eng. J.* 170, 353–362. doi: 10.1016/j.cej.2010.12.002

Wei, W., Yue, X. J., Cui, H. L., Lu, X. M., and Xie, J. M. (2013). Hydrothermal synthesis and properties of $BiVO_4$ photocatalysts. *J. Mater. Res.* 28, 3408–3416. doi: 10.1557/jmr.2013.366

Xu, H., Li, H. M., Wu, C. D., Chu, J. Y., Yan, Y. S., and Shu, H. M. (2008). Preparation, characterization and photocatalytic activity of transition metal-loaded $BiVO_4$. *Mat. Sci. Eng. B. Solid.* 147, 52–56. doi: 10.1016/j.mseb.2007.11.011

Xu, X., Du, M., Chen, T., Xiong, S., Wu, T., Zhaoa, D., et al. (2016). New insights into Ag-Doped $BiVO_4$ microspheres as visible light photocatalysts. *RSC Adv.* 6:98788. doi: 10.1039/C6RA20850A

Xu, X., Zhou, S. Y., Long, J., Wu, T. H., and Fan, Z. H. (2017). Synthesis of a core-shell photocatalyst material YF_3:Ho^{3+}@TiO_2 and investigation of its photocatalytic properties. Mat*erials* 10:302 doi: 10.3390/ma10030302

Yang, C. Y., Li, F., and Li, T. H. (2015). A one-step ionic liquid-assisted ultrasonic method for the preparation of BiOCl/m-$BiVO_4$ heterojunctions with enhanced visible light photocatalytic activity. *Crystengcomm* 17, 7676–7683. doi: 10.1039/C5CE01312G

Ye, L., Liu, J., Gong, C., Tian, L., Peng, T., and Zan, L. (2012). Two different roles of metallic Ag on Ag/AgX/BiOX (X = Cl, Br) visible light photocatalysts: surface plasmon resonance and Z-scheme bridge. *ACS Catalysis* 2, 1677–1683. doi: 10.1021/cs300213m

Zhang, A. P., and Zhang, J. Z. (2009). Characterization of visible-light-driven $BiVO_4$ photocatalysts synthesized via a surfactant-assisted hydrothermal method. *Spectrochim. Acta A* 73, 336–341. doi: 10.1016/j.saa.2009.02.028

Zhang, C. L., Shou, J., and Li, H. (2015). Current situation and countermeasures of water body pollution in rural areas of China. *Mat. E.R.* 63, 42–47.

Zhang, F, Zhao, J, and Shen, T, Hidaka, H., Pelizzetti, E., and Serpone, N., (1998). TiO_2-assisted photodegradation of dye pollutants IAdsorption, I., and degradation kinetics of eosin in TiO_2 dispersions under visible light irradiation. *Phys. Chem. Chem. Phys*. 16, 16606–16614.

Zhang, L., Chen, D., and Jiao, X. (2006). Monoclinic structured $BiVO_4$ nanosheets: hydrothermal preparation, formation mechanism, and coloristic and photocatalytic properties. *J. Phys. Chem. B*. 110, 2668–2673. doi: 10.1021/jp056367d

Zhang, X., Liu, X., Zhang, L., Li, D., and Liu, S. (2016). ChemInform abstract: novel porous Ag_2S/ZnS composite nanospheres: fabrication and enhanced visible-light photocatalytic activities. *Chemistry* 47, 38–43. doi: 10.1002/chin.201604015

Zhang, Z., Wang, W., Shang, M., and Yin, W. (2010). Photocatalytic degradation of rhodamine B and phenol by solution combustion synthesized $BiVO_4$, photocatalyst. *Catal. Comm*. 11, 982–986. doi: 10.1016/j.catcom.2010.04.013

Zhao, D., Zong, W., Fan, Z., Fang, Y.-W., Xiong, S., Du, M., et al. (2017). Synthesis of carbon-doped nanosheets m-$BiVO_4$, with three-dimensional (3D) hierarchical structure by one-step hydrothermal method and evaluation of their high visible-light photocatalytic property[J]. *J. Nanopart. Res.* 19:124. doi: 10.1007/s11051-017-3818-6

Zhao, D., Zong, W., Fan, Z., Xiong, S., Du, M., Wu, T., et al. (2016). Synthesis of carbon doped $BiVO_4$@Multi-walled carbon nanotubes with high visible light absorption behavior and evaluation of its photocatalytic property. *CrystEngComm* 47, 9007–9015. doi: 10.1039/C6CE01642A

Zhou, B., Zhao, X., Liu, H., Qua, J., and Huangac, C. P. (2011). Synthesis of visible-light sensitive M–$BiVO_4$, (M = Ag, Co, and Ni) for the photocatalytic degradation of organic pollutants. *Separat. Purific. Technol*. 77, 275–282. doi: 10.1016/j.seppur.2010.12.017

Zhou, Z., Long, M., Cai, W., and Cai, J. (2012). Synthesis and photocatalytic performance of the efficient visible light photocatalyst Ag–AgCl/$BiVO_4$. *J. Mol. Catal. A Chem*. 353, 22–28. doi: 10.1016/j.molcata.2011.10.025

Conflict of Interest Statement: The authors declare that the research was conducted in the absence of any commercial or financial relationships that could be construed as a potential conflict of interest.

The handling Editor declared a shared affiliation, though no other collaboration, with one of the authors, FZ.

frontiers in Chemistry

ORIGINAL RESEARCH
published: 01 March 2018
doi: 10.3389/fchem.2018.00037

Ti_4O_7/g-C_3N_4 Visible Light Photocatalytic Performance on Hypophosphite Oxidation: Effect of Annealing Temperature

Wei Guan[1], *Gaoge Sun*[2], *Lei Yin*[3], *Zhenghua Zhang*[4*†] *and Shichao Tian*[5*†]

[1] Chongqing Key Laboratory of Environmental Materials and Remediation Technologies, Chongqing University of Arts and Sciences, Chongqing, China, [2] Department of Chemistry, Tsinghua University, Beijing, China, [3] Heibei Yinfa Meifute Environmental Engineering Co., Ltd., Shijiazhuang, China, [4] Research Institute of Environmental Engineering and Nano-Technology, Graduate School at Shenzhen, Tsinghua University, Shenzhen, China, [5] Shenzhen Environmental Science and New Energy Technology Engineering Laboratory, Tsinghua-Berkeley Shenzhen Institute, Shenzhen, China

OPEN ACCESS

Edited by:
Fan Dong,
Chongqing Technology and Business University, China

Reviewed by:
Hongwei Huang,
China University of Geosciences, China
Michael Nolan,
University College Cork, Ireland

***Correspondence:**
Zhenghua Zhang
zhenghua.zhang@sz.tsinghua.edu.cn
Shichao Tian
18812672619@163.com

[†] These authors have contributed equally to this work.

Specialty section:
This article was submitted to Catalysis and Photocatalysis, a section of the journal Frontiers in Chemistry

Received: 04 December 2017
Accepted: 14 February 2018
Published: 01 March 2018

Citation:
Guan W, Sun G, Yin L, Zhang Z and Tian S (2018) Ti_4O_7/g-C_3N_4 Visible Light Photocatalytic Performance on Hypophosphite Oxidation: Effect of Annealing Temperature. Front. Chem. 6:37. doi: 10.3389/fchem.2018.00037

The oxidation of hypophosphite to phosphate is the key to recover the phosphorus resource from the hypophosphite wastewater. In the present work, Ti_4O_7/g-C_3N_4 composites were synthesized at two different temperatures (100 and 160°C) and their performance on photocatalytic oxidation of hypophosphite under visible light irradiation and the corresponding mechanism were evaluated. A hydrolysis method using g-C_3N_4 and Ti_4O_7 was applied to synthesize the Ti_4O_7/g-C_3N_4 composites with their hybrid structure and morphology confirmed by X-ray diffraction (XRD), scanning electron microscopy (SEM), and X-ray photoelectron spectra (XPS). The annealing temperature significantly affected the photocatalytic performance of Ti_4O_7/g-C_3N_4 that the 160-Ti_4O_7/g-C_3N_4 composite (fabricated at 160°C) showed the highest oxidation efficiency of hypophosphite of 81% and the highest photocatalytic oxidation rate of 0.467 h^{-1} comparing with the 100-Ti_4O_7/g-C_3N_4 composite (fabricated at 100°C) and pure g-C_3N_4. The enhanced photocatalytic performance of 160-Ti_4O_7/g-C_3N_4 could be ascribed to the effective charge separation and enhanced photoabsorption efficiency. Additionally, electron spin resonance (ESR) results showed that hydroxyl radicals and superoxide anion radicals were mainly responsible to the oxidation of hypophosphite with superoxide anion radicals accounting for a more significant contribution. Moreover, Ti_4O_7/g-C_3N_4 photocatalysts showed the remarkable stability in the repetitive experiments.

Keywords: graphitic carbon nitride, sub-stoichiometric titanium oxides, hypophosphite, hydroxyl radicals, superoxide anion radicals

INTRODUCTION

Hypophosphite is commonly used as a reducing agent in metallurgy industries especially in the processes of plating and surface finishing thereby generating large amounts of hypophosphite wastewater (Bulasara et al., 2011; Li et al., 2015). The hypophosphite contaminant should be further treated before being discharged into the river or lake, because it may lead to algae growth

and cause eutrophication (Wang et al., 2016; Ge et al., 2017). In addition, phosphorus is a non-renewable resource mainly used as a nutrient in agricultural production (Montangero and Belevi, 2007). Due to an increase in the global demand for phosphorus resource, it will be depleted in the next 50–100 years (Takeda et al., 2010; Ye Y. Y. et al., 2017; Ye Z. L. et al., 2017). Therefore, the phosphorus recovery from wastewater is of considerable interest. However, a high solubility constant of the hypophosphite precipitants limits the transformation of hypophosphite into the precipitated products. In contrast, phosphate is easier to be recovered than hypophosphite by precipitation. As such, a highly efficient approach for the pre-oxidation of hypophosphite to phosphate becomes of great importance for phosphorus recovery. Photocatalysis, a nano-enabled technology, has been recognized for its promising applications with the generation of activated radicals such as hydroxyl radicals and superoxide anion radicals, which herein can be applied for hypophosphite oxidation.

Semiconductor photocatalysts have been recognized as a potential strategy to solve some serious challenges of the twenty-first century, such as energy shortage, environmental pollution, and global warming (Lin et al., 2017). TiO_2 photocatalyst has attracted much attention due to its strong oxidizing power, low cost and high chemical stability. However, a large band gap (3.2 eV) of TiO_2 means that it can only absorb ultraviolet light (only about 3–5% of total sunlight), which greatly limits its performance in industrial applications (Teng et al., 2017; Noman et al., 2018). Therefore, it is urgent to develop novel semiconductor photocatalysts that respond to visible light.

Recently, graphitic carbon nitride (g-C_3N_4), constituted by numerous layers of two-dimensional (2D) counterparts, has attracted enormous attention given its advantages such as low cost and visible light driven semiconductor photocatalyst (Huang et al., 2017b; Liu et al., 2017a,b; Tian et al., 2017; Wang et al., 2017). The metal free g-C_3N_4 can work as photocatalyst under visible light irradiation with a suitable band gap of 2.7 eV. In addition, g-C_3N_4 possesses excellently structural stability, which is suitable for chemical modification. Nevertheless, the photocatalytic property of g-C_3N_4 is still limited for its low surface area, low photoabsorption efficiency and high recombination rate of photo-induced electron-hole pairs (Jourshabani et al., 2017; Shao et al., 2017).

Decreasing the recombination of photo-induced carriers during the photocatalytic process would enhance the photocatalytic activity of the as-prepared g-C_3N_4 photocatalyst (Li J. D. et al., 2017). Therefore, some methods, such as porosity engineering, doping with foreign elements, and compositing with other semiconductors to facilitate charge separation, were developed to enhance the photocatalytic performance of g-C_3N_4. For example, the horn-like hollow mesoporous ultrathin g-C_3N_4 tubes were fabricated with high surface area, drastically boosted bulk charge separation, carrier density and surface charge transfer efficiency and showed the remarkably photocatalytic performance for H_2 evolution (Liu et al., 2017a). Meanwhile, the 3D mesoporous g-C_3N_4 established by ultrathin self-doped nanosheets exhibited the superior photocatalytic performance on hydrogen evolution (Tian et al., 2017). Additionally, the porous and thin g-C_3N_4 nanosheets, prepared via a novel thiourea-assisted melamine-precursor hydrothermal pre-treatment followed by a traditional thermal polymerization method, profoundly enhanced visible-light photocatalytic performance on H_2 evolution and NO removal from the gaseous phase (Huang et al., 2017b). Moreover, the Cl intercalated mesoporous g-C_3N_4 showed outstanding photocatalytic performance for water splitting into H_2, CO_2 reduction, liquid and air contaminants removal (Liu et al., 2017b).

Substoichiometric titanium oxides, known as Magnéli phases (Sun et al., 2016), comprise a series of compounds with the generic formula Ti_nO_{2n-1} ($4 \leq n \leq 10$) (Kolbrecka and Przyluski, 1994; Guo et al., 2016). Among these compounds, Ti_4O_7 possesses high electrical conductivity, thermal stability, and corrosion resistance in harsh conditions (Oturan et al., 2017). Therefore, Ti_4O_7 is wildly used as catalyst coated material (Li et al., 2010), wastewater treatment material (You et al., 2016), support material in fuel cell (Chisaka et al., 2016), and additive to positive materials in batteries (Cao et al., 2017). However, it was also reported that pure Ti_4O_7 as the photocatalyst had limited photocatalytic activity with the band gap of 2.9 eV (Maragatha et al., 2017). Herein, coupling Ti_4O_7 and intrinsic g-C_3N_4 to construct the well-matched Ti_4O_7/g-C_3N_4 heterojunction would be an alternative novel pathway to address the intrinsic drawbacks of g-C_3N_4 for photocatalytic applications.

In this study, novel Ti_4O_7/g-C_3N_4 photocatalysts were synthesized at two different temperatures (100 and 160°C) and their performance in photocatalytic oxidation of hypophosphite under visible light irradiation and the corresponding mechanism were compared and investigated. Ti_4O_7/g-C_3N_4 photocatalysts exhibited an enhanced photocatalytic activity for hypophosphite oxidation under visible light irradiation and the annealing temperature significantly affected the photocatalytic performance. The separation mechanism of photogenerated electrons and holes of the photocatalysts was investigated by UV-Vis diffuse reflectance spectra, photoluminescence emission spectra, cyclic voltammetry (CV), and electrochemical impedance spectroscopy (EIS). The activated species generated in the photocatalytic process were measured by electron spin resonance (ESR). The enhanced photocatalytic performance could be ascribed to the efficient charge separation and transfer across the heterojunction interface and the enhanced photoabsorption efficiency. Our work demonstrated that the rational design and construction of isotype heterojunction was an effective strategy for the development of efficient photocatalysts under visible light irradiation.

MATERIALS AND METHODS

Chemicals

Melamine ($C_3H_6N_6$), urea [$CO(NH_2)_2$], sub-stoichiometric titanium oxide (Ti_4O_7), sodium hypophosphite (NaH_2PO_2), sodium sulfate (Na_2SO_4), isopropanol [IPA, $(CH_3)_2CHOH$], ethylenediaminetetraacetic acid disodium salt ($C_{10}H_{14}N_2Na_2O_8$), sodium hydroxide (NaOH), and sulfuric acid (H_2SO_4) were provided by Sinopharm Chemical Reagent Co., Ltd. (Beijing, China). 5,5-dimethylpyrroline-N-oxide (DMPO)

was bought from Dojindo Co., Ltd. (Shanghai, China). The entire chemical reagents were analytical grade and all solutions were prepared using Milli-Q water (Millipore, 18.2 MΩ cm).

Synthesis of g-C_3N_4 Materials

The g-C_3N_4 materials were prepared using a liquid-based growth method (Sun et al., 2018). In a typical process, the mixture of melamine and urea (molar ratio = 1:1) was dissolved with 50 mL deionized water and then vigorously stirred for 1 h at room temperature. After that, the mixture suspension was centrifuged at 7,500 r/min for 15 min, and then dried at 60°C for 24 h under the vacuum to obtain the white powder. After that, the prepared white powders were further grinded into smaller powders in a mortar and placed in a muffle furnace. The powders were then annealed at 550°C in a muffle furnace for 4 h in static air at a ramp rate of 2.5°C min^{-1}. The resulting yellow products were collected for further usage.

Preparation of $Ti_4O_7/g\text{-}C_3N_4$ Photocatalysts

The preparation procedure of $Ti_4O_7/g\text{-}C_3N_4$ photocatalysts was shown below: g-C_3N_4 powder (2.0 g) and Ti_4O_7 (1.0 g) were dispersed into 100 mL NaOH (0.1 mol/L) by ultrasonication for 0.5 h. Subsequently, the mixed liquor was transferred to reaction still and then annealed in different temperatures (100 and 160°C) for 20 h. After that, the obtained precipitates were collected by centrifugation and washed with distilled water, and then dried at 60°C for 12 h. Samples fabricated at different annealing temperatures were noted as 100-$Ti_4O_7/g\text{-}C_3N_4$ (fabricated at 100°C) and 160-$Ti_4O_7/g\text{-}C_3N_4$ (fabricated at 160°C), respectively.

Samples Characterization

The concentration of NaH_2PO_2 was measured by ion chromatography using a 732 IC detector (McDowell et al., 2004). The crystal phase composition and fineness of the samples were analyzed by X-ray diffraction (XRD) with Cu Kα radiation in the scanning range of 2θ = 5–80° (model D/max RA, Rigaku Co., Japan). The surface morphology of the as-developed samples was examined by scanning electron microscopy (SEM) (JEOL JSM-6701F). The valence state of the deposition was measured by X-ray photoelectron spectra (XPS) (PHI-5300/ESCA, ULVAC-PHI, INC). The UV–vis diffuse reflection spectra (UV–vis DRS) of the samples was obtained by a UV–vis spectrophotometer (UV-2450, Shimadzu, Japan). Electrochemical properties of the $Ti_4O_7/g\text{-}C_3N_4$ and g-C_3N_4 photocatalysts, including photocurrents (PC), CV, and EIS, were measured on a CHI 660B electrochemical system. Electron spin resonance (ESR) (ESRA-300, Bruker, Germany) signals were recorded by the probe molecular 5,5-dimethyl-1-pyrroline-N-oxide (DMPO) to identify the radicals generated under visible light irradiation (λ > 420 nm) (Tian et al., 2015).

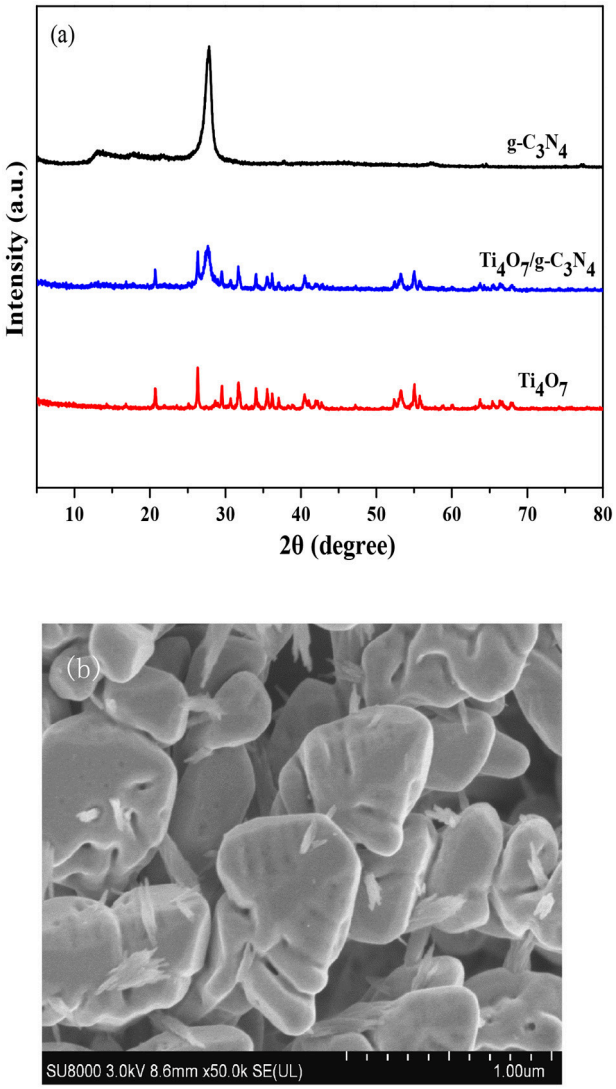

FIGURE 1 | Structure and morphology analyses. **(a)** XRD patterns of the g-C_3N_4, Ti_4O_7 and 160-$Ti_4O_7/g\text{-}C_3N_4$ photocatalysts; **(b)** SEM image of the 160-$Ti_4O_7/g\text{-}C_3N_4$ photocatalyst.

Evaluation of Photocatalytic Activity

The photocatalytic activities of as-synthesized samples were evaluated by the oxidation of hypophosphite in aqueous solution under visible light irradiation. For hypophosphite oxidation, the light source was a 35 W metal-halide lamp (Philips) with a 420 nm UV-cutoff filter. The lamps were located 12 cm away from the surface of reaction solution (about 5 mW cm^{-2}). In each experiment, photocatalyst (10 mg) was dispersed in hypophosphite (100 ml, 100 mg L^{-1}) aqueous solution. Before irradiation, the solution was continuously stirred in the dark for 2 h to reach adsorption-desorption equilibrium between the hypophosphite and the photocatalyst. During the photocatalytic reaction, the solutions were kept magnetically stirring, and 4 ml mixture was collected at 1 h intervals followed by centrifugation (10,000 rpm, 5 min) to remove the photocatalyst.

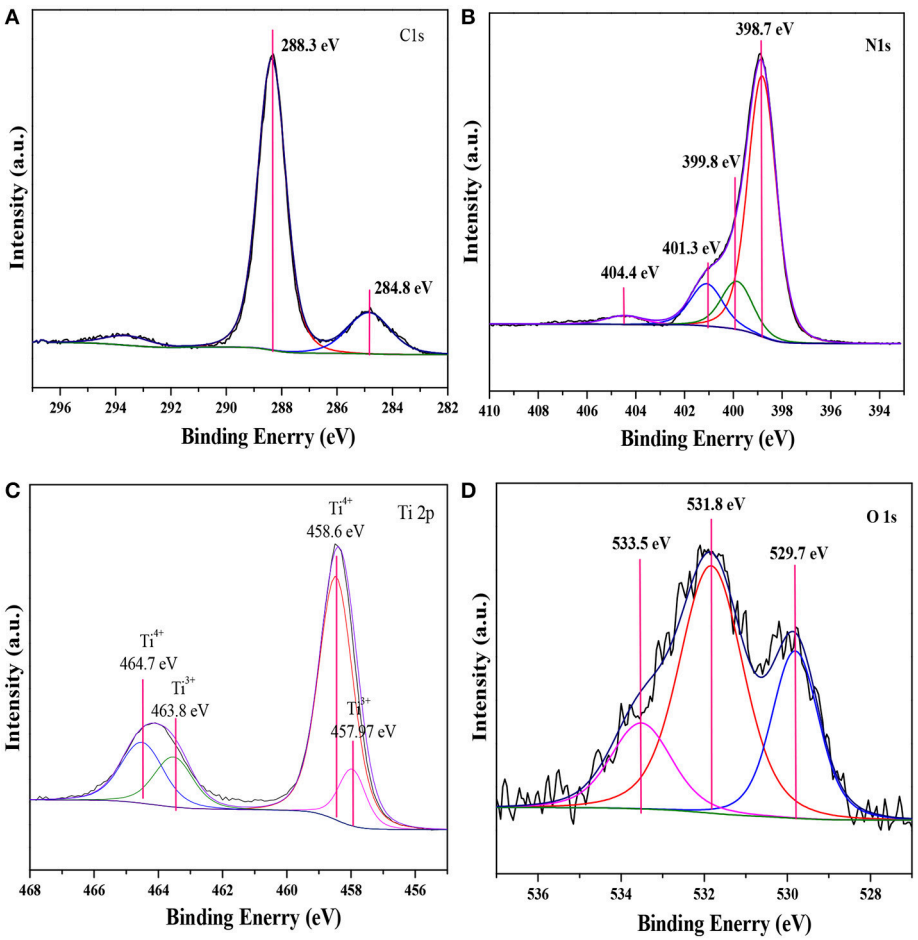

FIGURE 2 | XPS spectra of the 160-Ti_4O_7/g-C_3N_4 photocatalyst. **(A)** C 1 s; **(B)** N 1 s; **(C)** Ti 2 p; **(D)** O 1 s.

Radicals Quencher Experiment for Photocatalysis

In order to identify the contributions of the radicals generated in the photocatalytic oxidation process, IPA and N_2 purging were applied with IPA acting as the ·OH radicals quencher and N_2 purging reducing the superoxide $\cdot O_2^-$ radicals (Yang et al., 2016). Adding different radical scavengers into reaction solutions would affect the photocatalytic performance. As such, the contributions of ·OH radicals and $\cdot O_2^-$ radicals on photocatalytic oxidation of hypophosphite under visible light irradiation can be evaluated based on the change of photocatalytic oxidation efficiency of hypophosphite with and without IPA (1 mM) and N_2 purging (continuous purging).

RESULTS AND DISCUSSION

Structure and Morphology Analyses

The crystal structures of g-C_3N_4, Ti_4O_7, and 160-Ti_4O_7/g-C_3N_4 photocatalysts were characterized by XRD. As shown in **Figure 1a**, two pronounced diffraction peaks in pure g-C_3N_4 were observed at 13.20° and 27.60°, respectively. The peak at 13.20° was corresponded to (1 0 0) plane of tri-s-triazine units (Zhang et al., 2012a). The peak at 27.60°indexed as (0 0 2) peak was due to the interlayer-stacking of aromatic systems as in graphite (Zhang et al., 2012b). The characteristic peaks of Ti_4O_7 were matched well with the standard card (JCPDF 50-0787). The main diffraction peaks of 160-Ti_4O_7/g-C_3N_4 photocatalyst did not change obviously, indicating that the fabrication process did not destroy the main structure of both counterparts. The microstructure of the 160-Ti_4O_7/g-C_3N_4 photocatalyst was shown in **Figure 1b**. It was mainly composed of spheroidal crystals, and the shape of synthesized 160-Ti_4O_7/g-C_3N_4 photocatalyst was relatively uniform.

XPS measurements were carried out to investigate the compositions and elemental chemical states of the samples. As shown in **Figure 2**, the XPS spectra revealed that the elements of C, N, Ti and O existed on the surface of 160-Ti_4O_7/g-C_3N_4 photocatalyst. The corresponding high resolution spectra of C 1s, N 1s, Ti 2p, and O 1s were also analyzed. The XPS spectra of C 1s core level for 160-Ti_4O_7/g-C_3N_4 photocatalyst was shown

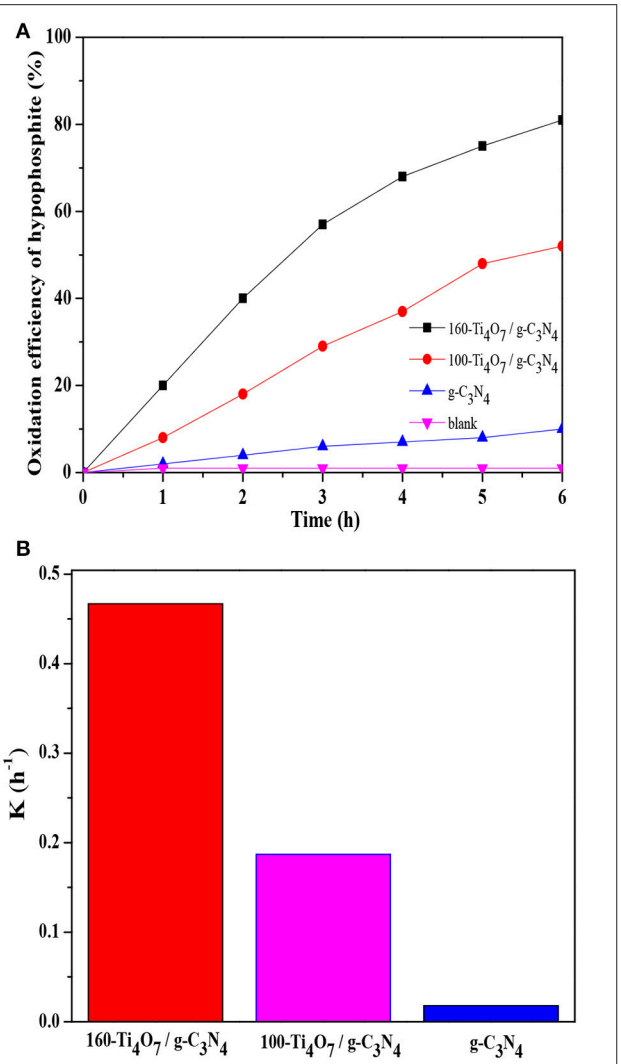

FIGURE 3 | Photocatalytic activity of different photocatalysts. **(A)** The oxidation efficiency of hypophosphite; **(B)** The comparison of oxidation rate constant k.

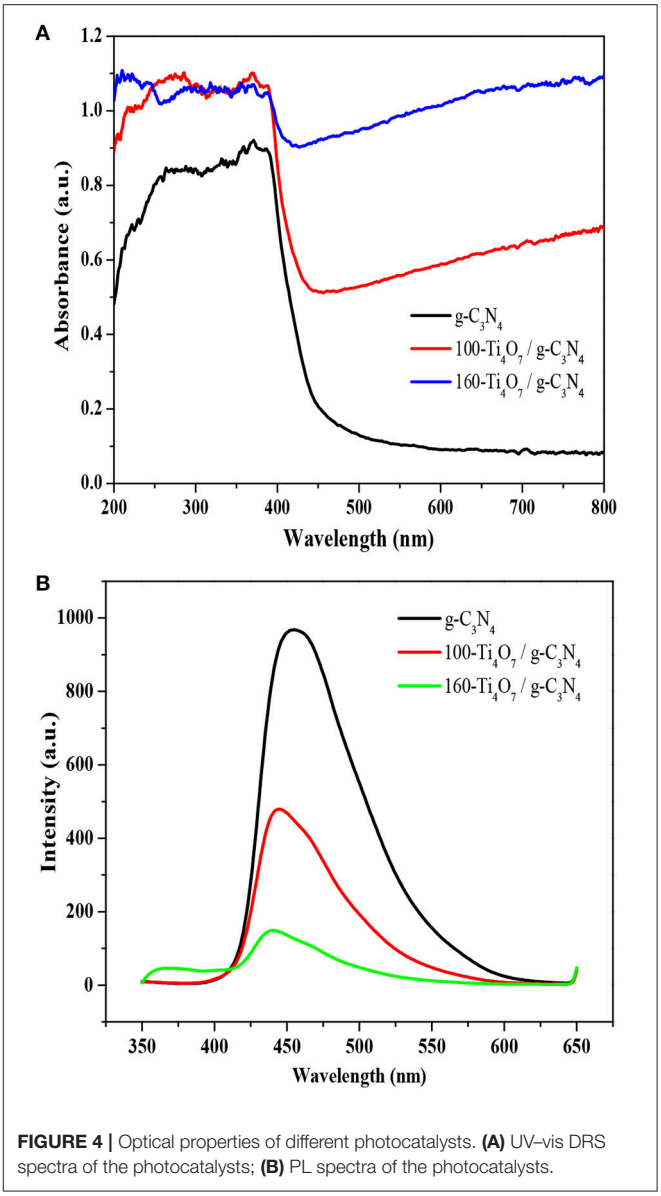

FIGURE 4 | Optical properties of different photocatalysts. **(A)** UV–vis DRS spectra of the photocatalysts; **(B)** PL spectra of the photocatalysts.

in **Figure 2A** that it could be divided into two components including the standard reference carbon (284.8 eV) and the sp^2 bonded C in N=C(–N)$_2$ (288.3 eV) (Jo and Natarajan, 2015). The N 1s spectra of Ti_4O_7/g-C_3N_4 could be divided into four peaks as shown in **Figure 2B**. The main peak at 398.7 eV was assigned to sp^2 nitrogen (C=N–C) involved in triazine rings, and the peak at 399.8 eV originated from the tertiary nitrogen bonded to carbon atoms in the form of N–(C)$_3$ (Wu et al., 2013). The peak at 401.3 eV was ascribed to amino functions (C–N–H). Another peak centered at 404.4 eV was associated to charging effects or positive charge localization in heterocycles (Gao et al., 2014). These assignments of C 1s and N 1s were agreed well with the XPS results of g-C_3N_4 reported previously. Ti_4O_7 is a mixed-valence compound with two evenly occupied Ti^{4+} ($3d^0$) and Ti^{3+} ($3d^1$) configurations. As shown in **Figure 2C**, two broad peaks at about 458.6 and 464.7 eV were observed, corresponding to the characteristic Ti $2p_{1/2}$ and Ti $2p_{3/2}$ peaks of Ti^{4+}, respectively. Additionally, two peaks at 457.97 and 463.8 eV corresponding to Ti^{3+} also appeared, as reported elsewhere (Zeng et al., 2017). The O 1 s spectra of Ti_4O_7/g-C_3N_4 were shown in **Figure 2D**. The peak with binding energy of 533.5 eV was assigned to the C–O functional groups, and the peaks centered at the binding energies of 531.8 and 529.7 eV were ascribed to the OH–Ti and O–Ti bonds (Li Z. Q. et al., 2017). These results confirmed the presence of Ti_4O_7 on the g-C_3N_4 surface with covalent bonds.

Photocatalytic Activity Analysis

The photocatalytic oxidation of hypophosphite over various samples was analyzed. As shown in **Figure 3A**, the blank experiment indicated that the concentration of hypophosphite

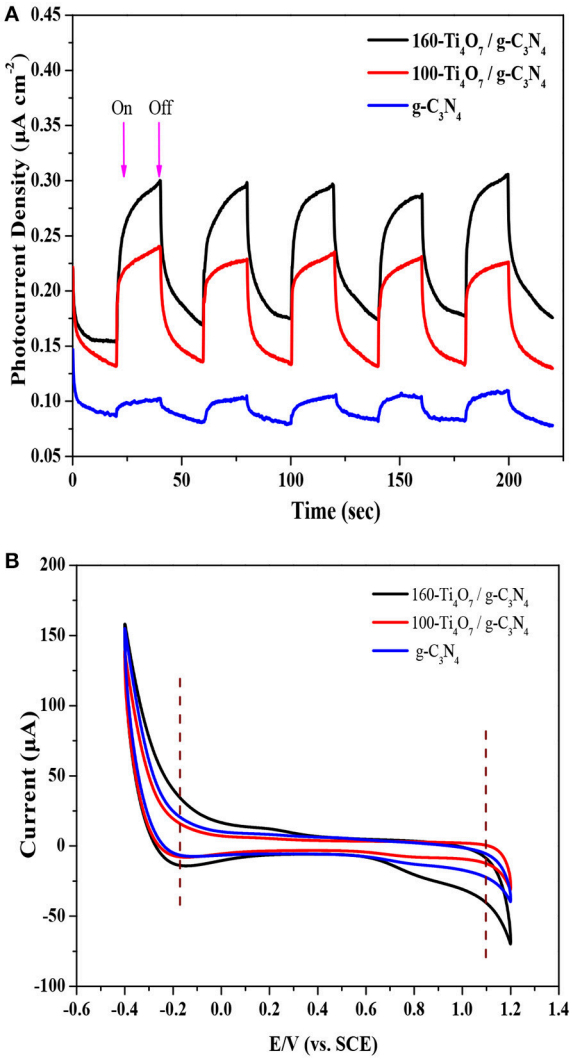

FIGURE 5 | Electrochemical properties analysis of the 160-Ti_4O_7/g-C_3N_4 photocatalyst. **(A)** photocurrent density of different photocatalysts; **(B)** cyclic voltammogram scan of different photocatalysts.

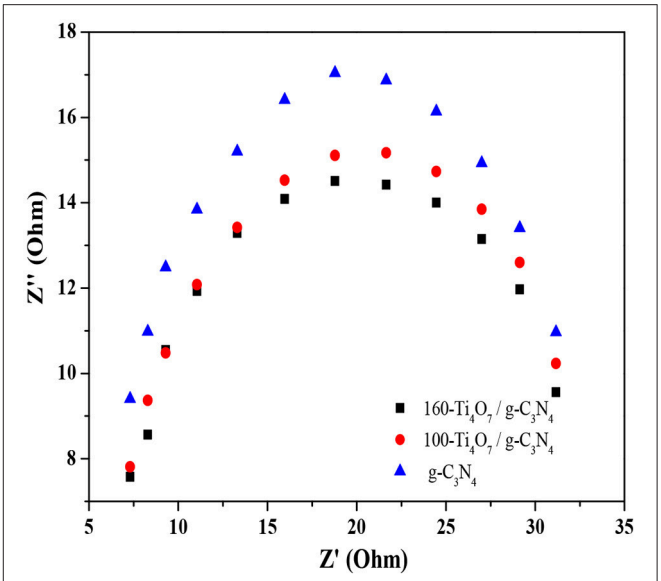

FIGURE 6 | EIS Nyquist plots of the g-C_3N_4, 100-Ti_4O_7/g-C_3N_4, and 160-Ti_4O_7/g-C_3N_4 photocatalysts under visible light irradiation.

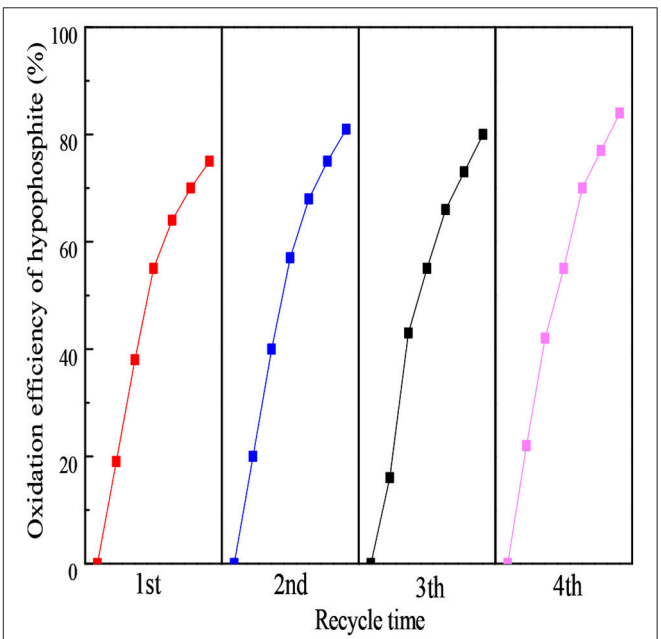

FIGURE 7 | The stability analysis of the 160-Ti_4O_7/g-C_3N_4 photocatalyst under repetitive experiments.

was stable under visible light irradiation ($\lambda > 420$ nm) if there was no photocatalyst presented. Pure g-C_3N_4 showed weak photocatalytic activity with the oxidation efficiency of only 10% possibly owing to the rapid recombination of photo-generated charge carriers and low charge transfer ability (Shi et al., 2017). The 160-Ti_4O_7/g-C_3N_4 photocatalyst had the highest photocatalytic activity with the oxidation efficiency of 81% compared with the pure g-C_3N_4 and 100-Ti_4O_7/g-C_3N_4 photocatalysts.

The photocatalytic oxidation kinetic of the prepared samples was fitted by a pseudo-first-order model, which was depicted by the following Equation (1) (Lu et al., 2018):

$$\ln (C_0/C) = kt \quad (1)$$

Where C_0 and C are the hypophosphite concentrations in solution at times 0 and t, respectively, and k is the first-order rate constant. As shown in **Figure 3B**, the 160-Ti_4O_7/g-C_3N_4 photocatalyst showed the highest photocatalytic oxidation rate of 0.467 h^{-1}, which was 2.5 and 26 times higher than that of 100-Ti_4O_7/g-C_3N_4 and pure g-C_3N_4, respectively. Therefore, the results showed that the 160-Ti_4O_7/g-C_3N_4 photocatalyst

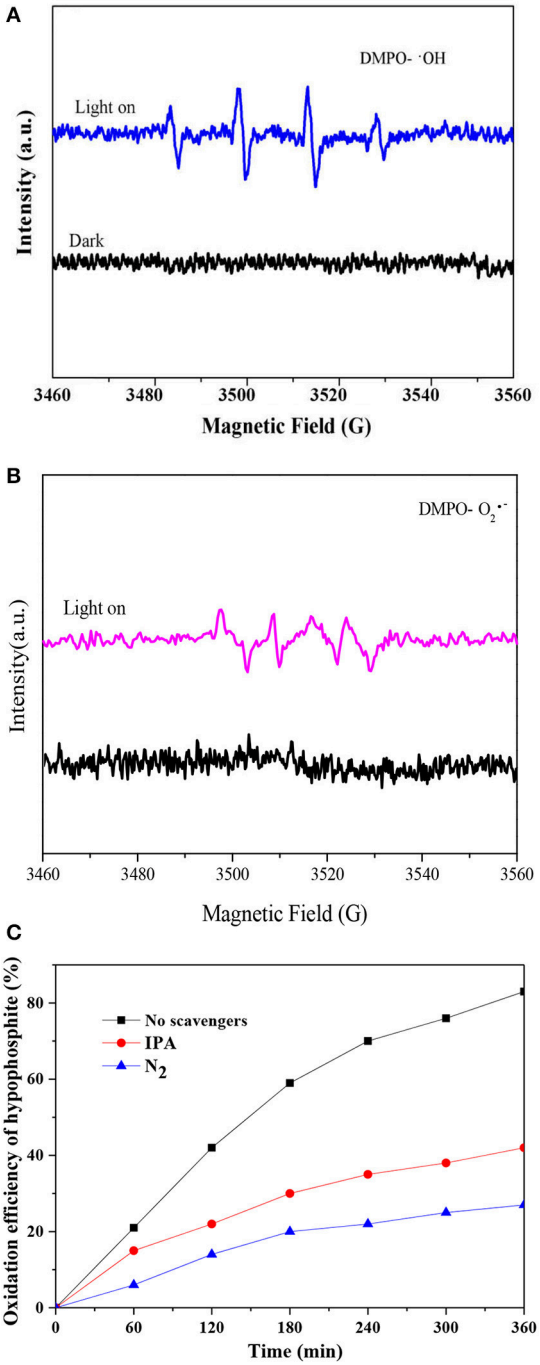

FIGURE 8 | Radials analyses. **(A)** DMPO spin-trapping ESR spectra for ·OH radials analysis; **(B)** DMPO spin-trapping ESR spectra for $\cdot O_2^-$ radials analysis; **(C)** Effect of scavengers on the photocatalytic oxidation process.

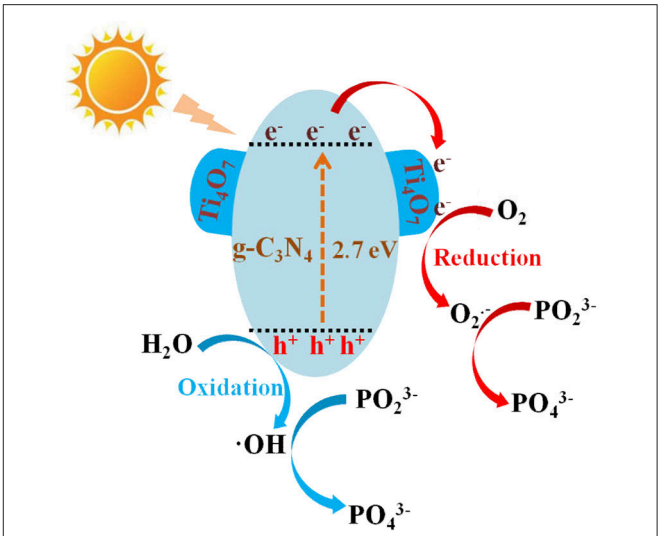

FIGURE 9 | The mechanism of the hypophosphite oxidation over the Ti_4O_7/g-C_3N_4 photocatalyst under visible light irradiation.

exhibited an excellent activity in photocatalytic oxidation of hypophosphite under visible light irritation.

The enhanced photocatalytic activity of Ti_4O_7/g-C_3N_4 and the effect of annealing temperature on Ti_4O_7/g-C_3N_4 photocatalytic activity were further investigated and explained from the perspectives of photoabsorption efficiency, band gap, separation, transformation, and recombination processes of photogenerated carriers in the following sections.

Optical Properties Analysis

The optical properties of Ti_4O_7/g-C_3N_4 and pure g-C_3N_4 photocatalysts were evaluated by UV–vis diffuse reflectance spectra. As shown in **Figure 4A**, the photoabsorption efficiency of Ti_4O_7/g-C_3N_4 was remarkably enhanced compared with the pure g-C_3N_4. The pure g-C_3N_4 held an absorption edge of around 430 nm while the Ti_4O_7/g-C_3N_4 photocatalysts showed a distinct red-shift, indicating that the Ti_4O_7/g-C_3N_4 photocatalysts were more efficient in light harvesting under visible light irradiation. The enhanced photoabsorption efficiency of Ti_4O_7/g-C_3N_4 was due to the narrowed band gap. The band energy gap of the photocatalysts was determined from the formula $\alpha h\nu = A\ (h\nu - E_g)^{n/2}$ (*Eg, α, h, ν, and A* indicate the band gap, optical absorption coefficient, Plank's constant, photonic frequency and a proportionality constant, respectively) (Huang et al., 2017b; Liu et al., 2017a,b; Tian et al., 2017). The band gap calculated from the plot of absorption$^{1/2}$ vs. energy was 2.70, 2.32, and 2.13 eV for g-C_3N_4, 100-Ti_4O_7/g-C_3N_4, and 160-Ti_4O_7/g-C_3N_4, respectively.

Photoluminescence (PL) spectra was used to investigate the separation, transformation and recombination processes of photogenerated carriers. The band–band PL spectrum can directly reflect the separation performance of photo-induced charge carriers, viz. the stronger of the band-band PL signal, the higher of the recombination rate of photo-induced carriers. The PL spectroscopy of the photocatalysts was shown in **Figure 4B**. All photocatalysts exhibited a broad emission peak centered at around 460 nm, which was mainly caused by the recombination of photogenerated electrons and holes produced by g-C_3N_4 (Shi et al., 2017). The PL emission intensity was highest for the pure g-C_3N_4, while the intensity was

significantly lowered for $Ti_4O_7/g\text{-}C_3N_4$. This indicated that the charge carrier recombination was effectively suppressed for the $Ti_4O_7/g\text{-}C_3N_4$ photocatalysts. It is well known that the noble metals, such as Ti_4O_7, are good conductors with excellent electric properties. After formation of noble metals-semiconductors heterostructures, the photogenerated electrons of semiconductors could transfer through these noble metals rapidly and the lifetime of these electrons and holes are prolonged (Cui et al., 2017). In addition, the PL intensity of 160-$Ti_4O_7/g\text{-}C_3N_4$ was much lower than that of 100-$Ti_4O_7/g\text{-}C_3N_4$, indicating that 160-$Ti_4O_7/g\text{-}C_3N_4$ had the effectively decreased charge carrier recombination compared with 100-$Ti_4O_7/g\text{-}C_3N_4$. The higher annealing temperature could etch and tailor $g\text{-}C_3N_4$ with the possibly smaller and thinner nanosheet structure of 160-$Ti_4O_7/g\text{-}C_3N_4$ compared with 100-$Ti_4O_7/g\text{-}C_3N_4$ and thus shortened the distance between the photogenerated electrons and the heterostructure surface, which suppressed the recombination probability of photo-generated electron–hole pairs with the photogenerated electrons rapidly transferring through Ti_4O_7 (Dong et al., 2015).

Electrochemical Properties Analysis

The PC responses of $g\text{-}C_3N_4$, 100-$Ti_4O_7/g\text{-}C_3N_4$, and 160-$Ti_4O_7/g\text{-}C_3N_4$ photocatalysts under visible light irradiation were evaluated to further offer information about the separation and transformation efficiency of photogenerated electrons and holes. As shown in **Figure 5A**, the transient PC responses of all photocatalysts at light on and light off were reversible and stable, and the PC density of 160-$Ti_4O_7/g\text{-}C_3N_4$ was much higher (0.30 $\mu A\ cm^{-2}$) than that of 100-$Ti_4O_7/g\text{-}C_3N_4$ (0.23 $\mu A\ cm^{-2}$) and $g\text{-}C_3N_4$ (0.10 $\mu A\ cm^{-2}$). This indicated that the $Ti_4O_7/g\text{-}C_3N_4$ heterostructures promoted the separation of photogenerated charge carriers (Kang et al., 2016), in line with the PL spectra results as shown in **Figure 4B**. Additionally, this was also supported by the CV test. As shown in **Figure 5B**, a reduction peak at about −0.18 V was observed in $g\text{-}C_3N_4$, 100-$Ti_4O_7/g\text{-}C_3N_4$, and 160-$Ti_4O_7/g\text{-}C_3N_4$, but 160-$Ti_4O_7/g\text{-}C_3N_4$ photocatalyst possessed much higher reduction current, which indicated faster electron transfer in 160-$Ti_4O_7/g\text{-}C_3N_4$ photocatalyst (Samanta and Srivastava, 2017).

Electrochemical impedance spectroscopy was used to investigate the photogenerated charge separation process on the photocatalysts. The radius of the circular arc reflected the resistance of the interfacial charge transfer and separation efficiency of the electron-hole pairs (Leng et al., 2005; Liang and Zhu, 2016). As shown in **Figure 6**, the arc radius decreased gradually when Ti_4O_7 was doped onto the $g\text{-}C_3N_4$ photocatalyst. This meant that the photogenerated charge separation process occurred more easily on $Ti_4O_7/g\text{-}C_3N_4$ compared with the pure $g\text{-}C_3N_4$ because of the decreased energy barrier that the electrode reaction needed to overcome. Moreover, the arc radius of 160-$Ti_4O_7/g\text{-}C_3N_4$ was smaller than that of 100-$Ti_4O_7/g\text{-}C_3N_4$, meaning that the separation of the photogenerated electron–hole pairs was more effective and the interfacial charge transfer of the electron donor/electron acceptor was faster on the 160-$Ti_4O_7/g\text{-}C_3N_4$ photocatalyst.

Catalyst Stability Analysis

The stability was another vital consideration for an excellent photocatalyst. To evaluate the stability of the as-prepared 160-$Ti_4O_7/g\text{-}C_3N_4$ photocatalyst, the repetitive experiments of photocatalytic oxidation of hypophosphite were carried out. As shown in **Figure 7**, the oxidation efficiency of hypophosphite in the four-round continuous reaction tests using 160-$Ti_4O_7/g\text{-}C_3N_4$ photocatalyst was 75, 81, 80, and 84%, respectively. The repetitive experiments results showed that the fabricated $Ti_4O_7/g\text{-}C_3N_4$ photocatalysts had a stable structure possibly with the strong binding force. The N-H groups or conjugated structures in $g\text{-}C_3N_4$ could tightly bond with Ti^{4+} ($3d^0$) and Ti^{3+} ($3d^1$) in Ti_4O_7, which effectively reduced the dissolution of bulk $g\text{-}C_3N_4$ material during the photocatalytic process.

Proposed Mechanism

To clarify the reaction mechanism of photocatalytic oxidation of hypophosphite, the ROS generated under visible light irradiation were analyzed by ESR technique (with DMPO). As shown in **Figure 8A**, no ESR signals were observed in the dark while ·OH was observed under visible light irradiation with four peaks with intensities of 1:2:2:1 attributing to DMPO-·OH generated via a hole oxidative process on H_2O and/or OH^- (Tu et al., 2017). Moreover, $\cdot O_2^-$ was also observed under visible light irradiation with a four-line spectrum with the relative intensities of 1:1:1:1 assigned to DMPO-$\cdot O_2^-$ adduct derived from O_2 reduction by electrons (Huang et al., 2015), however, no ESR signals were observed in the dark as shown in **Figure 8B**. Therefore, both ·OH and $\cdot O_2^-$ would contribute to the photocatalytic oxidation of hypophosphite and their contributions were further investigated with and without radical scavengers. Isopropanol (IPA) and N_2 purging were applied with IPA acting as the ·OH radicals quencher and N_2 purging reducing the superoxide $\cdot O_2^-$ radicals (Yang et al., 2016). As shown in **Figure 8C**, the photocatalytic oxidation efficiency of hypophosphite decreased from 83% (without radical scavengers) to 42% (with IPA) and even 27% (with N_2 purging). These results confirmed that both ·OH and $O_2\cdot^-$ radicals were the major active radical species for hypophosphite oxidation in the photocatalytic process with $O_2\cdot^-$ accounting for a more significant contribution. Note that the photocatalytic oxidation efficiency of hypophosphite did not decrease to zero with the lowest efficiency of 27% in the presence of N_2 purging, indicating that holes and some other radicals may also contribute to the photocatalytic oxidation process to some extent. It was reported that reactive oxygen species (ROS), such as superoxide ($\cdot O_2^-$), hydroxyl radicals (·OH), singlet oxygen ($^1O_2$), peroxyl ($RO_2\cdot$), and alkoxyl (RO-) as well as hypochlorous acid (HOCl) are basically produced in the photocatalytic process (Huang et al., 2017a), which may also contribute to the photocatalytic oxidation of hypophosphite in this case.

According to the above results and those reported in the literature, the possible photocatalytic mechanism of $Ti_4O_7/g\text{-}C_3N_4$ on hypophosphite oxidation was illustrated in **Figure 9**.

The possible photocatalytic processes were as follows:

$$Ti_4O_7/g\text{-}C_3N_4 + h\nu \rightarrow g\text{-}C_3N_4(e^- + h^+) \quad (2)$$

$$g\text{-}C_3N_4\ (e^-) + Ti_4O_7 \rightarrow Ti_4O_7\ (e^-) \quad (3)$$

$$Ti_4O_7 + h\nu \rightarrow Ti_4O_7\ (e^-) \quad (4)$$

$$Ti_4O_7\ (e^-) + O_2 \rightarrow \cdot O_2^- \quad (5)$$

$$\cdot O_2^- + PO_2^{3-} \rightarrow PO_4^{3-} \quad (6)$$

$$g\text{-}C_3N_4\ (h^+) + OH^- \rightarrow \cdot OH \quad (7)$$

$$\cdot OH + PO_2^{3-} \rightarrow PO_4^{3-} \quad (8)$$

$$g\text{-}C_3N_4\ (h^+) + PO_2^{3-} \rightarrow PO_4^{3-} \quad (9)$$

Firstly, the electrons (e^-) in valence band of g-C_3N_4 under visible light irradiation could be excited to the conduction band, leaving the holes (h^+) in valence band of g-C_3N_4 (Equation 2). Then the photogenerated electrons in the conduction band of g-C_3N_4 would continually transfer to Ti_4O_7 until the same Fermi levels reached (Equation 3). Thus, the photogenerated electrons and holes were located at Ti_4O_7 and g-C_3N_4, respectively, leading to the effective separation of the photoinduced charge carriers. Furthermore, the electrons might be also generated from the Ti_4O_7 particles (Equation 4) with the product easily reacting with the adsorbed oxygen molecules to produce $\cdot O_2^-$ (Equation 5) followed by the oxidation of hypophosphite to phosphate (Equation 6). Meanwhile, the photogenerated holes as the strong oxidants could oxidize OH^- to ·OH radicals, and then the hypophosphite was directly oxidized to phosphate (Equations 7 and 8). In addition, some photogenerated holes could directly oxidize hypophosphite to phosphate (Equation 9).

CONCLUSION

The enhancement of Ti_4O_7/g-C_3N_4 visible light photocatalytic performance on hypophosphite oxidation and the effect of annealing temperature and the corresponding mechanism were investigated in this study. 160-Ti_4O_7/g-C_3N_4 (fabricated at 160°C) photocatalyst showed the highest oxidation efficiency of hypophosphite of 81% and the highest photocatalytic oxidation rate of 0.467 h^{-1} comparing with 100-Ti_4O_7/g-C_3N_4 (fabricated at 100°C) and pure g-C_3N_4. The enhanced photocatalytic performance of 160-Ti_4O_7/g-C_3N_4 could be ascribed to the effective charge separation and enhanced photoabsorption efficiency. Additionally, ESR results showed that hydroxyl radicals and superoxide anion radicals were mainly responsible to the oxidation of hypophosphite with $O_2\cdot^-$ accounting for a more significant contribution. Moreover, Ti_4O_7/g-C_3N_4 photocatalysts showed the remarkable stability in the repetitive experiments. Our work demonstrated that the rational design and construction of isotype heterojunction was an effective strategy to develop the efficient photocatalysts under visible light irradiation.

AUTHOR CONTRIBUTIONS

All authors listed have made a substantial, direct and intellectual contribution to the work, and approved it for publication.

FUNDING

This work was supported by National Natural Science Foundation of China (No. 51608086); Science and Technology Project from Chongqing (CSTC2015JCYJA20027); Scientific and Technological Research Program of Chongqing Municipal Education Commission (KJ1501103); Chongqing Key Laboratory of Environmental Materials and Remediation Technology, Chongqing University of Arts and Sciences (CKE1407); Natural Science Foundation of Yongchuan, Chongqing (Ycstc, 2014ac4001); Scientific Research Foundation of Chongqing University of Arts and Sciences (R2014CH08).

REFERENCES

Bulasara, V. K., Thakuria, H., Uppaluri, R., and Purkait, M. K. (2011). Effect of process parameters on electroless plating and nickel-ceramic composite membrane characteristics. *Desalination* 268, 195–203. doi: 10.1016/j.desal.2010.10.025

Cao, X. C., Sun, Z. H., Zheng, X. J., Tian, J. H., Jin, C., Yang, R. Z., et al. (2017). $MnCo_2O_4$ decorated Magnéli phase titanium oxide as a carbon-free cathode for Li–O_2 batteries. *J. Mater. Chem. A* 5, 19991–19996. doi: 10.1039/c7ta06152h

Chisaka, M., Ando, Y., Yamamoto, Y., and Itagaki, N. (2016). A carbon-support-free titanium oxynitride catalyst for proton exchange membrane fuel cell cathodes. *Electrochim. Acta* 214, 165–172. doi: 10.1016/j.electacta.2016.08.032

Cui, W., Li, J. Y., Cen, W. L., Sun, Y. J., Lee, S. C., and Dong, F. (2017). Steering the interlayer energy barrier and charge flow via bioriented transportation channels in g-C_3N_4: enhanced photocatalysis and reaction mechanism. *J. Catal.* 352, 351–360. doi: 10.1016/j.jcat.2017.05.017

Dong, F., Li, Y. H., Wang, Z. Y., and Ho, W. K. (2015). Enhanced visible light photocatalytic activity and oxidation ability of porous graphene-like g-C_3N_4 nanosheets via thermal exfoliation. *Appl. Surf. Sci.* 358, 393–403. doi: 10.1016/j.apsusc.2015.04.034

Gao, D. Q., Xu, Q., Zhang, J., Yang, Z. L., Si, M. S., Yan, Z. J., et al. (2014). Defect-related ferromagnetism in ultrathin metal-free C_3N_4 nanosheets. *Nanoscale* 6, 2577–2581. doi: 10.1039/c3nr04743a

Ge, C., Chai, Y., Wang, H., and Kan, M. (2017). Ocean acidification: one potential driver of phosphorus eutrophication. *Mar. Pollut. Bull.* 115, 149–153. doi: 10.1016/j.marpolbul.2016.12.016

Guo, L., Jing, Y., and Chaplin, B. P. (2016). Development and characterization of ultrafiltration TiO_2 magnéli phase reactive electrochemical membranes. *Environ. Sci. Technol.* 50, 1428–1436. doi: 10.1021/acs.est.5b04366

Huang, H., Han, X., Li, X., Wang, S., Chu, P., and Zhang, Y. (2015). Fabrication of multiple heterojunctions with tunable visible-light-active photocatalytic reactivity in BiOBr–BiOI full-range composites based on microstructure modulation and band structures. *ACS Appl. Mater. Interfaces* 7, 482–492. doi: 10.1021/am5065409

Huang, H., Tu, S., Zeng, C., Zhang, T., Reshak, A., and Zhang, Y. H. (2017a). Macroscopic polarization enhancement promoting photo- and piezoelectric-induced charge separation and molecular oxygen activation. *Angew. Chem. Int. Edn.* 56, 11860–11864. doi: 10.1002/anie.201706549

Huang, H. W., Xiao, K., Tian, N., Dong, F., Zhang, T. R., Du, X., et al. (2017b). Template-free precursor-surface-etching route to porous, thin g-C_3N_4 nanosheets for enhancing photocatalytic reduction and oxidation activity. *J. Mater. Chem. A* 5, 17452–17463. doi: 10.1039/c7ta04639a

Jo, W. K., and Natarajan, T. S. (2015). Influence of TiO_2 morphology on the photocatalytic efficiency of direct Z-scheme g-C_3N_4/TiO_2 photocatalysts for isoniazid degradation. *Chem. Eng. J.* 281, 549–565. doi: 10.1016/j.cej.2015.06.120

Jourshabani, M., Shariatinia, Z., and Badiei, A. (2017). Facile one-pot synthesis of cerium oxide/sulfur-doped graphitic carbon nitride (g-C_3N_4) as efficient nanophotocatalysts under visible light irradiation. *J. Colloid Interface Sci.* 507, 59–73. doi: 10.1016/j.jcis.2017.07.106

Kang, K., Watanabe, S., Broch, K., Sepe, A., Brown, A., Nasrallah, I., et al. (2016). 2D coherent charge transport in highly ordered conducting polymers doped by solid state diffusion. *Nat. Mater.* 15, 896–902. doi: 10.1038/NMAT4634

Kolbrecka, K., and Przyluski, J. (1994). Sub-stoichiometric titanium oxides as ceramic electrodes for oxygen evolution—structural aspects of the voltammetric behaviour of Ti_nO_{2n-1}. *Electrochim. Acta* 39, 1591–1595. doi: 10.1016/0013-4686(94)85140-9

Leng, W. H., Zhang, Z., Zhang, J. Q., and Cao, C. N. (2005). Investigation of the kinetics of a TiO_2 photoelectrocatalytic reaction involving charge transfer and recombination through surface states by electrochemical impedance spectroscopy. *J. Phys. Chem. B* 109, 15008–15023. doi: 10.1021/jp051821z

Li, J. D., Zhang, X. L., Raziq, F., Wang, J. S., Liu, C., Liu, Y. D., et al. (2017). Improved photocatalytic activities of g-C_3N_4 nanosheets by effectively trapping holes with halogen-induced surface polarization and 2,4-dichlorophenol decomposition mechanism. *Appl. Catal. B Environ.* 218, 60–67. doi: 10.1016/j.apcatb.2017.06.038

Li, L. Y., Takahashi, N., Kaneko, K., Shimizu, T., and Takarada, T. (2015). A novel method for nickel recovery and phosphorus removal from spent electroless nickel-plating solution. *Sep. Purif. Technol.* 147, 237–244. doi: 10.1016/j.seppur.2015.04.029

Li, X. X., Zhu, A. L., Qu, W., Wang, H. J., Hui, R., Zhang, L., et al. (2010). Magneli phase Ti_4O_7 electrode for oxygen reduction reaction and its implication for zinc-air rechargeable batteries. *Electrochim. Acta* 55, 5891–5898. doi: 10.1016/j.electacta.2010.05.041

Li, Z. Q., Qi, M. Y., Tu, C. Y., Wang, W. P., Chen, J. R., and Wang, A. J. (2017). Highly efficient removal of chlorotetracycline from aqueous solution using graphene oxide/TiO_2 composite: properties and mechanism. *Appl. Surf. Sci.* 425, 765–775. doi: 10.1016/j.apsusc.2017.07.027

Liang, F. F., and Zhu, Y. F. (2016). Enhancement of mineralization ability for phenol via synergetic effect of photoelectrocatalysis of g-C_3N_4 film. *Appl. Catal. B Environ.* 180, 324–329. doi: 10.1016/j.apcatb.2015.05.009

Lin, F., Shao, B., Li, Z., Zhang, J. Y., Wang, H., Zhang, S. H., et al. (2017). Visible light photocatalysis over solid acid: enhanced by gold plasmonic effect. *Appl. Catal. B Environ.* 218, 480–487. doi: 10.1016/j.apcatb.2017.06.076

Liu, C. Y., Huang, H. W., Ye, L. Q., Yu, S. X., Tian, N., Du, X., et al. (2017a). Intermediate-mediated strategy to horn-like hollow mesoporous ultrathin g-C_3N_4 tube with spatial anisotropic charge separation for superior photocatalytic H_2 evolution. *Nano Energy* 41, 738–748. doi: 10.1016/j.nanoen.2017.10.031

Liu, C. Y., Zhang, Y. H., Dong, F., Reshak, A. H., Ye, L. Q., Pinna, N., et al. (2017b). Chlorine intercalation in graphitic carbon nitride for efficient photocatalysis. *Appl. Catal. B Environ.* 203, 465–474. doi: 10.1016/j.apcatb.2016.10.002

Lu, X. J., Wang, Y., Zhang, X. Y., Xu, G. Q., Wang, D. M., Lv, J., et al. (2018). NiS and MoS_2 nanosheet co-modified graphitic C_3N_4 ternary heterostructure for high efficient visible light photodegradation of antibiotic. *J. Hazard. Mater.* 341, 10–19. doi: 10.1016/j.jhazmat.2017.07.004

Maragatha, J., Rani, C., Rajendran, S., and Karuppuchamy, S. (2017). Microwave synthesis of nitrogen doped Ti_4O_7 for photocatalytic applications. *Physica E* 93, 78–82. doi: 10.1016/j.physe.2017.05.020

McDowell, M. M., Ivey, M. M., Lee, M. E., Firpo, V. V., Salmassi, T. M., Khachikian, C. S., et al. (2004). Detection of hypophosphite, phosphite, and orthophosphate in natural geothermal water by ion chromatography. *J. Chromatogr. A* 1039, 105–111. doi: 10.1016/j.chroma.2003.11.056

Montangero, A., and Belevi, H. (2007). Assessing nutrient flows in septic tanks by eliciting expert judgement: a promising method in the context of developing countries. *Water Res.* 41, 1052–1064. doi: 10.1016/j.watres.2006.10.036

Noman, M. T., Wiener, J., Saskova, J., Ashraf, M. A., Vikova, M., Jamshaid, H., et al. (2018). *In-situ* development of highly photocatalytic multifunctional nanocomposites by ultrasonic acoustic method. *Ultrason. Sonochem.* 40, 41–56. doi: 10.1016/j.ultsonch.2017.06.026

Oturan, N., Ganiyu, S. O., Raffy, S., and Oturan, M. A. (2017). Sub-stoichiometric titanium oxide as a new anode material for electro-Fenton process: application to electrocatalytic destruction of antibiotic amoxicillin. *Appl. Catal. B Environ.* 217, 214–223. doi: 10.1016/j.apcatb.2017.05.062

Samanta, S., and Srivastava, R. (2017). Thermal catalysis vs. photocatalysis: a case study with $FeVO_4$/g-C_3N_4 nanocomposites for the efficient activation of aromatic and benzylic C–H bonds to oxygenated products. *Appl. Catal. B Environ.* 218, 621–636. doi: 10.1016/j.apcatb.2017.06.043

Shao, H. X., Zhao, X., Wang, Y. B., Mao, R., Wang, Y., Qiao, M., et al. (2017). Synergetic activation of peroxymonosulfate by Co_3O_4 modified g-C_3N_4 for enhanced degradation of diclofenac sodium under visible light irradiation. *Appl. Catal. B Environ.* 218, 810–818. doi: 10.1016/j.apcatb.2017.07.016

Shi, A. Y., Li, H. H., Yin, S., Liu, B., Zhang, J. C., and Wang, Y. H. (2017). Effect of conjugation degree and delocalized π-system on the photocatalytic activity of single layer g-C_3N_4. *Appl. Catal. B Environ.* 218, 137–146. doi: 10.1016/j.apcatb.2017.06.017

Sun, S. P., Liao, X. M., Yin, G. F., Yao, Y. D., Huang, Z. B., and Pu, X. M. (2016). Enhanced electrochemical performance of TiO_2 nanotube array electrodes by controlling the introduction of substoichiometric titanium oxides. *J. Alloy. Compd.* 680, 538–543. doi: 10.1016/j.jallcom.2016.04.171

Sun, X., Jiang, D., Zhang, L., and Wang, W. Z. (2018). Alkaline modified g-C_3N_4 photocatalyst for high selective oxide coupling of benzyl alcohol to benzoin. *Appl. Catal. B Environ.* 220, 553–560. doi: 10.1016/j.apcatb.2017.08.057

Takeda, I., Somura, H., and Mori, Y. (2010). Recovery of phosphorus from natural water bodies using iron-oxidizing bacteria and woody biomass. *Ecol. Eng.* 36, 1064–1069. doi: 10.1016/j.ecoleng.2010.04.019

Teng, W., Wang, Y. M., Huang, H. H., Li, X. Y., and Tang, Y. B. (2017). Enhanced photoelectrochemical performance of MoS_2 nanobelts-loaded TiO_2 nanotube arrays by photo-assisted electrodeposition. *Appl. Surf. Sci.* 425, 507–517. doi: 10.1016/j.apsusc.2017.06.297

Tian, N., Zhang, Y. H., Li, X. W., Xiao, K., Du, X., Dong, F., et al. (2017). Precursor-reforming protocol to 3D mesoporous g-C_3N_4 established by ultrathin self-doped nanosheets for superior hydrogen evolution. *Nano Energy* 38, 72–81. doi: 10.1016/j.nanoen.2017.05.038

Tian, S. C., Li, Y. B., and Zhao, X. (2015). Cyanide removal with a copper/active carbon fiber cathode via a combined oxidation of a Fenton-like reaction and *in situ* generated copper oxides at anode. *Electrochim. Acta* 180, 746–755. doi: 10.1016/j.electacta.2015.09.006

Tu, S. C., Huang, H. W., Zhang, T. R., and Zhang, Y. H. (2017). Controllable synthesis of multi-responsive ferroelectric layered perovskite-like $Bi_4Ti_3O_{12}$: photocatalysis and piezoelectric-catalysis and mechanism insight. *Appl. Catal. B Environ.* 219, 550–562. doi: 10.1016/j.apcatb.2017.08.001

Wang, D., Chen, N., Yu, Y., Hu, W. W., and Feng, C. P. (2016). Investigation on the adsorption of phosphorus by Fe-loaded ceramic adsorbent. *J. Colloid Interface Sci.* 464, 277–284. doi: 10.1016/j.jcis.2015.11.039

Wang, W., Fang, J. J., Shao, S. F., Lai, M., and Lu, C. H. (2017). Compact and uniform TiO_2@g-C_3N_4 core-shell quantum heterojunction for photocatalytic degradation of tetracycline antibiotics. *Appl. Catal. B Environ.* 217, 57–64. doi: 10.1016/j.apcatb.2017.05.037

Wu, G. S., Thind, S. S., Wen, J. L., Yan, K., and Chen, A. C. (2013). A novel nanoporous α-C_3N_4 photocatalyst with superior high visible light activity. *Appl. Catal. B Environ.* 142–143, 590–597. doi: 10.1016/j.apcatb.2013.05.070

Yang, X. L., Qian, F. F., Zou, G. J., Li, M. L., Lu, J. R., Li, Y. M., et al. (2016). Facile fabrication of acidified g-C_3N_4/g-C_3N_4 hybrids with enhanced photocatalysis performance under visible light irradiation. *Appl. Catal. B Environ.* 193, 22–35. doi: 10.1016/j.apcatb.2016.03.060

Ye, Y. Y., Ngo, H. H., Guo, W. S., Liu, Y. W., Li, J. X., Liu, Y., et al. (2017). Insight into chemical phosphate recovery from municipal wastewater. *Sci. Total Environ.* 576, 159–171. doi: 10.1016/j.scitotenv.2016.10.078

Ye, Z. L., Deng, Y. Y., Lou, Y. Y., Ye, X., Zhang, J. Q., and Chen, S. H. (2017). Adsorption behavior of tetracyclines by struvite particles in the process of phosphorus recovery from synthetic swine wastewater. *Chem. Eng. J.* 313, 1633–1638. doi: 10.1016/j.cej.2016.11.062

You, S. J., Liu, B., Gao, Y. F., Wang, Y., Tang, C. Y. Y., Huang, Y. B., et al. (2016). Monolithic porous magnéli-phase Ti_4O_7 for electro-oxidation treatment of industrial wastewater. *Electrochim. Acta* 214, 326–335. doi: 10.1016/j.electacta.2016.08.037

Zeng, X. K., Wang, Z. Y., Wang, G., Gengenbach, T. R., McCarthy, D. T., Deletic, A., et al. (2017). Highly dispersed TiO_2 nanocrystals and WO_3 nanorods on reduced graphene oxide: Z-scheme photocatalysis system for accelerated photocatalytic water disinfection. *Appl. Catal. B Environ.* 218, 163–173. doi: 10.1016/j.apcatb.2017.06.055

Zhang, J. S., Zhang, G. G., Chen, X. F., Lin, S., Möhlmann, L., Dołega, G., et al. (2012a). Co-monomer control of carbon nitride semiconductors to optimize hydrogen evolution with visible light. *Angew. Chem. Int. Ed.* 124, 3237–3241. doi: 10.1002/anie.201106656

Zhang, J. S., Zhang, M. W., Zhang, G. G., and Wang, X. C. (2012b). Synthesis of carbon nitride semiconductors in sulfur flux for water photoredox catalysis. *ACS Catal.* 2, 940–948. doi: 10.1021/cs300167b

Conflict of Interest Statement: Author LY was employed by company of Heibei Yinfa Meifute Environmental Engineering Co., Ltd.

The other authors declare that the research was conducted in the absence of any commercial or financial relationships that could be construed as a potential conflict of interest.

frontiers in Chemistry

MINI REVIEW
published: 28 February 2018
doi: 10.3389/fchem.2018.00033

Understanding Mechanism of Photocatalytic Microbial Decontamination of Environmental Wastewater

Chhabilal Regmi[1†], *Bhupendra Joshi*[1†], *Schindra K. Ray*[1], *Gobinda Gyawali*[1*] *and Ramesh P. Pandey*[2,3*]

[1] Department of Environmental and Bio-chemical Engineering, Sun Moon University, Asan-si, South Korea, [2] Department of Life Science and Bio-chemical Engineering, Sun Moon University, Asan-si, South Korea, [3] Department of BT-Convergent Pharmaceutical Engineering, Sun Moon University, Asan-si, South Korea

OPEN ACCESS

Edited by:
Fan Dong,
Chongqing Technology and Business University, China

Reviewed by:
Leny Yuliati,
Universitas Ma Chung, Indonesia
Martin Reli,
Technical University of Ostrava, Czechia
Yuanguo Xu,
Jiangsu University, China

***Correspondence:**
Gobinda Gyawali
ggobinda@sunmoon.ac.kr
Ramesh P. Pandey
pandey@sunmoon.ac.kr

[†]These authors have contributed equally to this work.

Specialty section:
This article was submitted to Catalysis and Photocatalysis, a section of the journal Frontiers in Chemistry

Received: 16 November 2017
Accepted: 09 February 2018
Published: 28 February 2018

Citation:
Regmi C, Joshi B, Ray SK, Gyawali G and Pandey RP (2018) Understanding Mechanism of Photocatalytic Microbial Decontamination of Environmental Wastewater. Front. Chem. 6:33. doi: 10.3389/fchem.2018.00033

Several photocatalytic nanoparticles are synthesized and studied for potential application for the degradation of organic and biological wastes. Although these materials degrade organic compounds by advance oxidation process, the exact mechanisms of microbial decontamination remains partially known. Understanding the real mechanisms of these materials for microbial cell death and growth inhibition helps to fabricate more efficient semiconductor photocatalyst for large-scale decontamination of environmental wastewater or industries and hospitals/biomedical labs generating highly pathogenic bacteria and toxic molecules containing liquid waste by designing a reactor. Recent studies on microbial decontamination by photocatalytic nanoparticles and their possible mechanisms of action is highlighted with examples in this mini review.

Keywords: photocatalysis for environment, microbial inactivation, mechanisms of action, semiconductors, environmental pollutants

The natural ecosystem is being deteriorated continuously because of unrestrained flow of wastewater from various industries, hospital wastes, and laboratories due to rapid and poorly-planned urbanization in developing countries and development of mega cities. The urban population is rising unprecedentedly. The socio-economic disparities is exacerbating while creating unsanitary conditions that facilitates the outbreaks. The natural water bodies are contaminated with (i) pathogens originated from hospitals and biomedical laboratories, (ii) different hazardous materials such as organic dyes, chemicals, and toxins from industries. Meanwhile, fertile agricultural lands are also affected with those chemicals and excessively used hazardous pesticides, herbicides, and plastics while unduly used fertilizers are causing algal blooms in natural water bodies (Rosen et al., 2017; West et al., 2017). Ultimately, these harmful chemicals are entering to humans to cause deadly diseases *via* food chain from plants and animals. In some instances, the contaminated water and foods caused severe epidemics and pandemics due to super-bacteria resistant to almost all drugs. In another hand, the genetic disorders caused by chemical mutagens leaving thousands of people with deadly non-transmissible diseases such as cancers, reproductive disorders and adverse pregnancy outcomes, physical disorders, and disabilities (Frazier and Hage, 1998). All these factors are amplifying the global risks (www.weforum.org). Thus, the environment protection is always crucial to secure the human life and animals on the planet. Though governments of different nations issued standard guidelines to discharge treated effluents, sewerage, and other wastages to the environment, yet excessive discharge of waste is maltreating

the environment and the ecosystem. Hence, there is an urgent need for a highly efficient system to treat waste for complete degradation of toxic molecules into simpler non-toxic forms while inactivating highly pathogenic multidrug-resistant superbugs to make water free of pathogens.

Many industries and laboratories treat chemical wastages using various approaches prior to discharge them. Commonly practiced approaches include- (1) physical methods- sedimentation, floatation, filtration; (2) biological oxidation methods- includes trickling filters, rotating biological contractor, activated sludge, lagoons, and various aerobic and anaerobic methods; and (3) chemical treatment methods such as coagulation and flocculation by lime added with ferric chloride and lime added with aluminum sulfate. Hospitals and biomedical laboratories treat microbially contaminated wastes by either physical means such as autoclaving and irradiation, or chemical treatment methods using organic solvents and detergents to remove or inactivate pathogens prior to discharge. All these methods have their own merits and demerits. The major demerit lies in the incomplete removal of these wastage products as well as the formation of intermediates which are more toxic than the parent pollutants.

Recently, photocatalysis, a novel green technology which is based on advance oxidation processes (AOPs') and is capable of generating different reactive species such as reactive oxygen species (ROS), reactive nitrogen species (RNS), oxygen radicals ($\cdot O_2^-$), hydroxyl radicals ($\cdot$OH) have attracted the great attention for their potential application for the degradation of organic and biological wastes (Cavassin et al., 2015; Ramazanzadeh et al., 2015; Waiskopf et al., 2016; Nosaka and Nosaka, 2017; Podporska-Carroll et al., 2017). In this method, the synthesized semiconductor NPs are activated by light of different wavelength (1) UV light, (2) visible light, and (3) NIR light depending on the energy band gap they possess (Sarina et al., 2013). The activated semiconductor degrade the organic and microbial cells by a simple photocatalytic redox mechanism. In recent year, extensive research has been carried out for the efficient removal of the toxic molecules and pathogenic microbes from wastewater using semiconductor photocatalytic NPs. Moreover, various modification on the photocatalytic nanoparticles such as formation of heterojunction, tuning the morphology, doping of metals/non-metals, and decorating of nanoparticles onto the photocatalytic surface have been carried out in order to make efficient inactivation of microorganism in waste water under visible light. Regmi et al. (2017a) have fabricated Fe doped $BiVO_4$ visible light active semiconductor and showed efficient removal of ibuprofen and *Escherichia coli* in water. Recently, the synthesis of Bi_2MoO_6 on g-C_3N_4 nanosheet is reported with enhanced photocatalytic hydrogen evolution and disinfection of *E. coli* under the visible light (Li et al., 2017). Meanwhile, Meng et al. (2017) used synthesized MoS_2 quantum dots interspersed Bi_2WO_6 heterostructure for efficient detoxification and disinfection in wastewater. Doping of different size of metals such as Ag further improved the photocatalytic antibacterial activities (Esfandiari et al., 2014). Ning et al. (2017) synthesized dual couples Bi metal depositing and Ag@AgI islanding on BiOI 3D architectures showed synergistic bactericidal mechanism of *E. coli* under visible light. Similarly, Booshehri et al. (2014) studied the effect of depositing silver nanoparticles on $BiVO_4$ to enhance visible light photocatalytic inactivation of bacteria in water. Other illustrations of microbial inactivation using semiconductors include the heterogeneous photocatalytic inactivation of *B. stearothermophilus* endospores in aqueous suspensions under artificial and solar irradiation (Berberidou et al., 2012), visible light inactivation of bacteria and fungi by modified titanium dioxide (Mitoraj et al., 2007), and the efficient inactivation of *E. coli* by ZnO–Ag nanoparticles under solar radiation (Adhikari et al., 2015). Similarly, visible light driven morphology tuned α-$NiMoO_4$ photocatalyst were used to inactivate multidrug resistant *Staphylococcus aureus* (Ray et al., 2018). Diverse microbes such as pathogenic bacteria, viruses, fungi, protozoa, and other organisms are inactivated thus making the water devoid of microbes and safe to human, animal, and environment.

Another key importance of semiconductor NPs is its multiple applications in medicine, bio-imaging, drugs delivery, the coating of implantable devices, wound dressings, dental material, bone cement as well as personal care products (Smith and Nie, 2010; Pan et al., 2016; Wang et al., 2017). They can also prevent pathogenic microbes to restrict the biofilm formation. Biofilm-forming bacteria such as *S. aureus* is one of the deadliest superbugs which is getting resistant to almost all kinds of drugs. NPs such as MgF_2, Au-based NPs (Yu et al., 2016), AgBr-Ag-Bi_2WO_6 (Zhang et al., 2010), Ag and Mg-based NPs (Lellouche et al., 2012; Markowska et al., 2013), ZnO, CuO, Fe_3O_4, TiO_2 and YF photocatalytic NPs are capable of inhibiting such microbes from developing biofilm (Wang et al., 2017).

Harmful algal bloom is another major problem in natural water bodies where the dissolved oxygen is extremely low, killing marine lives. Some of these algae produce toxins, algal toxins and metabolites such as domoic acid, brevotoxin, saxitoxin, microcystin, geosmin, anabena, nodularin etc. which are also detrimental to the health of the marine animals (Sivonen and Jones, 1999). As these harmful algae last for several months to years in the water bodies, these dead zones lost all forms of plants and marine animals while causing significant loss of environmental health, ecosystem, and economies. Thus, photocatalytic materials could play a potential role in decreasing such harmful algal blooms and preventing natural waters and different form of lives and ecosystem. The Ni-doped $BiVO_4$ photocatalyst exhibited the efficient algae inactivation under visible light irradiation while Co-BiVO4 degraded malachite green and inactivated harmful microorganisms in wastewater including green tides (Regmi et al., 2017b,c). Similarly, Ag-TiO_2 has shown efficient UV-photo elimination of harmful algal bloom (Rodríguez-González et al., 2010).

The multiple applications of photocatalytic NPs lead to discovering the modes of action of these particles in decomposing organic molecules to simpler form such as CO_2 and H_2O and disabling actively growing pathogens from multiplying and reproducing. This potential of NPs has huge benefits to make the environment clean by eliminating toxic molecules and pathogens while keeping the entire ecosystem healthy.

The mechanisms of destruction of the microorganisms, algae, and various organic toxic molecules is different. Although several studies have been reported till now to explain the possible mechanism of degradation of organic compounds and killing of microbes, the antimicrobial mechanism of photocatalytic NPs has to be explored yet. The photocatalytic process which is based on AOPs' is considered as green technique for treatment of polluted water containing harmful microbes. In this process a semiconductor upon absorption of a photon of suitable energy (≥band gap energy) can act as a photocatalytic substrate by producing highly reactive radicals that can that can degrade indiscriminately micropollutants including harmful micro-organism present in wastewater (Pillai et al., 2017). But during the process majorities of the produced charges undergo recombination within the bulk/surface of photocatalyst, with the release of heat as a byproduct, before they are transferred to the adsorbate species creating the decrease in photocatalytic efficiency often greater than 90%. Thus, impurities substitution, lattice defects, and vacancies formation on the semiconductor can provide possible alternative pathways for the enhancement of photogenerated electrons and holes thus, prevent recombination.

The semiconductor photocatalyst on irradiation to light with energy equal or greater to its band gap energy produces an oxidative and reductive entity. In its first step, photo-generated holes and electrons are formed in the valence band (h^+_{VB}) and the conduction band (e^-_{CB}), respectively. Consequently, these photogenerated charge carriers then react with water or dissolved oxygen to produce reactive oxidizing species such as OH and O_2^- that decompose pollutants into smaller molecules as well as inactivate micro-organisms.

$$\text{Photocatalyst} + h\nu \rightarrow e^-_{CB} + h^+_{VB}$$
$$h^+_{VB} + H_2O \rightarrow \cdot OH + H^+$$
$$h^+_{VB} + OH^- \rightarrow \cdot OH_{ad}$$
$$e^-_{CB} + O_2 \rightarrow \cdot O_2^- \rightarrow^{2H+} H_2O_2 \rightarrow^{e-} \cdot OH + OH^-$$
$$\cdot OH + \text{pollutants/cellular constituent (micro} - \text{organism)}$$
$$+ O_2 \rightarrow \text{simpler products (salts, } CO_2, H_2O \text{ etc.,)}$$
$$\cdot OH_{ad} \rightarrow \cdot OH_{free} + \text{pollutants} \rightarrow \text{simpler oxidation products}$$

Photocatalytic materials when come in contact with microbes via different energy such as electrostatic attraction, hydrophobic interactions, van der Waals forces and receptor-ligand interactions, they exert their effect on the bacterial cell membrane and starts to influence the basic metabolism of the cells by various mechanisms. The cells could also experience different stresses such as oxidative stresses, membrane permeability imbalance, changes in cell shape, protein inhibition and alteration in metabolism and DNA damages. As shown in **Figure 1**, various reactive radicals generated by photocatalytic NPs on receiving the photon energy higher than the band gap energy enters to the cells and brings disorders to the cells' metabolism and gene expression (Wang et al., 2015). Single NP can also have multiple modes of actions (Hajipour et al., 2012). Thus, the exact mechanism of cell death caused by NPs is currently unknown. Currently understood mechanisms of destruction of microbes are discussed with examples henceforward. (i) Oxidative stress induction; in which the excess ROS, generated as a result of redox process, favors the oxidation process in the cells that leads to the peroxidation of lipid membrane and eventually attack proteins, depress the activity of certain periplasmic enzyme, and eventually interact with DNA and damage it. (ii) Metal ion release; where the metal ions released from metal oxide semiconductors are percolated through the cell membrane and directly interact with the –SH, -NH and –COOH group of nucleic acid and protein and finally damaging them. However, this method is less lethal than the other. Since detail studies of metal ion release on antimicrobial mechanism has not been carried out yet; it is not considered as the major cause of cell death (Hussein-Al-Ali et al., 2014). (iii) The non-oxidative mechanism involves the inactivation of microbes by decreasing the critical cellular metabolism such as protein, amino acid, nucleotide, energy, and carbohydrate metabolism without oxidative stress induction. The mechanism of non-oxidative stress cell death is poorly understood with very few MgO NP (Leung et al., 2014). Among these three possible mechanisms of antibacterial activities of NPs, the first mechanism has attracted the most attention of the researchers.

In general different types of ROS ($\cdot O_2^-$, ·OH, H_2O_2,) are generated by NPs by reducing O_2 molecules (**Figure 1**). These ROS exert a different level of stress reactions to the cells to damage the cell components such as peptidoglycan layer, electron transport chain system, genomic materials (DNA, RNA), proteins, ribosomes etc. ROS alters the cell permeability by attacking the components of the cell membrane which changes cell integrity and release of cytoplasmic contents (Ansari et al., 2015; Huang et al., 2017; Ray et al., 2017). Moreover, ROS also depress the activities of various proteins essential for physiological processes in the cell (Padmavathy and Vijayaraghavan, 2011). H_2O_2 is able to enter the cell membrane and damage cell components while increasing the expression pattern of oxidative stress-induced genes (Xu et al., 2013).

The usefulness of photocatalysis for the disinfection of water has been shown by the destruction effects it has on a wide range of micro-organisms i.e. bacteria, viruses, fungi and protozoa (Laxma Reddy et al., 2017; Ray et al., 2017). The disinfection efficiency of photocatalysis depends upon pH, chemical nature of bacterial suspension medium, photocatalyst type, size, surface morphology, specific surface area, structure, zeta potential, high surface energy, and atomic ligand deficiency, concentration, light intensity, and treatment time as well as the nature of the targeted organism. The accepted sequence of events which take place when micro-organisms undergo photocatalytic experience are thought to be an attack of the cell wall constituent by the hydroxyl radical produced during the catalysis process. These radicals being the strongest agent could break many organic covalent bonds, such as C-C, C-H, C-N, C-O, and H-O present in biomolecules such as carbohydrates, nucleic acid, proteins, amino acid, and even DNA (Wu et al., 2016; Laxma Reddy et al., 2017; Xu et al., 2018).

Even though several modes of cell death based on reactive radicals are proposed and elucidated in recent publications, the exact mechanism of the antibacterial mechanism of NPs is not understood yet and warrants further research. Since there

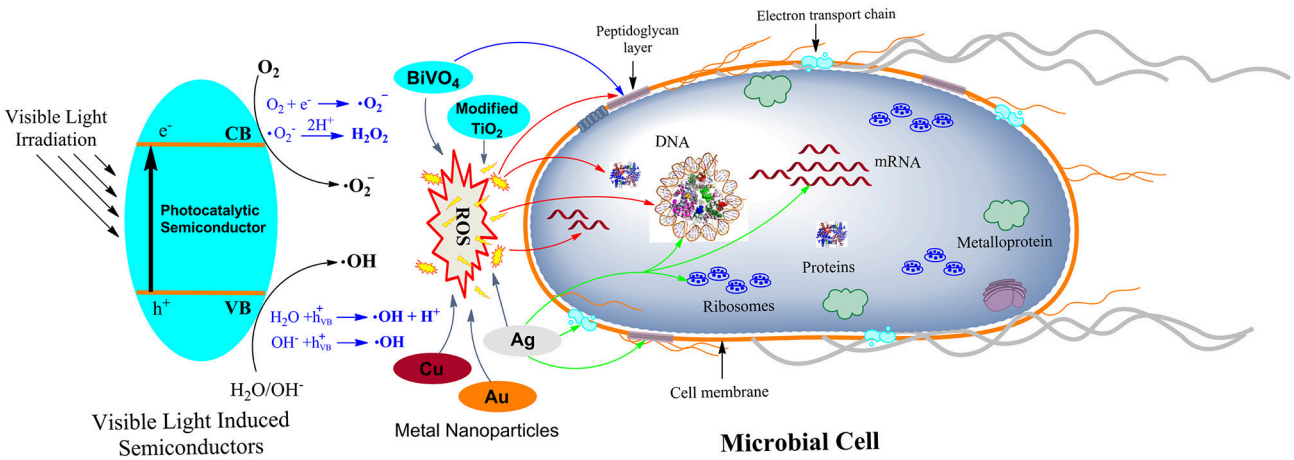

FIGURE 1 | The possible mechanisms of antimicrobial activities exhibited by different photocatalytic semiconductors. In the left side of the figure, the activation of the photocatalytic semiconductor by visible light is shown. Red colored arrows point the targets of reactive oxygen species (ROS) generated by various semiconductors. The blue color arrow represents the target of $BiVO_4$. Ag, Cu, and Au metal nanoparticles are also known to generate ROS and targets different parts in the cell. The green color arrow represents targets of Ag nanoparticle. Different targets in the microbial cells are labeled within the cell.

is variation in the type of NPs, strains, and environmental conditions used for antibacterial tests; it is very difficult to generalize the exact mechanism of killing of microbes by NPs. Different NPs exhibit different antibacterial activities over different strains. Thus, it is essential to bring such topics in the discussion forum for comprehensive analysis and elucidation of the exact mechanism of action of NPs. Several issues including entry of NPs to different cells having different structural integrity has to be elucidated. Moreover, the exact mechanism of NPs on protein degradation, DNA damage, and alteration of cells' basic metabolic pathways are hugely unknown.

Understanding the real mechanism of inhibiting and destroying cells during photocatalytic disinfection helps to fabricate more efficient semiconductor photocatalyst by (1) tuning the morphology, (2) incorporating transition metal ions such as Ag, Au, Cu, Fe, or Ni and (3) designing heterojunction photocatalysts capable of utilizing efficient energy source such as sunlight (Guo et al., 2015; Podporska-Carroll et al., 2017). Upon getting insights into the mechanism of the photocatalytic bactericidal phenomenon of semiconductor NPs, the system could be employed for large-scale decontamination of environmental wastewater or industries and hospitals/biomedical labs generating highly pathogenic bacteria and toxic molecules containing liquid waste by designing a reactor. Moreover, designing of semiconductor NPs which can utilize the large fraction of the solar spectrum (visible light) further expand the reactor's promiscuity without the expense of energy. More importantly, if these semiconductor NPs are reusable, non-toxic, and easily synthesizable; the waste treatment system will be highly cost-effective and sustainable. Another important point is that microbes need significant alteration to overcome the bactericidal activity exerted by NPs. NPs act on wide target sites in the cell at a time, thus bacteria could not make such big changes in metabolism by making mutational changes in the genomes and bringing changes in the metabolism in short period of time. This eliminates the concern of pathogens getting resistance to such treatment systems. Not only wastewaters, such reactors can also be designed for different purposes such as disinfection of hospital medical utensils, detoxifying textile wastes, and inactivation of algal bloom in large water bodies.

AUTHOR CONTRIBUTIONS

CR, BJ, SR, GG, and RP wrote the manuscript. CR and BJ equally contributed to this article.

ACKNOWLEDGMENTS

This research was supported by grant from National Research Foundation of Korea to Ramesh Prasad Pandey (Grant No: 2017R1C1B5018056).

REFERENCES

Adhikari, S., Banerjee, A., Eswar, N. K. R., Sarkar, D., and Madras, G. (2015). Photocatalytic inactivation of *E. coli* by ZnO–Ag nanoparticles under solar radiation. *RSC Adv.* 5, 51067–51077. doi: 10.1039/C5RA06406F

Ansari, M. A., Khan, H. M., Alzohairy, M. A., Jalal, M., Ali, S. G., Pal, R., et al. (2015). Green synthesis of Al2O3 nanoparticles and their bactericidal potential against clinical isolates of multi-drug resistant *Pseudomonas aeruginosa*. *World J. Microbiol. Biotechnol.* 31, 153–164. doi: 10.1007/s11274-014-1757-2

Berberidou, C., Paspaltsis, I., Pavlidou, E., Sklaviadis, T., and Poulios, I. (2012). Heterogenous photocatalytic inactivation of *B. stearothermophilus* endospores in aqueous suspensions under artificial and solar irradiation. *Appl. Catal. B Environ.* 125, 375–382. doi: 10.1016/j.apcatb.2012.06.005

Booshehri, A. Y., Goh, S. C., Hong, J., Jinag, R., and Xu, R. (2014). Effect of depositing silver nanoparticles on BiVO4 in enhancing visible light photocatalytic inactivation of bacteria in water. *J. Mater. Chem. A* 2, 6209–6217. doi: 10.1039/C3TA15392D

Cavassin, E. D., de Figueiredo, L. F., Otoch, J. P., Seckler, M. M., de Oliveira, R. A., Franco, F. F., et al. (2015). Comparison of methods to detect the *in vitro* activity of silver nanoparticles (AgNP) against multidrug resistant bacteria. *J. Nanobiotechnol*. 13, 64. doi: 10.1186/s12951-015-0120-6

Esfandiari, N., Simchi, A., and Bagheri, R. (2014). Size tuning of Ag-decorated TiO2 nanotube arrays for improved bactericidal capacity of orthopedic implants. *J. Biomed. Mater. Res. A* 102, 2625–2635. doi: 10.1002/jbm.a.34934

Frazier, L. M., and Hage, M. L. (1998). *Reproductive Hazards of the Workplace*. New York, NY: John Wiley & Sons.

Guo, B. L., Han, P., Guo, L. C., Cao, Y. Q., Li, A. D., Kong, J. Z., et al. (2015). The antibacterial activity of Ta-doped ZnO nanoparticles. *Nanoscale Res. Lett*. 10:1047. doi: 10.1186/s11671-015-1047-4

Hajipour, M. J., Fromm, K. M., Ashkarran, A. A., Jimenez de Aberasturi, D., de Larramendi, I. R., Rojo, T., et al. (2012). Antibacterial properties of nanoparticles. *Trends Biotechnol.* 30, 499–511. doi: 10.1016/j.tibtech.2012.06.004

Huang, S., Xu, Y., Xie, M., Liu, Q., Xu, H., Zhao, Y., et al. (2017). A Z-scheme magnetic recyclable Ag/AgBr@$CoFe_2O_4$ photocatalyst with enhanced photocatalytic performance for pollutant and bacterial elimination. *RSC Adv*. 7, 30845–30854. doi: 10.1039/C7RA03936K

Hussein-Al-Ali, S. H., El Zowalaty, M. E., Hussein, M. Z., Geilich, B. M., and Webster, T. J. (2014). Synthesis, characterization, and antimicrobial activity of an ampicillin-conjugated magnetic nanoantibiotic for medical applications. *Int. J. Nanomed.* 9, 3801–3814. doi: 10.2147/IJN.S61143

Laxma Reddy, P. V., Kavitha, B., Kumar Reddy, P. A., and Kim, K. H. (2017). TiO_2-based photocatalytic disinfection of microbes in aqueous media: a review. *Environ. Res*. 154, 296–303. doi: 10.1016/j.envres.2017.01.018

Lellouche, J., Friedman, A., Lahmi, R., Gedanken, A., and Banin, E. (2012). Antibiofilm surface functionalization of catheters by magnesium fluoride nanoparticles. *Int. J. Nanomed*. 7, 1175–1188. doi: 10.2147/IJN.S26770

Leung, Y. H., Ng, A. M., Xu, X., Shen, Z., Gethings, L. A., Wong, M. T., et al. (2014). Mechanisms of antibacterial activity of MgO: non-ROS mediated toxicity of MgO nanoparticles towards *Escherichia coli*. *Small* 10, 1171–1183. doi: 10.1002/smll.201302434

Li, J., Yin, Y., Liu, E., Ma, Y., Wan, J., Fan, J., et al. (2017). *In situ* growing Bi2MoO6 on g-C3N4 nanosheets with enhanced photocatalytic hydrogen evolution and disinfection of bacteria under visible light irradiation. *J. Hazard. Mater*. 321, 183–192. doi: 10.1016/j.jhazmat.2016.09.008

Markowska, K., Grudniak, A. M., and Wolska, K. I. (2013). Silver nanoparticles as an alternative strategy against bacterial biofilms. *Acta Biochim. Pol*. 60, 523–530.

Meng, X., Li, Z., Zeng, H., Chen, J., and Zhang, Z. (2017). MoS2 quantum dots-interspersed Bi2WO6 heterostructures for visible light-induced detoxification and disinfection. *Appl. Catal. B Environ*. 210, 160–172. doi: 10.1016/j.apcatb.2017.02.083

Mitoraj, D., Janczyk, A., Strus, M., Kisch, H., Stochel, G., Heczko, P. B., et al. (2007). Visible light inactivation of bacteria and fungi by modified titanium dioxide. *Photochem. Photobiol. Sci*. 6, 642–648. doi: 10.1039/B617043A

Ning, S., Lin, H., Tong, Y., Zhang, X., Lin, Q., Zhng, Y., et al. (2017). Dual couples Bi metal depositing and Ag@AgI islanding on BiOI 3D architectures for synergistic bactericidal mechanism of *E. coli* under visible light. *Appl. Catal. B Environ*. 204, 1–10. doi: 10.1016/j.apcatb.2016.11.006

Nosaka, Y., and Nosaka, A. Y. (2017). Generation and detection of reactive oxygen species in photocatalysis. *Chem. Rev*. 117, 11302–11336. doi: 10.1021/acs.chemrev.7b00161

Padmavathy, N., and Vijayaraghavan, R. (2011). Interaction of ZnO nanoparticles with microbes – a physio and biochemical assay. *J. Biomed. Nanotechnol*. 7, 813–822. doi: 10.1166/jbn.2011.1343

Pan, W. Y., Huang, C. C., Lin, T. T., Hu, H. Y., Lin, W. C., Li, M. J., et al. (2016). Synergistic antibacterial effects of localized heat and oxidative stress caused by hydroxyl radicals mediated by graphene/iron oxide-based nanocomposites. *Nanomedicine* 12, 431–438. doi: 10.1016/j.nano.2015.11.014

Pillai, S. C., McGuinness, N. B., Byrne, C., Han, C., Lalley, J., Nadagouda, M. N., et al. (2017). "Photocatalysis as an effective advanced oxidation process," in *Advanced Oxidation Processes for Water Treatment: Fundamentals and Applications*, ed. M. I. Stefan (London: IWA Publishing), 333–381.

Podporska-Carroll, J., Myles, A., Quilty, B., McCormack, D. E., Fagan, R., Hinder, S. J., et al. (2017). Antibacterial properties of F-doped ZnO visible light photocatalyst. *J. Hazard. Mater*. 324, 39–47. doi: 10.1016/j.jhazmat.2015.038

Ramazanzadeh, B., Jahanbin, A., Yaghoubi, M., Shahtahmassbi, N., Ghazvini, K., Shakeri, M., et al. (2015). Comparison of antibacterial effects of ZnO and CuO nanoparticles coated brackets against *Streptococcus mutans*. *J. Dent.* 16, 200–205.

Ray, S. K., Dhakal, D., Pandey, R. P., and Lee, S. W. (2017). Ag-$BaMoO_4$: $Er3^+$/$Yb3^+$ photocatalyst for antibacterial application. *Mater. Sci. Eng. C Mater. Biol. Appl*. 78, 1164–1171. doi: 10.1016/j.msec.2017.04.115

Ray, S. K., Dhakal, D., Regmi, C., Yamaguchi, T., and Lee, S. W. (2018). Inactivation of *Staphylococcus aureus* in visible light by morphology tuned α-$NiMoO_4$. *J. Photochem. Photobiol. A Chem*. 350, 59–68. doi: 10.1016/j.jphotochem.2017.09.042

Regmi, C., Kim, T. H., Ray, S. C., Yamaguchi, T., and Lee, S. W. (2017c). Cobalt-doped BiVO4 (Co-BiVO4) as a visible-light-driven photocatalyst for the degradation of malachite green and inactivation of harmful microorganisms in wastewater. *Res. Chem. Intermed*. 43, 5203–5216. doi: 10.1007/s11164-017-3036-y

Regmi, C., Kshetri, Y. K., Kim, T., Pandey, R. P., Ray, S. K., and Lee, S. W. (2017b). Fabrication of Ni-doped BiVO4 semiconductors with enhanced visible-light photocatalytic performances for wastewater treatment. *Appl. Surf. Sci*. 413, 253–265. doi: 10.1016/j.apsusc.2017.04.056

Regmi, C., Kshetri, Y. K., Kim, T. H., Pandey, R. P., and Lee, S. W. (2017a). Visible-light-induced Fe-doped $BiVO_4$ photocatalyst for contaminated water treatment. *Mol. Catal*. 432, 220–231. doi: 10.1016/j.mcat.2017.02.004

Rodríguez-González, V., Obregón Alfaro, S., Torres-Martínez, L. M., Cho, S. H., and Lee, S. W. (2010). Silver–TiO_2 nanocomposites: Synthesis and harmful algae bloom UV-photoelimination. *Appl. Catal. B Environ*. 98, 229–234. doi: 10.1016/j.apcatb.2010.06.001

Rosen, B. H., Davis, T. W., Gobler, C. J., Kramer, B. J., and Loftin, K. A. (2017). *Cyanobacteria of the 2016 Lake Okeechobee Waterway Harmful Algal Bloom: U.S.* Geological Survey Open-File Report 2017–1054, 34.

Sarina, S., Waclawik, E. R., and Zhu, H. (2013). Photocatalysis on supported gold and silver nanoparticles under ultraviolet and visible light irradiation. *Green Chem*. 15, 1814–1833. doi: 10.1039/c3gc40450a

Sivonen, K., and Jones, G. (1999). "Cyanobacterial toxins," in *Toxic Cyanobacteria in Water: A Guide to their Public Health Consequences, Monitoring and Management*, eds I. Chorus and J. Bartram (London, UK: E & FN. Spon), 41–110.

Smith, A. M., and Nie, S. (2010). Semiconductor nanocrystals: structure, properties, and band gap engineering. *Acc. Chem. Res*. 43, 190–200. doi: 10.1021/ar9001069

Waiskopf, N., BenShahar, Y., Galchenko, M., Carmel, I., Moshitzky, G., Soreq, H., et al. (2016). Photocatalytic reactive oxygen species formation by semiconductor–metal hybrid nanoparticles. toward light-induced modulation of biological processes. *Nano Lett*. 16, 4266–4273. doi: 10.1021/acs.nanolett.6b01298

Wang, L., Hu, C., and Shao, L. (2017). The antimicrobial activity of nanoparticles: present situation and prospects for the future. *Int. J. Nanomed.* 12, 1227–1249. doi: 10.2147/IJN.S121956

Wang, W., Huang, G., Yu, J. C., and Wong, P. K. (2015). Advances in photocatalytic disinfection of bacteria: Development of photocatalysts and mechanisms. *J. Environ. Sci*. 34, 232–247. doi: 10.1016/j.jes.2015.05.003

West, M., Fenner, N., Gough, R., and Freeman, C. (2017). Evaluation of algal bloom mitigation and nutrient removal in floating constructed wetlands with different macrophyte species. *Ecol. Eng.* 108, 581–588. doi: 10.1016/j.ecoleng.2017.07.033

Wu, D., Wang, W., Ng, T. W., Huang, G., Xia, D., Yip, H. Y., et al. (2016). Visible-light-driven photocatalytic bacterial inactivation and mechanism of zinc oxysulfide under LED light irradiation. *J. Mater. Chem. A* 4, 1052–1059. doi: 10.1039/C5TA08044D

Xu, X., Chen, D., Yi, Z., Jiang, M., Wang, L., Zhou, Z., et al. (2013). Antimicrobial mechanism based on H2O2 generation at oxygen vacancies in ZnO crystals. *Langmuir* 29, 5573–5580. doi: 10.1021/la400378t

Xu, Y., Liu, Q., Liu, C., Zhai, Y., Xie, M., Huang, L., et al. (2018). Visible-light-driven Ag/AgBr/$ZnFe_2O_4$ composites with excellent photocatalytic activity for *E. coli* disinfection and organic pollutant degradation. *J. Colloid Interface Sci.* 512, 555–566. doi: 10.1016/j.jcis.2017.10.077

Yu, Q., Li, J., Zhang, Y., Wang, Y., Liu, L., and Li, M. (2016). Inhibition of gold nanoparticles (AuNPs) on pathogenic biofilm formation and invasion to host cells. *Sci. Rep.* 6:26667. doi: 10.1038/srep26667

Zhang, L. S., Wong, K. H., Yip, H. Y., Hu, C., Yu, J. C., Chan, C. Y., et al. (2010). Effective photocatalytic disinfection of *E. coli* K-12 using AgBr-Ag-Bi_2WO_6 nanojunction system irradiated by visible light: the role of diffusing hydroxyl radicals. *Environ. Sci. Technol.* 44, 1392–1398. doi: 10.1021/es903087w

Conflict of Interest Statement: The authors declare that the research was conducted in the absence of any commercial or financial relationships that could be construed as a potential conflict of interest.

frontiers in Chemistry

ORIGINAL RESEARCH
published: 12 December 2017
doi: 10.3389/fchem.2017.00114

A Green Desulfurization Technique: Utilization of Flue Gas SO_2 to Produce H_2 via a Photoelectrochemical Process Based on Mo-Doped $BiVO_4$

Jin Han†, *Kejian Li*†, *Hanyun Cheng and Liwu Zhang**

Shanghai Key Laboratory of Atmospheric Particle Pollution and Prevention, Department of Environmental Science and Engineering, Fudan University, Shanghai, China

OPEN ACCESS

Edited by:
Fan Dong,
Chongqing Technology and Business University, China

Reviewed by:
Guangming Jiang,
Chongqing Technology and Business University, China
Hongwei Huang,
China University of Geosciences, China
Yanhui Ao,
Hohai University, China

***Correspondence:**
Liwu Zhang
zhanglw@fudan.edu.cn

†*These authors have contributed equally to this work.*

Specialty section:
This article was submitted to Catalysis and Photocatalysis, a section of the journal Frontiers in Chemistry

Received: *27 October 2017*
Accepted: *27 November 2017*
Published: *12 December 2017*

Citation:
Han J, Li K, Cheng H and Zhang L (2017) A Green Desulfurization Technique: Utilization of Flue Gas SO_2 to Produce H_2 via a Photoelectrochemical Process Based on Mo-Doped $BiVO_4$. Front. Chem. 5:114. doi: 10.3389/fchem.2017.00114

A green photoelectrochemical (PEC) process with simultaneous SO_2 removal and H_2 production has attracted an increasing attention. The proposed process uses flue gas SO_2 to improve H_2 production. The improvement of the efficiency of this process is necessary before it can become industrial viable. Herein, we reported a Mo modified $BiVO_4$ photocatalysts for a simultaneous SO_2 removal and H_2 production. And the PEC performance could be significantly improved with doping and flue gas removal. The evolution rate of H_2 and removal of SO_2 could be enhanced by almost three times after Mo doping as compared with pristine $BiVO_4$. The enhanced H_2 production and SO_2 removal is attributed to the improved bulk charge carrier transportation after Mo doping, and greatly enhanced oxidation reaction kinetics on the photoanode due to the formation of SO_3^{2-} after SO_2 absorption by the electrolyte. Due to the utilization of SO_2 to improve the production of H_2, the proposed PEC process may become a profitable desulfurization technique.

Keywords: hydrogen, sulfur dioxide, solar energy, Photoelectrochemical (PEC), Mo-doped $BiVO_4$

INTRODUCTION

Sulfur dioxide (SO_2), as one of the acid gases, could transform into some atmospheric products (e.g., sulfate, sulfuric acid aerosol) through the chemical process in the atmosphere. It and its atmospheric products are detrimental to human health, and cause lots of environmental problems such as smog formation, acid deposition, and degradation of visibility. As is well-known, the SO_2 mainly enters the atmosphere through the anthropogenic processes, e.g., combustion and release of petroleum, fossil fuel, etc. (Lelieveld and Heintzenberg, 1992; McDonald-Buller et al., 2016). Till now, to remove SO_2 released from the burning of fossil fuels, several effective methods has been developed (Srinivasan and Grutzeck, 1999; Bashikova et al., 2001; Xia et al., 2011; Kaplan et al., 2013; Yang et al., 2013). Among these technologies, Wet Flue Gas Desulfurization (WFGD) has been one of the state-of-the-art technologies for SO_2 removal with high efficiency, simple equipment and obtaining multi-useful byproducts (Yang et al., 2012; Lu et al., 2013). Unfortunately, there are some inevitable drawbacks with the WFGD process: for example, the oxidation process energy of SO_3^{2-} to final SO_4^{2-} is wasted and it is not consistent with the sustainable principles. In order to solve this problem, our group proposed a solar-to-H_2 energy conversion with SO_2 removal

simultaneously via a solar water splitting process for the first time (Han et al., 2017). Since the oxidation of SO_3^{2-} (formed during desulfurization process) needs much lower activation energy and 2 electrons than that of water, acted as a sacrificing reagent during the process, thus it could significantly improve the evolution rate of H_2. This method not only utilizes the waste energy during the desulfurization process, also realizes the energy production by using air pollutants, which could achieve the zero release of SO_2.

Though we have reported a photoresponse semiconductor ($BiVO_4$) for H_2 generation with SO_2 removal, but it is still a challenge to facilitate the performance due to the intrinsic low mobility of photogenerated charges of $BiVO_4$. Lots of methods have been proposed to solve this problem, such as controlling the morphology (McDonald and Choi, 2012; Kim and Choi, 2014; Zhou et al., 2014), metal and nonmetal doping (Jo et al., 2012; Chen et al., 2015; Huang H. et al., 2015; Huang H. W. et al., 2015; Huang et al., 2017), forming heterojunctions (Hong et al., 2011; Luo et al., 2011; Seabold and Choi, 2012; Zhang et al., 2016). These modifications have improved the properties of $BiVO_4$ greatly by reducing the band-gap energy or improving the charge carrier transport. It has been reported that Mo^{6+} ion substitute the V site in monoclinic sheelite $BiVO_4$ could improve the photoinduced carriers, which could facilitate the oxidation while in water splitting reaction system theoretically and experimentally (Luo et al., 2011, 2013; Parmar et al., 2012; Ding et al., 2014; Park et al., 2014; Seabold et al., 2014; Zhou et al., 2014; Jiang et al., 2015, 2017; Kuang et al., 2016; Nair et al., 2016; Pattengale and Huang, 2016). However, Mo-doped $BiVO_4$ has not been studied as photoanode for flue gas SO_2 removal. Here, we prepared Mo-doped $BiVO_4$ for enhancing H_2 generation with simultaneous SO_2 removal. Moreover, the importance of the amount of Mo-dopants on the performance of $BiVO_4$ with SO_2 removal was also studied. Besides we prepared a series of Mo-doped $BiVO_4$ films with different content. The structure characterizations of the obtained films are investigated by XRD, SEM, Raman, UV-vis. Furthermore, we studied the performance of H_2 generation and efficiency of SO_2 removal.

EXPERIMENT

Synthesis of the Catalysts

In this work, the deionized water (DI water) was used throughout the whole experiment, and all the chemical reagents are analytical grade and used without any further purification.

F-doped SnO_2 coated glass (FTO) were purchased from China Southern Glass Co. Ltd, and the FTO glasses were sonicated by immersing in acetone, ethanol and DI water for removing the impurities on the surface of the glass. For comparison, the pristine $BiVO_4$ was also prepared. All of the electrodes were synthesized by drop-coating method. The precursor solution was dropped onto the conducting side of FTO, followed by annealing in air. The precursor solutions were synthesized by the following procedure (Zhang et al., 2014): diethylene-etriaminepentaacetic acid (DTPA) and ammonia in water (13.0 mol L^{-1}) were added into hot deionized water. After dissolution, the stoichiometric $Bi(NO_3)_3{\bullet}5H_2O$, V_2O_5 powder and moderate ammonium molybdate tetrahydrate ($H_{24}Mo_7N_6O_{24}{\cdot}4H_2O$) were added into sequence as listed. The resulted mixture was stirred and heated for an hour to promote the dissolution and reaction (complexation of Bi^{3+}, V^{5+}, and Mo^{6+} with DTPA) until the mixture turned into a transparent solution. Here, we prepared three different samples with the content of Mo ranging from 1, 3, to 5. The amounts of doped Mo were 1 atom%, 3 atom%, 5 atom%, and were denoted as $BiVO_4$(Mo-1), $BiVO_4$(Mo-3), $BiVO_4$(Mo-5), respectively. Then, 40 μl prepared solutions were dropped onto the conducting side of FTO (1 × 2 cm) respectively. After dried at 60° C in oven, the films were annealed at 500° C for 3 h with a ramping rate of 2° C min^{-1} in air. The above process was repeated by three times for the synthesis of the electrode.

Characterization of the Samples

The crystal structures of the as-prepared samples were determined using an X-Ray Diffraction (XRD) with Cu Kα radiation ranging from 10 to 60°. The crystallite sizes of the samples were calculated using the Scherrer formula:

$$D = \frac{K\lambda}{\beta\cos\theta} \quad (1)$$

Where D is the average crystallite size (nm), λ is the wavelength of the X-ray radiation (0.154 nm), K is the shape factor (0.9), β is the peak width at half-maximum height, corrected for instrumental broadening, and $2\theta = 28.7°$. The micromorphology and the microstructure of the samples were determined by using field emission scanning electron microscopy (FE-SEM, Hitachi S-4800, Japan). UV-vis transmission spectra of the as-prepared catalysts were measured using a UV-Vis spectrophotometer (SHIMADZU UV-2600) with an integrating sphere attachment. $BaSO_4$ used as a standard. Raman spectra were recorded with a Raman spectrometer (HORIBA, X-plo RA Plus), a green laser (532 nm) were used as excitation sources.

PEC Measurement

The apparatus for the PEC tests was a gastight photoreactor. The PEC performance were conducted with a typical three-electrode configuration by using a potentiostat (CHI 660E, Shanghai Chenhua Co. Lid. China). The synthesized pure $BiVO_4$ or Mo-doped $BiVO_4$ electrode was used as working electrode, Pt wire was used as counter electrode and Hg/HgO electrode was used as reference electrode. The electrolyte solutions for the PEC tests were prepared by absorbing SO_2 gas with NaOH solutions of certain concentration (detailed in **Table 1**). We bubbled SO_2 of concentration is 1,000 ppm successively to NaOH aqueous with the flow rate of 200 ml min^{-1} to form Na_2SO_3 with a specific concentration. Eventually, the obtained electrolytes for PEC tests were 0.1 M NaOH−0.025 M Na_2SO_3 [denoted as NaOH(aq)+SO_2(g)-1], 0.1 M NaOH-0.05 M Na_2SO_3 [denoted as NaOH(aq)+SO_2(g)-2], 0.1 M NaOH-0.075 M Na_2SO_3 [denoted as NaOH(aq)+SO_2(g)-3]. For comparison, the NaOH (aq, 0.1 M) solution was also prepared. The PEC tests were measured under illumination by using a 300 W Xe lamp solar simulator with AM 1.5 G filter (100 mW cm^{-2}) from the back side of the working electrode, as well as in dark conditions. Liner Sweep Voltammetry (LSV) was measured with the sweep rate of 10 mV s^{-1}.

The structures of prepared $BiVO_4$ and Mo-doped $BiVO_4$ bulk were optimized by using the CASTEP code (Ding et al., 2014). The primitive cell of pure monoclinic sheelite $BiVO_4$ was relaxed using 400 eV energy cut off for the plane-wave expansion. The structural model of Mo-doped monoclinic sheelite $BiVO_4$ was built by substituting one V atom in a relaxed $(2 \times 1 \times 2)$ supercell of monoclinic sheelite $BiVO_4$ with one Mo atom.

Hydrogen Evolution

The reactor for hydrogen evolution experiments is identical with the apparatus used for PEC tests, which use a two-electrode configuration. The electrolyte was NaOH solution bubbled with SO_2 gas. The experiments were conducted under illumination using a 300 W Xe lamp with AM 1.5 G filter (100 mW cm^{-2}) from the back side of the photoanodes in a 150 ml reactor with 100 ml electrolytes filled in and the external bias was 1.6 V. The amount of H_2 was analyzed by gas chromatography using a thermal conduction detector (TCD) once an hour. The pH values of the solution during the PEC tests were detected by Ohaus (STARTER 2100). The theoretical evolution rate of H_2 is calculated according to the following equation:

$$v = \frac{I \times t}{Z \times F \times A \times 3600} \tag{2}$$

Where, v indicates the evolution rate of H_2 (mol cm^{-2} h^{-1}); I indicates the average current (A); t indicates the time (s); Z indicates the transferred electron number (1); F is the Faraday's constant (96,500 C mol^{-1}); A is the area of the film (cm^2).

The equation for the calculation of Faradaic efficiency is:

$$Faradaic\ efficiency\ (\%) = \frac{m \times n \times F}{I \times t} \times 100\% \tag{3}$$

Where, m is the experimental value of H_2 (mol); n is the reacted electron number (1); F is the Faraday's constant (96,500 C mol^{-1}); I is the average current (A); t is the time (s).

TABLE 1 | The detailed information of electrolyte and SO_2 absorbing efficiency.

Items	NaOH(aq)-SO_2(g)-1	NaOH(aq)-SO_2(g)-2	NaOH(aq)-SO_2(g)-3
Concentration of NaOH/M	0.150	0.200	0.250
Concentration of SO_2/ppm	1,000	1,000	1,000
SO_2 flow rate/ml min^{-1}	200	200	200
SO_2 inletting time/min	112	224	336
Resulted concentration of SO_3^{2-}/M	~0.025	~0.050	~0.075
SO_2 absorbing efficiency/%	~99	~98	~98

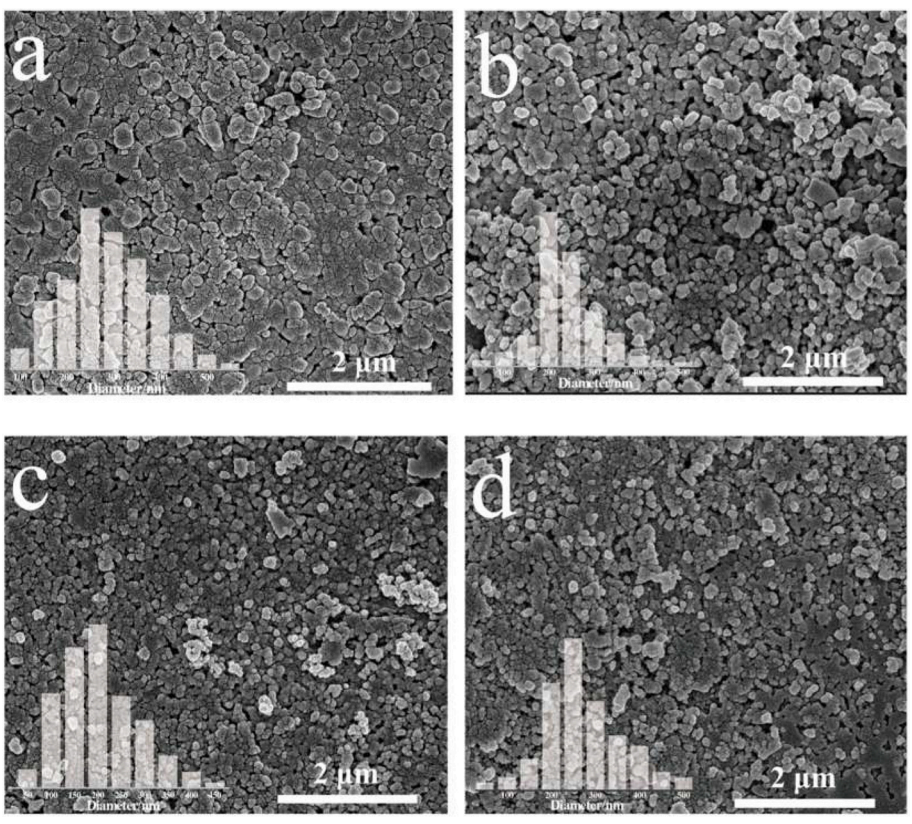

FIGURE 1 | SEM images and particle range of **(a)** pure $BiVO_4$; **(b)** $BiVO_4$(Mo-1); **(c)** $BiVO_4$(Mo-3); **(d)** $BiVO_4$(Mo-5).

RESULTS AND DISCUSSION

Structure and Physical Properties of the Photoelectrode

The SEM (Scanning Electron Microscopy) images of pristine $BiVO_4$ and Mo-doped $BiVO_4$ films are shown in **Figure 1**. All of the films present nanoparticle structure while a rougher, more disordered structure can be observed in the $BiVO_4$ films. Besides, the incorporation of Mo could decrease the average size of $BiVO_4$ with decreasing aggregation of the particles. The average diameter of pure $BiVO_4$ is about 280 nm (**Figure 1a**), and the average diameter of Mo-doped $BiVO_4$ are ranging from 200 to 250 nm, which are smaller than that of pure $BiVO_4$ (**Figures 1b–d**). Besides, the smaller particle size of the as-prepared photocatalyst could provide more available active sites, which could be in favor of the PEC performance.

Figure 2A compares the XRD (X-Ray Diffraction) patterns of pure and Mo-doped $BiVO_4$ films with different concentrations of Mo dopant. All the diffraction peaks are assigned to phase-pure monoclinic sheelite $BiVO_4$ structure (JCPDS No. 14-0688). Since the films are very thin, the diffraction peaks of FTO substrate are also observed in XRD. No noticeable peaks of MoO_3 is detected in the Mo-doped $BiVO_4$, the results are consistent with previous study (Berglund et al., 2012; Luo et al., 2013; Chen et al., 2015; Nair et al., 2016; Thalluri et al., 2016). Additionally, the main peaks of the monoclinic $BiVO_4$ structure shift to lower intensity and higher scattering angles in the Mo-doped $BiVO_4$ films since the radius of Mo is higher than that of V. This represents a shrinkage or an enlargement of the *d* spacing of corresponding crystal planes due to incorporation of dopant cations into V sites of $BiVO_4$ (Parmar et al., 2012). As the pure phase and modification in *d* spacing, it can be calculated that the Mo have been effectively incorporated into the crystal lattice of $BiVO_4$ with the monoclinic phase unchanged (Parmar et al., 2012). Furthermore, the crystallite sizes calculated by using the Scherrer formula are 110, 117, 83, 85 nm for the $BiVO_4$, $BiVO_4$(Mo-1), $BiVO_4$(Mo-3), $BiVO_4$(Mo-5), respectively.

Though XRD shows some trace that Mo have been doped in the crystal of pure $BiVO_4$. However, it is too rough to identify the doping sites in the crystal lattice because of the low doping concentration. To probe the doping sites and local distortions of Mo-doped $BiVO_4$, the Raman spectra were measured and the results are shown in **Figure 2B**. The Raman mode located at 829 cm^{-1} is assigned to the symmetric stretching mode of VO_4^{3-} units. It is clear that the symmetric stretching mode in Mo-doped $BiVO_4$ shifts to a lower wave number, which suggests Mo^{6+} substitutes V^{5+} in the VO_4^{3-} tetrahedron (Luo et al., 2013; Zhang et al., 2014).

Optical properties of the films are very important for the PEC performance. **Figure 3A** displays the UV-Vis DRS absorption

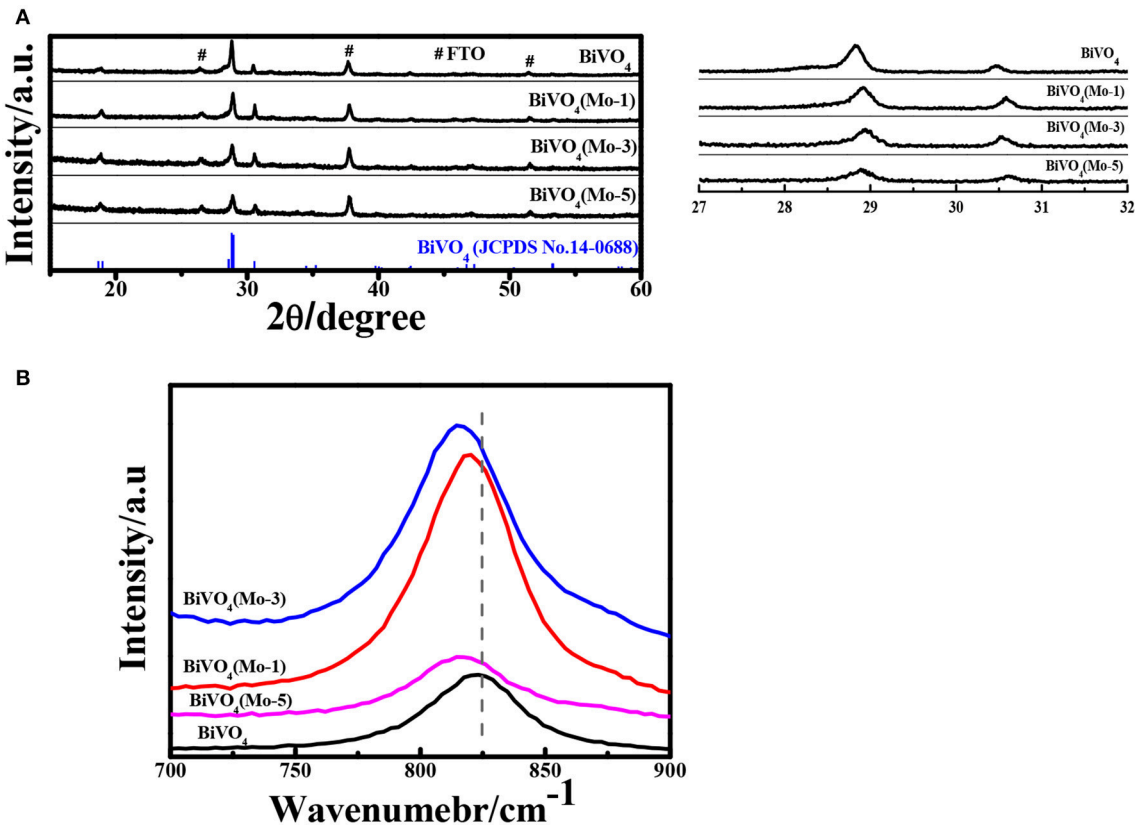

FIGURE 2 | (A) XRD patterns; (#: FTO) **(B)** Raman spectra of pure $BiVO_4$ and Mo doped $BiVO_4$ with different concentration.

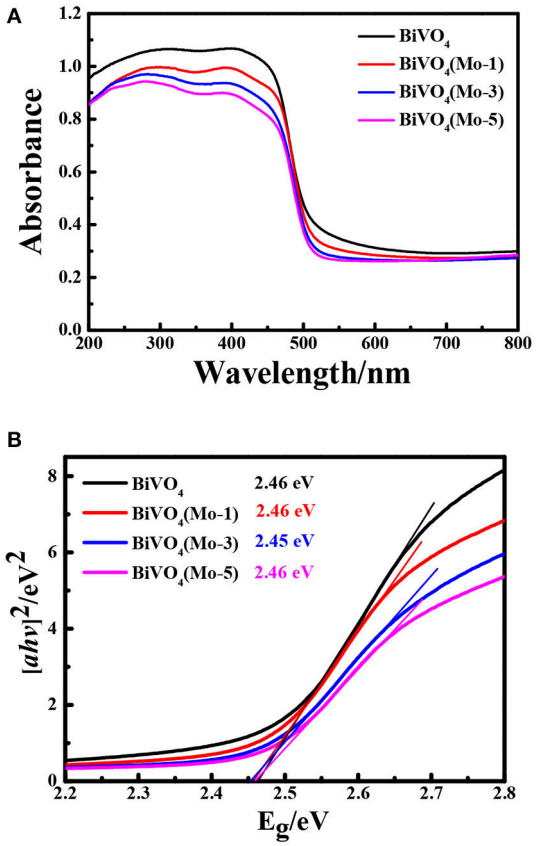

FIGURE 3 | (A) UV-Vis DRS spectra and **(B)** Tauc plots of pure $BiVO_4$ and Mo doped $BiVO_4$ with different concentration.

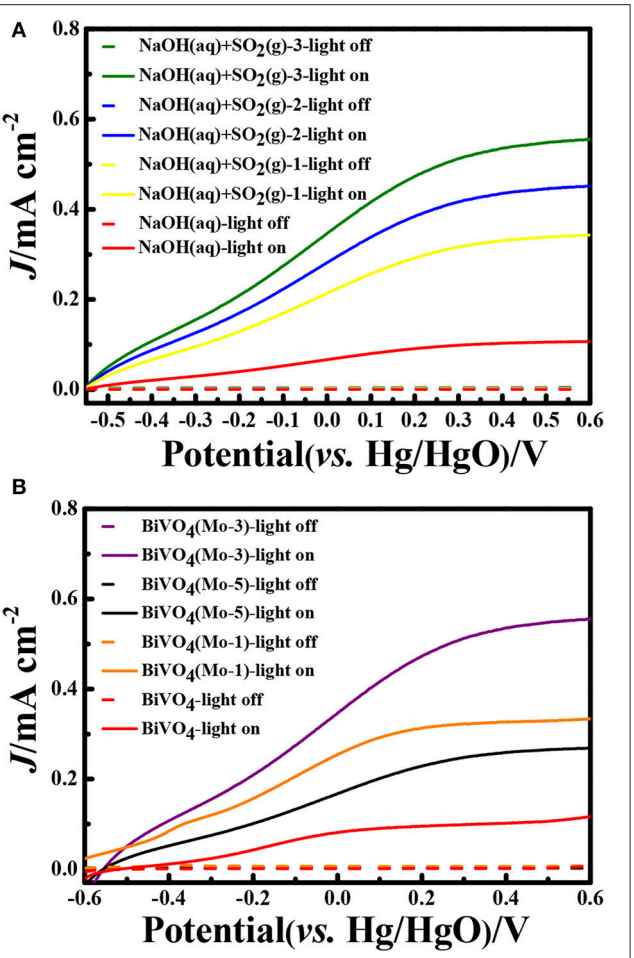

FIGURE 4 | Linear Sweep Voltammograms (LSV) curves **(A)** $BiVO_4$(Mo-3) in different electrolyte systems; **(B)** different photoanodes in NaOH(aq)+SO_2(g)-3 electrolyte. (Scan speed: 10 mV s^{-1}).

spectra of the four films. All of the films present a strong absorption in the UV-Vis range, and the incorporation of Mo can hardly affect the absorption edges of $BiVO_4$. Besides, there isn't any peak shift in the UV-Vis spectra of Mo-doped films, which indicates there is not existence of the phase transfer from monoclinic to tetragonal structures with doping of Mo (**Figure 3A**; Pattengale and Huang, 2016). As the pure $BiVO_4$ shows a larger optical absorbance at wavelengths (>325 nm), thus the pure $BiVO_4$ are less porous than the Mo-doped $BiVO_4$ (Nair et al., 2016).

The optical band gap energy can be calculated by the following equation:

$$\alpha h\nu = A(h\nu - E_g)^{n/2} \quad (4)$$

where, α, $h\nu$, A, and E_g are the absorption coefficient, photo energy, constant and band gap energy, respectively. The value of n depends on whether the transition is direct ($n = 1$) or indirect ($n = 4$). The bandgap of all the films are about 2.5 eV (**Figure 3B**), which is consistent with the reported band gap of $BiVO_4$ (Zhang et al., 2014). This result indicates that the incorporation of low amount of Mo could hardly influence the bandgap of $BiVO_4$, and it is considered to be the characteristic band gap of monoclinic phase of $BiVO_4$.

In the experiments, the SO_2 gas was absorbed by NaOH solutions and the concentration of SO_3^{2-} was detected. Through analyzing, the removal efficiencies of SO_2 gas were about 98%, it indicated that the absorption method could removal SO_2 completely. In order to determine the PEC properties of the photoelectrodes, the Linear Sweep Voltammograms (LSV) were measured both in dark and under AM 1.5 G illumination (100 mW cm^{-2}; **Figure 4**). After analyzing the photocurrent densities of the photoanodes in different electrolyte systems after absorbing SO_2 (**Figure 4A**), it is concluded: (1) the photocurrent densities are negligible under dark conditions in different electrolyte systems; (2) the photocurrent densities could be significantly enhanced after inletting SO_2 into electrolyte. Since the introduction of SO_2 into electrolyte, the concentration of SO_3^{2-} could be increased, and the oxidation reaction of SO_3^{2-} needs lower activation energy and kinetically faster than that of water, thus the formed SO_3^{2-} consumes the photogenerated holes instantaneously and generates a higher photocurrent density than that of water. Though the doping of Mo could decrease the light-absorbing slightly (**Figure 3A**), but it could

significantly enhance the bulk charge carrier transportation of $BiVO_4$. Therefore, the PEC performance of Mo-doping $BiVO_4$ is higher than that of $BiVO_4$. The photocurrent density is greatly dependent on the amount of SO_2 absorbed in the electrolyte. In NaOH(aq)+SO_2(g)-3, the photocurrent density is improved by 1.2 times, 1.6 times, and 5 times than that of NaOH(aq)+SO_2(g)-2, NaOH(aq)+SO_2(g)-1, NaOH(aq) at 0.5 V vs. Hg/HgO, respectively. The photocurrent density is significantly improved by 5 times as compared with our previous research on porous $BiVO_4$ (Han et al., 2017).

Compared with the four different electrode films in NaOH(aq)+SO_2(g)-3 electrolyte, it is clear that $BiVO_4$(Mo-3) displayed an outstanding PEC performance. The photocurrent density of $BiVO_4$(Mo-3) is 1.7 times than that of $BiVO_4$(Mo-1), 2 times than that of $BiVO_4$(Mo-5), and 5 times than that of $BiVO_4$ at 0.5 V vs. Hg/HgO (**Figure 4B**). The current densities of $BiVO_4$(Mo-3) in NaOH(aq) with and without SO_2(g)-3 at 0.6 V vs. Hg/HgO are ca. 0.6 and 0.1 mA cm^{-2}, respectively; the current density in NaOH(aq)+SO_2(g)-3 is 6 times higher than that in NaOH(aq). On the other hand, the evolution rate of H_2 in NaOH(aq)+SO_2(g)-3 (39.4 μmol h^{-1} cm^{-2}) is more than 40 times higher than that in NaOH (0.92 μmol h^{-1} cm^{-2}) in the **Table 2**. The above results indicate that the amount of Mo at 3 atom% could be an optimal choice.

The experiments for H_2 evolution in different systems were measured with a two-electrode configuration at a bias of 1.6 V under AM 1.5G irradiation. **Figure 5A** shows the amount of H_2 evolved in different systems and **Table 2** summarized the data of current densities, theoretical/ experimental evolution rates of H_2 and the Faradaic efficiencies in the different systems. Comparing each photoanodes in different solution systems, it is clear that the SO_2 removal could significantly facilitate the current density and evolution rate of H_2, which is in good agreement with our previous research (Han et al., 2017). Besides, the current density and evolution rates for $BiVO_4$(Mo-1, 3, 5) under light irradiation are higher than that under the dark condition. Furthermore, all of the Mo doped $BiVO_4$ photoanodes show more attractive performance than that of pure $BiVO_4$, and the $BiVO_4$(Mo-3) performed the best H_2 generation activities. As calculated, a highest H_2 evolution rate of 39.4 μmol h^{-1} cm^{-2} is realized in NaOH(aq)+SO_2(g)-3 with $BiVO_4$(Mo-3) as photoanode, and the H_2 evolution rate is only 0.19 μmol h^{-1} cm^{-2} in NaOH(aq) with the $BiVO_4$ as photoanode, suggesting the H_2 production can be enhanced about 200 times with the removal of SO_2 simultaneously with 3 atom% Mo-doped $BiVO_4$. Furthermore, the theoretical evolution rates of H_2 are close to theoretical rates in each system, indicating a high Faradaic efficiency of H_2 production (higher than 95%). Besides, the catalysts could not dissolve although the solution is a strong basic aqueous solution.

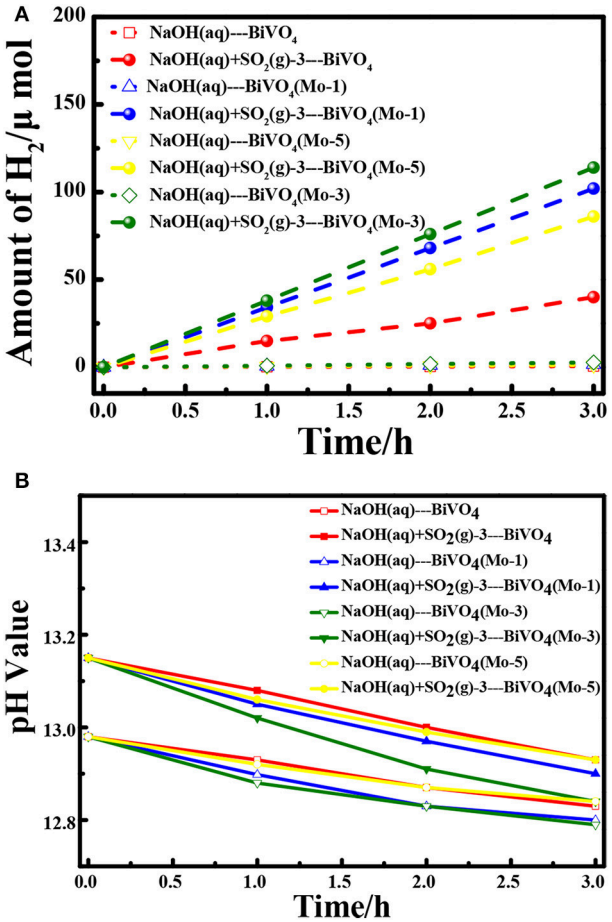

FIGURE 5 | (A) Hydrogen generation at an applied potential of 1.6 V in two-electrode configuration for 3 h; **(B)** The variation of pH values of electrolytes during the process.

TABLE 2 | The current density, theoretical and experimental evolution rate of H_2, and the Faradaic efficiency in different electrolytes [A—0.1 M NaOH; B—NaOH(aq)+SO_2(g)-3].

Items	$BiVO_4$		$BiVO_4$(Mo-1)			$BiVO_4$(Mo-3)			$BiVO_4$(Mo-5)		
	A	B	A		B	A		B	A		B
	L	L	D	L	L	D	L	L	D	L	L
Current density/mA cm^{-2}	0.01	0.8	0.005	0.03	1.85	0.007	0.05	2.1	0.004	0.023	1.6
Theoretical evolution rate of H_2/μmol h^{-1} cm^{-2}	0.19	14.8	0.092	0.55	34.2	0.13	0.92	39.4	0.075	0.43	29.6
Experimental evolution rate of H_2/μmol h^{-1} cm^{-2}	0.18	14.4	0.088	0.54	33.7	0.126	0.90	38.8	0.071	0.41	29.2
Faradaic efficiency/%	95	97	96	98	99	97	98	98	95	95	99

In order to better understand the structure reconstruction with/without Mo doping, the geometric structures of pristine and the Mo-doped $BiVO_4$ were compared in **Figure 6**. It is clear that the doping of Mo could increase the length of Bi-O bonds. This phenomenon indicates that the original coordinated O atoms are "shifted" toward the doped Mo sites, and introduce "oxygen vacancies." As well-known, the oxygen vacancies could play an important role in improving the photocatalytic performance. Besides, the Mo^{6+} ion substitute the V site in monoclinic sheelite $BiVO_4$ could improve the transportation of photoinduced carriers, which could facilitate the charge carrier separation and leads to suppressed bulk recombination (Ding et al., 2014). Therefore, the photocatalytic activity is enhanced significantly after Mo-doping, as shown in **Figure 4**.

With the existence of flue gas SO_2 removal, SO_3^{2-} was formed in electrolyte solution. Then the photo-generated holes could be more quickly consumed by the formed SO_3^{2-} than that without SO_3^{2-} (pure NaOH solution), because oxidation of SO_3^{2-} has a much lower activation energy and kinetically much faster than water oxidation or OH^- oxidation (McDonald and Choi, 2012; Seabold and Choi, 2012). The oxidation of SO_2 is thus proposed to replace the oxygen evolution reaction in water splitting, which can improve the water splitting efficiency and reduce the cost of H_2 production. The whole process for SO_2 removal with simultaneous production of H_2 is thus summarized and illustrated in **Figure 7**. Mo-doped $BiVO_4$ is first excited to generate e^- in conduction band (CB) and create hole (h^+) in the valence band (VB) at the same time. With the assistance of space charge layer and extra bias, the e^- transfer to the cathode and participate in cathode reaction for H_2 production. While the formed of SO_3^{2-} after flue gas SO_2 absorption is oxidized by the holes on the photoanode. As the Mo incorporated in $BiVO_4$ could improve the electronic conductivity of pure $BiVO_4$ (Luo et al., 2011; Pilli et al., 2011), therefore, the e^- produced in Mo doped

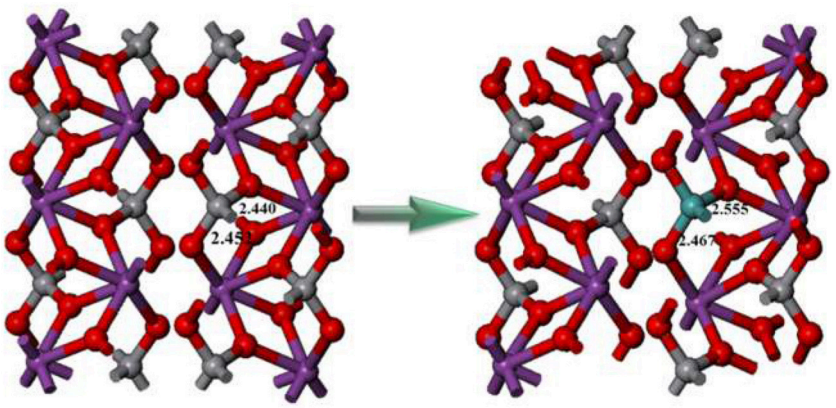

FIGURE 6 | The conventional cell of pure monoclinic sheelite $BiVO_4$ **(left)** and supercell of Mo doped monoclinic sheelite $BiVO_4$ **(right)**.

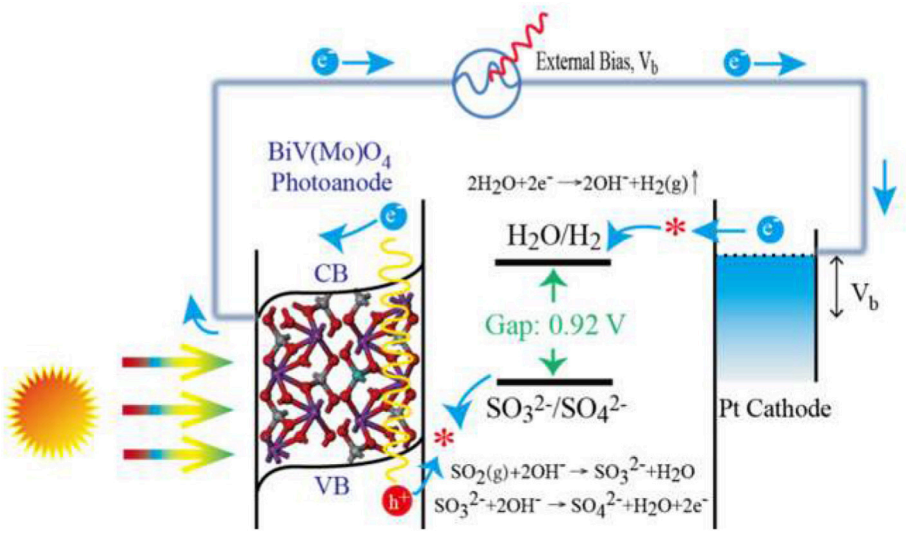

FIGURE 7 | Schematic illustration of H_2 generation during the PEC process with SO_2 removal.

$BiVO_4$ moves faster than that produced in $BiVO_4$, and shows a significantly increased photocurrent density (**Figure 4**) and rate of H_2 production (**Figure 5**). The reactions are summarized as following:

$$SO_2(g) + OH^- \rightarrow HSO_3^- \quad (5)$$

$$HSO_3^- + OH^- \rightarrow SO_3^{2-} + H_2O \quad (6)$$

Reaction on photoanode (Mo-doped $BiVO_4$ film):

$$SO_3^{2-} + 2OH^- \rightarrow SO_4^{2-} + H_2O + 2e^- \quad (7)$$

Reaction on cathode (Pt wire):

$$2H_2O + 2e^- \rightarrow H_2(g) + 2OH^- \quad (8)$$

The total reaction:

$$SO_2(g) + 2OH^- \xrightarrow{hv} H_2(g) + SO_4^{2-} \quad (9)$$

CONCLUSIONS

In summary, the effect of Mo doping on $BiVO_4$ used as photoanode for H_2 production with simultaneously flue gas SO_2 removal is investigated. The 3 atom% Mo-doped $BiVO_4$ ($BiVO_4$(Mo-3)) possessed the best PEC activity due to its better charge carrier transportation. With the help of Mo, the H_2 evolution rate and SO_2 removal rate of Mo-doped $BiVO_4$ almost 3 times higher than pristine $BiVO_4$. Through this process, the SO_2 in flue gas is removed and collected to produce H_2, which could greatly reduce the cost of desulfurization process, and even make it profitable.

AUTHOR CONTRIBUTIONS

JH: assisted in design of the experiments and wrote the manuscript; KL: performed the experiments and wrote the manuscript; HC: assisted in the analysis and interpretation of the data; LZ: planned the project, designed the experiments, and also wrote the manuscript.

ACKNOWLEDGMENTS

The authors gratefully acknowledge financial support from National Natural Science Foundation of China (No. 21507011 and No. 21677037), and Ministry of Science and Technology of the People's Republic of China (2016YFE0112200 and 2016YFC0203700).

REFERENCES

Bashikova, S., Bagreev, A., Locke, D. C., and Bandosz, T. J. (2001). Adsorption of SO_2 on sewage sludge-derived materials. *Environ. Sci. Technol.* 35, 3263–3269. doi: 10.1021/es010557u

Berglund, S. P., Rettie, A. J., Hoang, S., and Mullins, C. B. (2012). Incorporation of Mo and W into nanostructured $BiVO_4$ films for efficient photoelectrochemical water oxidation. *Phys. Chem. Chem. Phys.* 14, 7065–7075. doi: 10.1039/c2cp40807d

Chen, L., Toma, F. M., Cooper, J. K., Lyon, A., Lin, Y. J., Sharp, I. D., et al. (2015). Mo-Doped $BiVO_4$ photoanodes synthesized by reactive sputtering. *ChemSusChem* 8, 1066–1071. doi: 10.1002/cssc.201402984

Ding, K. N., Chen, B., Fang, Z. X., Zhang, Y. F., and Chen, Z. F. (2014). Why the photocatalytic activity of Mo-doped $BiVO_4$ is enhanced: a comprehensive density functional study. *Phys. Chem. Chem. Phys.* 16, 13465–13476. doi: 10.1039/c4cp01350f

Han, J., Zheng, X. Z., Zhang, L. W., Fu, H. B., and Chen, J. M. (2017). Removal of SO_2 on a nanoporous photoelectrode with simultaneous H_2 production. *Environ. Sci. Nano* 4, 834–842. doi: 10.1039/C6EN00638H

Hong, S. J., Lee, S., Jang, J. S., and Lee, J. S. (2011). Heterojunction $BiVO_4/WO_3$ electrodes for enhanced photoactivity of water oxidation. *Energy Environ. Sci.* 4, 1781–1787. doi: 10.1039/c0ee00743a

Huang, H., Li, X., Wang, J., Dong, F., Chu, P. K., Zhang, T., et al. (2015). Anionic group self-doping as a promising strategy: band-gap engineering and multi-functional applications of high-performance CO_3^{2-}-doped $Bi_2O_2CO_3$. *ACS Catal.* 5, 4094–4103. doi: 10.1021/acscatal.5b00444

Huang, H., Tu, S., Zeng, C., Zhang, T., Reshak, A. H., and Zhang, Y. (2017). Macroscopic polarization enhancement promoting photo- and piezoelectric-induced charge separation and molecular oxygen activation. *Angew. Chem. Int. Ed.* 56, 11860–11864. doi: 10.1002/anie.201706549

Huang, H. W., He, Y., Du, X., Chu, P. K., and Zhang, Y. H. (2015). A General and facile approach to heterostructured core/shell $BiVO_4$/BiOI *p-n* junction: room-temperature *in situ* assembly and highly bootsed visible-light photocatalysis. *ACS Sustain. Chem. Eng.* 3, 3262–3273. doi: 10.1021/acssuschemeng.5b01038

Jiang, G., Lan, M., Zhang, Z., Lv, X., Lou, Z., Xu, X., et al. (2017). Identification of active hydrogen species on palladium nanoparticles for an enhanced electrocatalytic hydrodechlorination of 2,4-dichlorophenol in water. *Environ. Sci. Technol.* 51, 7599–7605. doi: 10.1021/acs.est.7b01128

Jiang, G. M., Zhu, H. Y., Zhang, X., Shen, B., Wu, L. H., Zhang, S., et al. (2015). Core/Shell face-centered tetragonal FePd/Pd nanoparticles as an efficient non-Pt catalyst for the oxygen reduction reaction. *ACS Nano* 9, 11014–11022. doi: 10.1021/acsnano.5b04361

Jo, W. J., Jang, J. W., Kong, K. J., Kang, H. J., Kim, J. Y., Jun, H., et al. (2012). Phosphate doping into monoclinic $BiVO_4$ for enhanced photoelectrochemical water oxidation activity. *Angew. Chem. Int. Ed.* 51, 3147–3151. doi: 10.1002/anie.201108276

Kaplan, V., Wachtel, E., and Lubomirsky, I. (2013). Carbonate melt regeneration for efficient capture of SO_2 from coal combustion. *RSC Adv.* 3, 15842–15849. doi: 10.1039/c3ra42654h

Kim, T. W., and Choi, K. S. (2014). Nanoporous $BiVO_4$ photoanodes with dual-layer oxygen evolution catalysts for solar water splitting. *Science* 343, 990–994. doi: 10.1126/science.1246913

Kuang, Y. B., Jia, Q. X., Ma, G. J., Hisatomi, T., Minegishi, T., Nishiyama, H., et al. (2016). Ultrastable low-bias water splitting photoanodes via photocorrosion inhibition and *in situ* catalyst regeneration. *Nat. Energy* 2:16191. doi: 10.1038/nenergy.2016.191

Lelieveld, J., and Heintzenberg, J. (1992). Sulfate cooling effect on climate through in-colud oxidation of anthropogenic SO_2. *Science* 258, 117–120.

Lu, Z. F., Streets, D. G., Foy, B., and Krotkov, N. A. (2013). Ozone monitoring instrument observations of interannual increases in SO_2 emissions from indian coal-fired power plants during 2005-2012. *Environ. Sci. Technol.* 47, 13993–14000. doi: 10.1021/es4039648

Luo, W. J., Wang, J. J., Zhao, X., Zhao, Z. Y., Liab, Z. S., and Zou, Z. G. (2013). Formation energy and photoelectrochemical properties of $BiVO_4$ after doping at Bi^{3+} or V^{5+} sites with higher valence metal ions. *Phys. Chem. Chem. Phys.* 15, 1006–1013. doi: 10.1039/C2CP43408C

Luo, W. J., Yang, Z. S., Li, Z. S., Zhang, J. Y., Liu, J. G., Zhao, Z. Y., et al. (2011). Solar hydrogen generation from seawater with a modified $BiVO_4$ photoanode. *Energy Environ. Sci.* 4, 4046–4051. doi: 10.1039/c1ee01812d

McDonald, K. J., and Choi, K. S. (2012). A new electrochemical synthesis route for a BiOI electrode and its conversion to a highly efficient porous $BiVO_4$

photoanode for solar water oxidation. *Energy Environ. Sci.* 5, 8553–8557. doi: 10.1039/c2ee22608a

McDonald-Buller, E., Kimura, Y., Craig, M., McGaughey, G., Allen, D., and Webster, M. (2016). Dynamic management of NO_x and SO_2 emissions in the texas and Mid-Atlantic electric power systems and implications for air quality. *Environ. Sci. Technol.* 50, 1611–1619. doi: 10.1021/acs.est.5b04175

Nair, V., Perkins, C. L., Lin, Q. Y., and Law, M. (2016). Textured nanoporous Mo:$BiVO_4$ photoanodes with high charge transport and charge transfer quantum efficiencies for oxygen evolution. *Energy Environ. Sci.* 9, 1412–1429. doi: 10.1039/C6EE00129G

Park, Y., Kang, D., and Choi, K. S. (2014). Marked enhancement in electron-hole separation achieved in the low bias region using electrochemically prepared Mo-doped $BiVO_4$ photoanodes. *Phys. Chem. Chem. Phys.* 16, 1238–1246. doi: 10.1039/C3CP53649A

Parmar, K. P. S., Kang, H. J., Bist, A., Dua, P., Jang, J. S., and Lee, J. S. (2012). Photocatalytic and photoelectrochemical water oxidation over metal-doped monoclinic $BiVO_4$ photoanodes. *ChemSusChem* 5, 1926–1934. doi: 10.1002/cssc.201200254

Pattengale, B., and Huang, J. (2016). The effect of Mo doping on the charge separation dynamics and photocurrent performance of $BiVO_4$ photoanodes. *Phys. Chem. Chem. Phys.* 18, 32820–32825. doi: 10.1039/C6CP06407H

Pilli, S. K., Furtak, T. E., Brown, L. D., Deutsch, T. G., Turner, J. A., and Herring, A. M. (2011). Cobalt-phosphate (Co-Pi) catalyst modified Mo-doped $BiVO_4$ photoelectrodes for solar water oxidation. *Energy Environ. Sci.* 4, 5028–5034. doi: 10.1039/c1ee02444b

Seabold, J. A., and Choi, K. S. (2012). Efficient and stable photo-oxidation of water by a bismuth vanadate tPhotoanode coupled with an iron oxyhydroxide oxygen evolution catalyst. *J. Am. Chem. Soc.* 134, 2186–2192. doi: 10.1021/ja209001d

Seabold, J. A., Zhu, K., and Neale, N. R. (2014). Efficient solar photoelectrolysis by nanoporous Mo:$BiVO_4$ through controlled electron transport. *Phys. Chem. Chem. Phys.* 16, 1121–1131. doi: 10.1039/C3CP54356K

Srinivasan, A., and Grutzeck, M. W. (1999). The adsorption of SO_2 by zeolites synthesized from fly ash. *Environ. Sci. Technol.* 33, 1464–1469. doi: 10.1021/es9802091

Thalluri, S. M., Hernández, S., Bensaid, S., Saracco, G., and Russo, N. (2016). Green-synthesized W- and Mo-doped $BiVO_4$ oriented along the {040} facet with enhanced activity for the sun-driven water oxidation. *Appl. Catal. B Environ.* 180, 630–636. doi: 10.1016/j.apcatb.2015.07.029

Xia, D. H., He, C., Zhu, L. F., Huang, Y. L., Dong, H. Y., Su, M. H., et al. (2011). A novel wet-scrubbing process using Fe(VI) for simultaneous removal of SO_2 and NO. *J. Environ. Monit.* 13, 864–870. doi: 10.1039/c0em00647e

Yang, Z. Z., He, L. N., Song, Q. W., Chen, K. H., Liu, A. H., and Liu, X. M. (2012). Highly efficient SO_2 absorption/activation and subsequent utilization by polyethylene glycol-functionalized Lewis basic ionic liquids. *Phys. Chem. Chem. Phys.* 14, 15832–15839. doi: 10.1039/c2cp43362a

Yang, Z. Z., He, L. N., Zhao, Y. N., and Yu, B. (2013). Highly efficient SO_2 absorption and its subsequent utilization by weak base/polyethylene glycol binary system. *Environ. Sci. Technol.* 47, 1598–1605. doi: 10.1021/es304147q

Zhang, L. W., Lin, C. Y., Valev, V. K., Reisner, E., Steiner, U., and Baumberg, J. J. (2014). Plasmonic enhancement in $BiVO_4$ photonic crystals for efficient water splitting. *Small* 10, 3970–3978. doi: 10.1002/smll.201400970

Zhang, L., Ye, X., Boloor, M., Poletayev, A., Melosh, N. A., and Chueh, W. C. (2016). Significantly enhanced photocurrent for water oxidation in monolithic Mo:$BiVO_4$/SnO_2/Si by thermally increasing the minority carrier diffusion length. *Energy Environ. Sci*. 9, 2044–2052. doi: 10.1039/C6EE00036C

Zhou, M., Bao, J., Xu, Y., Zhang, J. J., Xie, J. F., Guan, M. L., et al. (2014). Photoelectrodes based upon Mo: $BiVO_4$ inverse opals for photoelectrochemical water splitting. *ACS Nano* 8, 7088–7098. doi: 10.1021/nn501996a

Conflict of Interest Statement: The authors declare that the research was conducted in the absence of any commercial or financial relationships that could be construed as a potential conflict of interest.

The reviewer, GJ, and handling Editor declared their shared affiliation.

Advantages of publishing in Frontiers

OPEN ACCESS
Articles are free to read for greatest visibility and readership

FAST PUBLICATION
Around 90 days from submission to decision

HIGH QUALITY PEER-REVIEW
Rigorous, collaborative, and constructive peer-review

TRANSPARENT PEER-REVIEW
Editors and reviewers acknowledged by name on published articles

Frontiers
Avenue du Tribunal-Fédéral 34
1005 Lausanne | Switzerland

Visit us: www.frontiersin.org
Contact us: info@frontiersin.org | +41 21 510 17 00

REPRODUCIBILITY OF RESEARCH
Support open data and methods to enhance research reproducibility

DIGITAL PUBLISHING
Articles designed for optimal readership across devices

FOLLOW US
@frontiersin

IMPACT METRICS
Advanced article metrics track visibility across digital media

EXTENSIVE PROMOTION
Marketing and promotion of impactful research

LOOP RESEARCH NETWORK
Our network increases your article's readership